Nano Geochemistry of Low Salinity Enhanced Oil Recovery

RIKAN MOHAMMED ALI KAREEM

Nano Geochemistry of Low Salinity Enhanced Oil Recovery

Rikan Kareem

A Thesis presented for the degree of
Doctor of Philosophy

The Layered Mineral Geochemistry Group
Department of Earth Sciences
University of Durham
England

November 2016

Nano Geochemistry of Low Salinity Enhanced Oil Recovery

Rikan Kareem

Submitted for the degree of Doctor of Philosophy
November 2016

Abstract

In this thesis a wide range of analytical techniques were used to characterise several petrophysical properties of Berea sandstone, including the mineral distribution at the pore surface and its pore structure, both playing a crucial role in determining its response to low salinity enhanced oil recovery (EOR) investigations. In addition, the role of different cations in affecting the wettability state of pure quartz and Berea sandstone was experimentally investigated in order to gain an insight on the behaviour of sandstone reservoirs during low salinity waterflooding EOR.

Results from the multi-technique, multi-scale characterisation of Berea indicate that the mineralogy exposed to the pore spaces is highly heterogeneous across different length scales, going down to the often-neglected nanoscale were significant amounts of phases identified as grain coatings. In addition, analysis of the porosity and pore-connectivity also requires a multi-length approach for its full characterisation to be realised. Both aspects are crucial to understand the role of mineral surface chemistry in determining oil/water and oil/minerals interactions in both experiments and field conditions.

Investigations on wettability alteration using environmental scanning electron microscopy (ESEM) and contact angle measurements on ideal quartz surfaces showed that reduced salinity leads to a more water-wet state. These measurements were complemented with atomic force microscopy adhesion measurements on quartz surfaces, the results giving further insight into the role of nano-scale roughness on quartz surfaces in wettability alteration by increasing the amount of oil retained on the surface.

Finally, similar wettability alteration experiments were performed on Berea sections. The effect of brine was consistent, reproducible and reversible and again showed a low salinity effect, i.e. a change to more water-wet conditions with lower salinity. The results also demonstrate that quartz surfaces always contributes at least in part to the low salinity effect, decreasing oil wettability when salinity is low. In addition, we demonstrate that the ESEM can be an essential tool in studying the wettability alteration of rocks and minerals.

Declaration

The work in this thesis is based on research carried out at the Nano Geochemistry of Low Salinity Enhanced Oil Recovery, Department of Earth Sciences, and Durham University, United Kingdom. No part of this thesis has been submitted elsewhere for any other degree, diploma or other qualification and it is all my own work unless referenced to the contrary in the text. All parts of the thesis are my individual contribution.

How to Cite

Rikan, Kareem. *Nano geochemistry of Low Salinity Enhanced Oil Recovery,* Department of Earth Science, Durham University, United Kingdom, 2016

Acknowledgements

Studying as a Ph.D. student at the University of Durham was truly a magnificent and challenging experience for me. I am extremely grateful for having been honored with the chance to pursue my education in the Ph.D. program at the University of Durham, and I am thankful to all the individuals who made this experience possible. I owe my deepest gratitude to Professor Chris Greenwell, for being a fantastic supervisor. Chris has been an incredibly dedicated and supportive supervisor throughout. His support is highly appreciated and became invaluable in my final year at Durham. I surely would not be where I am today, or have enjoyed some of the successes that I have, without his guidance.

My sincere thanks also go to Dr. Pablo Cubillas, who has been an equally helpful, supportive and enthusiastic supervisor. Both Chris and Pablo have seemingly had much faith in me when I sometimes have had very little in myself, and have provided me with opportunities and the means to travel to several international conferences and workshops which have helped me to mature both personally and academically, and provided me with much inspiration for my work. Thanks you Pablo for all the hours you have put into teaching me how to use the AFM, proof-reading work and always being available for helpful advice and encouragement. However, more than that, I would like to express my gratitude for your friendship; I feel privileged to have been able to work with you over the past three years. I also cannot thank my third supervisor, Professor Jon Gluyas, who has had an undeniable contribution to the characterisation part of the project. His thoughtful discussions and collaborations in all the steps are much appreciated.

I would like also to acknowledge a KRG-HCDP scholarship program and additional funding from BP that enabled me not only to cover consumables, but also provided the opportunity to present my results at different international conferences outside of the UK. I also extend sincere thanks to Dr Ian Collins and Dr Peter Salino for your much-needed feedback and comments. Much of this work would not have been possible without the support and assistance of many people in various labs, especially when I was venturing into unfamiliar territory: thank you to Dr Sina Gomari at Teesside University for the use of your labs and for your time spent showing me how to use some of your equipment. I'd also like to thank Dr. Darren Gröcke for TOC measurements, Leon Bowen for SEM training and helping image processing, and to Ian Chaplin for your patience and expertise in sectioning some "challenging" materials. Many thanks also to Miss Helen Riggs for helping and training with the ESEM. I also extend sincere thanks to my examiners, Dr. Sam Krevor (Imperial College) and Dr. Stuart Jones (Durham), whose feedback improved this thesis.

That the last few years were immensely enjoyable is down to so many people. In particular, I thank my housemate: Amjed Rasheed for his friendship. I also thank Muhammad Salih, Foad Lotfifar, Hakim Taha, and Hoshiar S. Sangawi for their friendship and many others in Chris Greenwell's groups such as Valentina, Nipada, Tom, Munira, Rosanne, and Catriona. I greatly appreciate their friendship and believe in me. My special thanks to my family, for all their support throughout this thesis and throughout my life. Ardalan, Nizar, Alan who have always been with me in rough times, Rebaz and Rawand, I

feel lucky to have you guys as my siblings. Mum and Dad, who were my source of inspiration and energy, thank you for everything. I cannot express how grateful I am for the sacrifices you made for us over the years. I'd like also to thank my mother- and father-in-law for their awareness as well as their supportive. Last but certainly not least I'd like to thank my beloved wife (Hevi). Over the past three years and particularly over the past eight months you have given so much support and encouragement that I am grateful for. I love you, thank you for everything!

So thanks you all.

Dedicated to

Dedicated to my wonderful wife Hevi & son Yani; to my parents;
to my brothers, my uncle, Adil Kareem and my friends for all their support

Contents

List of Figures

Chapter 2

Chapter 3.

Chapter 4.

Chapter 5.

Chapter 6.

List of Tables

Chapter 2.

Chapter 4.

Chapter 5.

Chapter 6.

Chapter 1

Introduction to Low Salinity Enhanced Oil Recovery in Sandstone Reservoir

1.1. Introduction

In the last 45 years, the global crude oil consumption, which is the principal fuel source, has sharply increased from 45 million barrels of oil equivalent per day (mbed/d) to 90 mbed/d; and it is projected to grow to over 100 mbed/d by 2040 (Organization of Petroleum Exporting Countries, 2014). In this period of time, recovery methods have also improved their efficiency, going from 30 to 50% recovery of the original oil in place (OOIP) (Farouq-Ali and Stahl, 1970; Castor et al., 1981; Kokal and Al-Kaabi, 2010). However, this still means that over 50 % of the OOIP is not currently available to supply the world energy markets (Kokal and Al-Kaabi, 2010). This situation has spurred the investment on so-called enhanced oil recovery (EOR) methods that aim to increase the maximum oil yield achievable.

Growth in oil demand, oil price, and conflict between some oil-rich countries are but a few reasons why oil and gas companies have been looking at different methods to optimize oil recovery rates within existing oil reservoirs, which are porous rocks containing oil and gas at high temperatures and pressures deep underground over the past few decades. Such techniques are referred to as enhanced oil recovery (EOR). Although Oil & Gas Journal's exclusive biennial EOR survey indicates that EOR processes have

weathered the low oil price environment of the last two years, EOR techniques in oil reservoirs still contribute significant oil production in both the US and elsewhere.

In general, it has been found that such techniques are increasingly driven by cost and technology. Development of new methods and enhancing existing knowledge with feedback from fields' implementation remain the challenges for EOR projects. In this context, the current scenario of low oil prices and a slowdown in the projects may create an opportunity for oil and gas companies to focus on EOR programs to identify the factors that influence the oil recovery of conventional reservoirs.

1.2. Why is Oil Recovery So Low?

Water flooding is currently the preferred recovery technique for most reservoirs because of the higher sustained oil production rates, which are obtained compared with the case if water were not injected. Oil production without injection is often termed primary recovery. Primary oil recovery is the initial production stage where the only source energy dedicated to the recovery process is the natural energy existing in the rock reservoirs in the form of overpressure. The underground surplus pressure brings oil to the surface through the production well. This driving force can be generated by the displacement of connate water oil downward into the well, the expansion of the natural gas at the top of the reservoir, the expansion of gas initially dissolved in the crude oil, or the gravity drainage resulting from the movement of oil within the reservoir from the upper to the lower parts where the wells are located. For primary production, around 5-30 % of OOIP can be recovered, depending on the type of hydrocarbon and the reservoir complexities (Ahmed and McKinney, 2005). For example, Dromgoole and Speers (1997) found that lower reservoir complexity correlates with higher recovery.

Primary production can be continued for some time in any field, where reservoir pressure is well above the bubble point before additional pressure support is required to prevent gas coming out of solution in the reservoir. As the pressure is lowered, the pressure at which the first gas begins to evolve from the oil is defined as the bubble point. Occasionally, primary production becomes relatively inefficient and economically not viable due to the high amount of gas produced as a result of pressure depletion in the oil reservoir. After this natural reservoir drive diminishes, secondary recovery methods are commonly applied to increase reservoir pressure (Ahmed, 2010). Traditional, secondary oil

recovery involves the injection of either water or gas (which already exists in the reservoir), to maintain a reservoir pressure and to displace the oil towards the production wells. Water injection is normally referred to as waterflooding by the oil and gas community (Green and Willhite, 1998a). Waterflooding was first attempted to keep the oil reservoir pressure during production stages. In the case of gas injection, gas is usually injected either into a gas cap for pressure maintenance and gas cap expansion or the oil column to displace the immiscible oil towards producing wells. After the secondary production phase the total oil recovered varies between 30 % and 70% of OOIP (Toole and Grist, 2003; McGuire et al., 2005; Muggeridge et al., 2014). Of the remaining oil, it is believed that much of it is trapped or bypassed in volumes that cannot be accessed by secondary recovery due to unfavorable wettability states, capillary traps, and unfavorable oil reservoir conditions (Muggeridge et al., 2014). Reservoir heterogeneity (significant permeability contrast between lithologies) is the most common cause for oil to be trapped (Castor et al., 1981; Baviere, 1991).

Tertiary (enhanced) oil recovery is additional recovery above what could be recovered by primary and secondary recovery techniques. It should be noted that, in some cases, the chronological oil production classification of primary, secondary and tertiary recovery can be misleading due to technical and economic factors. For this reason, the designation “enhanced oil recovery” (EOR) is a more appropriate term that has become more broadly used than tertiary recovery (Green and Willhite, 1998a). EOR is defined by Baviere (1991) as: “EOR consists of methods aimed at increasing ultimate oil recovery by injecting appropriate agents not normally present in the reservoir, such as chemicals, solvents, oxidizers and heat carriers to induce new mechanisms for displacing oil.” Zhang and Morrow (2006) also suggested the definition of EOR as any process aiming to improve the fluid flow by changing the physical properties of the reservoir rock or fluids, including wettability, interfacial tension, permeability, porosity, etc. The Society of Petroleum Engineers (SPE) offers the additional definition of EOR as “one or more of a variety of processes that seek to improve the recovery of hydrocarbon from a reservoir after the primary production phase” (SPE E&P Glossary, 2009). Alvarado and Manriqu (2010), however, commented that the Society of Petroleum Engineers’ definition seems more ambitious than other definitions because standardising hydrocarbon production in the reservoir is not universally undertaken after primary and secondary recoveries.

Injection of liquids or gasses during EOR operations not only enhances the natural pressure in the oil reservoir but also helps in lowering the interfacial tension between oil and water which creates favorable displacement. Nearly all tertiary oil recovery methods may be categorised into three main techniques: thermal processes, chemical processes, and miscible processes (Muggeridge et al., 2014). Although the water flooding method is normally classified as a secondary recovery method, when dramatically changing the chemical composition of the injected brine is considered as tertiary recovery method (Austad et al., 2008, 2010a). If an injection method is applied, the injection fluid is not solely enhancing the pressure in the rock reservoir, but it also changes both physical and chemical properties of the reservoir rock/fluids or their interactions to improve the sweep efficiency at various lengths and timescales. These interactions might, for example, lead to the alteration of the interfacial tensions (IFT), fluid viscosities, wettability state or favorable phase behavior (Green and Willhite,1998a).

In addition, there are wide ranges of EOR methods, the most common can be grouped in: CO_2 injection, steam injection, in situ combustion, and chemical flooding (polymer, surfactants, alkaline, seawater, and diluted seawater injection) (Green and Willhite, 1998b; Doghaish, 2009), which are often used in sandstone rock reservoirs compared to other reservoirs (Alvarado and Manrique, 2010). Improved oil recovery may be obtained by CO_2 injection to displace and dissolve some of the remaining oil (Blunt et al., 1993). In general, it has been found that such a tertiary processes can enhance oil recovery by 8 to 16% of the OOIP (Rogers and Grigg, 2000). Designed water flooding, such as low salinity waterflooding is another technique that can enhance oil recovery through lowering the concentration of brine of the injection water. It is part of an emerging EOR theme built on the notion that not only the physical properties of the reservoir matter but that also the brine chemical properties are of great importance for determining additional oil recovery from a reservoir.

Currently, the extensive research being undertaken highlights low salinity water as critical for improved oil recovery and reducing the residual oil saturation in sandstone/clay reservoir systems. It is believed that according to the following reasons injected low salinity water can be more successful than thermal, chemical and solvent based EOR methods. Firstly, water is relatively easy to inject into the oil bearing sandstone rock reservoirs. Secondly, water is an efficient injection fluid to displace oil through the

sandstone reservoir. Finally, water is available, and commonly, inexpensive in most of the regions studied when compared to other compounds.

1.3. Low-Salinity Water Flooding as an Enhanced Oi Recovery (LSEOR) Techniques

In the tertiary oil recovery, the target oil is the immobile oil which interfaces with the pore-lining minerals (oil-wet state). Injection of diluted seawater (better known as low salinity EOR or LSEOR) can change the wettability state of the reservoir to water-wet state. LSEOR was documented by (Martin, 1959), for the first time when fresh water was injected to displace viscous oil into the reservoir cores from Maracaibo Basin in Venezuela. This work was continued (experimentally) by Bernard (1967), who flooded both outcrop samples (Berea sandstone) and reservoir sandstone cores (from Wyoming) with fresh water and brines with a different ionic concentration of NaCl. Injection of the low salinity brine showed a significant potential for increasing oil recovery when reducing the NaCl solution composition from 1 to 0.1%. Despite the promising results, this work did not receive attention from the oil industry at that time. During the last decade, however, low salinity waterflooding EOR has gained increased interest in industry because the injection water can be produced in-situ from dilution or modification of seawater which is a low-cost substance, environment-friendly and sustainable (Thomas et al., 2010). In addition, LSEOR has been shown to be capable of increasing the oil yield in both core injection experiments and oilfield test (Tang and Morrow, 1997; Lager et al., 2006). However, the underlying mechanisms that drive the reservoir change in wettability, from oil-wet to water-wet state, during LSEOR are not fully understood. These mechanisms, of course, are critical in the search for the screening criteria that could help us to predict the reservoirs where the method would have the best chance of working.

From the UK's perspective, over the last 20 years, low salinity EOR procedures have been studied for the sandstone reservoirs in the North Sea, which are the UK's dominant petroleum reserves. Most of the experimental work and full field tests have been performed by British Petroleum (BP) and have shown promising results. BP's laboratory core floods have resulted in increased oil recovery (Lager et al., 2006, 2008; Lee et al., 2010; Robbana et al., 2012). Moreover, the single-well tracer tests and log-inject-log measurements have illustrated that LSEOR improves the oil recovery (Webb et al., 2004; McGuire et al.,

2005). Recently, PB started construction of a low salinity EOR operation in the Clair field, North Sea, and it should start producing oil in 2017 (Robbana et al., 2012).

1.4. Factors that control Low Salinity Water Flooding

From most of experimental and field conditions, it is possible to see what properties of a reservoir might make it a potential candidate for low salinity waterflooding, although none of these is without exception and principally relate to application in secondary mode. These properties are: the salinity and saturation of connate water, the reservoir's initial wettability, along with the presence of clay minerals and polar oil components. The listed conditions for low salinity effects are generally related to the systematic experimental work by Tang and Morrow (1999a), Pu et al. (2008, 2010), Austad et al. (2010b), and RezaeiDoust et al.(2011) but some points have also been taken from the works by Lager et al. (2006), Alotaibi et al. (2011), and Shaker Shiran and Skauge (2013).

1.4.1. Sandstone

EOR by injection of low salinity waters is frequently documented in clay-rich sandstones from both, laboratory and field trials (Somerton and Radke, 1983; Law et al., 2015; Sheng, 2015). Nearly all studies of LSEOR in sandstone core rocks have been made on clay-rich sandstones. Although clay mineral commonly forms only a minor part most of the sandstone composition (Blatt, 1982; Worden and Morad, 1999), they commonly disseminate as a matrix which coats the pores of the rock. It has been suggested that the clay minerals are involved with oil migration, because they interact heavily with the crude oil (Hancock and Taylor, 1978; Bjørlykke, 1992; Bjorlykke, 1998; Marcussen et al., 2010). Tang and Morrow (1999a) noticed that clay mineral-containing sandstones produced more oil recovery than clean sand, and they stated that for a low salinity flood to be successful, clay minerals must be present in the core. They also described the fine clay migration mechanisms whereby the low salinity brine disturbs the fine clay, leading to mobilisation. This migration leads to lower permeability, and water flows through the other flow paths to remove the crude oil. However, the well observations of Lager et al.(2006); and Zhang et al. (2007b) did not show permeability reduction, and Cissokho et al. (2010) and Soraya et al. (2009) said that although their experiments detected higher pressure in core samples; they did not increase oil recovery effectiveness. Due to the contradictory results in the study of this physical mechanism, the study of chemical reactions on the clay mineral has attracted more research. Additional work has been conducted on clay-free sandstones, with initial results failing to show sensitivity to composition of the brine (Tang and Morrow,

1999a). However,recently published results by Farzaneh et al. (2015) suggested that low salinity water has a positive response in a homogeneous borosilicate core that is absence of clay (clay-free silica core). It has also been proposed that clay may not always be needed for observing increased recovery from low salinity brine. Although the recent study shows that we are almost seen additional oil recovery in silica core (Farzaneh et al., 2015).

1.4.2. Polar Crude Oil Fraction

With regards to oil recovery by low salinity brine injection, crude oil is the most important factors in the reservoir (Moradi et al., 2013). Crude oil components are separated, based on their polarity properties, into two fractions: non-polar (saturates and aromatics), and polar (resins and asphaltenes) (Fan and Buckley, 2002). The polar fraction usually contains oxygen, in the form of carboxylic acids (-COOH) or hydroxyl (-OH) groups (Anderson, 1986a; Kumar et al., 2012; Haugvaldstad, 2014). The polar components, which are most appropriate to adsorb onto rock minerals, are thought to have acidic or basic properties (Alvarado et al., 2014)

The minor polar fraction contains sulphur (namely sulphides, triophenes, and mercaptans); and nitrogen compounds (including carbazoles, amides, porphyrins, and quinolines) (Anderson, 1986a). Tang, (1998) argued that the oil polar components be essential for chemical interaction in LSEOR, as these components will interact more with the mineral surfaces available at the pore space. Since the polar components attached to the clay mineral surfaces act as anchoring molecules for crude oils, the wetting tendencies of crude oils/brine/rock system is for sandstone rocks to be naturally to oil-wet state (Donaldson and Tiab, 2004; RezaeiDoust et al., 2011). Kumar et al. (2005) and Abdallah et al. (2007) also supported the idea that the polar fraction of the crude oil was involved in the enhanced oil recovery mechanism since it induced wettability alteration. Zhang et al. (2007a) investigated LSEOR with crude oil and refined oil; and found that the refined oil, which did not contain the polar fraction, did not give incremental recovery oil.

1.4.3. Formation Brine and Brine Injection

A brine, or saline water, is an aqueous solution that contains significant amounts of dissolved salts. The United States Geological Survey (USGS) classified saline water into three types. These being: slightly saline water of around 1,000 to 3,000 ppm (parts per million) of total dissolved solid (TDS); moderately saline water of approximately 3,000 to

10,000 ppm TDS; highly saline water which contains about 10,000 to 35,000 ppm TDS. Typical compounds used to prepare synthetic brines in the laboratory include deionised water, and common salts such as NaCl, $CaCl_2$, $MgCl_2$, KCl and $SrCl_2$ (Karnanda et al., 2012; Tverdal, 2013; Aghaeifar et al., 2015; Hosseinzade Khanamiri et al., 2016).

Formation brine (water) occurs naturally within the pores of the rock. Formation water, the results of water mixing and other physical-chemical process, can have a wide range of salinities about 7000 to 270000 ppm TDS (Warren, 2006). An understanding of the salinity variation of the formation waters in oil reservoir is significant for many geochemical processes, such as the fluid-rock interaction, the migrating paths of fluid and the entrapment mechanisms of hydrocarbon In one of the pioneer studies on the LSEOR, Morrow and co-workers observed a different brine composition correlated with the amount of oil recovery (Morrow et al., 1998). Sharma and Filoco (2000) and McGuire et al. (2005) argued that low concentration formation water is important in LSEOR.

Tang and Morrow (1997), for their part, were interested in the effluent composition. They injected diluted sea water through sandstone core plugs without attention to the proportion of monovalent or divalent cations. The investigation reported higher oil recovery when flooding by 0.01 dilution factors (1 ml brine + 99 ml water. Yildiz and Morrow (1996) extended the investigation of the Moutray crude oil core waterflooding by controlling the effluent concentration of $CaCl_2$ and NaCl which are the more represented divalent and monovalent cations in sea water. The experiment showed that 2% $CaCl_2$ brine waterflooding gave an increase in extraction of 5.5 % OOIP compared to the use of 0.5% $CaCl_2$ brine, and they asserted that some divalent ions in brine composition improved oil recovery. Conversely, when Yildiz et al. (1999a) repeated the waterflooding experiments with Prudhoe Bay crude oil core and brine containing 4% NaCl + 0.5% $CaCl_2$, this yielded 16% greater oil recovery than the brine containing 2% $CaCl_2$. On a separate study using the single-well chemical tracer test (SWCTT) method in an Alaskan reservoir, McGuire et al. (2005) reported that a necessary point is not only the relative percentage of cations but also their concentration, because they observed no effective oil recovery when the injected brine concentration was higher than 7000 ppm. In the same way, Webb et al., (2004) tested with diluted brine at 5% (for a total concentration of 1000–4000 ppm); while Zhang et al. (2007b) diluted connate water to 5% for a concentration of 1500 ppm. In the latter case (Zhang et al. ,2007a) they found a higher recovery respect to not only percent dilution but also TDS (total dissolved solid). Finally, Jerauld et al. (2008) suggested that the proper

concentration should be 10–25% of formation water or 1000- 2000 ppm. Thereby, the potential effluent should be diluted 5 to 25% and range from 1000 to 7000 ppm. In most of the published cases, higher oil recovery was obtained when the salinity of injection water is in the range of 500–3,000 ppm of TDS, and no more than 5,000 ppm (Webb et al., 2004; Jerauld et al., 2008). From the somewhat conflicting results of these laboratory and field studies, it became clear that the underlying mechanisms for low salinity EOR could not be fully understood. This gave rise to a large number of more fundamental studies that have attempted to shed light on these fundamental mechanisms.

1.5. Motivation behind the Project

EOR projects are going to become increasingly common worldwide in the future, despite concerns about greenhouse gas emissions, as demand for oil will continue to increase (Florini, 2011) while at the same time it becomes harder to find new oilfields due to crises and instability in the Middle East and North Africa. EOR technology has been around for decades, and BP has been researching and using it for over forty years. Many suggestions for which mechanism causes this effect have been presented over the last decade, but researchers cannot seem to agree on what the dominating factor is. To date, studies have proposed more than seventeen separate mechanisms by which low-salinity waterflooding can enhance oil recovery. These are explained in some detail in the recent review by Sheng (2014). In Chapter 2 four of the frequently suggested mechanisms are discussed. The only thing on which authors seem to agree on is that LSEOR tends to alter the rock wettability towards a more water-wet state (Anderson, 1986a, 1986b; Tang and Morrow, 1999a; Buckley et al., 1996; Austad et al., 2010b). Laboratory experiments and yield trials have often reported contradictory findings. Nevertheless, significant factors of the oil/brine/rock system seem to be the presence of clay material such as kaolinite and illite in rock, the presence of an initial water saturation, and exposure to crude oil to create mixed-wet conditions (Morrow and Buckley 1999).

The potential for improving oil recovery by injected low salinity water in sandstone rock reservoirs has high attention when compared with other EOR methods due to the relatively low cost and being environmental aspects. The improvement of oil recovery by LSEOR from core plugs rich in clays was reported as early as 1967 (Bernard 1967). At present, most of the core flooding experiments are regularly conducted on sandstone core plugs (Alvarado and Manrique,2010). Since Berea core plugs have relatively high porosity

and permeability makes it a good reservoir, Berea sandstone rocks have been recognised by the petroleum industry as a representative model siliciclastic rock for some years.

In contrary, only incomplete data has been reported in the literature regarding its petrographic, geochemical, and petrophysical properties. In particular knowledge of the mineral distribution along the pore walls is particularly scarce, despite the fact that mineral exposed in the pore space will be crucial in determining the rock-fluid interactions that occur during core-flooding experiments. This research has focused on the characterisation of Berea core plugs (with four different permeability ranges from < 50 mD, 50-100 mD. 100-200 mD, and 500-1000 mD), so an interesting step further could be to investigate the effect of different brine on mineral surfaces. The motivation behind this approach is to use a pre-characterised rock sample to investigate the interaction between mineral surfaces and reservoir fluids.

Although wettability has received growing attention over the recent years, the effect of wettability on quartz mineral has not been systematically investigated compared to clay minerals. This research seeks to understand the brine salinity effects on wettability behavior on model quartz crystal surface at multiple length scales (nano-scale to macro-scale). Previously performed investigations revealed that quartz mineral surface is between neutral to oil-wet states due to the adsorption of the natural surfactants present in the crude oil. To examine the effects of polar compounds oil model compounds will be used. These kinds of experiments are desired and useful because no systematic investigation has reported the sole effect of these polar compounds on the wettability variation. There are also some authors investigated the wettability change at a microscopic scale, by measuring the contact angles of oil droplets over rock surfaces, or measuring the contact angles of oil droplets on the single mineral surface. Just a few authors observe wettability behaviors in a porous medium. Therefore, this study attempts to examine the effects of NaCl and $CaCl_2$, salts concentrations (0.001M−1.0M) on the detrital quartz surfaces in Berea sandstone with respect to the presence of polar compounds using oil model compounds (e.g. decanoic acid, dodecane) and crude oil. The surface chemistry of minerals in sandstone rock is the main cause of the wettability during low-salinity waterflooding. Thus the understanding of salinity brine influencing the contact angle on single mineral in porous medium and fluid is of key important.

1.6. Thesis Objectives

This thesis is an experimental study of LSEOR, with an emphasis on studying the wetting properties of oil model compounds (decanoic acid) and crude oil (after treatment with solutions of different salinities of multi-cation) on quartz crystals, as an alternative to sandstone rock, and Berea core sandstone as a model of sandstone reservoir rock. An extensive literature review of low salinity waterflooding in sandstone rock has been performed to obtain a theoretical base for discussions and conclusions. The main objectives of this thesis are as follows.

a) Characterise the properties of Berea sandstone (porosity and permeability) and link these to a detailed characterisation of both bulk and pore lining mineralogy.
b) Understand the nature of quartz-oil interactions. Pendant drop shape, environmental scanning electron microscopy, atomic force microscopy and zeta-potential techniques will give complementary insight into the oil/quartz/ brines interfaces.
c) Ascertain how different cations affect the oil/brine and brine/rock interface. In conjunction with the techniques in (b), spontaneous imbibition test will also give insight into wettability state on score scale as parameters are varied.

Regarding the above objectives, the contributions of the thesis are as follows.

1.7. Thesis Outline

The main results of the thesis are presented as three "journal-style" chapters (Chapters 4-6), in addition to this introductory chapter (Chapter 1), which describes the thesis aims, a literature review (Chapter 2) of what is known about the LSEOR, details of specific methodologies specifically with regards to sampling procedures (Chapter 3) and a final conclusions chapter (Chapter 7). A brief synopsis of each of the research chapters are included below. Some appendices are also included at the end of this thesis, the contents of which are outlined below.

Chapter 2: *"Theoretical background and literature review."*

This chapter is divided into four main sections. In the first section, an outline of the sandstone rock compositions. The second section provides an overview of EOR processes

in siliciclastic sedimentary reservoirs in various oil fields. Section three presents an overview of the concept of wettability, a reservoir property that is one of the major targets of this study, and how it can be measured experimentally. Fourthly, a detailed of the proposed low salinity water flooding EOR mechanisms in tertiary mode is discussed.

Chapter 3: *"Experimental Techniques and Data Analysis."*

Chapter 3 delivers an overview of the multiple characterisation techniques utilised for the project, with emphasis on their application to investigate LSEOR. It also presents a detail of the procedure used during the experimental work. The main instruments used are optical microscopy, which was used in order to characterise the detrital grains in the studied thin sections of Berea core sandstone; X-ray diffraction (XRD) was used to determine the mineral compositions of Berea core plugs; Scanning electron microscopy (SEM) was used to characterise the pore structure in the matrix part of Berea core chips; Energy-dispersive X-ray (EDX) is used to analysis the elemental composition of each of mineral surface to compute the area fractions of minerals in the studied thin sections of Berea core sandstone; Environmental scanning electron microscopy (ESEM) allows direct observation of fluid distribution as well as wettability alteration in the presence of various brine; X-ray computed tomography (X-ray CT) was used to identify and compute the internal structures (e.g. porosity and permeability) within Berea core samples to a resolution of less than one micron; Atomic force microscopy (AFM) provided an insight into the surface structure, as well as capturing dynamic properties such as adhesion within different fluids (e.g. High and low concentration of brines); Mercury capillary injection porosimetry (MICP) was used to examine the pore size distribution of studied Berea core sandstone; Infrared (IR) spectroscopy is one of the spectroscopic techniques was identified the structure of crude oil and oil model compound; Pendant drop shape was used to measure the contact angle between different phase; Zeta (ζ)-potential techniques was used for measuring the charges of oil/brine/rock interfaces.

Chapter 4: ***"****Multi-technique Approach to the Petrophysical Characterization of Berea Sandstone Core Plugs (Cleveland Quarries, USA)"*

This chapter has been published in its presented form in the Journal of Petroleum Science and Engineering (Appendix A): *Kareem, R., Cubillas, P., Gluyas, J., Bowen, L., Hillier, S., & Greenwell, H. C. (2016). Multi-technique Approach to the Petrophysical Characterization of Berea Sandstone Core Plugs (Cleveland Quarries, USA). Journal of Petroleum Science and Engineering*

Chapter 4 provides a literature review of sedimentary petrology and deals with the multi-length scale characterisation of Berea core sandstone. It also contains methodology of quantitative image analysis. In this work, four Berea sandstone samples (with 4 different permeability ranges from < 50 mD, 50-100 mD. 100-200 mD, and 500-1000 mD) were subjected under the same condition to a multi-technique characterisation with an emphasis on determining the mineral composition, and distribution at the pore surface as well as pore structure and connectivity analysis. Therefore, the mineral distribution was measured in two-dimensions by chemical mapping using energy dispersive X-ray spectroscopy-scanning electron microscopy (SEM–EDX). The bulk composition of the Berea sandstone thin section was also measured by X-ray diffraction and micro-X-ray computed tomography. In addition to SEM, it should be noted that the atomic force microscopy was also used in order to detect the nano mineral phase that cannot be observed within SEM resolution. The pore structure within the four different Berea samples was studied using a combination of X-ray computed tomography, mercury injection porosimetry and high resolution scanning electron microscopy. Performing a full "multi-scale" characterisation, therefore, will be critical in the planning, execution, and analysis of core flood experiments in the lab.

Chapter 5: *"An Experimental Investigation into Role of Salinity, and Ionic strength on Wettability Regime in Quartz-Based Substrates."*

A part of this chapter has been published and presented in IOR 2015-18th European Symposium on Improved Oil Recovery (Appendix B): *Kareem, R. (2015, April). Towards a Nanoscopic Understanding of Oil-sandstone Wettability-Implications for Enhanced Oil Recovery, In IOR 2015-18th European Symposium on Improved Oil Recovery*

Chapter 5 introduces the general aspects related to wettability alteration, a property that is central to this part of the thesis. It includes the definition, previous research on the topic and as well as how wettability may be altered. Quartz crystal as a model mineral surface was used to gain a better insight on oil/brine/quartz interactions. The study of wettability on model quartz crystal surfaces was based on contact angle measurements through pendant drop shape technique. The results are analysed, discussed and compared with similar finding obtained by ESEM techniques. In addition, the wettability alteration of quartz surfaces was investigated at the nanoscale (using AFM) as a result of measuring adhesion force within different brine solutions. It should be noted that the effects of the surface roughness on wettability were observed during running adhesion experiments. This

mimicked the natural roughness pore surfaces in real reservoir rocks and induced a different wetting state not previously studied for quartz surface. Finally, results of the ζ-potential analysis are presented for quartz particles studied at similar conditions. Therefore, the effect of brine salinity, cation type on all measurement is examined. It has to be mentioned that all measurements are presented for samples have been used in a clean state, brine salinity and aged crude oil as well as decanoic acid in dodecane. The correlation and comparison of zeta-potential measurements and wettability derived from contact angle measurements with adhesion data were then made. An expansion of the electrical charges in well with changes in contact angle towards more water-wet as salinity is decreased.

Chapter 6: ***"****An Integrated Study of Wettability Alteration and Oil Recovery Improvement in Berea Sandstone as A-model of Sandstone Reservoir."*

A part of this chapter has been published in its presented in 78th EAGE Conference and Exhibition 2016 (Appendix C): *Kareem, R., Cubillas, P., Riggs, H. J., Gluyas, J., Gröcke, D. R., & Greenwell, H. C. (2016, May). Insights of Berea Sandstone Wettability Alteration as A-model of Sandstone Reservoir through Contact Angle Measurement, In 78th EAGE Conference and Exhibition 2016*

Chapter 6 contains a summary of a literature review of the LSEOR technique, including previous research on the topic and the proposed mechanisms behind the low salinity EOR effect. It should be noted, in this part of the thesis, only Berea sandstone was used. The pendant drop shape technique was used to measure contact angles in aged Berea slices in crude oil and decanoic in dodecane the alterations induced by brine salinity and composition. ESEM was used to replicate the same experiment via Peltier stage. The measurements were performed on the quartz overgrowth surfaces that are present in Berea core sandstone. Total organic carbon measurements were also performed to measure the amount of carbon in pre-treatment and treatment samples aged in crude oil. Additionally, results from ζ-potential analysis of Berea particles are shown. Z-Potential measurements and wettability measurements are presented for samples have been used in used in a clean state, brine salinity and aged crude oil as well as decanoic acid. Finally, spontaneous imbibition experiments were performed on restored-Berea core plugs at room temperature and 70°C. Although the literature of LSEOR contains numerous experimental results on Berea sandstones, to our knowledge, it lacks data on Berea core plugs aged in decanoic acid in dodecane. In the end, the impact of lowering the salinity brine on altering the wettability of Berea sandstone was examined.

Chapter 7: *Conclusions and Recommendations*

This chapter summarises the conclusion from each experimental chapter study to provide the overall picture of results directly related to the thesis objectives. In the end, Chapter 7 provides recommendations for future focus area, which could be used to improve in this study or the relevant researches.

The author conducted the experimental work, with assistance from Dr. Pablo Cubillas, Mr. Leon Bowen, Ms. HJ Riggs at Durham University and Dr. Sina Rezaei Gomari in the school of Sciences & Engineering at Teesside University. Except for the XRD technique as well as the MICP technique, the author performed all data processing and wrote the manuscript after supervisory discussions with Prof Chris Greenwell, Dr. Pablo Cubillas, Prof Jon Gluyas, and Dr. Sina Rezaei Gomari, who also provided editorial comments and some suggestions on the manuscript.

1.8. Appendices

Appendix A contains additional experimental data and methodological observations to complement the data presented in Chapter 4. It is also included the published version of Chapter 4.

Appendix B contains details of contact angle measurements, additional experimental data of zeta potential in Quartz particles, and data tables to complement the data presented in Chapter 5. It is also included the published version of conference paper of chapter 5.

Appendix C contains details of contact angle measurements, additional experimental data of zeta potential in Berea sandstone particles, and data tables to complement the data presented in Chapter 6. It is also included the published version of an extended abstract of chapter 6.

1.9. References

Abdallah, W. et al., 2007, Fundamentals of Wettability: Oilfield Review, p. 17.

Aghaeifar, Z., S. Strand, T. Austad, T. Puntervold, H. Aksulu, K. Navratil, S. Storås, and D. Håmsø, 2015, Influence of Formation Water Salinity/Composition on the Low-Salinity Enhanced Oil Recovery Effect in High-Temperature Sandstone Reservoirs: Energy & Fuels, v. 29, no. 8, p. 4747–4754, doi:10.1021/acs.energyfuels.5b01621.

Ahmed, T., 2010, Chapter 14 - Principles of Waterflooding, *in* Reservoir Engineering Handbook (Fourth Edition): Boston, Gulf Professional Publishing, p. 909–1095.

Ahmed, T., and P. D. McKinney, 2005, 2 - Water Influx, *in* Advanced Reservoir Engineering: Burlington, Gulf Professional Publishing, p. 149–185.

Alotaibi, M. B., R. A. Nasralla, and H. A. Nasr-El-Din, 2011, Wettability Studies Using Low-Salinity Water in Sandstone Reservoirs: SPE Reservoir Evaluation & Engineering, v. 14, no. 6, p. 713–725, doi:10.2118/149942-PA.

Alvarado, V., G. Garcia-Olvera, P. Hoyer, and T. E. Lehmann, 2014, Impact of Polar Components on Crude Oil-Water interfacial Film Formation: A Mechanisms for Low-Salinity Waterflooding: Society of Petroleum Engineers, doi:10.2118/170807-MS.

Alvarado, V., and E. Manrique, 2010, Enhanced Oil Recovery: An Update Review: Energies, v. 3, no. 9, p. 1529–1575, doi:10.3390/en3091529.

Anderson, W. G., 1986a, Wettability Literature Survey- Part 1: Rock/Oil/Brine Interactions and the Effects of Core Handling on Wettability: Journal of Petroleum Technology, v. 38, no. 10, p. 1,125-1,144, doi:10.2118/13932-PA.

Anderson, W., 1986b, Wettability Literature Survey- Part 2: Wettability Measurement: Journal of Petroleum Technology, v. 38, no. 11, p. 1,246-1,262, doi:10.2118/13933-PA.

Austad, T., A. Rezaeidoust, and T. Puntervold, 2010, Chemical Mechanism of Low Salinity Water Flooding in Sandstone Reservoirs: Society of Petroleum Engineers, doi:10.2118/129767-MS.

Austad, T., S. Strand, M. V. Madland, T. Puntervold, and R. I. Korsnes, 2008, Seawater in Chalk: An EOR and Compaction Fluid: SPE Reservoir Evaluation & Engineering, v. 11, no. 4, p. 648–654, doi:10.2118/118431-PA.

Baviere, M. (ed.), 1991, Basic Concepts in Enhanced Oil Recovery Processes: Springer, 432 p.

Bernard, G. G., 1967, Effect of Floodwater Salinity on Recovery Of Oil from Cores Containing Clays: Society of Petroleum Engineers, doi:10.2118/1725-MS.

Bjorlykke, K., 1998, Clay mineral diagenesis in sedimentary basins; a key to the prediction of rock properties; examples from the North Sea Basin: Clay Minerals, v. 33, no. 1, p. 15–34.

Bjørlykke, K., 1992, Clay Minerals in North Sea Sandstones.

Blatt, H., 1982, Sedimentary petrology.

Blunt, M., F. J. Fayers, and F. M. Orr Jr., 1993, Carbon dioxide in enhanced oil recovery: Energy Conversion and Management, v. 34, no. 9–11, p. 1197–1204, doi:10.1016/0196-8904(93)90069-M.

Buckley, J. S., C. Bousseau, and Y. Liu, 1996, Wetting Alteration by Brine and Crude Oil: From Contact Angles to Cores: SPE Journal, v. 1, no. 3, p. 341–350, doi:10.2118/30765-PA.

Castor, T. P., W. H. Somerton, and J. F. Kelly, 1981, Recovery Mechanisms of Alkaline Flooding: p. 249–291, doi:10.1007/978-1-4757-0337-5_14.

Cissokho, M., H. Bertin, S. Boussour, P. Cordier, and G. Hamon, 2010, Low Salinity Oil Recovery On Clayey Sandstone: Experimental Study: Petrophysics, v. 51, no. 5.

Doghaish, N. M., 2009, Analysis of Enhanced Oil Recovery Processes---a Literature Review: Dalhousie University (Canada), 102 p.

Donaldson, E. C., and D. Tiab, 2004, Petrophysics: Theory and Practice of Measuring Reservoir Rock and Fluid Transport Properties: Gulf Professional Publishing, 916 p.

Dromgoole, P., and R. Speers, 1997, Geoscore; a method for quantifying uncertainty in field reserve estimates: Petroleum Geoscience, v. 3, no. 1, p. 1–12, doi:10.1144/petgeo.3.1.1.

Farouq-Ali, S. M., and C. D. Stahl, 1970, Increased oil recovery by improved waterflooding: Earth Miner. Sci.; (United States), v. 39:4.

Farzaneh, S. A., M. Sohrabi, J. R. Mills, P. Mahzari, and K. Ahmed, 2015, Oil Recovery Improvement from Low Salinity Waterflooding in a Clay-free Silica Core: doi:10.3997/2214-4609.201412100.

Florini, A., 2011, The International Energy Agency in Global Energy Governance: Global Policy, v. 2, p. 40–50, doi:10.1111/j.1758-5899.2011.00120.x.

Green, D. W., and G. P. Willhite, 1998a, Enhanced Oil Recovery. SPE textbook series.: Richardson, Texas, Society of Petroleum Engineers, 545 p.

Green, D. W., and G. P. Willhite, 1998b, Enhanced Oil Recovery. SPE textbook series,6.: Richardson, Texas, Society of Petroleum Engineers.

Hancock, N. J., and A. M. Taylor, 1978, Clay mineral diagenesis and oil migration in the Middle Jurassic Brent Sand Formation: Journal of the Geological Society, v. 135, no. 1, p. 69–72, doi:10.1144/gsjgs.135.1.0069.

Haugvaldstad, E., 2014, Clay minerals in sandstone reservoirs: implications for “smart water” injection.

Hosseinzade Khanamiri, H., I. Baltzersen Enge, M. Nourani, J. Å. Stensen, O. Torsæter, and N. Hadia, 2016, EOR by Low Salinity Water and Surfactant at Low Concentration: Impact of Injection and in Situ Brine Composition: Energy & Fuels, v. 30, no. 4, p. 2705–2713, doi:10.1021/acs.energyfuels.5b02899.

Jerauld, G. R., K. J. Webb, C.-Y. Lin, and J. C. Seccombe, 2008, Modeling Low-Salinity Waterflooding: SPE Reservoir Evaluation & Engineering, v. 11, no. 6, p. 1,000-1,012, doi:10.2118/102239-PA.

Karnanda, W., M. S. Benzagouta, A. AlQuraishi, and M. M. Amro, 2012, Effect of temperature, pressure, salinity, and surfactant concentration on IFT for surfactant flooding optimization: Arabian Journal of Geosciences, v. 6, no. 9, p. 3535–3544, doi:10.1007/s12517-012-0605-7.

Kokal, S., and A. Al-Kaabi, 2010, Enhanced oil recovery:challenges & opportunities: p. 64–69.

Kumar, K., E. Dao, and K. K. Mohanty, 2005, AFM study of mineral wettability with reservoir oils: Journal of Colloid and Interface Science, v. 289, no. 1, p. 206–217, doi:10.1016/j.jcis.2005.03.030.

Kumar, B., H. Yarranton, and E. Baydak, 2012, Effect of Salinity on the Interfacial Tension of Crude Oil: doi:10.3997/2214-4609.20143757.

Lager, A., K. . Webb, C. J. . Black, M. Singleton, and K. . Sorbie, 2006, Low salinity oil recovery an experimental investigation Paper, *in* Torndheim,Norway: Paper SCA 2006-36.

Lager, A., K. J. Webb, I. R. Collins, and D. M. Richmond, 2008, LoSal Enhanced Oil Recovery: Evidence of Enhanced Oil Recovery at the Reservoir Scale: Society of Petroleum Engineers, doi:10.2118/113976-MS.

Law, S., A. McDonald, S. Fellows, J. Reed, and P. G. Sutcliffe, 2015, Influence of Clay Content and Type on Oil Recovery Under Low Salinity Waterflooding in North Sea Reservoirs: Society of Petroleum Engineers, doi:10.2118/175506-MS.

Lee, S. Y., K. J. Webb, I. Collins, A. Lager, S. Clarke, O&apos, M. Sullivan, A. Routh, and X. Wang, 2010, Low Salinity Oil Recovery: Increasing Understanding of the Underlying Mechanisms: Society of Petroleum Engineers, doi:10.2118/129722-MS.

Marcussen, Ø., T. E. Maast, N. H. Mondol, J. Jahren, and K. Bjørlykke, 2010, Changes in physical properties of a reservoir sandstone as a function of burial depth – The Etive Formation, northern North Sea: Marine and Petroleum Geology, v. 27, no. 8, p. 1725–1735, doi:10.1016/j.marpetgeo.2009.11.007.

Martin, J. C., 1959, The Effects of Clay on the Displacement of Heavy Oil by Water: Society of Petroleum Engineers, doi:10.2118/1411-G.

McGuire, P. L., J. R. Chatham, F. K. Paskvan, D. M. Sommer, and F. H. Carini, 2005, Low Salinity Oil Recovery: An Exciting New EOR Opportunity for Alaska's North Slope: Society of Petroleum Engineers, doi:10.2118/93903-MS.

Moradi, M., E. Topchiy, T. E. Lehmann, and V. Alvarado, 2013, Impact of ionic strength on partitioning of naphthenic acids in water–crude oil systems – Determination through high-field NMR spectroscopy: Fuel, v. 112, p. 236–248, doi:10.1016/j.fuel.2013.05.024.

Morrow, N. R., G. Tang, M. Valat, and X. Xie, 1998, Prospects of improved oil recovery related to wettability and brine composition: Journal of Petroleum Science and Engineering, v. 20, no. 3–4, p. 267–276, doi:10.1016/S0920-4105(98)00030-8.

Muggeridge, A., A. Cockin, K. Webb, H. Frampton, I. Collins, T. Moulds, and P. Salino, 2014, Recovery rates, enhanced oil recovery and technological limits: Phil. Trans. R. Soc. A, v. 372, no. 2006, p. 20120320, doi:10.1098/rsta.2012.0320.

Pu, H., X. Xie, P. Yin, and N. R. Morrow, 2008, Application of Coalbed Methane Water to Oil Recovery from Tensleep Sandstone by Low Salinity Waterflooding: Society of Petroleum Engineers, doi:10.2118/113410-MS.

Pu, H., X. Xie, P. Yin, and N. R. Morrow, 2010, Low-Salinity Waterflooding and Mineral Dissolution: Society of Petroleum Engineers, doi:10.2118/134042-MS.

RezaeiDoust, A., T. Puntervold, and T. Austad, 2011, Chemical Verification of the EOR Mechanism by Using Low Saline/Smart Water in Sandstone: Energy & Fuels, v. 25, no. 5, p. 2151–2162, doi:10.1021/ef200215y.

Robbana, E., T. A. Buikema, C. Mair, D. Williams, D. J. Mercer, K. J. Webb, A. Hewson, and C. E. Reddick, 2012, Low Salinity Enhanced Oil Recovery - Laboratory to Day One Field Implementation - LoSal EOR into the Clair Ridge Project: Society of Petroleum Engineers, doi:10.2118/161750-MS.

Rogers, J. D., and R. B. Grigg, 2000, A Literature Analysis of the WAG Injectivity Abnormalities in the CO2 Process: Society of Petroleum Engineers, doi:10.2118/59329-MS.

Shaker Shiran, B., and A. Skauge, 2013, Enhanced Oil Recovery (EOR) by Combined Low Salinity Water/Polymer Flooding: Energy & Fuels, v. 27, no. 3, p. 1223–1235, doi:10.1021/ef301538e.

Sharma, M. M., and P. R. Filoco, 2000, Effect of Brine Salinity and Crude-Oil Properties on Oil Recovery and Residual Saturations: SPE Journal, v. 5, no. 3, p. 293–300, doi:10.2118/65402-PA.

Sheng, J. J., 2014, Critical review of low-salinity waterflooding: Journal of Petroleum Science and Engineering, v. 120, p. 216–224, doi:10.1016/j.petrol.2014.05.026.

Sheng, J. J., 2015, Status of surfactant EOR technology: Petroleum, v. 1, no. 2, p. 97–105, doi:10.1016/j.petlm.2015.07.003.

Somerton, W. H., and C. J. Radke, 1983, Role of Clays in the Enhanced Recovery of Petroleum From Some California Sands: Journal of Petroleum Technology, v. 35, no. 3, p. 643–654, doi:10.2118/8845-PA.

Soraya, B., C. Malick, C. Philippe, H. J. Bertin, and G. Hamon, 2009, Oil Recovery by Low-Salinity Brine Injection: Laboratory Results on Outcrop and Reservoir Cores: Society of Petroleum Engineers, doi:10.2118/124277-MS.

SPE E&P Glossary, 2009, Category:Glossary -: <http://petrowiki.org/Category%3AGlossary> (accessed June 26, 2016).

Tang, G.-Q., 1998, Brine Composition and Waterflood Recovery for Selected Crude Oil/brine/rock Systems: University of Wyoming, 215 p.

Tang, G.-Q., and N. R. Morrow, 1999, Influence of brine composition and fines migration on crude oil/brine/rock interactions and oil recovery: Journal of Petroleum Science and Engineering, v. 24, no. 2–4, p. 99–111, doi:10.1016/S0920-4105(99)00034-0.

Tang, G. Q., and N. R. Morrow, 1997, Salinity, Temperature, Oil Composition, and Oil Recovery by Waterflooding: SPE Reservoir Engineering, v. 12, no. 4, p. 269–276, doi:10.2118/36680-PA.

Thomas, B. G., A. Iliyas, T. E. Johansen, K. Hawboldt, and F. Khan, 2010, Towards Sustainable and Environmentally Friendly Enhanced Oil Recovery in Offshore Newfoundland, Canada: Offshore Technology Conference, doi:10.4043/20385-MS.

Toole, S. T., and D. M. Grist, 2003, Oil and Gas Recovery Behaviour in the UKCS Basins: Society of Petroleum Engineers, doi:10.2118/83982-MS.

Tverdal, T. F., 2013, The Effect of Salinity on Surfactant Flooding: A Literature Review and an Experimental Study: 126.

Warren, J. K., 2006, Evaporites: Sediments, Resources and Hydrocarbons: Berlin, Heidelberg, Springer Berlin Heidelberg.

Webb, K. J., C. J. J. Black, and H. Al-Ajeel, 2004, Low Salinity Oil Recovery - Log-Inject-Log: Society of Petroleum Engineers, doi:10.2118/89379-MS.

Worden, R. H., and S. Morad, 1999, Clay Minerals in Sandstones: Controls on Formation, Distribution and Evolution, *in* R. H. Worden, and S. Morad, eds., Clay Mineral Cements in Sandstones: Blackwell Publishing Ltd., p. 1–41.

Yildiz, H. O., and N. R. Morrow, 1996, Effect of brine composition on recovery of Moutray crude oil by waterflooding: Journal of Petroleum Science and Engineering, v. 14, no. 3, p. 159–168, doi:10.1016/0920-4105(95)00041-0.

Yildiz, H. O., M. N. R. Valat, and N. R. Morrow, 1999, Effect of brine composition on wettability and oil recovery of a Prudhoe Bay Crude oil: Journal of Canadian Petroleum Technology, v. 38, no. 1, p. 26–31.

Zhang, Y., and N. R. Morrow, 2006, Comparison of Secondary and Tertiary Recovery With Change in Injection Brine Composition for Crude-Oil/Sandstone Combinations: Society of Petroleum Engineers, doi:10.2118/99757-MS.

Zhang, P., M. T. Tweheyo, and T. Austad, 2007a, Wettability alteration and improved oil recovery by spontaneous imbibition of seawater into chalk: Impact of the potential determining ions Ca2+, Mg2+, and SO42−: Colloids and Surfaces A: Physicochemical and Engineering Aspects, v. 301, no. 1–3, p. 199–208, doi:10.1016/j.colsurfa.2006.12.058.

Zhang, Y., X. Xie, and N. R. Morrow, 2007b, Waterflood Performance By Injection Of Brine With Different Salinity For Reservoir Cores: Society of Petroleum Engineers, doi:10.2118/109849-MS.

Chapter 2

Theoretical Background

This chapter reviews literature related to the key objectives of the thesis in four main parts. Firstly, an introduction on the origin and mineralogical composition of sandstone rock is given. Secondly, the concept of wettability will be defined and the different wettability classes that are possible to be observed in sandstone reservoir rocks will be presented, along with a description on the techniques used in oil industry for wettability measurements. Thirdly, the factors affecting the wettability of reservoir rocks are discussed. Fourthly, the mechanisms behind wettability alteration, and their role on oil recovery (in particular, with relevance to low salinity EOR) are explained in detail.

2.1. Sandstone

2.1.1. Sedimentary Environment

Sandstones are sedimentary rocks, formed due to physical and chemical processes such as compaction and diagenesis acting on accumulated clastic materials derived from pre-existing rocks. Typically, these clastic materials have been transported away from different sources (igneous, metamorphic or sedimentary rocks), and are deposited in various depositional enviornments such as foreland basins, alluvial fans, coastlines, flood plains and/or deltas (Zolotukhin and Ursin, 2000; Nichols, 2009). The clastic sediments are normally attributed to high and low energy environments. Sand grains have a normal size ranging from 63 μm to 2 mm and sandstone is defined as a rock composed of grains in this size range (Nichols, 2009). As the grains are buried, the increasing overburden temperature, pressure and dissolution of minerals cause compaction and cementation of the grains, in a process referred to as diagenesis. Although many types of sandstone contain

mainly quartz grains, the term sandstone carries no implication about the amount of quartz present in the rock (Nichols, 2009).

2.1.2. Petrography and Mineralogy of Sandstone

2.1.2.1. Detrital Grains

Due to their detrital nature, a range of minerals may occur in sandstone reservoirs, among which quartz (SiO_2) is the most abundant. Quartz is most abundant mineral in most sandstone due to the chemical stability of quartz crystal as the bonds between silicon and shared oxygen ions are strong (Blatt, 1982). Also, quartz contains no metallic cations that could be replaced by hydrogen ions during weathering, in contrast to feldspar, for example. Because about two-thirds of the detrital fraction of the average sandstone is quartz, a wide range of literature exists concerning its physical and chemical character of detrital rocks.

Feldspars are less stable in sedimentary environment than quartz. Although feldspar is often altered to clay minerals (Boggs, 2009), it still forms 10-15% of dertial fraction of the average sandstone rock (Blatt,1982). The feldspars are a group of minerals that have similar characteristics due to a analogous structure. Often, feldspars are simply referred to as plagioclase and orthoclase (a K-feldspar) because identification to greater precision is difficult with ordinary methods. In addition, accessory minerals are often observed to be a part of sandstone composition.

2.1.2.2. Accessory Minerals

The accessory minerals are defined by Blatt (1982) as including all detrital minerals except quartz and feldspar, although micas are typically excluded from accessary mineral due to their extremely platy shape. Typically, the accessory minerals are referred to as heavy minerals. Due to the desegregated, then the accessory minerals in the sandstone can easily be identified from detrital grains on the basis of density and texture(Blatt ,1982). It is widely recognised that the amount of accessory minerals in sandstone is based on the abundance of each mineral in the source rocks. Based on Blatt (1982) the accessory minerals can be divided into three groups, as shown in the table below.

Table 2.1: Common accessory minerals in sandstone rock and their source

Igneous rocks	Metamorphic rocks	Indeterminate rocks
Aegerine	Actinolite	Enstatite
Augite	Andalusite	Hornblende
Chromite	Chloritoid	Hypersthene
Ilmenite	Cordierite	Magnetite
Topaz	Diopside	Sphene
	Epidote	Tourmaline
	Garnet	Zircon
	Glaucophane	
	Kyanite	
	Rutile	
	Sillimanite	
	Staurolite	
	Tremolite	
	Wollastonite	

Table 2.1gives the names of the accessory mineral in sandstone and the type of crystalline rock from which it originates. A description of each accessory mineral is presented in Blatt (1982). Beside the accessory minerals in sandstone rocks, most of the sandstones observed contains mica, biogenic particles (made of carbonate or silica), different types of cements (carbonate, silica, etc) and clay minerals.

2.1.2.3. Clay minerals

Research on the role of clays on sandstone reservoirs has been conducted for more than 50 years, but still the presence of clay minerals in these types of reservoirs presents a challenge for petroleum production. Early studied showed that the presence of clay minerals can sometimes affect reservoir quality negatively in sandstone reservoirs due to their small particle dimension of less than 5 μm (Ahmed and McKinney, 2005; Civan, 2007, 2015). In addition, the amount, distribution pattern and morphology of clay minerals can also affect sandstone reservoir properties in terms of porosity, permeability and reactivity to various EOR process (Worden and Morad, 1999).

The word ‘clay mineral’ refers to different groups of minerals that are members of the hydrous aluminous phyllosilicates, where as the word ‘clay’ is strictly a grain-size term, classically for particle diameters less than 3.9 μm (Meunier, 2005). Unfortunately, in sedimentary petrology, the term clay’ is frequently used synonymously with ‘clay mineral.' Typically, “clay” is a generic term, referring to different types of phyllosilicate minerals of clay fraction size. They are composed mostly of silica, alumina, and water and commonly

contain several other cations, such as iron, magnesium, sodium, calcium and potassium as ion substitutions within the framework, or as charge balancing ions. The clay minerals commonly identified in sandstone are formed from two different types of layers, a SiO_4-rich tetrahedral layer (which can contain Al as substitutions for Si) and an $Al_2(OH)_6)_n$ octahedral layer (which can also contain Fe or Mg or other divalent or trivalent cations). The tetrahedra result from the close packing of four O^{2-} ions, with the space between them occupied by a Si^{4+} ion or, to a lesser extent, an Al^{3+} ion (Worden and Morad, 2002). The octahedral layer results from the close packing of six anions that are dominantly oxygen but also can include some hydroxyl (OH) ions. It is well known that each layer result from the association of several ionic sheets, according to a limited number of combinations (Meunier, 2005). Hence, each of ionic sheets is formed by three ionic planes. The presence of isomorphic substitutions in the tetrahedrla (Al for Si) and octahedral layers, leads to the appearance of a permantent charge in the framework. To ensure charge balance, cations, such as Ca, Mg, and K (in addition to hydration water), are present in the interlayer space (Worden and Morad, 2002). A characteristic of clay minerals that distinguishes them from the other silicate mineral in rocks is the existence of a permanent, and largely pH independent, negative charge on the basal surfaces. These negative charges derive from the substitution of the cations within the structure (e.g. substitution of Si^{4+} by Al^{3+} in the tetrahedral and substitution of Al^{3+} by for instance Fe^{2+} in the octahedral units). In addition, the presence of broken bonds at the edges of the clay structure will results in additional charges (total charge and identity in this case being pH dependent). These sites of negative charge attract positively charged ions from the surrounding pore fluid to acquire neutrality.

Clays are referred to as cation exchange minerals, due to their ability to exchange cations with surrounding solutions in the external or internal surfaces (interlayer spaces) of the clay structure (Meunier, 2005). The cation exchange capacity (CEC) is a measure of the clay's capacity to retain and hold cations from the surrounding solution and is defined as the quantity of exchangeable cations trapped by the clay at a given pH, usually pH 7, and is expressed in milliequivalents (meq) per 100 g of clay (Meunier, 2005). As indicated by the CEC term, the external CEC depends on the number of bonding sites of cations on the outer surfaces. The internal CEC, however, depends on the permanent charges of clay minerals. Cations in solution are attracted and held with weak quasi-bonding forces, including electrostatic and van der Waals forces. Cations can readily be exchanged if they

are weakly adsorbed. Thus, the relative replacing power of a particular cationic species depends on the strength of binding. The relative replacing power is affected by salinity concentration, temperature, pressure, and pH. The relative replacing the power of the common cations in clays at the room temperature is believed to be in this order (Meunier, 2005).

$$Li^{+} < Na^{+} < K^{+} < Mg^{2+} < Ca^{2+} < Sr^{2+} < Ba^{2+} < H^{+}$$

This means that Ca^{2+} ions will replace both Mg^{2+} ions and (two) Na^{+} ions and Mg^{2+} will replace (two) Na^{+} ions. Note, however, that high concentrations of Na^{+} can reverse the process (as happens when NaCl is added to the ion exchanger in a dishwasher). Ions with a low relative replacing power may be able to replace ions with a higher relative replacing power if the concentration of the solution of the low replacing power ion is sufficiently higher than that of the higher replacing power ion. Some of the characteristics of various clays common in sandstone oil reservoirs, such as CEC and surface charge, are given in Table 2.2.

Table 2.2: Properties and behaviours of the most abundant clay minerals in sandstone rocks (Meunier, 2005).

Property	**Kaolinite**	**Illite**	**Montmorillonite**	**Chlorite**
Structure	1:1	2:1	2:1	2:1:1
Surface area (m^2/gm)	15-25	50-110	30-80	140
Surface charge	No charge	Negative	Negative	Positive
CEC (meq/100g)	3-15	10-40	80-150	10-40
Particle size (micron)	5-0.5	Large sheets to 0.5	2-0.1	5-0.1

The variability of clay mineral types is depended on how the tetrahedral silica and octahedral aluminum sheets link together to form the essential units that the clay is made up and also on the chemical composition (and substitutions) of these layers. Of the many different clay minerals that occur in sandstone rocks the four most common (Tucker, 2001) are shown in Figure 2.1.

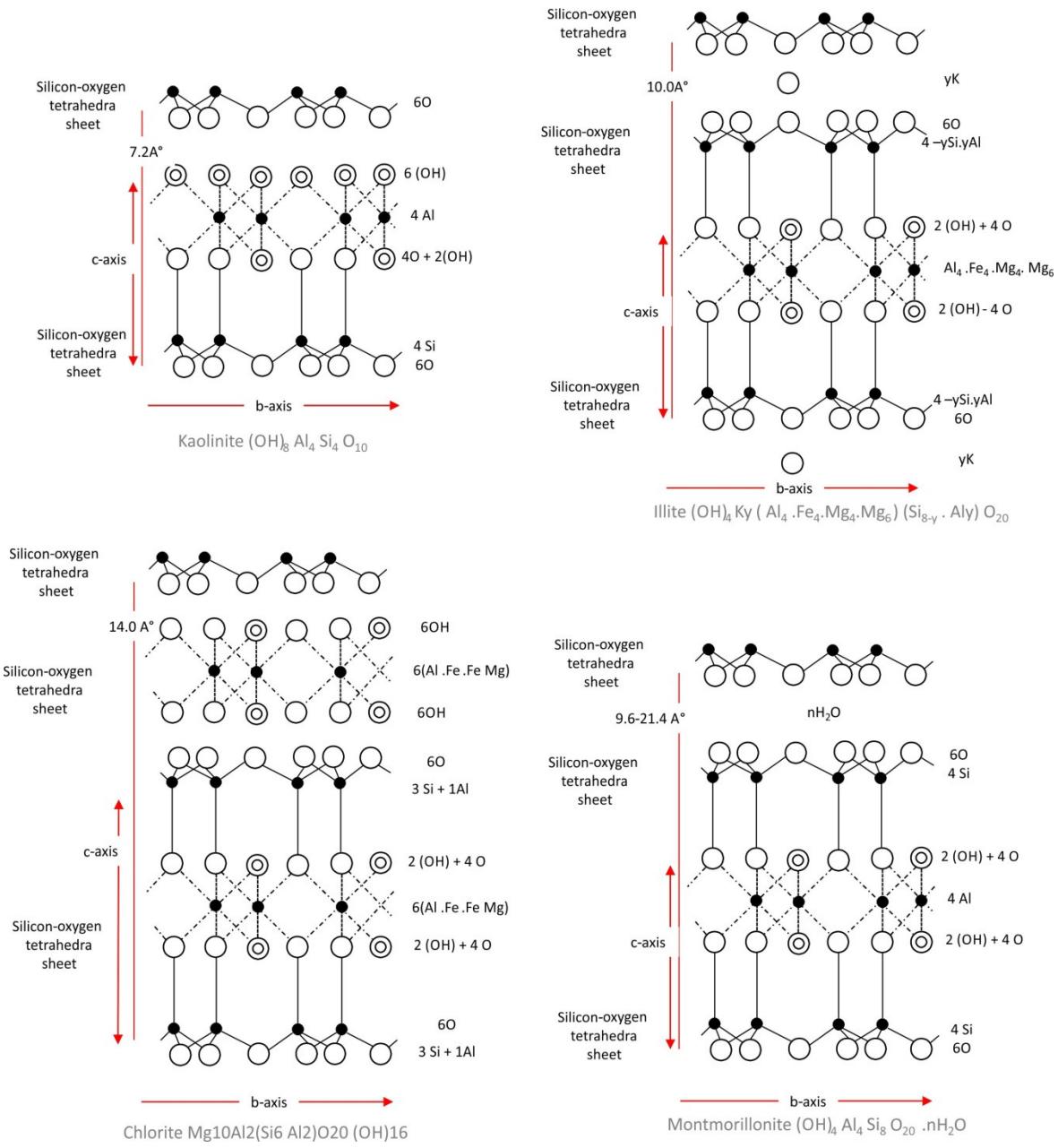

Figure 2.1: Schematic description showing the crystal structure of some of the more common clay minerals in sandstone rock, extracted from (Meunier, 2005).

Kaolinite, chemical formula of ideal kaolinite is $Al_2Si_2O_5(OH)_4$ (Meunier, 2005), is the commonest type of clay mineral in sandstones (Civan, 2007) and is comprised of one tetrahedral layer linked to one octahedral layer with no interlayer cations and, for this reason, is referred to as a 1:1 type structure (Figure 2.1). Silica tetrahedra are arranged in a hexagonal pattern in the silica sheet; three oxygens of each tetrahedron are shared with three other tetrahedra, and the fourth oxygen is shared with two alumina octahedra in the alumina sheet. In the alumina sheet, an aluminum atom is bonded to four hydroxyls (OH)

groups and two oxygens from the tetrahedral sheet. Layers are joined by hydrogen bonds between adjacent silica and alumina sheets (Grim, 1968).

In its purest form kaolinite will possess no structural charge (therefore no charge balancing cations will be present within its layer), however, this is almost never the case, and therefore a small, permanent, charge in the siloxane surface will occur.The charge in the aluminol face, is pH dependent, as its controlled by protonation, deprotonation of hydroxyl groups (Mugele et al., 2014, 2016,Grim, 1953; Gupta and Miller, 2010; Gupta et al., 2011). In addition, the edges of kaolinite particles are composed of broken bonds whose charge will also depend on protonation/deprotonation reaction and therefore, will be pH dependent(Wang and Siu, 2006; Gupta and Miller, 2010).

Characteristically, kaolinite's morphology is described as pseudohexagonal plates that are commonly stacked, in a book - or wormlike, vermicular habit, as shown in Figure 2.2, which do not break up under chemical treatment, due to of their relatively large particle size (up to 5µm). Kaolinite can cause severe plugging of pore throats and loss of permeability near near-wellbore if mobilised by liquid flow (Meunier, 2005, Mungan, 1965; Civan, 2007). In general, kaolinite transforms due to deep burial and with increasing temperatures (70°C to 130°C) into its high-temperature equivalent, dickite with blocky pseudohexagonal crystals (Worden and Morad, 2002). Transformation of kaolinite to dickite indicates neomorphic change to a better-ordered, thicker crystal (up to 8 µm thickness) and more stable crystal structure (Ehrenberg et al., 1993; McAulay, 1994; Lanson et al., 2002). In addition, illitization of kaolinite in reservoirs can start around 70°C (Worden and Morad, 2002), however, has mostly been reported at higher temperatures of 120°C to 140°C (Lanson et al., 2002).

The name **illite** was proposed by Grim, Bray and Bradley in 1937 for the mica-type mineral occurring in argillaceous sediments (Grim, 1953). It was explicitly stated that "the term is not proposed as a specific mineral name, but as a general term for the clay mineral constituent of argillaceous sediments belonging to the mica group." Illite is a three-layer clay mineral comprised of one octahedral layer sandwiched between two tetrahedral layers and so is labelled a 2:1 structure. O -K- O bonds connect two opposing tetrahedral layers. The general chemical formula for illite is $K_{0.8}(Al_{1.8}Mg_{0.2})(Si_{3.4}Al_{0.6})O_{10}(OH)_2$ (Meunier, 2005), where y is typically significantly less than 2. The K^+ cation is needed for charge balance the negative framework charge arising from the partial substitution of Al^{3+} for Si^{4+} in the tetrahedral layer and the substitution of divalent cations for Al^{3+} in the octahedral.

The O-K-O bonding is strong and prevents swelling behaviour in illite (Worden and Morad, 2002).

Illite minerals in sandstone can often be observed: as delicate fibres or hair-like crystals that protrude perpendicular to the grain surface into the pore space; as irregularly shaped flakes that coat framework grains; in mixed layers with smectite (Figure 2.2) (Desbois et al., 2011; Luffel et al., 1993; Wilson et al., 2014; Wilson and Pittman, 1977). Variations in size bring about changes in crystal shape. Thus, under diagenetic conditions, the morphological shape of a crystal of illite is often altered according to whether they were formed in sandstones or in shales (Varajao and Meunier, 1995). The typical problem caused by illite in sandstone reservoirs is plugging of pore throats, which leads to permeability reduction; through migration during liquid flooding (Civan, 2000). Civan (200) explained that leaching of potassium ions will change illite to an expandable clay type, which could be prone to swelling. The process causes the expansion of the interlayer in illite leading to permeability reduction of the host rock. Illite can also be dislodged and liberated during swelling process. It should be noted that this phenomenon is referred to as fines generation by discontinuous jumps or microquakes. Consequently, formation damage often occurs in two ways: (1) the permeability of sandstone rock decreases by reduction of porosity by swelling process (Civan et al., 1989; Mohan and Fogler, 1997); and (2) the particles entrained from the pore surface by the flowing fluid are carried towards the pore throats and captured by a jamming process. Thus, the permeability decreases by obstruction and or plugging of pore throats (Mohan and Fogler, 1997; Civan, 2015).

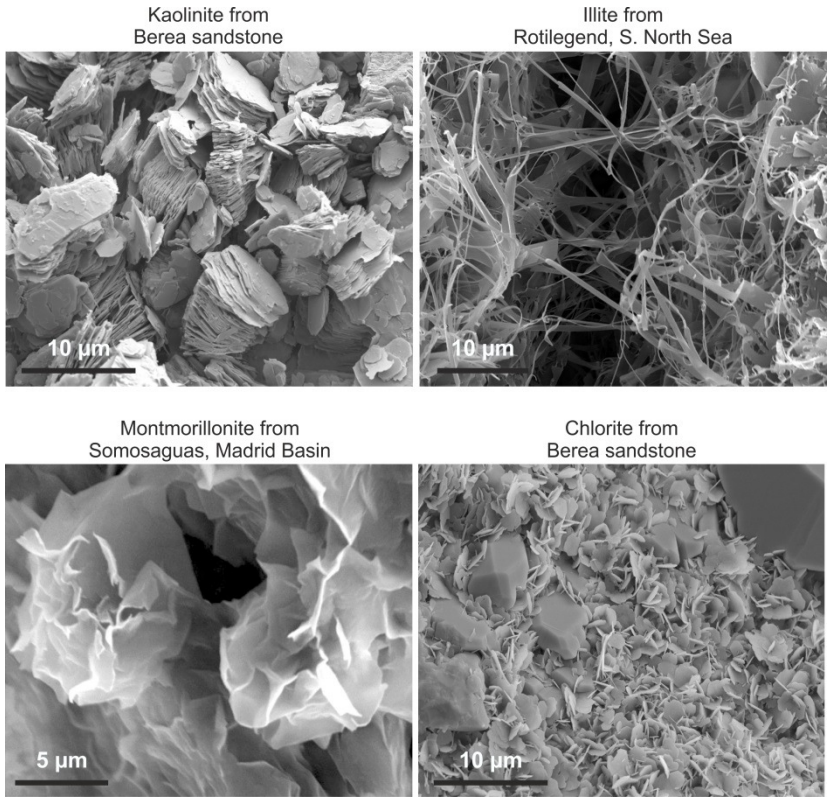

Figure 2.2: Scanning electron microscope (SEM) micrographs showing morphology of the most common clay mineral in sandstone rock.

Montmorillonite has a similar structure to illite, being a 2: 1 clay mineral with one octahedral layer sandwiched between two tetrahedral layers. It is recognised that the ideal chemical formula is $(1/2Ca,Na)_{0.7}(Al,Mg,Fe)_4[(Si,Al)_8O_{20}]\bullet nH_2O$ (Meunier, 2005). The octahedral layer of the clay typically contains one Mg atom for every three Al atoms. Regarding its morphology, montmorillonite usually occurs as wrinkled sheets which form webs or honeycomb-type structures or a rose-like texture, when attached to the detrital sand grain surfaces (Figure 2.2). The montmorillonite mineral structure, shown in Figure 2.1, has a large cation exchange capacity (Table 2.1) and will readily adsorb Na^+ and other cations, all leading to a high degree of swelling and dispersion.

Under favourable conditions, in aqueous media,Ca^{2+}-montmorillonite platelets remain practically intact, close to each other, while the Na^+-montmorillonite aggregates readily swell and the platelets separate widely. Water can easily invade the open space between the platelets and form thicker water envelopes around the sodium-montmorillonite platelets than the calcium-montmorillonite platelets (Goyal, 2007).Changes in the chemistry of the aqueous medium would change the amount of swelling, and the type and amount of exchangeable cations present between montmorillonite layers(Zhou, 1995).

Chlorite is a significant rock forming mineral being the one of main clay minerals in sandstone rocks. It is importance also relies on the fact that is one of the few common minerals that is sensitive to acid and oxygenated waters (Blatt, 1982). In these conditions, it will precipitate gelatinous Fe $(OH)_3$ which will not pass through pore throats during liquid flooding (Civan, 2000).The general formula is $(Mg,Fe^{2+},Fe^{3+},Mn,Al)_{12}$ $[(Si,Al)_8O_{20}](OH)_{16}$ (Deer et al., 1992).The term chlorite, in fact, refers to clays with a composition intermediate along several end members: Clinochlore (Fe-rich), Chamosite (Mg-rich), and Pennantite (Mn-rich) (Civan, 2000; Peng et al., 2009).The structure of chlorite is 2:1:1 comprised of a negatively charged 2:1 tetrahedral-octahedral-tetrahedral layered structure inter-layered with an additional octahedral layer that is positively charged and consisting of cations and hydroxyl ions (see Figure 2.1) (Worden and Morad, 2002). In general, chlorite exists in two different mineralogical polytypes, the 1b polytype, and the 2b polytype. It has been proposed that the type 1 polytype may be prevalent at lower diagenetic temperatures, with the type 2 polytype forming as diagenetic at higher temperatures (150°C - 200°C) (Worden and Morad, 2002; Peng et al., 2009).

Morphologically, chlorite in most sandstones is described as platy, honeycomb, cabbage head rosette or fan, as shown in Figure 2.2. The pore-filling chlorite and grain coating in sandstone is diagenetic and controlled by the mineralogical composition of the reservoir, clay mineral precursor, and the pore fluid chemistry as well as the temperature (Chen et al., 2011). Recently, Stricker and Jones (2016) reported the role played by chlorite coatings in the Skagerrak Formation in the Central North Sea. They examined the role played by chlorite coatings is significant in reducing quartz cementation, which has a direct connection to reservoir quality.

2.2. EOR in Sandstone Reservoirs

The sandstone reservoir systems show the highest potential to implement EOR than other reservoir types (e.g., carbonates and turbidites), and most of the technologies that have been tested and used at the pilot and commercial scales are mostly in this kind of lithology (Alvarado and Manrique, 2010). Buracica and Carmópolis (Brazil), and Karazhanbas (Kazakhstan) are good examples of fields that have been subjected to several EOR technologies at pilot scale in sandstone reservoirs. Secondly, from the UK perspective, sandstone reservoirs predominate in the UK sectors of the North Sea. Finally, most carbonate reservoirs are naturally fractured. The fractures exist at all scales, from microscopic fissures to kilometer sized structures called fracture swarms or corridors,

creating complex flow networks in the reservoir. As a consequence, the movement of hydrocarbons and other fluids is often not as expected or predicted (Ehrenberg and Nadeau, 2005). Just a few very large fracture corridors can be highways for fluids in the middle of a carbonate reservoir. On the contrary, sandstone rocks provide an ideal environment for the storage and extraction of hydrocarbon, due to their high porosity and permeability properties, as shown in Figure 2.3.

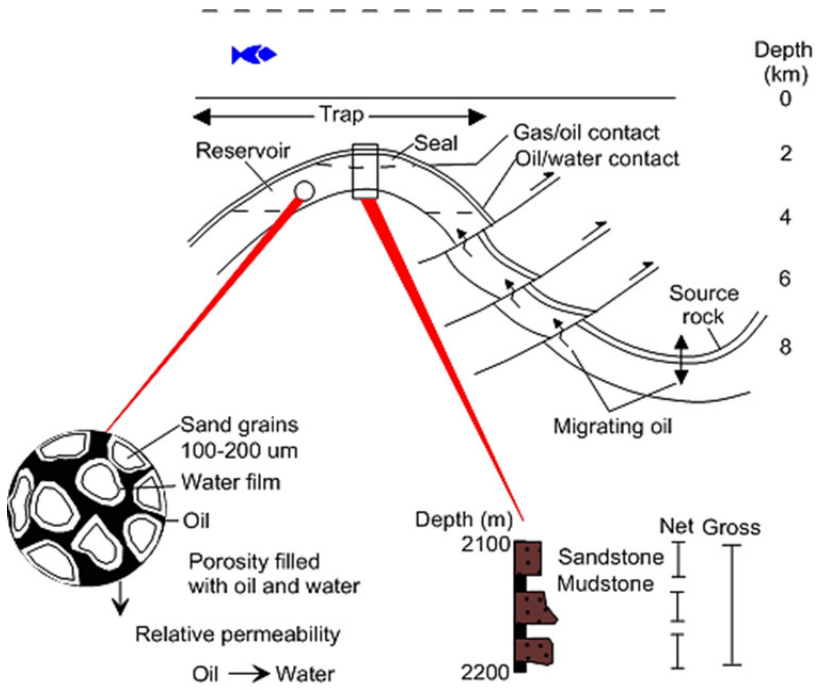

Figure 2.3: Cross section of oil reservoir basin; Extracted from Gluyas and Swarbrick. (2003).

2.3. Forces of Oil Displacement

In an oil reservoir, water, gas and oil are often subjected to several different types of forces. Gravitational forces, viscous forces, and capillary forces are the most important ones. These three forces will be briefly discussed in the following sections.

2.3.1. Gravitational Forces

Gravity forces in porous media are necessary for fluid flow, especially in cases where there exists a high-density difference between multiphase fluids (density of injected fluid is less than displaced fluid), and also in cases with low oil-water interfacial tension (IFT) conditions. IFT is defined by Willhite (1986) as the energy required for increasing the area of the interface by one unit. The buoyancy force, given by equation 2.1, is always

active when the immiscible fluids (oil/water, oil/gas, water/gas, or oil/water and gas) in reservoir rocks co-exist. As a result, the lighter phase experiences a pressure pointing upwards, causing the fluids to segregate.

$$\Delta P_g = \Delta \rho g H \tag{2.1}$$

Where:

- ΔP_g Pressure difference between phases due to gravity
- $\Delta \rho$ Density difference between phases
- g Acceleration due to gravity, equal to 9.8 m/s^2
- H Height of the hydrostatic column

2.3.2. Viscous Forces

The viscous forces in a porous medium are reflected in the pressure gradient generated by the flow of fluid through a porous medium. The viscous force must be larger than the magnitude of the capillary forces for flow to occur through a pore (Green and Willhite,1998a).The pressure gradient is proportional to the viscosity and the fluid velocity and inversely proportional to the conductivity of the medium.Viscous force in a circular capillary tube can be calculated by the following equation 2.2 (Green and Willhite, 1998a).

$$\Delta P = 8\mu L V_{avg} / r^2 g_c \tag{2.2}$$

Where:

- V_{avg} = fluid velocity, cm/sec
- r = capillary tube radius, cm
- ΔP = pressure loss over length L, (N/m)
- μ = fluid viscosity
- L = length over which pressure loss is measured, cm
- g_c = Conversion factor

2.3.3. Capillary Forces

The capillary forces are the result of the combined effect of the surface and interfacial tensions of the rock and fluids in a petroleum reservoir, the pore size and geometry, and the wetting characteristics of the system (Ahmed, 2010). Capillary pressure is the difference in pressure between two immiscible fluids across a curved interface at equilibrium, which determines the basic behaviour of immiscible displacement in reservoir

rocks (Tiab and Donaldson, 2012). The capillary pressure is defined as the pressure in the oil phase minus the pressure in the water phase for a water/oil system. Since larger pressure exists in the non-wetting phase, the capillary can be positive and negative depending on which is the wetting phase. Laplace's equation 2.3 gives the capillary pressure across a curved surface regarding its radii of curvature.

$$P_c = P_o - P_w = \sigma_{ow} (1/R_1 + 1/R_2) \quad (2.3)$$

Where:

- P_c = Capillary pressure.
- P_o = Pressure in the oil phase.
- P_w = Pressure in the water phase.
- σ_{ow} = Interfacial tension between oil and water.
- R_1, R_2 = curvature Radii of interface between oil and water.

Due to complex geometrical aspects, the capillary pressure can be approximated by a bundle of capillary tubes, which reduces equation 2.3 to:

$$P_c = 2\sigma_{ow} \cos\theta / r \quad (2.4)$$

Where:

- P_c = Capillary pressure, pressure difference existing across the interface.
- σ_{ow} = Interfacial tension between the two immiscible phases.
- θ = Contact angle measured through the water phase.
- r = Radius of cylindrical pore channel.

From Eq-4, its clear that, the interfacial tension, the size of the capillary and the relative wettability of the fluids are decisive parameters to predict capillary pressure. The displacement of one fluid, e.g., oil and water, by another in the pores of a porous media is either aided or opposed by the surface forces of capillary pressure (Ahmed, 2010). It should be noted that real rocks contain an array of pores of different sizes connected by pore throats of differing size, which will limit the applicability of simple equations, like the above (4). The impact of the capillary pressure on fluid flow is commonly dependent on the type of lithology in the oil reservoir. It should be noted, in fractured reservoirs, spontaneous imbibition of water into the matrix due to strong capillary forces is significant for the displacement efficiency of a waterflood. Sandstone reservoirs, however, are usually not very fractured. For such reservoirs, strong capillary forces during waterflooding can always cause trapping of oil and high residual oil saturation, which is known as the "end

effect" (Anderson, 1987a). In the context of a reservoir, oil saturation in a reservoir, represented as S_{or}, and following primary and secondary phase, sets an upper limit to the total amount of oil that could be produced using any EOR technique, no matter how good its performance may be (Ahmed, 2010).

2.3.4. Interrelation between Different Forces

The influence of gravity forces depends on the relative magnitude of capillary forces and gravity forces. The lower IFT is, the better the effect of reducing injection pressure is, and the greater the extent of improving oil recovery is (Amaefule and Handy, 1982; Gaonkar, 1992; Kumar et al., 2012). In general, when interfacial tension is low it translates into lower viscous forces required to mobilise discrete droplets of oil and coalesce them together to form a continuous oil phase as a sheet like-film in the pores of sandstone rock reservoirs (Taber, 1969). In a recent publication, researchers have shown that residual oil saturation is a function of capillary number (N_c), which is the dimensionless ratio between the viscous and capillary forces as shown in equation 2.5.

$$N_c = u\mu / \gamma \tag{2.5}$$

Where:

- Nc = Capillary Number.
- u = Darcy velocity.
- μ = Viscosity of displacing fluid.
- γ = interfacial tension between two phases.

2.4. Wettability

2.4.1. General Aspects

Fluid distribution in porous rocks is affected not only by capillary, viscous and gravity forces but also by forces present at liquid/solid interfaces (Green and Willhite, 1998a), and therefore reflect the balance between cohesive and adhesive forces. Molecules of one fluid are attracted to another fluid by an electrostatic force referred to as cohesion; the basic property of this is interfacial tension. The molecules of a fluid are also, to some degree, attracted to the molecules of an adjoining solid by an electrostatic force called adhesion. In general, wettability is the term used to describe the relative adhesion of two fluids to a solid surface. In a porous medium, this is described as the tendency of one liquid to spread on, or adhere to, a solid's surface in the presence of another (immiscible) fluid. The liquid that can spread over the solid surface is called the wetting liquid (Zolotukhin

and Ursin, 2000; Drummond and Israelachvili, 2002, 2004), which, in the most extreme cases, can displace the non-wetting fluid from a surface completely. When it comes to EOR, wetting can influence the oil recovery process due to its effect on location, flow and distribution of the fluid within reservoir rocks(Anderson, 1986c).

In the brine-oil-rock system (Figure 2.4), the wettability can range from strongly oil-wet to strongly water-wet depending on the brine interactions with the rock surface. If no preference is shown by the rock to either fluid, the system is said to exhibit neutral wettability or intermediate wettability (Figure 2.4), a condition that one might visualize as being equally wet by both fluids (50%/50% wettability) (Anderson, 1987; Abdallah et al., 2007). If the rock surface is preferentially strongly oil-wet, even though it may be saturated with water, oil is present as a thin film covering the rock and occupies the smaller pores (Abdallah et al., 2007). The formation brine is located in the centre of the pores as droplets. Oil-wet rocks are characterized by early water breakthrough. A significant amount of the oil is recovered after water breakthrough. Water breakthrough on injection occurs initially along the shortest (least resistant) flow path between injector and producer, while oil is still being swept along other flow paths (Alotaibi et al., 2010). On the contrary, in strongly water-wet rock, water will occupy the smaller pores and will be in contact with most of the rock surface (Abdallah et al., 2007). The oil in the pores will be located at the centre of the larger pores as disconnected globules, formed by a snap-off mechanism, or even extending over several pores.

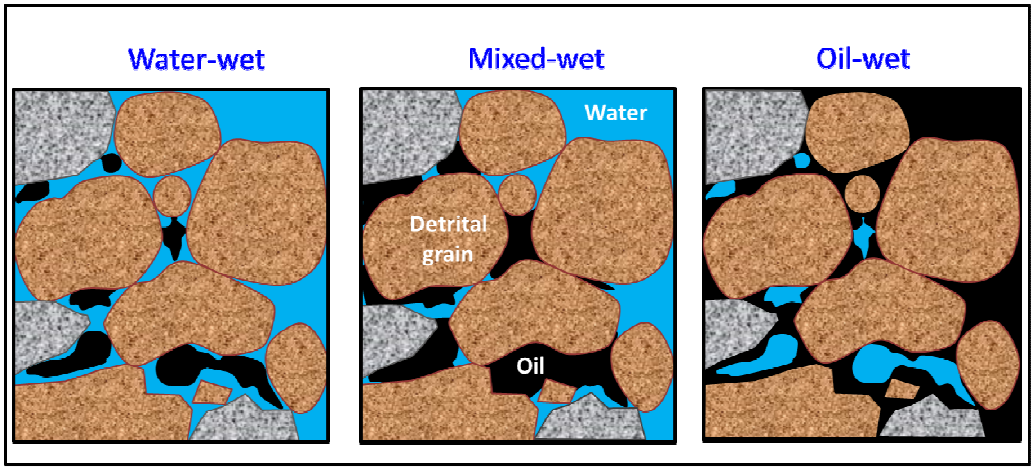

Figure 2.4: Schematic view showing the state of wettability in porous media. In a water-wet reservoir (left), oil remains in the centre of pores. In the mixed-wet case, oil has displaced water from some of the mineral grains surfaces (middle). In oil-wet reservoirs, the aqueous fluids are isolated from being in contact with the mineral grains by a coat of oil.

The wettability varies throughout a reservoir due to the variation in the composition of it's constitute rock, which often comprises a variety of detrital minerals, clay mineral

types, and pore structure. Different terms are used to describe the wettability in the heterogeneity patterns found in rock reservoirs. Fractional wettability (Fatt and Klikoff, 1959; Bradford and Leij, 1995; Tsakiroglou and Fleury, 1999; Beatty and Smith, 2010) is the wettability state of an oil reservoir that has local areas that are strongly oil-wet, whereas the rest of reservoir is strongly water-wet (Anderson, 1986b). Fractional wettability is different from neutral wettability, which is used to imply that all minerals of the rock's reservoir have a similar preference for water or oil.

Mixed wettability, introduced by Salathiel (Salathiel, 1973), refers to a particular type of fractional wettability with continuous water-wet paths and oil-wet paths, where smaller pores are occupied by water and are water-wet, and the larger pores of the rock are still oil-wet. The existence of a continuous filament of oil (oil-wet) area in the larger pores of the porous media allows oil displacement at very low oil saturations so that it can be recovered through waterflooding until a very low saturation is reached (Anderson, 1986b; Donaldson et al., 1969). Mixed wettability usually occurs when the oil, containing interfacial-active polar organic compounds, occupies a water-wet rock saturated with brine (Anderson, 1986c).The interfacial-active compounds act as a modifier when they react with the rock's surface, and displace the aqueous film lining the large pores and, thus, converting them into an oil-wet state.

2.4.2. Evaluation of Wettability

Evaluation of relative oil/water wetting is a vital aspect of oil reservoir exploration, as it has a major influence on oil production rates, the water/oil production ratio after water breakthrough, the oil production rates of the residual oil saturation of a reservoir at abandonment, and EOR. Over the past fifty years, a few quantitative or qualitative techniques for determining wettability have been developed to study this phenomena on different types of solid surfaces as well as porous media (Anderson, 1986b; Glover, 2002). Some of the most important of these methods are briefly summarised below:

- Microscopic examination: This involves the direct observation and measurement of contact angles of fluid droplets over solid surfaces. Some of the techniques that are commonly used to measure contact angles include: the conventional telescope-goniometer method, the Wilhelmy balance and the more recently pendant drop shape methods. Notably, techniques of contact angle can be as simple as taking readings of contact angle using photos by a digital camera or as complicated as

taking high-resolution images using environmental scanning electron microscope (ESEM) (Wei et al., 2003; Kareem et al., 2016), and atomic force microscopy (AFM) (Zhang et al., 2012; Yu et al., 2013). The measurements are often difficult, and good images relies significantly on a good sample preparation and methodology (Donald et al., 2000; Donald, 2003; Guan et al., 2003). Recently, Yuan and Lee, (2013) provided a comprehensive review of limitations of these techniques and their impact on contact angle measurement

- Amott and Amott-Harvey: This is a macroscopic test that can measure the wettability of a rock to given fluids. In this technique, different amounts of oil and water are imbibed by a sample spontaneously and/or by force (Anderson, 1986b).
- U.S. Bureau of Mines (USBM): This is a macroscopic mean test for wettability of a rock to given fluids. It is similar to the Amott method but considers the work required to do a forced fluid displacement. (Anderson, 1986b).
- Nuclear magnetic resonance (NMR): evaluates changes in longitudinal relaxation time (Guan et al., 2002; Vevle, 2011; Prather et al., 2016).
- Reservoir logs: resistivity logs before and after injection of a reverse wetting agent (Spinler, 1997; Hamon, 2000).
- Flotation method: measures the distribution of grains at water/oil or air/water interfaces (Anderson, 1986b; Williams and Fuerstenau, 1987; Ozkan and Yekeler, 2003).
- Relative permeability method: allows determination of the shape and magnitudes of relative-permeability curves for oil (K_{ro}) and relative-permeability curves for water (K_{rw}) (Anderson, 1986b; Tang and Morrow, 1999a; Morrow et al., 1998; Alotaibi et al., 2010; Austad et al., 2010a; Nasralla et al., 2011).
- Glass slide method: measures the displacement of the non-wetting fluid from a glass slide (Anderson, 1986b; Maghzi et al., 2010; Khajepour et al., 2014).

Although no single accepted method exists, the first three methods are the most common within the oil industry. The wettability criteria for the three methods are described in greater detail in the next sections. The remaining tests in the list are qualitative, each with somewhat different criteria to determine the degree of water or oil wetness.

For most of the cases, the contact angle method (sessile drop method) is the most widely-used technique for the direct measuring of the wetting properties of the rock

surfaces with respect to a liquid in the presence of another immiscible liquid (Shedid and Ghannam, 2004; Stalder et al., 2010). As mentioned earlier, ESEM has been used in some wettability studies to identify oil wetted, and water wetted rock surface in the local environment (Stokes and Donald, 2000; Guan et al., 2002; Wei et al., 2003; Yang et al., 2015). The wetting state of the rock surface can be understood by contact angle as shown in Table 2.3. Wettability close to intermediate wet, but on the water-wet side of the neutral point, is beneficial for recovery of oil from water (Yildiz and Morrow, 1996; Tang and Morrow, 1997, 1999a).

Table 2.3: Wettability expressed by contact angles(Glover, 2011).

Contact angle(°)	**Wettability preferences**
0	Extremely water wet
0-30	Significantly water-wet
30- 60	Moderately water-wet
60-90	Weakly water-wet
90	Neutral wet
90-120	Weakly oil-wet
120-150	Moderately oil-wet
150-180	Significantly oil-wet
180	Extremely oil-wet

For a static oil/water/solid system, such as that shown in Figure 2.5, the three interfacial tensions, σ_{os}, σ_{ws} and σ_{ow} are in mechanical equilibrium. This equilibrium is expressed by Young's equation 2.6 (Anderson, 1986b).

$$\sigma_{os} = \sigma_{ws} + \sigma_{ow} \cos\theta \tag{2.6}$$

Where

- θ = Contact angle measured through the denser phase.
- σ_{os} = Oil-solid interfacial tension.
- σ_{ow} = Oil-water interfacial tension.
- σ_{ws} = Water-solid interfacial tension.

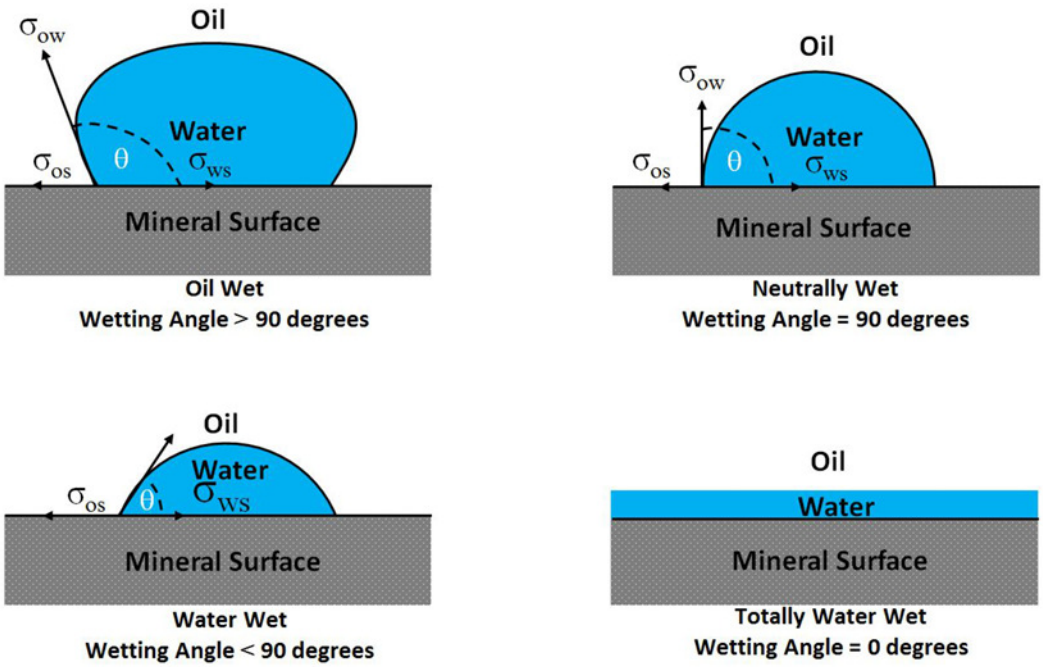

Figure 2.5: Contact angle measurement for an oil drop through water phase showing various wetting states. Extracted from (Glover, 2011).

It should be noted that a contact angle is easiest to examine when the contact plane is flat since a non-flat surface can led to incorrect measured values (θ apparent vs. θ true in Figure 2.5). However, pore walls are mostly rough, and typically more than one mineral species composes the matrix surrounding the pores, thus complicating contact angle evaluations in real rocks. This said, there is no strong evidence in the literature on whether it is more representative to measure contact angle on "single" mineral plates or porous rock chips. Obviously, it is not always possible to reproduce reservoir wettability behaviours from contact angles measured at room temperature.Nevertheless, wettability measurements can give a guide to the relative oil or brine wetting tendencies of reservoir rocks. This can be crucial in the selection of relative permeability test methods to generate data relevant to a particular reservoir situation.

The Amott-Harvey imbibition method is a macroscopic, average wettability, measurement for a solid/fluid system. Quantitatively, the Amott method was the first one that could be used for core reservoirs rocks. The method involves measuring the amount of both spontaneous and forced imbibition of fluid in a rock core. The principle is that the wetting fluid will imbibe spontaneously into the core, displacing the non-wetting fluid. It assumes that a strongly wetting fluid will spontaneously imbibe until the residual saturation of the non-wetting fluid is obtained and reflects the ease with which the wetting

fluid will displace the non-wetting fluid. The Amott wettability neglects the hysteresis of the capillary pressure curve which can lead to the misleading results when the sample is fractionally wet (McDougall and Sorbie, 1995). By measuring the imbibition of oil and brine on test cores of the sample, a wettability index can be obtained (Anderson,1986a). An index of 1.0 indicates a strongly wetting fluid, and an index of 0.0 is a strongly non-wetting fluid (Anderson, 1986b; Thakur and Satter, 1998).

An Amott wettability measurement consists of the following four steps (Figure 2.6): (1) immersion of the core in oil, and measurement of the volume of water displaced by the spontaneous (free) imbibition; (2) centrifugation of the core in oil until the irreducible water saturation is reached, and measurement of the total amount of water displaced, including the volume displaced by spontaneous imbibition; (3) immersions of the core in brine, and measurement of the volume of oil spontaneously displaced by imbibition; and (4) centrifugation of the core in oil until residual oil saturation is reached, and measurement of the total amount' of oil displaced.

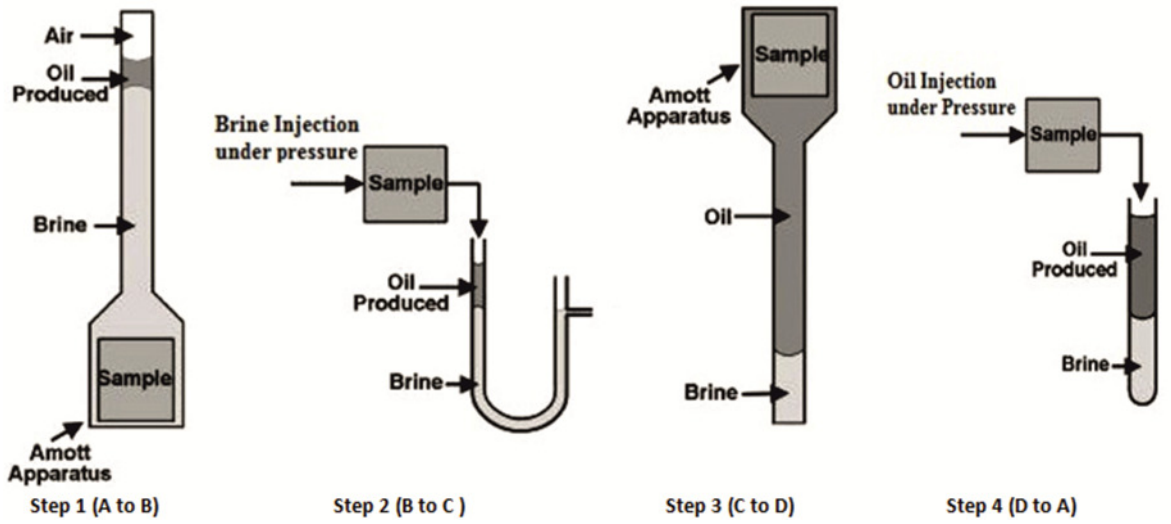

Figure 2.6: Graphical illustration of the steps performed in Amott wettability (natural and forced displacement) test (Glover, 2011).

The third quantitative method is the USBM method, which was first introduced by Donaldson et al. (1969). Like the Amott method, the USBM method is a macroscopic average wettability measurement for a solid/fluid system. The capillary pressure curves are obtained by alternately displacing water and oil from small cores using a centrifuge. The areas under the capillary pressure curves represent the thermodynamic work that is

required for the respective fluid displacements, as can be seen in Figure 2.7. Displacement of a non-wetting phase by a wetting phase requires less energy than the displacement of a wetting phase by a non-wetting phase. Therefore, the ratios of the areas under the capillary pressure curves (between S_{iw}, and S_{wor}) are a direct indicator of the degree of wettability. The logarithm of the area ratio of oil displacing water, A1 (from S_{or} to S_{iw}), to water displacing oil, A2 (from S_{iw} to S_{or}), is used as a convenient scale for the wettability index (W):

$$W = log\left(\frac{A1}{A2}\right) \tag{2.7}$$

Where

- A1= is the area under the drainage curve.
- A2= is the area under the imbibition curve.

Increasing positive values to +∞ indicates strongly water-wet. However, increasing negative values to -∞ indicate strongly oil-wet. It should be noted that, a value of zero represents uniform wetting of rock by both fluids. The USBM index gives a measure of the energy needed to make the forced displacement, making it an independent indicator of wettability while the Amott-Harvey index is based on the relative change in saturation. Table 2.4 provides the approximate relationship between wettability and the common experiments/measurements previously described.

Table 2.4: The approximate relationship between wettability state, contact angle, Amott-Harvey wettability indices and the USBM (Glover, 2011).

Quantitative method		**Water-wet**	**Neutral-wet**	**Oil-Wet**
Contact Angles	Min	0°	60° to 75°	105° to 120°
	Max	60° to 75°	105° to 120°	180°
Ammot Wettability Index	Iw	>0	0	0
	Io	0	0	>0
USBM Wettability Index		1	0	-1

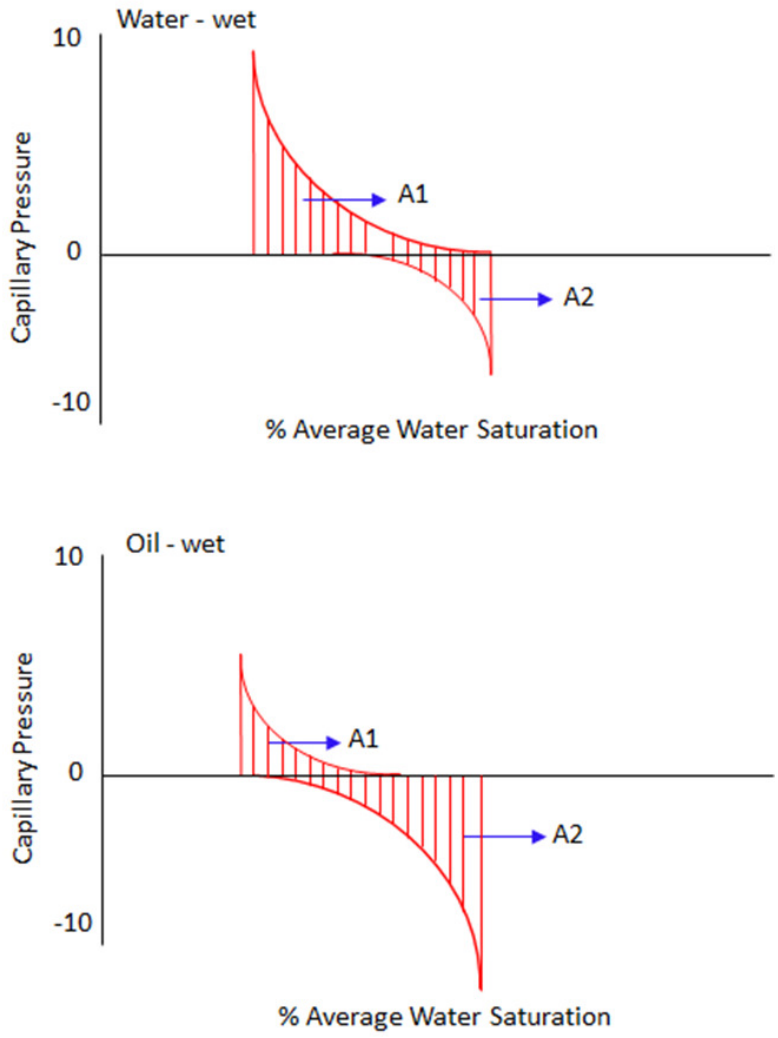

Figure 2.7: USBM Method to determine wettability (León-Pabón et al., 2014)

2.5. Factors Affecting Wettability State

Rock wettability has long been studied. Many studies have shown that the interaction between rock/brine/crude oil can have a significant effect on the wetting condition (Anderson, 1986b; Cuiec, 1984; Buckley and Liu, 1998; Bera et al., 2012). Thus, a significant amount of effort has been directed at trying to understand rock wetting at a more fundamental level. Several factors can affect or control the wettability condition of an oil reservoir, these include: the type of mineral surfaces that line the pore spaces of the rock, brine composition; the presence of surface active agents in the crude oil; initial water saturation of the reservoir and reservoir temperature and pressure are among the earlier parameters identified (Anderson, 1986a).

2.5.1. Effect of Reservoir Rock (Mineral Type)

Numerous investigators have reported upon the factors that can cause wetting conditions in laboratory core tests to be different from those in the reservoir. Welge' perhaps was among the first to recognize that restored-state test procedures may not deliver flow characteristics representative of the reservoir (Welge, 1949). Studies by other researchers have revealed that the important factors that can contribute to changes in core-wetting behavior depends upon the adsorption of polar components of crude oil onto the different constituent mineral phases exposed within the rock's pore space (e.g. quartz, mica, or clay);which tend to make these surfaces oil-wet (Tang and Morrow, 1999a; Zhang et al., 2007a; Yang et al., 2015).

The active surface chemistry in the case of clays increases this effect more than in quartz. Several studies have been made regarding the adsorption of asphaltenes and resins onto clays, and found that adsorption can make the clay more oil-wet (Somerton and Radke, 1983). Clementz (1977) found that some compounds can be adsorbed rapidly onto montmorillonite, forming stable clay-organic compounds and changing the wettability from water-wet to oil-wet. The adsorption also reduced the expansion of swelling clays, clay surface area, cation exchange capacity, and water sensitivity; however, the adsorption of asphaltenes on Berea sandstone cores in the presence of water did not reduce water sensitivity of the kaolinite contained in the core (Mohan et al., 1993a).

The influence of mineral composition on the surface properties of sandstone core rocks can be adequately quantified through the CEC and the measurement of the electrochemical potential of the rock sample. These measurements can be performed on samples of the whole rock and then will reflect the contributions of all the different minerals present on the sample, including common minerals such as quartz and clays. As has been discussed before (2.1.2.3.), some authors have focused on evaluating the effects of the type of clays (kaolinite, illite or montmorillonite, and chlorite) and their amount, which have been proved to significantly affect the wettability in a sandstone reservoir (Baptist and White, 1957; Morrow, 1990; Yariv, 1992; Borysenko et al., 2009; Wu and Firoozabadi, 2010).The effect of quartz surface will be discussed in more details later in this thesis.

2.5.2. Effect of Brine Composition

It is now well known that, initial brine composition, salinity and pH can all affect the chemical composition of mineral surfaces. Several researchers have studied the effects of pH and brine, and they reported that they might increase or decrease or even change the surface charge of the rock reservoir (Fogden, 2011; Liu et al., 2016). The forces acting between charged surfaces (like the interaction of rock surface/brine and oil/brine interfaces through the water film) can be described by the DLVO theory, named after Derjaguin, Landau, Verwey, and Overbeek (Derjaguin and Landau, 1941; Verwey et al., 1948). This theory describes the balance between two forces, electrostatic repulsion and van der Waals attraction. An EDL consists of a negatively charged mineral surface in direct contact with a liquid phase, whose cations adjacent to the mineral form parallel layers. The structure can be broken down into three layers. Firstly, more strongly bound, the film is known as the Stern layer which consists of ions of opposite charge tightly held to the surface, as can be seen in Figure 2.11. These ions are considered immobile and screen the surface charge. Secondly, there is a region bound by the slipping plane containing ions of both charges. These ions may exchange with the electrolyte but are not able to move freely. Thirdly, diffuse layer, which is in Brownian motion with the bulk liquid phase. Together, the van der Waals and electrostatic repulsions create a neutral electric double layer. The formation of this electrical double layers in a brine phase, can lead to a significant screening off the original surface charge. A decrease in the salinity of the brine or valence of cations present in the brine causes an expansion of the electrical diffuse double layer. This implies a reduction in the ability to screen the charge and an increase in the electrical potential at the slipping surface between the charged surface and the brine solution is observed. It has been proved that brine pH and composition have a profound effect on the wettability of all types of rocks (Austad et al., 2008; RezaeiDoust et al., 2009; Fogden, 2011; Liu et al., 2016). As a result, the existence and some multivalent ions and total salinity of the brine are among the factors which effect of rock wettability (Anderson, 1986a; Tang and Morrow, 1999b; Yildiz et al., 1999b; Lager et al., 2007; Farzaneh et al., 2015).

2.5.3. Effect of Oil Composition

Since crude oils are composed of such a diverse range of molecules with different functional groups (Chapter 1), it's easy to see that this can lead a wide variety of interactions with the mineral surfaces exposed in a the pores of a rock. This said,

heteroatoms compounds are expected to interact more heavily with mineral surfaces on the basis of their larger size and variety of functional groups. This molecules are most common in the heavier fractions of crude oil, especially in the asphaltenes and resins (Anderson, 1986b; Speight, 2014). Asphaltenes are large complex molecules composed mostly of carbon and hydrogen. Resins are smaller molecules, and in general have a higher amount of the nitrogen, sulfur, and oxygen. In the presence of water, the rock and the oil interfaces become charged. The polar functional groups belonging to both the mineral and the crude oil phase can behave as acids (giving up a proton and becoming negatively charged) and bases (gaining a proton and thus getting a positive charge) (Buckley et al., 1998). Nearly all reservoirs rocks are filled and saturated with water during deposition and are believed to be initially strongly water-wet. As oil migrates into the reservoir, the rock can either remain water-wet for a period as the connate water would keep the surface from being directly contacted by the oil, or its wettability can change as certain as certain polar components of the oil are adsorbed by mineral surfaces (Anderson, 1986a).

Notably, (Donaldson et al. (1969), (Cuiec, 1975) and Buckley et al. (1998) pointed out that composition of crude oil is crucial to wetting alteration in two different ways:

1. Polar components present in the crude oil, especially in the heavy asphaltenes and resin fraction, are those that exhibit a higher affinity for mineral surfaces and influence wetting conditions in rocks reservoirs.
2. Solvency of crude oil affects the tendency of the active components of the oil to aggregate and even separate between the oil and water phases.

Although the solubility of polar components into the water phase is commonly low, over geologic time, they can travel through the protective water film and contact the rock surface. Based on experimental results, however, it is believed that the ability to adsorb onto the rock in the presence of a water film is low and is not strong enough to initiate wettability alteration within a few hours (Kaminsky and Radke, 1997).

2.5.4. Effect of Initial Water Saturation

The pore spaces in rocks that form oil and gas reservoirs are always completely saturated with fluid. Initially, when sediments were being deposited (usually in an aqueous environment), the pores were completely saturated with water (i.e., water saturation was 100% of the pore space). Later, during deep burial, compaction, and partial cementation,

the water may have changed in composition, but the saturation remained 100% unless hydrocarbons entered the pores and forced the water out.

During hydrocarbon accumulation in the reservoir, water saturation can be reduced by 5 to 40 %, after which no more water can escape from the pores. This occurs when water saturation becomes immobile, at the irreducible water saturation. Saturation is defined as that fraction, or percent, of the pore volume occupied by a particular fluid (oil, gas, or water), and It is expressed by the following relationship (Ahmed, 2010):

$$\text{Fluid saturation (Si)} = \frac{\text{total volume of fluid}}{\text{pore volume}} \times 100 \qquad (2.8)$$

All saturations are based on pore volume not the gross volume of the reservoir. The saturation of each phase ranges between zero to 100 percent. By definition, the sum of the saturations is 100%, therefore

$$S_{oil} + S_{gas} + S_{water} = 100$$

Petroleum science literature contains several symbols for water saturation, including S_{wi}, S_{wc}, S_{wir}. Care must be taken to ensure correct interpretation of the symbol. The following definitions should help.

1) S_{wir} = irreducible water saturation, below which water cannot flow.
2) S_{wc} = connate water saturation existing on the discovery of the reservoir. It may or may not be irreducible.
3) S_{wi} = may mean irreducible, connate, or interstitial, which means saturation among the interstices, or pores. Interstitial may or may not signify irreducible. It may be the value at the time of discovery of the reservoir, or the value at any time after that. S_{wi} may also mean initial or original, which truly means the water saturation on discovery, but it, may or may not be irreducible.

The presence of a water film separating the mineral surfaces and oil protects the mineral surfaces from interaction with the polar components of the oil. This means that the initial water saturation will affect the wetting behaviour of the mineral surfaces (Salathiel, 1973). Salathiel found that there was a certain range of initial water saturation, which

provides the lowest residual oil saturation by LSEOR. To illustrate the effectiveness of initial water saturation in LSEOR, an experimental study revealed an increase in water-wetness in sandstone core rock as the original water saturation increased (Buckley, 1995; Jadhunandan and Morrow, 1995; Tang and Morrow, 1997; Zhou et al., 2000).The interrelationship of wettability, initial water saturation, and oil recovery has been studied by spontaneous imbibition and waterflooding (Zhou et al., 2000). Zhou et al. (2000) successfully documented the effect of initial water saturation on wettability using different Berea sandstone samples. Experiments were conducted at three values of initial water saturation, around 15%, 20%, and 25% respectively. It was found that both imbibition rate and final oil recovery in terms of oil originally in place (OOIP) increased with an increase in initial water saturation, whereas oil recovery by waterflooding decreased.

2.5.5. Effect of Temperature and Pressure

Besides the parameters noted before, it has been shown that the brine/oil interfacial tension can increase with temperature (McCaffery, 1972; Okasha and Al-Shiwaish, 2010; Rajayi and Kantzas, 2011), making this parameter relevant to the wettability changes.

Experimentally, observations of contact angle have indicated that mineral surfaces behave as water-wet at full reservoir conditions compared to room condition (Hjelmeland and Larrondo, 1986) where they do not. Different opinions in the literature regarding the influence of high temperature on the wettability of sandstone were documented by Rajayi and Kantzas (2011). Using contact angle measurements, they showed that sandstone might acquire oil-wet or water-wet state at high temperature. However, other researches have reported contradictory results when increasing the temperature in their experiments, as described below.

Civan (2015) Showed that an increase in temperature often, but not always, increases the sandstone's affinity to water and that no influence was observed for carbonate rocks. Based on core flooding experiments, Jadhunandan and Morrow (1995) reported that an increase in aging temperature decreased both primary oil recovery as well as tertiary recovery of oil from sandstone cores, which was understood as a reduction in water wetness as temperature increased. Schembre et al. (2006) observed, on the contrary, that cores of sandstone can become more water-wet at high temperature. This was attributed to fines detachment from the rock surface at elevated temperatures. Moreover, they mentioned that the water film on pore surfaces becomes more stable at high temperature.

Regarding the effect of pressure, there is no clear evidence that it can directly affect the wettability state in oil reservoirs (Anderson, 1986a). Several researchers reported that they have been able to restore the cores to their native state of wettability in the laboratory when the cores were restored at reservoir temperature and ambient pressure (Mungan, 1972; Cuiec, 1975). However, Zhou et al. (1997) used variable aging times to obtain cores with different degrees of wettability to develop a correlation between spontaneous imbibition and wettability. The rate and amount of water imbibition decrease as the cores change from strongly water-wet toward neutral or oil-wet conditions. Thus, a correlation to the wettability index could be made from the area under the imbibition capillary pressure curve (displacement energy or pseudo work) and the advancing contact angle at the point of 50% oil recovery by imbibition. Researchers show the importance of a hydraulic continuity for the achievement of maximum recovery.

2.6. Mechanisms of Wettability Alteration

It is generally believed that oil reservoirs were originally water-wet before the oil migration, and trapping, in the formation took place (Alagic et al., 2011). When oil migrates into an originally water-wet reservoir, the saturation history will change. Surface wetting is induced by saturation history, reservoir temperature and pressure, which leads to an equilibrium condition between multiple phases. The degree of change in wettability in the rock surfaces can be determined by the interaction of the oil components, the mineral surfaces, and brine chemistry (Anderson, 1986a; Buckley, 1996). As mentioned in section 2.5.3 oil composition is central in changing a water-wet surface towards more oil-wet. Polar crude oil components, especially in the heavy asphaltene and resin fractions, can adsorb on mineral surfaces and alter their wetting properties towards a less water-wet condition (Buckley et al., 1998). Buckley et al. (1998) studied the mechanisms of wetting alteration by crude oils through experimental observations of contact angles and identified four different mechanisms in which polar crude oil components can alter the rock wettability state. These are polar interactions, surface precipitation, acid/base interactions and ion binding between charged sites and higher valence ions.

It is suggested that the American Petroleum Institute (API) gravity, acid number (AN), and base number (BN), can be used to evaluate the potential for wettability alteration for a given crude oil (Liu and Buckley 1999).When a brine is present, the oil and mineral surfaces become charged. Their polar components behave as acids and bases by giving up a proton and becoming negatively charged, and gaining a proton and becoming positively

charged, respectively (Buckley and Liu, 1998). These surface charges influence the adsorption behavior and thus wettability during injection LSEOR. The API gravity, is a stock-tank oil gravity obtained when flashing reservoir fluid from bubble-point pressure directly to the atmosphere (Labedi, 1992): if its API gravity is greater than 10, it is lighter and floats on water; if less than 10, it is heavier and sinks. In general, the acid number (AN) is defined as the amount of potassium hydroxide (KOH) in milligrams, required for neutralizing 1 g of the petroleum acid in the crude oil, and reversely, the base number (BN) is defined as the amount of KOH in milligrams, required neutralizing 1 g of the petroleum base (Green and Willhite, 1998).

2.6.1 Polar Interactions

Early work has shown that the wetting properties of a reservoir rock are due to the presence or absence of polar organic compounds in crude oil Benner and Bartel (1941). Denekas et al. (1959) have presented a detailed study of the effect of crude oil components on the wetting properties of reservoir rocks. The wettability alteration of a reservoir rock by adsorption of polar compounds has been investigated by several authors (Denekas et al., 1959; Clementz, 1977), as summarised by Anderson, (1986a). Adsorption through polar interactions is the predominant adsorption mechanism in the absence of a water film between the oil and the mineral surfaces. A natural crude oil/brine/ rock system involves complex interactions of the fluid-fluid and fluid-solid surface.

Recently, it has been shown that the main parameters that influence adsorption include the type of mineral and its cation exchange capacity, the nitrogen content of the oil, and the solvent in which the polar compounds are dissolved (Buckley et al., 1998). In cases with specific oil-wet minerals (that are hydrophobic) present in the rock (Anderson, 1986a) or in reservoirs where the rock is both source and reservoir and thus have organic coatings on pore surfaces(Cuiec, 1984), direct contact between the oil and rock surface becomes possible. The extent of polar interaction, as studied by the contact angle method is not affected by aging time and aging temperature and it is obviously different for different crude oils (Buckley, 1996).

2.6.2. Surface precipitation

In general, high molecular polar components that exist in oil can interact with minerals surfaces and alter the wettability state. The limited ability of the crude oil to act as a solvent for the asphaltenic fraction in the pore spaces and fluid pathways can potentially

influence the dissolution, and precipitation of dissolved material onto the mineral surface (Buckley, 1996). The parameter that can explain the mechanism for which a given crude oil may alter the rock wettability are API gravity and refractive index (Liu and Buckley, 1999). The gravity of oil and the refractive index is an indicator of the oil's solvent quality. If the oil is a poor solvent for its asphaltenes, the tendency for wetting alteration is enhanced, and as illustrated in Figure 2.8.

Buckley (1995) and Al-Maamari and Buckley (2003) pointed out that precipitation of asphaltenes could change the wettability of the rock surface to the less water-wet condition. In their experimental work, Buckley (1995) observed the wettability alteration of Berea core sandstones due to the precipitation of asphaltenes. The changing in wettability behaviours was dependent on the type and amount of asphaltenic fraction adsorbed on the mineral surface in the Berea rock studied. Their result has shown the role of oil solvent quality to the interactions between a crude oil and mineral surfaces.

2.6.3. Ion-Bridging

Another type of adsorption is ion bridging where cations, like Ca^{2+}, act as bridges in the brine phase between a negatively charged polar end, such as the carboxylate group in crude oil, and negatively charged sites on the mineral surfaces exposes in the pore space (Lager et al., 2008). Several interactions have been proposed such as oil/Ca^{2+}/oil, mineral/Ca^{2+}/mineral, and oil/Ca^{2+}/mineral, when multivalent cations, such as Ca^{2+} ions masks the mineral surfaces as illustrated in Figure 2.8 (Buckley et al., 1998).

In the case of sandstone rock reservoirs, oils with a high acid number and low base number are dependent on this type of mechanism to define their wettability state in the wetting process (Buckley et al., 1998).The ion bridging mechanism provides the possibility for negatively charged carboxylates to change the wetting condition of the negatively charged clay mineral surfaces towards a less water-wet condition, and it is possibly that this is the most dominant interaction which results in wettability alteration towards an oil-wet condition in sandstone reservoirs containing acidic oil (Buckley, 1996).

2.6.4. Acid/Base Interactions

The mineral surfaces of the rock respond differently to acidic and basic component of the oil due to their relative charges (Buckley, 1996). It has been shown that water plays a vital role in mediating oil/rock interactions. In the presence of water between the oil and rock phases, the water can causes the formation of charged oil/brine and brine/mineral

interfaces due to acid/base dissociation. In such a condition both interfaces act as acids or as bases by giving up or gaining a proton (Cuiec, 1975). Basically, the main phenomenon in which the wettability alteration can happen through acid/base interactions between crude oil, brine, and mineral surfaces, as can be seen in Figure 2.8. The water film which is in contact with the minerals surface of the rock can become less stable (Liu et al., 2010) and adsorption of ionized oil components from the oil/brine interface occurs.

The surface charge depends on the extent of acid/base dissociation interactions at the interface which, in turn, depends on pH of the film near the surface and the brine composition. It is generally assumed that, when repulsion occurs between oil components and the mineral surfaces, the water film is stable and thick, i.e. strongly water-wet conditions can be maintained. If the water film is unstable and thin, the film can break, resulting in direct contact with oil to the minerals surface and adsorption of polar components on pore walls.

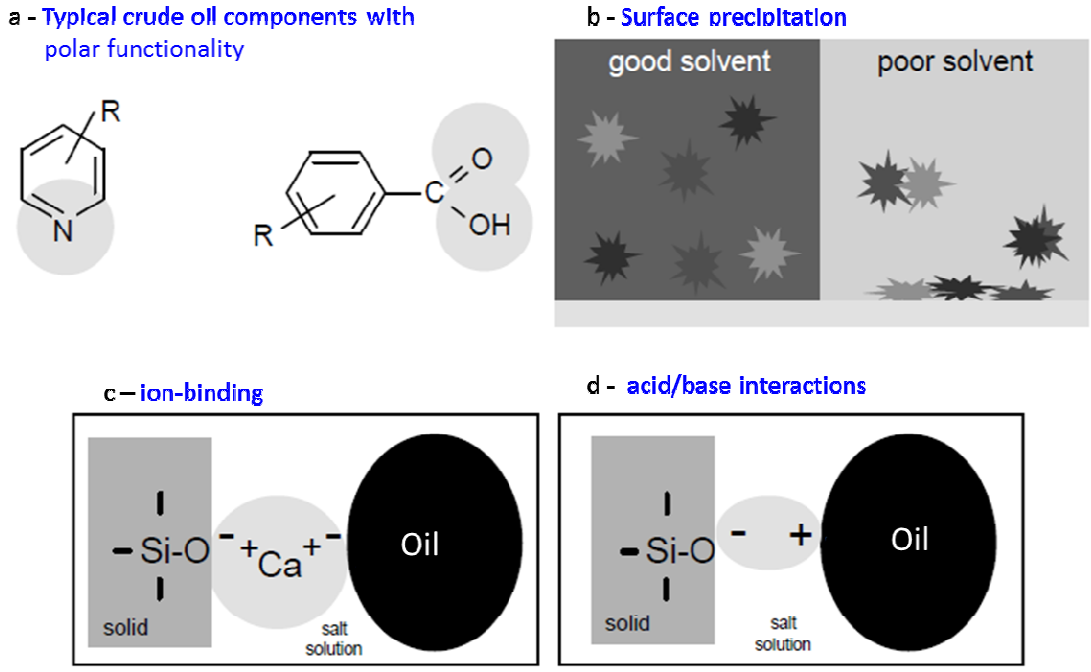

Figure 2.8: Mechanism of interactions leading to wettability alteration (Buckley, 1996).

Finally, it should be noted that the mechanism (s) by which wettability alteration occurs in sandstone rock reservoirs is now a major issue of debate in the LSEOR literature. Several mechanisms have been proposed and developed, but none of them have definitively been shown to be the primary one (Suijkerbuijk et al., 2012a). This is due to the complex nature of the brine/oil/rock interactions and is further complicated by a

number of conflicting observations from experimental studies (Al-Shafei and Okasha, 2009). To understand the wettability alteration, it is important to note that crude oil/brine and brine/rock interfaces can be explained by through the theory of intermolecular forces. For this reason, it is necessary to present some basic information of intermolecular forces in the next sub-section.

2.7. Intermolecular forces

Intermolecular forces (IMFs) are forces of attraction or repulsion, which act between neighboring particles such as atoms, molecules, or ions. These forces include, but are not limited to Van der Waals interactions, electric double layer forces, salvation forces, steric interaction forces and hydrophobic interaction forces. All these types of interactions have been considering when explaining the fundamental mechanisms behind the LSEOR, but its Van der Waals attractive forces and the aforementioned double layer effects which have been more widely invoked in studies through DLVO theory.

Van der Waals forces are relatively long range attractive forces which arise from interactions between dipoles, both permanent and induced. They comprise three different interaction forces: dipole-dipole interactions (Keesom forces); dipole-induced dipole interactions (Deby forces) and interactions between induced dipoles (London or dispersive forces), (Israelachvili, 2011).

2.8. Low Salinity Water Flooding Mechanism

The aspiration of operators using waterflooding on mature fields is to maximise the effective recovery of the remaining oil after low salinity waterflooding at the lowest investment cost possible. For this reason, low salinity injection has been widely studied in the last two decades in most international laboratories and across a multitude of field tests.

Although it is generally accepted that the improved oil recovery by low salinity flooding is caused by wettability alteration, how low salinity water flooding works, i.e. the mechanisms that give rise to incremental recovery, are not well understood, even despite numerous laboratory studies. The reasons behind this lack of consensus are varied, but mostly stem from the complicated interaction between the various minerals present in a given rock, with the water and oil phases inside the pores (Morrow and Buckley, 2011). Sheng (2014) summarised various mechanisms that have been suggested to explain low-salinity waterflooding. These mechanisms are: fine migration (Tang and Morrow, 1999a); mineral dissolution (Buckley and Morrow, 2010); limited release of mixed-wet particles

(Buckley and Morrow, 2010); increased pH effect and reduced interfacial tension (IFT) (McGuire et al.,2005); emulsification/snap-off (McGuire et al., 2005);saponification (McGuire et al., 2005); surfactant-like behavior (McGuire et al., 2005); multicomponent ion exchange (MIE) (Lager et al., 2007); double layer effects (Ligthelm et al., 2009); particle-stabilized interfaces/lamella (Buckley and Morrow, 2010; Morrow and Buckley, 2011); salt-in effects (RezaeiDoust et al., 2009); osmotic pressure (Buckley and Morrow, 2010); salinity shock (Buckley and Morrow, 2010); wettability alteration (to more water-wet) (Buckley and Morrow, 2010); wettability alteration (to less water-wet) (Buckley and Morrow, 2010); viscosity ratio (Buckley and Morrow, 2010); and end effects (Buckley and Morrow, 2010).

Most of the proposed mechanisms are linked to each other. For instance, to have fine mobilization, fines must be available in the injection fluid. The possible fines could be the product of mineral dissolution and precipitation or released particles. Thus, the limited release of mixed-wet particles and mineral dissolution can be related to fines migration (Tang and Morrow, 1999a). As a result of dissolution, the viscosity of the low salinity flood increases. Saponification, surfactant-like behavior, and emulsification/snap off are all related to pH and IFT effects. Osmotic pressure and salinity shock are directly related to salinity contrasts between the initial water and displacing water. The end effect occurs in laboratory scale. In this chapter, the main recommended mechanisms e.g. fines migration, multi-ion Exchange (MIE), double layer effect (EDL), and pH will be discussed in more detailed.

2.8.1. Fines Migration

Clay hydration using freshwater is known to result in swelling of the basal spacing located between the clay layers, resulting in damage to the producing formation by decreasing pore volume and permeability, and also increasing the tendency for the clay particles (fines) to disperse. Furthermore, the addition of dissolved salts in flood water may not have the ability to stabilise the clay particles and therefore can also give rise to fine migration. Numerous reports in the literature have detailed various effects associated with fine migration; these include: mobilization of fines with permeability decline caused by waters of decreasing brine concentration, increased flow velocity, altered water pH or temperature (Mungan, 1966; Lever and Dawe, 1984; Civan, 2000, 2015).

Morrow and co-workers suggested partial stripping of mixed-wet particles from the pore walls of Berea sandstone during low salinity water injection as a feasible explanation

for improved oil recovery (Tang and Morrow, 1999a; Zhang et al., 2012). Often in these tests a few particles, which mainly consisted of kaolinite clay fragments, were observed in the effluent. They proposed that the mechanism for improved oil recovery during low salinity water injection was the reduction of water relative permeabilities (reduction in water swept zone) due to fines mobilization, migration and stirring Figure 2.9.

At low salinity conditions, the partial mobilization of mixed wet particles reduces the residual oil saturation and increases the oil recovery. In principle, clay minerals (e.g. kaolinite) are attached to the surface of detrital grains by a balance between mechanical forces such as capillary forces and colloidal forces (Israelachvili, 2011). Colloidal forces depend on the balance of electrostatic repulsion forces and van der Waals attractive forces. During brine injection, the electrical double layer in the water phase between particles is expanded, and the tendency to strip fines is increased. The stripped fines migrate and aggregate so that the oil coalesces. Subsequently, partial mobilisation of residual oil was observed via the detachment and flow of the fines (Figure 2.9), but only when the ionic strength was less than the critical flocculation concentration, at which the fines would otherwise aggregate (Sheng, 2014). Thus limited removal of mixed-wet fines from pore walls results in a change in the wetting pattern towards a more water wet situation, with the consequent increase in oil mobilisation and recovery.

In general, recent investigations have proven that clay-rich sandstone shows water-wet behaviour during low salinity waterflooding compared with high salinity brines where the clays remain undisturbed and therefore, the rock's initial wetting state is retained (Tang and Morrow, 1999a; Lager et al., 2007).

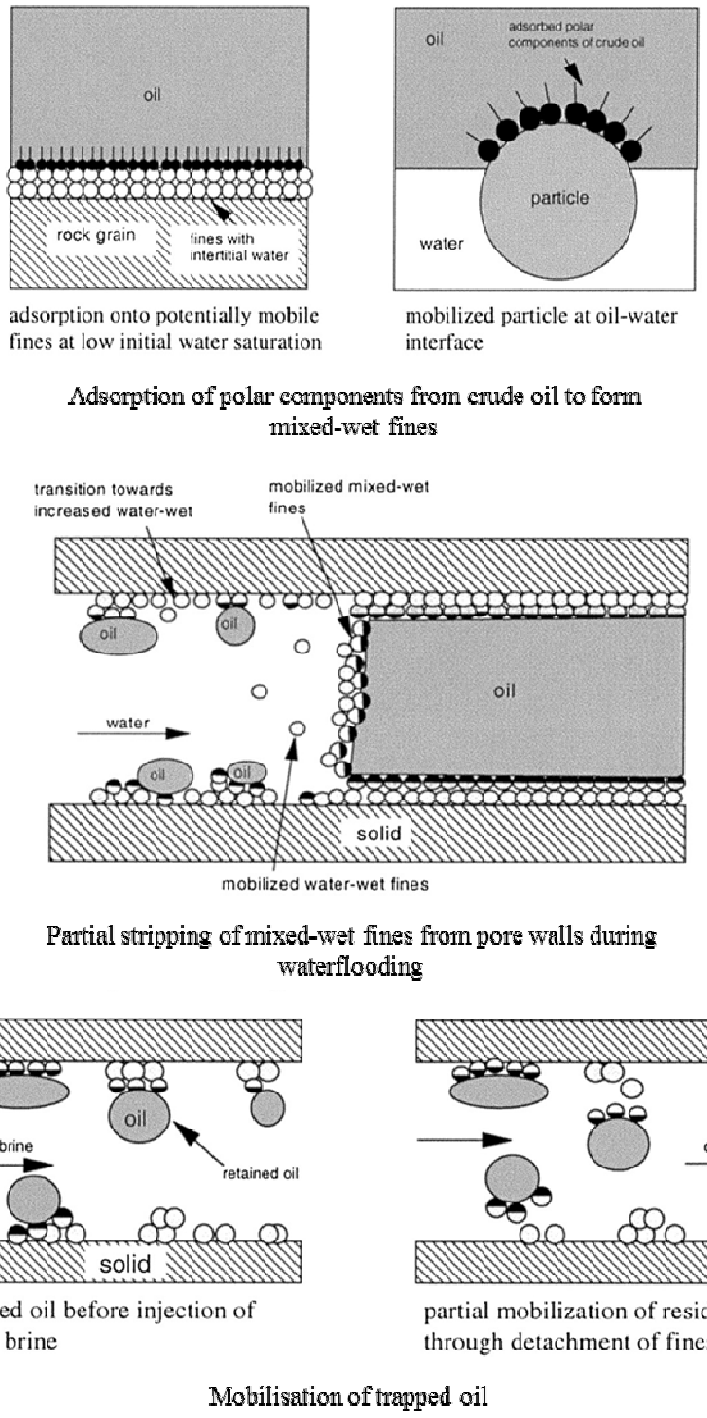

Figure 2.9: Schematic drawing showing the role of clay particles in mobilisation of oil during low salinity water flooding. Extracted from Tang and Morrow (1999).

The pioneering work by Bolandtaba et al. (2009) suggested a new explanation of how partial mobilization of fines provides the condition for enhancing oil recovery. In their study, Bolandtaba used a new experimental method (based on an analogy to the EOR technique) where a polymer or silica particles are dispersed in the injected solution. He suggested that the released clay particles due polymer or silica particles injection will plug

pore throats and reduce permeability. This would result in the water having to take different paths through the reservoir into non-swept pores and improve the microscopic sweep efficiency. Even though linked polymer particles are much smaller than the pore throats in sandstone, in several laboratory and field tests (in China), it was reported that injection of linked polymer gels is more efficient than frequent polymer flooding to improve oil recovery (Bolandtaba et al., 2009). Therefore, the observed increased oil recovery could be the result of improved microscopic sweep efficiency rather than the wettability change process (in a similar way to the explanation of how linked polymer gels improve oil recovery), so this mechanism appears in the pressure/permeability category.

Evidence Supporting Fine Migration Mechanism of Enhanced Oil Recovery Methods:

The fine migration mechanism is supported by several experiments where a recovery enhancement was reported. Khilar and Fogler (1984) results showed a 30% reduction in permeability when the pre-treatment was carried out with cesium-salt solutions, a reduction of more than 95% with a sodium-salt pre-treatment, and virtually no reduction when the cation in the solution was divalent. In core flooding experiments, Bernard (1967) observed additional oil recovery only when associated with an increase in pressure drop (at a constant rate) consistent with formation damage. Tang and Morrow (1999a) in series of experiments concluded that fine (particle) mobilization (mainly kaolinite) increased recovery associated with in increase in pressure drop. Their experiments were of two types (a) In a first batch Berea cores where fired to deactivate the clay to swelling, therefore stabilising the clays inside the sample. This cores where later flushed with different salinities but did not show the sensitivity of salinity on oil recovery on the contrary, experiments performed on as-received Berea showed an increase in oil recovery with the decrease in salinity.(b) in the second batch experiments cleaned and as-received cores where flushed with different brines, and those that were pre-cleaned showed a smaller increase in the oil recovered than those containing clay minerals.A result from both batches of experiments supports the proposed mechanism for fines migration.

Another reason behind the mechanism is the direct relation between the amounts of initial clay exists in the reservoir and the level of increased oil recovery. Berg et al. (2010) tried to capture this process using a video camera to view the release of crude oil droplets from a montmorillonite surface, within a flow cell. An average 66 % oil recovery was

recorded alongside clay swelling, but it was not possible to completely exclude the separation of clay together with oil, due to experimental restrictions.

Evidence Against Fine Migration Mechanism of an Enhanced Oil Recovery Method:

Although, there are supporting results, many contradicting indications exist. Fines migration has sometimes been observed in low salinity core flooding, but some researchers claim never to have seen particles of clay minerals in the effluent brine (Lager et al., 2007). Lager and co-workers have concluded that the 12 % increase in oil recovery and absence of fines in the effluent brine was due to an alteration in wettability condition, towards a more water-wet state. This is believed to be initiated by the divalent cation concentration within the reservoir, since aged core samples absent of Mg^{2+} and Ca^{2+} ions showed, for the first time in EOR investigations, no improved oil recovery results with low salinity water flooding. This concept was also proven by Rivet et al. (2010) when they did not see fines migration in effluent solution. In addition, tests with no evidence of fines release or any increase in pressure drop have been reported, despite an additional oil production (Lager et al., 2007, 2008a; Jerauld et al., 2008; Pu et al., 2008; Rivet et al., 2010). This suggests that fines migration and associated permeability changes are not always associated with the LSEOR and vice versa.

Regarding pressure drop, Soraya et al. (2009) further observed significant production of fines and an increased pressure drop during the experiment, but without any incremental oil recovery. However, lack of observation of fines in core flood out flow does not rule out the possible local migration of in-situ the fines at pore scale, especially when the core contains oil-wet particles, which are hard to detect in the produced oil phase (Fogden et al., 2011). In that sense, it was concluded that the presence of kaolinite in the core is essential for a successful low salinity project, but recently Cissokho et al. (2010) reported an increase of about 10% OOIP by injection of low salinity brine in kaolinite free sandstone cores that contained only illite and chlorite . This proved that improved oil recovery could be observed in cores that contain no kaolinite. Moreover, it is clear that clay swelling and/or fines migration cannot explain the LSEOR observed in carbonates (Mohan et al., 1993).

2.8.2. Multi-Component Ion Exchange

Multicomponent ionic exchange (MIE), is considered as one of the possible mechanisms that explain the causes of the low salinity effect (Lager et al., 2008). This mechanism explains the release of oil that is adsorbed directly to the clay mineral surfaces in a rock. Eight different mechanisms for adsorption of organic functional groups on soil minerals have been suggested by Sposito (Sposito, 2008), as shown in Table 2.5. Among these mechanisms, it is assumed that four out of eight (cation exchange, cation bridging, ligand exchange and van der Waals interactions) are the dominant adsorption mechanism (Lager et al., 2008) (see Figure 2.10). Cation exchange is a mechanism whereby positively charged organics ions, such as amine/ammonium groups or heterocyclic rings containing nitrogens, can replace the inorganics cations that usually charge balances a clay surface. Cation bridging is a weak adsorption mechanism in which a cation acts as a bridge between the negatively charged mineral surface and the functional groups of the organic material (Arnarson and Keil, 2000). Ligand exchange usually occurs, when carboxylate groups of acidic material substitute hydroxyl groups on the minerals surface. Van der Waals forces are short-range, attractive forces that are only important at high ionic strengths since high ionic strengths give low electrostatic repulsion forces according to DLVO theory. This allows particles to be located close to each other.

Various papers have reported on experimental observations that seem to validate the crucial role of the MIE mechanism for LSEOR. Lager et al. (2007) showed that the presence of divalent cations, especially Ca^{2+}, in the formation brine is the necessary condition for an increase in recovery by injecting a brine of low salinity (and low divalent ion content) (Lager et al., 2007). In addition, the results of geochemical analyses of the effluents, compared to the invading and connate brines, showed a strong reduction in the concentration of multivalent cations, especially in the concentration of Mg^{2+} indicating that this ion was strongly adsorbed, presumably by the clay minerals. A similar, but a much smaller change in the concentration of Ca^{2+} was also identified. However, from this study, it was not clear what the concentrations needed to be to achieve additional oil recovery. According to Lager et al. (2008), the concentrations of both these divalent ions need to be lower than the connate water concentrations, although not zero, but these constraints have been violated in many of the low salinity water floods and have still resulted in additional recovery (Suijkerbuijk et al., 2012; Fjelde et al., 2014; Yang et al., 2015). MIE has been proposed to work in the following way:

Table 2.5: Eight proposed adsorption mechanisms between organic compounds and clay minerals (Sposito, 2008).

Mechanism	**Organic functional group**
Cation Exchange	amino, ring NH, heterocyclic N (aromatic ring)
Cation Bridging	carboxylate, amines, carbonyl, alcoholic OH
Ligand Exchange	carboxylate
Van der Waals Interactions	uncharged organic units
Anion Exchange	carboxylate
Hydrogen Bonding	amino, carbonyl, carboxyl, phenolic OH
Water Bridging	amino, carboxylate, carbonyl, alcoholic OH
Protonation	amino, heterocyclic N, carbonyl, carboxylate

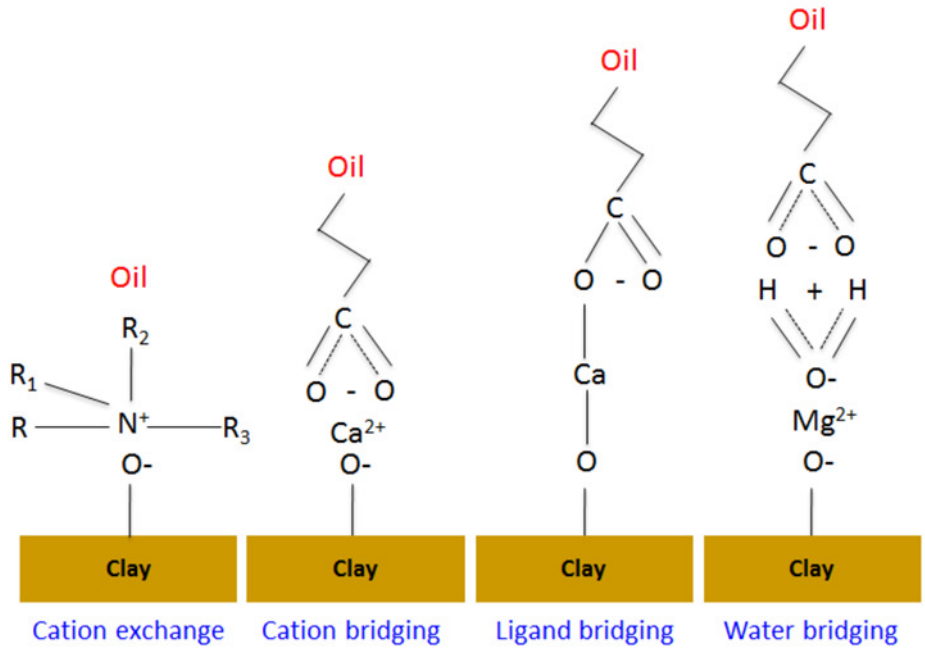

Figure 2.10: Representation of the mechanisms occurring between clay mineral surfaces and crude oil during low salinity water injection. Extracted from Lager et al. (2006)

When the low salinity water that contains low concentrations of Ca^{2+} and Mg^{2+} is injected into a rock core, monovalent ions will exchange with the multivalent cations bridging the oil molecules to the clay surface. Then the divalent ions exchange with either cationic organic compounds or with bases due to the change in ion exchange equilibrium. The consequences are the removal of polar organic compounds and the organometallic complexes from the mineral surfaces (clay minerals) leaving behind them uncomplexed monovalent cations. At a result, the bonded oil will become mobile, and the wettability is altered towards a more water-wet state (Lager et al., 2006, 2008; Lee et al., 2010).

Additionally, it has been suggested that injection of the low salinity brine leads to expansion of the electric double layer related to the MIE mechanism and thereby facilitate desorption of oil from the clay. This will lead to an increase in the water-wetness of the formation, as shown in Figure 2.10 (Lager et al., 2006; Lee et al., 2010; Al-adasani et al., 2012).

Evidence Supporting Multi-Component Ion Exchange Mechanism of Enhanced Oil Recovery Methods:

In general, MIE has been often observed when fresher formation water invades a more saline sandstone reservoirs having clay minerals (or other ion exchangers) and multivalent ions (e.g. (Valocchi et al., 1981; Appelo, 1994), and also in clay-bearing sandstone corefloods at the residual oil saturation (Almada et al., 2013). Lager et al. (2006) tested the link between MIE and the LSEOR by removing all Ca^{2+} and Mg^{2+} from the clay mineral surfaces in a sandstone core and then flooding with high and then low salinity NaCl brine. Lager et al. (2006) reported that, by replacing all Ca^{2+} and Mg^{2+} cations present on the mineral surface by Na^{+} prior to introducing oil and aging, the primary high salinity flood resulted in a higher recovery compared to the same test without removal of the multivalent cations. This sequence indicated that the higher water wetness of the minerals surfaces due to the absence of adsorption by ligand formation and multivalent cation bridging. Subsequently, they noted that oil recovery was not sensitive to salinity gradient when divalent cations were striped out from the formation brine. All these observations lead to the authors to conclude that MIE was the predominant mechanism behind increased oil recovery observed.

MIE can be invoked to explain the absence of a LSE observed by Tang and Morrow (1999) after firing of their Berea core sample, as this will prevention exchange with the clay minerals (Lager et al., 2006). Another supporting result for the MIE mechanism came from studying the macroscopic wettability alteration with the microscopic release of the hydrophobic layers (organic acid layers) from mineral surfaces in Berea sandstone particles during low salinity waterflooding. Recently, evidence to link MIE and the wettability alteration has been studied by Yang et al. (2015). Yang et al. (2015) found that lowering the salinity of the injected brine, especially the reduction of the multivalent cations Ca^{2+} ions, changes the electrical charges at both oil/brine and brine/rock interfaces to strongly negative, which causes higher repulsive forces between the two interfaces, and

as a result, the wet state was changed towards more water-wet state and markedly improved oil recovery.

Evidence Against Multi-Component Ion Exchange Mechanism of Enhanced Oil Recovery Methods:

Based on the MIE hypothesis, it is necessary that the invading brine has a low concentration of monovalent cations to replace (exchange) those connected to the clay minerals and forming organometallic complexes and promoting oil wetness. Although this seemed to be a logical conclusion, experimental evidence by Cissokho (Cissokho et al., 2010) indicates that the presence of divalent cations does not always leads to an increase in oil recovery when switching from a high salinity brine to a low salinity brine.

Lager et al. (2006) argue that clay minerals act as ion exchangers, suggesting those with high CEC are optimal, yet kaolinite has been closely associated with the LSE despite its relatively low CEC (Table 2.2; (Lager et al., 2007; Seccombe et al., 2008)). The MIE mechanism alone does not explain the several coreflooding investigations where the conditions for MIE were met, but no low salinity effects were observed. Ligthelm et al. (2009) observed that the double-layer expansion mechanism could take place as can explain numerous coreflooding experiments, (further elaborated in the following section).

2.8.3. Double-Layer Effects

Recently, the double-layer effect (EDL) has received considerable support to be the dominant mechanism for low salinity water flooding, rather than just a secondary effect (Nasralla and Nasr-El-Din, 2014). Ligthelm et al. (2009) suggested that expansion of the EDL at mineral-brine interfaces, as a result of low salinity brine injection, is the primary mechanism leading to the low salinity effects.

The thickness of the EDL (Figure 2.11) refers to the distance over which the ion distribution differs, which is a function of the electrolyte concentration and ion valency, measured regarding a zeta potential; the potential difference between the bulk low salinity water flood and the Stern layer (Lee et al., 2010; Sheng, 2014). From this, the thickness of the double layer is related to the concentration of ions in the water phase and the charge of the ions (Hiemenz and Rajagopalan, 1997; Lee et al., 2010; Nasralla and Nasr-El-Din, 2014a).

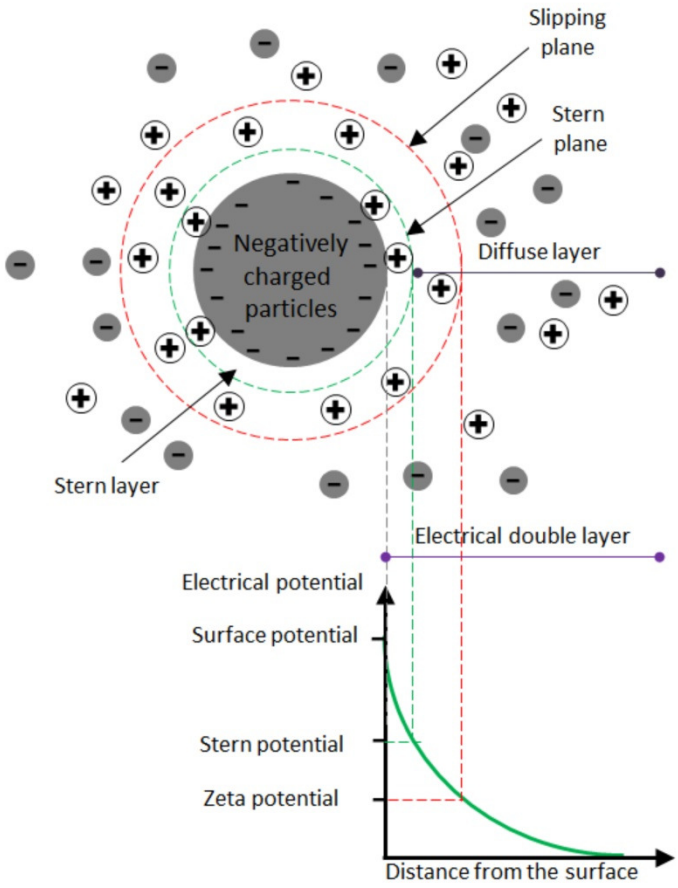

Figure 2.11: Schematic of the electrical double layer. Extracted from Nasralla and Nasr-El-Din (2014)

Ligthelm et al. (2009) argued that injection of low salinity brine causes the electrical double layer to expand, resulting in increased electrostatic repulsion between charged clay mineral surfaces in the sandstone and adsorbed polar oil components as there are less cations available to screen off the negative charge of the minerals, so the negative electric field produced by it increases its range (essentially).When this repulsion exceeds the binding forces for the organo-metallic complexes, the polar oil components desorb yielding more water-wet mineral surfaces, consistent with Derjaguin-Landau-Verwey-Overbeek (DLVO) theory and some previous studies of wettability alteration (Anderson, 1986a; Evans and Wennerström, 1999) and references therein; (Buckley et al., 1989, 1998). It should be noted that during a low salinity waterflooding, if the brine concentration is further reduced, DLE then causes clay particles to detach, leading to deflocculation, clay mobilization, and possibly formation damage (RezaeiDoust et al., 2011). Thus there is an optimum injection brine salinity which is low enough to cause desorption of oil and

wettability alteration, but not fines release and formation damage (see also (Almada et al., 2013)).

Evidence Supporting Double-Layer Effects Mechanism of Enhanced Oil Recovery Methods:

Several results support this mechanism as the most important in driving LSEOR. Ligthelm et al. (2009) performed flooding tests with formation brine of high salinity containing sodium, calcium, and magnesium. After the oil production had stopped, the injection composition was altered to contain only sodium chloride, with the same ionic strength, and a small increase in oil production was observed, which was attributed to the cation exchange mechanism. This was because it seemed reasonable to think that the injection of high salinity pure sodium chloride brine had stripped off the divalent cations attached to the rock surface. Then, the brine was changed to low salinity water with 100 times lower salinity, and a significant increase in recovery was observed. These results were explained by double layer expansion mechanism, and contribution of ion exchange was believed to be small.

Lee et al. (2010) from laboratory tests also proposed the double layer expansion as the main oil recovery mechanism. These authors reported the results of experiments to measure the thickness of the diffuse layer around silica particles dispersed in oil, with the electrochemical properties of the surface of the particles adjusted to be clay-like. The results indicate that the lower the salinity, the thicker the layer, with monovalent cations giving less variation in thickness than divalent ions. Moreover, it was suggested that the exchange of divalent ions for monovalent ions at low concentrations could enhance the thickness of the water layer. Double layer expansion is also investigated by Nasralla and Nasr-El-Din (2014); they claimed this theory is behind oil recovery. For this reason, they measured the zeta potential under low and high pH state in low salinity. It was suggested that reducing the pH of the low salinity brine makes the electrical charges at both oil-brine and brine-mineral interfaces weakly negative which reduce the repulsive forces between oil polar components and mineral surface and this will reduce the expansion of double layer. As a result, the mineral surfaces become strongly oil wet in the system. To obtain a positive effect from the low salinity injection, the pH of low salinity brine must be kept high to maximise the electrostatic repulsion forces between the mineral surfaces and polar oil compounds.

Double-layer expansion can be related to force measurements from atomic force microscopy (AFM). AFM has been used to measure the adhesion, between quartz grains removed from sandstone cores and CH_3 functionalised (mimic oil molecules) probes whilst immersed on brines of different salinity (Hilner et al. 2015). Hilner et al. (2015) found a significant decrease in adhesion between nonpolar oil molecules and natural quartz surfaces at a similar threshold salinity to that at which the low salinity effects is typically observed, and argued that DLE will always play a role in the low salinity even if other mechanisms also involved.

Evidence Against Double-Layer Effects Mechanism of Enhanced Oil Recovery Methods:

The DLE mechanism assumes that electrostatic forces play a critical role in wettability behaviours; specifically, it assumes that the polar oil components of interest and/or the brine/oil interface have the same polarity as the mineral surfaces at reservoir pH, so will be repelled as the salinity decreases yielding desorption and more water-wetting behaviour. This is often inconsistent with adhesion tests that suggest increased adhesion of oil as salinity decreases at fixed pH (Buckley et al., 1989, 1998).

Furthermore, DLE has failed so far to explain why the low salinity effect is not always observed with a low number of ionic strength. DLE as the fundamental explanation fro LSEOR still needs to be confirmed at the reservoirs conditions; as the majority of experimental studies have been confided to relatively low salinity and temperature conditions, as well as been perforemd on particle samples, and in the absence of crude oil (Hussain et al., 1996; Vinogradov et al., 2010; Nasralla and Nasr-El-Din, 2014b; Hou et al., 2015; Shehata and Nasr-El-Din, 2015; Yang et al., 2015). Recently, a molecular dynamic (MD) simulation study was undertook to attempt to understand the role of the EDL mechanism in LSEOR (Underwood et al., 2015). Underwood et al. (2015) performed MD computational simulations to investigate montmorillonite-organic matter interactions under different salinity condition. Results from computational simulation found that the pH surrounding clay's basal plane, and hence the protonation and charge of acid molecules, is the most important parameter driving LSEOR, whereas the electric double layer expansion is not able to fully explain the effects of low-salinity brine.

2.8.4. Local pH Effects

Austad et al. (2010) recently proposed a new chemical mechanism, based on experimental observations, to explain the effectiveness of LSEOR, along with several pre-conditions required. The proposed mechanism also invokes ion exchange but, in contrast to the MIE mechanism (Lager et al., 2006), they suggested that injection of low salinity brine leads to desorption of surface-active cations from clay mineral surfaces and replacement by protons. This causes a concomitant increase in local pH, which is sufficient to release previously adsorbed acidic and basic organic materials.

Initially, as in multicomponent ionic effects, organic matter (both acidic and basic) is adsorbed onto clay mineral surfaces via inorganic cation bridging, especially through bridging by multivalent ions such as Ca^{2+}, from the formation water. It has been found that, because of the presence of dissolved CO_2 and H_2S, the initial pH of the formation water is normally 5 or less. When the low salinity water is injected into the reservoir with an ion concentration much lower than that in the initial formation brine, equilibrium is achieved through brine and rock interactions, specifically through the desorption (and replacement) of cations, especially multivalent ions like Ca^{2+}. Protons, H^+, from the water close to the clay mineral surfaces, can adsorb onto the clay and replace the Ca^{2+}. As a result, the local pH close to the clay surface increases, as in the following equation (Austad et al., 2010a):

$$\text{Clay-}Ca^{2+} + H_2O \leftrightharpoons \text{Clay-}H^+ + Ca^{2+} + OH^- \quad (2.9)$$

The increased local pH close to the clay mineral surfaces, and a reaction between OH^- and the adsorbed acidic and protonated basic material causes the organic material to desorb from the clay surface. Consequently, the rock surface as a whole becomes more water wet and increased oil recovery is observed. This process is shown by equations 2.10 and 2.11 and in the diagram on Figure 2.12:

$$\text{Clay-}RNH_3 + OH^- \leftrightharpoons \text{Clay} + RNH_2 + H_2O \quad (2.10)$$

$$\text{Clay-}RCOOH + OH^- \leftrightharpoons \text{Clay} + RCOO^- + H_2O \quad (2.11)$$

The source of OH^- comes mostly from injected brines, as the concentration of OH^- in the formation is relatively small. Finally competition for the OH^- ions will occur through interactions with divalent cations, specially Mg^{2+}, which have a relatively high affinity for this anion.

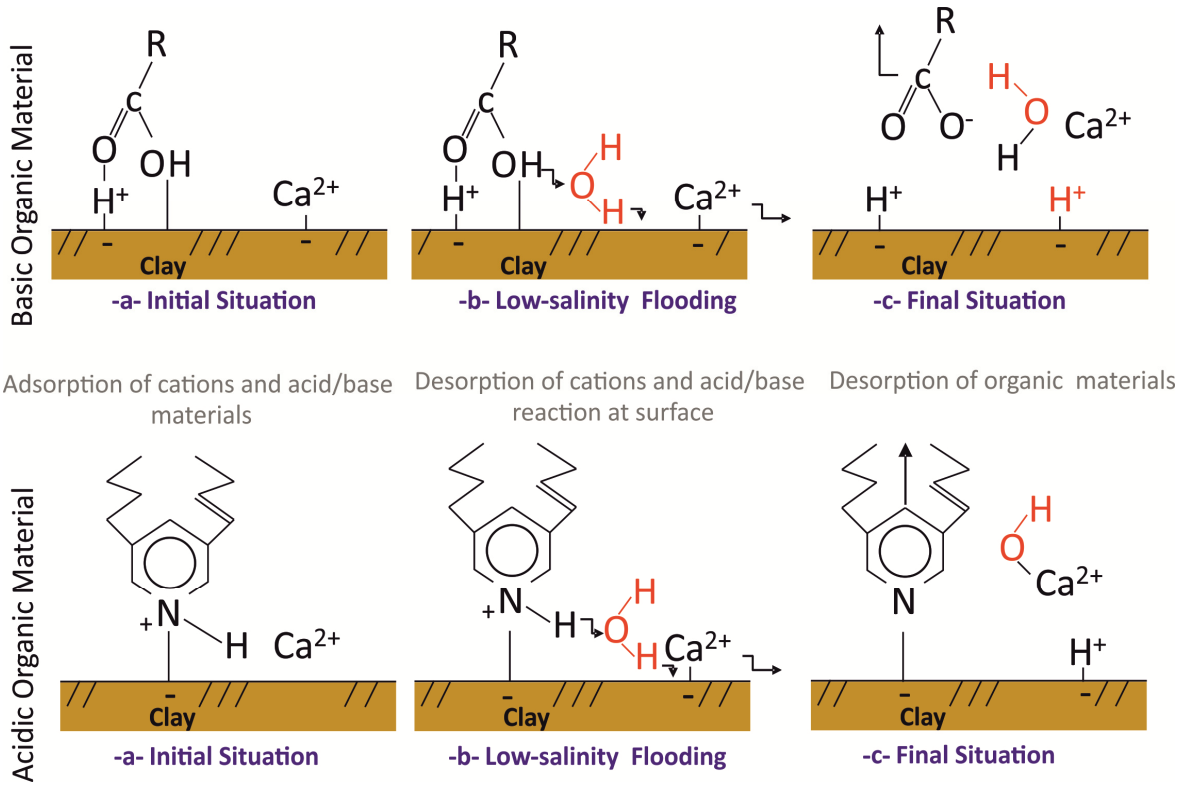

Figure 2.12: Simple schematic of proposed mechanism showing desorption of basic (upper) and acidic (lower) polar components of oil in low salinity water brines. Extracted from Austad et al. (2010b).

Evidence Supporting Local pH Effects Mechanism of Enhanced Oil Recovery Methods:

Austad and co-workers observed that many coreflooding experiments show an increase in pH following the injection of low salinity brine (e.g.(Kia et al. ,1987)); moreover, Rezaeidoust et al. (2010) found that pH increase depended upon the prevalent cation affinity to clay mineral surfaces in sandstone rock, with low salinity NaCl brines displaying the largest pH increase consistent with the low affinity of Na^+. It also reported that a strong pH dependence of both acidic and basic organic adsorption on clay minerals (Aksulu et al., 2012; Rezaeidoust et al., 2010; Austad et al., 2010), consistent with the requirements of their proposed mechanism. Rezaeidoust et al. (2010) injected high salinity NaCl brine into a set of a cores containing crude oil and $CaCl_2$ brine; then reported that the variations observed in the experimental results could be related to the differing affinities of Na^+ and Ca^{2+} cations toward the clay mineral surfaces which is consistent with the proposed mechanism.

Evidence Against Local pH Effects Mechanism of Enhanced Oil Recovery Methods:

Several core flooding experimental studies report little or no change in effluent pH associated with the low salinity effect; moreover, in the reservoir, such a global pH change is unlikely to occur owing to the presence of pH buffers such as CO_3^{2-} species. Several studied have observed effluent pH increases in experiments but no associated low salinity effects (Cissokho et al., 2010; Hege et al., 2010).The initial investigation of pH effect was reported by (Kia et al.,1987). Experiments carried out on Berea sandstones by Kia et al. (1987) were undertaken where the injection of fresh water and salts, at ca. pH 6.5, into core plugs, generated a measurable pH increase within the effluent of up to 8.3. This, however, does not provide substantial evidence for increased oil recovery by low salinity water flooding but appears to disprove the associated reduced interfacial tension theory, which relies on an alkali environment of pH > 9 to drive in-situ surfactant formation and subsequent oil release (Sheng, 2014).

Austad et al. (2010a) proposed that the decrease in Mg^{2+} and Ca^{2+} observed in the laboratory experiments of Lager et al. (2006) was caused by deposition of $Mg(OH)_2$ and $Ca(OH)_2$ rather than MIE mechanism. Ca $(OH)_2$ deposition, however, was predicted to occur only at pH > 11; such high pH was not reported.

Finally, Austad (2013) has concluded that the resulting pH of low salinity water flooding cannot possibly be used to determine or verify a mechanism for EOR because the outcome is entirely reliant on the chemical reactions within the reservoir rock and hence the sandstone composition. For example, the solubilisation of trace amounts of calcite, which cement quartz grains together, may result in an increase in effluent pH but have no impact on the magnitude of oil recovery (Kia et al., 1987). It should be noted that the pH mechanism does not explain those coreflooding experiments where pH change was recorded and the other low salinity effect requirements were met, but no LSE was observed. Studies are still ongoing to confirm or refute the proposed mechanism.

2.8.5. Other Mechanisms

Apart from the electro- and pressure-osmosis explanations, all mechanisms invoked to explain LSEOR involve chemical reactions at the rock/fluid interface that lead to wettability changes. This means that all the methods, except osmosis, could have been placed in the “alteration of wettability” category. In situ osmosis may be an intuitive

explanation for how low salinity water works, as the mechanism, matches well with the presence of clay minerals, high salinity connate water and low salinity injection water. If clay particles form tiny membranes in pore throats the pressure will rise on the high salinity side; which may lead to the displacement of oil droplets under an osmotic pressure gradient. Sandengen and Arntzen (2013) proposed that such osmotic gradient relocates oil by expanding an otherwise inaccessible aqueous phase in a porous rock medium.

This mechanism should work regardless of the composition of crude oil. However, the experimental core study by Rivet et al. (2010) and Buckley (2009) using mineral oil (that is, oil without polar compounds) show no enhanced recovery with injection low salinity water, so this explanation is no longer popular. Finally, according to Buckley (2009), low salinity water flooding also works in reservoirs with low salinity connate brine, which again showing fails the osmosis theory.

2.9. References

Abdallah, W. et al., 2007, Fundamentals of Wettability: Oilfield Review, p. 17.

Ahmed, T., 2010, Chapter 14 - Principles of Waterflooding, *in* Reservoir Engineering Handbook (Fourth Edition): Boston, Gulf Professional Publishing, p. 909–1095.

Ahmed, T., and P. D. McKinney, 2005, 2 - Water Influx, *in* Advanced Reservoir Engineering: Burlington, Gulf Professional Publishing, p. 149–185.

Aksulu, H., D. Håmsø, S. Strand, T. Puntervold, and T. Austad, 2012, Evaluation of Low-Salinity Enhanced Oil Recovery Effects in Sandstone: Effects of the Temperature and pH Gradient: Energy & Fuels, v. 26, no. 6, p. 3497–3503, doi:10.1021/ef300162n.

Al-adasani, A., B. Bai, and Y.-S. Wu, 2012, Investigating Low Salinity Waterflooding Recovery Mechanisms in Carbonate Reservoirs: Society of Petroleum Engineers, doi:10.2118/155560-MS.

Alagic, E., K. Spildo, A. Skauge, and J. Solbakken, 2011, Effect of crude oil ageing on low salinity and low salinity surfactant flooding: Journal of Petroleum Science and Engineering, v. 78, no. 2, p. 220–227, doi:10.1016/j.petrol.2011.06.021.

Al-Maamari, R. S. H., and J. S. Buckley, 2003, Asphaltene Precipitation and Alteration of Wetting: The Potential for Wettability Changes During Oil Production: SPE Reservoir Evaluation & Engineering, v. 6, no. 4, p. 210–214, doi:10.2118/84938-PA.

Almada, P., M. B, S. G. J. Pieterse, A. H. M. Marcelis, V. Haasterecht, M. J. T, N. J. Brussee, V. D. Linde, and H. A, 2013, Experimental Investigation on the Effects of Very Low Salinity on Middle Eastern Sandstone Corefloods: Society of Petroleum Engineers, doi:10.2118/165180-MS.

Alotaibi, M. B., R. Azmy, and H. A. Nasr-El-Din, 2010, A Comprehensive EOR Study Using Low Salinity Water in Sandstone Reservoirs: Society of Petroleum Engineers, doi:10.2118/129976-MS.

Al-Shafei, M. A., and T. M. Okasha, 2009, Wettability Studies at the Pore Level of Saudi Aramco Reservoirs: Society of Petroleum Engineers, doi:10.2118/126088-MS.

Alvarado, V., and E. Manrique, 2010, Enhanced Oil Recovery: An Update Review: Energies, v. 3, no. 9, p. 1529–1575, doi:10.3390/en3091529.

Amaefule, J. O., and L. L. Handy, 1982, The Effect of Interfacial Tensions on Relative Oil/Water Permeabilities of Consolidated Porous Media: Society of Petroleum Engineers Journal, v. 22, no. 3, p. 371–381, doi:10.2118/9783-PA.

Anderson, W. G., 1986a, Wettability Literature Survey- Part 1: Rock/Oil/Brine Interactions and the Effects of Core Handling on Wettability: Journal of Petroleum Technology, v. 38, no. 10, p. 1,125-1,144, doi:10.2118/13932-PA.

Anderson, W., 1986b, Wettability Literature Survey- Part 2: Wettability Measurement: Journal of Petroleum Technology, v. 38, no. 11, p. 1,246-1,262, doi:10.2118/13933-PA.

Anderson, W. G., 1987a, Wettability Literature Survey- Part 4: Effects of Wettability on Capillary Pressure: Journal of Petroleum Technology, v. 39, no. 10, p. 1,283-1,300, doi:10.2118/15271-PA.

Anderson, W. G., 1987b, Wettability Literature Survey Part 5: The Effects of Wettability on Relative Permeability: Journal of Petroleum Technology, v. 39, no. 11, p. 1,453-1,468, doi:10.2118/16323-PA.

Anderson, W. G., 1986c, Wettability Literature Survey-Part 3: The Effects of Wettability on the Electrical Properties of Porous Media: Journal of Petroleum Technology, v. 38, no. 12, p. 1,371-1,378, doi:10.2118/13934-PA.

Appelo, C. a. J., 1994, Cation and proton exchange, pH variations, and carbonate reactions in a freshening aquifer: Water Resources Research, v. 30, no. 10, p. 2793–2805, doi:10.1029/94WR01048.

Arnarson, T. S., and R. G. Keil, 2000, Mechanisms of pore water organic matter adsorption to montmorillonite: Marine Chemistry, v. 71, no. 3–4, p. 309–320, doi:10.1016/S0304-4203(00)00059-1.

Austad, T., 2013, Chapter 13 - Water-Based EOR in Carbonates and Sandstones: New Chemical Understanding of the EOR Potential Using "Smart Water" A- Sheng, James J., *in* Enhanced Oil Recovery Field Case Studies: Boston, Gulf Professional Publishing, p. 301–335.

Austad, T., A. Rezaeidoust, and T. Puntervold, 2010a, Chemical Mechanism of Low Salinity Water Flooding in Sandstone Reservoirs: Society of Petroleum Engineers, doi:10.2118/129767-MS.

Austad, T., S. Strand, M. V. Madland, T. Puntervold, and R. I. Korsnes, 2008, Seawater in Chalk: An EOR and Compaction Fluid: SPE Reservoir Evaluation & Engineering, v. 11, no. 4, p. 648–654, doi:10.2118/118431-PA.

Baptist, O. C., and E. J. White, 1957, Clay Content and Capillary Behavior of Wyoming Reservoir Sands.

Beatty, S. M., and J. E. Smith, 2010, Fractional wettability and contact angle dynamics in burned water repellent soils: Journal of Hydrology, v. 391, no. 1–2, p. 97–108, doi:10.1016/j.jhydrol.2010.07.007.

Benner, F. C., and F. E. Bartel, 1941, The Effect Of Polar Impurities Upon Capillary And Surface Phenomena In Petroleum Production: American Petroleum Institute.

Bera, A., K. S, K. Ojha, T. Kumar, and A. Mandal, 2012, Mechanistic Study of Wettability Alteration of Quartz Surface Induced by Nonionic Surfactants and Interaction between Crude Oil and Quartz in the Presence of Sodium Chloride Salt: Energy & Fuels, v. 26, no. 6, p. 3634–3643, doi:10.1021/ef300472k.

Berg, S., A. W. Cense, E. Jansen, and K. Bakker, 2010, Direct Experimental Evidence of Wettability Modification By Low Salinity: Petrophysics, v. 51, no. 5.

Bernard, G. G., 1967, Effect of Floodwater Salinity on Recovery Of Oil from Cores Containing Clays: Society of Petroleum Engineers, doi:10.2118/1725-MS.

Blatt, H., 1982, Sedimentary petrology.

Boggs, S., 2009, Petrology of Sedimentary Rocks: <http://www.cambridge.org/gb/academic/subjects/earth-and-environmental-science/sedimentology-and-stratigraphy/petrology-sedimentary-rocks-2nd-edition?format=HB&isbn=9780521897167> (accessed October 26, 2016).

Bolandtaba, S. F., A. Skauge, and E. MacKay, 2009, Pore Scale Modelling of Linked Polymer Solution (LPS) – A New EOR Process: doi:10.3997/2214-4609.201404822.

Borysenko, A., B. Clennell, R. Sedev, I. Burgar, J. Ralston, M. Raven, D. Dewhurst, and K. Liu, 2009, Experimental investigations of the wettability of clays and shales: Journal of Geophysical Research: Solid Earth, v. 114, no. B7, p. B07202, doi:10.1029/2008JB005928.

Bradford, S. A., and F. J. Leij, 1995, Fractional wettability effects on two-and three-fluid capillary pressure-saturation relations: Journal of Contaminant Hydrology, v. 20, no. 1, p. 89–109, doi:10.1016/0169-7722(95)00027-S.

Buckley, J. S., 1995, Asphaltene Precipitation and Crude Oil Wetting: SPE Advanced Technology Series, v. 3, no. 1, p. 53–59, doi:10.2118/26675-PA.

Buckley, J. S., 2009, “Low Salinity Waterflooding - An Overview of Likely Mechanisms,” on-line presentation.

Buckley, J. S., 1996, Mechanisms and consequences of wettability alteration by crude oils, Ph.D.: Heriot-Watt University.

Buckley, J. S., and Y. Liu, 1998, Some mechanisms of crude oil/brine/solid interactions: Journal of Petroleum Science and Engineering, v. 20, no. 3–4, p. 155–160, doi:10.1016/S0920-4105(98)00015-1.

Buckley, J. S., Y. Liu, and S. Monsterleet, 1998, Mechanisms of Wetting Alteration by Crude Oils: SPE Journal, v. 3, no. 1, p. 54–61, doi:10.2118/37230-PA.

Buckley, J., and N. Morrow, 2010, Improved Oil Recovery by Low Salinity Waterflooding, *in* University of Calgary, Calgary, Alberta, Canada.

Buckley, J. S., K. Takamura, and N. R. Morrow, 1989, Influence of Electrical Surface Charges on the Wetting Properties of Crude Oils: SPE Reservoir Engineering, v. 4, no. 3, p. 332–340, doi:10.2118/16964-PA.

Chen, G., G. Du, G. Zhang, Q. Wang, C. Lv, and J. Chen, 2011, Chlorite cement and its effect on the reservoir quality of sandstones from the Panyu low-uplift, Pearl River

Mouth Basin: Petroleum Science, v. 8, no. 2, p. 143–150, doi:10.1007/s12182-011-0127-z.

Cissokho, M., H. Bertin, S. Boussour, P. Cordier, and G. Hamon, 2010, Low Salinity Oil Recovery On Clayey Sandstone: Experimental Study: Petrophysics, v. 51, no. 5.

Civan, F., 2007, CHAPTER 1 - OVERVIEW OF FORMATION DAMAGE, *in* Reservoir Formation Damage (Second Edition): Burlington, Gulf Professional Publishing, p. 1–9.

Civan, F., 2015, Reservoir Formation Damage: Gulf Professional Publishing, 1044 p.

Civan, F., 2000, Reservoir Formation Damage: Fundamentals, Modeling, Assessment, and Mitigation: Gulf Professional Publishing, 768 p.

Civan, F., R. M. Knapp, and H. A. Ohen, 1989, Alteration of permeability by fine particle processes: Journal of Petroleum Science and Engineering, v. 3, no. 1, p. 65–79, doi:10.1016/0920-4105(89)90033-8.

Clementz, D. M., 1977, Clay Stabilization in Sandstones Through Adsorption of Petroleum Heavy Ends: Journal of Petroleum Technology, v. 29, no. 9, p. 1,061-1,066, doi:10.2118/6217-PA.

Cuiec, L. E., 1975, Restoration of the Natural State of Core Samples: Society of Petroleum Engineers, doi:10.2118/5634-MS.

Cuiec, L., 1984, Rock/Crude-Oil Interactions and Wettability: An Attempt To Understand Their Interrelation: Society of Petroleum Engineers, doi:10.2118/13211-MS.

Deer, W. A., P. R. A. Howie, and P. J. Zussman, 1992, An Introduction to the Rock Forming Minerals: Prentice Hall, 712 p.

Denekas, M. O., C. C. Mattax, and G. T. Davis, 1959, Effects of Crude Oil Components on Rock Wettability.

Derjaguin, and L. Landau, 1941, Theory of the Stability of Strongly Charged Lyophobic Sols and of the Adhesion of Strongly Charged Particles in Solutions of Electrolytes: Acta Phys. Chim. URSS, v. 14, p. 633–662.

Donald, A. M., 2003, The use of environmental scanning electron microscopy for imaging wet and insulating materials: Nature Materials, v. 2, no. 8, p. 511–516, doi:10.1038/nmat898.

Donald, A. M., C. He, C. P. Royall, M. Sferrazza, N. A. Stelmashenko, and B. L. Thiel, 2000, Applications of environmental scanning electron microscopy to colloidal aggregation and film formation: Colloids and Surfaces A: Physicochemical and Engineering Aspects, v. 174, no. 1–2, p. 37–53, doi:10.1016/S0927-7757(00)00520-3.

Donaldson, E. C., R. D. Thomas, and P. B. Lorenz, 1969, Wettability Determination and Its Effect on Recovery Efficiency: Society of Petroleum Engineers Journal, v. 9, no. 1, p. 13–20, doi:10.2118/2338-PA.

Drummond, C., and J. Israelachvili, 2004, Fundamental studies of crude oil–surface water interactions and its relationship to reservoir wettability: Journal of Petroleum Science and Engineering, v. 45, no. 1–2, p. 61–81, doi:10.1016/j.petrol.2004.04.007.

Drummond, C., and J. Israelachvili, 2002, Surface forces and wettability: Journal of Petroleum Science and Engineering, v. 33, no. 1–3, p. 123–133, doi:10.1016/S0920-4105(01)00180-2.

Ehrenberg, S. N., P. Aagaard, M. J. Wilson, A. R. Fraser, and D. M. L. Duthie, 1993, Depth-dependent transformation of kaolinite to dickite in sandstones of the Norwegian continental shelf: Clay Minerals, v. 28, no. 3, p. 325–352.

Ehrenberg, S. N., and P. H. Nadeau, 2005, Sandstone vs. carbonate petroleum reservoirs: A global perspective on porosity-depth and porosity-permeability relationships: AAPG Bulletin, v. 89, no. 4, p. 435–445, doi:10.1306/11230404071.

Evans, D. F., and H. Wennerström, 1999, The Colloidal Domain: Where Physics, Chemistry and Biology Meet: New York, Wiley-Blackwell, 672 p.

Farzaneh, S. A., M. Sohrabi, J. R. Mills, P. Mahzari, and K. Ahmed, 2015, Oil Recovery Improvement from Low Salinity Waterflooding in a Clay-free Silica Core: doi:10.3997/2214-4609.201412100.

Fatt, I., and W. A. J. Klikoff, 1959, Effect of Fractional Wettability on Multiphase Flow Through Porous Media: Journal of Petroleum Technology, v. 11, no. 10, p. 71–76, doi:10.2118/1275-G.

Fjelde, I., A. V. Omekeh, and Y. A. Sokama-Neuyam, 2014, Low Salinity Water Flooding: Effect Of Crude Oil Composition: Society of Petroleum Engineers, doi:10.2118/169090-MS.

Fogden, A., 2011, Effect of Water Salinity and pH on the Wettability of a Model Substrate: Energy & Fuels, v. 25, no. 11, p. 5113–5125, doi:10.1021/ef200920s.

Fogden, A., M. Kumar, N. R. Morrow, and J. S. Buckley, 2011, Mobilization of Fine Particles during Flooding of Sandstones and Possible Relations to Enhanced Oil Recovery: Energy & Fuels, v. 25, no. 4, p. 1605–1616, doi:10.1021/ef101572n.

Gaonkar, A. G., 1992, Effects of salt, temperature, and surfactants on the interfacial tension behavior of a vegetable oil/water system: Journal of Colloid and Interface Science, v. 149, no. 1, p. 256–260, doi:10.1016/0021-9797(92)90412-F.

Glover, P. W., 2011, Chapter 7: Wettability. Formation Evaluation MSc Cource Notes.

Glover, P. W., 2002, Formation evaluation: 79-80 p.

Goyal, K. L., 2007, A review of: “Drilling and Drilling Fluids”, by G. V. Chilingarian and P. Vorabutr; published in 1981 by Elsevier Scientific Publishing Co., P.O. Box 211, 1000 AE Amsterdam, The Netherlands; distributed by El-sevier/North-Holland, Inc., 52 Vanderbilt Avenue, New York, N. Y. 10017; 767 pp., photos, illustrations,

appendices, glossary; $136.50, U.S.: 1228.50, Rs: Energy Sources, doi:10.1080/00908318308928521.

Green, D. W., and G. P. Willhite, 1998a, Enhanced Oil Recovery. SPE textbook series.: Richardson, Texas, Society of Petroleum Engineers, 545 p.

Grim, R. E., 1968, Clay mineralogy: McGraw-Hill, 616 p.

Grim, R. E., 1953, Clay mineralogy: McGraw-Hill, 408 p.

Guan, H., D. Brougham, K. S. Sorbie, and K. J. Packer, 2002, Wettability effects in a sandstone reservoir and outcrop cores from NMR relaxation time distributions: Journal of Petroleum Science and Engineering, v. 34, no. 1–4, p. 35–54, doi:10.1016/S0920-4105(02)00151-1.

Guan, H., G. M. Graham, and A. Juhasz, 2003, Investigation of Wettability Alteration Following Scale Inhibitor Adsorption onto Carbonate and Clastic Reservoir Core Material - Static Tests and ESEM Studies: Society of Petroleum Engineers, doi:10.2118/80231-MS.

Gupta, V., M. A. Hampton, J. R. Stokes, A. V. Nguyen, and J. D. Miller, 2011, Particle interactions in kaolinite suspensions and corresponding aggregate structures: Journal of Colloid and Interface Science, v. 359, no. 1, p. 95–103, doi:10.1016/j.jcis.2011.03.043.

Gupta, V., and J. D. Miller, 2010, Surface force measurements at the basal planes of ordered kaolinite particles: Journal of Colloid and Interface Science, v. 344, no. 2, p. 362–371, doi:10.1016/j.jcis.2010.01.012.

Hamon, G., 2000, Field-Wide Variations of Wettability: Society of Petroleum Engineers, doi:10.2118/63144-MS.

Hege, C., Wideroee, H. Rueslaatten, T. Boassen, C. M. Crescente, M. Raphaug, G. H. Soerland, and H. Urkedal, 2010, Investigation of Low Salinity Water Flooding by NMR and Cryo ESEM: n paper sca 2010-26 presented at the 24th International Symposium of Core Analysts, Halifax, Canada (pp. 4-7).

Hiemenz, P. C., and R. Rajagopalan, 1997, Principles of Colloid and Surface Chemistry, Third Edition, Revised and Expanded: CRC Press, 676 p.

Hilner, E., M. P. Andersson, T. Hassenkam, J. Matthiesen, P. A. Salino, and S. L. S. Stipp, 2015, The effect of ionic strength on oil adhesion in sandstone – the search for the low salinity mechanism: Scientific Reports, v. 5, p. 9933, doi:10.1038/srep09933.

Hjelmeland, O. S., and L. E. Larrondo, 1986, Experimental Investigation of the Effects of Temperature, Pressure, and Crude Oil Composition on Interfacial Properties: SPE Reservoir Engineering, v. 1, no. 4, p. 321–328, doi:10.2118/12124-PA.

Hou, B., Y. Wang, and Y. Huang, 2015, Mechanistic study of wettability alteration of oil-wet sandstone surface using different surfactants: Applied Surface Science, v. 330, p. 56–64, doi:10.1016/j.apsusc.2014.12.185.

Hussain, S. A., Ş. Demirci, and G. Özbayoğlu, 1996, Zeta Potential Measurements on Three Clays from Turkey and Effects of Clays on Coal Flotation: Journal of Colloid and Interface Science, v. 184, no. 2, p. 535–541, doi:10.1006/jcis.1996.0649.

Israelachvili, J. N., 2011, 17 - Adhesion and Wetting Phenomena, *in* Intermolecular and Surface Forces (Third Edition): San Diego, Academic Press, p. 415–467.

Jadhunandan, P. P., and N. R. Morrow, 1995, Effect of Wettability on Waterflood Recovery for Crude-Oil/Brine/Rock Systems: SPE Reservoir Engineering, v. 10, no. 1, p. 40–46, doi:10.2118/22597-PA.

Jerauld, G. R., K. J. Webb, C.-Y. Lin, and J. C. Seccombe, 2008, Modeling Low-Salinity Waterflooding: SPE Reservoir Evaluation & Engineering, v. 11, no. 6, p. 1,000-1,012, doi:10.2118/102239-PA.

Kaminsky, R., and C. J. Radke, 1997, Asphaltenes, Water Films, and Wettability Reversal: SPE Journal, v. 2, no. 4, p. 485–493, doi:10.2118/39087-PA.

Kareem, R., P. Cubillas, H. J.Riggs, J. Gluyas, D. R. Gröcke, and H. C. Greenwell, 2016, Insights of Berea Sandstone Wettability Alteration as A-model of Sandstone Reservoir through Contact Angle Measurement: doi:10.3997/2214-4609.201600762.

Khajepour, H., M. Mahmoodi, D. Biria, and S. Ayatollahi, 2014, Investigation of wettability alteration through relative permeability measurement during MEOR process: A micromodel study: Journal of Petroleum Science and Engineering, v. 120, p. 10–17, doi:10.1016/j.petrol.2014.05.022.

Khilar, K. C., and H. S. Fogler, 1984, The existence of a critical salt concentration for particle release: Journal of Colloid and Interface Science, v. 101, no. 1, p. 214–224, doi:10.1016/0021-9797(84)90021-3.

Kia, S. F., H. S. Fogler, M. G. Reed, and R. N. Vaidya, 1987, Effect of Salt Composition on Clay Release in Berea Sandstones: SPE Production Engineering, v. 2, no. 4, p. 277–283, doi:10.2118/15318-PA.

Kumar, B., H. Yarranton, and E. Baydak, 2012, Effect of Salinity on the Interfacial Tension of Crude Oil: doi:10.3997/2214-4609.20143757.

Labedi, R., 1992, Improved correlations for predicting the viscosity of light crudes: Journal of Petroleum Science and Engineering, v. 8, no. 3, p. 221–234, doi:10.1016/0920-4105(92)90035-Y.

Lager, A., K. J. Webb, and C. J. J. Black, 2007, Impact of Brine Chemistry on Oil Recovery.

Lager, A., K. J. Webb, C. J. J. Black, M. Singleton, and K. S. Sorbie, 2008, Low Salinity Oil Recovery - An Experimental Investigation1: Petrophysics, v. 49, no. 1.

Lager, A., K. Webb, C. J. Black, M. Singleton, and K. Sorbie, 2006, Low salinity oil recovery an experimental investigation Paper, *in* Torndheim,Norway: Paper SCA 2006-36.

Lanson, B., D. Beaufort, G. Berger, A. Bauer, A. Cassagnabère, and A. Meunier, 2002, Authigenic kaolin and illitic minerals during burial diagenesis of sandstones: a review: Clay Minerals, v. 37, no. 1, p. 1–22, doi:10.1180/0009855023710014.

Lee, S. Y., K. J. Webb, I. Collins, A. Lager, S. Clarke, O&apos, M. Sullivan, A. Routh, and X. Wang, 2010, Low Salinity Oil Recovery: Increasing Understanding of the Underlying Mechanisms: Society of Petroleum Engineers, doi:10.2118/129722-MS.

Lever, A., and R. A. Dawe, 1984, Water-Sensitivity and Migration of Fines in the Hopeman Sandstone: Journal of Petroleum Geology, v. 7, no. 1, p. 97–107, doi:10.1111/j.1747-5457.1984.tb00165.x.

Ligthelm, D. J., J. Gronsveld, J. Hofman, N. Brussee, F. Marcelis, and H. van der Linde, 2009, Novel Waterflooding Strategy By Manipulation Of Injection Brine Composition.: Society of Petroleum Engineers, doi:10.2118/119835-MS.

Liu, L., and J. S. Buckley, 1999, Alteration of wetting of mica surfaces: Journal of Petroleum Science and Engineering, v. 24, no. 2–4, p. 75–83, doi:10.1016/S0920-4105(99)00050-9.

Liu, J., H. Vu, S. S. Yoon, R. A. Jepsen, and G. Aguilar, 2010, SPLASHING PHENOMENA DURING LIQUID DROPLET IMPACT: Atomization and Sprays, v. 20, no. 4, doi:10.1615/AtomizSpr.v20.i4.30.

Liu, Y., W. Yao, G. Wang, Y. Wang, A. S. Moita, Z. Han, and L. Ren, 2016, Reversibly switchable wettability on aluminum alloy substrate corresponding to different pH droplet and its corrosion resistance: Chemical Engineering Journal, v. 303, p. 565–574, doi:10.1016/j.cej.2016.06.038.

Maghzi, A., A. Mohebbi, R. Kharrat, and M. H. Ghazanfari, 2010, Pore-Scale Monitoring of Wettability Alteration by Silica Nanoparticles During Polymer Flooding to Heavy Oil in a Five-Spot Glass Micromodel: Transport in Porous Media, v. 87, no. 3, p. 653–664, doi:10.1007/s11242-010-9696-3.

McAulay, G. E., 1994, Palaeohydrodynamic Fluid Flow Regimes During Diagenesis of the Brent Group in the Hutton-NW Hutton Reservoirs: Constraints from Oxygen Isotope Studies of Authigenic Kaolin and Reverse Flexural Modelling: Clay Minerals, v. 29, no. 4, p. 609–625, doi:10.1180/claymin.1994.029.4.16.

McCaffery, F. G., 1972, Measurement of Interfacial Tensions And Contact Angles At High Temperature And Pressure: Journal of Canadian Petroleum Technology, v. 11, no. 3, doi:10.2118/72-03-03.

McDougall, S. R., and K. S. Sorbie, 1995, The Impact of Wettability on Waterflooding: Pore-Scale Simulation: SPE Reservoir Engineering, v. 10, no. 3, p. 208–213, doi:10.2118/25271-PA.

McGuire, P. L., J. R. Chatham, F. K. Paskvan, D. M. Sommer, and F. H. Carini, 2005, Low Salinity Oil Recovery: An Exciting New EOR Opportunity for Alaska's North Slope: Society of Petroleum Engineers, doi:10.2118/93903-MS.

Meunier, A., 2005, Clays: Berlin ; New York, Springer, 488 p.

Mohan, K. K., and H. S. Fogler, 1997, Colloidally induced smectitic fines migration: Existence of microquakes: AIChE Journal, v. 43, no. 3, p. 565–576, doi:10.1002/aic.690430302.

Mohan, K. K., R. N. Vaidya, M. G. Reed, and H. S. Fogler, 1993a, Water sensitivity of sandstones containing swelling and non-swelling clays: Colloids and Surfaces A: Physicochemical and Engineering Aspects, v. 73, p. 237–254, doi:10.1016/0927-7757(93)80019-B.

Mohan, K. K., R. N. Vaidya, M. G. Reed, and H. S. Fogler, 1993b, Water sensitivity of sandstones containing swelling and non-swelling clays: Colloids and Surfaces A: Physicochemical and Engineering Aspects, v. 73, p. 237–254, doi:10.1016/0927-7757(93)80019-B.

Morrow, N. R., 1990, Wettability and Its Effect on Oil Recovery: Journal of Petroleum Technology, v. 42, no. 12, p. 1,476-1,484, doi:10.2118/21621-PA.

Morrow, N., and J. Buckley, 2011, Improved Oil Recovery by Low-Salinity Waterflooding: Journal of Petroleum Technology, v. 63, no. 5, p. 106–112, doi:10.2118/129421-JPT.

Morrow, N. R., G. Tang, M. Valat, and X. Xie, 1998, Prospects of improved oil recovery related to wettability and brine composition: Journal of Petroleum Science and Engineering, v. 20, no. 3–4, p. 267–276, doi:10.1016/S0920-4105(98)00030-8.

Mugele, F., I. Sîretanu, N. Kumar, B. Bera, L. Wang, M. A. Maestro, M. H. G. Duits, H. T. M. van den Ende, and I. Collins, 2014, Charge Control And Wettability Alteration At Solid-liquid Interfaces, *in* Society of Petroleum Engineers journal, Tulsa, Oklahoma, USA: Society of Petroleum Engineers.

Mugele, F., I. Siretanu, N. Kumar, B. Bera, L. Wang, R. de Ruiter, A. Maestro, M. Duits, D. van den Ende, and I. Collins, 2016, Insights From Ion Adsorption and Contact-Angle Alteration at Mineral Surfaces for Low-Salinity Waterflooding: SPE Journal, v. 21, no. 4, p. 1,204-1,213, doi:10.2118/169143-PA.

Mungan, N., 1966, Certain Wettability Effects In Laboratory Waterfloods: Journal of Petroleum Technology, v. 18, no. 2, p. 247–252, doi:10.2118/1203-PA.

Mungan, N., 1965, Permeability Reduction Through Changes in pH and Salinity: Journal of Petroleum Technology, v. 17, no. 12, p. 1,449-1,453, doi:10.2118/1283-PA.

Mungan, N., 1972, Relative Permeability Measurements Using Reservoir Fluids: Society of Petroleum Engineers Journal, v. 12, no. 5, p. 398–402, doi:10.2118/3427-PA.

Nasralla, R. A., M. B. Alotaibi, and H. A. Nasr-El-Din, 2011, Efficiency of Oil Recovery by Low Salinity Water Flooding in Sandstone Reservoirs: Society of Petroleum Engineers, doi:10.2118/144602-MS.

Nasralla, R. A., and H. A. Nasr-El-Din, 2014a, Double-Layer Expansion: Is It a Primary Mechanism of Improved Oil Recovery by Low-Salinity Waterflooding? SPE Reservoir Evaluation & Engineering, v. 17, no. 1, p. 49–59, doi:10.2118/154334-PA.

Nichols, G., 2009, Sedimentology and Stratigraphy: Chichester, UK ; Hoboken, NJ, Wiley-Blackwell, 432 p.

Okasha, T. M., and A.-J. A. Al-Shiwaish, 2010, Effect of Temperature and Pressure on Interfacial Tension and Contact Angle of Khuff Gas Reservoir, Saudi Arabia: Society of Petroleum Engineers, doi:10.2118/136934-MS.

Ozkan, A., and M. Yekeler, 2003, A new microcolumn flotation cell for determining the wettability and floatability of minerals: Journal of Colloid and Interface Science, v. 261, no. 2, p. 476–480, doi:10.1016/S0021-9797(03)00130-9.

Peng, J., J. Liu, Y. Wang, and J. Liu, 2009, Origin and controlling factors of chlorite coatings—an example from the reservoir of T3x Group of the Baojie area, Sichuan Basin, China: Petroleum Science, v. 6, no. 4, p. 376–382, doi:10.1007/s12182-009-0057-1.

Prather, C. A., J. M. Bray, J. D. Seymour, and S. L. Codd, 2016, NMR study comparing capillary trapping in Berea sandstone of air, carbon dioxide, and supercritical carbon dioxide after imbibition of water: Water Resources Research, v. 52, no. 2, p. 713–724, doi:10.1002/2015WR017547.

Pu, H., X. Xie, P. Yin, and N. R. Morrow, 2008, Application of Coalbed Methane Water to Oil Recovery from Tensleep Sandstone by Low Salinity Waterflooding: Society of Petroleum Engineers, doi:10.2118/113410-MS.

Rajayi, M., and A. Kantzas, 2011, Effect of Temperature and Pressure on Contact Angle and Interfacial Tension of Quartz/Water/Bitumen Systems: Journal of Canadian Petroleum Technology, v. 50, no. 6, p. 61–67, doi:10.2118/148631-PA.

Rezaeidoust, A., T. Puntervold, and T. Austad, 2010, A Discussion of the Low-Salinity EOR Potential for a North Sea Sandstone Field: Society of Petroleum Engineers, doi:10.2118/134459-MS.

RezaeiDoust, A., T. Puntervold, and T. Austad, 2011, Chemical Verification of the EOR Mechanism by Using Low Saline/Smart Water in Sandstone: Energy & Fuels, v. 25, no. 5, p. 2151–2162, doi:10.1021/ef200215y.

RezaeiDoust, A., T. Puntervold, S. Strand, and T. Austad, 2009, Smart Water as Wettability Modifier in Carbonate and Sandstone: A Discussion of Similarities/Differences in the Chemical Mechanisms: Energy & Fuels, v. 23, no. 9, p. 4479–4485, doi:10.1021/ef900185q.

Rivet, S., L. W. Lake, and G. A. Pope, 2010, A Coreflood Investigation of Low-Salinity Enhanced Oil Recovery: Society of Petroleum Engineers, doi:10.2118/134297-MS.

Salathiel, R. A., 1973, Oil Recovery by Surface Film Drainage In Mixed-Wettability Rocks: Journal of Petroleum Technology, v. 25, no. 10, p. 1,216-1,224, doi:10.2118/4104-PA.

Seccombe, J. C., A. Lager, K. J. Webb, G. Jerauld, and E. Fueg, 2008, Improving Wateflood Recovery: LoSalTM EOR Field Evaluation: Society of Petroleum Engineers, doi:10.2118/113480-MS.

Shedid, S. A., and M. T. Ghannam, 2004, Factors affecting contact-angle measurement of reservoir rocks: Journal of Petroleum Science and Engineering, v. 44, no. 3–4, p. 193–203, doi:10.1016/j.petrol.2004.04.002.

Shehata, A. M., N. El-Din, and H. A, 2015, Spontaneous Imbibition Study: Effect of Connate Water Composition on Low-Salinity Waterflooding in Sandstone Reservoirs: Society of Petroleum Engineers, doi:10.2118/174063-MS.

Shehata, A. M., and H. A. Nasr-El-Din, 2015, Zeta Potential Measurements: Impact of Salinity on Sandstone Minerals: Society of Petroleum Engineers, doi:10.2118/173763-MS.

Sheng, J. J., 2014, Critical review of low-salinity waterflooding: Journal of Petroleum Science and Engineering, v. 120, p. 216–224, doi:10.1016/j.petrol.2014.05.026.

Somerton, W. H., and C. J. Radke, 1983, Role of Clays in the Enhanced Recovery of Petroleum From Some California Sands: Journal of Petroleum Technology, v. 35, no. 3, p. 643–654, doi:10.2118/8845-PA.

Soraya, B., C. Malick, C. Philippe, H. J. Bertin, and G. Hamon, 2009, Oil Recovery by Low-Salinity Brine Injection: Laboratory Results on Outcrop and Reservoir Cores: Society of Petroleum Engineers, doi:10.2118/124277-MS.

Speight, J. G., 2014, The Chemistry and Technology of Petroleum, Fifth Edition: Boca Raton, CRC Press, 953 p.

Spinler, E. A., 1997, Determination of In-Situ Wettability from Laboratory and Well Log Measurements for a Carbonate Field: Society of Petroleum Engineers, doi:10.2118/38733-MS.

Sposito, G., 2008, The Chemistry of Soils: Oxford University Press, USA, 342 p.

Stalder, A. F., T. Melchior, M. Müller, D. Sage, T. Blu, and M. Unser, 2010, Low-bond axisymmetric drop shape analysis for surface tension and contact angle measurements of sessile drops: Colloids and Surfaces A: Physicochemical and Engineering Aspects, v. 364, no. 1–3, p. 72–81, doi:10.1016/j.colsurfa.2010.04.040.

Stokes, D. J., and A. M. Donald, n.d., In situ mechanical testing of dry and hydrated breadcrumb in the environmental scanning electron microscope (ESEM): Journal of Materials Science, v. 35, no. 3, p. 599–607, doi:10.1023/A:1004720209547.

Stricker, S., and S. J. Jones, 2016, Enhanced porosity preservation by pore fluid overpressure and chlorite grain coatings in the Triassic Skagerrak, Central Graben, North Sea, UK: Geological Society, London, Special Publications, v. 435, p. SP435.4, doi:10.1144/SP435.4.

Suijkerbuijk, B., J. Hofman, D. J. Ligthelm, J. Romanuka, N. Brussee, H. van der Linde, and F. Marcelis, 2012a, Fundamental Investigations into Wettability and Low Salinity Flooding by Parameter Isolation: Society of Petroleum Engineers, doi:10.2118/154204-MS.

Taber, J. J., 1969, Dynamic and Static Forces Required To Remove a Discontinuous Oil Phase from Porous Media Containing Both Oil and Water: Society of Petroleum Engineers Journal, v. 9, no. 1, p. 3–12, doi:10.2118/2098-PA.

Tang, G.-Q., and N. R. Morrow, 1999, Influence of brine composition and fines migration on crude oil/brine/rock interactions and oil recovery: Journal of Petroleum Science and Engineering, v. 24, no. 2–4, p. 99–111, doi:10.1016/S0920-4105(99)00034-0.

Tang, G. Q., and N. R. Morrow, 1997, Salinity, Temperature, Oil Composition, and Oil Recovery by Waterflooding: SPE Reservoir Engineering, v. 12, no. 4, p. 269–276, doi:10.2118/36680-PA.

Thakur, G. C., and A. Satter, 1998, Integrated Waterflood Asset Management: PennWell Books, 436 p.

Tiab, D., and E. C. Donaldson, 2012, Petrophysics: Theory and Practice of Measuring Reservoir Rock and Fluid Transport Properties: Gulf Professional Publishing, 971 p.

Tsakiroglou, C. D., and M. Fleury, 1999, Resistivity index of fractional wettability porous media: Journal of Petroleum Science and Engineering, v. 22, no. 4, p. 253–274, doi:10.1016/S0920-4105(98)00085-0.

Tucker, M., 2001, Sedimentary Petrology: Oxford ; Malden, MA, Wiley-Blackwell, 272 p.

Underwood, T., V. Erastova, P. Cubillas, and H. C. Greenwell, 2015, Molecular Dynamic Simulations of Montmorillonite–Organic Interactions under Varying Salinity: An Insight into Enhanced Oil Recovery: The Journal of Physical Chemistry C, v. 119, no. 13, p. 7282–7294, doi:10.1021/acs.jpcc.5b00555.

Valocchi, A. J., R. L. Street, and P. V. Roberts, 1981, Transport of ion-exchanging solutes in groundwater: Chromatographic theory and field simulation: Water Resources Research, v. 17, no. 5, p. 1517–1527, doi:10.1029/WR017i005p01517.

Varajao, A., and A. Meunier, 1995, Particle morphological evolution during the conversion of I/S to illite in Lower Cretaceous shales from Sergipe-Alagoas basin, Brazil: Clays and clay minerals, v. 43, no. 1, p. 14–28.

Verwey, E. J. W., J. T. G. Overbeek, and K. van Nes, 1948, Theory of the Stability of Lyophobic Colloids: The Interaction of Sol Particles Having an Electric Double Layer: Elsevier Publishing Company, 205 p.

Vevle, J., 2011, NMR measurements of wettability alternation in Berea Sandstone.

Vinogradov, J., M. Z. Jaafar, and M. D. Jackson, 2010, Measurement of streaming potential coupling coefficient in sandstones saturated with natural and artificial brines at high salinity: Journal of Geophysical Research: Solid Earth, v. 115, no. B12, doi:10.1029/2010JB007593.

Wang, Y. H., and W. K. Siu, 2006, Structure characteristics and mechanical properties of kaolinite soils. I. Surface charges and structural characterizations: Canadian Geotechnical Journal, v. 43, no. 6, p. 587–600.

Wei, Q. F., R. R. Mather, A. F. Fotheringham, R. Yang, and J. Buckman, 2003, Esem Study of Oil Wetting Behaviour of Polypropylene Fibres: Oil & Gas Science and Technology, v. 58, no. 5, p. 593–597, doi:10.2516/ogst:2003041.

Welge, H. J., 1949, Displacement of Oil from Porous Media by Water or Gas: Transactions of the AIME, v. 179, no. 1, p. 133–145, doi:10.2118/949133-G.

Willhite, G. P., 1986, Waterflooding: Society of Petroleum Engineers, 348 p.

Williams, M. C., and D. W. Fuerstenau, 1987, A simple flotation method for rapidly assessing the hydrophobicity of coal particles: International Journal of Mineral Processing, v. 20, no. 1–2, p. 153–157, doi:10.1016/0301-7516(87)90023-8.

Worden, R., and S. Morad (eds.), 2002, Clay Mineral Cements in Sandstones: Malden, MA, Wiley-Blackwell, 520 p.

Worden, R. H., and S. Morad, 1999, Clay Minerals in Sandstones: Controls on Formation, Distribution and Evolution, *in* R. H. Worden, and S. Morad, eds., Clay Mineral Cements in Sandstones: Blackwell Publishing Ltd., p. 1–41.

Wu, S., and A. Firoozabadi, 2010, Effect of Clay, Brine and Chemical Treatment in the Wettability Alteration of Berea Rock: Society of Petroleum Engineers, doi:10.2118/129542-MS.

Yang, J., Z. Dong, M. Dong, Z. Yang, M. Lin, J. Zhang, and C. Chen, 2015, Wettability Alteration during Low Salinity Waterflooding and The Relevance of Divalent Ions in This Process: Energy & Fuels, doi:10.1021/acs.energyfuels.5b01847.

Yariv, S., 1992, Wettability of Clay Minerals: p. 279–326, doi:10.1007/978-1-4899-1176-6_11.

Yildiz, H. O., and N. R. Morrow, 1996, Effect of brine composition on recovery of Moutray crude oil by waterflooding: Journal of Petroleum Science and Engineering, v. 14, no. 3, p. 159–168, doi:10.1016/0920-4105(95)00041-0.

Yuan, Y., and T. R. Lee, 2013, Contact Angle and Wetting Properties: p. 3–34, doi:10.1007/978-3-642-34243-1_1.

Yu, J., H. Wang, and X. Liu, 2013, Direct measurement of macro contact angles through atomic force microscopy: International Journal of Heat and Mass Transfer, v. 57, no. 1, p. 299–303, doi:10.1016/j.ijheatmasstransfer.2012.10.041.

Zhang, R., N. Qin, L. Peng, K. Tang, and Z. Ye, 2012, Wettability alteration by trimeric cationic surfactant at water-wet/oil-wet mica mineral surfaces: Applied Surface Science, v. 258, no. 20, p. 7943–7949, doi:10.1016/j.apsusc.2012.04.139.

Zhang, P., M. T. Tweheyo, and T. Austad, 2007, Wettability alteration and improved oil recovery by spontaneous imbibition of seawater into chalk: Impact of the potential determining ions Ca2+, Mg2+, and SO42−: Colloids and Surfaces A: Physicochemical and Engineering Aspects, v. 301, no. 1–3, p. 199–208, doi:10.1016/j.colsurfa.2006.12.058.

Zhou, Z., 1995, Construction and Application of Clay-Swelling Diagrams by Use of XRD Methods: Journal of Petroleum Technology, v. 47, no. 4, p. 306–306, doi:10.2118/29224-PA.

Zhou, D., M. Blunt, and F. M. Orr, 1997, Hydrocarbon Drainage along Corners of Noncircular Capillaries: Journal of Colloid and Interface Science, v. 187, no. 1, p. 11–21, doi:10.1006/jcis.1996.4699.

Zhou, X., N. R. Morrow, and S. Ma, 2000, Interrelationship of Wettability, Initial Water Saturation, Aging Time, and Oil Recovery by Spontaneous Imbibition and Waterflooding: SPE Journal, v. 5, no. 2, p. 199–207, doi:10.2118/62507-PA.

Zolotukhin, A. B., and J.-R. Ursin, 2000, Introduction to petroleum reservoir engineering: Kristiansand, Norway, Høyskoleforlaget, Norwegian Academic Press.

Chapter 3

Experimental Techniques and Data Analysis

In this research project an extensive range of characterisation techniques and different approaches have been employed for the following purposes:

1- To characterise and study the petrophysical properties of Berea sandstone core plugs;
2- Investigating the role of brine in wettability alteration on model mineral surfaces (quartz crystal).
3- To compare the model quartz crystal wettability with the wettability of quartz grains surface in Berea sandstone cores.
4- Determining spontaneous imbibition in Berea core plugs.

A general background, as well as a detailed description of the sample preparation and methodology of these experimental techniques is presented in this chapter. Details of specific experiments and procedures are summarised in the next chapters.

3.1. Optical Thin Section Analysis

3.1.1. Optical Microscopy

The optical microscope frequently referred to as light microscope, is a kind of microscope, which uses visible light and a system of lenses to enlarge images of small specimens. The optical microscope is a fundamental part of Earth Sciences research methods, which plays a role in the petrographic study for the composition of different types of rock. Basic optical microscopes can be very simple, although there are many complex designs, which aim to improve resolution and specimen contrast. In this study, a

Leica DM2500P and DM750P were used for the textural characterisation and quantitative analysis of studied samples. The images were often taken at varying magnifications, from 5× to 50×, using both transmitted and crossed polarisers.

3.1.2. Rock Used

Cleveland Quarries is in the business of quarrying and fabricating sandstone and has the exclusive trademark on Berea Sandstone™. For the past 30 years Berea sandstone core plugs have been widely acknowledged by the oil and gas industry as an ideal homogenous rock sample for testing enhanced oil recovery (Oak et al., 1990; Tang and Morrow, 1997; Nasralla et al., 2011a, 2011b). Use of Berea sandstone core plugs rather than core reservoir plugs for this fundamental study is attractive and significant since Berea sandstone core plugs are readily commercially accessible, inexpensive and believed to be relatively homogenous (Ramirez et al., 1986; Churcher et al., 1991; Ma and Morrow, 1994). In total, sixty Berea sandstone core plugs, all obtained from Cleveland Quarries, USA, were studied. However, of these, twenty-six Berea core samples were used for characterisation, when the rest was used in the investigation of wettability behaviours. These samples can be grouped into four permeability ranges. Details of the properties of these permeability ranges are presented in Chapter 4.

3.1.3. Sample Preparation

Thin sections were prepared at the Rock Sectioning Laboratory in the Department of Earth Sciences at Durham University. Polished and non-polished thin sections of Berea cores were made by cutting the core sample into 10 mm thick slices using a bench-mounted circular disc cutter with a fine diamond impregnated blade and water as a lubricant. Samples were then trimmed to height and width to be able to fit a standard glass slide (25.4 x 76.2 mm). Before attaching the sample to a glass plate, it was necessary to prepare the bonding surface. This involved polishing the cut rock samples surface using 20 μm and 10 μm abrasives, then the core samples were lapped on a glass slide. This process was completed by hand.

The next step was to ‘lap’ the glass slide that holds the thin section (which makes the glass frosted to allow for a better bond with the rock) using the same process of polishing by hand using a flat glass surface and Al_2O_3 powder (9.5 μm) paste before washing with water and drying with air. Once the glass was frosted, it was placed on a hot plate at 60 °C. To mount the prepared rock sample on the prepared glass slide an epoxy resin (EpoTek

301) was used. The resin was mixed and then applied to the sample before it was bonded to the glass slide ensuring that there were no bubbles present between the rock sample and the glass slide. Once the resin was set, the samples were re-sectioned. Re-sectioning involved cutting the rock sample (bonded to the slide) on a diamond impregnated disc to a thickness of 500 μm. The samples were then ground to a 100 μm thickness before the final manual polishing procedure, as described previously, using Al_2O_3 powder (9.5 μm) paste was repeated until the the finished thickness of 15 μm for optical thin sections and 50 μm for SEM thin sections was achieved. After this, the samples were then either covered with a cover slip (used for optical microscope only) or further polished using a 0.3 μm aluminium oxide paste (used in both optical and scanning electron microscopy – Chapter 4).

Mineralogical composition quantification was achieved by the point counting method. This technique is used to determine the components of a sample and the percentages that represent each component in it (Shand, 1916; Wentworth, 1923; Gatlin et al., 1993; Larrea et al., 2013). The method is often applied in biological, geological and materials science domains. Point counting is a statistical technique and involves "defining" a matrix of points superimposed to the slide, recording exactly what component is seen at each point and then assembling a description from all the information recorded. Point counting is normally conducted either by hand only, or manually through different devices. Although there are automated image processing techniques for counting features on microscope slides in other fields, particularly in biology, these techniques are not easily adapted to petrographic thin sections. Because of the characteristics of the petrographic slide, the color of each conceptual unit is not homogeneous enough to be interpreted as a single component by an automated image processing technique, based on colour or grey scale images.

In this thesis, point counting was conducted using a point counting stage (PETROG-Conwy Valley Systems Limited) linked to a standard petrographic microscope (Leica DM2500P and DM750P) that is capable of moving the sample at regular steps. Firstly, an image of a petrographic thin section was loaded. Secondly, the regular grid was created. Finally, the grid is superimposed onto the image, and the counting process can start. Performing point counting on a petrographic thin section requires observations to be made at regular positions on the sample. At each location, it was decided to which mineral the respective grid point and its local neighbourhood belonged. By counting the number of points found for each mineral the percentages of each mineral phase present in the sample

was calculated. These percentages represent the relative proportions of the minerals in the sample (Larrea et al., 2013). Concerning the statically correct number of counts required for quantitative examinations, the image to be manipulated must contain at least 300 points (Stricker and Jones, 2016).

3.2. X-ray Diffraction

3.2.1. Powder X-ray Diffraction

X-ray diffraction is a powerful technique that can be used to identify samples. In general, mineral phases are identified using X-ray diffraction techniques. X-rays are focused into an incident beam using slits and directed onto the surface of the randomly oriented powdered sample. This technique then measures X-rays as they are diffracted from the sample. In ordered solids, diffraction occurs at a regular spacing (d-spacing) related to the unit cell of the solid.

In order to produce X-rays, a source, such as copper, is usually bombarded with high energy electrons, releasing Cu k_α radiation that is used as an X-ray source. This is generated when the bombardment of Cu with electrons can displace electron in the Cu k shell (n=1), creating an excited state. As electrons relax from the L (n=2) and M (n=3) shells into the K-shell, the excess energy of this process is released as an X-ray photon. The X-ray emitted from relaxation from M shell to the K shell are described as k_α radiation. For Cu k_α, the wave length of the X-ray is 0.154 nm. This X-ray source is used, since the wave lengths are required to be of ordered of interatomic spacing in order to produce interference (Bloss, 1994). Once generated, the X-ray is scattered off the sample to be probed at specific angles. Peaks will occur when two waves interfere constructively with each other, as shown in Figure 3.1. If the waves are not in phase, their interference is destructive, and no peak is observed.

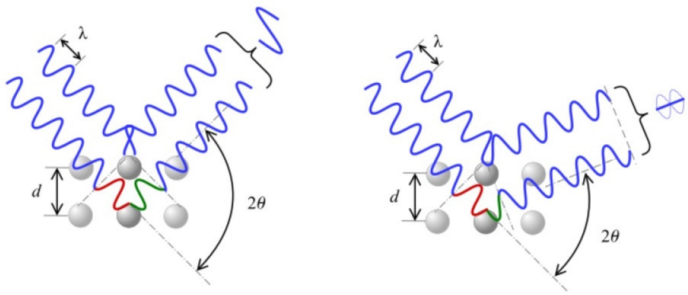

Figure 3.1: Schematic indicating scattering of X-rays by a crystal lattice and Bragg's Law, waves are X-ray paths. Left demonstrates constructive interference. Right shows destructive interference that occurs when the phase of the waves shifts and the signal is destroyed. Figure from Wikipedia, https://en.wikipedia.org/wiki/Bragg's_law.

The X-rays diffract from the periodic arrangements of atoms in a crystal, as with visible light diffracting from a grating. The diffraction from a crystal can be represented by Bragg's law and is described by equation 3.1 (Pecharsky and Zavalij, 2005).

$$n\lambda = 2d_{hkl} \sin\theta \quad (3.1)$$

Where:

- λ = Wavelength of X-rays.
- (n = a positive integer)
- d = Interplanar distance between lattice planes of the crystal.
- hkl = Miller index.
- θ = Scattering or Bragg's angle.

For a given *d*-spacing, a peak will occur in the diffractogram when the angle of incidence is such that constructive interference occurs between the scattered X-rays. By probing the sample over a range of angles, a pattern will arise corresponding to the angles at which constructive interference is achieved for different *d*-spacing within the sample. This pattern will be unique to the material being studied, and can thus be used to "fingerprint" in order to identify new samples by comparison to reference pattern, or allowing a full structure solution if needed (Pecharsky and Zavalij, 2005).

3.2.2. Sample Preparation

Powder X-ray diffraction (XRD) analysis of the Berea core samples was undertaken at the James Hutton Institute, Aberdeen. The samples were prepared by McCrone milling followed by spray drying. XRD patterns were recorded on a Bruker D8 Advance from 4-70°2θ, counting for 384 seconds per 0.0194° step, using a Lynxeye XE position sensitive detector and Ni-filtered Cu radiation. The mineralogical composition of examined core samples was obtained via whole-rock X-ray diffraction (XRD) analysis with a full pattern fitting reference intensity ratio (RIR) method, as described in Omotoso et al., (2006) and Ortiz et al., (2009).

Sample-specific clay mineralogy was also obtained by means of XRD analysis of the clay mineral fraction separated from the bulk XRD sample. XRD data was collected on a Siemens D5000 instrument using cobalt radiation. Clay fractions of < 2 μm were obtained by timed sedimentation, prepared as oriented mounts onto glass slides using the filter peel transfer technique and scanned from 2 - 45° (2θ) in the air-dried state, after glycolation (vapour pressure overnight), and after heating to 300 °C for one hour. For clay minerals

present in amounts > 10 wt. % uncertainty is estimated as better than ± 5 wt. % at the 95% confidence level. The technique used for preparation of samples is described in detail in Chapter 4.

3.3. Scanning Electron Microscopy (SEM)

3.3.1. Applications of SEM in the Geosciences

SEM is an essential observation technique to investigate micro-characteristics of samples in natural science; it has also been widely used in the field of geological scientific research. It provides direct, high-resolution data; offers a great depth of focus; and requires non-sophisticate sample preparations. SEM analysis in geoscience research is essentially used to provide estimates of the pore space, composition, and paragenesis of sedimentary rock samples. Image analysis for quantitative estimates of the pore space within a sample, for example, contribute to estimates of reservoir potential and fluid overpressure (Bera et al., 2011; Newport et al., 2016). Furthermore, SEM has become one of the most versatile instruments available for the investigation and study of the microstructural characteristics in the igneous rocks and metamorphic rocks (Bullock et al., 2014). Combined with a backscattered electron (BSE) detector, electron back-scattering diffraction (EBSD), energy dispersal X-ray spectroscopy (EDS) and cathodoluminescence spectrometry (CL), SEM can yield multiple ranges of observation about the different type of rock samples at the same time, such as superficial microstructure, CL analysis, BSE image, component analysis and crystal structure features (Chen et al., 2015).

3.3.2. Instrument Basics

The basic principle of SEM were established by Knoll and von Ardenne as well as Zworykin and Hillier, during the 1930s and early 1940s, when the electron beam of a transmission electron microscope was rastered, essentially creating a scanning transmission electron microscope. Since then, a microscope for imaging bulk sample was introduced by Zworkin in 1942, whilst commercially available microscopes have been available since 1965. The operation of the SEM is achieved by applying a voltage between a conducting sample and filament, resulting in electron emission from the filament to the sample. The electrons are then guided to the sample through a series of electromagnetic lenses in the electron column. A typical SEM schematic is shown in Figure 3.2. The beam current and

spot sizes are controlled by one or more consider lenses and the probe-forming objective lenses.

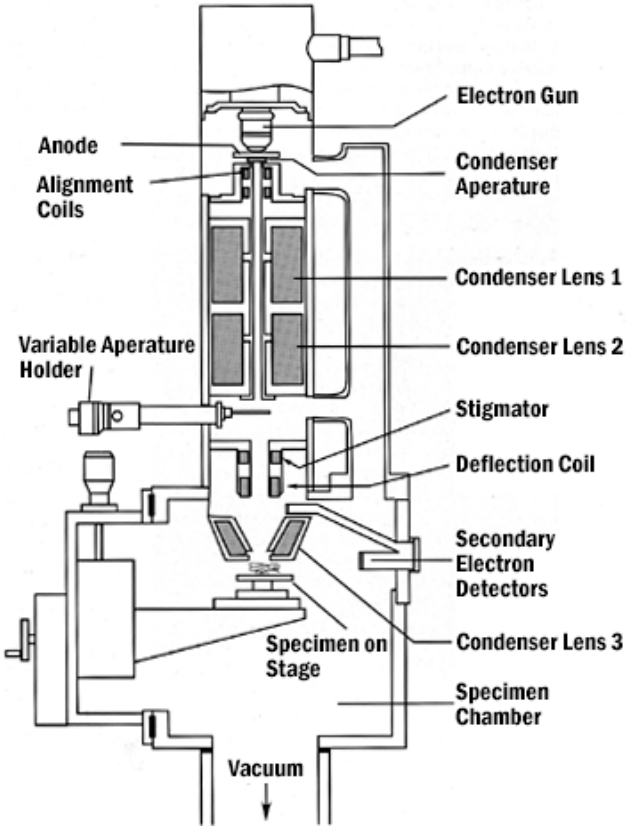

Figure 3.2: Typical schematic diagram of a generic SEM with the electron. Extracted from https://cmrf.research.uiowa.edu/scanning-electron-microscopy.

The beam interacts with the sample, leading to electrons being emitted from the sample, primarily as secondary electrons and backscattered electrons. It is the signal generated by secondary electrons that are observed. These secondary electrons are produced as a result of interactions between the electron beam and the weakly bound electrons in the conduction band of the sample. Some energy transferred to these from the beam, provides the energy for their escape as secondary electrons. These are low energy electrons (<50 eV) and therefore only those formed in the first few nanometres of the sample surface have enough energy to escape and be detected.

The escaping electrons are typically detected by an Everhart-Thornley detector. The resulting image is formed from the intensity of the secondary electron emission from the sample at each x; y data point during rastering of the electron beam across the surfaces. In order to perform the chemical analysis of the sample, emergent x-rays are measured. These

are element specific allowing quantification of the specimens elemental composition. This technique is known as energy dispersive x-ray spectroscopy.

3.3.3. Energy Dispersive X-ray (EDX) Spectroscopy

EDX spectroscopy can only be used for surface analysis; geological speaking, it is beneficial for identifying framework minerals that have a regular crystal structure but not for clay minerals, which may be composed of interlayered minerals (e.g. illite-smectite) and may contain impurities. EDX is mainly used to identify the specific minerals present when imaging under BSE conditions as the grey-scale colours produced are relative and cannot be used for mineral identification. EDX works by focussing high-energy electrons onto the surface of the sample that causes secondary electrons to be expelled. This results in the atom shifting to an excited state; to return to its normal state an electron from a higher shell moves to fill the electron hole and radiation is emitted in the form of X-rays, which are recorded by a detector (Welton, 1983). Each atom has unique energy levels that occur in electron transfer leading to distinct X-ray wavelengths being emitted by it, which allows for its unequivocal identification. To be able to quantify the amount of an element in a sample, a pure cobalt standard is used to calibrate virtual standards built into the INCA Energy EDS System, using equation 3.2.

$$Cspec = \frac{Nspec}{Nstd} Cstd = kCstd \tag{3.2}$$

Where:

- C_{spec} = Concentration of an element within a sample.
- N_{spec} = Number of counts from a sample.
- N_{std} = Number of counts from the standard.
- C_{std} = Concentration of the standard.
- k = Constant.

3.3.3. Sample Preparation

Thin sections of Berea core plugs were characterised using a scanning electron microscope (Hall and Lloyd, 1981; Peters, 2009; Landrot et al., 2012). The prepared thin sections for an optical microscope, they were also used for SEM analysis (Logan and Semeniuk, 1976). For SEM analyses, thin sections of selected samples were carbon coated with a 20-40 μm thick (depending on sample composition) conductive layer of carbon prior to analysis using a Cressington 108 Carbon/ A coating machine, to reduce sample

charging. Selected samples were examined using a Hitachi SU-70 High-Resolution Analytical SEM, equipped with an Oxford Instrument Energy Dispersive X-ray (EDX) and microanalysis system (INCA Energy 700) at the G.J. Russell Microscopy Facility at Durham University.

3.3.4. Data Processing

One of the main objectives of this work was to interpret BSE images that are grey-scaled according to the atomic mass of the Berea sandstone composition, to quantify the surface fraction of various types of minerals. The full details of image processing and data analysis are presented in Chapter 4.

3.4. Atomic Force Microscopy

Atomic force microscopy (AFM) is a type of multipurpose technique that depends on the interaction of a sharp probe with a surface as it is scanned over it in order to produce a high-resolution image to characterise the surface topography of material at the nano-scale (Hassenkam et al., 2011, 2012; Pedersen et al., 2016; Siretanu et al., 2016). AFM can be operated under ambient conditions, and in solutions, without surface destruction. Furthermore, development has increased the range of conditions accessible with this technique, for example, there are now several hydrothermal AFM's, capable of imaging at reservoir temperature (150 °C) and pressures of up to 6 atm.

3.4.1. Instrument Basics

The AFM is classically governed by three basic components**.** Figure 3.3 shows a simple schematic of how an AFM operates. An extremely sharp tip (5-20 nm), attached to a cantilever, is rastered across a surface at low force (hundredths of pN to 100 nN). Vertical movement (deflection) and torsion of this cantilever is monitored using the so-called optical detection mechanisms. For AFM, this sharp probe is a tip that interacts directly with the surface of the solid object. These interactions can include both the attractive and repulsive forces that exist between the tip and the object surface. Though the information gathered, a three-dimensional topographic of the surface can be obtained (Johnson et al., 2009)

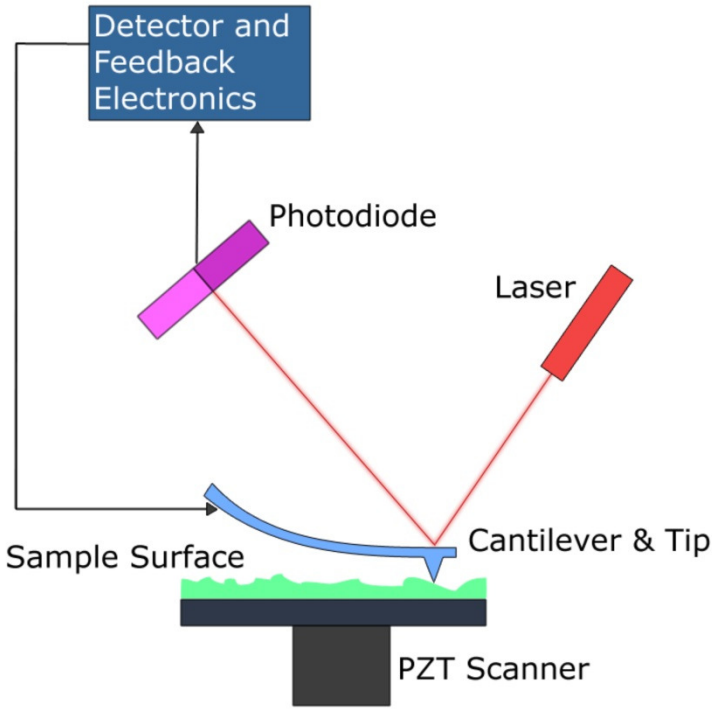

Figure 3.3: Schematic diagram of an AFM set- up, as the cantilever is displaced via its interaction with the surface, so too will the reflection of the laser beam be displaced on the surface of the photodiode from (Cubillas and Anderson, 2014).

A sharp tip attached to a flexible cantilever is used to scan the sample surface. As the tip is rastered a cross the sample surface, the cantilever bend/deflect as the interaction between the tip and the surface change, by measuring this bending, it is possible to measure the force between the tip and the sample surface. The cantilever can be considered as a spring, which obeys Hook's law. Primarily, the bending of the cantilever is measured by a laser shining on the back of the cantilever. A laser is reflected into a four-quadrant photodiode detector. Any deflection of the cantilever will result in movement of the laser spot on the photodiode detector, as can be seen in Figure 3.3.

3.4. 2. Scanning Modes

There are three main scanning modes of the AFM instrument; contact mode, non-contact mode and intermittent contact (or tapping) mode (Hansma et al., 1993). In any mode, the scanning can be performed in two different ways; either at a constant height or a constant force. Firstly, in constant height mode, the height of the cantilever is kept constant with respect to the object's surface. Secondly, in the scanning case, any surface features encountered will cause a deflection of the cantilever, resulting in a change in applied force.

This deflection is essentially taken as the measurement. However, this mode is rarely used, since the variation in forces means that both the sample and tip are at risk of damage. In general, the typical scanning mode often used in most of the experiments is the constant force mode. In this mode, the photodiode detector records the deflection of the cantilever. Using a feedback loop, the z piezoelectric scanner is then moved in order to return the cantilever to the original contact force. The height of the surface features can be plotted from the movement of the scanner. In Figure 3.4, a typical force distance curve for an AFM experiment is shown. This gives the relation between the distances of the tip from the sample surface.

At extended distance, there is an interaction between the tip and sample and so no force is recorded. As the tip moves closed to the sample, attractive forces as are the major component and the cantilever will bend as shown by the inset image. It is in this attractive region that non-contact AFM is performed. At one point, these attractive forces will cause the tip to “snap” into contact with the surface, shown by the sudden fall on the curve. After this point, the tip is in repulsive contact and moving the tip further toward the sample will increase this unfavourable interaction. It is in repulsive contact that contact mode AFM is performed, as shown in Figure 3.4. The cantilever deflection, in this case, is also shown inset. Moving in the opposite direction, there is a larger bending due to an attractive interaction measured in the curve. This extra bending is caused by adhesion interactions between the tip and samples as the tip moves out of contact with the surface. Although other forces are active in the attractive region, Van der Waals and Capillary forces van der Waals forces typically dominate at small distances.

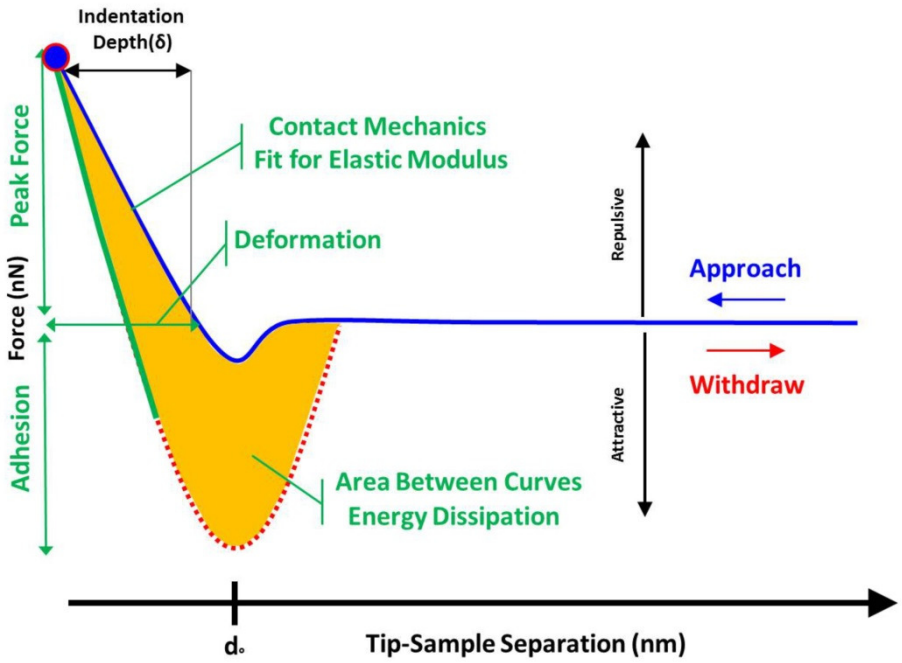

Figure 3.4: Schematic diagram of an adhesion experiment and the corresponding typical force curves for approach (blue) and retraction (red) from the surface from Li et al. (2015).

The most used imaging mode is the contact mode, when a certain force is applied to the surface by the cantilever, meaning that the tip is in constant repulsive contact with the surface as it rasters over it. In general, this procedure of imaging has some advantage and disadvantage. By being in repulsive contact, the cantilever will not snap in to a contact as can happen in non-contact AFM due to attractive forces. The possibility of sample damage can always be counted as a disadvantage of contact mode imaging (Ohnesorge and Binnig, 1993). Both non-contact and intermittent contact mode AFM can be described as a dynamic mode. In non-contact mode, the oscillating cantilever does not make contact with the surface, whilst in intermittent contact ode the tip makes repulsive contact with the surface during oscillation. The amplitude of oscillation is typically set between 10 and 100 nm, and the probe "taps" the surface at the bottom of its bounce. As the probe interacts with topographic features, the oscillation amplitude changes, and the feedback loop moves the sample up or down to maintain the amplitude set point. Since the probe is in contact with the surface for a fraction of its tapping period, lateral forces are greatly reduced due to lack of contact. A drawback of this method is that imaging in fluid e.g. oil model compounds and brines can be challenging.

3.4.3. Instrument Details for This Work

A multimode Bruker AFM, equipped with a Bruker Nanoscope V controller, was used in two force spectroscopy-imaging modes, PeakForce^{TM}(PF) and PeakForce Quantitative Nanomechanical (PFQNM). Both modes provide topographic information (as seen in the height map shown in next chapters), as well as the ability to measure adhesion forces. The main difference, however, being the resonance frequency of the cantilever; 2 KHz and 0.5-2 KHz for PF and PFQNM, respectively. Quantitative nanomechanical characterisation is achieved in real time by the system software, following contact mechanics theory (Trtik et al., 2012), which simultaneously derives four mechanical properties: reduced elastic modulus, adhesion, sample deformation and the work of adhesion (dissipation), all from the approach-retract cycle and at an unprecedented resolution. For our experiments, however, only the adhesion measurements (Figure 3.4) were of interest.

In addition to the measurements described using PFQNM, further adhesion was calculated using the traditional force-distance curves, courtesy of the 'Point and Shoot' facility of the NanoScope V 8.15® software, which allows numerous positions on an image to be selected and a standard force-distance curve to be recorded for each one. This was used instead of the more typical force-volume mode, which would have resulted in scans > 60 minutes in duration, thus unfeasible in this case owing to sample drift, which would have meant that the nanometer-sized particles could move out of the scan area during the actual imaging. In the majority of instances, the final images and combined data were saved and analysed, but on occasion, the raw data recorded using the PeakForce capture, namely each individual force-distance curve per image pixel, may be examined.

When using PFQNM, calibration of the cantilever's vertical spring constant and the sensitivity of the optical detection mechanism was required. The sensitivity calibration was performed by recording a force-distance curve over the surface of the sample and selecting the repulsive region to obtain a V/nm calibration factor. Afterwards, the spring constant was calibrated by means of the thermal tuning feature in the NanoScope V 8.15® software, which relies on calculations from Hutter and Bechhoefer (1993) to derive a formula relating the thermal noise of the cantilever at maximum Z displacement with its spring constant. Once these values have been obtained, the software automatically calculated the adhesion measurements and subsequent images display the data in newtons (N).

3.4. 4. Sample Preparation

Surface characterisation was carried out in order to determine the surface chemistry of detrital quartz composition of a range of Berea sandstone samples obtained from Cleveland Quarries, USA. Studied samples were chosen to represent the various range of permeability within the studied cores. The techniques used for the preparation of samples such as cut and gold-coated in preparation for analysis by AFM are described in detail in Chapter 4.

Geochemical analyses were also carried out to look at the crude oil /brine/quartz and oil model compounds/brine/quartz interactions. The quartz crystal specimens were used for wettability experiments; they have been saturated with formation water, then aged in oil and exposed in brines before analysis to replicate the sandstone reservoir conditions. The preparation of samples is described in detail in Chapter 5.

3.5. Micro -X-ray Computed Tomography

X-ray computed tomography (X-ray CT) is a non-destructive 3D imaging process capable of imaging and analysing the internal structure of solid samples to a resolution of less than one micron (Peng et al., 2012). The technique was first used for medical purposes (Hendee, 1979) followed quickly by an evaluation of its usefulness in material sciences (Reimers and Goebbels, 1983). A simple sketch of an X-ray CT machine setup is shown in Figure 3.5. The X-ray tube consists of a focused electron beam directed at a target which, when hit, decelerates the electrons and generates X-rays. This x-ray beam is then shaped into a cone as it passes through a circular aperture upon exiting the tube. The effectiveness of an X-ray source is controlled by:

- The focal spot size, which defines the possible source-detector paths that can intersect at any given point within the sample. A smaller spot size leads to less blurring and the ability to detect smaller features.
- The X-ray intensity, which affects directly the signal-to-noise ratio. Higher X-ray intensities improve the counting statistics and hence the image quality although they often require larger spot sizes which can increase blurring of images.
- The X-ray energy spectrum produced, which affects the level of detail achieved for differing density regions within a sample. Higher energy X-rays penetrate more effectively through a material, enabling the scanning of more dense samples, however, they are less sensitive to material a density and composition variation,

which reduces the identification of density fluctuations within the less dense regions of a sample.

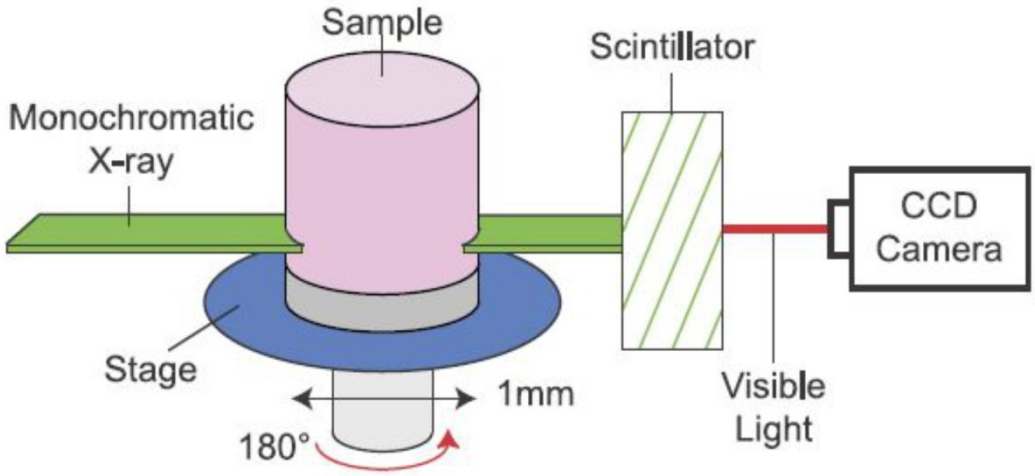

Figure 3.5: A simple sketch of a typical X-ray CT machine setup. A monochromatic X-ray (green) is transmitted through the bulk sample onto a scintillator (dashed-green), where it is converted to visible light (red), and recorded by a CCD camera. During a microtomography scanning, the sample is rotated 180° to create a series of cross-sectional data used to construct the 3D digital image from Miller et al. (2014).

As the X-rays pass through the sample, the signal is attenuated through scattering and absorption and the detector produces a 2D grey-scale image of the sample showing the attenuation of the X-rays having passed through the entire sample. The linear attenuation coefficient, μ, for each pixel, is defined using Beer's law (Eq. 33), where I is the intensity remaining after the X-ray has passed through the sample of thickness h and I_0 is the incident X-ray intensity (Wellington and Vinegar, 1987).

$$I/I_o = exp\,(-\mu h) \tag{3.3}$$

By rotating the sample in small known increments, through the use of the sample stage, a series of grey-scale attenuation images, or 2D projections, are captured and used to perform a mathematical reconstruction of the scanned sample. The mathematical reconstruction, via the means of a back filtered projection, converts the series of 2D X-ray absorption images, captured in the y-z plane, into a series of 2D greyscale slices in the x-z plane which provides an indication of the density at any point within the sample. The series

of 2D x-z plane slices are then stacked one above each other, and a 3D data set is created in which the sample is described by a series of voxels. Voxels are the 3D equivalent of pixels within a 2D image and therefore are cubes with a fixed edge length each containing a grey-scale value related to the X-ray attenuation of the sample at the voxel's location. The reconstructed 3D model of the scanned sample can be used for visual inspection and quantitative analysis. The reconstructed 3D data obtained following X-ray CT scanning will contain imperfections and anomalies not representative of the sample. These unwanted effects are referred to as image artefacts and can be problematic as they can obscure details of interest within the sample (Helliwell et al., 2013).

The XRadia/Zeiss XRM 410, shown in Figure 3.6, is a larger laboratory based machine designed to provide high-resolution scans to 1.0 µm was used. The XRM410 has a large working area within the machine enabling *in-situ* experimentation with purchased, stages. Three different sample sizes of each permeabilities group were scanned in the School of Engineering & Computing Sciences at Durham University. For all three sample sizes a 'small field of view' and a 'large field of view' were performed. The large field of view scan was set up to measure the largest amount of the sample possible whilst the small field of view sample scan was set up to obtain the maximum resolution possible, where a single macro lens (0.4×) for large field of view scans and three high-resolution lens (4×, 10× and 20×) for region of interest scans. All samples are scanned by The XRadia/Zeiss XRM 410, which ensures maximum scan quality.

Figure 3.6: An image of the XRM410 from http://www.dur.ac.uk/xrdur/facilities/xrct.

3.5.1. Data Processing

Avizo Fire, a commercial 3D analysis program capable of providing high-quality 3D visualisation, data processing and analysis techniques (FEI, 2014). Avizo Fire analyses held a major advantage, as it is capable of quickly and easily providing detailed geometric information on materials. For the data analysis, the Avizo Fire analysis was performed using single RAW or txm files. The analysis was performed on a Dell desktop (Intel Xeon E5-2603 CPU @ 1.8GHz, 128Gb of RAM, NVIDIA Quadro 6000 GPU with 71Gb of available graphics memory) in the Earth Sciences Department at Durham University. Since X-ray CT, images represent the density of each voxel within the reconstruction through the use of a greyscale value, the procedures of phase identification for all scanned Berea sandstone specimens is described in more detail in Chapter 4.

3.6. Mercury Injection Porosimetry

Mercury injection capillary porosimetry (MICP) is a technique used for characterising the pore size distribution of porous materials (Abell et al., 1999; Diamond, 2003; Vennat et al., 2009; Houben et al., 2013). The technique is based on the fact that mercury behaves as a non-wetting liquid in contact with the pore space when pressure is sufficiently high: the higher the pressure, the smaller the pore throats that are filled with mercury (Abell et al., 1999). Consequently, it does not penetrate into the openings and cracks of these porous materials without the application of pressure. The pressure (Pw) required is a function of the contact angle (θHg) of mercury with the porous material to be intruded, its gas/liquid surface tension (γHg) and pore radius. This relationship is given by the Younge Laplace law for the particular case of cylindrical pores as the Washburn equation (Kate and Gokhale, 2006):

$$r_p = \frac{2\gamma_{sHg} COS\theta_{Hg}}{P_w} \qquad (3.4)$$

Where:

- rp = Pore radius.
- γHg = Gas/liquid surface tension.
- θHg = The contact angle of mercury.
- Pw = Pressure differences.

This equation dictates that with increasing pressure, the mercury will intrude into progressively narrower pores for constant values of γ_{Hg} and θ_{Hg}. Based on a set of

assumptions on pore morphology, a pore size distribution curve is obtained from the intruded volume at each pressure step.

For this thesis, the mercury porosimetry experiments were carried out with a Micromeritics Poresizer 9320 at the School of Civil Engineering and Geosciences, at the University of Newcastle. The samples used in this analysis were subsamples of core Berea sandstone, dried at a temperature of 40 °C before MIP experiments. The samples were placed in the mercury filled sample cup in a pressure vessel. Then the pressure was slowly increased from 3 psi to 39,000 psi, which corresponds to a pore access diameter of three nm.

3.7. Environmental Scanning Electron Microscopy

Environmental scanning electron microscopy (ESEM) was developed about 25 years ago. A company called ElectroScan made the first ESEMs, and they were built on a chassis provided by Philips Electron Optics. Although ESEM has been commercially available for over a decade, it is only recently that it has begun to use in the diverse field of materials. The ESEM permits observation-hydrated materials in their original condition (e.g., Donald, 2003; Redwood et al., 2005). This increased versatility allowed application of the ESEM techniques to different research fields including, for example, the study of colloids (e.g., Donald et al., 2000). In reservoir rocks and petroleum engineering, the studies commonly focused on wettability alteration at different conditions (Fassi-Fihri et al., 1995; Robin et al., 1998; Robin, 2001; Al-Shafei and Okasha, 2009; Polson et al., 2010; Dodd et al., 2014).

3.7.1. Instrument Basics

The ESEM is a commercial SEM-type instrument that employs low to no vacuum near the specimen. ESEM differs from conventional SEM in that, instead of the sample chamber being held under a high vacuum, a gaseous environment of a few Torr can be maintained in the chamber whilst imaging is carried out, although the electron gun and electron column are both kept at the standard vacuum pressures of around 10^{-6} to 10^{-7} Torr. This is achieved by the use of differential pumped zones, separated pressure-limiting (or differential) apertures (see Figure 3.7).

As indicated above, the ESEM can operate with a gas pressure (up to ~20 Torr) in the sample chamber, and one of the commonly used gases is water vapour. The primary electron beam is very energetic, and it travels through the gas (penetrates the water vapour)

with little apparent scatter, scanning across the surface of the sample. Most scattering that could affect resolution occurs between the final pressure-limiting aperture at the bottom of the column and the sample surface; hence, there is the need to reduce this distance to a minimum.

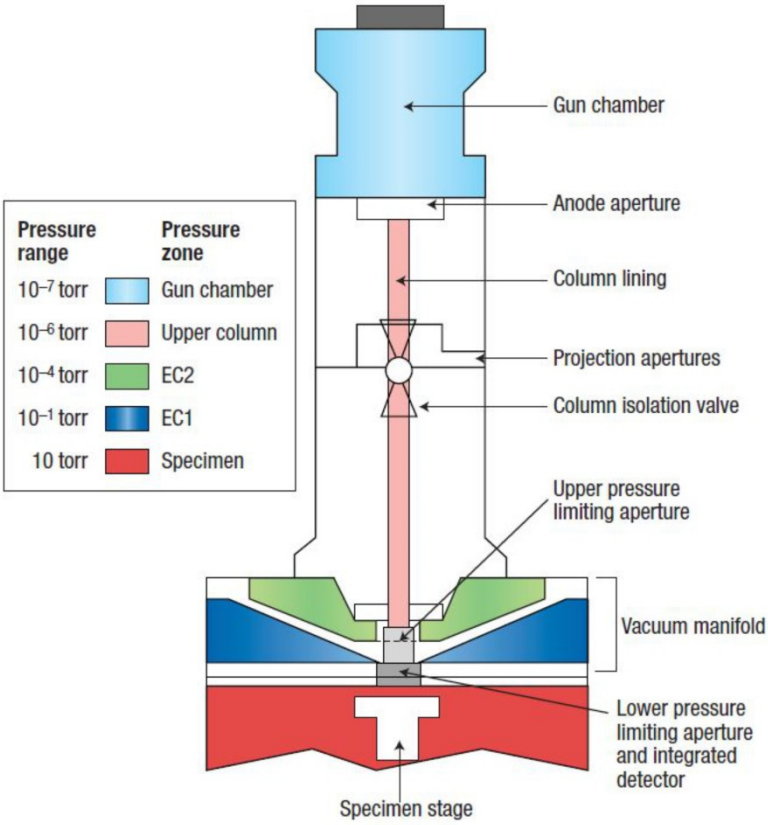

Figure 3.7: Multistage differential pressure pumping unit of a generic ESEM. The gun can be maintained at high vacuum, while a system of differential pumping- and pressure-limiting apertures allows the chamber to be maintained at a pressure of a few Torr. Extracted from Donald, (2003) after permission).

The secondary electrons in particular, because of their low energies, have a high collision cross-section with the gas molecules, and ionization of the molecules has a significant probability of occurring. Each such ionizing collision leads to the generation of an additional daughter electron, so that cascade amplification occurs, shown schematically in Figure 3.8. The amplified secondary electron signal is collected efficiently at the gaseous secondary electron detector (GSED), with its strong and local positive charge. The intensity of that signal is converted into a brighter or darker contrast.

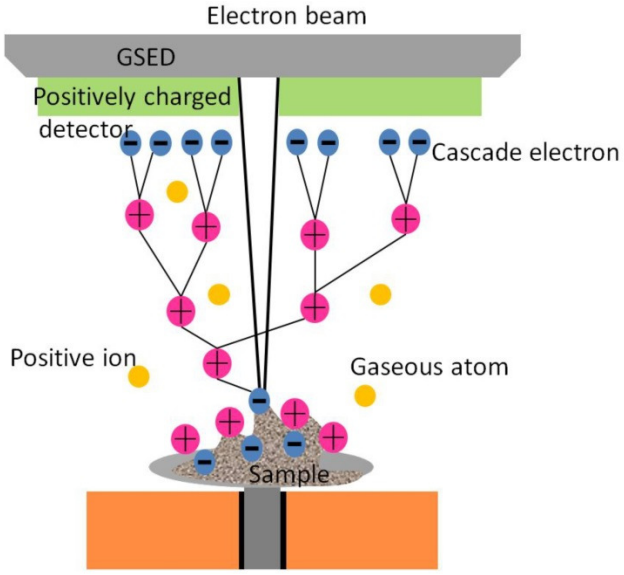

Figure 3.8: The cascade amplification process. This process occurs within the chamber, where the gas molecules are ionized by the secondary electrons emitted from the sample. Each ionizing collision gives rise to a daughter electron, which, like the original electron, is accelerated towards the positively charged detector, and further collisions can occur en-route to the detector. The positive ions generated drift back towards any negative charges the sample surface. Modified from Donald, (2003) after permission**.**

3.7.2. Sample Imaging-Wet State

To study wetting behaviour on minerals surfaces, the studied samples were necessarily cooled at 5 °C in the refrigerator before mounted on a Peltier stage in the ESEM chamber. As indicated above, the water vapour introduces into the specimen chamber via a separate valve that can be used to control the chamber pressure. At the same time, the temperature and chamber pressure, hydrated samples can be kept fully hydrated during the examination. The equilibrium phase diagram for water given in Figure 3.9 shows that when the pressure in the sample chamber is maintained at about 6.0 Torr, and the temperature of the sample is maintained at 5 °C, then as the relative humidity inside the chamber reaches 100%, water will condense as droplets onto the surface of the cooled sample, allowing observation of the contact angle between the sample and water droplets.

As indicated above, the ESEM can operate with a significant gas pressure around the sample. In principle, this means that "wet" mode allows visualisation of samples in the presence of fluids. In this case, quantitative assessment of the wettability was carried out in an FEI/Philips XL30 ESEM equipped with a gaseous secondary electron detector (GSED) and a Peltier stage capable of operating at +/-20 °C from ambient temperature (maximum range -5°C to +60 °C). The pre-cooled sample placed onto the Peltier stage, which was

maintained at 5 °C to minimise sample dehydration during pump down. The wet mode was selected from the ESEM controller, and the chamber was evacuated to 5.96 Torr and then flooded five times with water vapour from 5.96 Torr to 9.97 Torr, with the cycle terminating at 6 Torr/5.5 Torr.

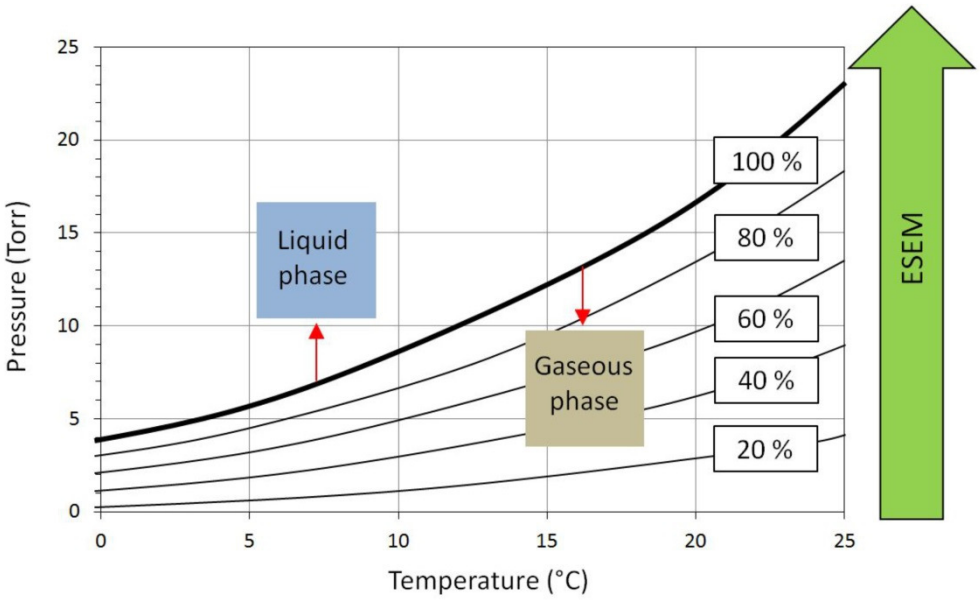

Figure 3.9: Saturated vapour pressure of water as a function of temperature. The useful ranges of working conditions for the ESEM are shown; it can be seen that the state of the sample can be changed by small alterations in temperature. Modified from Al-Shafei and Okasha, (2009).

These conditions produced a suitable atmosphere for providing the water vapour needed for the experiment, as shown in Figure 3.9, whilst also maintaining sample hydration, suppressing charge, and facilitating image amplification. After gaining an image of a suitable area of the sample, the pressure in the chamber was first reduced to 4.5 Torr and then increased incrementally until direct condensation of water onto the sample surface was observed. (Alternatively, the pressure was increased incrementally from 5.5 Torr.) In order to locate the best position to measure the contact angel, the image was, if necessary, scan-rotated. Micrographs were taken with high resolution and magnification, from which observations of droplet morphology and contact angle relative to the sample substrate were made. The pressure was increased until the condensed water droplets "grew" at an acceptable rate, and the experiment was terminated when the viewing surface was seen to be flooded with water. The typical pressures observed were 6.8 Torr and 7.1 Torr during this study. Usually, the pressure used was based on the type of brine such as NaCl and $CaCl_2$.

3.7.3. Sample Preparation

Contact angles were measured on quartz crystals, and Berea core chips, by using ESEM. This set up includes a serious of preparation step, including saturation of samples in formation water, and aging, which is used to examine the effect of brine on aged samples. Additionally, similar steps were also replicated in other techniques. The preparation of samples is described in detail in Chapter 5 and Chapter 6.

3.8. Pendant Drop Shape Technique

Regarding the scale of the observations, it is significant to obtain reproducible data from the ESEM techniques and correlate them with the conventional method (drop shape analysis) to evaluate wettability behaviours. The wettability plays an important role in the determination of residual oil saturation and recovery efficiency during waterflooding in sandstone rock (Nasralla et al., 2013). An analysis of the drop profile is commonly used for the contact angle measurement between the liquid drop and sample surface. However, in many cases such as ESEM, it is difficult to carry out this measure; therefore, it is necessary to evaluate the shape of the drop from optical view.

3.8.1. Drop Shape Method

Numerous methods have been developed to determine the contact angle and liquid surface tension from the pendant drop techniques, the shape of a sessile drop, or captive bubble. The applications and limitations of these techniques are described in the literature (Yuan and Lee, 2013). The pendant drop technique is a simple and accurate method for measuring the interfacial or surface tension that exists when two phases are present. These phases can be brine/oil, or brine/oil model compounds. A droplet of one liquid is created in a cell containing the second liquid (immiscible with the first one). This is done by injecting the liquid through a needle tip. The drop is attached to the needle-tip by capillary forces, and a picture of the droplet is taken. The shape of the pendant drop is determined by the size of the drop and the interfacial tension between the two immiscible liquids (Gentle and Barnes, 2005). Since the shape and size can be directly measured, IFT can then be calculated from the picture. The evaluation of the drop shape is based on the Young-Laplace equation (Bashforth and Adams, 1883). This equation defines the pressure difference (Laplace pressure) between the areas inside and outside of a curved liquid surface/interface with the principle radii of curvature.

$$\Delta p = (P_{int} - P_{ext}) = \sigma \left(\frac{1}{R_1} + \frac{2}{R_2}\right) \quad (3.5)$$

Where:

- $P_{int} - P_{ext}$ = Pressure on the concave and convex sides of the surface, respectively.
- σ = Interfacial tension.
- R_1 and R_2 = Two principal radii of curvature of the surface.

The forces that determine the shape of the pendant drop are the surface tension and gravitation. The surface tension seeks to minimise the surface area and get the drop into a spherical shape. Gravitation, on the other hand, stretches the drop from this spherical shape and the typical pear-like shape results. Gravitation causes a pressure difference across the z-axis according to Pascal's law (hydrostatic pressure). Therefore the Laplace pressure ΔP (z) at a distance z from an arbitrary reference plane with Laplace pressure ΔP_0 is:

$$\Delta P\,(z) = \Delta P_0 \pm \Delta P \rho g z \quad (3.6)$$

Where:

- ρ = Density of fluid on the concave and convex side of the surface.
- g = Acceleration due to gravity.

For a pendant drop, the principal radii of curvature at the vertex (lowest point of the drop) are $R_1=R_2=R$. Thus, it is convenient to place the reference plane at this point. For every point above it holds R2=x/sin Φ (see figure 3.10). The mentioned equations lead to:

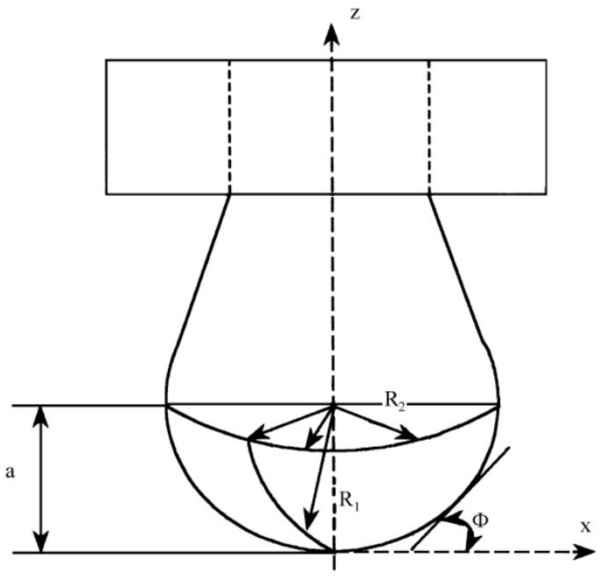

Figure 3.10: Geometric treatment at the apex of the pendant drop from (Arashiro and Demarquette, 1999).

$$\frac{1}{R_1} + \frac{\sin \Phi}{x} = \frac{2}{R} + \frac{\Delta \rho g z}{\sigma} \tag{3.7}$$

The numerical fit of the theoretical drop shape to the shape recorded by the camera eventually yields the surface tension. The described considerations also apply when the surrounding phase is not air but another liquid. It is important that the pendant drop is at least a certain minimum size. If the droplet is not large enough, the diameter of the pendant drop will come too close to the needle tip and the calculation will not be correct.

3.8.2. Drop Shape Analysis

The Young-Laplace fit can also be used to analyse the deformation of a drop sitting on a solid surface for determining the contact angle in the sessile drop method.During the early years of contact angle measurement, the θ/2 method was once widely used to analyse the profile of a sessile drop. In this analysis, contact angles can also be examined with an optical contact angle measuring and contour analysis system. The high-resolution camera is used to capture an image of a liquid droplet that sits on a solid (sessile drop) and to subsequently analyse it with software. The evaluation of the grey scale values of the recorded image allows for the detection of the so-called baseline (contact between the droplet and solid) and the drop outline. In general, the Young-Laplace method yields the most reliable results, especially for large contact angles and big drops. It has to be kept in mind, however, that with the Young-Laplace method one always obtains a common contact angle for the left and right intersection with the base line because the calculation assumes a symmetric drop. A drop-shape analyser (Kruss DSA 100) apparatus was used at room temperature and pressure (as seen in Chapter 5 in Figure 5.6). DSA100 is a high-quality technique for measurement of both the equilibrium interfacial tension and the contact angle.

3.8.3. Sample Preparation

Although drop shape can be used to satisfactorily identify the wettability behaviours in different mineral surfaces (such as quartz, calcite, and mica) that are the main commonly encountered minerals in the composition of rock samples, it is generally not possible to measure the contact angle on non-polish surfaces, due to the impact of surface roughness on the measured contact angle. As such, model polished surfaces offer advantages for

wetting observation. For sample preparation, a similar approach as has been used in previous techniques was applied. A more detailed description is provided in Chapter 6.

3.9. Zeta Potential Measurements

Recently, modification of the salinity of the injected brine in sandstone reservoirs has been widely used to improve oil recovery. Several possible low-salinity waterflooding mechanisms in sandstone rock reservoir have been investigated in order to understand the effect of brine salinity on rock-wettability alteration to provide a better understanding of low salinity waterflooding. Therefore, the effect of changing salinity on electrokinetic charges is investigated by use of zeta potential technique to explain the causes of wettability behaviours by low salinity brine. The zeta potential is defined as the electrical potential developed at a solid-liquid interface in response to the relative movement of solid particles and water (Schulthess and Sparks , 1986). Surface charge is believed to play a major role of the low salinity waterflooding performance. In general, it is believed that the surface charge alternates at the interface in the boundary of hydrodynamic shear between a solid surface and ions as a product of the electrostatic repulsion and attractive force related to the Van der Waal's forces (Shehata and Nasr-El-Din, 2015).

3.9.1. Surface Charge Formation

One of the key parameters characterising the stability of a colloidal suspension is the charge of the particles that define it. The surface charge is the electrical potential difference between the inner and outer surface of the dispersed phase in a colloid (Korpi and de Bruyn, 1972). As a colloidal particle moves through a solution, due to an applied constant voltage field, the ions present in the solution move with it. This phenomenon is known electrophoresis (Zasoski, 2008). Surface charge practically always appears on the particle surface when it contacts with fluids. Most fluids contain ions, positive (cations) and negative (anions). These ions interact with the object surface. In general, there are two different mechanisms that can lead to a surface being charged, the acid-base reactions between the surface functional group and an aqueous solution, and adsorption of ions.

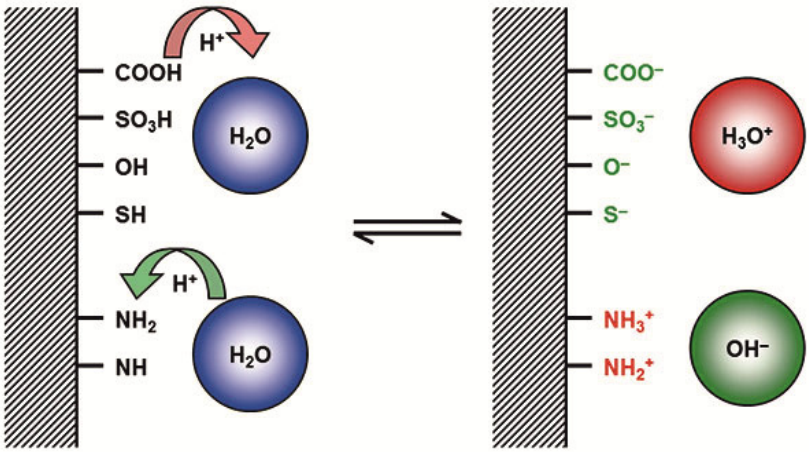

Figure 3.11: Schematic presentation of charge formation at the solid-liquid interface for a hydrophilic material surface with acidic or base functional groups, extracted from Luxbacher, (2014).

An acid group such as carboxylic acid and hydroxyl groups as demonstrated in Figure 3.11 dissociate in water and remain negatively charged. Basic groups such as amine groups used in this example undergo protonation in water and therefore assume a positive charge. This means that the surface charges generated by those acid-base reactions are directly linked to the functional groups that are chemically bound to the surface (Luxbacher, 2014). The equilibrium of the surface charging process depends on the area density of surface functional groups and the pH of the aqueous solution. A high surface group density may inhibit complete dissolution of acidic groups or protonation of basic groups due to the electrostatic repulsion between a charged group and its neighbours. The pH of an aqueous solution is the driving forces of acid-base reaction. At high pH levels, dissociation of acid groups will be enhanced, but protonation of basic groups will be suppressed.

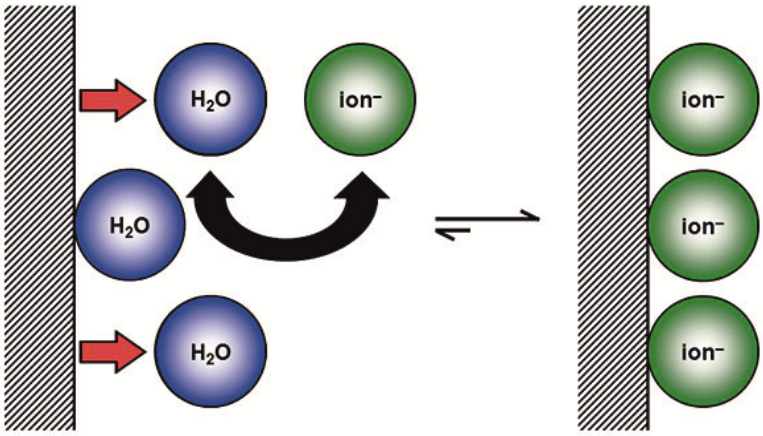

Figure 3.12: Schematic presentation of charge formation at the solid-liquid interface for a hydrophobic material with no functional groups, extracted from Luxbacher, (2014).

The lack of functional groups on some surfaces does not prevent the ability to determine a zeta potential. This means that charging behavior contrasts from the acid-base reactions. The material surfaces in aqueous solutions that do not possesses functional groups behave hydroponically. As it can be seen in Figure 3.12, the presences of the hydrophobic surface affect the water molecules. These water molecules are replaced with water ions such as hydroxide (OH^-) or hydronium (H_3O^+). In this situation, pH once again plays an important role in the sign and number of the surface charges. At high pH, OH^- ion concentration increases, which results in a negative surface charge. At low pH, H_3O^+ concentration becomes dominant, and the surface charge becomes positive.

3.9.2. Electrokinetic phenomena

The measurement of electrokinetic effect is crucial in the determination of zeta potential. It is highly dependent on the size and type of the solid particles and the composition of the surrounding liquid. The surface chemistry and physical structure of particles and liquid properties commonly controls an electrokinetic behavior. The direction and velocity of the particles depend on the dielectric constant and viscosity of the suspending liquid and to the electrical potential at the boundary between the moving particle and the liquid. At some distance from the particle, there exists a “boundary” beyond which ions do not move with the particle. This boundary is known as the slip plane, or (the surface of hydrodynamic shear), and is usually defined as the point where the Stern layer and the diffuse layer meet. The potential exists at the slipping plane that is defined as zeta potential. Zeta analyser used in the experiments, facilities electrokinetic

phenomena in the form of streaming potential and this will be the focus of the successive section.

3.9.3. The Streaming Potential Techniques

It was Georg Hermann Quincke, who for the first time described the streaming potential in 1859. Hermann von Helmholtz in 1879 then described a correlation between the streaming potential and electrical potential difference at the solid-liquid interfaces. The streaming potential is obtained by the tangential flow of liquid phase across the often-stationary solid surface. This technique involves four main steps that illustrate below:

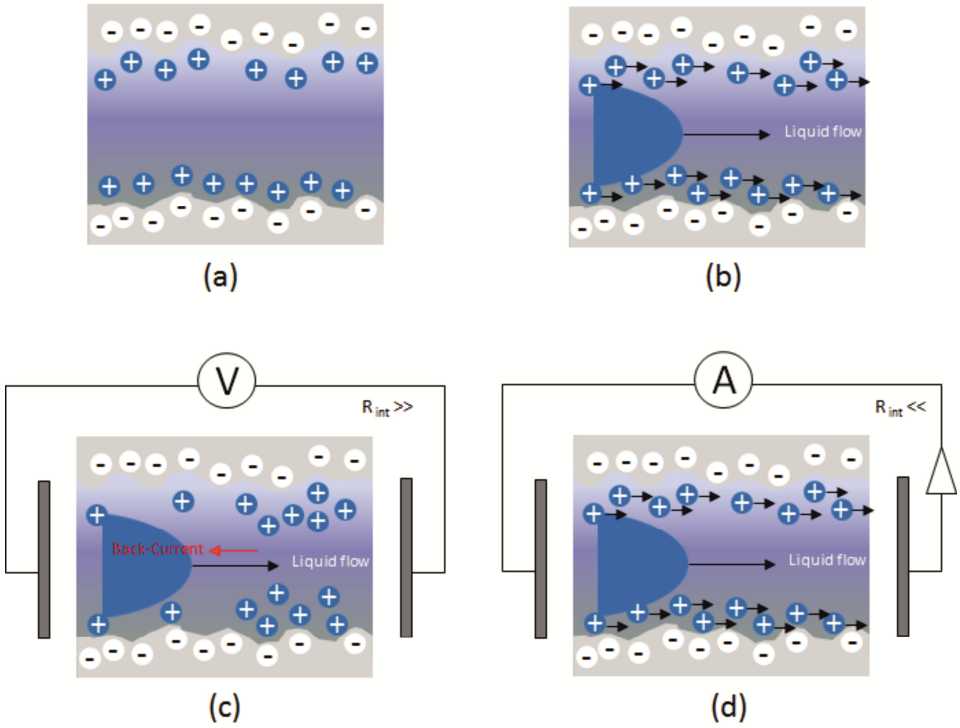

Figure 3.13: Schematic presentation of the streaming potential and the streaming current. a) Soil-liquid interface (charge equilibrium).b) Movement of surface charge compensated ions(due to liquid flow). c) Streaming potential measurement (equilibrium between streaming current/liquid flow and back current/impedance electronic circuit). d) Streaming current measurement (flow impedance electronic circuit), extracted from Luxbacher, (2014).

Once the solid material is contacted with water, a surface charge is generated and is directly compensated by counter-ions in the aqueous solution, as can be seen in Figure 3.13a. An equilibrium of this electrochemical double layer (EDL) is necessary for reliable streaming potential measurement. Since the water is streamed in a capillary system (an e.g. irregular shape such as void between particles of powder), sharing forces act upon the

counterions that compensate the surface charge. Therefore, the sharing forces move these ions in the direction of liquid flow (Figure 3.13b)

Zeta analyser used an electronic circuit of high internal resistance to take measurement of streaming potential. This allows for a charge separation between the inlet and out let of the capillary system. The charges separation leads to the introduction of electric forces that counteracts the liquid flow. Back current of charges forms (red arrow Figure 3.13c) that compensates the current of ions in the liquid flow direction (black arrow Figure 3.13c). The electrical potential difference is observed due to net charge separation, and streaming potential is detected between the two electrodes located at each end of the capillary system. In order to measure the streaming current Figure 3.13d, a different electric circuit is used. In this circuit, a low internal resistance is applied. Once again, aqueous solution, streaming through a capillary system causes the counter ions to shear off, which are moved towards the outlet electrode. Those moving charges initiate an electric current. Streaming current is measured through an interfacial ion electrode charge transfer. Both streaming current and streaming potential measurement depend on volume flow rate, ionic strength and the size of flow channel/capillary system.

3.9.4. Zeta Potential Analysis

Electrokinetic phenomena of the streaming potential and streaming current are represented by the Helmholtz-Smoluchowski equation. The zeta potential is determined using SurPass Electronic Analyser (Anton Paar). In this study, the following equation is used in Attract software for the calculation of the zeta potential:

$$Zeta\ Potential = \frac{dI_{str}}{d\Delta P} X \frac{\eta}{\varepsilon \varepsilon_0} X \frac{L}{A} \qquad (3.8)$$

Where:

- $\frac{dI_{str}}{d\Delta P}$ = Streaming current confident.
- η = Viscosity of electrolyte solution.
- $\varepsilon X \varepsilon_0$ = Dielectric coefficient of electrolyte solution.
- $\frac{L}{A}$ = Cell constant (the gap between two adjacent solid samples).

All materials used in this experiment that mimic the sandstone reservoir rocks exist in granular form. This means that the application of Equation is invalid as the cell constant (L/A) is unknown. This means that it must be another derivation of this equation that the zeta analyser is using in order to approximate the zeta potential, thus leading to findings of Helmholtz-Smoluchowski equation.

This equation uses the definition of electrical conductivity (k),

$$K = \frac{1}{R} X \frac{L}{A} \tag{3.9}$$

This rearrange to;

$$kR = \frac{L}{A} \tag{3.10}$$

Using this, equation is replaced by Equation;

$$Zeta\ Potential = \frac{dI_{str}}{d\Delta P} X \frac{\eta}{EXE_0} X\ kR \tag{3.11}$$

3.10. Infrared Spectroscopy

Infrared (IR) spectroscopy is one of the spectroscopic techniques. Absorbing groups in the infrared region absorb within a certain wavelength region (including gamma and x-rays) to very long wavelengths (including microwaves and broadcast radio waves). The absorption peaks within this region are usually sharper when compared with absorption peaks from the ultraviolet and visible regions (Michaelian, 2003). In this way, IR spectroscopy can be very sensitive to determination of functional groups within a sample since different functional group absorbs different particular frequency of IR radiation (Shabib-Asl et al., 2014). Therefore, each molecule has a characteristic spectrum often referred to as the fingerprint.IR spectroscopy is very useful in the identification and structure analysis of a variety of materials, including both organic and inorganic compounds (Michaelian, 2010).

A spectroscopy technique is useful to characterize and measure the absorption and transmission of a variety of an important material such as liquid sample, and solid sample. Absorbance spectroscopy, commonly referred to as spectrophotometry, is the analytical technique based on measuring the amount of light absorbed by a sample at a given wavelength. In this way, infrared spectroscopy is used as a qualitative measurement of a

sample. IR spectroscopy technique has some advantages and dis advantages. Infrared Spectra could give us lots of structural information of the analyses, such as the type of compound, the functional group of compound and the stereoscopic structure of compound. Depending on the available information form the functional part and the fingerprint. In unstable substance, the scan will be finish before it starts to decompose since IR spectroscopy can get information for the whole range of frequency simultaneously, within one second. The disadvantages of IR spectroscopy include, sample constraints and quantification of data that depend on certain conditions.

The infrared (IR) spectroscopy (Spectrum Two™ from PerkinElmer) was used, which includes Spectrum 10 software and delivers a scan range of 8,300-350cm^{-1}, while offering 0.5cm^{-1} resolution and 9,300:1 peak-peak signal-to-noise for 4 second scan.

3.11. Total Organic Carbon

Total organic carbon is a non-specific test, which means TOC analysis will not determine which particular compounds are present in the sample (most samples are complex mixtures that contain thousands of different organic carbon compounds). Instead, TOC will evaluate the sum of all organic carbon within those compounds. TOC of the samples was performed at Durham University using a Costech Elemental Analyser (ECS 4010) connected to a Thermo Finnigan Delta V Advantage isotope ratio mass spectrometer. Sample preparation for TOC involved weighing the mass of the sample followed by a 50 ml treatment of 3M hydrochloric acid that de-calcified the powdered samples. Samples were then rinsed with de-ionised water until pH neutrality was obtained, and then dried in an oven at 60 °C. In addition, the technique used for preparation of samples such as water saturation, aging with oil and washing in brines is described in detail in Chapter 6.

3.12. References

Abell, A. B., K. L. Willis, and D. A. Lange, 1999, Mercury Intrusion Porosimetry and Image Analysis of Cement-Based Materials: Journal of Colloid and Interface Science, v. 211, no. 1, p. 39–44, doi:10.1006/jcis.1998.5986.

Al-Shafei, M. A., and T. M. Okasha, 2009, Wettability Studies at the Pore Level of Saudi Aramco Reservoirs: Society of Petroleum Engineers, doi:10.2118/126088-MS.

Bashforth, F., and J. C. Adams, 1883, An attempt to test the theories of capillary action by comparing the theoretical and measured forms of drops of fluid. With an explanation of the method of integration employed in constucting the tables which give the theoretical forms of such drops: Cambridge [Eng.] University Press, 162 p.

Bera, B., S. K. Mitra, and D. Vick, 2011, Understanding the micro structure of Berea Sandstone by the simultaneous use of micro-computed tomography (micro-CT) and focused ion beam-scanning electron microscopy (FIB-SEM): Micron, v. 42, no. 5, p. 412–418, doi:10.1016/j.micron.2010.12.002.

Bloss, F. D., 1994, Crystallography and Crystal Chemistry: An Introduction: Mineralogical Society of Amer.

Bullock, R. J., N. De Paola, R. E. Holdsworth, and J. Trabucho-Alexandre, 2014, Lithological controls on the deformation mechanisms operating within carbonate-hosted faults during the seismic cycle: Journal of Structural Geology, v. 58, p. 22–42, doi:10.1016/j.jsg.2013.10.008.

Chen, L., J. Xu, and J. Chen, 2015, Applications of scanning electron microscopy in earth sciences: Science China Earth Sciences, v. 58, no. 10, p. 1768–1778, doi:10.1007/s11430-015-5172-9.

Churcher, P. L., P. R. French, J. C. Shaw, and L. L. Schramm, 1991, Rock Properties of Berea Sandstone, Baker Dolomite, and Indiana Limestone: Society of Petroleum Engineers, doi:10.2118/21044-MS.

Diamond, S., 2003, A DISCUSSION OF THE PAPER “Effect of Drying on Cement-Based Materials Pore Structure as Identified by Mercury Porosimetry - Comparative Study between Oven-, Vacuum-, and Freeze-Drying” by C. Galle: Cement and Concrete Research, v. 33, no. 1.

Dodd, N. et al., 2014, Pore-Scale Imaging of Oil and Wettability in Native-State, Mixed-Wet Reservoir Carbonates.

Donald, A. M., 2003, The use of environmental scanning electron microscopy for imaging wet and insulating materials: Nature Materials, v. 2, no. 8, p. 511–516, doi:10.1038/nmat898.

Donald, A. M., C. He, C. P. Royall, M. Sferrazza, N. A. Stelmashenko, and B. L. Thiel, 2000, Applications of environmental scanning electron microscopy to colloidal aggregation and film formation: Colloids and Surfaces A: Physicochemical and

Engineering Aspects, v. 174, no. 1–2, p. 37–53, doi:10.1016/S0927-7757(00)00520-3.

Fassi-Fihri, O., M. Robin, and E. Rosenberg, 1995, Wettability Studies at the Pore Level: A New Approach by the Use of Cryo-Scanning Electron Microscopy: SPE Formation Evaluation, v. 10, no. 1, p. 11–19, doi:10.2118/22596-PA.

Gatlin, C. L., E. S. Schaberg, W. H. Jordan, B. L. Kuyatt, and W. C. Smith, 1993, Point counting on the Macintosh. A semiautomated image analysis technique: Analytical and Quantitative Cytology and Histology / the International Academy of Cytology [and] American Society of Cytology, v. 15, no. 5, p. 345–350.

Gentle, I., and G. Barnes, 2005, Interfacial Science: An Introduction: Oxford University Press, 247 p.

Hall, M. G., and G. E. Lloyd, 1981, The SEM examination of geological samples with a semiconductor back-scattered electron detector: American Mineralogist, v. 66, no. 3–4, p. 362–368.

Hansma, H. G., R. L. Sinsheimer, J. Groppe, T. C. Bruice, V. Elings, G. Gurley, M. Bezanilla, I. A. Mastrangelo, P. V. Hough, and P. K. Hansma, 1993, Recent advances in atomic force microscopy of DNA: Scanning, v. 15, no. 5, p. 296–299.

Hassenkam, T., A. C. Mitchell, C. S. Pedersen, L. L. Skovbjerg, N. Bovet, and S. L. S. Stipp, 2012, The low salinity effect observed on sandstone model surfaces: Colloids and Surfaces A: Physicochemical and Engineering Aspects, v. 403, p. 79–86, doi:10.1016/j.colsurfa.2012.03.058.

Hassenkam, T., C. S. Pedersen, K. Dalby, T. Austad, and S. L. S. Stipp, 2011, Pore scale observation of low salinity effects on outcrop and oil reservoir sandstone: Colloids and Surfaces A: Physicochemical and Engineering Aspects, v. 1–3, no. 390, p. 179–188, doi:10.1016/j.colsurfa.2011.09.025.

Helliwell, J. R., C. J. Sturrock, K. M. Grayling, S. R. Tracy, R. J. Flavel, I. M. Young, W. R. Whalley, and S. J. Mooney, 2013, Applications of X-ray computed tomography for examining biophysical interactions and structural development in soil systems: a review: European Journal of Soil Science, v. 64, no. 3, p. 279–297, doi:10.1111/ejss.12028.

Hendee, W., 1979, Medical Radiation Physics: Chicago, Year Book Medical Publishers, 517 p.

Houben, M. E., G. Desbois, and J. L. Urai, 2013, Pore morphology and distribution in the Shaly facies of Opalinus Clay (Mont Terri, Switzerland): Insights from representative 2D BIB–SEM investigations on mm to nm scale: Applied Clay Science, v. 71, p. 82–97, doi:10.1016/j.clay.2012.11.006.

Hutter, J. L., and J. Bechhoefer, 1993, Calibration of atomic-force microscope tips: Review of Scientific Instruments, v. 64, no. 7, p. 1868–1873, doi:10.1063/1.1143970.

Johnson, D., N. Hilal, and W. R. Bowen, 2009, Atomic Force Microscopy in Process Engineering: doi:10.1016/B978-1-85617-517-3.00001-8.

Kate, J. M., and C. S. Gokhale, 2006, A simple method to estimate complete pore size distribution of rocks: Engineering geology, v. 84, no. 1–2, p. 48–69.

Korpi, G. K., and P. L. de Bruyn, 1972, Measurement of streaming potentials: Journal of Colloid and Interface Science, v. 40, no. 2, p. 263–266, doi:10.1016/0021-9797(72)90015-X.

Landrot, G., J. B. Ajo-Franklin, L. Yang, S. Cabrini, and C. I. Steefel, 2012, Measurement of accessible reactive surface area in a sandstone, with application to CO2 mineralization: Chemical Geology, v. 318–319, p. 113–125, doi:10.1016/j.chemgeo.2012.05.010.

Larrea, M. L., S. M. Castro, and E. A. Bjerg, 2013, A software solution for point counting. Petrographic thin section analysis as a case study: Arabian Journal of Geosciences, v. 7, no. 8, p. 2981–2989, doi:10.1007/s12517-013-1032-0.

Logan, B. W., and V. Semeniuk, 1976, Dynamic Metamorphism: Processes and Products in Devonian Carbonate Rocks, Canning Basin, Western Australia: Geological Society of Australia, 154 p.

Ma, S., and N. R. Morrow, 1994, Effect of Firing on Petrophysical Properties of Berea Sandstone: SPE Formation Evaluation, v. 9, no. 3, p. 213–218, doi:10.2118/21045-PA.

Michaelian, K. H., 2003, Photoacoustic Infrared Spectroscopy: Wiley-Interscience, 360 p.

Michaelian, K. H., 2010, Photoacoustic IR Spectroscopy: Instrumentation, Applications and Data Analysis: John Wiley & Sons, 404 p.

Nasralla, R. A., M. B. Alotaibi, and H. A. Nasr-El-Din, 2011, Efficiency of Oil Recovery by Low Salinity Water Flooding in Sandstone Reservoirs: Society of Petroleum Engineers, doi:10.2118/144602-MS.

Nasralla, R. A., M. A. Bataweel, and H. A. Nasr-El-Din, 2013, Investigation of Wettability Alteration and Oil-Recovery Improvement by Low-Salinity Water in Sandstone Rock: Journal of Canadian Petroleum Technology, v. 52, no. 2, p. 144–154, doi:10.2118/146322-PA.

Newport, L. P., A. C. Aplin, J. G. Gluyas, H. C. Greenwell, and D. R. Gröcke, 2016, Geochemical and lithological controls on a potential shale reservoir: Carboniferous Holywell Shale, Wales: Marine and Petroleum Geology, v. 71, p. 198–210, doi:10.1016/j.marpetgeo.2015.11.026.

Oak, M. J., L. E. Baker, and D. C. Thomas, 1990, Three-Phase Relative Permeability of Berea Sandstone: Journal of Petroleum Technology, v. 42, no. 8, p. 1,054-1,061, doi:10.2118/17370-PA.

Ohnesorge, F., and G. Binnig, 1993, True atomic resolution by atomic force microscopy through repulsive and attractive forces: Science (New York, N.Y.), v. 260, no. 5113, p. 1451–1456, doi:10.1126/science.260.5113.1451.

Omotoso, O., D. K. McCarty, S. Hillier, and R. Kleeberg, 2006, Some Successful Approaches to Quantitative Mineral Analysis as Revealed by the 3rd Reynolds Cup Contest: Clays and Clay Minerals, v. 54, no. 6, p. 748–760, doi:10.1346/CCMN.2006.0540609.

Ortiz, J. D., L. Polyak, J. M. Grebmeier, D. Darby, D. D. Eberl, S. Naidu, and D. Nof, 2009, Provenance of Holocene sediment on the Chukchi-Alaskan margin based on combined diffuse spectral reflectance and quantitative X-Ray Diffraction analysis: Global and Planetary Change, v. 68, no. 1–2, p. 73–84, doi:10.1016/j.gloplacha.2009.03.020.

Pecharsky, V., and P. Zavalij, 2005, Fundamentals of Powder Diffraction and Structural Characterization of Materials: Springer Science & Business Media, 732 p.

Pedersen, N. R., T. Hassenkam, M. Ceccato, K. N. Dalby, K. Mogensen, and S. L. S. Stipp, 2016, Low Salinity Effect at Pore Scale: Probing Wettability Changes in Middle East Limestone: Energy & Fuels, v. 30, no. 5, p. 3768–3775, doi:10.1021/acs.energyfuels.5b02562.

Peng, S., Q. Hu, S. Dultz, and M. Zhang, 2012, Using X-ray computed tomography in pore structure characterization for a Berea sandstone: Resolution effect: Journal of Hydrology, v. 472–473, p. 254–261, doi:10.1016/j.jhydrol.2012.09.034.

Peters, C. A., 2009, Accessibilities of reactive minerals in consolidated sedimentary rock: An imaging study of three sandstones: Chemical Geology, v. 265, no. 1–2, p. 198–208, doi:10.1016/j.chemgeo.2008.11.014.

Polson, E. J., J. O. Buckman, D. G. Bowen, A. C. Todd, M. M. Gow, and S. J. Cuthbert, 2010, An Environmental-Scanning-Electron-Microscope Investigation Into the Effect of Biofilm on the Wettability of Quartz: SPE Journal, v. 15, no. 1, p. 223–227, doi:10.2118/114421-PA.

Ramirez, W. F., A. C. Oen, J. F. Strobel, J. L. Falconer, and H. E. Evans, 1986, Surface Composition of Berea Sandstone: SPE Formation Evaluation, v. 1, no. 1, p. 23–30, doi:10.2118/11972-PA.

Redwood, P. S., J. R. Lead, R. M. Harrison, I. P. Jones, and S. Stoll, 2005, Characterization of humic substances by environmental scanning electron microscopy: Environmental Science & Technology, v. 39, no. 7, p. 1962–1966.

Reimers, P., and J. Goebbels, 1983, New possibilities of non-destructive evaluation by x-ray computed tomography: Materials Evaluation, v. 41, p. 732–737.

Robin, M., 2001, Interfacial Phenomena: Reservoir Wettability in Oil Recovery: Oil & Gas Science and Technology, v. 56, no. 1, p. 55–62, doi:10.2516/ogst:2001007.

Robin, M., R. Combes, and L. Cuiec, 1998, Two SEM Techniques To Investigate Reservoir-Rock Wettability: Journal of Petroleum Technology, v. 50, no. 11, p. 77–79, doi:10.2118/1198-0077-JPT.

Schulthess, C. P., and D. L. Sparks, 1986, Backtitration technique for proton isotherm modeling of oxide surfaces: Soil Science Society of America journal (USA).

Shabib-Asl, A., M. A. A. Mohammed, M. Kermanioryani, and P. P. J. Valentim, 2014, Effects of Low Salinity Water Ion Composition on Wettability Alteration in Sandstone Reservoir Rock: A Laboratory Investigation: Journal of Natural Sciences Research, v. 4, no. 13, p. 34–41.

Shand, S. J., 1916, A Recording Micrometer for Geometrical Rock Analysis: The Journal of Geology, v. 24, no. 4, p. 394–404, doi:10.1086/622346.

Shehata, A. M., and H. A. Nasr-El-Din, 2015, Zeta Potential Measurements: Impact of Salinity on Sandstone Minerals: Society of Petroleum Engineers, doi:10.2118/173763-MS.

Siretanu, I., D. van den Ende, and F. Mugele, 2016, Atomic structure and surface defects at mineral-water interfaces probed by in situ atomic force microscopy: Nanoscale, v. 8, no. 15, p. 8220–8227, doi:10.1039/C6NR01403H.

Stricker, S., and S. J. Jones, 2016, Enhanced porosity preservation by pore fluid overpressure and chlorite grain coatings in the Triassic Skagerrak, Central Graben, North Sea, UK: Geological Society, London, Special Publications, v. 435, p. SP435.4, doi:10.1144/SP435.4.

Tang, G. Q., and N. R. Morrow, 1997, Salinity, Temperature, Oil Composition, and Oil Recovery by Waterflooding: SPE Reservoir Engineering, v. 12, no. 4, p. 269–276, doi:10.2118/36680-PA.

Trtik, P., J. Kaufmann, and U. Volz, 2012, On the use of peak-force tapping atomic force microscopy for quantification of the local elastic modulus in hardened cement paste: Cement and Concrete Research, v. 42, no. 1, p. 215–221, doi:10.1016/j.cemconres.2011.08.009.

Vennat, E., C. Bogicevic, J.-M. Fleureau, and M. Degrange, 2009, Demineralized dentin 3D porosity and pore size distribution using mercury porosimetry: Dental Materials: Official Publication of the Academy of Dental Materials, v. 25, no. 6, p. 729–735, doi:10.1016/j.dental.2008.12.002.

Wellington, S. L., and H. J. Vinegar, 1987, X-Ray Computerized Tomography: Journal of Petroleum Technology, v. 39, no. 8, p. 885–898, doi:10.2118/16983-PA.

Welton, J. E., 1983, SEM Petrology Atlas: American Association of Petroleum Geologists.

Wentworth, C. K., 1923, An Improved Recording Micrometer for Rock Analysis: The Journal of Geology, v. 31, no. 3, p. 228–232, doi:10.1086/623009.

Yuan, Y., and T. R. Lee, 2013, Contact Angle and Wetting Properties: p. 3–34, doi:10.1007/978-3-642-34243-1_1.

Zasoski, R. J., 2008, Zeta potential: p. 841–845, doi:10.1007/978-1-4020-3995-9_644.

Chapter 4

Multi-technique Approach to the Petrophysical Characterization of Berea Sandstone Core Plugs (Cleveland Quarries, USA)

4.1. Introduction

In an age of increasing energy use, coupled with the depletion of conventional global oil resources, the development and optimization of enhanced oil recovery (EOR) techniques is critical to sustain oil supplies and to ensure maximum value is delivered from producing oilfield assets. Oil-production from EOR projects continues to supply an increasing percentage of the world's oil. About 3% of the worldwide production now comes from EOR (Aghaeifar et al., 2015). Therefore, the importance of choosing the "best" recovery method becomes increasingly important to petroleum engineers. Low-salinity (LS) water flooding EOR has attracted considerable attention in the last decade due to its potential low-cost as an EOR technique (Tang and Morrow, 1999; Webb et al., 2004; Lager et al., 2006; Sorbie and Collins, 2010). However, despite numerous studies, the main mechanism underpinning increased hydrocarbon recovery by low salinity EOR remains unresolved, particularly in sandstone reservoirs (Strand et al. 2014).

Sandstone reservoirs show the best potential for implementation of EOR projects when compared with other reservoir lithologies and the majority of the pilot and commercial scale studies are in sandstones (Alvardo and Eduardo, 2010). Typically, the heterogeneity of pore-lining minerals in sandstone reservoir rock samples has been postulated to be important in determining underpinning mechanisms during EOR as these have a key role in changing the wettability and modifying fluid flow properties. Use of a

standard, model sandstone for test and investigation has been encouraged and the Berea sandstone of eastern Ohio, western Pennsylvania, western West Virginia, and eastern Kentucky has been used extensively in studies of transport mechanisms at the pore scale (denoted hereafter as BST) (Alotaibi et al., 2010; Nasralla et al., 2011b; Zhang et al., 2012). The BST used in the present study is from a single sandstone unit deposited above the Bedford shale formation, representing a cycle of deposition during an oscillation in the land and sea level (at first subaerially as a delta, and later as a marine pavement that formed as the sea inundated this delta) between two periods of tectonic quiescence of the Devonian period (Pashin and Ettensohn, 1995). Previous studies have deployed various high resolution imaging techniques to characterize reservoir sandstones, including scanning electron microscopy (SEM) and micro X-ray computer tomography (µ-XCT), as the basis for statistical models of the volumetric and effective mineralogy distribution within different sandstone samples, including BST (Peters (2009); Bera et al., (2011); Landrot et al., (2012); Golab et al., (2013); Waldmann et al., (2014); and Lai and Krevor (2014)). However, these studies have not been conclusive in quantifying the amount and distribution of clay minerals in sandstones (and in particular, within the pore space). This is very important, owing to the potential reactivity of clay mineral surfaces with pore fluids. There has also been a substantial discussion of the uncertainties associated with measuring the reactivity of surface-coating minerals (e.g. the importance of edge surface areas for phyllosilicate clay minerals such as smectites (Metz et al., 2005), or etched surfaces in quartz grains (Gautier et al., 2001).

In this work, pore-lining, reactive minerals, which include minerals other than quartz and K-feldspar (e.g., kaolinite, illite and surface coating nanoparticles), were studied using SEM mineral mapping techniques, and then compared with volumetric mineralogy obtained using X-ray diffraction (XRD) and µ-XCT. Atomic force microscopy (AFM) was used to characterize nanoparticles covering the pore-lining minerals, and therefore, gain a level of understanding unachievable by conventional and even high-resolution SEM imaging. Finally, a study of the pore distribution and connectivity within BST was undertaken using µ-XCT and mercury injection capillary porosimetry (MICP). The overarching goal of this study is to identify inter- and intra-mineral heterogeneity on the pore surfaces of BST to demonstrate the use of a multi-technique/multi-scale approach for rock characterization. Since selected core plugs exhibit macroscopic and nanoscopic heterogeneities associated with changes in the depositional environment and diagenesis, it

is beyond the scope of this study to characterise the full range of variability in BST. However, representative samples have been chosen from each of the four permeabilities to study the variations. The information gathered in this study will be used to design future core-scale low salinity EOR studies, where a detailed knowledge of surface mineral reactivity and post-flood changes will be needed.

4.2. Methods and Characterisation

In this chapter, twenty six Berea core samples, obtained from Cleveland Quarries, USA, were studied. These samples can be grouped into 4 permeability ranges, referred to BST.1 to BST.4 (Table 1) Four samples of BST.1, five samples of BST.2, thirteen samples of BST.3, and four samples of BST.4 were studied. It should be noted that the permabilities of all Berea samples reported are air permability and were measured by the supplier. Details of the characterized properties are presented in Table.1. The core samples chosen for the study were shipped to the UK as drilled to a small 1 ½" diameter x 2" long core from the corner of the quarried blocks which were approximately 7' x 4 ½' x 4' (Darlene Ondercin, personal communication, April 6, 2016). A request was made in order to ensure that bedding plane orientation was parallel to the length of the requested cores.

4.2.1. Bulk Composition

4.2.1. Optical Microscopy Petrographic Study

In this study, a detailed optical microscopy study on 52 thin sections was performed using a Nikon Eclipse 50iPOL polarizing microscope. Two thin sections from each of the 26 core samples were characterized (see Figure 4.1). One thin section was parallel to the length of the BST core plugs (bedding plane orientation), and the other was a plane perpendicular to the length of core plugs. Although these thin sections are susceptible to local heterogeneities in the BST core samples, taken together, two thin sections were taken to be sufficient to adequately represent the main composition of the entire Bulk sample (Figure 4.1). Standard thin section, included sectioning impregnating with epoxy resin, and polishing was performed for the 26 BST core samples; with a typical thickness of each section ca ~50 µm.

All thin sections were prepared by the thin section service in the Department of Earth Sciences at Durham University. Primarily, optical microscopy informed the selection of samples for additional analysis. The objective of the optical analysis was to quantify the

detrital and authigenic mineralogy, texture, and spatial pore distribution. This was accomplished by using the standard point-count technique (300 points per thin section).

Table 4.1: Petrophysical properties of studied BST core plugs

Plug No	ID	Permeability mD	Description		Bulk Volume (cm^3)	Density	Porosity
			Dimeter (mm)	Length (mm)			
1	BST.1	<50	19.2	51.4	14.8	1.0	20.1
2		<50	19.2	51.3	14.8	1.0	19.7
3		<50	19.1	51.3	14.7	1.0	19.9
4		<50	19.1	50.5	14.5	1.0	20.4
5	BST.2	50-100	20.1	50.8	16.0	1.0	20.4
6		50-100	20.1	51.3	16.2	1.0	16.8
7		50-100	20.1	50.9	16.1	1.0	20.8
8		50-100	20.1	51.9	16.4	1.0	20.1
9		50-100	20.1	50.5	16.0	1.0	20.1
10	BST.3	100-200	20.0	50.0	15.7	1.0	20.7
11		100-200	20.1	50.0	15.8	1.0	21.8
12		100-200	20.0	50.0	15.7	1.0	18.1
13		100-200	19.9	50.0	15.5	1.0	22.1
14		100-200	20.0	50.0	15.7	1.0	21.7
15		100-200	20.0	50.0	15.7	1.0	20.0
16		100-200	20.0	50.0	15.7	1.0	17.4
17		100-200	20.0	50.0	15.7	1.0	18.5
18		100-200	20.0	51.1	16.0	1.0	20.5
19		100-200	20.0	51.4	16.1	1.0	21.3
20		100-200	20.0	51.0	16.0	1.0	20.8
21		100-200	20.0	50.7	15.9	1.0	20.0
22		100-200	20.0	51.1	16.0	1.0	20.1
23	BST.4	500-1000	19.8	51.5	15.9	1.0	23.4
24		500-1000	19.9	50.5	15.7	1.0	23.9
25		500-1000	20.0	52.7	16.5	1.0	24.5
26		500-1000	20.0	52.2	16.3	1.0	25.6

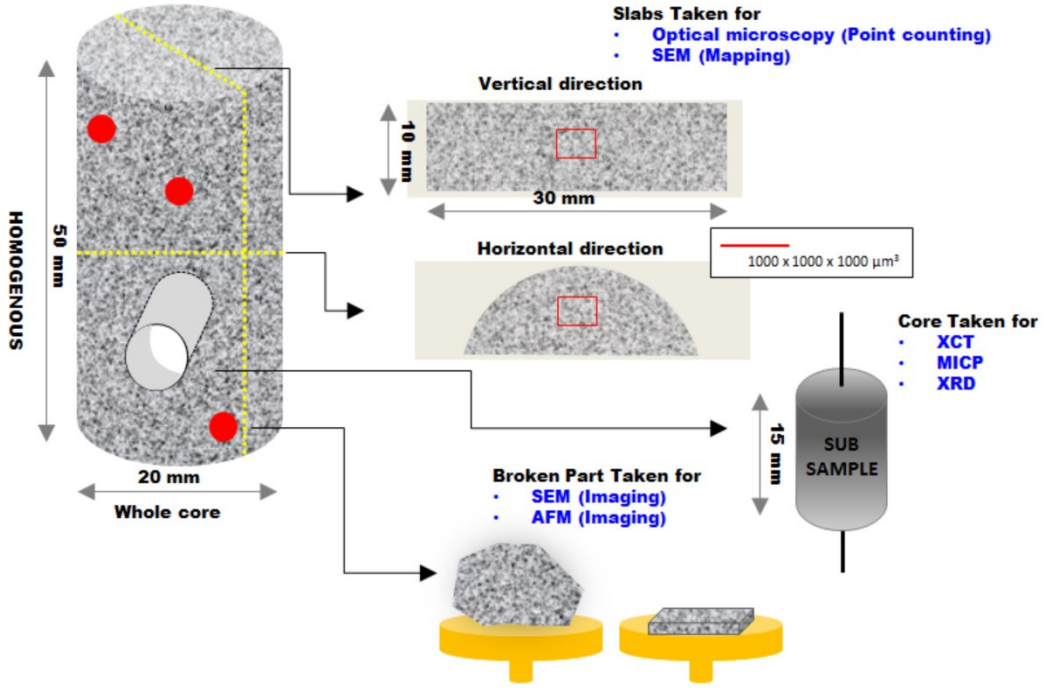

Figure 4.1: A diagram showing the location of subsamples along the BST core plugs.

4.2.2. X-Ray diffraction - Mineralogical Identification

In this study, the mineralogical composition of selected samples, one from each of the 4 permeability ranges of BST studied, was obtained via whole-rock X-ray diffraction (XRD) analysis with a full pattern fitting reference intensity ratio (RIR) method, as described in Omotoso et al. (2006), at the James Hutton Institute, Aberdeen. For each of selected cores, a small 1 cm dia x 1cm long piece was drilled perpendicular to the main core length (bedding planes) in order to use the same subsample for XRD and X-ray CT characterisation (Figure 4.1). For whole rock XRD samples were prepared by McCrone milling followed by spray drying. XRD patterns were recorded on a Bruker D8 Advance from 4-70°2θ, counting for 384 seconds per 0.0194° step, using a Lynxeye XE position sensitive detector and Ni-filtered Cu radiation. The weight percentage of each mineral phase was converted to a volume fraction and grouped into four categories (as discussed below) in order to compare with X-ray CT data for the purpose of determining the volumetric fraction of mineralogy. Details on how this conversion is done can be found in the following subsection.

Mineral weight percentages were estimated from XRD measurements performed at the James Hutton Institute, Aberdeen. These were obtained via whole rock XRD analysis with a full pattern fitting reference intensity ratio (RIR) method as described in Omotoso et

al. (2006). The mass of common minerals in BST has converted to volume in order to align the data with the XCT analysis. Density is one of the several intrinsic physical properties of minerals that relate to the composition of the mineral and to the pattern in which the mineral's atoms are arranged. The density of some common minerals in BST is quartz = 2.62 g/cm^3, feldspar = 2.6 g/cm^3, muscovite = 2.8 g/cm^3, kaolinite = 2.6 g/cm^3, illite = 2.75 g/cm^3, chlorite = 2.9 g/cm^3, anatase = 3.9 g/cm^3, and carbonate = 2.9 g/cm^3. The way we measure volume is to divide the mass or weight of each mineral by its density. Written out, the formula for calculating volume is: The mineral weight percentage data is shown in Table 1B.

$$V = M/D \tag{4.1}$$

Where:

- V = volume (cm^3)
- M = mass (g)
- D = density (g/cm^3)

Sample-specific clay mineralogy was also obtained by means of X-ray diffraction (XRD) analysis of the clay mineral fraction separated from the bulk XRD sample, also performed at the James Hutton Institute, Aberdeen. XRD data was collected on a Siemens D5000 instrument using cobalt radiation. Clay fractions of < 2 μm were obtained by timed sedimentation, prepared as oriented mounts onto glass slides using the filter peel transfer technique and scanned from 2 - 45° (2θ) in the air-dried state, after glycolation (vapor pressure overnight), and after heating to 300 °C for one hour. For clay minerals present in amounts > 10 wt. % uncertainty is estimated as better than ± 5 wt. % at the 95% confidence level.

4.2.3. Scanning Electron Microscopy

In this section, BST samples were analysed for detrital and authigenic mineralogy, porosity and pore connectivity, texture, and mineral distribution through a combination of SEM images of broken samples and backscattered electron (BSE) microscopy with an energy dispersive X-ray (EDX) analysis on thin sections. For determination of the relative percentage of mineral area within BST core samples AZtecEnergy - EDS software was used. The same optical thin sections, oriented parallel to the length of the BST core plugs (bedding plane orientation) were used in the BSE analysis. The thin sections were carbon

coated (25 nm) using a Cresington 108 carbon/A (see Figure 4.1).The typical thickness of each thin section was ca ~50 µm. Observations of thin sections used a Hitachi SU-70 high-resolution analytical SEM, equipped with an Oxford Instruments energy dispersive X-ray spectroscopy (EDS) microanalysis system (INCA Energy 700), at the G. J. Russell Electron Microscopy Facility, Durham University. BSE imaging of thin sections allowed relative identification of minerals (Dilks and Graham, 1985; Tovey and Krinsley, 1991) within the BST. For each of the 26 thin sections, one set of large-scale images (1 mm by 1 mm) were obtained for large area chemical phase map montage production. For all the images, the locations were assigned randomly. EDS were obtained for mineral phase identification. Phase identification was achieved via offline using Oxford Instruments AZtecEnergy - EDS software, giving the area fraction of each specific mineral.

The mineral phases identified in the BST polished thin sections were divided into several mineral groups: quartz, K-feldspar, plagioclase, muscovite, ankerite, siderite, anatase, chlorite, kaolinite and illite/smectite which correspond with the phases identified directly by XRD (Section 4.2.2). Measured mineral area fractions were normalized to the "total pore area" within the section to better reflect the true representation of the mineral within the pore space.Details on process for estimating the area fraction from electron microscopy images can be found in the following subsection. The "total pore area" includes the actual empty space in addition to the area occupied by the pore lining minerals (i.e. the space delimited by the detrital grains). The normalized measurements allowed comparison with the µ-XCT data (Section 4.2.4). BSE images of each BST thin section specimen (3072 × 2304 pixels) were collected at 20 kV acceleration voltage, 4000 nA beam current, 30 µm aperture size and a 15 mm free working distance. For identification of, cementation in the BST polish thin sections, cathode luminescence SEM (SEM-CL) was used. For this purpose, a representative sample was chosen from the studied thin sections to provide detailed information about the type of cement and quartz overgrowths (Milliken and Lauback, 2000). CL images were taken with an accelerating voltage of 15 kV (in contrast to 20 kV for BSE), 8 nA beam current, and 15 mm working distance. The topography and texture of detrital grains, clay minerals, and pore connectivity were assessed using SEM imaging, in both secondary electron (SE) and backscattered electron (BSE) modes. Three broken samples (ca ~1-1.5 cm2) per core plug were selected for this purpose; the locations were assigned randomly (Figure 4.1). To avoid artifacts arising from sample preparation, this work follows the processes developed by Soeder (1986), where

the effects of sample preparation on porosity were critically assessed. The broken specimens were not dried in a dehumidified oven, in order to prevent damage to the internal pore structures as well as clay minerals.

4.2.3.1. Area Fraction from Electron Microscopy Images

In this section, the specimens were examined in BSE mode at 20kV acceleration voltage, 15 mm working distance and a resolution of 2048x1920 pixels. Microanalytical energy dispersive X-ray spectroscopy (EDX) was used for chemical determination. The technique generates a set of the elemental map, including Al, Ca, Cl, Fe, K, Mg, Mn, Na, P, S, Ti and Si (Figure 4.2).The elemental maps were thresholded into two phases to indicate the significant concentration of each element and background. This step was automated and generated with the Aztec software. On the other hand, in some cases, the segmentation may explicitly require some degree of manual input to improve image acquisition.

Based on the relative elemental concentrations and grain boundaries, the software assigns a phase/mineral identity to each identifiable grain. Although highly accurate, mineral data identification was further refined by considering the XRD analysis of the same samples, i.e. in those cases where the software assigned a phase not identified by XRD, this was reassigned. Further data processing with Aztec allows quantifying the area fraction of each mineral phase within the scanned area. The minerals identified by the software were: Quartz, k-feldspar, plagioclase, muscovite, ankerite, siderite, anatase, chlorite, kaolinite, and illite/smectite.

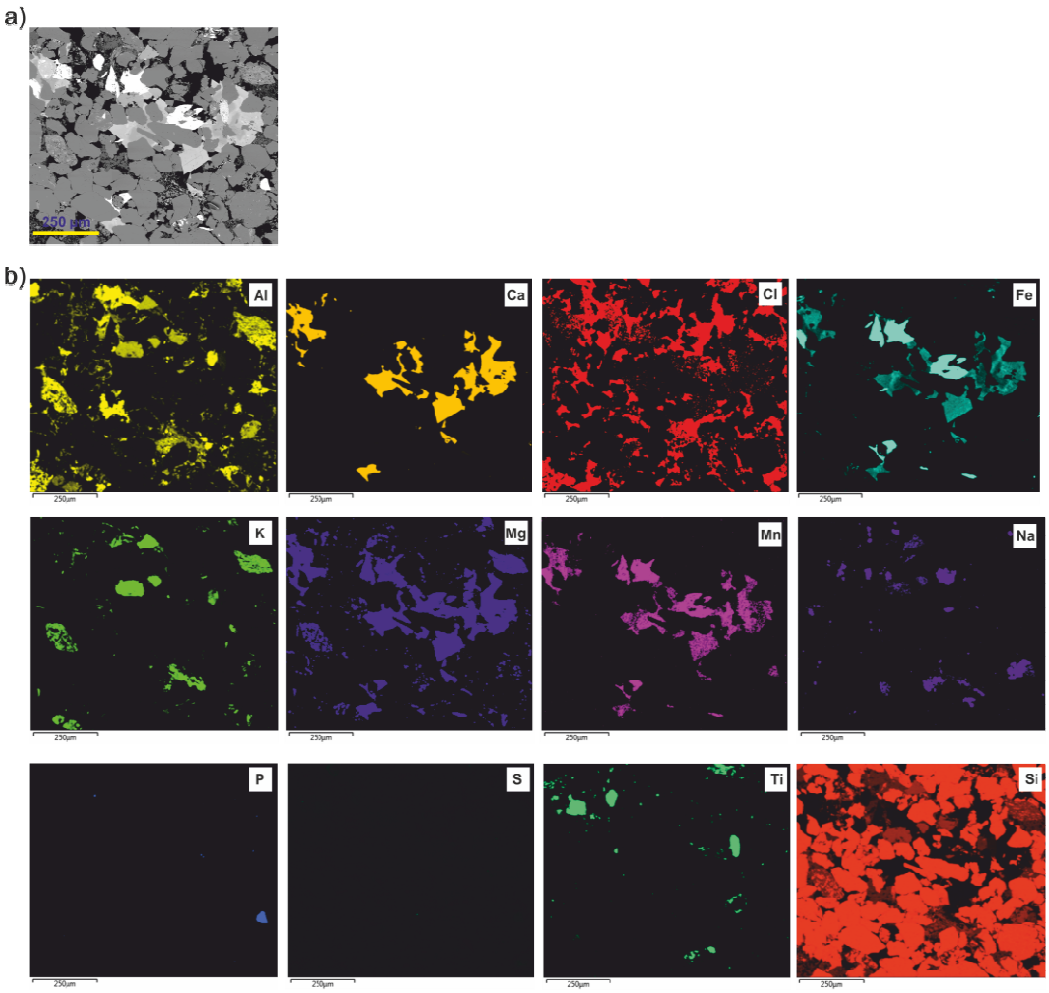

Figure 4.2: (a) Backscattered electron (BSE) image of BST sample measuring 1mm^2. (b) Energy dispersive spectroscopy (EDS) overlaid on the BSE to create a false colour elemental map.

4.2.4. Micro-X-ray Computed Tomography

4.2.4.1. Imaging

In this part of work, tomographs were taken from small cylindrical specimens with dimensions of 10 mm in diameter and 15 mm in height. These were sampled from a representative BST core in the 4 permeability groups (as shown in Figure 4.1). A small sample diameter was chosen so that the specimen fitted in the field of view during high-resolution scans, ensuring the highest quality, so that an exact comparison of the pore space can be validated with porosimetry analysis. Tomograms were obtained and processed using a Zeiss XRadia-410 CT scanner. Details of scan parameter for all studied sample sizes can be found in the Table1 in appendix A.3. The X-ray source was set to 80 kV and 140 µA, a Bremsstrahlung filter was used to enhance the performance of the detector for the X-ray photons to acquire 3201 projections of 2048 pixel^2 over 24 hours.

The projection set covered a *ca* 1 mm^3 cube at the center of the studied BST specimen, scanning about the midpoint to minimize the long scan time producing motion artifacts. The projections were typically reconstructed to a 3-dimensional (3D) raw tomogram, with a voxel size of 1.03 μm/voxel resolution. Tomogram data was processed with Avizo™ 9, a commercially available software package from FEI, to identify surface and pore mineral phases (Buchwalter et al. 2015). Further details of the data processing method are presented in the following subsections.

Table 4.2: Description of the X-ray segmentation groups for the Berea sandstone

Group name	**Major Mineral**	**Minor Mineral**
Quartz	Quartz	
Feldspar	alkali feldspar	plagioclase, albite, and muscovite
Clay	Kaolinite	illite, and chlorite
Other	Ankerite	siderite, calcite, and anatase

4.2.4.2. Image Processing.

In a tomographic image, the value of each volume voxel represents the average X-ray attenuation property of that material in that specific volume. The degree of attenuation depends on the elemental composition and bulk density of the material. This gives the technique the potential for mineral phase identification. In recent years, image acquisition methods applied in mineral identification derived from X-ray CT scanning have improved considerably as shown by Peter (2009), Landrot et al. (2012), Golab et al. (2013), Hezel et al (2013), and Lai et al (2015). In this work, BST specimen data were resolved from artifacts using a non-local mean filter (Buadeseta et al. 2005). Once the noise had been reduced to an adequate level, in Avizo™ 9, watershed segmentation was applied for both binary and multiphase segmentation. Segmentation is a procedure by which the grayscale data is transformed into binary data required for quantitative analyses. During setting of gray scale thresholds, special focus was set on the conservation and representation of grain and pore boundaries, which were selected manually. The specific parameters, such as the gray intensity range for each mineral group used per BST specimen, are provided in the Supplementary Information. The solid phase of the BST specimens was further segmented into mineral groups using a similar approach to that reported by Golab et al. (2013) and Lai et al. (2015). Table 4.2 summarises the definition of the segmentation groups used for the

BST specimens. The quartz group consisted of only quartz. The feldspar group consists of feldspars plus muscovite since it has a similar attenuation to feldspars. Kaolinite, illite/smectite, and chlorite comprised the clay mineral group. Calcite, ankerite and siderite, and remaining oxides such as anatase, formed the last group (other).

For each of 8 scanned samples from the 4 BST groups, we selected several representative subvolumes and characterised their porosity, pore size distribution, and pore volume in order to increase efficiency of computation. The size of those subvolumes ranged from 4000×4000×4000 μm^3 to 1000 × 1000 ×1000 μm^3. The higher the atomic number or density, the more X-rays are absorbed, creating darker regions in the tomography (Cnudde, 2009). After implementing segmentation manually, a "hole filling" function in Avizo™ 9 was employed on the data so that any isolated black voxels (isolated holes within minerals) were converted into white voxels (i.e. counted as solid matrix). The solid matrix was removed and the pore space converted into a pseudo-solid matrix and quantified. The number of pores and their volume distribution was computed for all BST core samples (Houston et al. 2013). A similar approach was implemented to quantify detrital grains and their distribution in the scanned BST specimens.

4.2.4.3. X-ray Imaging and Segmentation (Mineral Identification)

In this part of work, implementation of simple thresholding for mineral identification was avoided, as this technique would only produce a segmentation image containing a single phase for a given grayscale. Since a certain amount of manual input is required in the routine, repeating the operation for all 4 mineral groups (with 4 different gray scales) will introduce artefacts and errors in the quantification. For these reasons, this work implemented the watershed module which provides an effective solution for these issues by performing the phase separation (based on different gray scales) in a single pass.

The contrast in X-ray light attenuation characterised as a greyscale contrast in the reconstructed images was the main differentiator for identifying mineral phases in the X ray images. The difference in attenuation are related to variations in the atomic number and therefore on the relative chemical composition of the different components that constitute BST. Table 4.3 shows the intensity gradient of each mineral group during segmentations process. The grayscale contrast between mineral groups was showed in Figure 4.3.

Table 4.3: Intensity gradient of each mineral group during segmentation processing

Sample ID	BST.1 Core Plug	BST.2 Core Plug	BST.3 Core Plug	BST.4 Core Plug
No. of phases	5	5	5	5
Range of intensity	Pores	Pores	Pores	Pores
Min	4440	4440	5169	3880
Max	6216	5820	9395	7280
Range of intensity	Clay	Clay	Clay	Clay
Min	1776	1820	8456	7280
Max	6750	6510	10334	7850
Range of intensity	Quartz	Quartz	Quartz	Quartz
Min	6217	6796	10335	7850
Max	7990	8650	11745	9225
Range of intensity	Alkali feldspar	Alkali feldspar	Alkali feldspar	Alkali feldspar
Min	7998	8252	10800	9700
Max	8800	9300	12680	10195
Range of intensity	Others	Others	Others	Others
Min	6662	9300	12680	10679
Max	21760	23785	20669	48540

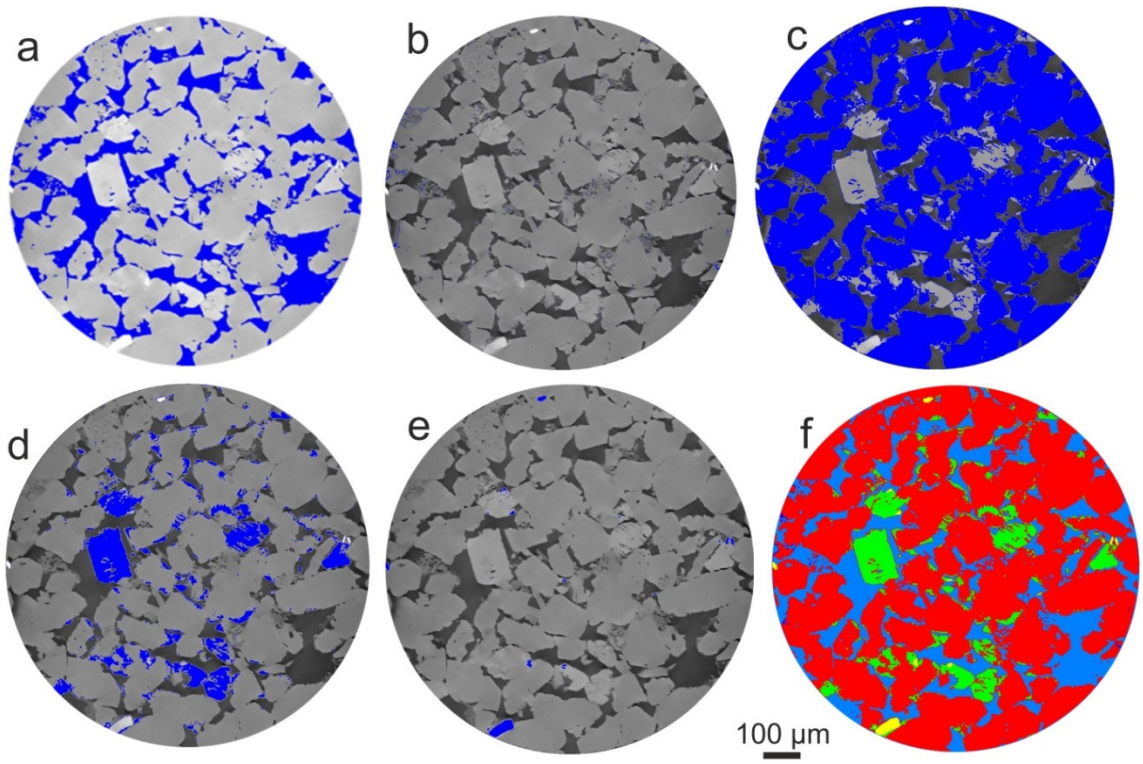

Figure 4.3: Segmentation process in the mineral phase identification of Berea sandstone sample: (a) Gradient mask of pores, and initial labels for (b) clay, (c) quartz, (d) feldspar (e) other minerals, and (f) Segmented Berea core sample.

The detrital grain distribution for each of BST core specimens was quantified using the interactive thresholding module. This module created a binary image. For binary images, the Avizo™ 9 displays the voxel of intensity 1 with blue color. In order to reduce noise and artifacts once again, the morphological opening operator was applied to the binary image, which gives a second binary image. This second pass removes all small objects and makes the boundary between objects smoother. Finally, the separated objects module was applied to detect all the surfaces that separate agglomerated particles. Separated surfaces were subtracted from the initial image; see Figure 1 in appendix A.3. The labeling module was then applied in order to identify and label each separated particle. Grain size analysis is the equivalent diameter measure was used to compute the diameter of the spherical particles of the same volume. The equivalent diameter is given by the following formula:

$$\text{Eq Diameter} = \sqrt[3]{6 \times Volume\ 3d \div \pi} \tag{4.2}$$

For the four BST core specimens, the computed equivalent grain diameters are shown in Table 2 in appendix A.3.

4.2.5. Atomic Force Microscopy Characterisation

In this part of study, a multimode Bruker atomic force microscopy (AFM), equipped with a Bruker Nanoscope V controller, was used to characterize the surface of selected BST mineral grains exposed in the core pores. A representative section of a BST.4 core specimen was cut using a low speed saw to produce a sample of 10mm × 10mm × 1mm dimensions. The specimen was studied using SEM to identify an adequate area to scan with the AFM. Flat crystal surfaces with an orientation approximately parallel to the sample holder surface were used and were placed in a gold sputtering apparatus, and covered with a small foil disk with a 20 µm aperture in the center. A small gold reference mark was created on the center of the sample to locate the same area scanned on the SEM with the optical microscope attached to the AFM. SEM images at different magnifications were collected so a length scale similar to images produced by the optical microscope (attached to the AFM) could be easily obtained and then allow comparison. Special emphasis was placed on areas that showed well developed (therefore flat) quartz surfaces from selected samples to scan using the AFM. Details of methodology can be found in the Figure 1 in appendix A.4. All scans were performed using PeakForce™ tapping mode and

scanasyst-air probes (Bruker probes). Image analysis was carried using Nanoscope Analysis version 1.5 (Bruker).

4.2.6. Mercury Injection Porosimetery

In this part of study, mercury injection capillary porosimeter (MICP) is a method used for characterizing the distribution of pore throat structure (Hildenbrand & Urai, 2003; Yven et al., 2007) in a porous material. The method is based on the fact that a non-wetting liquid can intrude the pore space when pressure is sufficiently high: the higher the pressure, the smaller the pore throats that are filled with mercury (Abell et al., 1998). By using the Washburn equation (Washburn, 1921), the pressure differences can be converted to pore access diameters, assuming that the porous material consists of a bundle of nonintersecting tubes (Howard, 1991). Based on a set of assumptions on pore morphology, a pore throat size distribution curve is obtained from the intruded volume at each pressure step. The samples used in this analysis were first scanned using X-ray CT, and after this, they were analysed using MIP. Mercury injection on smaller core plugs (1cm in diameter and 1.5cm long) drilled out of the representative of BST core samples (Figure 4.1). Ideally, a sample analysed by MICP should be as large as possible. However, a small sample diameter was chosen so that an exact comparison of the pore space can be validated with μ-XCT analysis. The samples were placed in the mercury filled sample cup in a pressure vessel at the School of Civil Engineering and Geosciences, at the University of Newcastle. Then the pressure was slowly increased from 3 psi to 39,000 psi.

4.3. Results and Discussion

4.3.1. Berea Sandstone and Bulk Composition

The Upper BST unit at the Cleveland Quarries locality, from which the cores in this study originate, is a fine to medium grain size, well-sorted sandstone with closely spaced planar bedding (Churcher et al. 1991). The two main components of BST are detrital grains, such as quartz, alkali feldspar, and plagioclase, and a matrix composed mostly of clay minerals, such as kaolinite and illite/smectite (Pepper, 1944; Lai et al. 2015).

4.3.1.1. Detrital Grains

Observations made with transmitted light plane-polarized and in bright-field reflected light on BST thin sections allowed the identification of the percent value of framework grains. Modal analysis results for the average 52 studied thin sections (i.e., two thin sections from each of the 26 BST core samples) are presented in Table 4.4, Table 1 and Table 2 in the appendix A.1. In terms of mineralogical composition, the detrital grains can be divided into quartz (Q), feldspar (F) and lithic fragments (L).

Table 4.4: Averages of multiple thin section data set from BST core samples showing quartz as the main component with their size distribution from selected samples.The range of uncertainty is about ± 15% as three parameters have used in the analysis.Q = Quartz, F = Feldspar, L = Lithic fragments, % QFL=Percent value of framework grains in each sample, and Eq = Equivalent.

Sample No.	Composition			EqDiameter XCT (µm)		
	%Qtz	%F	%L	Minimum	Maximum	Mean
BST.1	83	8	9	13.1	330.6	172.0
BST.2	85	7	8	15.4	284.0	149.8
BST.3	84	8	8	13.2	347.5	184.5
BST.4	91	1	7	13.2	416.6	215.1

SEM images showing details of each mineral component are given in Figure 4.4. Quartz is represented mainly as monocrystalline grains (Figure 4.4a and Figure 4.4b) and feldspar as K-feldspar with negligible amounts of mica (Figure 4.4b). Additionally, most of the observed K-feldspar grains in BST show signs of partial to almost total dissolution (honeycombed grains), leading to increased surface area when compared to undissolved grains (Figure 4.4c and Figure 4.4d). The total K-feldspar content of sandstones decreases

due to diagenetic processes leading to the formation of intra-granular kaolinite and illite (Bjorlykke 1998). Significant amounts of kaolinite and illite clay minerals arising from the dissolution of feldspar cover large areas of most of the quartz detrital grains (Figures 4.4a, 4.4e and 4.4f). Different types of rock fragments, including igneous and sedimentary, are present in the studied samples. Microquartz grains, with an average abundance of 2%, are the most abundant lithic components. Sedimentary rock fragments, averaging 7%, are mostly composed of authigenic clays.

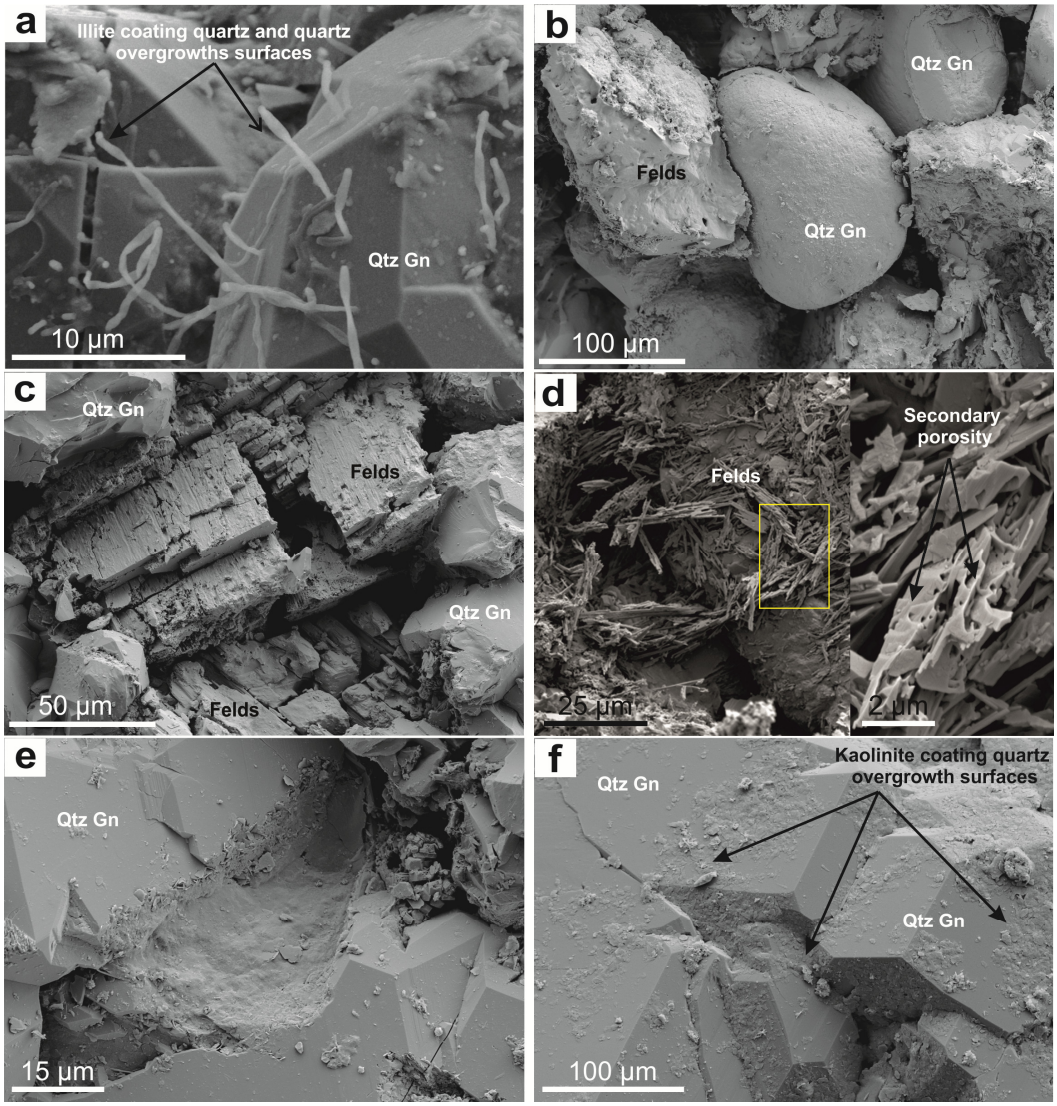

Figure 4.4: SEM micrographs of BST detrital grains, a) Detrital quartz grains in BST.1 coated by diagenetic clay minerals (hairy authigenic illite) and quartz overgrowths. b) Example of well-rounded quartz crystal from sample BST.4 (classified as a mature quartz arenite). Visible as well are several feldspar grains, showing clear signs of dissolution, and authigenic clay fractions interspersed within the quartz grains. c) Detailed view of detrital K-feldspar grains that are partially dissolved (creating secondary intergranular porosity); in contrast quartz detrital grains show no signs of dissolution. d) Detailed view of secondary porosity in a dissolved K-feldspar grain in BST.2 which is surrounded by detrital quartz grains and kaolinite crystals generated by extensive dissolution of detrital K-feldspar grain during diagenesis. Although this type of dissolution clearly creates intragranular pores, without further dissolution of other phases, such pores can remain largely unconnected, and thus may not significantly affect permeability. e) Quartz overgrowth in BST.4. In addition a layer of kaolinite over growth is visible covering part of the quartz crystals. f) Well-formed quartz overgrowths in BST.4. The growth of a thin clay coating (probably kaolinite), as seen here, would ultimately help to prevent further cementation. Qtz = quartz and Felds = feldspar.

Using the sandstone classification of Folk (1980), the petrographic point counting data indicates that samples from the BST.1, BST.2, and BST.3 are quartz sublitharenites, whereas BST.4 are quartz arenites (Figure 4.5a). The result of the equivalent grain

diameter analysis (conducted using the µ-XCT data) of all BST specimens show a wide range of grain sizes from coarse (240 µm) to very fine (13 µm) (Figure 4.5). The average equivalent diameter of the detrital grains in the cores of BST.1 and BST.3 groups are relatively close to each other, with values of 171 µm and 184 µm, respectively (Figure 4.5b and Figure 4.5d), as reported in Table 4.4. Based on frequency distribution (Figure 4.5c), the average equivalent diameter for BST.2 is smaller (149 µm) than that of BST.1 and BST.3, whereas the average equivalent diameter for BST.4 is the largest, at 215 µm (Figure 4.5e). From quantitative XRD analysis, the volume fraction of quartz is similar for samples BST.1, BST.2 and BST.3 (just above 80%). However, for sample BST.4 the volume of detrital quartz grains is 95.05% of the bulk volume. Notably, the segmented quartz volume values calculated from the µ-XCT data show excellent agreement with the total volume fraction of quartz minerals measured using XRD (Table 4.5).

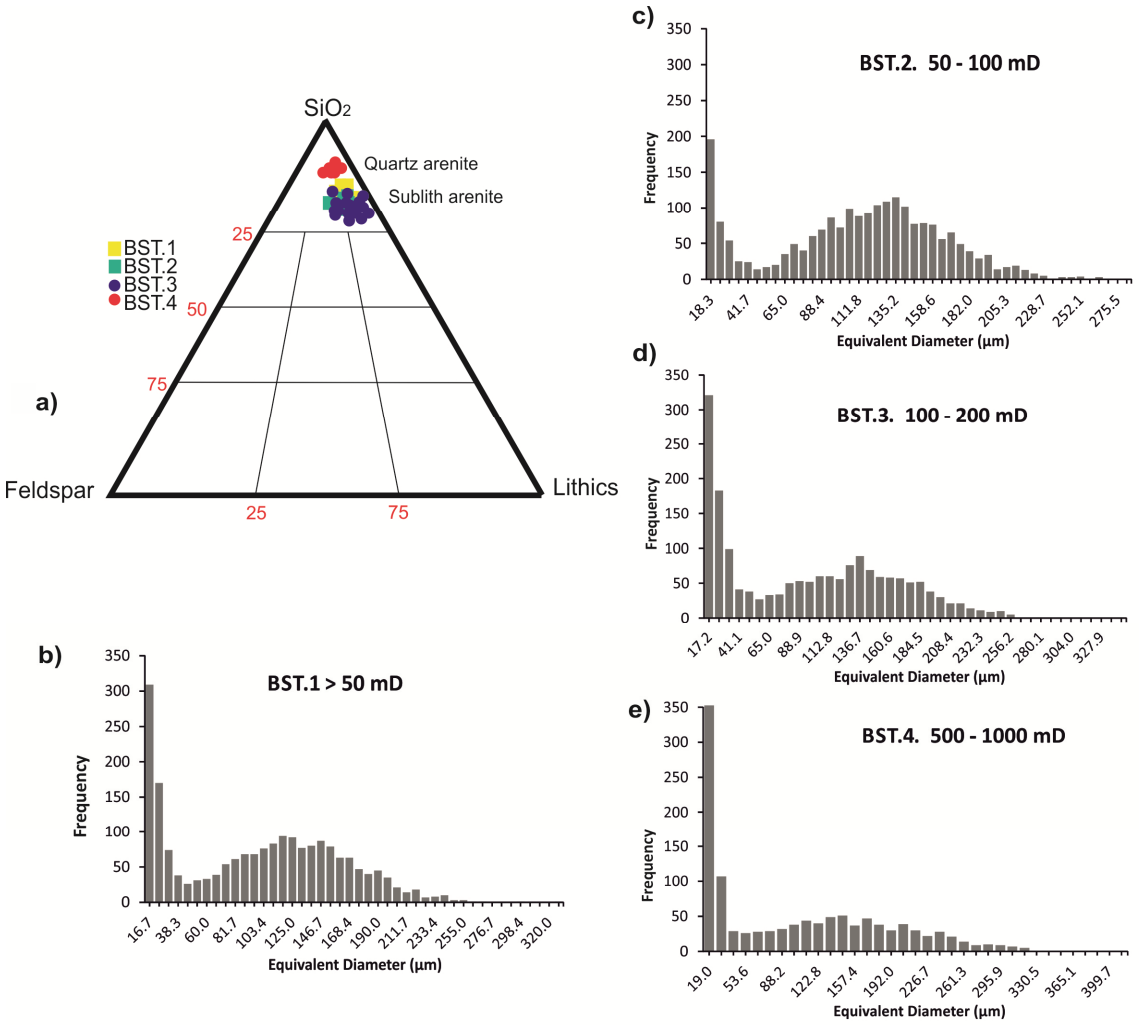

Figure 4.5: a) Ternary diagram showing the framework composition (based on the classification of Folk (1980)) for the 4 BST samples studied. BST.1, BST.2, and BST.3 are classified as litharenites, and BST.4 as a quartz arenite. Grain size distribution plots obtained from µ-XCT data for: b) BST.1, c) BST.2, d) BST.3, and e) BST.4.

Table 4.5. Mineral volume fraction and area fraction for all BST core sample from XRD, X-ray CT, and SEM/EDX.

Sample ID	Group	Wt% from XRD	Volume fraction		Area fraction
			XRD	XCT	SEM
BST.1	Quartz	81.5	81.9	83.7	61.1
	Feldspar	6.50	6.60	6.20	7.00
	Clay	8.20	8.00	9.10	16.7
	Other	3.70	3.40	0.90	15.1
		99.9	99.9	99.9	99.9
BST.2	Quartz	84.5	84.9	83.8	76.2
	Feldspar	5.80	5.80	6.90	8.30
	Clay	6.80	6.70	7.80	11.7
	Other	2.80	2.50	1.40	3.70
		99.9	99.9	99.9	99.9
BST.3	Quartz	82.7	83.1	82.9	75.0
	Feldspar	7.00	7.00	6.90	4.00
	Clay	7.10	6.90	8.40	14.4
	Other	3.10	2.70	1.70	6.50
		99.9	99.7	99.9	99.9
BST.4	Quartz	95.1	95.3	94.9	95.1
	Feldspar	0.80	0.80	1.10	0.00
	Clay	3.40	3.30	3.60	4.60
	Other	0.60	0.50	0.30	0.20
		99.9	99.9	99.9	99.9

Based on quantitative XRD analysis, the volume fraction of K-feldspar is similar for samples in the BST.1, BST.2 and BST.3 (around 4% to 5%) groups. However, for samples in the BST.4 group, the volume of K-feldspar grains is less than 1% of the bulk volume. Remarkably, the total volume fraction of K-feldspar minerals measured using XRD (Table 4.5) matches with values obtained from the point counting method as can be seen in Table 4.4 and Table 1 (in the appendix A.2). In addition, the BSE phase maps (Figure 4.6) collected at 1000 μm^2 shows that the area of feldspar fraction appears to be higher in 3 of the 4 BST permeability groups. It is clear the total K-feldspar content decreased with an increasing permeability range. The area fractions of minerals (measured from the SEM mineral phase mapping) are shown in Table 4.5. The partial dissolution of detrital feldspar grains across all samples is a common feature and leads to an increasing exposed area in comparison to other detrital grains (Figure 4.4c and Figure 4.4d). In fact, different dissolution stages, from partial to complete dissolution, can be seen across the BST core plugs. Moreover, the dissolution of detrital feldspar grains would mean a large exposed area of the mineral to any pore fluids e.g. injected low salinity brine. From this, it is clear

the physico-chemical properties of the brine water/rock interactions depend on the accessibility and type of minerals in contact to the open pore system.

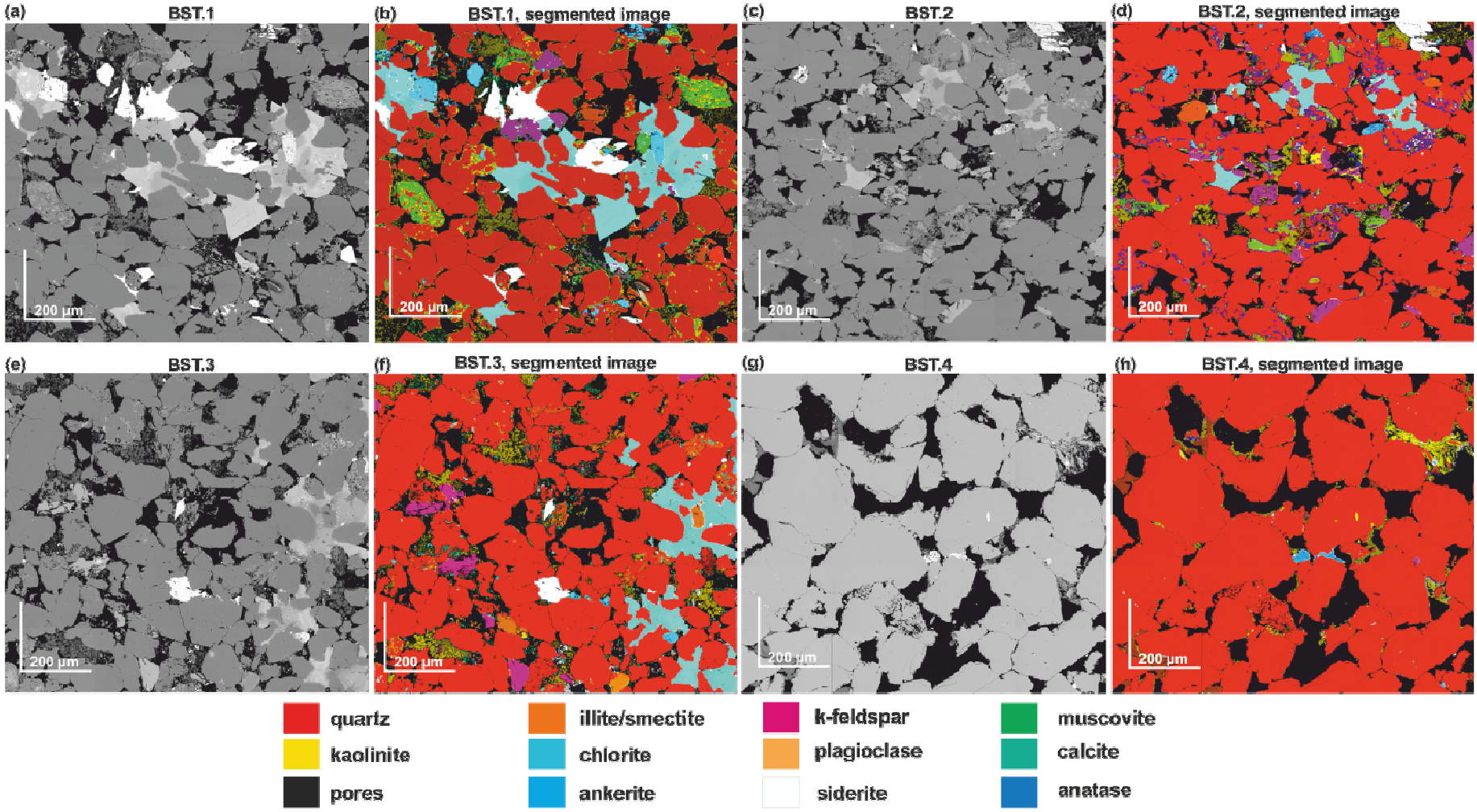

Figure 4.6: BSE and corresponding phase mapping images of BST.1 (a and b), BST.2. (c and d), BST.3 (e and f), and BST.4 (g and h). The analytical conditions were: beam intensity of 20 kV. Image interpretation data are shown in Table 4.

4.3.1.2. Matrix (Detrital and Authigenic Minerals)

Previous work on BST, based on SEM imaging, has shown that detrital grains are mainly cemented by authigenic minerals such as kaolinite, illite, and chlorite (Churcher et al. 1991). Although authigenic clay minerals are undoubtedly present in both the matrix and intergranular pore spaces, it can be difficult to distinguish authigenic clays from detrital clays either by petrography or by standard crystallographic techniques e.g. optical microscopy and X-ray diffraction (XRD). In addition, complex micro-textural and micro-chemical relationships (Hurst 1999) and low abundance complicate the use of many geochemical methods in characterizing clay minerals in reservoir sandstones. For the purpose of determining the matrix mineralogical composition, whole rock, and clay separate (< 2 μm) XRD analysis of a representative sample of each BST core plugs was performed. Results from these analyses are shown in Figure 4.7a and Figure 4.7b. From the XRD patterns, well-ordered kaolinite was identified (with a *d*-spacing of ca. 7.15 Å). SEM images corroborate this finding, as seen in Figure 4.10d, which shows large, well-formed, kaolinite crystals. Some of the more blocky forms are reminiscent of the habit often adopted by dickite, but close inspection of the random powder diffraction data failed to identify any dickite in the samples, only kaolinite was identified. Both illite and illite/smectite, the latter with about 15% expandable (smectite) layers, were identified as distinct minerals from the measured 10 Å spacing in the XRD patterns, and from the broad 'tails' to the 10 Å peak that change in response to glycolation and heating (Figure 4.7b). From SEM observations, however, it can be observed that most of the illite identified from XRD is detrital and is clearly incorporated in the clay matrix (Figure 4.10). Small amounts (< 1%) of discrete chlorite (*d*-spacing: 14 Å) also occur in all the BST core samples (Table 1 in the appendix A.2). In addition, during heating BST samples to 300 °C, for one hour, the chlorite shows some sensitivity which is often indicative of iron-rich chlorite possibly with berthierine interstratification (Figure 4.7b).

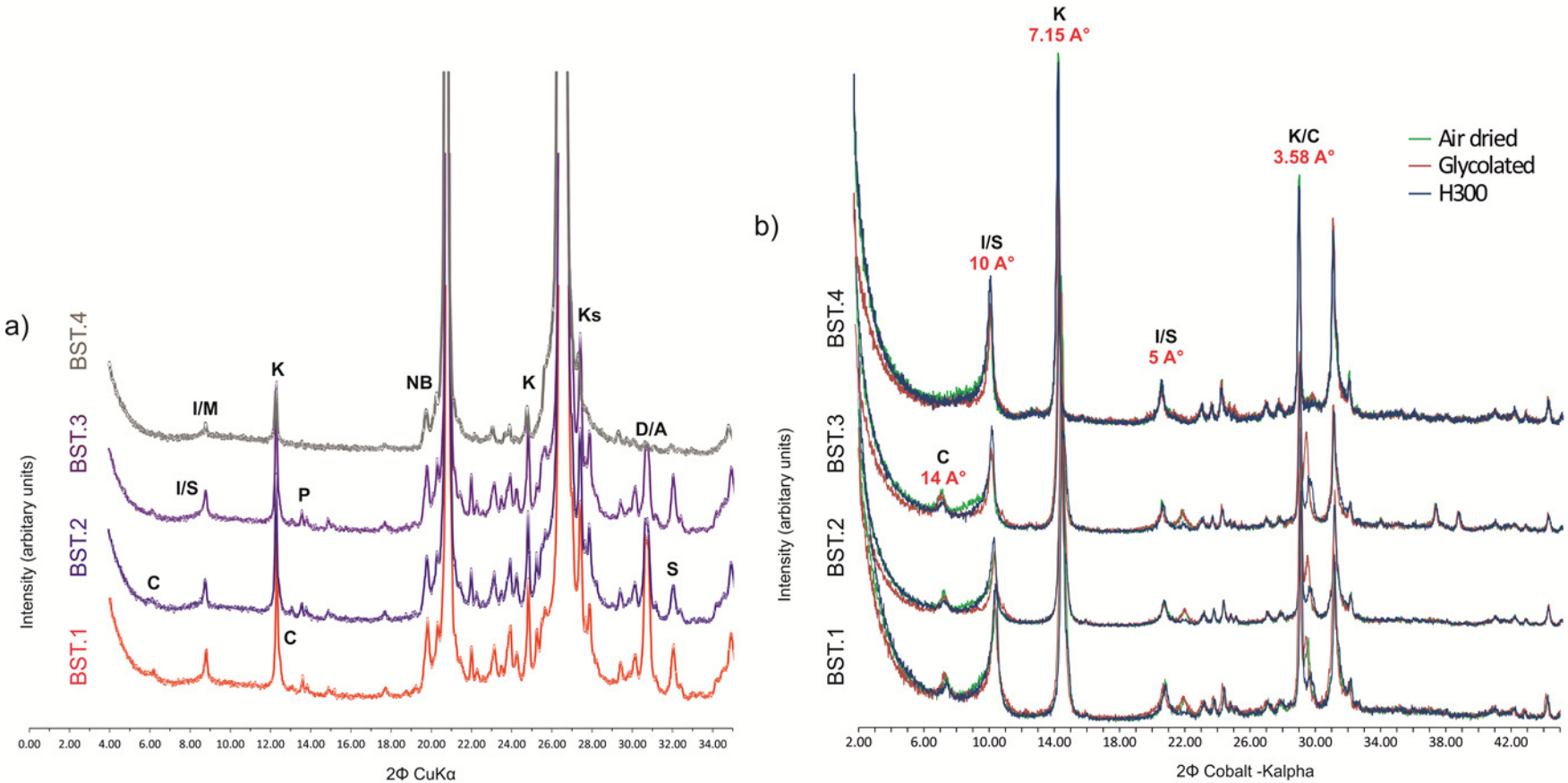

Figure 4.7: XRD patterns of all BST core samples. a) Whole-rock XRD patterns. Patterns are offset for clarity and main quartz peaks are off scale to show detail of other minerals present .b) XRD patterns from the clay fraction (2 < µm). The main peaks in the patterns are kaolinite, illite, illite/smectite, and chlorite; several other trace minerals (not labelled) are also present. I/M = Illite/mica, I/S = Illite/smectite, K = Kaolinite, C= Chlorite, P = Plagioclase, NB = non-basal clay Ks= K-feldspar, D/A = Dolomite/Ankerite, S = Siderite.

Figure 4.8 shows the calculated volumetric and area fractions of the clay minerals from XRD and from BSE/EDX images of the BST core samples, respectively. The results for estimating the area fraction are listed in Table 2 in the appendix A.2. The area fractions of kaolinite in BST.1, BST.2, BST.3, and BST.4 are 13.9%, 5.8%, 5.2%, 3.1%, respectively. For illite, the area fraction for the 4 BST groups is 2.1%, 6.0%, 2.7, and 1.6%, respectively. In comparison to illite, kaolinite shows a higher area fraction for samples BST.1, BST.3, and BST.4, as can be seen in Figure 4.9a and Figure 4.9b. In contrast, when compared with kaolinite in BST.2, illite crystals occupy most of the total pore space (see Figure 4.9c and Figure 4.9d). It is important to note at this point, that area fraction data was measured using BSE/EDX analysis of various areas of interest across a single thin section from a core sample. Since the SEM data is taken from a 2-D section of the core, it was not expected to completely agree with the volumetric data derived from XRD/XCT; nevertheless a reasonable good agreement exists among the different techniques (Table 4.5 and Figure 4.8).

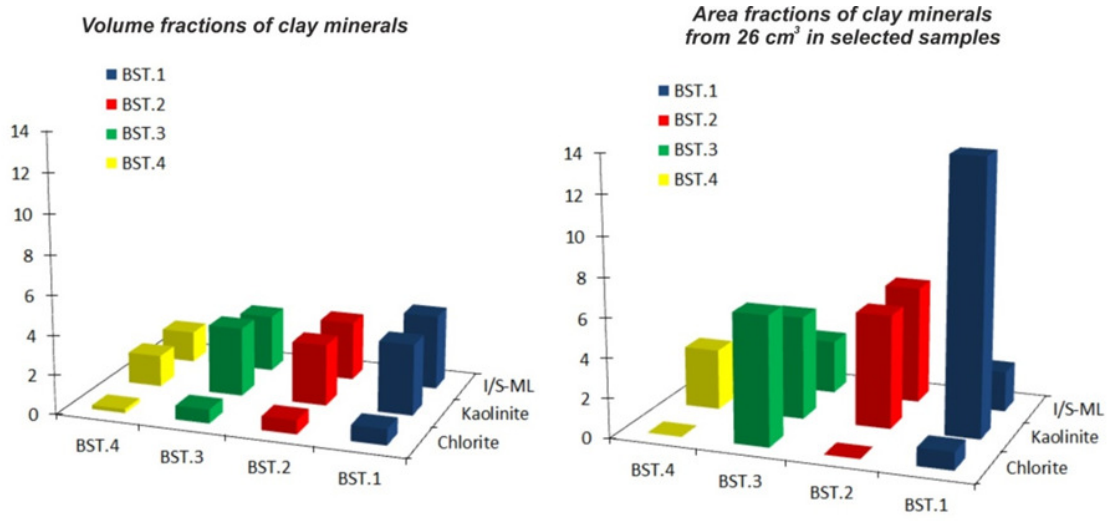

Figure 4.8: Volume fractions (%) and area fractions (%) of the main clay minerals present in each BST sample obtained from XRD and EDX data, respectively. These data are taken (Tables 1B and 1C in the Supplementary Information).

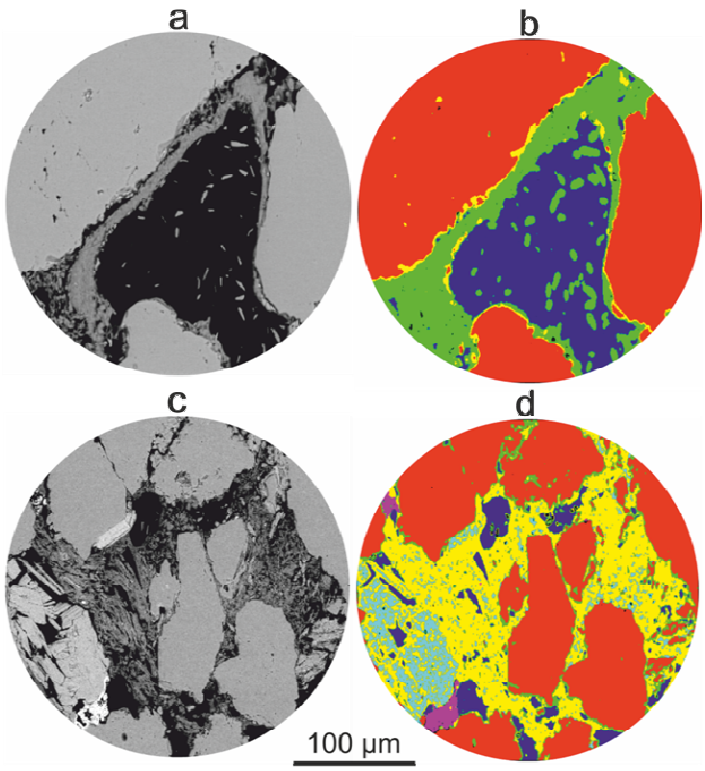

Figure 4.9: (a) and (b) Representative BSE and mineral map images (respectively) for sample BST. 1. (c) and (d) Representative BSE and mineral map images for sample BST. 2. Key: Red: quartz. Green: kaolinite. Yellow: Illite. Blue: pore. Light blue: K-feldspar. Purple: Anatase.

These differences in area fraction have implications for the BST quality parameters (e.g. porosity, permeability), as will be discussed below. According to SEM observations, kaolinite from BST scanned sections are widely dispersed throughout the pore structure in the form of pseudo-hexagonal (Figure 4.10a and Figure 4.10b), and sub-idiomorphic platy crystals loosely attached to pores walls (Figure 4.10c and Figure 4.10d). Kaolinite crystals occupy most of the "total" pore space and therefore are also more exposed to the "open" pore space (Figure 4.10c) than the other clay types. Based on the work of Soeder (1986), BST kaolinite crystals, such as those shown in Figure 4.10d, do not appear to have experienced significant damage during the sample preparation process. This suggests that the observed clay mineral geometry within BST pore spaces and observed SEM-scale pore connectivity relationships reflect the native rock conditions. In addition, the kaolinite agglomerates show a high degree of internal porosity, either in the "booklet" form (Figure 4.10a, Figure 4.10c and Figure 4.10d) or of those composed of more disaggregated crystals (Figure 4.10d). These two characteristics (over exposure in the pore system and additional intricate porosity) mean that most of the pore fluid in these BST core samples will be predominantly in contact with the kaolinite and this may have important implications for

EOR (it has been shown, clay mineral-oil interactions can affect the wettability of a rock) where Berea sandstone is used as model cores. For example; Lbedeva et al. (2010) and Fogden and Lebedeva (2011) showed that oil adhesion to kaolinite decreases at low brine salinity or pH. This shows that the distribution of clay minerals such as kaolinite has a significant effect on the sandstone rock wettability behavior during oil recovery.

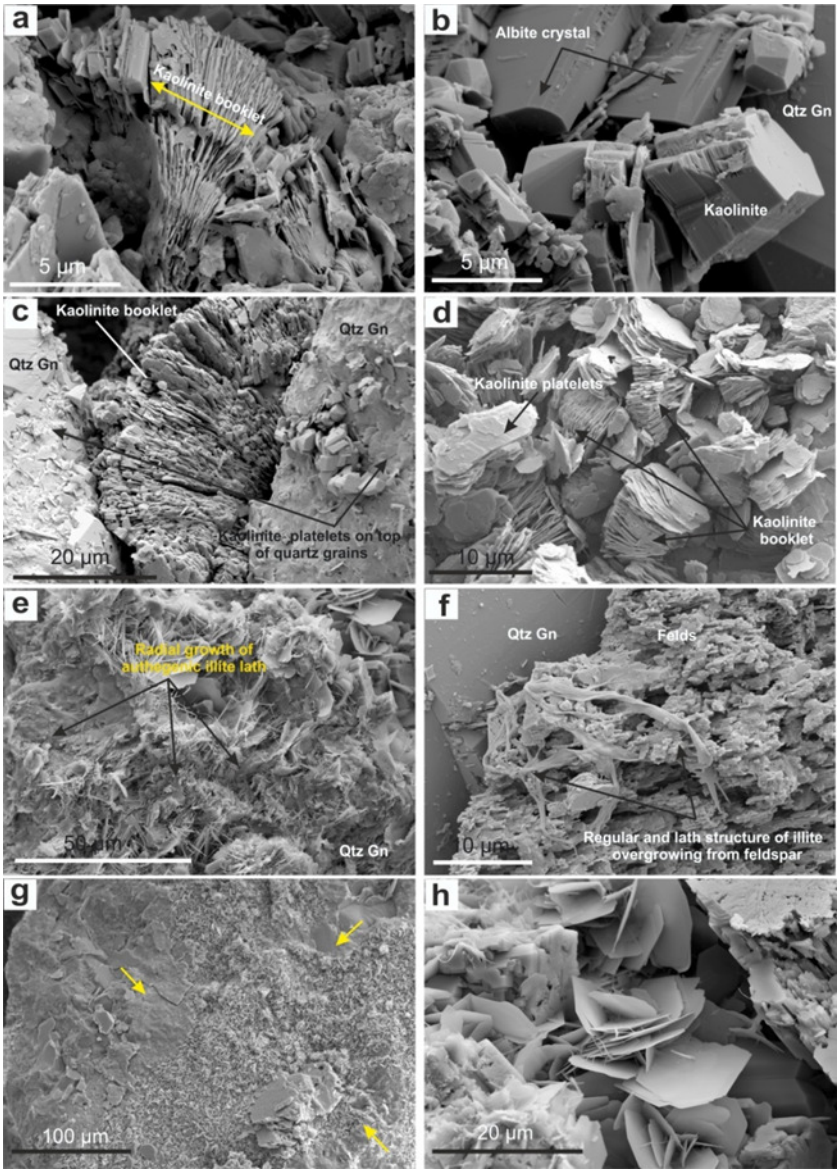

Figure 4.10: SEM micrographs of the clay matrix in BST samples. a) Detail of kaolinite coatings in BST.3. A well-developed kaolinite "booklet" can be clearly seen. b) Kaolinite crystals in contact with a prismatic, albite feldspar, and a larger detrital quartz grain in BST.4. c) Pore-filling, authigenic kaolinite in BST.3 showing booklet morphology. Smaller kaolinite crystals can also be seen covering the detrital quartz grain. d) Aggregates kaolinite booklets and platelets in BST.4. The plates consist of euhedral, subhexagonal crystal, which display high degree of elongation along the a- or b-axis direction. e) Detailed view of illite crystals with hairy-like morphology in BST.2 Formation of these clay crystals postdates quartz overgrowths. f) Illite crystals growing from a highly dissolved K feldspar grain in BST.2.g) Chlorite rich region showing intimately mixed between chlorite and another clay mineral in BST.1 (yellow arrows). h) Enlargement area in (g) showing chlorite crystals. Qtz = quartz.

In comparison, illite crystals are less represented in the open pores across the scanned area of BST core samples, with the exception of the BST.2 samples (Figure 4.6 and Figure 4.9c), but they can also exhibit a great variation of morphologies and internal porosity, which may also lead them to play a role in determining the overall wettability of BST (Figure 4.10e and Figure 4.10f).Based on SEM observation, the majority of illite identified from X-ray diffraction is of assumed detrital origin and is associated with the matrix (Figure 4.10). Only in a few cases was authigenic illite identified by SEM (Figure 4.10f) (Balthazar, 1991). Finally, the presence of large kaolinite crystals could have a significant impact on reducing intergranular pore volume (Wilson & Pittman, 1977), but more importantly, can act as migrating fines in the pore system (Neasham, 1977). Based on SEM observations, kaolinite crystals can be up to 50 µm thick along the *c axis* and may have a major impact in terms of pore obstruction during waterflooding studies, especially on those BST samples with lower permeability (and smaller pore throat sizes). Although fines migration has been discussed as a potential mechanism for EOR (Morrow et al., 1999), in the case of BST it may, in fact, hamper oil recovery. Chlorite is the third most prevalent clay in the studied BST core samples (see Table 1 and Table 2 in the appendix A.2).

Based on the paragenetic sequence of the Berea reservoir sandstones, the chlorite in BST core plugs is mostly diagenetic in origin (Balthazar, 1991). SEM imaging indicates that chlorite crystallites comprising the detrital grain coatings are generally well crystallized and show a preferred orientation with respect to the substrate (Figure 4.10h). Although in BST.3 samples the amount of chlorite is less than 1 vol. %, it has a large area fraction when compared to other authigenic clay minerals including kaolinite and illite (Table 2 in the appendix A.2). Chlorite is frequently responsible for the preservation of porosity in sandstones rocks (Zhang et al. 2015).However, chlorite in BST core samples is dominantly observed as a pore-lining material and rarely is found to be pore filling (Balthazar, 1991). Finally, the volumetric distribution of each mineral group in selected BST core samples was rendered using µ-XCT (Figure 4.11). The volumes shown in the figures represent a sample size of 400 µm × 400 µm × 400 µm. It can be seen that the extent of clay mineral distribution across the whole volume of the sample is relatively even (see Table 1 for XRD mineral volume fractions and Table 2 for BSE mineral area fractions in the appendix A.2).

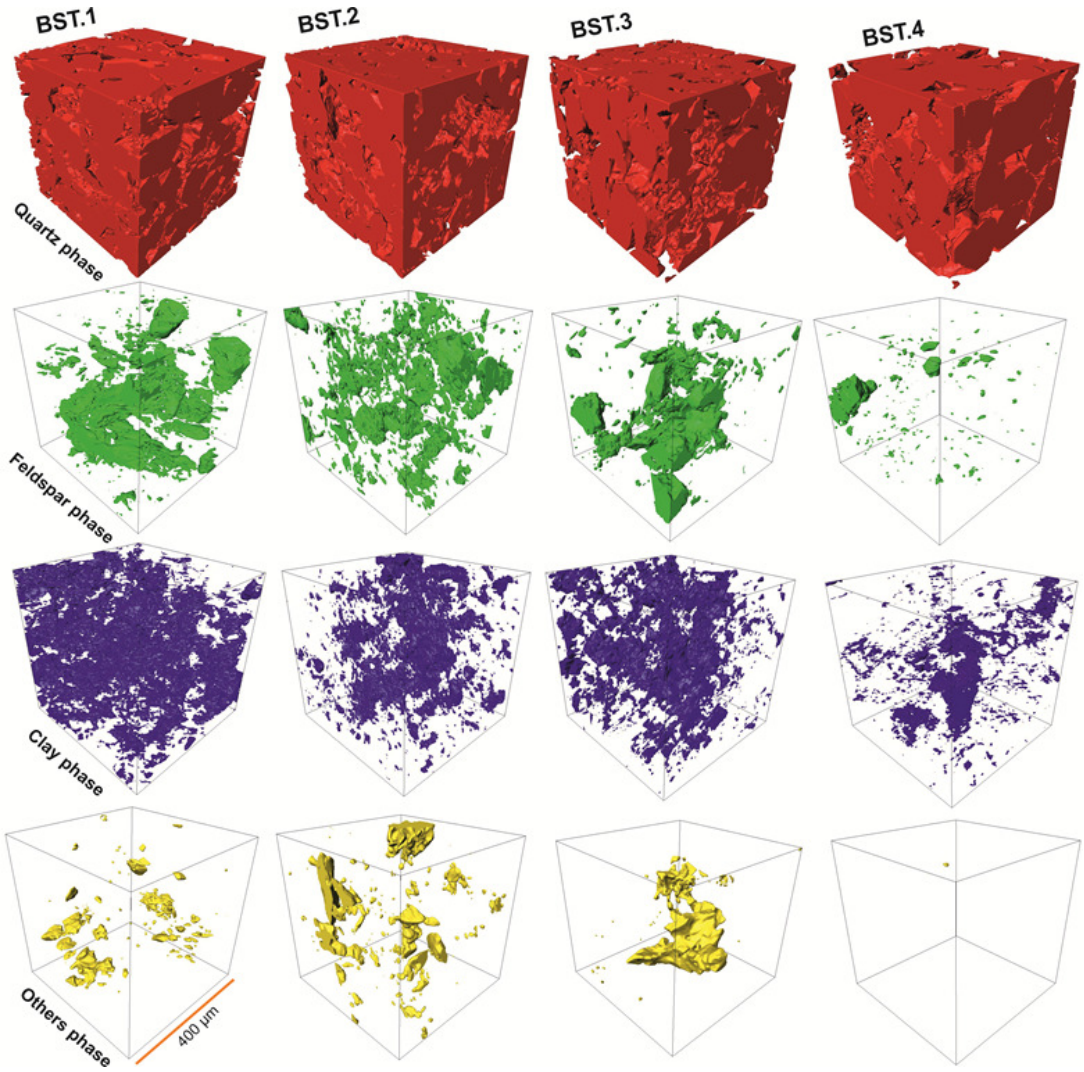

Figure 4.11: 3-D renderings map showing the volumetric distribution of each mineral phase for all BST samples. From top to bottom: Quartz, feldspar, clay minerals, and others (primarily carbonates and oxide).

4.3.1.3. Cementation in Berea Core Sandstone

Quartz, ankerite, and siderite are the commonest (non-clay) cement observed in the cores examined in this study as determined by SEM-CL and XRD (Figure 4.12. Also see Table 1 and Table 2 in the appendix A.1 and appendix A.2, respectively). Ankerite and siderite commonly exhibit a blocky habit and commonly occlude large portions of intergranular pore space (Figure 4.12a and Figure 4.12b). Ankerite and siderite cement also occlude secondary pores formed after feldspar dissolution (Figure 4.12a and Figure 4.12b).Thin section analysis reveals two generations of ankerite cement characterized by differing amounts of Fe and Mn. In all samples the amount of siderite (e.g., Figure 4.12a)

ranges between 0.1 vol. % and 0.8 vol. %, whereas the amount of ankerite (e.g., Figure 4.12b) ranges between 0.1 vol. % and 1-6 vol. % (Table 1 in the appendix A.2). In addition, it is clear from SEM images (Figure 4.6, Figure 4.12) that ankerite and siderite have an impact on porosity reduction and may also impact on permeability reduction in the BST core samples, depending on how these carbonate phases are distributed within a pore system.

Two types of quartz cement were identified in BST based on CL images: (1) thick macro-quartz overgrowths and, (2) thin micro-quartz grain coatings. Quartz cement is a volumetrically minor phase (≤ 4 %, Table 1 and Table 2 in the appendix A.1) and occludes the pore space in the most of the BST cores studied (Figure 4.12c and Figure 4.12d). It is likely, however, that even a small volume of quartz cement would be sufficient to block a number of the pore spaces. The term "macro-quartz overgrowth" is here used to describe syntaxial quartz overgrowths larger than 20 µm which can be observed between the detrital quartz grains and micro-quartz crystals ranging from 1 µm to 5 µm in optical continuity with detrital quartz grains, as can be seen in (Figure 4.12e). Quartz overgrowths are most common in the BST.4 samples (3.4%) and BST.3 samples (2.3%), though rare in BST.2 samples and BST.1 samples (1.4%, and 1.1% respectively) as can be seen in Table 1 and Table 2 in the appendix A.1. The decreased abundance of quartz cement in BST.1 and BST.2 samples is attributed to the early occlusion of pore space. SEM-CL shows that most of the detrital quartz grains have overgrowths, with the thickest being between 50µm and 100µm and usually present over monocrystalline, rounded to well-rounded quartz grains, as seen in (Figure 4.12f and Figure 4.12g). Figure 4.12h and Figure 4.12i also illustrate that some of the more frequently observed quartz cement are an early generation, which is located as syntaxial overgrowth on detrital grains. Based on a previous investigation on amorphous silica in sandstone rock, these syntaxial overgrowths on quartz grain surfaces in BST are possibly amorphous silica (Worden et al. 2012).Single microquartz crystals (< 5 µm) could be found in between the kaolinite crystals (Figure 4.12 j).

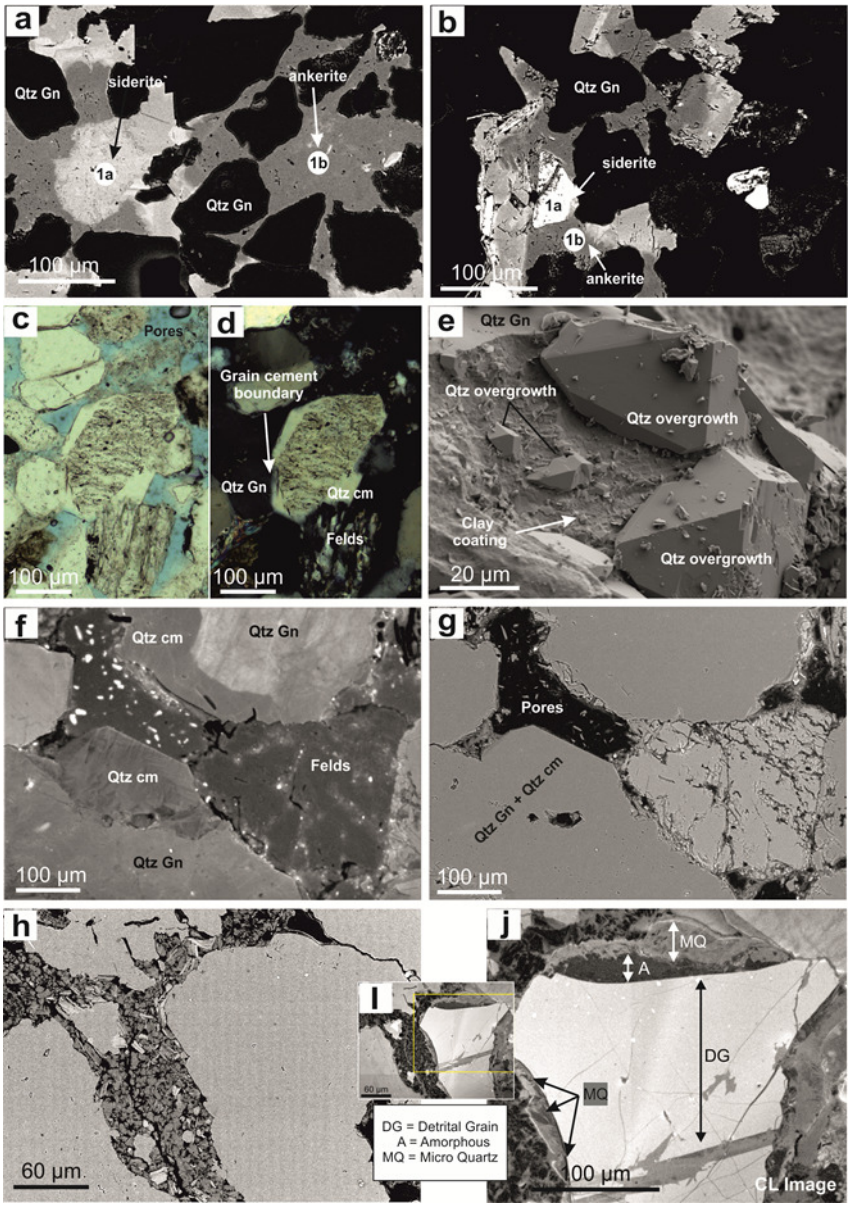

Figure 4.12: Representative photomicrographs showing porosity loss due to cementation. a) BSE image of detrital quartz grains surrounded by two generation of carbonate cement siderite (1a) and ankerite (1b) in BST.1. b) The same carbonate cement shown in (a) is blocking most of the pore spaces between detrital quartz grains in BST.2 c) Plane polarized image showing quartz cements occluding pores between the coarse detrital quartz grains in the BST.3. Optical micrograph (d), of the same area as shown in (c), shows the grain cement boundary (see white arrow). e) Secondary electron micrograph (BST.2) shows large, euhedral quart overgrowth (cement) filling a pore. Note the detrital grain had early, partial clay coating (see white arrow). f) SEM micrograph shows the advance stage of quartz overgrowth cementation in which a significant amount of primary pore space was filled. SEM-CL micrograph (g) of the same area shown in (f); BSE image (h) reveals that the grains and cements (BST.3) are composed of silica and SEM-CL images, (i) and (j), show isopachous layers of quartz cement, high resolution CL (j) distinguishes the detrital grain with bright luminescence (DG) from the dark amorphous silica layer dark or non-luminescing band (A), and the bright microcrystalline quartz (MQ). Qtz = quartz, cm = cement, Gn= grain, and Felds= feldspar.

4.3.2. Possible Nano-Scale Minerals on Mineral Surfaces

It has been documented that nano-scale particles, including possible clay minerals and organic coatings, can be present at sandstone pore surfaces (e.g., Hassenkam et. al., 2011, Matthiesen et al., 2014). Furthermore, the aforementioned studies discuss the potential role nanoparticles may play in EOR processes. To confirm the presence of nanoscale surface bound particles in the studied BST core plug samples, high-resolution SEM imaging of uncoated samples and atomic force microscopy (AFM) was used to study the exposed surfaces of quartz, feldspar and kaolinite crystals.

4.3.2.1. Quartz, Feldspar, and Anatase Surface Characteristics

As mentioned above, by volume, BST is dominated by detrital grains such as quartz and K-feldspar and based on SEM image analysis these are mostly covered by authigenic minerals such as kaolinite, illite, iron oxides, quartz, and carbonate (Figure 4.4 and Figure 4.10) with sizes in the micron range. Quartz overgrowths are frequently observed in BST, and appear in a variety of shapes and sizes (Figure 4.4 and Figure 4.13), generally showing relatively flat surfaces. High-resolution SEM observations of uncoated quartz overgrowths confirm the presence of sub-micron particles of different sizes and shapes (from subhedral to blade-like). Figure 4.13a and Figure 4.13b show examples of needle-shaped particles and nanometer sized kaolinite-like crystals on uncoated detrital quartz surfaces. Similar nanoscale objects are observed on the surface of feldspar and anatase crystals (Figure 4.13c and Figure 4.13d). These observations align with the nanometer range needle-shaped minerals observed by Gary and Rex (1966), who used SEM and XRD to analyze the effluent from core flooding performed on BST, and postulated these to be mica crystals. Figure 4.13e and Figure 4.13f show that these nanosized clay-shaped particles are probably forms of fibrous illite.

Nano-sized clay-shaped particles are of interest to the petroleum industry because these objects are challenging to characterize and may disproportionately affect hydrocarbon production (Gray and Rex, 1966; Stalder, 1973; Pallatt et al., 1984). To further characterize BST mineral surfaces with nanometer resolution, atomic force microscopy (AFM) was employed. AFM characterization revealed small particles (10 nm-400 nm) over the studied mineral surfaces. Figure 4.14 shows an SEM image of uncoated quartz overgrowth (BST.4 sample) and three AFM-PeakForce™ images taken at various positions on its surface. The AFM images show a multitude of small crystals (see Figure

4.14a), with different shapes (see Figures 4.14a, 4.14b and 4.14c), ranging from round to lath-like, and sizes up to ~ 400 nm, as shown in 4.14d and Figure 4.14e. The subhedral shape of some of these crystals resembled some of the micro-crystals imaged using the SEM (Figure 4.10) and are shown in Figure 4.14c. In other cases, subhedral particles resembling kaolinite were also observed (Figure 4.14a and Figure 4.14c). These type of crystals were also observed using SEM, as can be seen in Figure 4.13b.

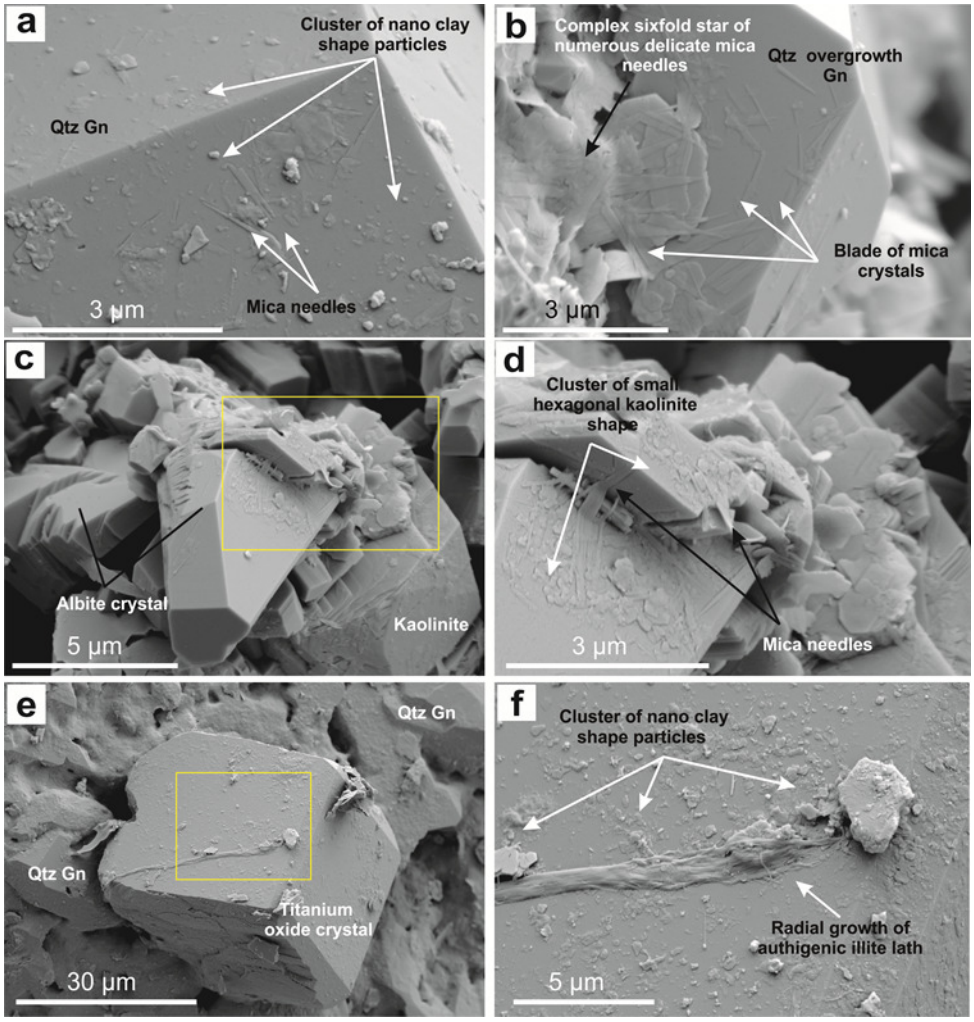

Figure 4.13: SEM micrographs showing different types of nanoparticles over detrital grains and clay minerals in BST. a) Electron micrograph of a quartz grain from the BST covered by numerous mica needles and clusters of nano-sized clay (lath-shaped). b) Electron micrograph of a hexagonal kaolinite crystal covered by numerous mica needles which extend over the underlying quartz overgrowth (BST.3). c) Electron micrograph of mica needles and clusters of nano-particles over albite and kaolinite crystals on BST.2. d) Enlargement of a part of albite crystal from (c) showing further details of the mica needles and a cluster of small hexagonal, nano-sized, kaolinite crystals. e) Electron photomicrograph of a truncated, octahedral, TiO_2 single crystal with exposed {001} and {101} facets lying on the detrital quartz grains which is coated with nano-sized clay crystals and authigenic illite (BST.4). f) Enlargement of the TiO_2 from (d) showing mica blades, and clusters of nano-sized clays, and authigenic illite laths collapsed on top of one another in a random manner. Qtz = quartz, and Gn= grain.

In their study, Gray and Rex (1966) also identified kaolinite-shaped nanoparticles, which corroborate our observations. SEM and AFM results show that only the authigenic blade- or needle-shaped crystals are probably illite and only the smallest crystals of authigenic kaolinite are mobile and coat the surfaces of other minerals, such as quartz in the BST core specimens. This finding agrees with Gray and Rex's observation that dispersion of mica needles and small kaolinite crystals are the principal cause of clay mineral based fines migration. These authors also suggested that the nanoparticles adsorbed to mineral surfaces via the Coulombic attraction of doubly charged ions such as calcium.

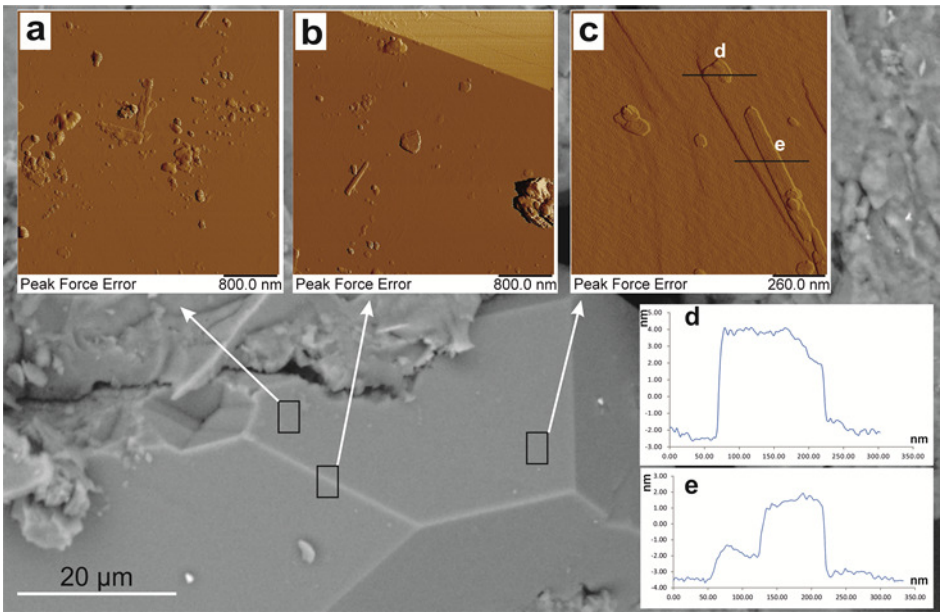

Figure 4.14: Background shows secondary electron photomicrographs of uncoated quartz overgrowth crystal from BST.4. a-c) AFM PeakForce™ images taken at the highlighted locations on the quartz surface showing nano-sized illite needles and a cluster of nano-sized hexagonal kaolinite-like crystals; d and e) show cross sections from nanoparticles in c).

4.3.2.2. Kaolinite Surfaces

High-resolution SEM images show that the kaolinite basal planes are also covered by significant amounts of nanoparticles (Figure 4.13b and Figure 4.13d), the shape and sizes of these nanoparticles is the same as those observed in the quartz crystals and therefore are also identified as nano-sized kaolinite and fibrous illite. The area occupied by these authigenic nano-particles could not be accurately measured, but as with quartz crystals surfaces, the presence of these minerals needs to be accounted for when assessing the reactivity of surfaces in contact with pore fluids.

Compared to the other main clay minerals present in BST (illite/smectite and chlorite) kaolinite crystal crystals show mostly a well-developed, pseudo-hexagonal shape (Figure 4.10) and, in most cases, it is the edge sites that are a the more exposed surface in the pore space, as opposed to the basal planes. This arrangement has important implications in terms of the oil retention capacity of the pore surfaces, as they are expected to be more reactive, and their reactivity pH dependent as well Nasralla and Nasr- El- Din (2014). As described by Nasralla and Nasr- El- Din (2014), the pH dependence and ion sorption reactions within the edges can create a negative site (dominated by SI:Al-O^- edge sites) for the particle at reservoir conditions. These sites will coordinate to oppositely charge dangling bonds in the oil fraction (– $COOCa^+$, – NH^+) and any complexed salt ions occur and electrostatic bridges form, whose quantity determines the strength of oil adhesion to the kaolinite surface. The non-basal (i.e. non 00*l*) surfaces are very pH sensitive relative to the basal surfaces and may show rapid changes in structure as a function of EOR flood chemistry (Brady et al. 2012). Brady et al. (2012) highlighted their model on clay minerals, specifically kaolinite since its morphology permits a high concentration of unfulfilled bonds at sheet edges and corners, as well as natural impurities, which therefore generate a high chemical, surface reactivity that has been suggested to dominate enhanced oil recovery.

4.3.3. Porosity Characterization

To obtain a detailed understanding of the pore network of the four BST samples two complementary techniques were used µ-XCT and MICP. It is notable that µ-XCT and MICP approaches can generate different results in porosity (Peng et al. 2012). This is in part due to the fact that MICP can account for pore volumes that are accessible via pore throat sizes with equivalent diameters between 3nm and 360 nm, whereas micro -XCT can only account for a “modeled” pore space resolvable above the 1.03 micron resolution limit.

4.3.3.3.1. µ-XCT Results.

Analysis of the porosity by µ-XCT was carried out using the maximum resolution possible (1.03 µm) in a volume of 1 mm^3. The volume and number of pores were calculated for each BST specimen and are summarized in Table 4.6.

Table 4.6: Overall porosity, the share of pores and apparent porosity for the four BST samples studied, as determined by µ-XCT and MIP.

Sample No.	µ-XCT					MICP
	Overall porosity in the range >1 µm (%)	Share of pores within the range of pore size (% Vol):				Porosity (%)
		1 - 10µm	10 - 100µm	100 – 250 µm	250 - 500 µm	
BST.1	16.1	45	32	23	0	17.4
BST.2	18.6	35.5	11.4	48	5.1	19.3
BST.3	16.9	47	30	23	0	17.2
BST.4	23.6	23.6	22.2	58.1	9.9	21.2

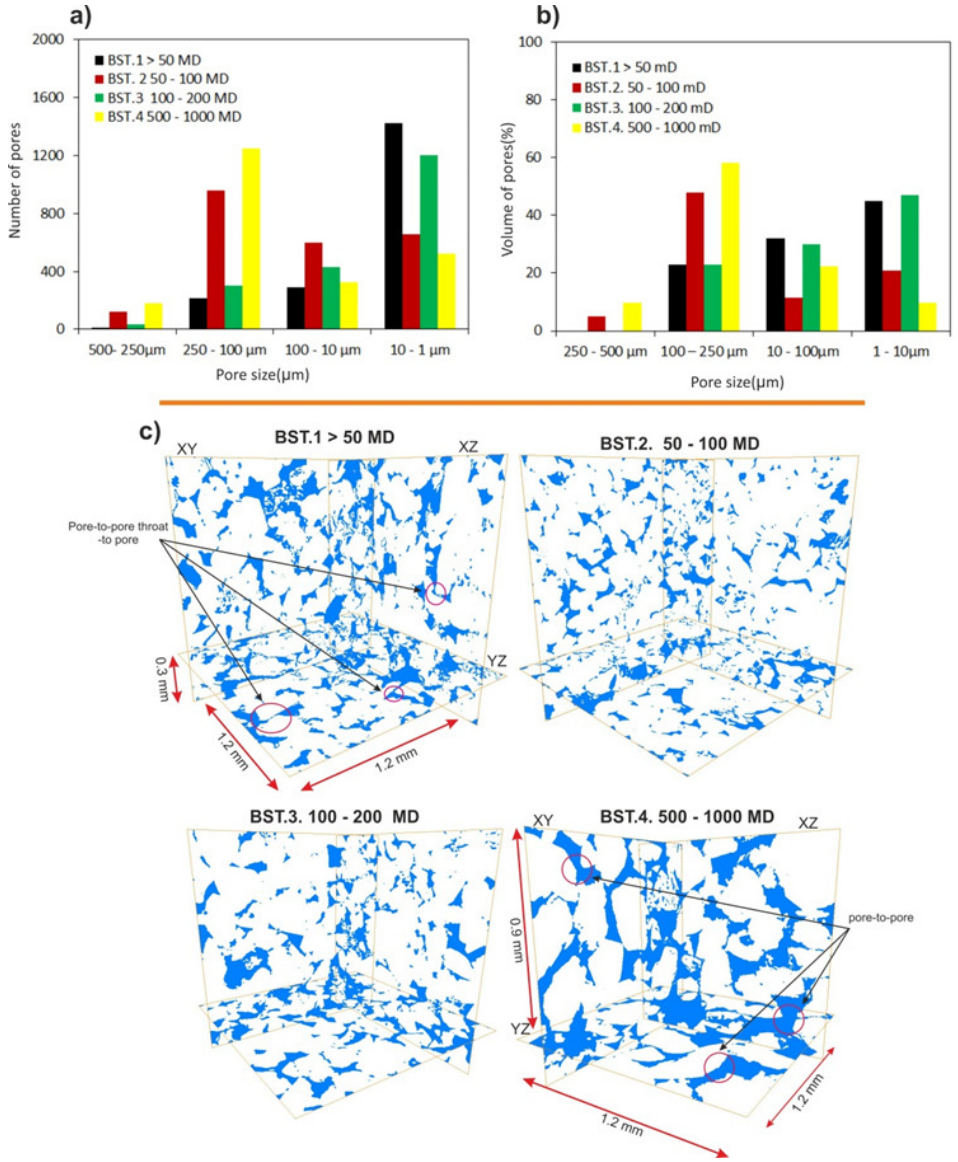

Figure 4.15: Porosity data obtained from analysis of µ-XCT data. a) Number of pores versus pore size fraction for the four BST samples studied. b) Volume of pores (%) versus pore size fraction. c) Three different cross-sectional views of the 3D reconstructed microstructure (at 100 slices), with XY, XZ and YZ sections at 1.2mm, 1.2mm and 1.2 mm, respectively.

As expected for sandstones dominated by primary intergranular pore systems, the permeability of BST samples increases with porosity (Table 4.6), as measured by micro-XCT. However this overall increase does not follow a linear trend and whereas the measured porosity (from µ-XCT measurements) increased from 16.1% to 18.6% for the BST.1 samples and BST.2 samples, respectively, it decreased to 16.9% for BST.3 samples and increased again to 23.6 % for BST.4 samples. Figure 4.15 shows the results from the quantification of the number and volume of pores within 4 pore size fractions (1-10 µm, 10-100 µm, 100-250 µm and 250-500 µm). Figure 4.15a shows most of the pores in the 4 sample sets have a size smaller than 100 µm. However, when the volume fraction of each sample is taken into account the relevance of the large pore fraction (> 100 µm) in the total porosity becomes clearer Figure 4.15b. Based on this, samples in the 4 BST permeability groups can be grouped into two categories, for samples BST.1 and BST.3 pores with a size larger than 100 µm represent just above 20% of the pore volume, whereas for samples BST.2 and BST.4 they represent more than 60% of the pore volume. Examples of the final 3D binary images showing the pore volume fraction for the four BST samples analysed are shown in Figure 4.15c. Additionally, results obtained from the analysis of BST.4 samples align well with the findings of the work of Berg et al. (2014), where an average permeability of 700 mD and a porosity of 19.9% were determined for 6 different BST core plugs. Furthermore, Leu et al. (2014) found that segmentation methods in BST core samples lead to different results for the computed physical properties such as porosity. The computed results in this study closely match with experimental values in the work of Peng et al. (2012), where MICP was used to determine a total porosity in the bulk sample without an epoxy coating of 23.2% based on the bulk density (2.03 g/cm^3).

Results from BST cores shows that the number of pores decreases exponentially as the pore-volume increases further. This is in agreement with the work of Bera et al. (2011) on BST, who found similar results in their FIB–SEM data, showing it is important to understand pore connectivity and the percolating network. Figure 4.15c furthermore shows that vuggy/moldic-like shapes (of size ≥ 200 µm) in BST.1 are connected through the edge of pore bodies (of size ~200 µm) and not directly to other vuggy/moldic-like body shapes. In contrast, it is seen that vuggy/moldic-like shapes are connected directly to other pore bodies in BST.2, BST.3 and BST.4 samples.

4.3.3.3.2. Pore Network Connectivity

Porosity was estimated by micro-XCT models and MICP using the same representative samples of each BST group. MICP porosity measurement results are shown in Table 4.6. In this work, MICP porosity results are typically 10% lower than porosity results obtained by micro-XCT. The difference in value is related to µ-XCT analysis since total porosity is including both accessible and isolated pores (Peng et al. 2012). The fact that the values are so comparable stems, in part, from using the highest resolution scan mode in the µ-XCT. It is clear that results show the same trend on porosity variation with respect to sample porosity as was measured with the µ-XCT. To gain a deeper understanding of the pore structure and connectivity across samples, a detailed high-resolution SEM study was undertaken. Figure 4.16 shows results from the mercury injection experiments for the four groups of samples (BST.1 – BST.4). From this figure, it can be clearly seen that BST.2 and BST.3 have a bimodal pore throat distribution, as opposed to the BST.1 and BST.4 samples, which show an unimodal distribution. Therefore, once again the results allowed grouping of the 4 sample sets into two categories. For BST.2 and BST.3the first peak (pore throat size) has its maximum between 0.1and 0.3µm correspond to (1P) and (1T), whereas the second peak (pore throat size) is, in both groups, located above 0.5µm, and up to 200µm correspond to (2p) and (2T). These samples encompass the two intermediate permeability values. In contrast, for BST.1 and BST.4 group of selected samples an unimodal distribution of pore throat sizes was only observed, the large (1k) peak in BST.1 corresponding to pore throat sizes between 0.5µm to 200µm. Although the large peak (1s) in BST.4 is also identified, the pore throat sizes are located between 0.5 µm to 500 µm as shown in Figure 4.16.

Despite the difference in permeabilities in the case of BST.1 and BST.4, both low and high permeability ranges exhibit unimodal and relatively larger pore throat sizes than those found in BST.2 and BST.3 samples. It is clear the MICP data for selected BST core sample reflect the entire pore throat. In addition to MIP and µ-XCT additional SEM observations were carried out to fully characterize the pore network and connectivity down to the nanometer scale, and therefore obtain a complete picture to link porosity to permeability. High-resolution SEM images indicate that the pores observed in equivalent samples can be assigned into two groups: inter-grain (pores along quartz contacts) and intra-grain (Figure 4.17a and Figure 4.17a c). Small size pores (< 1 µm) mostly exist within the clay mineral matrix, which, in the case of samples from BST.1, BST.3, and

BST.4 consists mostly of kaolinite compared to illite for BST.2 (Figure 4.17e and Figure 4.17f). Neasham (1977) proposed that the distribution of clay morphologies significantly affected sandstone porosity-permeability relationships, postulating that patchy discrete clay particles (e.g. kaolinite booklet-like micro aggregates) have less effect on fluid flow than clays lining the entire pore or congesting pore throats. As the degree of internal porosity of these kaolinite aggregates is smaller than that of the illite coatings (Figure 4.17c), this may explain the larger number of small-size pores observed by µ-XCT (Figure 4.15) in BST.1 and BST.3.

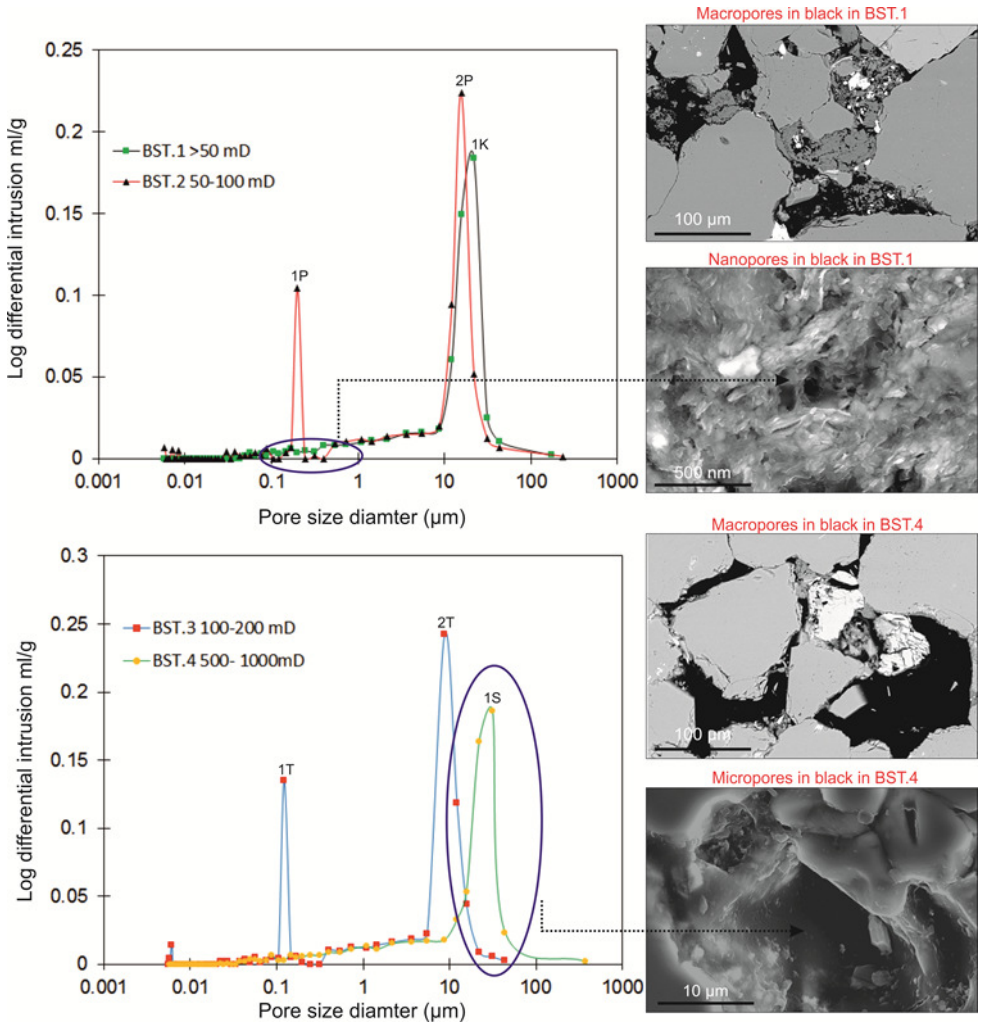

Figure 4.16: Mercury injection versus pore size curves for samples BST.1/2 (a) and BST.3/4 (b). SEM images show the different pore throat types associated to each peak in the curves.

SEM observations suggest that kaolinite aggregates could be one of the factors which are responsible for the permeability reduction in BST.1 compared with the rest of the BST samples, as the crystals are of relatively large size compared to the pore size and also appear to be only loosely attached to detrital grains. Figure 4.17e shows kaolinite-blocked cavities between detrital grains. This characteristic helps explain the MICP data for BST.1 samples, which suggested that the pore throats are not well connected (which will decrease overall permeability). In comparison to BST.1 samples, analysis of clay minerals in the BST.2 samples show illite to dominate the larger fractions.

Based on the SEM analysis, pore throats in illite aglomerates, which form the pathways in the pore network in BST.2 samples, tend to be more exposed to the open pore space. Examples of illite coatings are shown in Figure 4.17i. Due to the fibrous nature of illite, many pore throats within the illite matrix will be connected to the open main pore space. Intuitively, it might be expected that the BST.2 samples, with more authigenic fibrous illite, would have a greater loss of permeability, however, the results indicate that authigenic kaolinite in BST.1 samples reduces permeability more when compared with the BST.2 samples. This is in contrast to the analysis by Neasham (1977), who suggested that authigenic kaolinite filled pores would have the least effect on transport properties. In addition, clay minerals in the BST.3 samples show illite fractions in the scanned area are more dispersed between detrital grains when compared with BST.4 samples. This could be one of the main reasons that the small pore throats in BST.3 samples are exposed to the open pore spaces, as can be seen in (Figure 4.16).This indicates that the illite pore-lining clays in the BST.3 samples have the most effect on pore network properties. However, the high fraction of kaolinite shown by EDX in the BST.4 sample, suggests that it is unlikely that they contribute greatly to permeability reduction.

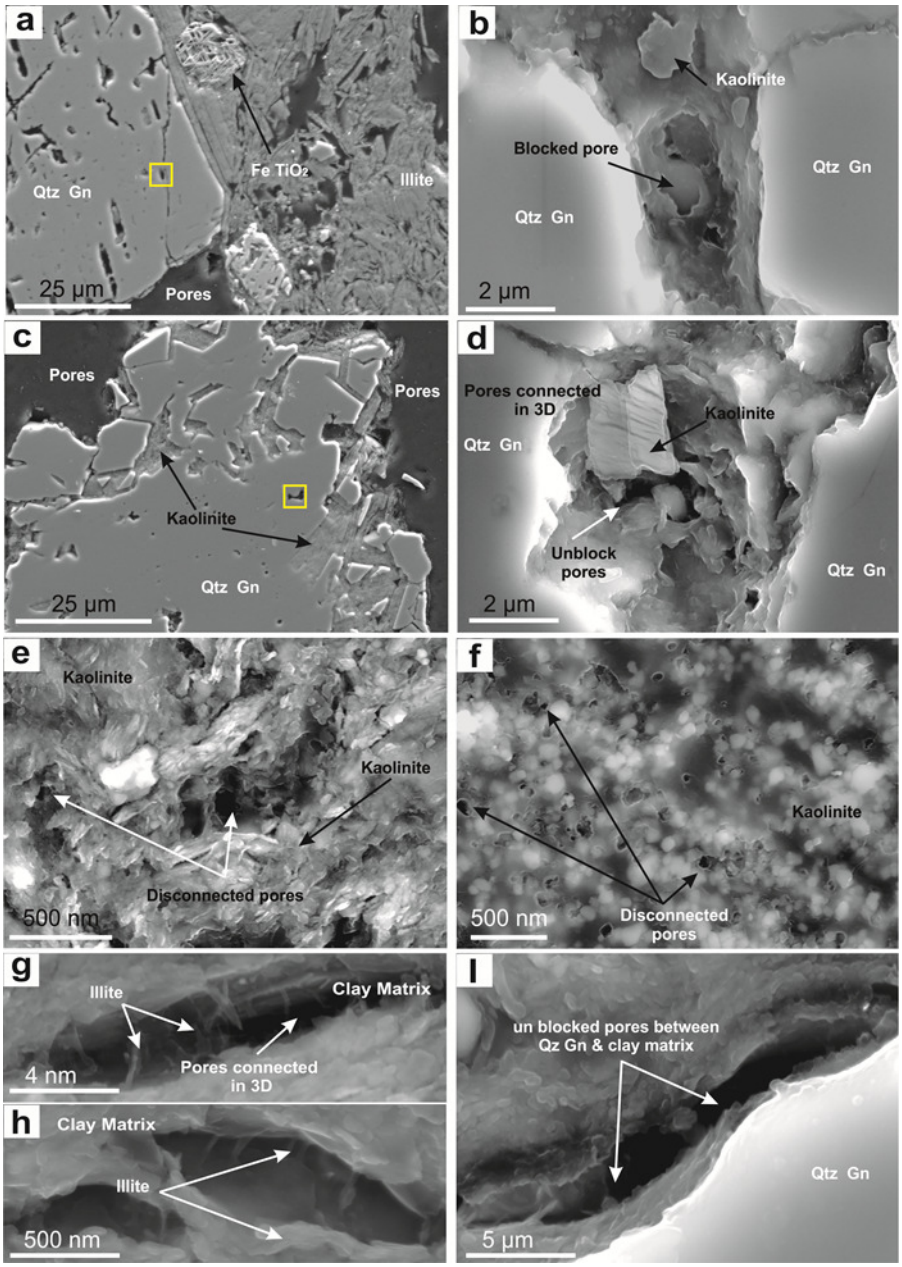

Figure 4.17: SEM and BSE micrographs showing the variation of pore distribution and pore connectivity in the BST cores studied: a) Example of intra-grain porosity in the detrital quartz grains in BST.1, as well as the porous framework of illite aggregates. b) Zoomed in, isolated pore (from (yellow box in a)). The pores in centre of the image are blocked by kaolinite which can significantly affect to overall porosity. c) BSE micrograph showing the kaolinite aggregates between detrital quartz grains in BST.2, which display a smaller internal porosity than illite agglomerates. d) Enlargement from yellow box in (c) showing pore lining kaolinite. e and f) High resolution images showing pore lining kaolinite in BST.1 and BST.3, respectively. Smaller pores in the aggregates show no sign of 3-D connectivity. g), and h), High resolution images from BST.3 showing elongated pores embedded with illite crystals. These pores are framed by fibrous illite minerals that allows for connectivity along the pore. i). High resolution images from BST.2

Results from the characterization show that the pore network in BST.1 is not well connected as the majority of clay minerals exposed to pore space are kaolinite, down to the

resolution of the SEM (Figure 4.16). Along with the pore connectivity in the clay mineral matrix, microstructural observations identify most of the pore throats as intra-grain which form the pathways in the pore network, and these are also blocked at and below the resolution of the SEM (i.e. < 2 μm width, Fig. 13b). The μ-XCT data identifies the heterogeneity in geometry in the pore network in BST.1 samples compared to other BST core plugs, as discussed in Section 4.3.3.3.1. This reveals that the permeability in BST.1 samples is mainly controlled by the pore connectivity in the clay mineral matrix, in intra-grain pores, as well as the geometry of the porous network. In contrast, analyses suggest that the clay mineral matrix is mostly connected to pore spaces in BST.2 and BST.3 samples (Figure 4.16).

When attempting to link intra-grain throats to permeability, it is important to know the connectivity of intra-grain pores (e.g. in quartz detrital grains). The observations from SEM images shows that the intra-grain pore throats are connected and have not been blocked by clay minerals such as kaolinite (see Figure 4.17d) owing to the larger pore-throat sizes being more abundant in BST.2, 3, and 4 samples compared with BST.1 samples. Comparing the computed geometry of the porous network in the BST cores studied, the pores in BST.2, BST.3 and BST.4 samples are often in direct contact with another pore through the body rather than at the edges of pores, as can be seen in (Figure 4.15). These results also offer an explanation as to why there is an increase in permeability within the studied samples. The above explanation may also apply for most sandstone reservoirs with a similar range of permeability.

EOR can partially be explained by permeability reduction in the water swept zone, due to fines migration when low salinity water brine is injected (Tang and Morrow, 1999; Lager et al., 2006). Recently, it has been observed that increased oil recovery could be the result of improved microscopic sweep efficiency rather than the wettability alteration processes (Li, 2008; Skauge et al., 2008). In fact, Tang and Morrow (1999) performed EOR experiments on Berea core sandstone and concluded that the fine (particle) mobilization (mainly kaolinite) increased oil recovery. In that sense, it is essential for a successful low salinity project to understand not only the morphology and identity of the main clay minerals in the samples studied but also their distribution with respect to the pore network, and in particular to pore throats. In the case of BST, that will be the case of either illite or kaolinite.

4.4. Conclusions

Berea core sandstone is widely used by industry as a proxy for one of the principal oil-bearing rocks. Therefore the characterization of its composition, pore structure and the distribution of minerals within the connected pore network is crucial for recovery correct analysis of core-flood experiments related to EOR, fine migrations or other type of studies. In this study, a wide range of techniques were used to characterize 4 types of samples of BST at scales ranging from nanometer to millimeter in order to address the pore surface chemistry as well as the heterogeneity in the mineral and pore sizes distribution. Differences in these parameters will determine the types and quantities of mineral surfaces accessible to react with oil, brine or other fluids and therefore will determine the type of response of Berea sandstone in coreflood experiments. The main conclusions of our characterisation study are:

1. The volumetric compositions of the selected BST are dominated (>87 %) by detrital quartz and K-feldspar. In terms of clay minerals, the volumetric fraction of each of the main clay types (kaolinite, illite/smectite, and chlorite) varied across the 4 different permeability ranges studied (from 3.4 to 9.1 %). This translates into a different amount of clay minerals contained within the total pore space. More importantly, perhaps, is the fact that the identity of the clay minerals exposed to the open pore space is different across the studied specimens.
2. Nano-sized clay-like crystals were observed over most quartz grains surfaces and on larger clay minerals such as kaolinite basal surfaces within the BST core specimens. Their origin, crystallography, chemical reactivity and surface-bonding relationships are in need of further study and future EOR experiments are ongoing to shed light on the importance of these nano-scale particles for reservoir management.
3. Carbonate cement is present, though localized in the BST. Silica cement is also prevalent in all of the BST specimens, including both as crystalline quartz and amorphous silica.
4. Porosity shows a positive, albeit non-linear, correlation with permeability across the BST cores studied. The permeability of the all BST core samples is mainly controlled by the pore connectivity within both the clay matrix and authigenic clays. Next to pore connectivity, pore morphology is also important, especially

when the large pores are connected through relatively smaller pores or edges, without being connected directly to the body of the pore.

Results from this work show that Berea sandstone cores can show significant variability and heterogeneity at both microscopic and nanoscopic scales, which undoubtedly will play a role in determining the rock's interaction with a fluid (being oil, brine or other solution). Performing a full "multi-scale" characterisation, therefore, will be critical in the planning, execution and analysis of core flood experiments in the lab.

4.5. References

Abell, A.B., Willis, K.L., Lange, D.A., 1998. Mercury intrusion porosimetry and image. analysis of cement-base materials. Journal of Colloid and Interface Science 211, 39–44.

Aghaeifar, Z., Strand, S., Austad, T., Puntervold, T., Aksulu, H., Navratil, K., & Håmsø, D. (2015). Influence of Formation Water Salinity/Composition on the Low-Salinity Enhanced Oil Recovery Effect in High-Temperature Sandstone Reservoirs. Energy & Fuels, 29(8), 4747-4754.

Alotaibi, M. B., Nasralla, R. A., & Nasr-El-Din, H. A. (2011). Wettability studies using low-salinity water in sandstone reservoirs. SPE Reservoir Evaluation & Engineering, 14(06), 713-725.

Al-Ramadan, K., Morad, S., Proust, J. N., & Al-Aasm, I. (2005). Distribution of diagenetic alterations in siliciclastic shoreface deposits within a sequence stratigraphic framework: evidence from the Upper Jurassic, Boulonnais, and NW France. Journal of Sedimentary Research, 75(5), 943-959.

Alvarado, V., & Manrique, E. (2010). Enhanced oil recovery: an update review. *Energies* **3**, 1529-1575.

Balthazor, D.A., 1991, Sedimentology of the Bedford-Berea sequence (Early Mississippian), Williams Field, Michigan: Kalamazoo, Western Michigan University, Master's Thesis, 144 p.

Baraka-Lokmane, S., Main, I. G., Ngwenya, B. T., & Elphick, S. C. (2009). Application of complementary methods for more robust characterization of sandstone cores. Marine and Petroleum Geology, 26(1), 39-56.

Baveye, P. C., Laba, M., Otten, W., Bouckaert, L., Sterpaio, P. D., Goswami, R. R., & Sezgin, M. (2010). Observer-dependent variability of the thresholding step in the quantitative analysis of soil images and X-ray microtomography data. Geoderma, 157(1), 51-63.

Beaufort, D., Cassagnabere, A., Petit, S., Lanson, B., Berger, G., Lacharpagne, J. C., & Johansen, H. (1998). Kaolinite-to-dickite reaction in sandstone reservoirs. Clay Minerals, 33(2), 297-316.

Bera, B., Mitra, S. K., & Vick, D. (2010). Understanding the micro structure of Berea Sandstone by the simultaneous use of micro-computed tomography (micro-CT) and focused ion beam-scanning electron microscopy (FIB-SEM).Micron, 42(5), 412-418.

Bera, B., Mitra, S. K., & Vick, D. (2011). Understanding the micro structure of Berea Sandstone by the simultaneous use of micro-computed tomography (micro-CT) and focused ion beam-scanning electron microscopy (FIB-SEM).Micron, 42(5), 412-418.

Berg, S., Armstrong, R., Ott, H., Georgiadis, A., Klapp, S. A., Schwing, A., ... & Enzmann, F. (2014). Multiphase flow in porous rock imaged under dynamic flow conditions with fast X-ray computed microtomography. Petrophysics, 55(04), 304-312.

Bjorlykke, K. 1998. 'Clay Mineral Diagenesis in Sedimentary Basins; a Key to the Prediction of Rock Properties; Examples from the North Sea Basin'. Clay Minerals 33 (1): 15–34. http://claymin.geoscienceworld.org/content/33/1/15.

Brady, P. V., & Krumhansl, J. L. (2012). A surface complexation model of oil–brine–sandstone interfaces at 100° C: Low salinity waterflooding. Journal of Petroleum Science and Engineering, 81, 171-176.

Buades, A., Coll, B., & Morel, J. M. (2005). A non-local algorithm for image denoising. In Computer Vision and Pattern Recognition, 2005. CVPR 2005. IEEE Computer Society Conference on (Vol. 2, pp. 60-65). IEEE.

Buchwalter, E., Swift, A.M., Sheets, J.M., Cole, D.R., Prisk, T., Anovitz, L.L., Ilavsky, J., Rivers, M., Welch, S. and Chipera, D., 2015. Mapping of Microbial Habitats in Organic-Rich Shale. Unconventional Resources Technology Conference (URTEC).

Churcher, P. L., French, P. R., Shaw, J. C., & Schramm, L. L. (1991). Rock properties of Berea sandstone, Baker dolomite, and Indiana limestone. In SPE International Symposium on Oilfield Chemistry. Society of Petroleum Engineers.

Civan, F. (2011). Reservoir formation damage. Gulf Professional Publishing.

Cnudde, V., Cwirzen, A., Masschaele, B., & Jacobs, P. J. S. (2009). Porosity and microstructure characterization of building stones and concretes. Engineering geology, 103(3), 76-83.

Dawson, G. K. W., Pearce, J. K., Biddle, D., & Golding, S. D. (2015). Experimental mineral dissolution in Berea Sandstone reacted with CO_2 or SO_2–CO_2 in NaCl brine under CO_2 sequestration conditions. Chemical Geology, 399, 87-97.

Dilks, A., & Graham, S. C. (1985). Quantitative mineralogical characterization of sandstones by back-scattered electron image analysis. Journal of Sedimentary Research, 55(3).

El-Ghali, M.A.K., Mansurbeg, H., Morad, S., Al-Aasm, I., Ajdanlisky, G., 2006b. Distribution of diagenetic alterations in fluvial and paralic deposits within sequence stratigraphic framework: evidence from the Petrohan terrigenous group and the svidol formation, lower Triassic, NW Bulgaria. Sedimentary Geology 190, 299e321.

Folk, R.L., (1980). Petrology of Sedimentary Rocks. Hemphill Publ. Co., Austin. 182 pp.

Garnes, W. T. (2014). Subsurface Facies Analysis of the Devonian Berea Sandstone in Southeastern Ohio (Doctoral dissertation, Bowling Green State University).

Gautier, J. M., Oelkers, E. H., & Schott, J. (2001). Are quartz dissolution rates proportional to BET surface areas?. Geochimica et Cosmochimica Acta, 65(7), 1059-1070.

Golab, A., Romeyn, R., Averdunk, H., Knackstedt, M., & Senden, T. J. (2013). 3D characterisation of potential CO_2 reservoir and seal rocks. Australian Journal of Earth Sciences, 60(1), 111-123.

Gray, D. H., & Rex, R. W. (1966). Formation damage in sandstones caused by clay dispersion and migration. In Proc (pp. 355-365). Clays and Clay Minerals 1966 14: 355-366.

Hassenkam, T., Pedersen, C. S., Dalby, K., Austad, T., & Stipp, S. L. S. (2011). Pore scale observation of low salinity effects on outcrop and oil reservoir sandstone. Colloids and Surfaces A: Physicochemical and Engineering Aspects, 390(1), 179-188.

Hezel, D. C., Elangovan, P., Viehmann, S., Howard, L., Abel, R. L., & Armstrong, R. (2013). Visualisation and quantification of CV chondrite petrography using micro-tomography. Geochimica et Cosmochimica Acta, 116, 33-40.

Hildenbrand, A., Urai, J.L., 2003. Investigation of the morphology of pore space in mudstones - first results. Marine Petroleum Geology 20, 1185–1200.

Houston, A. N., Schmidt, S., Tarquis, A. M., Otten, W., Baveye, P. C., & Hapca, S. M. (2013). Effect of scanning and image reconstruction settings in X-ray computed microtomography on quality and segmentation of 3D soil images. Geoderma, 207, 154-165.

Howard, J.J., 1991. Porosimetry measurement of shale fabric and its relationship to illite/smectite diagenesis. Clays and Clay Minerals 39 (3), 355–361.

Hurst, A. (1999).Textural and geochemical micro-analysis in the interpretation of clay mineral characteristics; lessons from sandstone hydrocarbon reservoirs. Clay Minerals, 34(1), 137-149.

Kilda, L., & Friis, H. (2002).The key factors controlling reservoir quality of the Middle Cambrian Deimena Group sandstone in West Lithuania. Bulletin of the Geological Society of Denmark, 49(1), 25-39.

Lager, A., Webb, K. J., Collins, I. R., & Richmond, D. M. (2008). LoSal enhanced oil recovery: Evidence of enhanced oil recovery at the reservoir scale. In SPE Symposium on Improved Oil Recovery. Society of Petroleum Engineers.

Lager, A., Webb, K.J. and Black, C.J.J., 2006. Impact of brine chemistry on oil recovery, Paper A24 presented at the 14th European Symposium on Improved Oil Recovery, Cairo, Egypt.

Lai, P., & Krevor, S. (2014). Pore scale heterogeneity in the mineral distribution and surface area of Berea sandstone. Energy Procedia, 63, 3582-3588.

Lai, P., Moulton, K., & Krevor, S. (2015). Pore-scale heterogeneity in the mineral distribution and reactive surface area of porous rocks. Chemical Geology, 411, 260-273.

Landrot, G., Ajo-Franklin, J. B., Yang, L., Cabrini, S., & Steefel, C. I. (2012). Measurement of accessible reactive surface area in a sandstone, with application to CO_2 mineralization. Chemical Geology, 318, 113-125.

Laškova L.N., 1987, The Cambrian: Oil fields of the Baltic region: Vilnius Mokslas p. 10–22 (in Russian)

Lebedeva, E. V., Fogden, A., Senden, T. J.,& Knackstedt, M. A.(2010). Kaolinite Wettability— The Effect of Salinity, pH and Calcium ,Society of Core Analysts.

Lebedeva, E.V.,&Fogden, A(2011). Wettability alteration of kaolinite exposed to crude oil in salt solutions. Colloids and Surfaces A: physicochemical and Engineering Aspects, 377(1), 115-122.

Lee, S. Y., Webb, K. J., Collins, I. R., Lager, A., Clarke, S. M., O'Sullivan, M., & Routh, A. F. (2011, April). Low Salinity Oil Recovery–Increasing Understanding of the Underlying Mechanisms of Double Layer Expansion. In IOR 2011.

Lee, S. Y., Webb, K. J., Collins, I., Lager, A., Clarke, S., O'Sullivan, M., & Wang, X. (2010, January). Low salinity oil recovery: Increasing understanding of the underlying mechanisms. In SPE Improved Oil Recovery Symposium. Society of Petroleum Engineers.

Leu, L., S. Berg, F. Enzmann, R. T. Armstrong, and M. Kersten. 2014. 'Fast X-Ray Micro-Tomography of Multiphase Flow in Berea Sandstone: A Sensitivity Study on Image Processing'. Transport in Porous Media 105 (2): 451–69. doi:10.1007/s11242-014-0378-4

Li, M., Linked polymer solution (LPS) and its application in EOR. The 29th IEA Workshop & Symposium, Beijing, China, Nov 3-5, 2008

Marle, C. M. (1991). Oil entrapment and mobilization. Basic Concepts in Enhanced Oil Recovery Processes, M. Baviere, Eds. Elsevier Applied Science, 3-39.

Matthiesen, J., Bovet, N., Hilner, E., Andersson, M. P., Schmidt, D. A., Webb, K. J.,& Stipp, S. L. S. (2014). How naturally adsorbed material on minerals affects low salinity enhanced oil recovery. Energy & Fuels, 28(8), 4849-4858.

Metz, V., Raanan, H., Pieper, H., Bosbach, D., & Ganor, J. (2005). Towards the establishment of a reliable proxy for the reactive surface area of smectite.Geochimica et Cosmochimica Acta, 69(10), 2581-2591.

Milliken, K. L., & Laubach, S. E. (2000). Brittle deformation in sandstone diagenesis as revealed by scanned Cathodoluminescence imaging with application to characterization of fractured reservoirs. In Cathodoluminescence in geosciences (pp. 225-243). Springer Berlin Heidelberg.

Morrow, N. R., Tang, G. Q., Valat, M., & Xie, X. (1998). Prospects of improved oil recovery related to wettability and brine composition. Journal of Petroleum science and Engineering, 20(3), 267-276.

Nasralla, R. A., Alotaibi, M. B., & Nasr-El-Din, H. A. (2011, January). Efficiency of oil recovery by low salinity water flooding in sandstone reservoirs. In SPE Western North American Region Meeting. Society of Petroleum Engineers

Neasham, J. W. (1977, January). The morphology of dispersed clay in sandstone reservoirs and its effect on sandstone shaliness, pore space and fluid flow properties. In SPE Annual Fall Technical Conference and Exhibition. Society of Petroleum Engineers.

Omotoso, O., McCarty, D. K., Hillier, S., & Kleeberg, R. (2006). Some successful approaches to quantitative mineral analysis as revealed by the 3rd Reynolds Cup contest. Clays and Clay Minerals, 54(6), 748-760.

Otten, W., Pajor, R., Schmidt, S., Baveye, P. C., Hague, R., & Falconer, R. E. (2012). Combining X-ray CT and 3D printing technology to produce microcosms with replicable, complex pore geometries. Soil Biology and Biochemistry, 51, 53-55.

Pallatt, N., Wilson, J., & McHardy, B. (1984). The relationship between permeability and the morphology of diagenetic illite in reservoir rocks. Journal of Petroleum Technology, 36(12), 2-225.

Peng, S., Hu, Q., Dultz, S., & Zhang, M. (2012). Using X-ray computed tomography in pore structure characterization for a Berea sandstone: resolution effect. Journal of Hydrology, 472, 254-261.

Pepper, J. F. et al. (1944) Map of the Second Berea sand in Gallia, Meigs, Athens, Morgan, and Muskingum Counties, Ohio, U. S. Geol. Survey, Oil and Gas Invest., Prelim, map no. 5

Pepper, J. F.; DeWitt, W.; and Demarest, D. F., 1954, Geology of the Bedford shale and Berea sandstone in the Appalachian Basin: U.S. Geol. Survey Prof. Paper 259, 111 p.

Peters, C. A. (2009). Accessibilities of reactive minerals in consolidated sedimentary rock: An imaging study of three sandstones. Chemical Geology, 265(1), 198-208.

Scholle, D., & Scholle, P. (n.d.). , (2014) A Color Guide to the Petrography of Sandstones, Siltstones, Shales and Associated Rocks.

Skauge, A.; Fallah, S.; McKay, E., Modeling of LPS Linked Polymer Solutions. The 29th IEA Workshop & Symposium, Beijing, China, Nov 3-5, 2008.

Soeder, D. J. (1986). Laboratory drying procedures and the permeability of tight sandstone core. SPE Formation Evaluation, 1(01), 16-22.

Sorbie, K. S., & Collins, I. (2010, January). A proposed pore-scale mechanism for how low salinity waterflooding works. In SPE Improved Oil Recovery Symposium. Society of Petroleum Engineers.

Stalder, P.J., 1973. Influence of crystallographic habit and aggregate structure of clay mineral on sandstone permeability. Geol. Mijnbouw, 52(4): 217--220.

Strand, Skule, Tor Austad, Tina Puntervold, Hakan Aksulu, Bjarne Haaland, and Alireza RezaeiDoust. 2014. 'Impact of Plagioclase on the Low Salinity EOR-Effect in Sandstone'. Energy & Fuels 28 (4): 2378–83. doi:10.1021/ef4024383

Tang, G.-Q, N. R. Morrow (1999). "Influence of brine composition and fines migration on crude oil/brine/rock interactions and oil recovery." Journal of Petroleum Science and Engineering 24(2–4): 99-111.

Tovey, N. K., & Krinsley, D. H. (1991). Mineralogical mapping of scanning electron micrographs. Sedimentary Geology, 75(1), 109-123.

Vosylius, G. (1998). Reservoir properties of Middle Cambrian rocks. In Proceedings of the International Scientific Conference "Prospectives of petroleum exploration in the Baltic Region". Lithuanian Geological Institute (pp. 43-48).

Waldmann, S., Busch, A., van Ojik, K., & Gaupp, R. (2014). Importance of mineral surface areas in Rotliegend sandstones for modeling CO_2–water–rock interactions. Chemical Geology, 378, 89-109.

Webb, K.J., C.J.J. Black, and I.J. Edmonds. Low salinity oil recovery - the role of reservoir condition core floods. in EAGE(Marle 1991) conference. 2005. Budapest, Hungary.

Wilson, M. D., & Pittman, E. D. (1977). Authigenic clays in sandstones: recognition and influence on reservoir properties and paleoenvironmental analysis. Journal of Sedimentary Research, 47(1).

Worden, R. H., French, M. W., & Mariani, E. (2012). Amorphous silica nanofilms result in growth of misoriented microcrystalline quartz cement maintaining porosity in deeply buried sandstones. Geology, 40(2), 179-182.

Yven, B., Sammartino, S., Geraud, Y., Homand, F., Villieras, F., 2007. Mineralogy, texture and porosity of Callovo-Oxfordian argillites of the Meuse/Haute-Marne region (eastern Paris Basin). Mémoires: Société Géologique de France 178, 73–90.

Zhang, F., She, Y. H., Li, H. M., Zhang, X. T., Shu, F. C., Wang, Z. L.& Hou, D. J. (2012). Impact of an indigenous microbial enhanced oil recovery field trial on microbial community structure in a high pour-point oil reservoir. Applied microbiology and biotechnology, 95(3), 811-821.

Zhang, P., Lee, Y. I., & Zhang, J. (2015). Diagenesis of tight-gas sandstones in the lower cretaceous denglouku formation, songliao basin, ne china: implications for reservoir quality. Journal of Petroleum Geology, 38(1), 99-114.

Chapter 5

An Experimental Investigation into Role of Salinity, and Ionic strength on Wettability Regime in Quartz-Based Substrates

5.1. Introduction

As has been mentioned in previous sections, although there is not a consensus on the main mechanism driving it, it is widely accepted that low salinity EOR produces a change in the wettability state of the reservoir to a more water wet state (Zhang and Morrow, 2006; Lager et al., 2008). In general, reservoir rocks as a whole may not show the same wettability states since wetting depends on the properties of the constituent minerals, the composition of oil and water salinity, in addition to the effect of temperature and pressure of the system (Nasralla et al., 2013). The wettability state of a reservoir rock is defined as oil-wet,water-wet, or intermediate-wet (Anderson,1986b). Recently, Pu et al.(2010) studied wettability alteration on mineral surfaces such as mica and kaolinite, as these have been shown to have a substantial impact on additional oil recovery (Somerton and Radke, 1983; Hassenkam et al., 2011, 2014).

According to Craig, (1971) wettability is a measurement relating to the degree of adhesive and cohesive forces which create a preference for one liquid (known as the wetting phase) to be in contact with a mineral surface, compared to another liquid (the non-wetting phase). The wetting phase will have a tendency to spread across the mineral surfaces, displacing the non-wetting liquid phase. To date, studies of crude oil/brine/rock

interactions have focused on contact angle measurements, which are considered to be a macrophysical parameter in petroleum engineering (e.g.Buckman et al. 2000; Shijkerbuij B. 2006). The conventional method of measuring the wettability when water and another immiscible fluid are in contact with a solid surface is by measuring the contact angle θ through the water phase, as shown in equation 2.6 (see Chapter 2). Figure 2.5 demonstrates the situation where the oil drop will be located on a solid surface in the presence of another immiscible liquid such as water. For oil/water system, if the contact angle is 0 to 75° the surface is water-wet, 75 to 115° is intermediate-wet, and 115 to 180° is considered oil-wet.

Wettability can be inferred at the core-scale indirectly by the use of the Amott wettability index (Anderson, 1986a) and low field nuclear magnetic resonance (NMR) (Al-Mahrooqi et al., 2003; Vevle, 2011). Traditionally, wettability behavior could only be accessed directly on a single mineral surface by the use of the dynamic sessile drop method (Abdallah et al., 2007; Nasralla et al., 2013) and in micromodel studies (Seyyedi et al., 2015). Since these early studies, an important and increasing number of papers have been published on wettability behavior at the micro-scale. These studies have demonstrated the wettability alteration on micro-scale levels using X-ray computed tomography (CT) (Andrew et al., 2014), X-ray photoelectron spectroscopy (XPS) (Pedersen et al., 2016), environmental scanning electron microscopy (ESEM) (Al-Shafei and Okasha, 2009; Polson et al., 2010) and, more recently, atomic force microscopy (AFM) (Hilner et al., 2015).

Wettability alteration has been examined on different mineral surfaces, such as quartz, mica, and kaolinite (Lebedeva and Fogden, 2011; Seiedi et al., 2011).The advantage of using single mineral surfaces is that it allows the observation of factors that can influence the wettability behavior in a more controlled way without the additional complexity caused by the pore geometry of a natural rock. For this reason, quartz is typically used as the model substrate to represent the sandstone wettability state (Bera et al., 2012a; Qi et al., 2013a). Recently, experimental investigations have been conducted to elucidate the mechanism responsible for wettability alteration of quartz surfaces (Bera et al., 2012; Qi et al., 2013b). However, very limited examinations have been performed on the adsorption of crude oils onto a quartz surface in the presence of brines (Saraji et al., 2013). From a series of flow experiments on mineral packs it was discovered that the total amount of adsorbed asphaltene on the surface of the minerals depends on to the stability of the thin brine film. Saraji et al. (2013) discovered that the adsorbed amount of asphaltene

on the quartz surface decreased at a higher salt concentration ($CaCl_2$) due to larger repulsive hydration forces, which stabilized the thin brine films on the quartz. However, in NaCl brine, the hydration forces may be not dominant resulting in higher adsorption at high ionic concentration. According to Buckley et al. (1998), during wettability alteration, four kinds of interactions exist among the system of oil, brine, and minerals. These are (i) polar interactions when there is no water film between the oil and mineral surface, (ii) surface precipitation of asphaltenes, (iii) acid/base interactions, and (iv) ion binding interactions (Buckley et al., 1998). In a sandstone reservoir, there is always a brine present, either as formation water or as low-salinity brine during the LSEOR process. The brine salinity has been shown to be a critical factor in determining wettability on any system (Al-Aulaqi et al., 2011) since it can affect the surface charge on the mineral and oil/brine interface (Buckley et al., 1998) which in turn can affect the wettability alteration. As a result, extensive research has been conducted on the brine, crude oil, and sandstone rock system, and it was examined that the brine composition of injected water can significantly alter the wettability of the oil reservoir during LSEOR (Jadhunandan and Morrow, 1995; Yildiz and Morrow, 1996; Arima and Iwata, 2007; Zhang et al., 2012; Qi et al., 2013a; Yang et al., 2015).

Taking into account all of these results, it would be interesting to find the effect of brines on the zeta potential (ζ) and wettability in the presence of crude oils and decanoic acid in dodecane on quartz surface at multiple length scales. These investigations are needed as well as being potentially beneficial since no systematic examination has previously reported the sole effect of the polar compounds on the ζ potential and wettability variation. Macroscopic examinations provide valuable indications, but micrometer and nanometer observations are vital for testing the conceptual models that are constructed using macroscopic data.

In this chapter, quartz crystals and quartz particles are used as the model substrate of sandstone rock, and the samples were aged with different methods to gain an oil-wet state. Then, the effect of brine concentration and composition into its adsorption was evaluated. Two types of chloride brines, Na^+ and Ca^{2+}, were taken into consideration during observations. The aim of this work is to elucidate crude oil and model oil adsorption rules on quartz surfaces in the presence of different brine ionic strengths and compositions, which would clarify wettability alteration during LSEOR processes.

5.2. Experimental Section

In this part of the chapter we describe the material, experimental procedures, and apparatus that have been used to study the wettability behavior of quartz surfaces at different scales, and the zeta potential analysis.

5.2.1. Materials Used

- Substrate: Quartz crystals used in these experiments were prepared at the rock preparation laboratory at the University of Manchester, and quartz powder.
- Brine: The brines used in these measurements were NaCl, $CaCl_2$ at concentrations of 0.001; 0.01; and 1.0M.
- Oil: Crude oil from one of North Sea reservoir and model oil compounds (decanoic acid-dodecane).

5.2.1.1. Substrate-Quartz Preparation

The purpose behind choosing various roughnesses was to allow a study of the effects of texture on the wetting states on a quartz substrate. Quartz is the most common mineral in mudrocks and sandstone reservoirs (Blatt and Schultz, 1976; Tiab and Donaldson, 2012), and it is temperature stable well above reservoir conditions. Its structure consists of densely packed tetrahedrons of Si-O bonds (Götze and Möckel, 2012). Quartz is often used as a representative mineral for the reservoir rock and, significantly, is highly wetted by water and oil in an atmosphere of air (Saraji et al., 2013).

Two types of quartz crystal were used in the experiments described here, with two very different degrees of roughness to assess its effect on the contact angles from several measurements (Figure 5.1). Hereafter, for ease of reference, they are referred to as flat (smooth surface) and non-flat (rough surface) quartz. Non-flat substrates were prepared from polished slides (with two orientations, parallel to the {100} face and perpendicular to the c-axis) of quartz crystals. These slides were prepared at the rock preparation laboratory at the University of Manchester. The polished slides were then treated with 1.0M KOH solutions (for different amounts of time) to induce the formation of etch pits and therefore to create roughness. Also, the natural face of a high-quality Herkimer quartz single crystal was used after a slice of the crystal was cut using a low-speed saw. Furthermore, the crystal was cleaned using a 0.1M KOH solution in addition to ethanol/methanol. Upon cleaning it was revealed that this natural face, in fact, exposes atomically flat surfaces

(Figure 5.1a and 5.2a). For the study, two non-flat crystals and a flat single crystal were used (Figure 5.1b). Each crystal was cleaned after the experiment to prevent cross-contamination (see below). In addition, quartz powder was prepared by grinding a quartz crystal (with a size range of 1-2 cm) in an agate mortar. Also, a portion of the crushed quartz powder passed through a 16-mesh mesh screen. Zeta potential measurements were performed on quartz powder with a size of 1mm (hereafter referred to as quartz powder) (Figure 5.2b). These measurements were performed on powders that have been in contact with crude oil and/ or decanoic acid-dodecane and saline solutions of different ionic strengths.

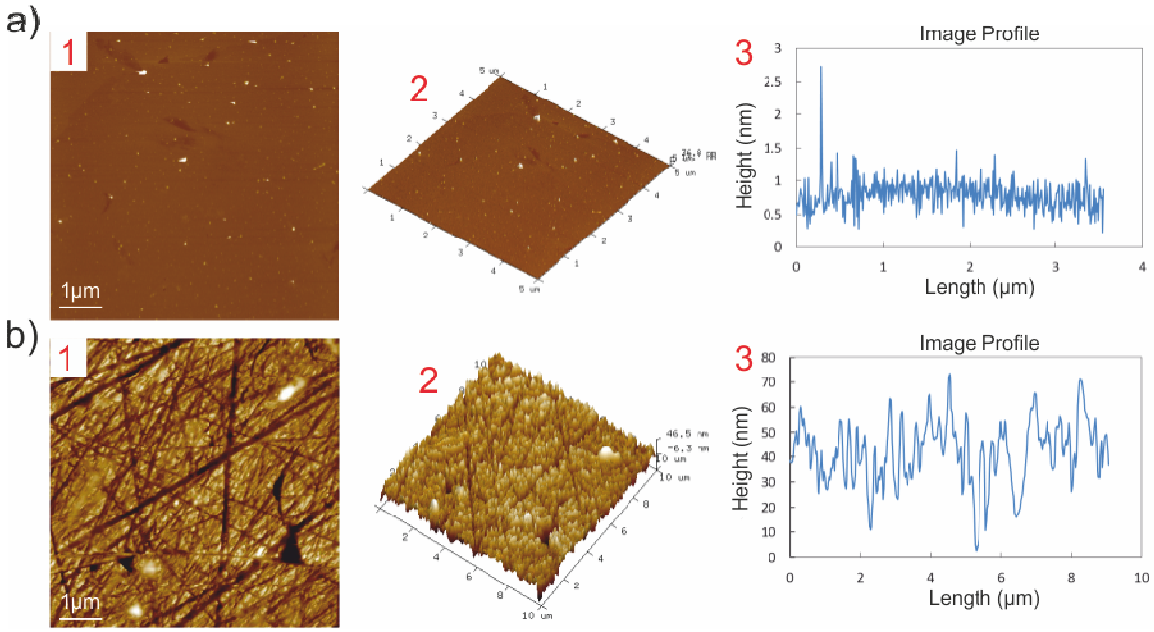

Figure 5.1: AFM characterization of quartz substrate with increasing levels of roughness at the nanoscale. 2D and 3D views of representative topographies are shown in the first and second column; in the third column, representative surface profiles are shown. (A (1), (2), (3)) Flat quartz substrate represents the natural face of a high-quality quartz single-crystal; (B (1), (2), (3)) surface topography, 3D views and profiles of quartz substrate batch (50 nm roughness). For all images the scan area is 1 x 1µm^2.

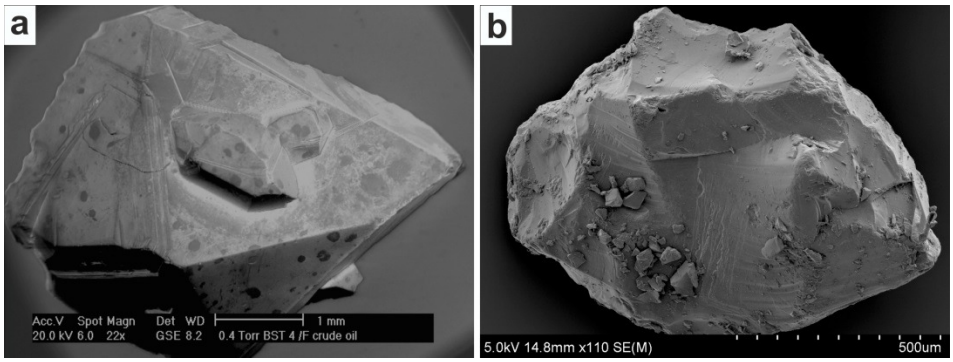

Figure 5.2: A represenatative SEM photomicrograph of quartz surface specimens. a) Flat quartz substrate represents high-quality quartz crystal. b) Micro quartz particles.

In this work, careful attention has been paid to the fluids used to ensure the purity of components and in avoiding contamination. While all efforts were employed to ensure cleanliness during tests, the experiments were not conducted within a clean-room environment.With this in mind, tests were implemented in line with a reputable standard operating process that avoided the introduction of artifacts (Treiber and Owens, 1972; Leirvik, 2010; Zhang et al., 2010).

Two types of brine were employed, formation water (FW), as shown in Table 5.1, and single salt solutions (of low, medium and high concentration and of single-cation such as sodium chloride and calcium chloride), Table 5.2. FW with the composition of the average North Sea connate water was used to treat the quartz substrates initially and, therefore, to replicate reservoir conditions. The preparations used MiliQ water and the corresponding salts (reagent grade, Sigma-Aldrich). The pH and density (at 25 °C) were found to be 5.51 and 1.16 g/cm^3 respectively. Low and high concentration single-ion brine solutions were also prepared using MiliQ water and the same chloride reagents. MiliQ water is a trademark created by Millipore Corporation to describe 'ultrapure' water of "Type 1", as defined by various authorities (e.g. ISO 3696), as well as their devices for producing such water.The chloride salt employed in this experiment are relatively soluble and should dissolve instantaneously. All solutions were regularly filtered (0.2 µm filter) to remove any undissolved impurities. New glassware was used for this wettability study and was not shared with other fluids. Single ion brine composition was chosen so that the specific effect of each cation (as well as low-high concentration) could be probed.

Table 5.1: Composition of the North Sea reservoir FW.

No	Ion	mol/L	Reagents	Reagents(mol)	Cl (from reagent)
1	Na	0.35	NaCl	0.90	0.54
2	Ca	0.01	$CaCl_2$	0.03	0.02
3	Mg	0.01	Mg Cl_2	0.02	0.02
4	K	0.01	KCl	0.12	0.06

Table 5.2: Composition of the low, medium and high concentration of brines.

Type of Brines	Synthetic Brines	mol/l
Low -brine concentration	NaCl	0.001
	$CaCl_2$	0.001
	NaCl	0.01
	$CaCl_2$	0.01
High-brine concentration	NaCl	1.0
	$CaCl_2$	1.0

5.2.1.3. Crude Oil and Decanoic Acid-Dodecane Properties

In this work, the chemical analysis of the used crude oil supplied by BP from one of the North Sea reservoir is shown in Table 5.3. Additionally, the result of infrared (IR) spectroscopy (Instrument: Spectrum Two™ from PerkinElmer) of an oil sample is shown in Figure 5.3. IR spectroscopy of crude oil makes it possible to identify the type of functional groups. Spectroscopic data in Figure 5.3 indicated the presence of sulfoxide, sulfone, acid, and carbonyl functions in the crude oil. In detail, the crude oil contained only small amounts of each phenolic, amine, and amide functionalities while the carboxyl signal has a high intensity, though care is needed in assigning relative amounts of groups in IR owing to orientation and relative intensity effects. In the aliphatic fraction, the C–H stretch range and CH_2 stretching dominate over CH_3. This corresponds to the cyclic structures and high total acid number (TAN= 1.2 mg KOH/g), which also suggest a relatively low number of terminal methyl groups may be present. Acidic components in crude oils consist of organic acids, inorganic acids, and some other compounds such as esters, phenols, amines and the pyrrole series, which affect the oil acidity status (Galimberti et al., 2000). The acidity of crude oil is most commonly expressed by its total acid number (TAN) (Lashkarbolooki et al., 2014a, 2014b). In the petroleum industry, if the TAN number of crude oil is higher than 0.5 mg KOH/g, the crude oil is considered an acidic crude oil (Groysman, 2014).

Table 5.3: Results of Gas Chromatography (GC) Analysis (provided by BP).

Hydrocarbon type (C < 36)	**wt %**	**Physical properties of C < 36**	
Normal paraffins	12.27	Density (25 °C)	0.8793
Isoparaffins	12.72	Viscosity (40 °C)	41.71
Aromatics	0.784		
Naphthenes	5.317		
Saturates (C17 < C < 25)	7.535		
Aromatics (C17 < C < 25)	10.22		
Unknowns (C < 25)	14.36		
$C36^{+}$	36.77		

In addition to oil, a so-called "model oil compound" was used throughout the wettability tests of the quartz substrate. This model compound was prepared using the decanoic acid and dodecane supplied by Sigma-Aldrich. The concentration of decanoic acid in dodecane was of 1.0 M. This was achieved by adding 176.26 g of decanoic acid to 1L of dodecane. The properties of both decanoic acid and dodecane used are summarised in Table 5.4.

Table 5.4: Oil-model compound properties.

Name	**polarity**	**Chemical formulation**	**Density**
Decanoic acid	Polar	$CH_3(CH_2)_8COOH$	0.893 g/mL^{-1}
Dodecane	Non-polar	$CH_3(CH_2)_{10}CH_3$	0.749 g mL^{-1}

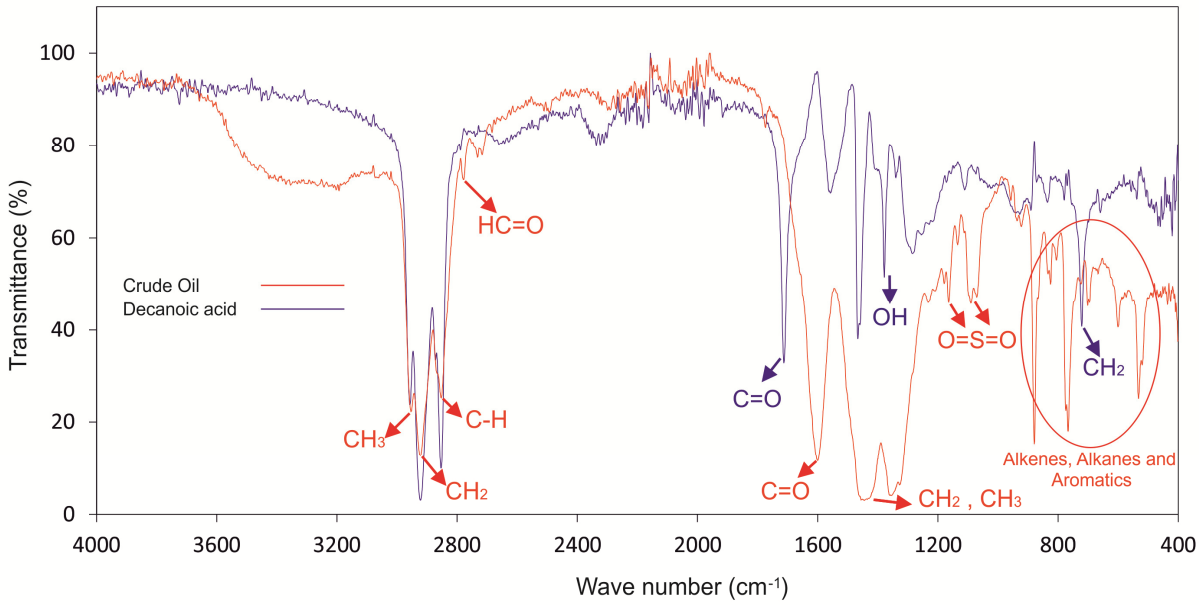

Figure 5.3: IR spectroscopy of used crude oil and decanoic acid-dodecane in this study.

5.2.2. Experimental Procedure

5.2.2.1. Substrate-Water Saturation

Before each experiment, quartz crystal specimens (or quartz powder) were thoroughly cleaned to prevent cross-contamination. Cleaning was done by immersing the crystals in ether and toluene to strip organic compounds and followed by a cycle of methanol and ethanol to remove any remnant of the brine solution. In all steps, sonication was performed (40 mins) using a sonic probe to improve the ability of the solvent to remove the surface contaminants.

This work follows the methodology developed by Leirvik (2010), where the effects of salts present in FW on the crystals were assessed. For the experiments performed with quartz powder, 5 g of the material, and a magnetic stirring rod, were placed into each prepared vial. For each gram of quartz powder used in this experiment, 5 ml of FW was used as an arbitrary measure. 25 ml of the relevant FW was measured out and placed in the corresponding vial. Once both the solid and liquid material were present in the vial, they were closed using ParaFilm®. Sealed vials were then put on magnetic stirring plates and left mixing at 400 rotations per minute (rpm) for one hour at room temperature (25 °C), to simulate the fluids being in contact with a reservoir rock. The samples were then dried in the oven for 12 hours at 40 °C, to complete the drying procedure. To saturate the quartz crystal specimens, the crystals were soaked in 5 ml of FW for one hour at 25 °C. When the samples were retrieved from the FW, the remaining FW was removed with a Teflon filter. This was because letting the water evaporate would leave too much salt on the quartz crystal surface,or alternatively gently letting the water absorb onto a piece of paper would possibly leave too little salt on the quartz crystal surface.

5.2.2.2. Substrate -Ageing

The wettability state of the quartz samples was changed by ageing them in oil or the 1.0 M decanoic acid-dodecane mixtures as per the following procedure. 4 g of quartz powder were weighed out and placed into a vial. For every gram of quartz powder used, 4 ml of oil / decanoic acid-dodecane mixture was needed. This optimum ratio was developed through trial and error, the first trial run, when smaller quantities of oil and decanoic acid-dodecane were used, failed to alter the wettability of the quartz adequately. In total, 16 samples of quartz powder were prepared, with eight of them being aged in oil and eight being aged in the decanoic acid-dodecane mixture. It is important to check the wettability

of aged samples (using drop shape analyser/and or ESEM) before the "washing" procedure (explained in the subsequent sections) is performed. To perform the ageing, the vials were put on a magnetic stirring plate and then they were each covered with electrical tape and foil and left mixing at 400 rpm for 30 days at 90 °C. A similar technique was used for aging a further 12 quartz crystals, with eight of them being aged in oil and four being aged in decanoic acid-dodecane. Each of the quartz crystals was placed into 20 ml of oil / and or decanoic acid-dodecane. The vials were each covered with foil before being placed in an oven for 30 days at 90 °C. This step mimics the reservoir charging process and equilibrates the quartz surface charges; a water surface film prevents the quartz surface from becoming strongly oil-wet.

5.2.2.3. Substrate-Brine Exposed

To obtain a range of wettability data i.e. reduce the contact angle from oil-wet to more water-wet in regular intervals, salinity injection on the quartz as a model substrate for sandstone were studied. It has been showed by (Qi et al., 2013b) that the presence of salts such NaCl and $CaCl_2$ contribute to wetting alteration. The phenomena behind the findings are described in the results section of this chapter. Once all the samples had been dried after aging, 20 ml of relevant chloride salt solution was measured and added to the corresponding vial, as can be seen in Figure 5.4. A magnetic stirrer was placed in each prepared vial for the powder samples, while a magnetic stirring rod was not used for the quartz crystal groups throughout the washing process. ParaFilm® was then applied to seal the vials; sealed vials were then placed on a magnetic stirring plate and left mixing at 400 rpm for 24 h at room temperature (25 °C). The samples obtained were then prepared for the investigations.

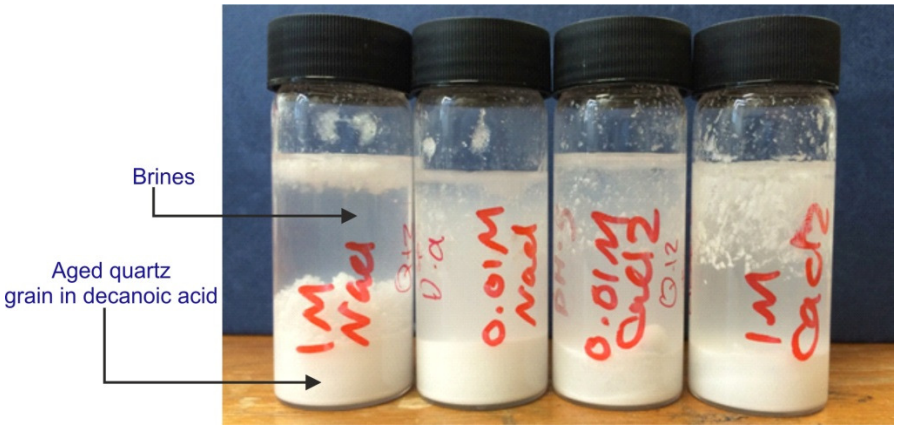

Figure 5.4: Washing process of aged quartz particles picture at room tempreature in 1.0M, and 0.01M of NaCl, and 1.0M and 0.01M of $CaCl_2$.

Using the procedures designed in the previous sections, samples were obtained for analysis as detailed in Figure 5.5. These samples were all in a dry powder to measure the ζ potential; a similar treatment was implemented for quartz crystals (non-flat surface) to measure the contact angles using different optical techniques.

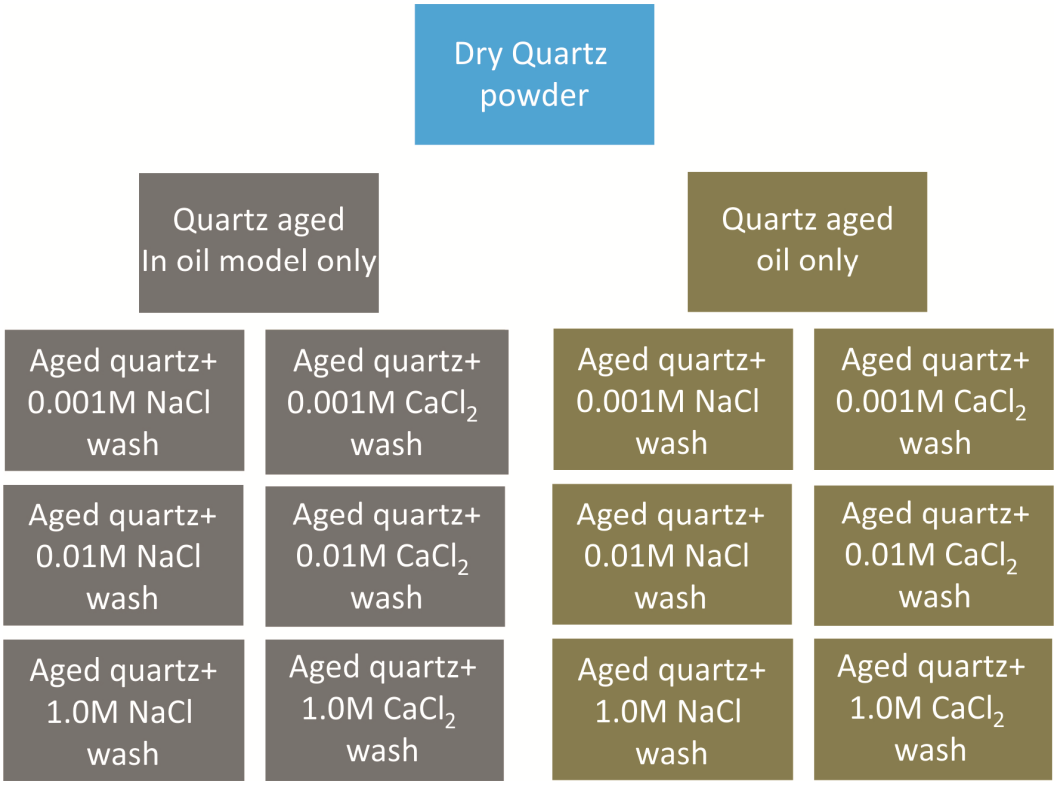

Figure 5.5: Diagramatic illustration of samples obtained from laboratory work.

In general, the effect of two different brines, in high and low concentrations, on non-flat quartz crystal was tested by measuring the contact angle for decanoic acid-dodecane, and crude oil on quartz surfaces. 1.0M NaCl and 1.0M $CaCl_2$ represent the high-concentration brine solution in this study (Table 5.2), while 0.01M and 0.001M of NaCl and $CaCl_2$ represent the low brine solutions. Therefore, in this study, the pH of the brines used in the measurements were not manipulated and set at 6.5 for all solutions. Solution pH was adjusted using hydrochloric acid for low pH and a NaOH buffer for high pH. Six samples were prepared for atomic force microscopy (AFM) analysis, eight samples were also prepared for environmental scanning electron microscope (ESEM) observations, and twelve different experiments were conducted using drop shape analysis. It should be noted that the above experiments were all done on the quartz crystal. In addition, twelve samples of quartz powder prepared for the ζ potential, the procedure for which was always the

same, except that a different concentration was used for each experiment, as can be seen in Figure 5.5.

5.2.3. Experimental Apparatus

In the present study, a wide range of techniques was used to observe the wettability alteration of the quartz mineral at scales ranging from nanometer (nm) to millimeter (mm) to clarify the wettability alteration mechanism in the presence of chloride salts.

5.2.3.1. Drop-Shape Analysis Apparatus

In this work, a drop-shape analyser (Kruss DSA 100) apparatus was used for the investigation of wetting and adhesion behavior. The DSA100 is a high-quality instrument for measurement of both the equilibrium interfacial tension (IFT) of the decanoic acid-dodecane mixture /oil and brine as well as contact angles. In comparison to other existing methods, the DSA100 system used for the pendant drop case is accurate for IFT measurements down to 0.05 $mN \cdot m^{-1}$. In addition, the technique is fully automatic and completely free of the operator's subjectivity (Qi et al., 2013b; Lashkarbolooki et al., 2014b). The results help to provide a picture of the interface contact between oil/brine/quartz mineral. In this experiment, the measurement was done through a water/solid/gas system. Thus the syringe was filled with de-ionised water, and the sample was immersed in oil. The DSA instrument is composed of the following main parts: sample table, syringe piston actuator, light source, lens, and CCD camera as well as computer software that records, interprets and displays data accurately (see Figure 5.6a).

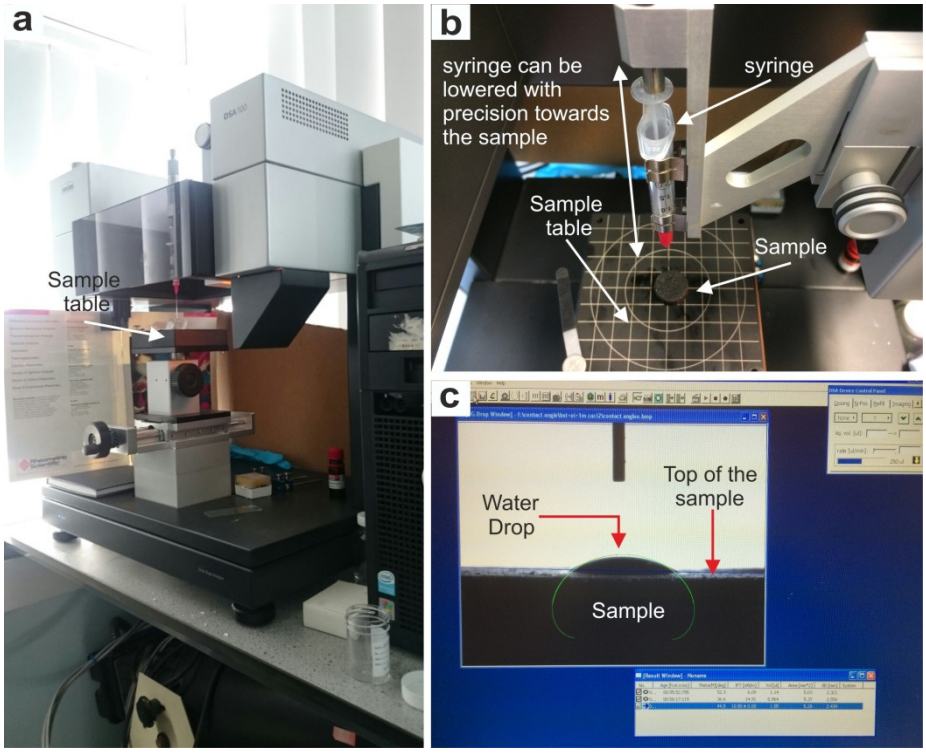

Figure 5.6: Components of drop shape anaylser instrument. a) Picture of the Kruss DSA100.b) Picture of the droplet dispensing syringe.c) Digital camerea feed visible within computer software.

In brief, for contact angle measurements, after the sample had been placed on the sample table (Figure 5.6b), the stage was adjusted to the required level for the digital camera to detect the flat surface of the sample as seen in Figure 5.6. Once the surface of the sample was positioned in optical clarity for the software, a water droplet was placed on the surface. The micro-syringe was lowered to accurately place a droplet of de-ionised water (5.00 ± 0.09 µl) onto the sample surface. Surprisingly, the literature does not provide a conclusive answer to the question as to the influence of the droplet volume V on contact angle θ. However, the shape of the drop is determined by the surface tensions involved and by gravity. Once a droplet had been put on the sample's surface, the silhouette of the droplet was viewed using a video camera, an image was taken of the water droplet, and subsequently the contact angles were evaluated (Figure 5.6c).

This process was repeated three times using different areas on the quartz surface. This method was used for all specimens to get a range of data to validate consistency and obtain an average. Also, through the application of computer image analysis and processing techniques, an accurate interfacial profile of the pendant water drop was obtained at different times. Therefore, along with each data point, error bars are depicted for better comparison between the various case.

5.2.3.2. Environmental Scanning Electron Microscopy Analysis

ESEM was used for performing contact angle measurements. An FEI/Philips XL30 ESEM equipped with a gaseous secondary electron detector (GSED) and a Peltier stage capable of operating at +/-20 ^{o}C from ambient temperature (maximum range -5 ^{o}C to +60 ^{o}C) was used. With the correct balance of temperature, pressure, and humidity, this is a system capable of condensing water onto a cooled surface. The prepared quartz crystal specimens were pre-cooled to approximately 5 ^{o}C in glass vials in a laboratory refrigerator. The pre-cooled samples were placed on a stainless steel stub, before being put on the Peltier stage in the ESEM chamber and held at a temperature of 5 ^{o}C, as can be seen in (Figure 5.7). For ease of viewing the contact angle of any condensed water, the stub had been placed at 45^{o,} and the Peltier stage was tilted to 30^{o}, giving the sample surface an overall viewing angle of 75^{o}.

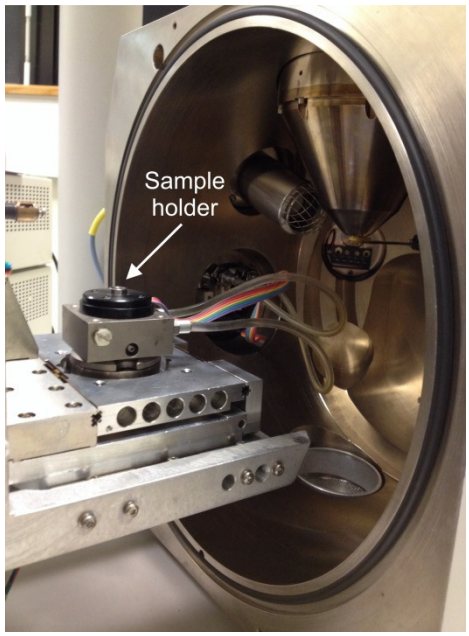

Figure 5.7: Peltier stage in side the ESEM chamber.

After closing the ESEM, the chamber was evacuated to 5.96 Torr and then flooded five times with water vapour from 5.96 Torr to 9.97 Torr, with the cycle terminating at 6 Torr./5.5 Torr. These conditions produced a suitable atmosphere for providing the water vapour needed for the experiment, as can be seen in Figure 5.8, (Buckman et al., 2000; Al-Shafei and Okasha, 2009; Polson et al., 2010), while also maintaining sample hydration, suppressing charge, and facilitating image amplification. After gaining an image of a suitable area of the sample, the pressure in the chamber was first reduced to 4.5 Torr, and

then increased incrementally until the direct condensation of water onto the sample surface was observed (alternatively, the pressure was increased incrementally from 5.5 Torr). For ease of interpretation and aesthetic reasons, the image was, if necessary, rotated. Micrographs were frequently taken at a magnification from which observations of droplet morphology and contact angle about the quartz substrate could be made. The pressure was increased until the condensed water droplets "grew" at an acceptable rate, and the experiment was terminated when the viewing surface was seen to be flooded with water.

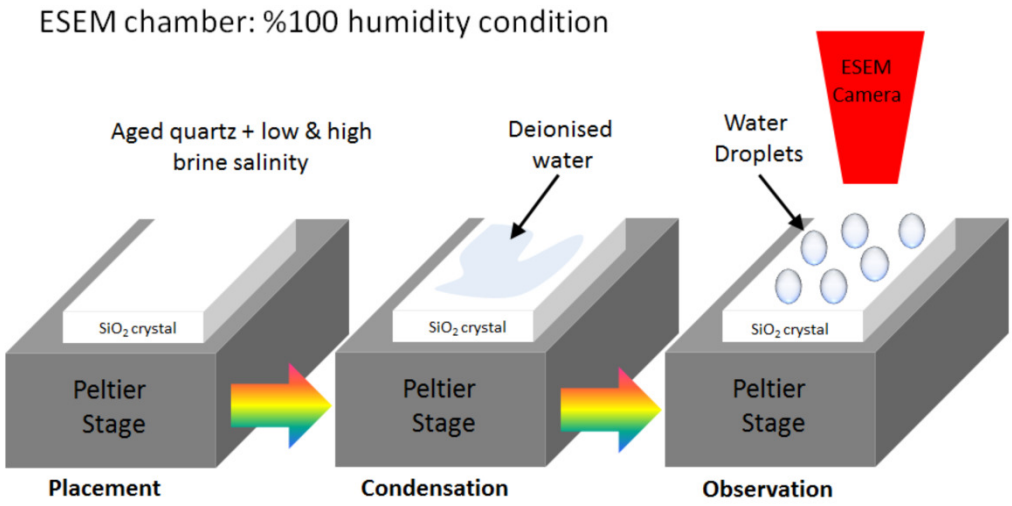

Figure 5.8: Schematic to show preparation and observation of the wetting state on a quartz substrate using low and high brine concentration. Brine is injected and placed on the substrate. By gradually increasing the humidity, water is precipitated and the contact angle between brine and substrate can be seen underneath.

The schematic diagram of the experimental setup for the contact angle method used to measure the wettability of quartz substrate is shown in Figure 5.8. The contact angle measurements were performed using the Drop analysis-LB software (ADSA), which uses a new method based on the Young-Laplace equation for measuring contact angles and surface tensions (Figure 5.9 a and b). This method was applied to measure the wettability state on an aged-quartz substrate (Stalder et al., 2010). The method is implemented as a Java plug-in for the ImageJ software (Stalder et al., 2010). The dynamic contact angle, which is the contact angle which occurs in the course of wetting (advancing angle) or de-wetting (receding angle) of a solid, are shown in Figure 5.9c. These were measured at different time intervals for all the brines. To test the ionic strength effect on the contact angles, the contact angle measurements were carried out at a constant temperature of 5 °C.

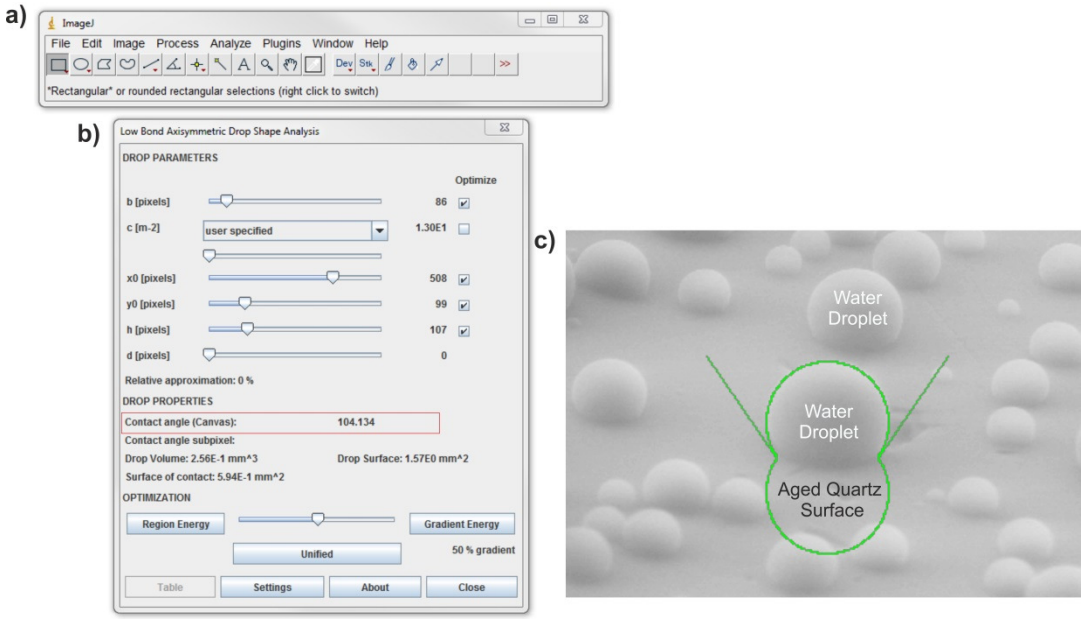

Figure 5.9: Approach for high precision contact angle measurement. a) ImageJ, a general purpose free image-processing package. b) Low-bond asymmetric drop shape analysis. c) A micrograph of the drop is recorded with the help of ESEM and transferred to the drop shape.

5.2.3.3 Atomic Force Microscopy Analysis

Atomic force microscopy measurements were performed using a Bruker Multimode AFM equipped with a Nanoscopic V controller. Two modes of operation were used, Peak Force (PF) and Peak Force Quantitative Nanomechanical (PFQNM). In this mode of operation the sample or probe is vibrated at low frequencies (0.5 KHz-2 KHz) with a sinusoidal function, effectively completing a force-distance curve in every cycle. Therefore, each cycle can be recorded and then analysed by the hardware/software, allowing the system to track the total force applied on the sample at every moment with high precision. Also, every approach/retract cycle can be analysed to obtain quantitative nanomechanical information, including adhesion. Scanassyst Fluid (Bruker) tips with a nominal spring constant of 0.7 nN were used. For these experiments, samples were pre-treated in the same way as mentioned earlier (See section 5.2.2). This procedure was repeated until all brine compositions were studied. Both flat and non-flat quartz samples were scanned. In addition to the adhesion measurements, quartz crystal samples were characterised by performing measurements in air using the Peak Force mode. Results from these measurements are shown in Figure 5.1 and show in detail the different roughnesses between the two samples studied. The non-flat crystal show polishing lines as well as dissolution features (product of their treatment with KOH), whereas the flat crystal, shows

an almost atomically flat termination perturbed by few features, which are probably the result of minor contamination.

5.2.3.3 Zeta-Potential

Zeta-potential reflects the potential difference between the 'shear' or 'slipping' plane and the bulk solution, as shown in Figure 2.10 and described in Chapter 2. Several authors have shown that the zeta-potential, which exists at the shear plane of any charged particle, has a major effect on surface properties (Jarrahian et al., 2012). It can be noted; wetting behavior studies benefit significantly from zeta-potential analysis as described in Chapter 2 and Chapter 3 because understanding the features of the electrical/ionic structure of mineral/brine interactions provides an important insight into wettability alteration due to ionic strength, oil type, and mineralogy.

Zeta potential was measured for both decanoic acid- dodecane/brine/quartz and crude oil/brine/quartz interfaces. Charges at interfaces are the main parameters that control the stability of the water film surrounding the quartz mineral, and hence the quartz wettability. A SurPass Electronic Analyser for solid surface analysis (Anton Paar) measured the electrophoretic mobility in a 0.1M of KCl suspension of quartz powder samples, and then the mobility was converted to ζ potential using the Smoluchowski equation (Luxbacher, 2014). All the measurements were conducted at 25 °C in the School of Science and Engineering at Teesside University. Before running ζ potential measurements, the aged quartz powder was washed with two different brines to provide a decanoic acid- dodecane /brine and crude oil/brine interface. NaCl and $CaCl_2$ solutions of various ionic strengths (0.001M, 0.01M and 1.0M) were used as the brines. The brine pH was adjusted at 6.5 using hydrochloric acid (HCl) for low pH and a NaOH buffer for high pH, to avoid the effect of pH on ζ potential. To perform the measurements, 500 mg of the prepared quartz powder sample was placed into a glass cylinder to run the ζ potential measurements (Figure 5.10). The particle size of the quartz powder was bigger than 500 µm to ensure that the quartz particles would not be washed out during flooding (see Figure 5.2b). To obtain a reliable measurement, pressure was checked after the filling and rinsing processes of the electrolyte hoses and measuring cell, and before starting the actual measurement.This can be examined through the pressure ramps (streaming potential versus pressure) for both flow directions to make sure that the system is filled without air and to check the flow performance (Luxbacher, 2014). Four runs were conducted for each sample to reduce

errors, and the average ζ potential was taken at pH 6.5. Also, along with each data point, error bars are depicted for better comparison between the different cases.

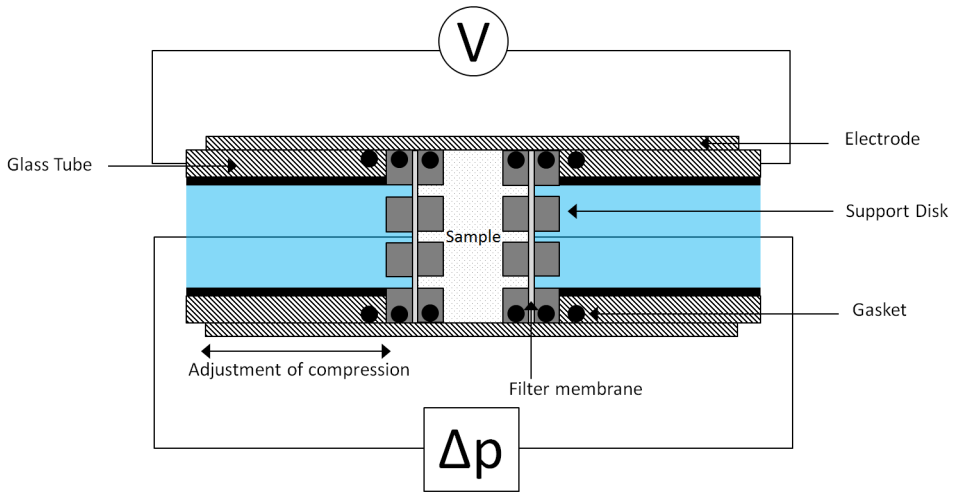

Figure 5.10: Schematic of powder and granular samples mounted in cylindrical cell in Anton-Paar Zeta analyser, extracted from (Luxbacher,2014).

5.3. Results and Discussion

In the following section, the results of contact angle observations at the micro and macro scale and ζ-potential measurements of quartz mineral are presented and discussed in the presence of low and high concentration NaCl, and $CaCl_2$ solution. The aim of this set of experiments is to examine the wettability states of quartz surfaces in the presence of different ionic strength, which would clarify the wettability alteration in the most of the sandstone reservoirs during low salinity EOR.

5.3.1. Surface Morphology and Quantitative Analysis of Quartz Substrates

In this section, the effect of roughness on the contact angle on an ideal quartz crystal are observed and discussed at a microscopic level. AFM images in Figure 5.1a and b show the morphology before any aging of the flat and non-flat quartz surfaces over an area of 10µm x 10µm. It can be observed from the image that the clean non-flat quartz substrate has etch pits. Representative ESEM micrographs of all experiments performed with both types of quartz surfaces (aged in decanoic acid -dodecane) are shown in Figure 5.11a/c. In total 4 different brines were used, NaCl (0.01M and 1.0M) and $CaCl_2$ (0.01M and 1.0M). Therefore, after condensation experiments in a Peltier stage ESEM, an average contact angle measurements across all experiments for both types of surfaces are also shown in Figure 5.11. Observations show that the measured contact angles do not change significantly with a change in the cation identity (as long as the concentration is

equivalent), but the contact angles do change once the concentration of the brine changes. For both, NaCl salt and $CaCl_2$ salt it was observed that an increase in the brine concentration leads to an increase in the measured contact angle. For NaCl solutions, the difference is approximately ~37°, while for $CaCl_2$ solutions is ~43 °. For comparison, the contact angle of all candidate droplets is listed in Appendix B.1.The average contact angle displayed in Figure 5.11 was calculated from these values.

To check the sole effects of roughness, the non-flat quartz crystals aged (in decanoic acid-dodecane) were employed for comparison. Data measured from the ESEM micrographs (see Figure 5.11c/d) show that measured contact angles (when compared to those measured on flat quartz) were of similar magnitude when measured on NaCl salt, but slightly larger when measured in $CaCl_2$ salt.The figure also shows differences stemming from the type of salt employed. In the case of $CaCl_2$ salt, the wettability of non-flat quartz crystal aged in decanoic acid-dodecane has been altered toward mixed-wet, as can be seen in Figure 5.11c. This significant change in wettability behavior occurs due to the surface tension of the quartz surface being changed more by using 0.01 M NaCl solution compared to $CaCl_2$ solution, leading to a reduced contact angle in the former case.

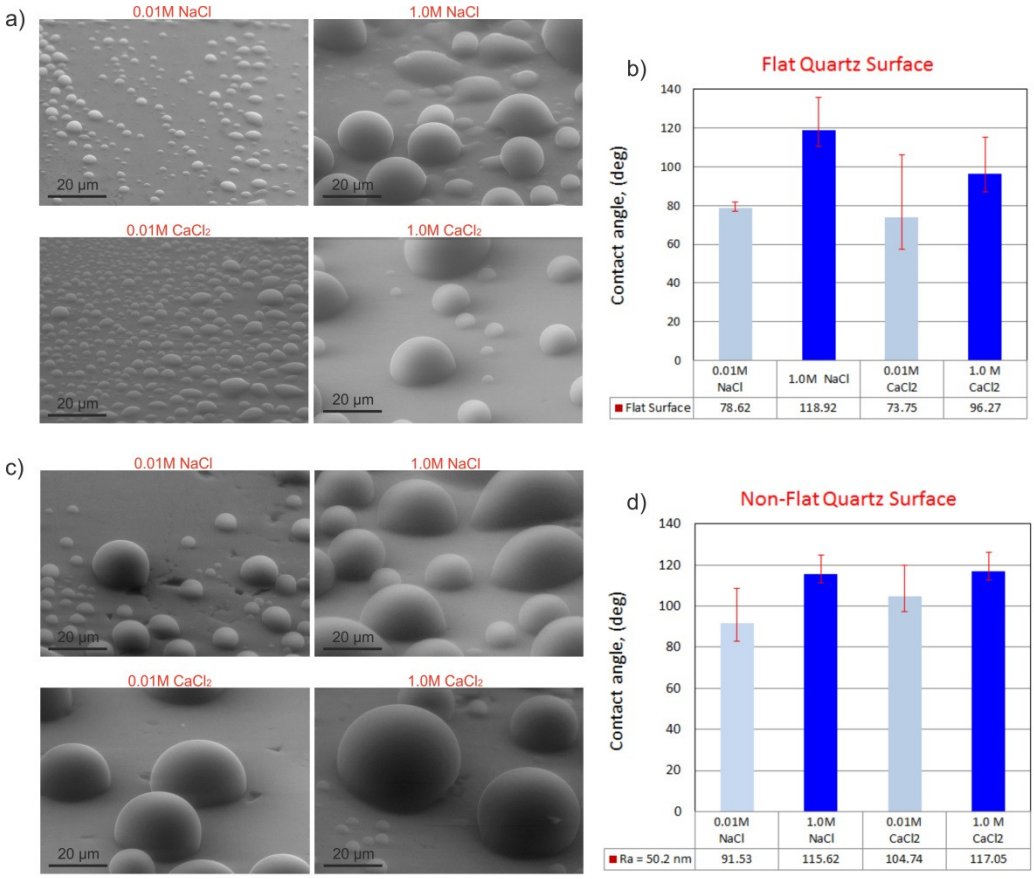

Figure 5.11: Effect of brines on dynamic contact angles on aged quartz surface at 5°Ca) ESEM photomicrographs of flat quartz aged in decanoic acid-dodecane exposed. b) Contact angle measurements on a flat quartz across the different brines utilised, c) ESEM photomicrographs of non-flat quartz aged in decanoic acid-dodecane.d) Contact angle measurements on a non-flat quartz across the different brines utilised. Error bars indicate standard deviations of several droplets.

Results indicate that the contact angles of water droplets increase with the mean roughness of the quartz crystal surface. So, as the surface roughness increases, so too does the solid-liquid contact area, leading to a large contact angle (Wenzel,1936). Although in this study different roughness of the surfaces were used, as obvious from AFM image in Figure 5.1 and Figure 5.11, which shows the wettability behavior is more related to brine concentration since the same trends of wettability with concentration were observed in the flat sample. Overall, it is clear that examination of quartz crystal surfaces aged in decanoic acid-dodecane showed the surface is sensitive to the roughness as well as brine salinities.

5.3.2. Wettability Examination at Multi-Scales

The effect of brine concentration and its composition on the wettability of non-flat quartz crystal surfaces has been determined by measuring the contact angles and adhesion force using AFM. Results of this experiment are discussed in the following subsections. The initial wettability of the representative condensate on quartz surfaces as measured by

drop shape analysis technique (macroscopic scale) is discussed in the first subsection. Additional ESEM results (microscopic scale) in the presence and absence of decanoic acid - dodecane and/or brine, on non-flat quartz surfaces, are given in the second subsection. The third subsection discusses AFM techniques (nanoscopic scale) which describe the effect of high and low salinity brine (0.01M and 1.0M of NaCl or $CaCl_2$) on wettability alteration.

5.3.2.1. Drop-Shape/ Contact Angle Measurements

Based on the previous investigation, it can be said that the non-flat quartz plate is relatively a good candidate as a model for sandstone rocks in wettability screening. In the results presented in this section, the water droplets deposited over a non-flat quartz surface aged in either, decanoic acid-dodecane or crude oil after being washed with different brines are examined. The optical images started recording as soon as the water droplet began to form on the non-flat quartz surface. The contact angle was measured after 30 s to ensure that the droplet was stabilised on the non-flat quartz surface. Images of water droplets on non-flat quartz crystal surfaces in different ionic strengths at room temperature and pressure are shown in Figures 5.12 and 5.13.

5.3.2.1.1. Macroscopic Observation of Quartz Aged in Decanoic Acid-Dodecane

To investigate the role of polar compounds on wettability behavior on the non-flat quartz crystal surfaces, the decanoic acid- dodecane model oil compounds were used. The effect of of the cation type was investigated by running different experiments by use of the decanoic acid in dodecane and two different brines on quartz crystals. The brine tested were NaCl salt (0.001M, 0.01M and 1M NaCl) comparing it to $CaCl_2$ at the same concentration (Table 5.2). The comparison is significant to observe the impact of cation type on quartz crystal. Pictures of water droplets on the surface of the quartz crystals, in different brine concentration at room temperature and pressure, are shown in Figure 5.12. The figures show a comparison between the contact angles of a water droplet containing NaCl and $CaCl_2$ brines of different ionic concentration in the presence of decanoic acid-dodecane. Each measured data point in the current investigation is the average of at least three independent measurements.

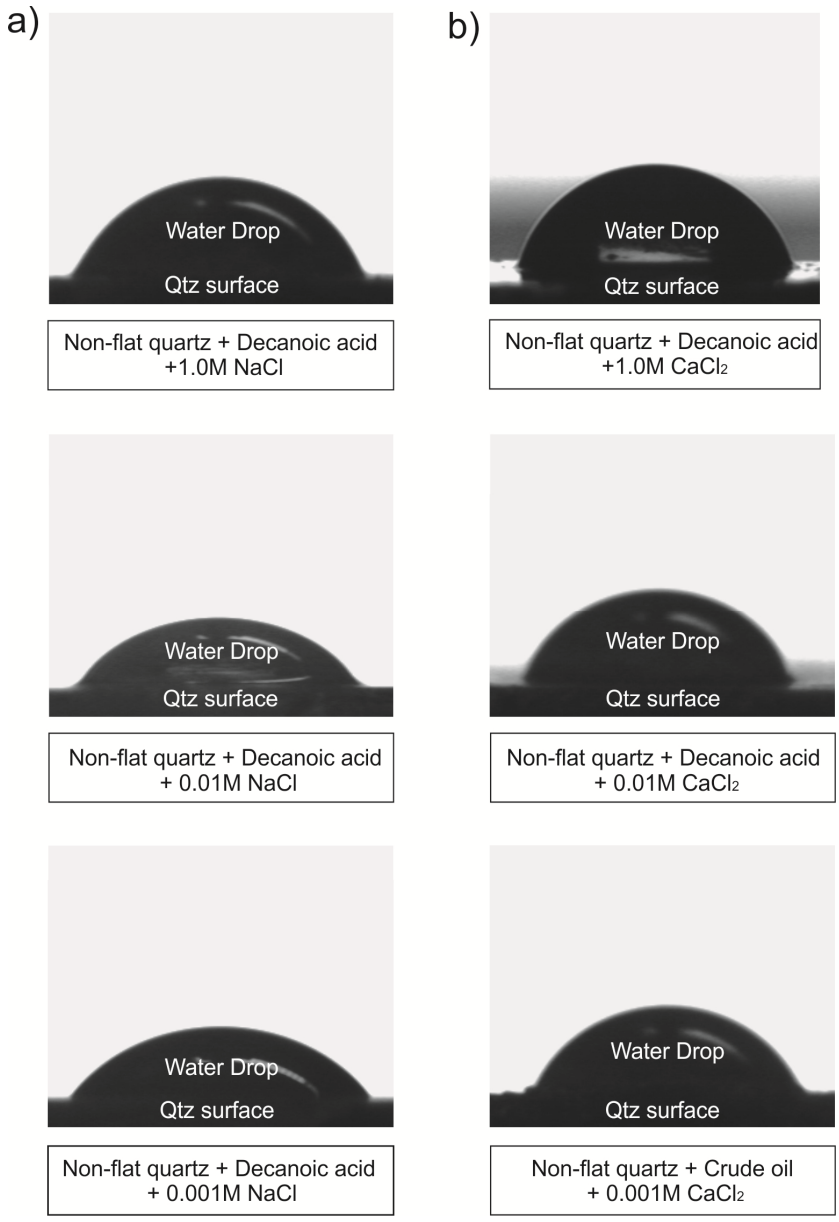

Figure 5.12: Contact angle images of brine droplets on non-flat quartz surface at room tempreature and pressure. a) Images recorded with different concentrations of NaCl . b) Images of $CaCl_2$ dropletes with different concentration.These images were scaled up from the real size of 2.5±0.5 mm 2.5±0.5 mm.

The average contact angles were measured as being 84.7°, 65.5°, and 53.6° for NaCl at 1.0M, 0.01M and 0.001M, respectively (Table 5.5).This shows that as the Na^+ concentration in the brine decreases, the contact angle value decrease as well (Figure 5.13). Therefore, the lower the Na^+ concentration, the more water wet the quartz surface becomes. In the case of $CaCl_2$ brines, the average of the three readings obtained from each were 86.1°, 73 ° and 71.9° for 1.0M, 0.01M and 0.001M, respectively (Table 5.5).

Table 5.5: Average contact angle of water droplets on non-falt quartz crystal aged in the decanoic acid- dodecane of NaClsolution and $CaCl_2$ solution along with their uncertainties at different concentrations.

Brines mol.kg-1	NaCl	$CaCl_2$
	Decanoic acid- dodecane	
	Theta (M) [deg]	Theta (M) [deg]
0.001	53.67 ± 0.1	71.91 ± 0.2
0.01	65.52 ± 0.1	73.00 ± 0.1
1	84.71 ± 0.1	86.17 ± 0.1

Therefore, Ca^{2+} shows a small increase in contact angle with increasing concentration (Figure 5.13), i.e., only has a limited effect on modifying the wetting state of quartz surfaces. A close look at Figure 5.13 shows that the contact angle decreases fast for both NaCl and $CaCl_2$ when the concentration decreases from 1.0M to 0.1 M, then this trend is interrupted with further increase in concentration for $CaCl_2$, but not for NaCl.

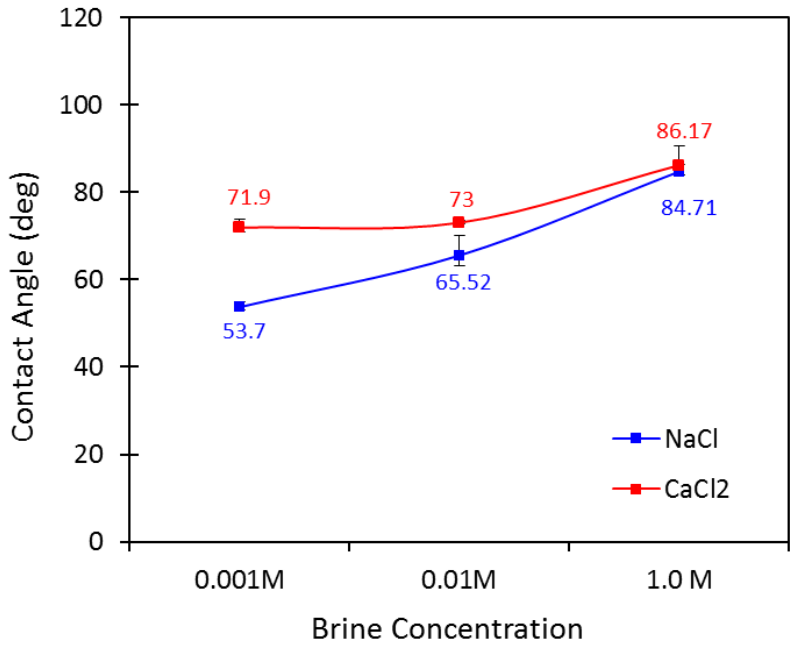

Figure 5.13: The avergae contatc angle is plotted versus the ion concentration at decanoic acid-dodecane shows the wetting states at non-flat quartz crystal at room tempreature and pressure. Error bars indicate standard deviations of several droplets.

The behaviour observed in these experiments agrees well with expectations from previous low-salinity investigations on rock and specific mineral surfaces (Hassenkam et al., 2014, 2016, Mugele et al., 2014, 2016), i.e. that a low concentration NaCl solution will induce a more water-wet state on the quartz surface. In our case, we can hipothesize that

treatment with low-salinity solutions will increase the desorption of oil molecules by breaking cation bridges and other bonds that the organic molecules could have formed on the quartz surfaces. $CaCl_2$ will have a smaller effect in reducing the contact angle as some bonds will be able to reform and therefore not affect the overall desorption mechanism, leaving behind a more oil-wet surface when compared to treatment with NaCl of the same concentration. The low salinity effect for NaCl may be explained by the fact that as the concentration is reduced the quartz surface will have a larger negative surface (larger surface charge density), as less Na^+ will be available to neutralize the negatively charged quartz surface. This will reduce the possibilities for oil molecules to reattach to the surface, leaving behind a water-wet surface.

Understanding wettability behaviors, in general, is one of the challenging difficulties in developing low salinity EOR technologies due to its role in all processes involved in three-phase interfacial phenomena. Two fundamental difficulties can be associated with contact angle behavior. The first is related to the type of solid surface and its surface roughness (see section 5.3.1), whereas the second is associated with the mutual interactions of immiscible liquids in contact with the solid surface. The wettability alteration of a quartz surface by adsorption of decanoic acid- dodecane (oil model compounds) leads to understanding the behavior of decanoic acid- dodecane/brine/quartz interactions under a certain condition. Typically, the quartz surface may not show the same wettability behavior as this will depend on oil composition and brine salinity of the system. In order to see if those trends were repeated (especially since they show a low salinity effect). in the next part of this study, crude oil was used, as it also may contribute to understanding the complexity of reservoir wettability.

5.3.2.1.2. Macroscopic Observation of Quartz Aged in Crude Oil

Crude oil is still dominated by polar organic compounds and thus might be expected to behave similarly to decanoic acid- dodecane; however, the role of the brines is examined to alter the behavior of oil/brine/quartz interactions. The effect of the cation type was examined by running different experiments by use of the same crude oil and two different brines on quartz crystals. The brine tested were NaCl salt (0.001M, 0.01M and 1M NaCl) comparing it to $CaCl_2$ at the same concentration (Table 5.2).This will allow to observe the impact of cation type on the quartz crystal. The investigation has been made on non-flat quartz aged in crude oil to observe the wettability alteration in the presence of asphaltene. Researchers believed that the adsorption of asphaltene on the reservoir rock may be a

major reason for wettability alteration (Taqvi et al., 2016). Pictures of water droplets on the surface of the non-flat quartz crystal, in different brine concentration at room temperature and pressure, are shown in Figure 5.14. Figure 5.14 shows the contact angle behavior in the presence of various concentration of NaCl and $CaCl_2$ on the quartz surface for brine droplets. Measured contact angles are reported in Table 5.6 and also listed in Appendix B.2.

Figure 5.14: Contact angle images of water droplet on non-flat quartz surface at room tempreature and pressure. a) Non-flat quartz aged in crude oil during exposed with various NaCl concentrations. b) Non-flat quartz aged in crude oil exposed with various $CaCl_2$ concentrations. These images were scaled up from the real size of 2.5±0.5 mm 2.5±0.5 mm.

For non-flat quartz crystal aged in crude oil, Figure 5.14a shows the contact angle of water droplets after treatment with low and high concentration of NaCl solution. The average contact angles were measured as being 86.4°, 72.6°, and 51.4° for NaCl at 1.0M, 0.01M and 0.001M, respectively (Table 5.6). It can be seen that the result indicates, again, that as the concentration of NaCl is decreased the measured contact angle value also goes down.Therefore, the lower the Na^+ concentration, the more water wet the quartz surface become. This trend is shown graphically in Figure 5.15. The figure shows that with a decrease in monovalent (Na^+), contact angle decreases.

Table 5.6: Average contact angle of water droplets on non-flat quartz aged in crude oil and treated with NaCl and $CaCl_2$ along with their uncertainties at different concentrations.

Brines mol.kg-1	**NaCl**	**$CaCl_2$**
	Crude oil	
	Theta (M) [deg]	**Theta (M) [deg]**
0.001	51.46 ± 0.1	78.75 ± 0.0
0.01	72.68 ± 0.1	81.55 ± 0.2
1	86.47 ± 0.2	84.08 ± 0.1

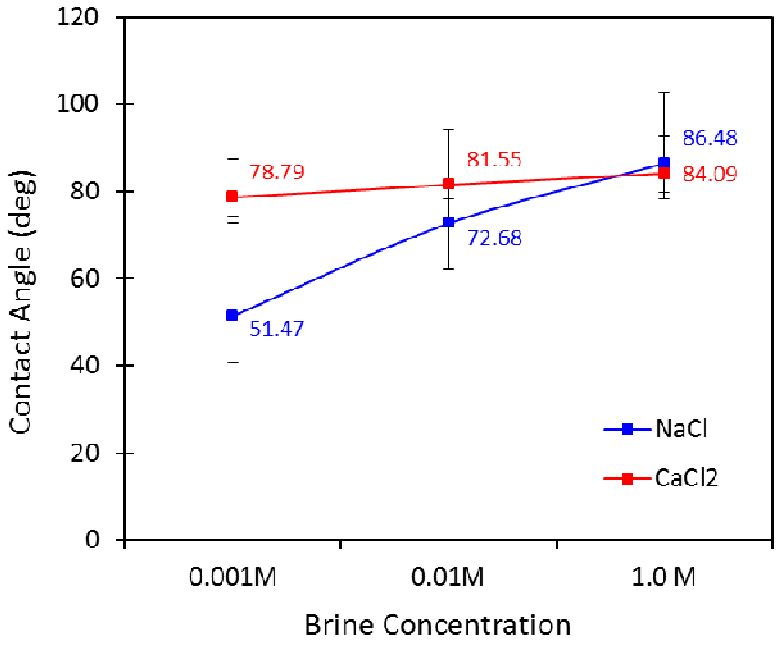

Figure 5.15: The avergae contact angle is plotted versus the ion concentration shows the wetting states at crude oil aged non-flat quartz crystal at room tempreature and pressure. Error bars indicate standard deviations of several droplets.

It can be noted, the presence of salts in the aqueous phase has a strong ability to increase the accumulation of the surface-active species available in the crude oil, at the crude oil-aqueous phase interface, and thereby reduce the tension and contact angle

(Standal et al., 1999). The effect of NaCl concentration on contact angle in the quartz surface has been studied by Bera et al. (2012), in a study using crude oil (TAN = 0.04 mg KOH/g), to alter the wettability of quartz surfaces toward the water-wet state. Bera et al. (2012) stated that acid had no significant effect on the wetting process compare with brine salinity and confirmed contact angles can be noticeably increased with the increases in NaCl concentration of 6-8 wt %. In addition, it is proposed that as salinity concentration of NaCl rises, then repulsive electrostatic double layer forces and repulsive hydration forces increase to avoid the spreading of oil on quartz surface (Bera et al., 2012).

In the case of $CaCl_2$ brines, Figure 5.14b shows the optical images of the droplets with different Ca^{2+} concentration.The average contact angle was measured as being 84°, 81.5° and 78.7°at 1.0M, 0.01M and 0.001M, respectively (Table 5.6). Figure 5.15 shows a plot of the contact angle data, and it can be seen that the Ca^{2+} concentration has no significant effect on altering the wetting state of the quartz surface (i,e., it has a low ability to remove the crude oil from the quartz surface). At all Ca^{2+} concentrations, the wetting state of the aged quartz surface is relatively mixed-wet. When comparing both sets of data, the much larger effect of Na^{+} on altering the quartz wettability state stands out. The higher contact angle measured on the surface treated with divalent ion solutions (at low and medium concentrations) indicates a different interaction between the oil molecules, the divalent ion, and the quartz surface. Qi et al. (2013a), for example, suggest that it is not easy for Ca^{2+} ions to bond with asphaltene molecules since the asphaltene molecules can interact with hydroxyls on the quartz surface by polar interaction.This means asphaltene molecules in the crude oil cannot be absorbed on the quartz surface with divalent cations ion binding. In general, observations reveal that the properties of crude oil have a different effect on the wettability alteration of non-flat quartz surface compared with decanoic acid - dodecane, although the crude oil is less acidic than decanoic acid- dodecane, as can be seen in Figure 5.3. Taking into account all of these different results due to effects of brine concentration, it seems interesting to find the effect of brine concentration on wettability alteration. To examine the repeatability of contact angle experiments on a smaller length scale, some of the experiment were repeated using ESEM and are discussed in more detailed in the next subsection.

5.3.2.2. Environmental Scanning Electron Microscopy/ Contact Angle Measurements

An ESEM technique was used to image the condensation process of polar compound in both a 2 component model oil and crude oil on a non-flat quartz surface. The results of this microscopic observation were again divided into two sub-sections to examine the wettability behavior in non-flat quartz crystal aged in the model oil (decanoic acid-dodecane) and crude oil, respectively.

5.3.2.2.1 Microscopic Observation of Aged Quartz in Decanoic Acid-Dodecane

The ESEM was used to determine the initial wettability of a non-flat quartz crystal. As a starting point (to obtain a baseline for comparison purposes) a sequence of ESEM experiments were carried out on untreated as well as model oil-aged quartz crystals. In the first test of first series experiments, aged non-flat quartz crystals were introduced without pretreatment into the ESEM chamber (Figure 5.16a). The similar sample was pretreated in decanoic acid-dodecane and introduced into the ESEM chamber, as shown in Figure 5.16b. For the rest of experiments as shown in (Figure 6.15c, d, e, and f), non-flat quartz crystals were pretreated in decanoic acid-dodecane and "washed" with different concentrations of NaCl salt, and $CaCl_2$ salt.

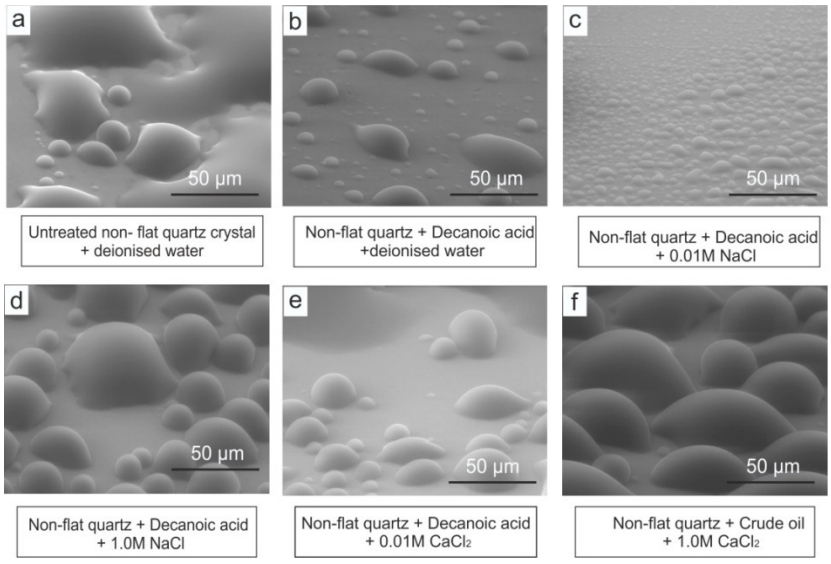

Figure 5.16: ESEM micrograph of non-flat quartz surfaces show the variation of the contact angle; a) untreated sample; The treated smaple in decanoic acid-dodecane (b). (c,d) non-flat quartz crystals were pretreated in decanoic acid-dodecane and "washed" with different 0.01M and 1.0M of NaCl salt, respectively. (d, e) non-flat quartz crystals were pretreated in decanoic acid-dodecane and "washed" with different concentration, 0.01M and 1.0M of $CaCl_2$ salt, respectively.

ESEM images were taken at 1200 to 1300 s after the start of the condensation experiments. Moreover, for non-flat quartz crystals, which were pretreated with decanoic acid-dodecane and brines, it should be noted here that the substrates show the water-wet state as displayed in Figure 5.16. Average measured contact angles are taken over several water droplets (Appendix B.2) and then plotted versus the different ion concentration of NaCl salt and $CaCl_2$ salt (see Figure 5.17) to show the reduction of the contact angle with chloride salt concentration. For reference, the average contact angle for an all candidate droplets is listed in Appendix B.2.The width of the calculated error bars (across several water droplets) proves the effect of roughnesses and heterogeneity of wettability behavior on the non-flat quartz crystal surface.

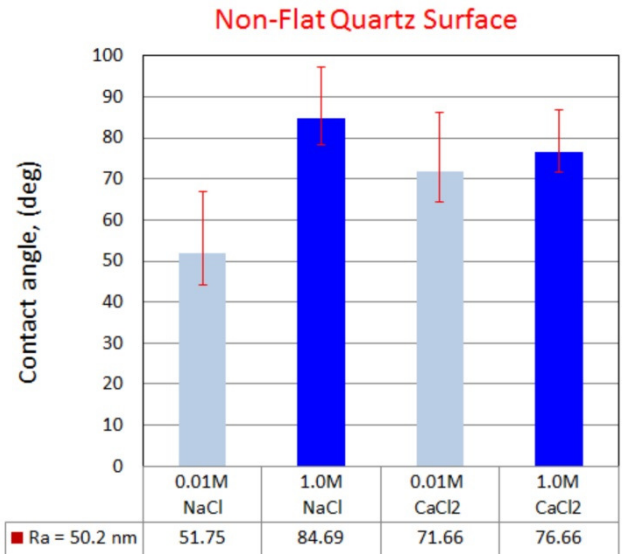

Figure 5.17: ESEM micrograph of non-flat quartz surfaces show the variation of the contact angle after injection with different brine concentrations. Error bars indicate standard deviations of several droplets.

It can be seen that the contact angles of water droplets in both brine salinity (Figure 5.17) is less than 90° (i.e. a water-wet state). More importantly, on the decanoic acid-dodecane treated samples, the contact angle at NaCl of 0.01M concentration is much lower. Therefore, it should be noted; these samples were only pretreated in decanoic acid-dodecane (not exposed to FW) before being introduced into the ESEM chamber, so here the FW has not affected. However, for those surfaces treated in FW before decanoic acid-dodecane aging, the contact angles are higher (see Figure 5.11b), indicating that FW may enhance the adsorption of decanoic acid-dodecane onto the quartz surface. Several researchers reported the effects of the water film on the quartz surface. Akhlaq et al. (1996)

and Qi et al. (2013) founded that the chemical composition of the adsorbed oil compounds be influenced by the presence of the water film on the sand and quartz surface.

In the next series of experiments, the effect of NaCl and $CaCl_2$ concentration on the measured contact angle was examined on non-flat aged quartz substrates in decanoic acid-dodecane. During contact angle measurements, water drops tend to spread on the quartz surfaces with time (as absorption of vapour alters the properties of the surface in the vicinity of the drop) and the volume of the drop may change due to evaporation or absorption of moisture. In this set of experiments, the variation of the contact angle with time was measured for the two types of brine composition at low and high concentrations.

For this purpose, a sequence of ESEM micrographs was taken off the non-flat aged quartz crystal to measure dynamic contact angles in the decanoic acid-dodecane/brine system at 5 °C and 6.8 Torr (ESEM /Peltier stage). From Figures 5.18 and 5.19, it can be seen that for NaCl and $CaCl_2$ brines on aged quartz crystal the wettability behaviors are different.Figure 5.18 shows a series of ESEM images taken as the experimental time progressed for the experiments performed with the various ionic strength of NaCl (0.01M and 1M). Figure.5.18a showed the morphology of droplets changing as a function of time up to a point when all droplets had collapsed at 1294 s after the tests were started. The ESEM micrographs collected during *in situ* experiments in Figure 5.18a showed that the average measured contact angle in the presence of 0.01M NaCl is $\theta = 80^{o}$ at 1090 s, which noticeably indicates intermediate wetting behavior. Two behaviors coexist in this sample: one showing trapped water droplets surrounded by oil until 1100 s, and two, condensed water spreading on the surface at 1294 s. However, when 1.0M of NaCl was introduced to the similar non-flat quartz under the same conditions, the morphology and contact angle of the droplets were stable and kept the same shape and an angle between 80° to 100° at 1300 s, as shown in (Figure 5.18b).

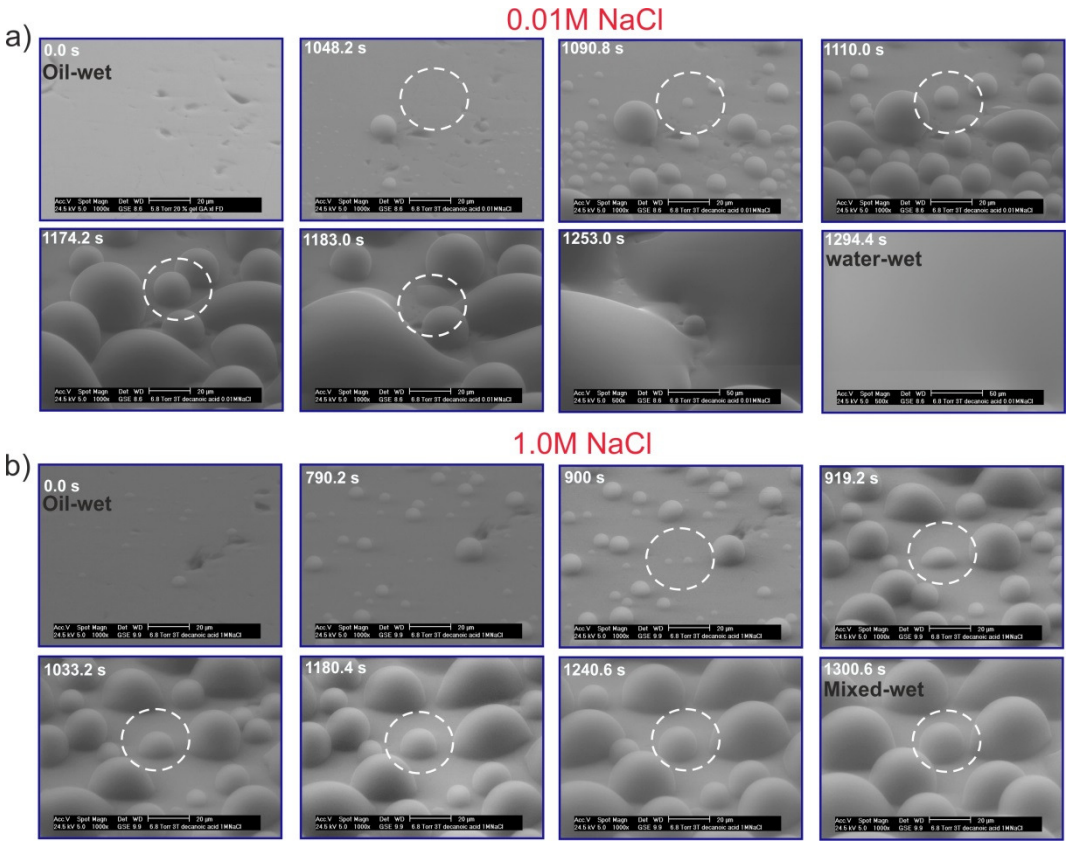

Figure 5.18: Micrographs show the variation of the contact angle with time after injection with low and high brine concentrations. a) after a certain time, the behavior of contact angle developed into a sheet-like cover on non-flat quartz aged in decanoic acid-dodecane when water began to condensate on the surface of the sample inside the ESEM chamber at 6.8 Torr. b) Condensed water appeared on the form of droplets in contact with aged sample as mentioned above with contact angle of θ =100.0° at 6.8 Torr.

The ESEM micrographs collected during *in situ* experiments in Figure 5.19a showed that the average calculated contact angle in the presences of 0.01M $CaCl_2$ is $\theta = 98^{o}$, which indicates intermediate wetting character. Notably, two different behaviors coexist in this sample: first showing trapped water droplets surrounded by oil until 1707 s, and the second showing condensed water developing into a sheet-like cover at 1707 s on the aged non-flat quartz surface when water began to condense on the surface of the aged quartz crystal inside the ESEM chamber at 7.1 Torr. The same experiment was repeated using 1.0M of $CaCl_2$ and the resulting ESEM micrograph (Figure 5.19b) showed the morphology and contact angle of the droplets were constantly stable and kept the same shape and an angle between 95° to 135° at 2652 sec to 3289 s.

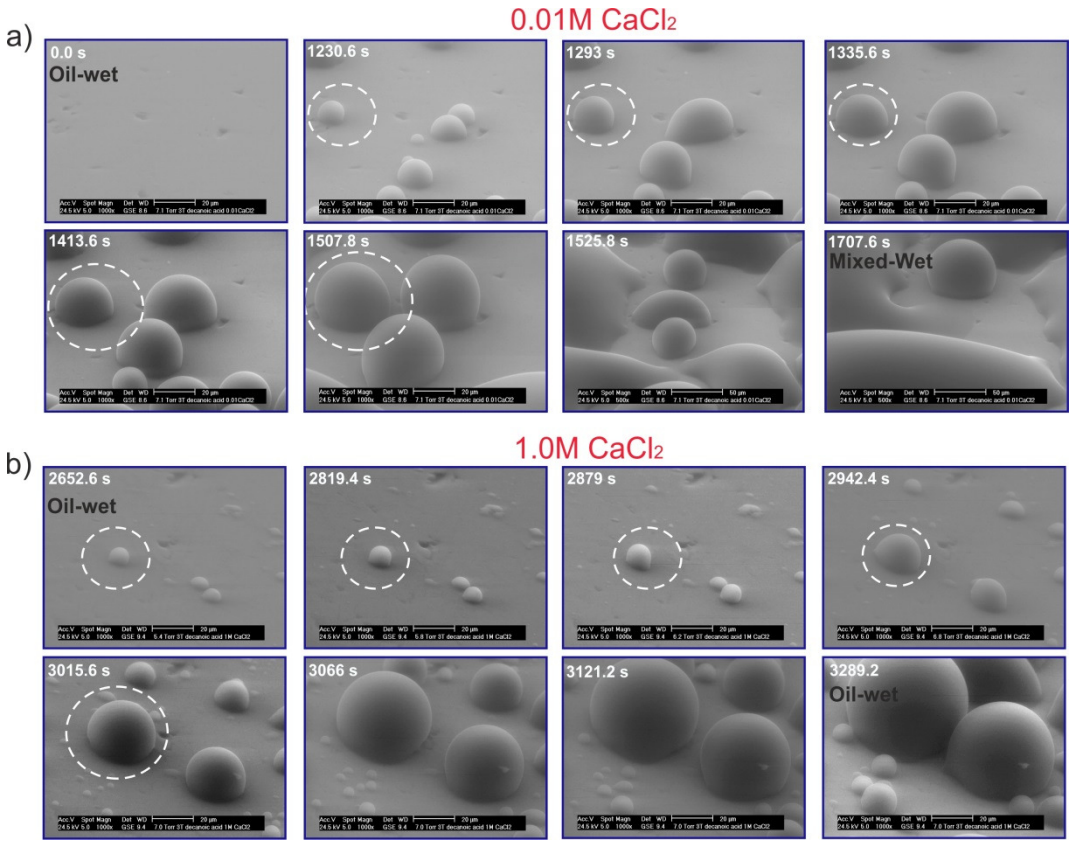

Figure 5.19: Micrographs show the variation of the contact angle with time after injection with low and high brine concentrations. a) Condensed water appeared on the form of droplets in contact with the surface of the aged crystal sample inside the ESEM chamber at a contact angle of =98.0° at 7.1 Torr. b) Photo micrographs showing condensed water at a contact angle of =132.0° at 6.8 Torr.

The measured dynamic contact angles are plotted against contact time in Figure 5.20 for both brine. Figure show a comparison between the dynamic contact angles of water droplets under the same conditions with a low and high concentration of NaCl and $CaCl_2$, versus time.

In low salinity concentration (0.01M) NaCl salt, the morphology of all water droplets changed as a function of time up to a point when the water droplets collapsed onto the quartz surface (water-wet). The average contact angles were 80°, as shown in (Figure 5.20a). The result indicates that low concentration of NaCl salt decreased the contact angle of water droplets; while high-salinity concentration (1.0 M) of NaCl salt shows high contact angles consistently throughout the duration of the whole experiment, this said, small shifts in the contact angle, between 80° to 90° were also observed (see Figure 5.20a). For those droplets formed on the quartz surface treated with 0.01M of $CaCl_2$ solution, the contact angles are is $\theta = 98^{o}$ (Figure 5.20b) and higher than the quartz surface treated with 0.01M NaCl salt, indicating that the 0.01M $CaCl_2$ salt treatment prevents the adsorption of

decanoic acid in dodecane compare with 0.01M NaCl salt. The morphology of droplets were consistently stable in 1.0M of $CaCl_2$ salt, and the contact angles were above 100°, as can be seen in Figure 5.20b.

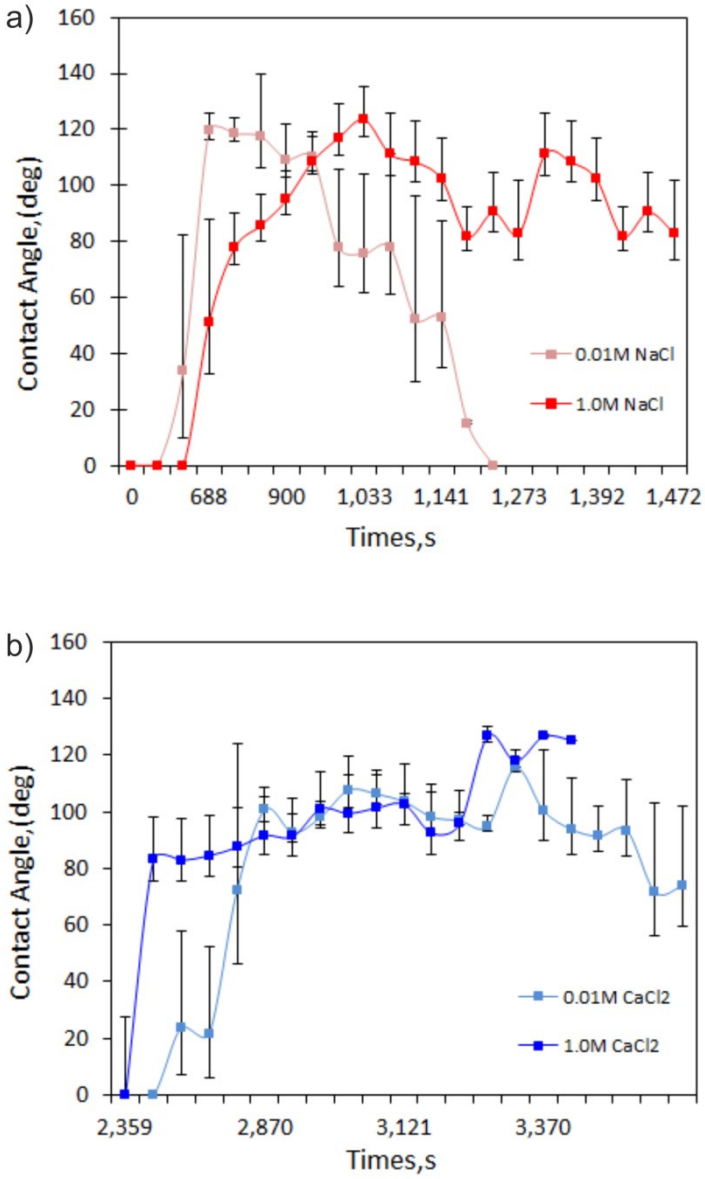

Figure 5.20: The average of dynamic contact angles plotted versus time for condensate on non-flat quartz aged in decanaoic acid-dodecane after each brine at 5°C. a) 0.01M and 1.0M of NaCl. b) 0.01M and 1.0M of $CaCl_2$. Each measured data point in the current investigation is the average of at least three independent droplets measurements. In addition, along with each data point, error bars are depicted for better comparison between the different cases. The width of the calculated error bars (across several water droplets) proves the effect of roughnesses and heterogeneity of wettability behavior on the non-flat quartz crystal surface.

For all of the brine concentrations, contact angles increase rapidly from ~10° to ~100°, and then become relatively stable, except for the experiment performed with 0.01 NaCl where contact angle decreases due to the coalescence of droplets into a brine film.In

general, observations show that for water droplets at 1.0M NaCl and $CaCl_2$, the contact angles are stable with time and kept the same relative shape. An experimental study has previously indicated a high concentration of salt often causes instability of water film over sand packs due to strong attractive forces (Saraji et al., 2013). This implies that the water film in the 1.0M NaCl and $CaCl_2$ solution was unstable due to strong attractive forces between decanoic acid- dodecane/brine and quartz/brine interfaces in this decanoic acid-dodecane /brine/quartz case, which allowed higher adhesion forces on quartz (Saraji et al., 2013). At the same time, the shifting in the angle of water droplets of 80° shown in Figure 5.20 demonstrates that the condensed water cannot attach to the quartz surface and therefore this system shows a strongly oil-wet nature at 5 °C and 6.8 Torr.

Results obtained by the pendant drop shape techniques appear to agree with the ESEM techniques observations. In general, the contact angle of water droplets on non-flat quartz surfaces aged in decanoic acid-dodecane have lower contact angles on similar quartz surface compared with the ESEM results in high and low salinity brine (0.01M and 1.0M of NaCl or $CaCl_2$). This change of a water droplet on non-flat quartz surface aged in decanoic acid/dodecane could be the effect of temperature and pressure (ESEM is not under high vacuum but is still under vacuum) on contact angle. It should be noted; the contact angles were measured though pendant drop shape at room temperature (27 °C). In contrast, the ESEM was operated at 5 °C in order to be able to examine the wettability behavior on the quartz crystal. This means that with an increase in temperature the contact angle of water droplets gradually decreases on the non-flat aged quartz surface.

It is clear temperature influences the oil (crude oil, decanoic acid- dodecane model oil) properties. Based on research by Bera et al. (2012), the interfacial interaction between decanoic acid- dodecane and the solution is also affected by temperature. As confirmed by Shedid and Ghannam, (2004) and Bera et al. (2012) the reduction in contact angle may also be attributed to the decrease in oil viscosity with the increase in temperature. The results obtained indicate that the decrease in contact angle of water droplets in the macroscopic investigation may also be attributed to the decrease in decanoic acid-dodecane viscosity with the increase in temperature. In general, Equation 2.6 shows that contact angle is related to the oil/liquid/solid interfacial tension (Wenzel, 1936). As temperature influences the density of decanoic acid- dodecane, interfacial tension between decanoic acid-dodecane/brines will also be affected by temperature and contact angle of droplets will also be changed.

5.3.2.2.2. Validation of Microscopic Observation

To examine the repeatability of the wettability behaviors obtained from the ESEM observations, two of the experiments were repeated on non-flat quartz crystal under the same conditions, 0.01M NaCl and 0.01M $CaCl_2$. For non-flat quartz aged in decanoic acid-dodecane treated in 0.01M of NaCl and 0.01M $CaCl_2$ solutions (Figure 5.21), no significant changes were observed of morphology and contact angle of water droplets in low concentration brines compared with the initial experiments (see Figure 5.18a and Figure 5.19a). Then, the contact angle was measured.

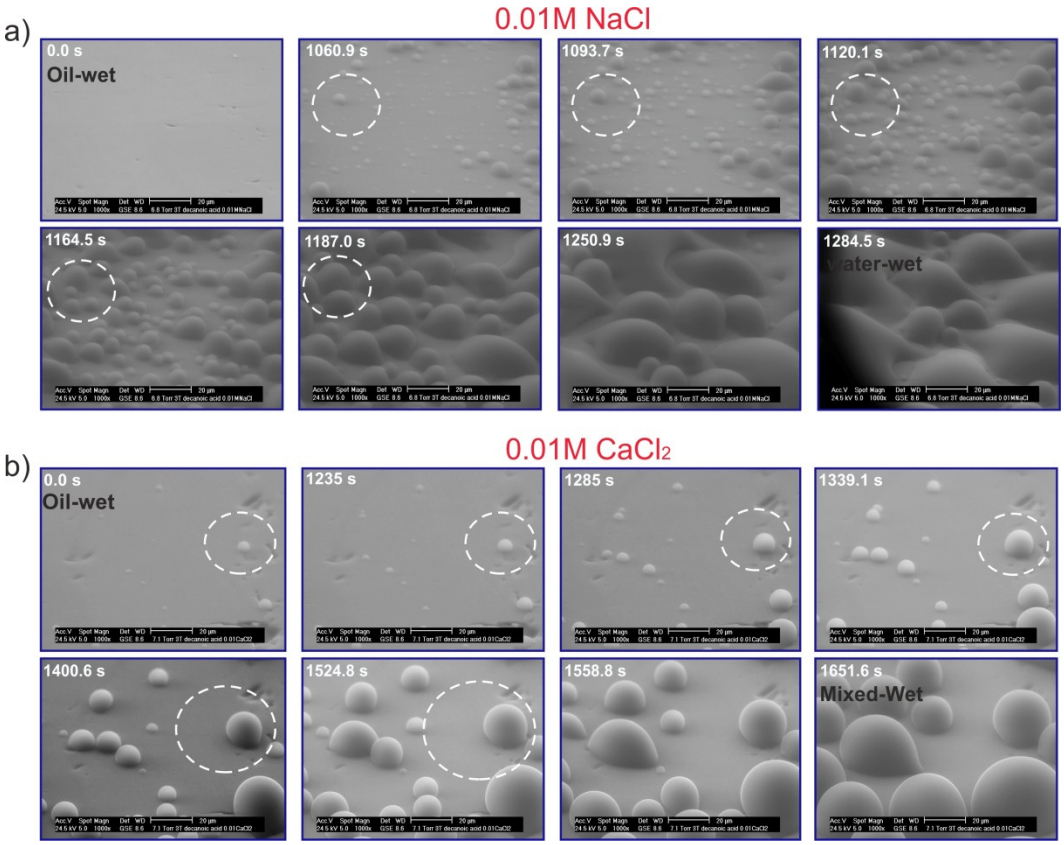

Figure 5.21: Micrographs show repoducibility of the contact angle with time after injection with low brine concentration at two different trials. a) after a certain time, the behavior of contact angle developed into a sheet-like cover on non-flat quartz aged in decanoic acid-dodecane when water began to condense on the surface of the sample inside the ESEM chamber at 6.8 Torr. b) Condensed water appeared in the form of droplets in contact with the surface of the aged crystal sample inside the ESEM chamber at a contact angle of =95.0° at 7.1 Torr.

Figure 5.22 shows the results. For both cases, the average angle values of 79° and 99° were obtained for 0.01M NaCl and 0.01M $CaCl_2$ solution, respectively (Figure 5.22). The results of the repeatability tests indicate that this non-flat quartz aged in decanoic acid-dodecane has a water-wet nature at low concentration of brine (0.01M NaCl), at 5 °C and 6.8 Torr. In contrast, the 0.01M $CaCl_2$ proves that decreasing water salinity could result in

wettability alteration of non-flat quartz aged in decanoic acid-dodecane towards a mixed-wet state at 5 °C and 7.1 Torr. It can be seen that, with the decrease of the salinity brine concentration, less time is needed for the contact angles to reach its maximum value (see Figure 5.22). After a 1300s the lowering of the contact angle in 0.01M of NaCl shows the time-independent behavior. On the other hand, the contact angle values of the 0.01M of $CaCl_2$ indicate different action among the decanoic acid- dodecane molecule, monovalent ion, and quartz surface.

The two cases also prove that the ESEM technique has the capability of reproducing contact angle measurements to within ± 3° for the purpose of characterising mineral surfaces such as quartz, calcite, and clay mineral wettability states. Generally, observations obtained with the ESEM technique cannot be directly generalised to core scale conditions since wettability is a function of mineralogy, pressure, temperature, fluid composition, and pH (Wang and Guidry, 1994). In addition, microscopic observation gives valuable information, but nanometer scale study is essential for examining the wettability behaviors that are constructed using microscopic data.

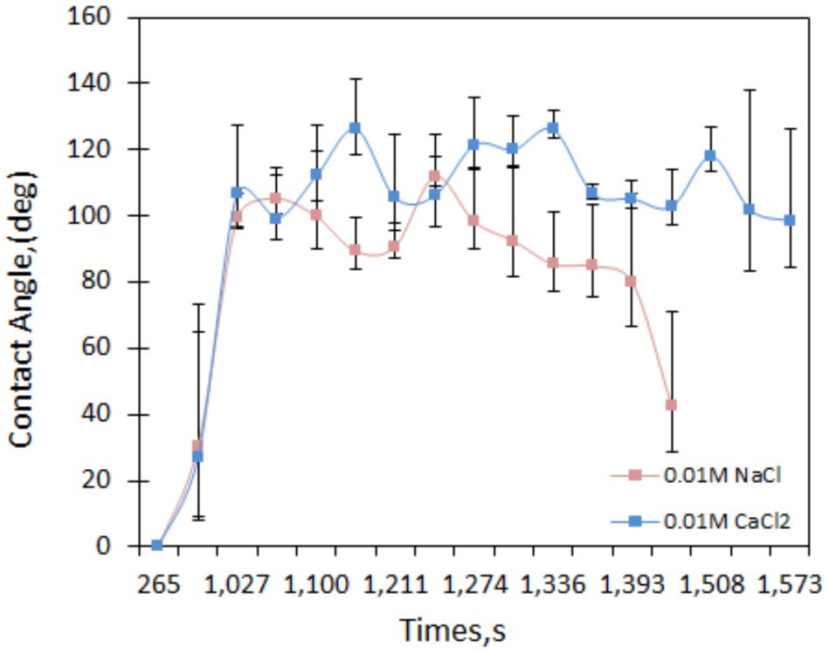

Figure 5.22: Reproducibility of the average of dynamic contact angles plotted versus time for condensate non-flat qaurtz aged in decanaoic acid-dodecane after each brine at 5°C. Each measured data point in the current investigation is the average of at least three independent droplets measurements. Error bars indicate standard deviations of several droplets.

5.3.2.3. Nanoscopic Observations

As stated previously AFM was used to investigate the effect of brine salinity and concentration on quartz wettability. For these experiments, samples were pre-treated in the

same way as with the ESEM samples but after the first sets of measurement in the AFM the brine was replaced with oil and left in contact with the crystal for 10-30 min, before being washed with a high and low salinity brine (0.01M and 1.0M NaCl or $CaCl_2$) and reintroduced in the AFM. It should be noted, in each of experiments 10 ml of brine was used. This procedure was repeated until all brine compositions were studied. In addition to the adhesion measurements, all quartz samples were characterised by performing measurements in air using the Peak Force mode. A non-flat quartz samples were scanned, as can be seen in Figure 5.1b.

Results from these measurements are shown in following experiments. As a starting point (to obtain a baseline for comparison purposes) a single AFM experiment was carried out on model oil-aged quartz crystals (Figure 5.23a, b, and c). For the rest of the experiments, non-flat quartz crystals were pre-treated in decanoic acid-dodecane and "washed" with different concentrations of NaCl brine, and $CaCl_2$ brine. Figure 5.23a shows a PeakForce image taken with the crystal immersed in decanoic acid-dodecane (no brine); the high roughness of the crystal is clear. Figure 5.23b shows the corresponding adhesion map.Note how there is almost no contrast in the adhesion signal, except a periodic variation which may be the product of some noise coupled to the cantilever vibration. Figure 5.23c shows a corresponding cross section taken over the adhesion map; on it, it can be seen again that there is almost no adhesion signal.

The next step in the investigation was to study the role of low concentration brine (0.01M of NaCl) in the first set of adhesion experiments. Figure 5.23d shows a PeakForce image of the same quartz crystal after it has been "flushed" with a NaCl (0.01 M) solution. This image does not show a significant difference with respect to the image taken in decanoic acid-dodecane, as in both cases the polishing features (grooves) are quite evident however, the adhesion maps do show a contrasting difference, with very high adhesion values along the polishing lines, this is interpreted as residual oil "stuck" on the grooves, which then causes an increase in adhesion as the tip contacts with it. A corresponding cross-section taken over the adhesion map illustrates the magnitude of the measured adhesion (Figure 5.23f). It can be seen that the aged non-flat quartz crystal in 0.01M NaCl now shows a higher adhesion than when measured under decanoic acid- dodecane (Figure 5.23f) and also how the adhesion due to the oil increases up to values of 2.5 nN. The AFM results indicate that significant amounts of decanoic acid- dodecane may be trapped within the "roughness" of the crystals, which explains why the mean measured contact angles are

larger than those measured for aged flat-quartz surface when exposed to 0.01M NaCl. (Figure 5.11).

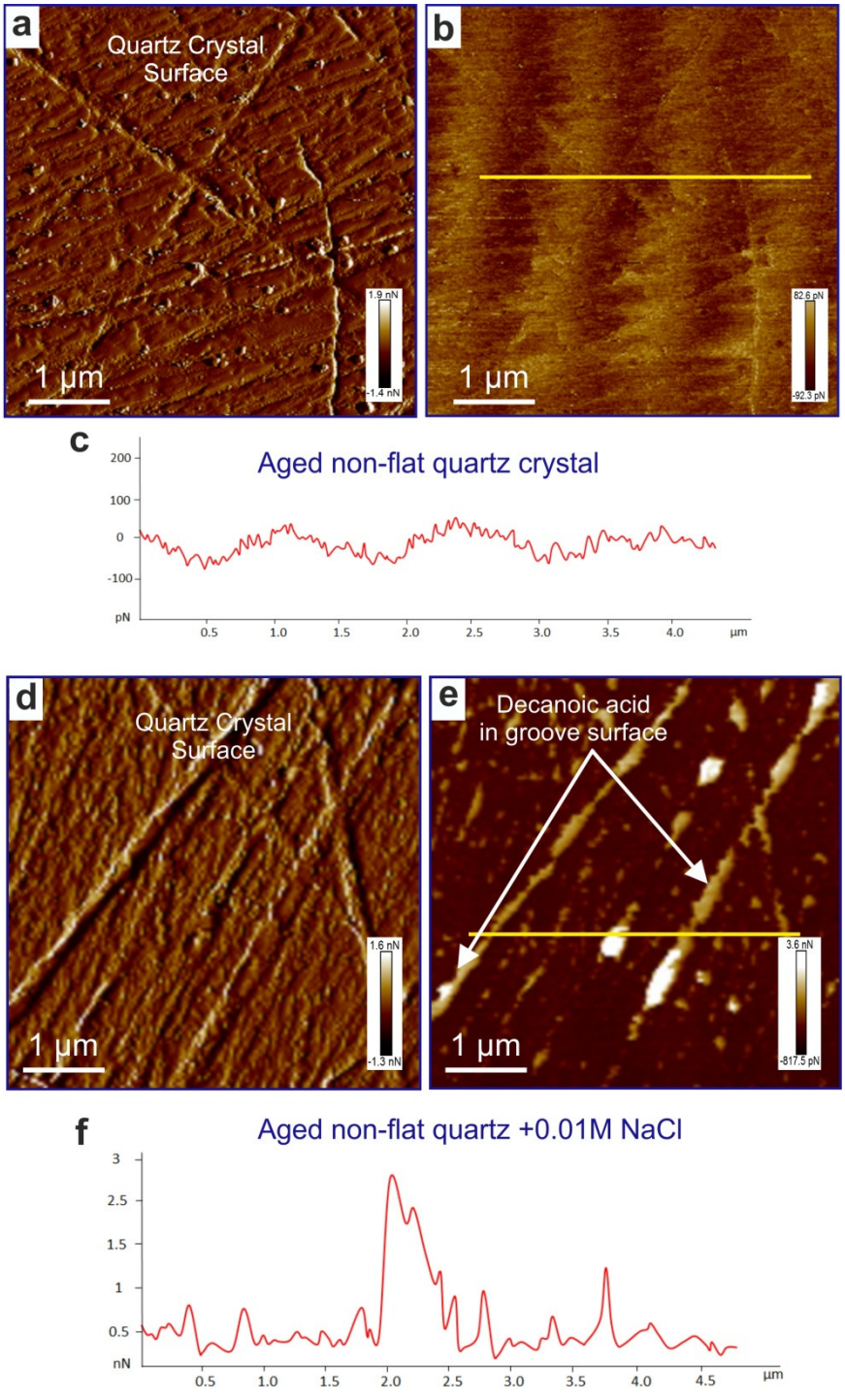

Figure 5.23: AFM images show a PeakForce image of non-flat quartz crystal. a) Non-flat clean quartz crystal immersed in decnaoic acid-dodecane (no brine). b) The corresponding adhesion map of image (a). c) A corresponding cross-section taken over the adhesion map (b). d) Non-flat quartz aged in decanoic acid-dodecane after flushing with a 0.01M of NaCl. e) The corresponding adhesion map of (d). f) The magnitude of the measured adhesion of (e) based on the chosen path.

Figure 5.24a shows the same crystal after it has been "flushed" with a $CaCl_2$ (0.01 M) brine. The same experiment was repeated on the same surface to examine the effect of 0.01M $CaCl_2$ on wettability alteration by a low concentration of brine at the nanometer-level. In this case, more oil (in the form of droplets) is apparent on the PeakForce image (Figure 5.24a). In this figure, there is some indication of remnants of the oil phase. These are much clearer in the adhesion image (Figure 5.24b) where this area has a much higher adhesion. In addition to this, a higher adhesion is observed along the polishing marks of the crystal, indicating that some of the decanoic acid- dodecane molecules are trapped in these regions. A corresponding cross-section is taken over the adhesion map shows the magnitude of the measured adhesion up to values of 4.0 nN (Figure 5.24c).

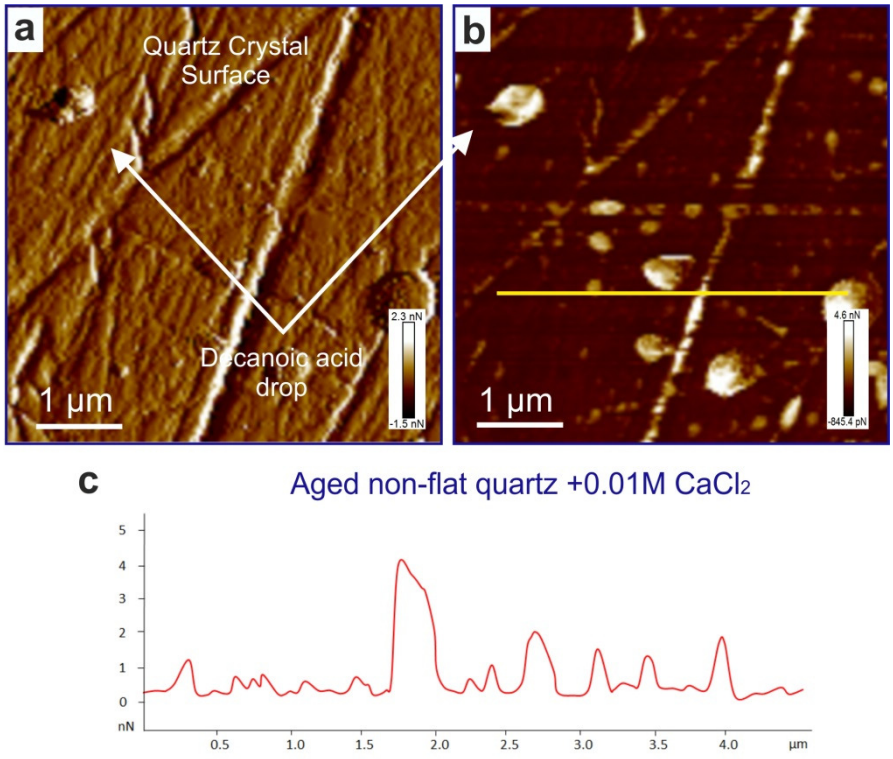

Figure 5.24: AFM images show a PeakForce image of non-flat quartz crystal. a) Non-flat quartz aged in decanaoic acid-dodecane after flushing with a 0.01M of $CaCl_2$. b) The corresponding adhesion map of (a). c) The magnitude of the measured adhesion of (b) based on the chosen path.

Next, it was our intention to compare the adhesion properties on surfaces of non-flat quartz crystals aged in decanoic acid-dodecane, after they have been exposed to 1.0M NaCl and $CaCl_2$ with non-flat crystal surfaces in the same condition that had previously been exposed to 0.01M of NaCl and $CaCl_2$. At a high concentration of NaCl and $CaCl_2$

(1.0M), the magnitude of adhesion across the aged non-flat quartz crystal increases compared with 0.01M for the same brine type. Figure 5.25a shows the same quartz crystal (see Figure 5.23a) after it has been "flushed" with a NaCl (1.0 M) solution. In this figure, there is more decanoic acid- dodecane (in the form of droplets) apparent on the PeakForce image compared with 0.01M NaCl; The adhesion map is presented in Figure 5.25b, which still shows significant adhesion along the polishing lines as well as on and in the flat areas. A corresponding cross-section taken over the adhesion map illustrates the magnitude of the measured adhesion(Figure 5.25c). The cross-section shows the height profile with adhesion data. Overall, adhesion is heterogeneous and ranges from low (2.5 nN) on the flat quartz area to higher (4.5 nN) along the edges, which is interpreted as t a significant amount of remnant decanoic acid-dodecane. The adhesion properties were investigated of the similar area on the non-flat quartz crystal aged in decanoic acid-dodecane after it had been exposed to 1.0M of $CaCl_2$ in the same way as those shown in Figure 5.25d and Figure 5.25e. In this case, the adhesion map (see Figure 5.25e) still shows significant adhesion. A corresponding cross-section taken over the adhesion map illustrates the magnitude of the measured adhesion up to values of 8.0 nN (Figure 5.25f).

On most of the samples, the response to changes in salinity was reproducible through three cycles or more, producing about the same magnitude of adhesion and the same amount of change in each cycling. Solution pH was not manipulated in these experiments, but this does not mean that pH cannot have a significant effect on the low salinity response in real rock reservoirs or in studies where the setup is different from ours (Austad et al., 2008; Rezaei-Doust et al., 2009; Hassenkam et al., 2011b). Beside, as well as the effectiveness of low salinity brine, all quartz crystals that were used in this AFM study were shown to contain residual decanoic acid-dodecane left in the surfaces, as shown in Figure 5.23 and Figure 5.24. AFM results presented by Hilner et al.(2015) support this observation, even though their experimental set up was quite different from ours. They used an AFM tip functionalised with CH_3 groups to observe the effect of ionic strength on oil adhesion in individual quartz particles. Overall, the adhesion is sensitive to brine-type as well as their concentration, and this is what this present study observed in the experiments.

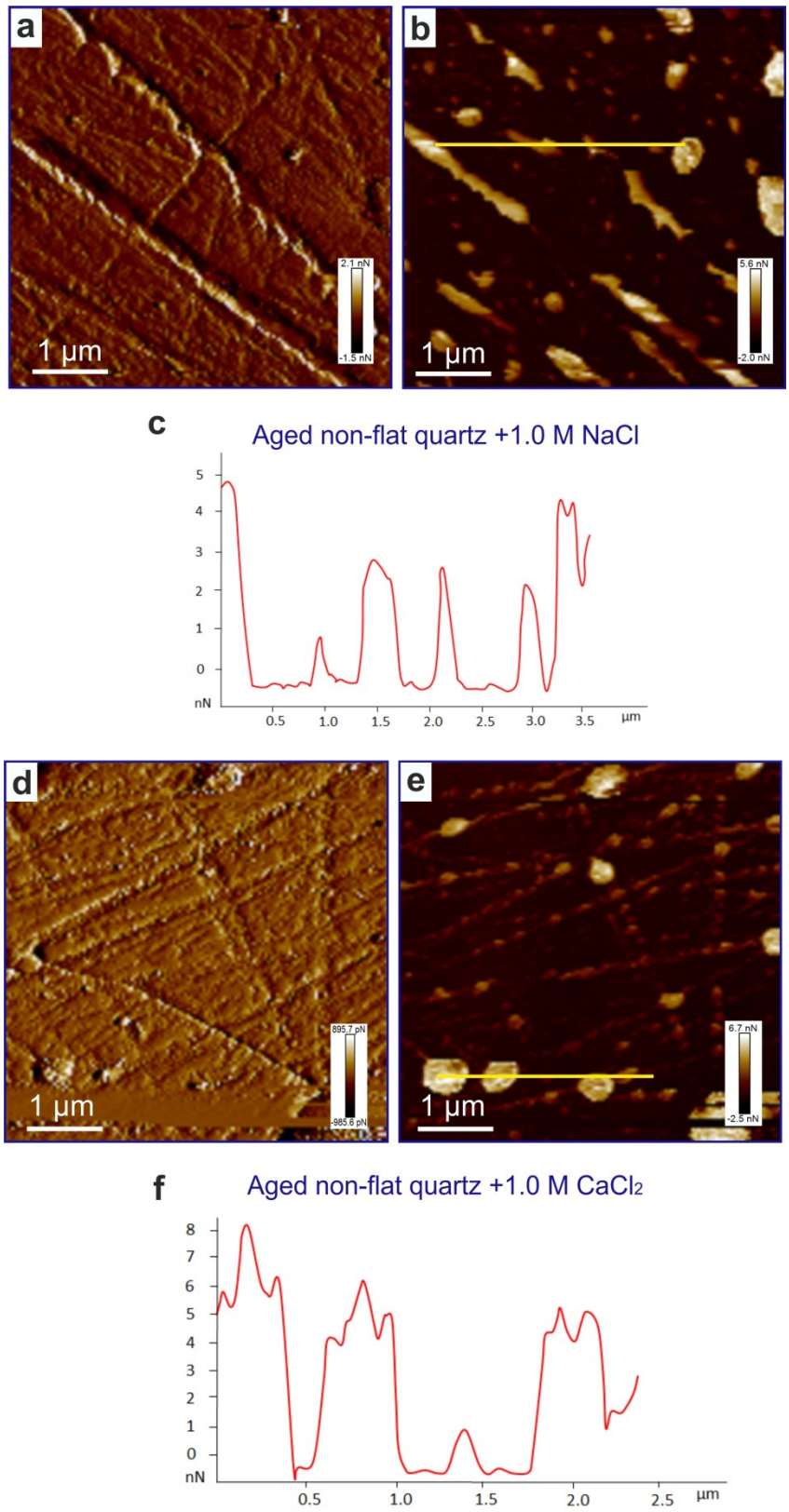

Figure 5.25: AFM images show a PeakForce image of non-flat quartz crystal. a) Non-flat quartz aged in decanaoic acid-dodecane after flushing with a 1.0M of NaCl. e) The corresponding adhesion map of (b). c) The magnitude of the measured adhesion of (b) based on chosen path. d) Non-flat quartz aged in decanaoic acid after flushing with a 1.0M of $CaCl_2$. b) The corresponding adhesion map of (e). f) The magnitude of the measured adhesion of (e) based on the chosen path.

5.3.3. Surface Charge on Quartz, Quartz Particles When Exposed to Potential Determining Ions

To have a better understanding of the impact of surface charge, the zeta potential of quartz powder was measured. Zeta potential for quartz crystals aged in decanoic acid-dodecane and crude oil could not be used in this experiment because of limitations of the SurPass Electronic Analyser. Zeta-potential measurements were conducted for quartz particles (powder) aged in either decanoic acid-dodecane or crude oil and then treated by NaCl and $CaCl_2$ brine at different salinities and compositions. The objectives of these tests were to examine the effect of the solution's salinity on the electrokinetic charge of oil/brine and quartz/brine interfaces and to link these changes to the dynamic changes in contact angle of water droplet observed at multi-length scale to explain how the concentration of brines water could modify the wettability at room temperature.

It can be seen that the quartz is quite stable in brine at a pH range of 1–10 (Drever, 1997). In the neutral and basic range of pH, the quartz surface acquires negative charges. It should be noted, the point of zero charge (pzc) for quartz is in the acidic region (~pH 2) (Ahmed and McKinney, 2005). The point of zero charge is the pH at which the charge of the mineral surface is zero and is usually determined by some form of acid-base titration. It is clear that the amphoteric dissociation of the surface silanol groups (SiOH) is responsible for the surface charges on quartz (Saraji et al., 2013). In acidic pH ranges, quartz becomes positively charged. In this study, the brine pH for quartz particles was in the neutral range of 6.5 and no pH modifier was used to manipulate the solution pH to align with contact angles measured.

In this section,0.001M, 0.01M, and1.0M rines were used, unlike the previous experiments when 0.01M and 1.0M were used (Table 5.2). In this test, as a starting point (to obtain a baseline for comparison purposes) a ζ potential measurement for untreated and treated quartz particles was carried out. The results obtained through ζ analysis are emphatic in this work. From Figure 5.26, it can be seen that the ζ potential at the untreated quartz particles is -47.98 mV (negative). In untreated cases, the zeta potential is negative, as observed in numerous previous studies of natural quartz at room temperature (see Kaya and Yukselen., 2011, and references therein).Kaya and Yukselen (2011) are Reported that the zeta potential for the quartz powder ranged from -302 mV at pH 3 to -64.4 mV at pH 11. After aging with decanoic acid-dodecane, the ζ potential at the surface of aged quartz crystal became positive (+10.24 mV), as shown in Figure 5.27. Moreover, the crude oil-

aged quartz shows an even more positive surface charge (+15.35 mV) (see Appendix B.3). In summary, these results provide an indication that the aging procedure in tests was successful.

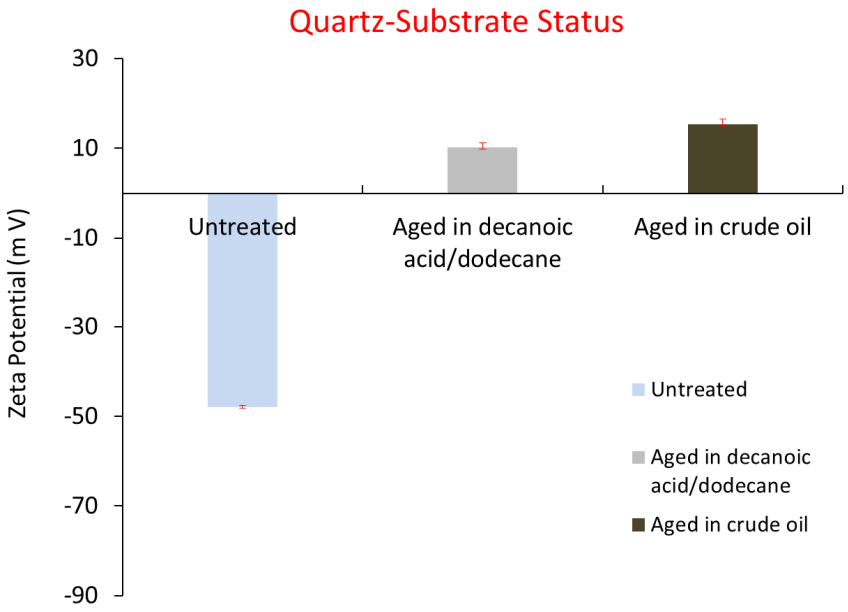

Figure 5.26: Results of ζ potential measurement for quartz powder: untreated, and treated with decanoic acid-dodecane and with crude oil. Error bars indicate standard deviations of four independent meaurments.

5.3.3.3.1. Surface Charge of Decanoic Acid-Dodecane/Brine/Quartz particles

Zeta potential measurements were conducted for decanoic acid- dodecane and quartz particles with NaCl and $CaCl_2$ at different salinities. The results show the ζ potential as a function of Na^+ concentration for each of the three NaCl concentrations studied, and as a function of Ca^{2+} concentration for three $CaCl_2$ concentrations examined. Therefore, the uncertainty of the ζ potential measurements for both brines was estimated by calculating the standard error of the different runs conducted on the same sample; the standard error varied from 0.5 to 2.2%.

The results of these measurements are listed in Table 5.7, and they are also displayed in Figure 5.27. 0.001M NaCl resulted in a negative charge with a higher magnitude (-54.81 mV) when compared to 0.001M $CaCl_2$ on the same surface (-47.43 mV) under the same conditions. It can be seen that the average ζ potential of aged quartz particles with remnant concentrations of NaCl was -42 mV and -29 mV for 0.01M NaCl and 1.0M NaCl, respectively. However, the average ζ potential of $CaCl_2$ solutions at the same salinity was -33 mV and -20 mV for 0.01M and 1.0M $CaCl_2$, respectively. Results

demonstrate that both NaCl and $CaCl_2$ solution and their concentration significantly and independently affect ζ potential as can be seen in Table 5.7 and Figure 5.27.

Table 5.7 Results of ζ potential measurement for untreated quartz powder, treated with decanoic acid-dodecane.

Sample	Ramp Nr	dU/dp [mV/mbar]	dU/dp R^2	dV/do [ml/min/mbar]	dV/dp R^2	pH	Conductivity [mS/m]	Gap Height [µm]	ζ [mV]
Qtz+0.001M NaCl	1	-0.28	1.00	0.57	0.99	7.98	24.80	0	-58.20
	2	-0.25	1.00	-0.72	0.96	7.98	24.83	0	-59.74
	3	-0.28	1.00	0.65	1.00	7.98	24.83	0	-50.21
	4	-0.25	1.00	-0.79	0.98	7.98	24.85	0	-51.09
Qtz+0.01M NaCl	1	-0.34	1.00	0.51	1.00	7.86	9.95	0	-35.81
	2	-0.35	0.99	-0.54	0.99	7.86	9.98	0	-33.01
	3	-0.33	1.00	0.67	1.00	7.86	9.98	0	-30.20
	4	-0.35	1.00	-0.70	1.00	7.86	9.99	0	-30.35
Qtz+1.0M NaCl	1	-0.10	1.00	4.97	0.99	7.86	20.76	0	-25.69
	2	-0.13	1.00	-6.24	0.99	7.86	20.88	0	-32.78
	3	-0.11	1.00	5.22	0.99	7.86	20.88	0	-26.61
	4	-0.13	1.00	-6.04	0.99	7.86	20.93	0	-31.95
Qtz+0.001M $CaCl_2$	1	-0.25	1.00	1.35	0.99	7.98	23.98	0	-48.12
	2	-0.24	1.00	-1.44	0.98	7.98	24.01	0	-46.19
	3	-0.25	1.00	1.45	0.99	7.98	24.02	0	-48.89
	4	-0.24	1.00	-1.56	0.99	7.98	24.04	0	-46.53
Qtz+0.01M $CaCl_2$	1	-0.16	1.00	1.84	0.99	7.86	16.48	0	-28.35
	2	-0.18	1.00	-1.80	0.99	7.86	16.51	0	-27.37
	3	-0.16	1.00	2.06	0.99	7.86	16.51	0	-28.77
	4	-0.17	0.99	-1.64	0.98	7.86	16.53	0	-27.39
Qtz+1.0M $CaCl_2$	1	-0.09	1.00	1.30	0.98	7.86	19.20	0	-20.56
	2	-0.08	0.99	-1.09	0.97	7.86	19.22	0	-19.56
	3	-0.09	1.00	1.40	0.98	7.86	19.22	0	-20.22
	4	-0.09	1.00	-1.22	0.97	7.86	19.23	0	-20.96

*Qtz = Quartz

In addition, the measured ζ potential of quartz particles surfaces decreased with increasing salt concentration for both NaCl and $CaCl_2$. Notably, the quartz samples treated with NaCl showed a consistent higher negative surface charge (10%) across all concentrations when compared to the values obtained for crystals treated with $CaCl_2$. In general, the reduction in the concentration of NaCl solutions changed the ζ potential from negative to more negative compare with $CaCl_2$ concentration, as can be seen in (Figure 5.28). From Figure 5.27, it can be concluded that for $CaCl_2$ solutions, when the concentration increases, the ζ potential value decreases, indicating that the negative charge of the aged non-flat quartz crystal decreases, which means that negatively charged polar molecules in decanoic acid-dodecane can bind with quartz surface more easily because of the diminished electrostatic repulsion (Israelachvili, 2011). In other words, there would be more decanoic acid- dodecane molecules adsorbed on the non-flat quartz crystal, and as

shown in Figure 5.14, the contact angles increase with the increase of the brine concentration.The reduction in ζ potential is due to the accumulation of more cations in the vicinity of negatively-charged aged quartz particles surfaces in decanoic acid-dodecane, which is based on diminished electrostatic repulsion.In addition, this shows that the cation type on quartz will have important effects on the electrical double layer (Nasralla et al., 2011; Qi et al., 2013; Keya et al., 2015).

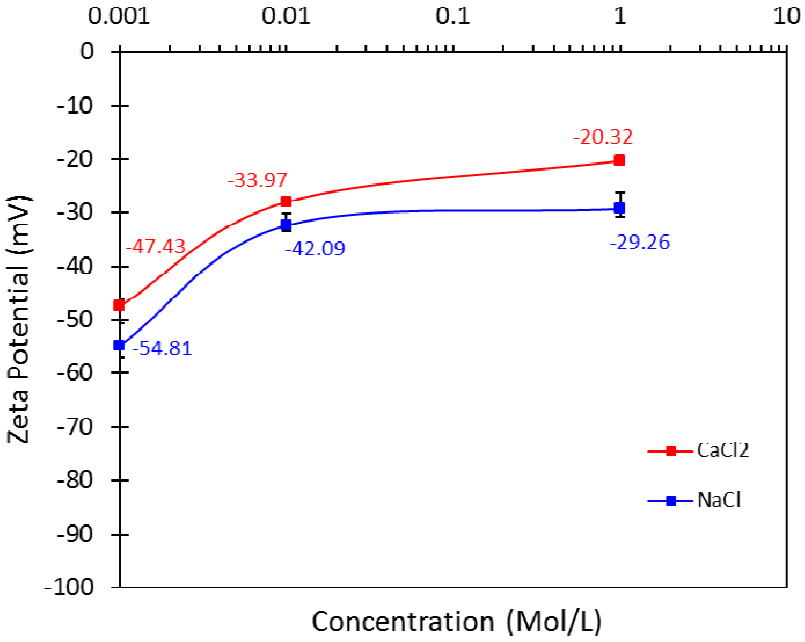

Figure 5.27: Impact of different concentration of NaCl, and $CaCl_2$ (0.001M,0.01M, and 1.0M) on quartz particles aged in decanoic aciddodecane.Error bars indicate standard deviations of 4 independent meaurments.

5.3.3.3.2. Surface Charge of Crude Oil/Brine/Quartz particles

Zeta potential measurements were conducted for crude oil/quartz particles at different salinities and compositions. The aim of these measurements was to study the effects of NaCl and $CaCl_2$ brine solution on the electrokinetic charge of quartz particles/ brine and oil/brine interfaces and relate these changes to electric charges to compare with the wettability behaviors in the similar system that contains decanoic acid-dodecane.

Tang and Morrow (1997) documented that the polar compounds in oil are essential in the interaction of oil/brine/mineral during EOR processes, as these compounds will interact more with the mineral surfaces available in the pore space (Standal et al., 1999). Therefore, Kumar et al. (2005) supported the same idea that the polar fraction of the crude oil is more involved in the EOR process since it induced wettability behavior. To examine the effects of crude oil compared with decanoic acid-dodecane (oil model compounds) in altering the

wettability state in a more controllable approach without more complexity caused by reservoir rock properties, the ζ potential was investigated on aged quartz powder in crude oil. Results of ζ potential measurement of crude oil with different brines are shown in Table 5.8. Figure 5.28 indicates that both chloride salt such as NaCl, and $CaCl_2$ solution and concentration affect ζ potential significantly.

Table 5.8 Results of ζ potential measurement for untreated quartz powder, treated with crude oil.

Sample	Ramp Nr	dU/dp [mV/mbar]	dU/dp R^2	dV/do [ml/min/mbar]	dV/dp R^2	pH	Conductivity [mS/m]	Gap Height [µm]	ζ [mV]
Qt+0.001M NaCl	1	-0.26	1.00	2.33	0.98	7.90	26.01	0	-44.95
	2	-0.26	0.99	-2.30	0.99	7.90	26.09	0	-46.28
	3	-0.27	1.00	2.44	1.00	7.90	26.09	0	-49.15
	4	-0.26	1.00	-2.38	0.99	7.90	26.05	0	-47.09
Qt+0.01M NaCl	1	-0.22	0.98	3.66	0.99	7.90	27.91	0	-28.38
	2	-0.21	0.99	-3.03	0.99	7.90	27.75	0	-24.21
	3	-0.22	0.98	3.64	0.99	7.90	27.75	0	-26.97
	4	-0.21	0.99	-3.11	0.99	7.90	27.96	0	-23.99
Qt+1.0M NaCl	1	-0.13	0.99	2.34	0.99	7.98	29.51	0	-17.96
	2	-0.17	0.99	-2.13	1.00	7.98	29.58	0	-22.33
	3	-0.14	1.00	2.43	0.99	7.98	29.58	0	-15.90
	4	-0.17	0.98	-2.15	1.00	7.98	29.64	0	-23.02
Qt+0.001M CaCl2	1	-0.24	1.00	1.91	0.99	7.98	24.22	0	-33.05
	2	-0.24	1.00	-1.92	1.00	7.98	24.27	0	-33.23
	3	-0.24	1.00	2.02	0.99	7.98	24.26	0	-33.47
	4	-0.23	1.00	-1.90	0.99	7.98	24.30	0	-31.31
Qt+0.01M CaCl2	1	-0.27	1.00	3.31	0.99	7.98	26.39	0	-22.96
	2	-0.26	1.00	-2.99	1.00	7.98	26.47	0	-21.85
	3	-0.27	1.00	3.46	0.99	7.98	26.47	0	-19.23
	4	-0.26	1.00	-3.18	1.00	7.98	26.43	0	-16.87
Qt+1.0M CaCl2	1	-0.27	1.00	2.21	1.00	7.98	26.82	0	-15.61
	2	-0.26	1.00	-2.16	1.00	7.98	26.95	0	-15.93
	3	-0.27	1.00	2.22	1.00	7.98	26.95	0	-18.44
	4	-0.25	1.00	-2.13	1.00	7.98	27.05	0	-20.48

*Qtz = Quartz

Noticeably, quartz samples treated with NaCl solutions showed again a larger negative charge than those treated with $CaCl_2$ (Table 5.8). The most negative charge was obtained with 0.001M NaCl, as can be seen in Figure 5.28. When the concentration of the brine was increased from 0.001 M to 0.01M, the concentration of cations (counterions) increased ten times, which reduced the ζ potential for NaCl from - 46 mV to -25 mV and for $CaCl_2$ from -32 mV to -20 mV (see Figure 5.28). The lowest negative charge obtained in 1.0M NaCl and $CaCl_2$ salt, however, is -19 mV and -17 mV, respectively. It should be noted, the variation in ζ potential is more uniform on NaCl and $CaCl_2$; the "jump" is between 0.01M and 1.0M. It can be seen that the results of this experimental work are well supported by prior experimental studies conducted by spectrophotometer (Saraji et al.,

2013) and electrophoretic mobility measurement (Qi et al., 2013). Increasing the ionic valency of salt cations from 1 to 2 resulted in lower ζ potential values of quartz (Figure 5.28). This is due to the much stronger ion binding of Ca^{2+} ion to quartz, as compared to Na^{+} (Israelachvili, 2011). The same trend was reported in a previous work (Saraji et al., 2013) during the dynamic adsorption of asphaltenes on quartz packs using low salinity (9 mM) and high concentration (90 mM) brines containing Na^{+}, Ca^{2+}, and Mg^{+} cations. In addition, ζ potential was measured for solutions of oil/brine, and solid/brine; on quartz surfaces (Nasralla and Nasr-El-Din, 2014), results showed that Na^{+} changes the electrical charge at both oil/ brine and quartz/brine interfaces to a highly negative value, which results in high repulsive forces between the two interfaces.

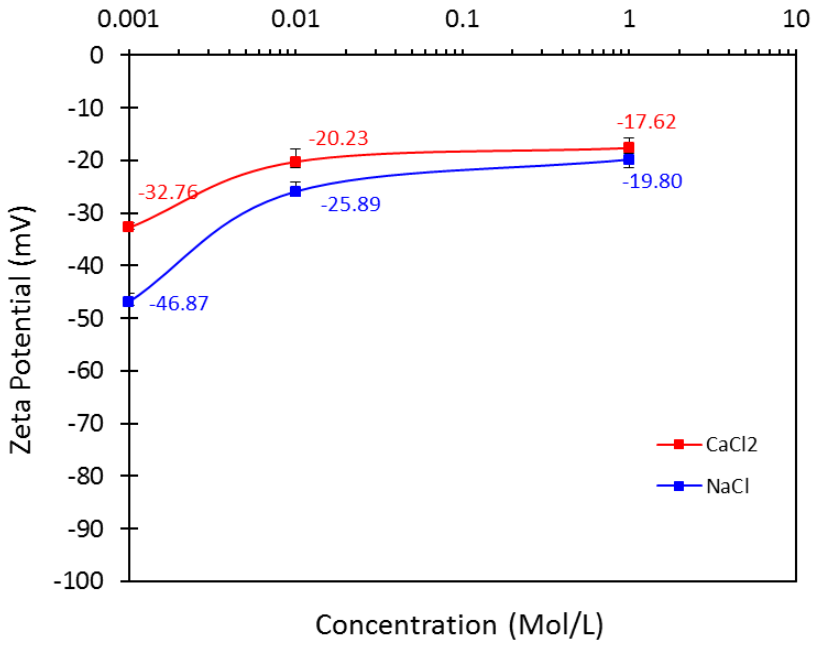

Figure 5.28: Impact of different concentration of NaCl and $CaCl_2$ (0.001M,0.01M, and 1.0M) on ζ potenial of quartz particles aged in crude oil.Error bars indicate standard deviations of 4 independent meaurments.

Finally, to explain the results in Figure 5.28, one needs to consider the polar compounds in crude oil. It is believed that the brines with higher valency cations always result-in a lower desorption of asphaltenes (Saraji et al., 2013). This implies that more adsorption concentration is the result of less stable water films. Asphaltene Adsorption on the quartz surface is explained by (Somasundaran and Zhang, 2006; Farooq et al., 2011; Qi et al., 2013) in more detail. In decanoic acid-dodecane experiments, the biggest drop in ζ potential in both brine salinity is from 0.001M to 0.01M; then it drops much less when

increasing to 1.0M. On the oil treated samples, however, the variation is uniform on NaCl, and on $CaCl_2$ the "jump" is between 0.01M and 1.0M. More importantly, the final ζ potential at NaCl 1M is much larger in oil (-19 mV) than on decanoic acid-dodecane (-29 mV) so here the NaCl has more screening effect. It seems clear that a full understanding of all the complex interactions involved (i.e., of both crude oil and quartz) could lead to new approaches and insights that are needed to improve oil production in sandstone reservoirs.

5.4. Conclusions

In this chapter, we presented results from a series of microscopic and nanoscopic observations aimed at assessing the influence of aging and brine composition/concentration on the wetting behavior on the quartz surfaces. After aging the quartz samples in crude oil and decanoic acid- dodecane, the wettability of the quartz surface changed from water-wet to oil-wet due to the adsorption and precipitation of organic material with polar compounds, including acids, which resulted in higher adhesion. Zeta potentials were measured using the streaming potential technique to examine the effect of cations on the repulsive forces between oil and rock and relate them to the wetting state. Based on the results obtained, the following conclusions can be drawn:

1. ESEM results show that roughness can have a major effect in changing the wetting characteristics of a decanoic acid- dodecane -treated quartz crystal. It was observed that the increase of nanoroughness value makes the quartz surface more oil-wet. This result can be interpreted using existing theories that relate roughness to contact angle.
2. AFM observations showed an increase (or decrease) of remnant oil after exposure to different brine compositions and concentrations. In particular, $CaCl_2$ solution showed more oil remnants on the non-flat quartz. These results demonstrate that both morphological and chemical properties of quartz surfaces at the nanoscale play a crucial role in determining its "macroscopic" wettability. Nevertheless, further work is required to examine the effects of more complex low salinity solutions than those used in current EOR operations.
3. Wettability observations illustrate that temperature has an effect on the contact angle measurement of oil/brine/quartz. The contact angle of a water droplet showed a reduction when the temperature increased, i.e. when the contact angles were measured at 5°C in the ESEM compared with the same experiment at room

temperature (25°C) using drop shape analysis. Results agree with some of the work in the literature.

4. The experimental study proves that lowering water salinity results in wettability alteration of non-flat quartz crystal. In general, due to the presence of asphaltenes in crude oil, and the polar character of the decanoic acid-dodecane, a dual effect can be observed for cation salt concentrations. For the case of low monovalent salt (NaCl) concentration, the polar character of the decanoic acid-dodecane leads to a greater reduction in the contact angles compared with the asphaltene content in crude oil in all cases, although as the concentration of salt was increased, the effect of polar character on contact angle reduction is dominant. Also, no significant change in wettability for $CaCl_2$ in ESEM was observed within the ranges studied.

The results of this study gain a better insight into the complex wettability behavior of quartz crystals as a model mineral surface. Quartz crystals present in real rock sandstone reservoirs may have different surface properties due to the adsorption of organic contaminants (clay minerals have a high affinity for organic material, where they could be strongly attached to the surface due to capillary forces and colloidal forces (Israelachvili, 2011), thus also changing the surface charge and adhesion properties). The results of this study can help understand the complex wettability behavior of sandstone reservoirs. Therefore, in the next chapter, we present data from analysis of the wetting properties of quartz surface in Berea sandstone samples. Also, it is important to note that there are other minerals present in sandstone rock (such as clay minerals) that can play a significant role in the wettability alteration of rocks. Therefore, further studies are necessary to understand the effect of these minerals on the wettability alteration of quartz overgrowths in sandstone rock.

5.5. References

Abdallah, W. et al., 2007, Fundamentals of Wettability: Oilfield Review, p. 17.

Ahmed, T., and P. D. McKinney, 2005, 2 - Water Influx, *in* Advanced Reservoir Engineering: Burlington, Gulf Professional Publishing, p. 149–185.

Akhlaq, M. S., D. Kessel, and W. Dornow, 1996, Separation and Chemical Characterization of Wetting Crude Oil Compounds: Journal of Colloid and Interface Science, v. 180, no. 2, p. 309–314, doi:10.1006/jcis.1996.0308.

Al-Aulaqi, T., C. Grattoni, Q. Fisher, Z. Musina, and S. Al-Hinai, 2011, Effect of Temperature, Oil Asphaltene Content, and Water Salinity on Wettability Alteration: Society of Petroleum Engineers, doi:10.2118/149071-MS.

Al-Mahrooqi, S. H., C. A. Grattoni, A. K. Moss, and X. D. Jing, 2003, An investigation of the effect of wettability on NMR characteristics of sandstone rock and fluid systems: Journal of Petroleum Science and Engineering, v. 39, no. 3–4, p. 389–398, doi:10.1016/S0920-4105(03)00077-9.

Al-Shafei, M. A., and T. M. Okasha, 2009, Wettability Studies at the Pore Level of Saudi Aramco Reservoirs: Society of Petroleum Engineers, doi:10.2118/126088-MS.

Anderson, W. G., 1986a, Wettability Literature Survey- Part 1: Rock/Oil/Brine Interactions and the Effects of Core Handling on Wettability: Journal of Petroleum Technology, v. 38, no. 10, p. 1,125-1,144, doi:10.2118/13932-PA.

Anderson, W., 1986, Wettability Literature Survey- Part 2: Wettability Measurement: Journal of Petroleum Technology, v. 38, no. 11, p. 1,246-1,262, doi:10.2118/13933-PA.

Andrew, M., B. Bijeljic, and M. J. Blunt, 2014, Pore-scale contact angle measurements at reservoir conditions using X-ray microtomography: Advances in Water Resources, v. 68, p. 24–31, doi:10.1016/j.advwatres.2014.02.014.

Arima, Y., and H. Iwata, 2007, Effect of wettability and surface functional groups on protein adsorption and cell adhesion using well-defined mixed self-assembled monolayers: Biomaterials, v. 28, no. 20, p. 3074–3082, doi:10.1016/j.biomaterials.2007.03.013.

Austad, T., S. Strand, M. V. Madland, T. Puntervold, and R. I. Korsnes, 2008, Seawater in Chalk: An EOR and Compaction Fluid: SPE Reservoir Evaluation & Engineering, v. 11, no. 4, p. 648–654, doi:10.2118/118431-PA.

Bera, A., K. S, K. Ojha, T. Kumar, and A. Mandal, 2012a, Mechanistic Study of Wettability Alteration of Quartz Surface Induced by Nonionic Surfactants and Interaction between Crude Oil and Quartz in the Presence of Sodium Chloride Salt: Energy & Fuels, v. 26, no. 6, p. 3634–3643, doi:10.1021/ef300472k.

Blatt, H., and D. J. Schultz, 1976, Size distribution of quartz in mudrocks: Sedimentology, v. 23, no. 6, p. 857–866, doi:10.1111/j.1365-3091.1976.tb00113.x.

Buckley, J. S., Y. Liu, and S. Monsterleet, 1998, Mechanisms of Wetting Alteration by Crude Oils: SPE Journal, v. 3, no. 1, p. 54–61, doi:10.2118/37230-PA.

Buckman, J. O., A. C. Todd, and P. I. Hill, 2000, Observations on Reservoir Rock Wettability Using an Environmental SEM: Microscopy and Analysis, p. 35–38.

Craig, F. F., 1971, The Reservoir Engineering Aspects of Waterflooding: H. L. Doherty Memorial Fund of AIME, 152 p.

Drever, J. I., 1997, The Geochemistry of Natural Waters: Surface and Groundwater Environments: Prentice Hall, 456 p.

Farooq, U., J. Sjöblom, and G. Øye, 2011, Desorption of Asphaltenes from Silica-Coated Quartz Crystal Surfaces in Low Saline Aqueous Solutions: Journal of Dispersion Science and Technology.

Galimberti, R., C. Ghiselli, and M. A. Chiaramonte, 2000, Acidic polar compounds in petroleum: a new analytical methodology and applications as molecular migration indices: Organic Geochemistry, v. 31, no. 12, p. 1375–1386, doi:10.1016/S0146-6380(00)00102-9.

Götze, J., and R. Möckel, 2012, Quartz: Deposits, Mineralogy and Analytics: Springer Science & Business Media, 366 p.

Groysman, A., 2014, Corrosion in Systems for Storage and Transportation of Petroleum Products and Biofuels: Identification, Monitoring and Solutions: Springer Science & Business Media, 306 p.

Hassenkam, T. et al., 2014, A Fast Alternative to Core Plug Tests for Optimising Injection Water Salinity for EOR: Society of Petroleum Engineers, doi:10.2118/169136-MS.

Hassenkam, T. et al., 2016, Could Atomic-Force Microscopy Force Mapping Be a Fast Alternative to Core-Plug Tests for Optimizing Injection-Water Salinity for Enhanced Oil Recovery in Sandstone? SPE Journal, v. 21, no. 3, p. 720–729, doi:10.2118/169136-PA.

Hassenkam, T., C. S. Pedersen, K. Dalby, T. Austad, and S. L. S. Stipp, 2011, Pore scale observation of low salinity effects on outcrop and oil reservoir sandstone: Colloids and Surfaces A: Physicochemical and Engineering Aspects, v. 390, no. 1–3, p. 179–188, doi:10.1016/j.colsurfa.2011.09.025.

Hilner, E., M. P. Andersson, T. Hassenkam, J. Matthiesen, P. A. Salino, and S. L. S. Stipp, 2015, The effect of ionic strength on oil adhesion in sandstone – the search for the low salinity mechanism: Scientific Reports, v. 5, p. 9933, doi:10.1038/srep09933.

Israelachvili, J. N., 2011a, 17 - Adhesion and Wetting Phenomena, *in* Intermolecular and Surface Forces (Third Edition): San Diego, Academic Press, p. 415–467.

Israelachvili, J. N., 2011b, Intermolecular and Surface Forces: Revised Third Edition: Academic Press, 704 p.

Jadhunandan, P. P., and N. R. Morrow, 1995, Effect of Wettability on Waterflood Recovery for Crude-Oil/Brine/Rock Systems: SPE Reservoir Engineering, v. 10, no. 1, p. 40–46, doi:10.2118/22597-PA.

Jarrahian, K., O. Seiedi, M. Sheykhan, M. V. Sefti, and S. Ayatollahi, 2012, Wettability alteration of carbonate rocks by surfactants: A mechanistic study: Colloids and Surfaces A: Physicochemical and Engineering Aspects, v. Complete, no. 410, p. 1–10, doi:10.1016/j.colsurfa.2012.06.007.

Kaya, A., and Y. Yukselen, 2011, Zeta potential of clay minerals and quartz contaminated by heavy metals: Canadian Geotechnical Journal, doi:10.1139/t05-048.

Kumar, K., E. Dao, and K. K. Mohanty, 2005, AFM study of mineral wettability with reservoir oils: Journal of Colloid and Interface Science, v. 289, no. 1, p. 206–217, doi:10.1016/j.jcis.2005.03.030.

Lager, A., K. J. Webb, C. J. J. Black, M. Singleton, and K. S. Sorbie, 2008, Low Salinity Oil Recovery - An Experimental Investigation1: Petrophysics, v. 49, no. 1.

Lashkarbolooki, M., S. Ayatollahi, and M. Riazi, 2014a, Effect of Salinity, Resin, and Asphaltene on the Surface Properties of Acidic Crude Oil/Smart Water/Rock System: Energy & Fuels, v. 28, no. 11, p. 6820–6829, doi:10.1021/ef5015692.

Lebedeva, E. V., and A. Fogden, 2011, Wettability alteration of kaolinite exposed to crude oil in salt solutions: Colloids and Surfaces A: Physicochemical and Engineering Aspects, v. 377, no. 1–3, p. 115–122, doi:10.1016/j.colsurfa.2010.12.051.

Leirvik, A., 2010, Evaluation of experimental methods to determine wettability: 29 p.

Mahani, H., A. L. Keya, S. Berg, W.-B. Bartels, R. Nasralla, and W. R. Rossen, 2015, Insights into the Mechanism of Wettability Alteration by Low-Salinity Flooding (LSF) in Carbonates: Energy & Fuels, v. 29, no. 3, p. 1352–1367, doi:10.1021/ef5023847.

Mugele, F., I. Sîretanu, N. Kumar, B. Bera, L. Wang, M. A. Maestro, M. H. G. Duits, H. T. M. van den Ende, and I. Collins, 2014, Charge Control And Wettability Alteration At Solid-liquid Interfaces, *in* Society of Petroleum Engineers journal, Tulsa, Oklahoma, USA: Society of Petroleum Engineers.

Mugele, F., I. Siretanu, N. Kumar, B. Bera, L. Wang, R. de Ruiter, A. Maestro, M. Duits, D. van den Ende, and I. Collins, 2016, Insights From Ion Adsorption and Contact-Angle Alteration at Mineral Surfaces for Low-Salinity Waterflooding: SPE Journal, v. 21, no. 4, p. 1,204-1,213, doi:10.2118/169143-PA.

Nasralla, R. A., M. B. Alotaibi, and H. A. Nasr-El-Din, 2011, Efficiency of Oil Recovery by Low Salinity Water Flooding in Sandstone Reservoirs: Society of Petroleum Engineers, doi:10.2118/144602-MS.

Nasralla, R. A., M. A. Bataweel, and H. A. Nasr-El-Din, 2013, Investigation of Wettability Alteration and Oil-Recovery Improvement by Low-Salinity Water in Sandstone

Rock: Journal of Canadian Petroleum Technology, v. 52, no. 2, p. 144–154, doi:10.2118/146322-PA.

Nasralla, R. A., and H. A. Nasr-El-Din, 2014, Impact of cation type and concentration in injected brine on oil recovery in sandstone reservoirs: Journal of Petroleum Science and Engineering, v. 122, p. 384–395, doi:10.1016/j.petrol.2014.07.038.

Pedersen, N. R., T. Hassenkam, M. Ceccato, K. N. Dalby, K. Mogensen, and S. L. S. Stipp, 2016, Low Salinity Effect at Pore Scale: Probing Wettability Changes in Middle East Limestone: Energy & Fuels, v. 30, no. 5, p. 3768–3775, doi:10.1021/acs.energyfuels.5b02562.

Polson, E. J., J. O. Buckman, D. G. Bowen, A. C. Todd, M. M. Gow, and S. J. Cuthbert, 2010, An Environmental-Scanning-Electron-Microscope Investigation Into the Effect of Biofilm on the Wettability of Quartz: SPE Journal, v. 15, no. 1, p. 223–227, doi:10.2118/114421-PA.

Pu, H., X. Xie, P. Yin, and N. R. Morrow, 2010, Low-Salinity Waterflooding and Mineral Dissolution: Society of Petroleum Engineers, doi:10.2118/134042-MS.

Qi, Z., Y. Wang, H. He, D. Li, and X. Xu, 2013, Wettability Alteration of the Quartz Surface in the Presence of Metal Cations: Energy & Fuels, v. 27, no. 12, p. 7354–7359, doi:10.1021/ef401928c.

RezaeiDoust, A., T. Puntervold, S. Strand, and T. Austad, 2009, Smart Water as Wettability Modifier in Carbonate and Sandstone: A Discussion of Similarities/Differences in the Chemical Mechanisms: Energy & Fuels, v. 23, no. 9, p. 4479–4485, doi:10.1021/ef900185q.

Saraji, S., L. Goual, and M. Piri, 2013, Dynamic adsorption of asphaltenes on quartz and calcite packs in the presence of brine films: Colloids and Surfaces A: Physicochemical and Engineering Aspects, v. 434, p. 260–267, doi:10.1016/j.colsurfa.2013.05.070.

Seiedi, O., M. Rahbar, M. Nabipour, M. A. Emadi, M. H. Ghatee, and S. Ayatollahi, 2011, Atomic Force Microscopy (AFM) Investigation on the Surfactant Wettability Alteration Mechanism of Aged Mica Mineral Surfaces: Energy & Fuels, v. 25, no. 1, p. 183–188, doi:10.1021/ef100699t.

Seyyedi, M., M. Sohrabi, and A. Farzaneh, 2015, Investigation of Rock Wettability Alteration by Carbonated Water through Contact Angle Measurements: Energy & Fuels, v. 29, no. 9, p. 5544–5553, doi:10.1021/acs.energyfuels.5b01069.

Shedid, S. A., and M. T. Ghannam, 2004, Factors affecting contact-angle measurement of reservoir rocks: Journal of Petroleum Science and Engineering, v. 44, no. 3–4, p. 193–203, doi:10.1016/j.petrol.2004.04.002.

Somasundaran, P., and L. Zhang, 2006, Adsorption of surfactants on minerals for wettability control in improved oil recovery processes: Journal of Petroleum Science and Engineering, v. 52, no. 1, p. 198–212, doi:10.1016/j.petrol.2006.03.022.

Somerton, W. H., and C. J. Radke, 1983, Role of Clays in the Enhanced Recovery of Petroleum From Some California Sands: Journal of Petroleum Technology, v. 35, no. 3, p. 643–654, doi:10.2118/8845-PA.

Stalder, A. F., T. Melchior, M. Müller, D. Sage, T. Blu, and M. Unser, 2010, Low-bond axisymmetric drop shape analysis for surface tension and contact angle measurements of sessile drops: Colloids and Surfaces A: Physicochemical and Engineering Aspects, v. 364, no. 1–3, p. 72–81, doi:10.1016/j.colsurfa.2010.04.040.

Standal, S., J. Haavik, A. M. Blokhus, and A. Skauge, 1999a, Effect of polar organic components on wettability as studied by adsorption and contact angles, *in* Journal of petroleum science & engineering: Elsevier, p. 131–144.

Tang, G. Q., and N. R. Morrow, 1997, Salinity, Temperature, Oil Composition, and Oil Recovery by Waterflooding: SPE Reservoir Engineering, v. 12, no. 4, p. 269–276, doi:10.2118/36680-PA.

Taqvi, S. T., A. Almansoori, and G. Bassioni, 2016, Understanding the Role of Asphaltene in Wettability Alteration Using ζ Potential Measurements: Energy & Fuels, v. 30, no. 3, p. 1927–1932, doi:10.1021/acs.energyfuels.5b02127.

Tiab, D., and E. C. Donaldson, 2012, Chapter 1 - Introduction to Mineralogy, *in* Petrophysics (Third Edition): Boston, Gulf Professional Publishing, p. 1–26.

Treiber, L. E., and W. W. Owens, 1972, A Laboratory Evaluation of the Wettability of Fifty Oil-Producing Reservoirs: Society of Petroleum Engineers Journal, v. 12, no. 6, p. 531–540, doi:10.2118/3526-PA.

Vevle, J., 2011, NMR measurements of wettability alternation in Berea Sandstone.

Wang, F. H. L., and L. J. Guidry, 1994, Effect of Oxidation-Reduction Condition on Wettability Alteration: SPE Formation Evaluation, v. 9, no. 2, p. 140–148, doi:10.2118/20504-PA.

Wenzel, R. N., 1936, RESISTANCE OF SOLID SURFACES TO WETTING BY WATER: Industrial & Engineering Chemistry, v. 28, no. 8, p. 988–994, doi:10.1021/ie50320a024.

Yang, J., Z. Dong, M. Dong, Z. Yang, M. Lin, J. Zhang, and C. Chen, 2015, Wettability Alteration during Low Salinity Waterflooding and The Relevance of Divalent Ions in This Process: Energy & Fuels, doi:10.1021/acs.energyfuels.5b01847.

Yildiz, H. O., and N. R. Morrow, 1996, Effect of brine composition on recovery of Moutray crude oil by waterflooding: Journal of Petroleum Science and Engineering, v. 14, no. 3, p. 159–168, doi:10.1016/0920-4105(95)00041-0.

Zhang, Y., and N. R. Morrow, 2006, Comparison of Secondary and Tertiary Recovery With Change in Injection Brine Composition for Crude-Oil/Sandstone Combinations: Society of Petroleum Engineers, doi:10.2118/99757-MS.

Zhang, R., N. Qin, L. Peng, K. Tang, and Z. Ye, 2012, Wettability alteration by trimeric cationic surfactant at water-wet/oil-wet mica mineral surfaces: Applied Surface Science, v. 258, no. 20, p. 7943–7949, doi:10.1016/j.apsusc.2012.04.139.

Zhang, L., Z.-L. Wang, Z.-Q. Li, L. Zhang, Z.-C. Xu, S. Zhao, and J.-Y. Yu, 2010, Wettability of a Quartz Surface in the Presence of Four Cationic Surfactants: Langmuir, v. 26, no. 24, p. 18834–18840, doi:10.1021/la1036822.

Chapter 6

An Integrated Study of Wettability Alteration and Oil Recovery Improvement in Berea Sandstone as A model of Sandstone Reservoir

6.1. Introduction

It is now widely accepted that sandstone oil reservoirs can have a range of wetting conditions depending not only on the oil composition and rock mineralogy, but also on the composition and amount of the brine phase, in addition to the effects of temperature and pressure. The brine salinity is counted to be essential in determining the wetting state (Austad et al., 2010a; Fogden, 2011; AlShaikh and Mahadevan, 2014).The evidence for low-salinity water flooding as a potential EOR technique in sandstone oil reservoirs typically comes from studying the crude oil/brine/rock interactions and how this controls wettability behaviours in a porous medium (Seyyedi et al., 2015). Crude oil/brine/mineral interactions have been constrained to duplicate mixed wetting conditions in laboratory samples that are more representative of wetting in a sandstone oil reservoir than either the strongly water-wet or strongly oil-wet extremes (Nasralla and Nasr-El-Din, 2011a; Tang and Morrow, 1999a; Zhang et al., 2007a; Alotaibi et al., 2010; Yang et al., 2015).In contrast, with multiple phases flowing in sandstone oil reservoirs and core flooding experiments, understanding wettability behaviours from pore scale to reservoir scale frequently can be quite problematic (Hendraningrat and Torsæter, 2014). In general, the

wetting phase will have a tendency to spread across the mineral surfaces, displacing the non-wetting liquid phase. However, as apparent in Chapter 4, the inherent heterogeneity of sandstone rock reservoirs, often comprising a variety of detrital minerals, clay mineral types and cement, will result in a variable surface chemistry, which will lead to a different wetting state for each mineral surface.

The issue of how each type and the amount of clay minerals (on sandstone rocks) affect wettability is important but not yet settled. As has been noted in previous chapters, clay minerals are commonly disseminated as a matrix which coats the pores of sandstone (Wilson et al., 2014). It has been suggested that the clay minerals are involved with oil migration, because they interact heavily with the crude oil (Hancock and Taylor, 1978; Marcussen et al., 2010; Bjørlykke, 2014). Tang and Morrow (1999a) noticed that clay mineral-containing sandstones produced more oil recovery than clean sand, and they stated that in order for a low salinity core-flooding experiment to be successful, clay minerals must be present in the core. However, they did not specify whether certain clay minerals play a more significant role than others. Lager et al. (2007) suggested that kaolinite plays the most important role and proposed a correlation between kaolinite content and additional oil recovered by low salinity waterflood EOR. However, recent work by Soraya et al. (2009) showed a positive response in kaolinite free sandstone rock after lowsal injection, and Austad et al. (2010) have proposed that kaolinite would be the least important clay because of its low cation-exchange capacity. Due to these apparent contradictions with respect to the role of kaolinite in oil recovery, the subject has attracted more research.

An additional complication could be arises from the presence of nano-mineral phases that attach to quartz overgrowth surfaces (or other mineral surfaces). In fact, investigations on the surface adhesion and internal pore surfaces characterisation in outcrop and reservoir sandstone using atomic force microscopy (AFM) process reveals widespread evidence of the presence of nano-mineral phases over the quartz grains (Hassenkam et al., 2016; Kareem et al., 2016). Previous work by the theses author shows nano-mineral phases attached on the quartz overgrowth surfaces in sandstone rocks (see Chapter 4 section 4.3.2.1) (Kareem et al., 2016). This work showed that most of the nano-size minerals on quartz surfaces have a kaolinite morphology, rather than illite or smectite. The presence of one type over the other is important, as illite and smectites are considered as water-wetting, while kaolinite is generally considered to be oil-wetting (Bantignies et al., 1997).

Wettability alteration has also been studied on different mineral surfaces, including clay minerals such as kaolinite, or illite (Bantignies et al., 1997; Lebedeva and Fogden, 2011; Mugele et al., 2016). In some cases, studies have been performed over "powders" containing many individual crystals (with impurities), but other have been performed in individual crystals, the advantage of the latter is that allows for the study of single parameters that can affect the wettability in a more controllable way. Quartz wettability has also been studies as a proxy or model substrate of sandstone (Alipour Tabrizy et al., 2011; Bera et al., 2012a, 2015; Qi et al., 2013a). However, as mentioned above, there is a number of experimental evidence that indicates that the surface of quartz crystal in reservoir rocks can be significantly different than that of the "model" crystal. It would be necessary to investigate the wettability behaviour and visualise fluid distribution over detrital quartz grain in porous media without any special preparation or metal coating. A number of sophisticated techniques have been employed to investigate the wettability state in porous media including (i) low field nuclear magnetic resonance (NMR) - capable of providing qualitative and quantitative wettability information and water/organic distribution of a reservoir rock material (Vevle, 2011; Prather et al., 2016), (ii) infrared spectroscopy (IR) and X-ray absorption spectroscopy (XAS) - able to study the local adsorption process at the microscopic level, these are functional group, it is element-selective and sensitive to the local environment(Bantignies et al., 1997; Qi et al., 2013b), and (iii) environmental scanning electron microscopy (ESEM) provides the potential to detect in-situ water "wetting" behaviour of a surface in dynamic experiments in a local environment level and without the additional complexity that results in difficulties in interpreting core-scale during waterflooding experiment (Al-Shafei and Okasha, 2009; Polson et al., 2010).

In this chapter, we present results from investigations on the wettability alteration of pretreated (with oil and model oil compounds) Berea sandstone samples following their interaction with different brine solutions. This was accomplished across several length scales (from macro to microscopic) by using ESEM, and the sessile drop (contact angle) method. In addition, the electrical charge at the oil/brine interface was measured against different brine ionic strengths using the zeta potential technique.The change in the electrokinetical charge of the oil/brine interface is related to the wettability alteration by low salinity water.Finally, spontaneous imbibition experiments were performed on restored Berea core plugs. These included tests at room temperature and at 70°C to macroscopically observe the effects of solution cations (Ca^{2+} and Na^{+}) and ionic strength on the wettability

alteration, and examine the effect of temperature on the performance of the low salinity waterflood(LSW). It should be noted, use of BST rather than cored oil reservoir material for the core-wettability study is crucial because it is commercially accessible, inexpensive, and homogeneous (Potts and Kuehne, 1988).Some reservoirs have the similar range of permeability and porosity as BST (Flores et al., 2008).

6.2. Experimental Section

In this part of the chapter we describe the materials used, experimental procedures, and apparatus used to study the wettability, as well as the zeta potential and to perform imbibition tests are presented.

6.2.1. Materials Used

The basic materials used were:

- Rock: Berea sandstone core plugs from Cleveland Quarries (See Chapter 2).
- Brine: The brines used in these measurements were NaCl, $CaCl_2$ at concentrations of 0.001; 0.01; and 1.0M.
- Oil: Crude oil from North Sea field and model oil compounds (decanoic acid-dodecane).

6.2.1.1. Core Sample Preparation and Characterisation

In this work, Berea cores from Cleveland Quarries are used in this chapter. They have a diameter D of ~2.0 cm, length L of ~ 5 cm, gas permeability k_g of 100-200 mD, and porosity $\emptyset$ ~ 17.0 (which corresponds to sample BST.3, described in Chapter 4). An examination of the morphology of grains and pores in the core samples, as well as an elemental analysis, was carried out using a Hitachi SU-70 high-resolution analytical SEM and integrated energy-dispersive X-ray spectroscopy (EDX) with AZtecEnergy software. Furthermore, the principle of each technique is mentioned in Chapter 2: Methodology and Chapter 3.

SEM analysis of the Berea sandstone sample reveals that a majority of the pore sizes are above several micrometers (Figure 6.1), while XRD confirms that the grains are mainly composed of quartz and alkali feldspar with minor contributions from authigenic clay minerals such as kaolinite and illite, as can be seen in Table 4.5. Additionally, a high-resolution SEM image (see Figure 6.1b) indicates that the studied Berea core sandstone

(denoted hereafter as BST) cores are mineralogically different. Although the SEM/EDX gives significant information on this, the best technique to interrogate the mineralogical composition is the XRD. The figure also shows kaolinite is the dominant clay minerals, and they are likely to be found sat on the surface of the quartz overgrowths. Further details on the bulk and pore-exposed mineralogy are discussed in Chapter 4. In addition, it was observed by means of SEM (uncoated samples, run at low voltage, 5 kV) and AFM that nano mineral phases are present over the pore lining minerals (quartz and clays mostly) as shown in Figure 6.1c. It should be noticed that Hassenkam et al.(2011) demonstrated and founded the role of clay nanoparticles, where attached to the sand grain surfaces, play a vital in the low salinity response in sandstone cores.

Mercury intrusion capillary pressure (MICP) was used to determine the pore size distribution in the samples used in this study. The measurements were conducted on a small piece of BST, representing an off-cut from the core plugs used in the wettability tests. The porosity is 17.2 %, similar to the µ-XCT values shown in Table 3.5.

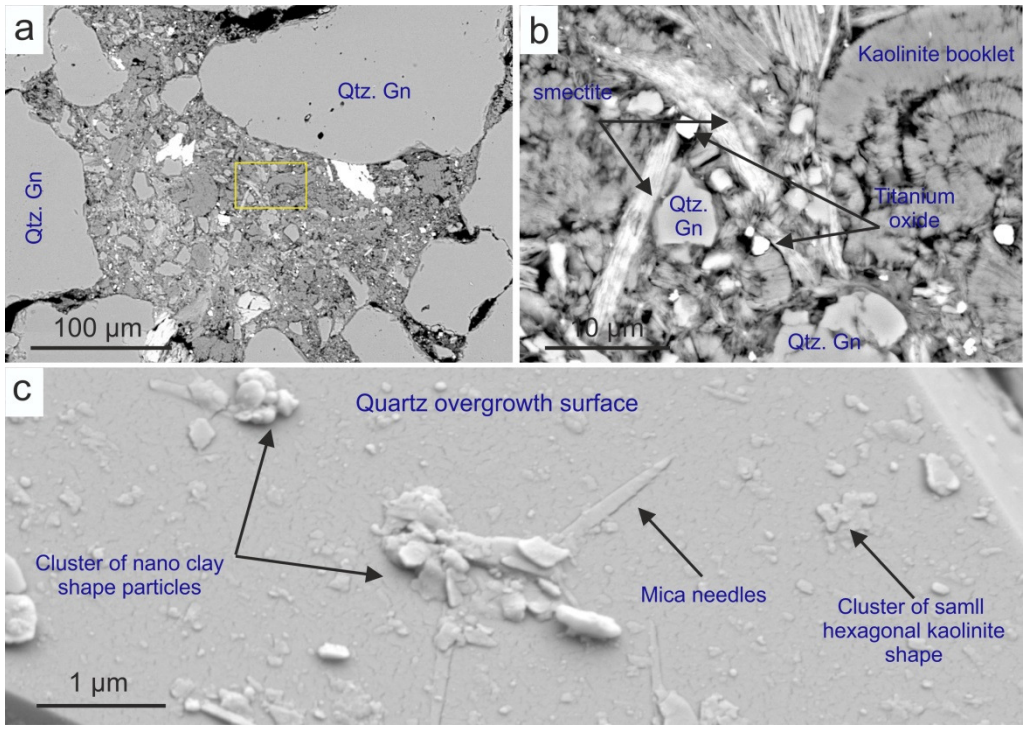

Figure 6.1: (a) SEM of the Berea sandstone with pores shown in black, quartz grains in light gray, and titanium oxide in white Color. (b) Higher magnification SEM image of matrix and porosity between quartz grains. (c) Electron photomicrograph showing the different types of nanoparticles over uncoated quartz overgrowth crystal.

It can be seen from Figure 6.2 that 80% of the pore throat diameter was centred on the 0.3-45.0 µm range, providing the average diameter of 81.07 µm, with 4 % pore of throat diameters below 10 nm. This throat size is smaller than that of some of the nanoparticles observed on quartz overgrowth surfaces, which implies that a small percentage of pore throats could easily be blocked by these clay nanoparticles.

Five sets of BST were prepared in this chapter. In the first set prepared (denoted hereafter as A1), thin slices of BST cores were prepared (all similar and sliced from core samples), each in the order of 10 mm diameter and approximately 3 mm thickness. Care was taken to produce the thinnest possible samples to ensure efficient cooling and maintenance of the correct sample surface temperature by the Peltier stage during ESEM analysis. The Logitech LP50 Lapping was employed for cutting BST core plugs. To avoid cleaning the samples, a new BST slice was invariably used for each of the performed measurements.

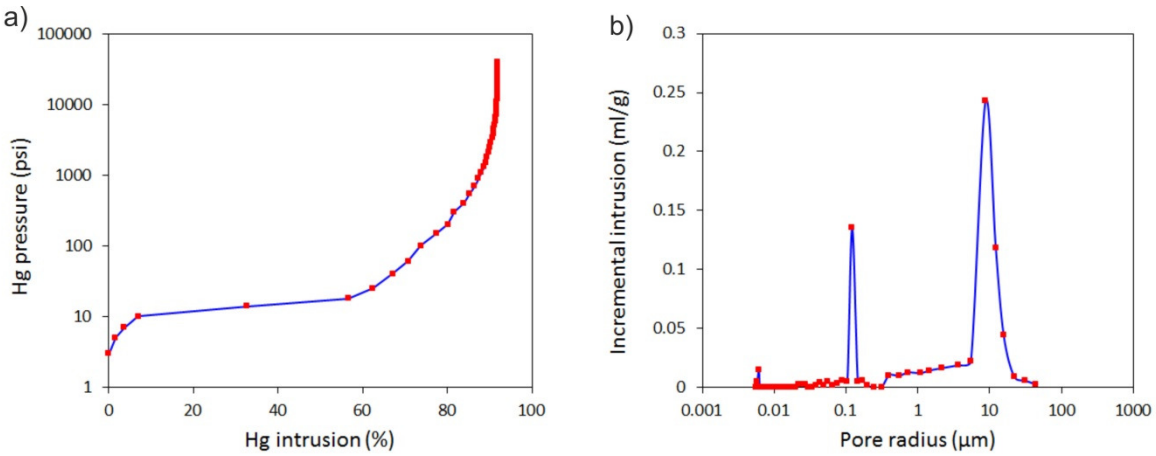

Figure 6.2: Core sample characterization by MICP. (a) Mercury injection capillary pressure curve showing (a) the pressure (y-axis) required to effect a change in mercury saturation in the sample (x-axis) and (b) Inverted pore throat radius spectrum showing a well-defined characteristic pore throat size.

The second sets of samples prepared (denoted hereafter as A2) were for the contact angle measurements using pendant drop shape analyser. In this case, BST core samples were cut and polished into several disks of 20 mm diameter and 5 mm thickness and used to investigate the effect of salinity on contact angle. In order to avoid the effect of surface roughness of pretreated BST slices during pendant drop shape analysis, the surface of BST slices needs to be relatively flat, smooth, and uncontaminated. It is, therefore, more practical to obtain flat surface specimens from relatively large size rocks. The BST core

plugs were cut with thicknesses varying from about 1 cm to about 2 cm using mechanical diamond saws (Logitech LP50 Lapping). The Logitech LP50 Lapping again was employed for cutting smaller size rocks. Although the diamond saws have done an excellent job in creating nice flat surfaces, there were still a few traces on the BST samples caused by the blades. To remove those traces and to reduce the amount of the roughness on the BST samples, a polishing test was undertaken using Buehler Ecomet Automate polishing machine (EcoMet^{TM} 250/300 Grinder-polisher). The polishing device has a circular plate which basically spins with the silicon carbide powder mixed with the water on the plate.

In order to achieve smoother surfaces, glass plates for specific silicon carbide grades were also used. In this stage of the polishing process, the silicon carbide grits were saturated with water on the glass plate surface until the mixture achieved the form of a paste. Then the aggregates were put onto the paste and moved around the surface of the glass with a uniform pressure applied by hand. BST slices were polished using number 220 (66 μm), 400 (22.1 μm), 600 (14.5 μm), and 1000 (9.2 μm) grade silicon carbide grits. The BST slices were also polished with 5-micron aluminum oxide powder in addition to number 220, 400, 600, and 1000 grade silicon carbide grits. The 5-micron aluminum oxide powder has a finer particle size and reduces the surface roughness further. This change has made a considerable difference in repeatability, precision, and standard deviation of contact angle measurements. To minimise the risk of surface contamination, the BST polished slices then were cleaned in an ultrasonic bath of distilled water in order to eliminate traces of the grit powder material. All the test results can be found in the results section.

The technique of polishing the slices is a recommended method from several renowned authors. The surface polishing process was initially suggested in the works of (Busscher et al., 1983), and shortly acknowledged as well as supported by (Vargha-Butler et al.,1986). Recently, (Yuan and Lee, 2013a), have reported that there is not a general guideline as to determine how smooth the solid surfaces must be for it to have an impact on the measured contact angle. Then again, the author recommended the use of a surface that has been prepared as smooth as possible. For such, a different approach was proposed different groups of researchers; and includes heat pressing, dip coating, solvent casting, and surface polishing (Vargha-Butler et al.,1986).

The third set of samples (denoted hereafter as A3) were prepared for TOC measurements, each with a diameter of approximately 20 mm diameter and 20 mm

thickness. The BST core plugs were cut using mechanical diamond saws. During this stage, care was taken to prepare samples with a relatively similar bulk volume. The fourth set of samples is BST grains. BST grains was prepared by grinding a BST core samples in an agate mortar. Also, a portion of the crushed BST samples passed through a 16-mesh mesh screen. Zeta potential measurements were performed on BST grains with a size of 1mm. These measurements were performed on BST grains that have been in contact with crude oil and/ or decanoic acid-dodecane and saline solutions of different ionic strengths. Fifthly, eight core plugs were used for imbibition experiment. Geometry and petrophysical properties of all cores are listed in Table 6.1. Figure 6.3 shows the sealed BST core plugs. The mineral analysis is given in Chapter 4, Table 4.5 and sees Appendix A.2.

Table 6.1: Petrophysical properties of BST core plugs used in the experiments.

Plug Name	Description		Dry weight (gm)	Bulk Volume (cm^3)	PV	Porosity (Ø)	S_{wi} %
	Dimeter (mm)	Length (mm)					
#1	20.0	50.0	33.9	15.7	3.2	20.7	25
#2	20.0	50.5	34.4	15.8	3.4	21.8	25
#3	20.0	50.2	34.1	15.8	3.4	21.6	25
#4	19.9	50.0	34.0	15.5	3.4	22.1	25
#5	20.0	50.0	34.1	15.7	3.4	21.7	25
#6	20.0	50.0	34.0	15.7	3.1	20.0	25
#7	20.0	50.0	34.0	15.7	3.3	20.7	25
#8	20.0	50.0	34.6	15.6	3.5	22.3	25

*PV= Pore volume.

Figure 6.3: Sealed desaturated BST core plugs.

6.2.1.2. Brines Properties

In this work, the brines used in the experiments described here were prepared by dissolving different amounts of chloride salts in MiliQ water. Formation water follows the compositions provided by BP Chapter 5 Table 5.1. In addition, low (0.001 M) and high (1M) concentration solutions were also prepared. The detailed of preparation was presented in the methodology (Section 5.21.3) of Chapter 5. Some of the properties of the low and high brines are also shown in Table 5.2.

6.2.1.3. Crude Oil and Decanoic Acid-Dodecane Properties

In selected experiments from this chapter, crude oil obtained from a sandstone rock reservoir was used. Prior to use, the crude oil was centrifuged for 45 min and filtered, first with a five μm Millipore filter and then a two μm Millipore filter, remove possible particles such as clay minerals that may damage the selected BST core plugs. Density and acidic number (AN) were provided by BP, see Table 5.3. The type of each of the functional groups in crude oil was identified in Chapter 5 (see Section 5.21.3). Additionally, decanoic acid ($C_{10}H_{20}O_2$) was employed as an oil model to represent polar compounds, which was supplied by Sigma-Aldrich. Dodecane ($CH_3(CH_2)_{10}CH_3$) obtained from Sigma-Aldrich, was then used as the non-polar oil component. Concentrations of 1.0 mole/liter decanoic acid- dodecane were prepared. Physical properties of decanoic acid and dodecane are given in Table 5.4.

6.2.2. Experimental Procedure

In this section, details of the laboratory experiments pursued for this chapter are given. Regarding wettability alteration, laboratory studies can provide a measure of oil recovery as a function of the injected brines composition, as well as information about the parameters that may affect the wettability during the brine injectivity process (scaling, and clay minerals mobilisation), and other waterflooding parameters. Finally, it can suggest the optimal chemical composition that induces and additional oil recovery.

6.2.2.1. Water Saturation/Aging/Washing in Berea Sandstone-Chips and Slices.

Initially, sample sets A1 and A3 were placed in a Binder 9030-0030 vacuum oven and dehydrated at 70 °C for 24 hours (see Figure 6.4). The second group of BST samples

(A2) were polished at the rock sectioning laboratory in the Earth Sciences Department at Durham University. Since the slices are dominated by detrital quartz grains, even the polished outer surface would consist of the same type of mineral. After polishing, the surfaces of the slices were cleaned by distilled water not to disturb the original wetting state inside the BST slices (Shabib-Asl et al., 2014), and then placed in a Binder 9030-0030 vacuum oven and dehydrated at 70 °C for 24 hours.Then, all the different sample groups were saturated with formation water by using the vacuum pump for 3 hours until no gas bubbles were exiting the rock slice, as shown in the schematic in Figure 6.4.To change the wettability state of selected BST samples, BST samples were aged in oil or the previously prepared oil-model compounds as follows: each sample in the three different BST groups was placed into a vial. For a sample of BST, 10ml of oil or oil model-compound was needed. This ratio was developed by previous trials and error. It was due to failure to alter the wettability of BST adequately on the early trial runs when smaller quantities of oil (3ml) and oil model compounds (4 ml) were used. Aging was performed after slicing and polishing the samples, as these procedures could have redistributed the brine/oil leading to artifacts and erroneous measurements.

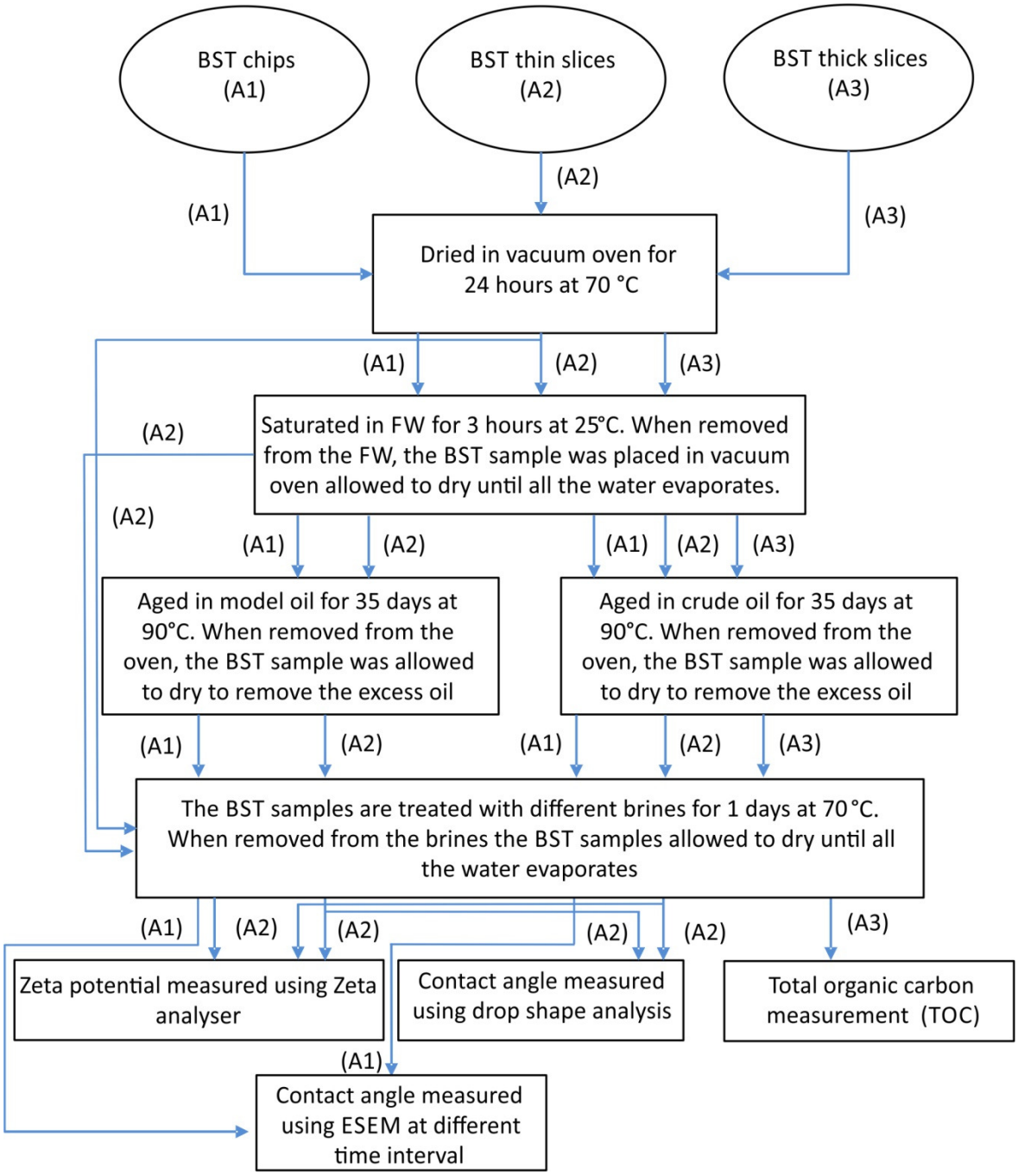

Figure 6.4: Flow chart indicating the different approaches used in Berea sandstone (BST) sample treatment. FW= formation water.

Next, the samples were placed in a Binder VD23 vacuum oven at 90 °C for approximately 35 days. In total, 16 samples of BST particles were prepared, as 8 of them were aged in oil and second half were aged in model oil compounds (see Figure 6.5). It is important to check the wettability of aged BST samples (using drop shape analyser/and or ESEM) before the"washing" procedure (as explained in Chapters 2 and 5) is

performed.This step mimics the reservoir charging process and equilibrates the mineral surface charges in the BST samples.

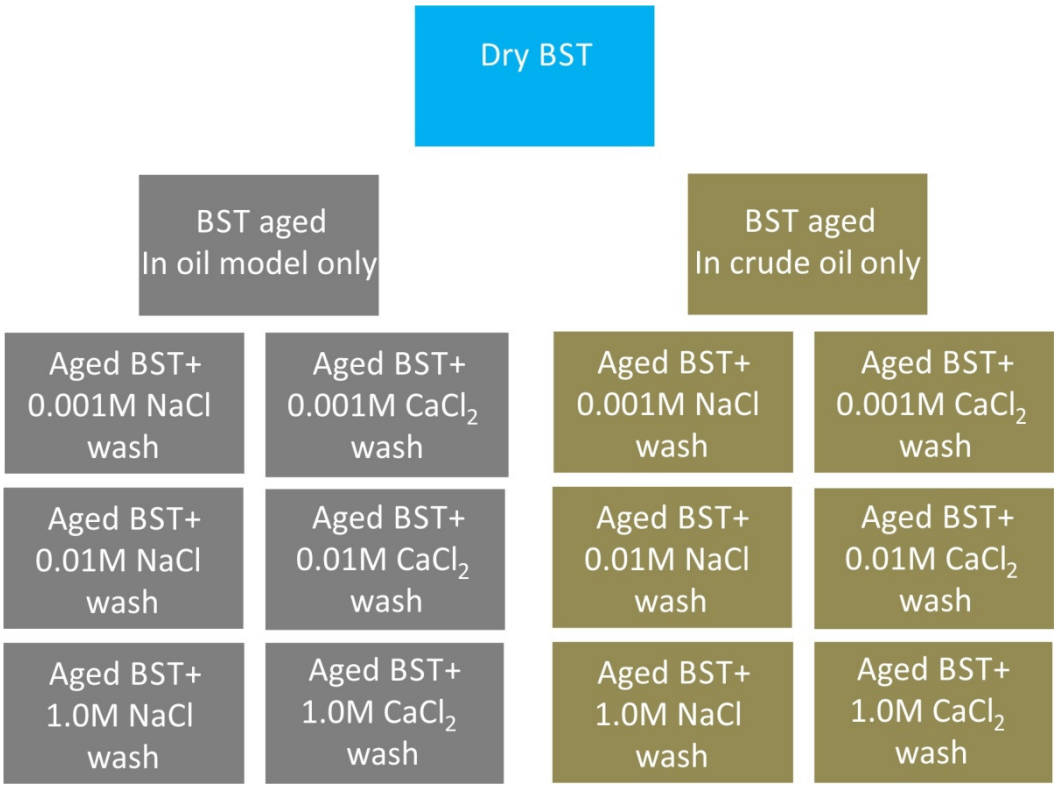

Figure 6.5: Diagram of samples used for laboratory work.

Finally, once all the samples were dried after taken out from crude oil or model oil aging, 15 ml of the relevant brine solution (either NaCl or $CaCl_2$) was added to each corresponding vial (see Figure 6.5). All solutions were regularly filtered (0.2 µm filter) to remove any undissolved impurities. Therefore, in this study, the pH of the brines used in the measurements were not manipulated and set at 6.5 for all solutions by adding a hydrochloric acid for low pH and a NaOH buffer for high pH. All measurements were performed in double repeats to ensure reliability.

6.2.2.2. Berea Sandstone-Core Handling for Imbibition Test

The spontaneous imbibition test is a qualitative method. The wettability determined in this experiment is relative, and only an estimate of alterated wettability can be determined. This experiment consists of two steps; core preparation and spontaneous imbibition. The procedure to prepare the cores used for imbibitions studies is explained in this subsection.

The objective of these experiments was to determine additional oil recovery from BST core plugs, aged with decanoic acid-dodecane, using low concentration (0.01M) of NaCl or $CaCl_2$ solution, where the core plugs were stored first in high concentration (1.0M) solutions. Although eight BST core plugs, #1 through #8, were prepared, only four were used in this work. Their physical properties are reported in Table 6.1. The facts behind BST core preparation is to restore the BST core samples back to its reservoir wettability state (which in this experiment is oil-wet using 1.0M of decanoic acid-dodecane) and saturation water state (connate water saturation). A core flooding apparatus was used for forced imbibition, where here we are interested in spontaneous imbibition. BST core is placed in the imbibition flask for spontaneous oil imbibition for an approximate time of six weeks. Below are the steps followed the BST for these tests.

6.2.2.2.1. Water saturation

All the cores, were initially dried in a Binder VD23 vacuum oven at 70 °C for 24 hours and weighted before each test and evacuated through the syringe, as shown in Figure 6.6. As soon the pressure gauge had attained a stable minimum value, the formation brine was introduced into the conical flask to saturate the BST core. After this, the weight of the saturated core was measured.

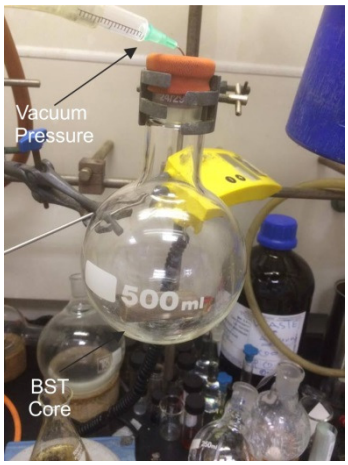

Figure 6.6: Saturation of BST core plug under vacuum pressure.

6.2.2.2.2. Pore Volume and Porosity Measurements

The pore volume calculation is based upon the weight difference between the dry and 100% saturated core and the measured density of the North Sea formation water (FW). The pore volume of the core is expressed by equation 6.1.

$$PV = \frac{W_s - W_d}{\rho_{North\ Sea\ FW}} \quad (6.1)$$

Where:

- PV =Pore volume of the core (cm^3)
- W_s =Weight of BSTcore 100% saturated with North Sea FW (g)
- W_d =Weight of dry BST core (g)
- $\rho_{North\ Sea\ FW}$ = Density of North Sea FW (g/cm^3)

The porosity calculated in this way is a measure of the pore volume that is capable of holding fluids in a BST core and can be defined as the percentage of void per 100% volume of material. The porosity is arithmetically expressed by equation 6.2 (Dandekar, 2013). The bulk volume/total volume of the core was calculated by Equation 6.3.

$$\emptyset = \frac{PV}{V_b} \times 100\% \quad (6.2)$$

Where:

- $\emptyset$ = Porosity of core (%)
- PV = Pore volume of the core (cm^3)
- V_b = Bulk volume of the core (cm^3)

$$V_b = \pi h r^2 \quad (6.3)$$

Where:

- V_b = Bulk volume of the core (cm^3)
- h = Height of the core (cm)
- r = Radius of the core (cm)

6.2.2.2.3. Initial Water Saturation

The initial water saturation (S_{wi}) of the BST cores was decided to be 25%. In actual reservoirs composed of porous rock, water saturation becomes relatively immobile, when water saturation reduces to 5-40 % (Ahmed, 2010). To replicate a sandstone reservoir conditions, S_{wi}=25% was achieved in all BST core plugs; formation water-saturated BST cores were desaturated on the unconfined porous plate at BP's Laboratory to that specific value. Although the procedure is not published, the BST core plugs were delivered in a sealed container, in contact with formation water. This was done to avoid evaporation and

release of further FW from the cores, which will result in a non-uniform distribution of S_{wi} across the core interior.

6.2.2.2.4. Oil Saturation

After an uniform S_{wi} throughout the BST, the core was obtained, it was then placed in a custom-made core holder (designed by Prof Chris Greenwell's group and fabricated in the Department of Physics's workshop at Durham University). The detail of the core flooding apparatus is discussed in the next section. Before flooding with the oil compound, the BST core plugs were placed under vacuum for 5 minutes, then a gas cap pressure (100 psi of N_2 gas) was applied. The vacuum helps remove trapped gas from the cores before decanoic acid-dodecane flowing. After this, the core was placed inside the flooding apparatus, and decanoic acid-dodecane was flown through to fully saturate with model oil (with the S_{wi} in place). In this work, a Leverett J-function was used to calculate the differential pressure between FW and decanoic acid-dodecane (see Equation 6.4) (Brown, 1951). This was the pressure applied during decanoic acid-dodecane flooding without displacing the S_{wi} in the desaturated BST plugs.

$$S_w = \frac{0.2166\, P_c}{\rho \cos(\theta)} \sqrt{\frac{K}{\emptyset}} \qquad (6.4)$$

Where:

- S_w =Leverett j-function.
- P_c =Capillary pressure,(psi).
- ρ =gas/water interfacial tension,(dyne/cm).
- θ =Contact angle.
- K =Permeability, (mD).
- $\emptyset$ =Porosity.

The interfacial tension (IFT) of nitrogen gas (N_2)/water was calculated to be a 69 mN.cm-1 at room temperature. Also, the contact angle of brine/ decanoic acid-dodecane was calculated to be 25.98° at room temperature.

The detailed procedure for oil flooding was as follows:

1. The desaturated BST core plug was loaded into a rubber sleeve with metal end pieces, which housed the fluid flow lines, and then the end pieces cable tied at both ends as shown in Figure 6.7.

2. Once assembled this was loaded into a core holder vessel, and a confining pressure of 300 psi was applied with hydraulic oil.
3. Decanoic acid-dodecane was injected from one side (inlet to outlet) with a rate of 0.1 ml/min, which is considered sufficient to create a one dimension horizontal flow.

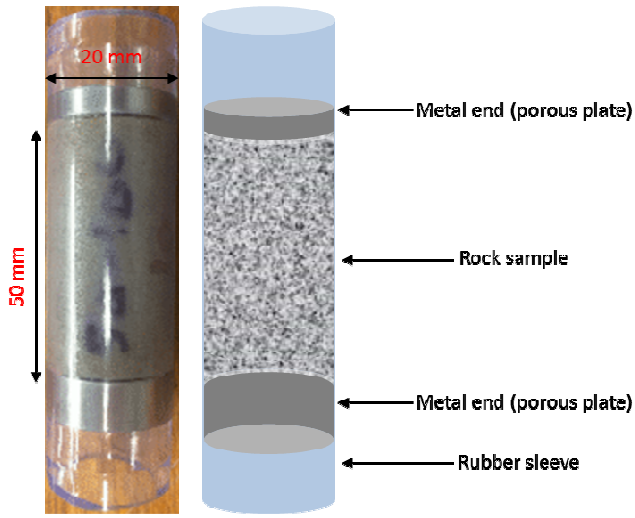

Figure 6.7: Image shows BST plug sample is loaded into a rubber sleeve with metal end pieces, housing the fluid flow lines which are cable tied at both ends.

4) The decanoic acid-dodecane injection was continued for six hr in each of the BST samples; this means that the decanoic acid-dodecane saturation has been reached for all BST plugs, and the cores were now ready for aging. Figure 6.8 illustrates a setup schematic of the setup of the saturation apparatus.

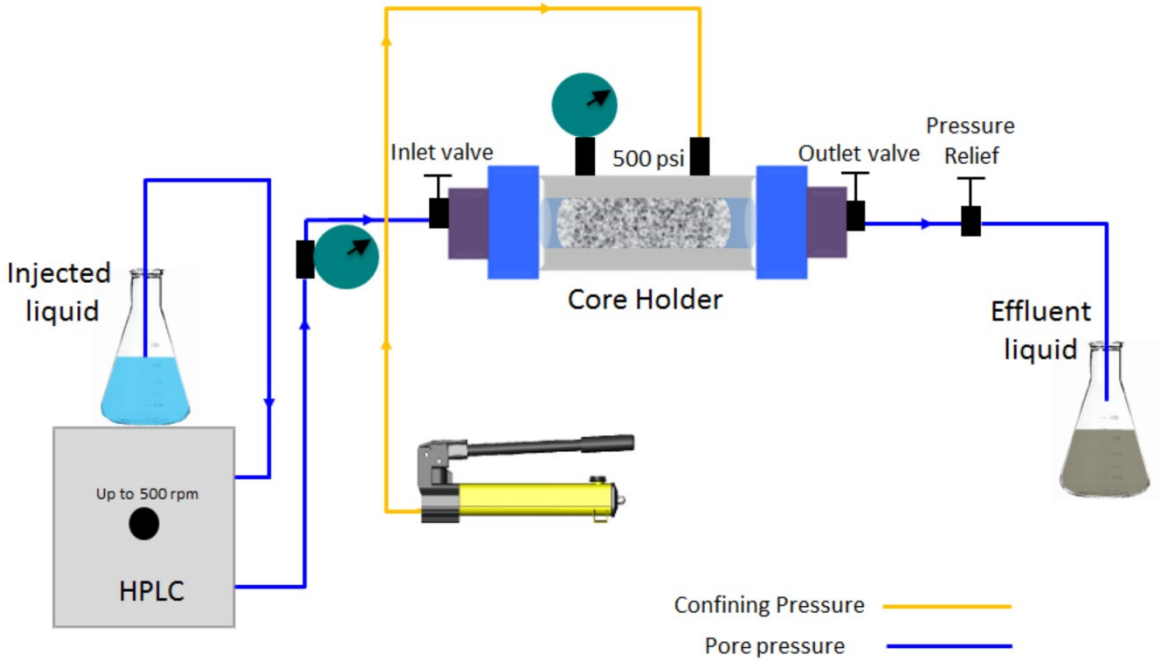

Figure 6.8: Illustration of oil saturation setup. The BST core plug was placed in the core holder, and the HPLC pump flooded the core with decanoic acid-dodecane. The floodingpath was regulated by opening and closing the valves accordingly. Back-pressure was regulated using a pressure relief valve.

Figure 6.8 shows the core flood equipment in this study as it consisted of a core holder, a high-performance liquid chromatography (HPLC) pump, a hydraulic pump, a back pressure (pressure relief) and accumulators. The BST core plugs were essentially placed in the core holder, a cylindrical core holder used in this study operates at up to 500 psi. The accumulator cell contains the decanoic acid-dodecane utilised for the flooding and is connected to the core holder. The confining pressure is applied to give a good seal between the core holder and the rubber sleeve (see Figure 6.7), and the backpressure is used to avoid any gas problems in the system.The instrument is connected to two pressure supplies one of 100 psi for the flowing decanoic acid-dodecane and one of up to 400 psi for the confining pressure. The pressure stability of the system is controlled by a valve, which enables control of the exchange the flow rate

6.2.2.2.5. Oil Aging

After the BST core plugs had been saturated with decanoic acid-dodecane and FW, the next step was aging the flooded BST cores. The aims of the aging process were to replicate an initial wetting condition similar to those found in the oil reservoir, i.e. making the decanoic acid-dodecane adsorb onto the mineral surfaces (i.e. oil wet). This will make

it possible to see a wetting alteration towards a more water-wet rock surface during the imbibition test. The saturated BST cores were wrapped in Teflon tape and placed in a steel aging cell that was already full of decanoic acid-dodecane. Details of the aging cell and set-up can be seen in Figure 6.9. The cores were then kept at the selected aging temperature of 120°C for ten weeks. A pressure of 100 psi N_2 gas pressure was applied to prevent boiling of formation water since the aging temperature is above the boiling of the initial water (100°C), and in order to prevent evaporation of oil's volatile components.

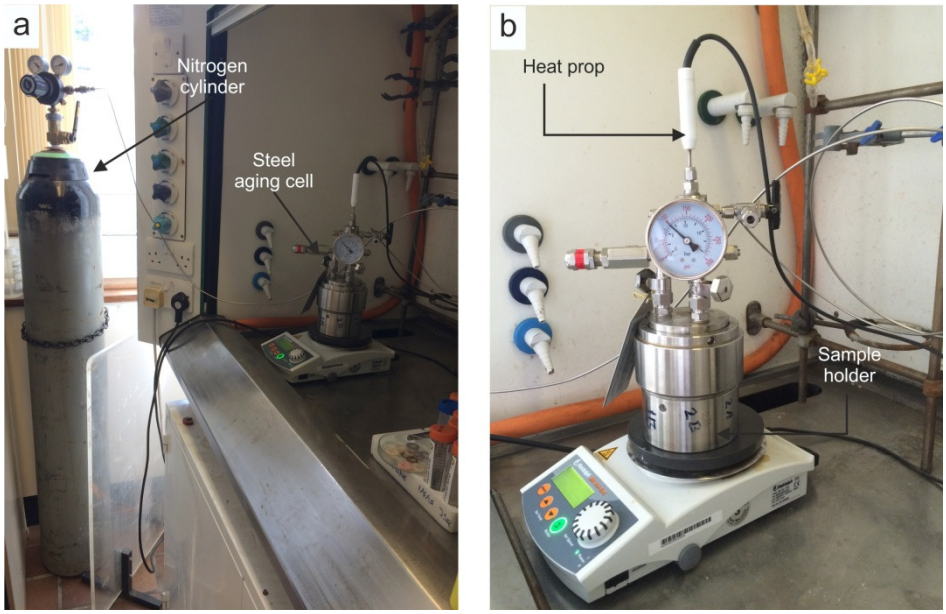

Figure 6.9: a) Aging BST core under reservoir temperature showing the full set up (120 °C) and b) a close up if the steel aging cell.

6.2.2.2.6. Oil Recovery Experiments

Long-term spontaneous imbibition studies were performed at room temperature and pressure for the #1 and #2 restored BST core plugs (Swi = 25% aged in decanoic acid-dodecane) in the imbibition cells for an approximate time of 45 days (Figure 6.10a). In this test the wetting fluid (brine) spontaneously imbibes into the pore spaces and displaces the less-wetting fluid (decanoic acid-dodecane) from the pore spaces of the aged BST core plugs. Initially, the #1 and #2 aged-BST core plugs were placed for 45 days in the high concentration (1.0M) of NaCl and $CaCl_2$ solutions, respectively. Then, both core plugs were placed in a low concentration (0.01M) of NaCl and $CaCl_2$ solutions. Depending on the efficiency of brine uptake, this experiment continues for 1-2 months until no more decanoic acid-dodecane (oil model compounds) was expelled from the plugs.

In a further experiment, in order to run the test in reservoir temperature, imbibition experiments were conducted at (70°C), by placing the imbibition flask (cells) in MOV-112-PE Electric Oven, as shown in (Figure 6.10b). Otherwise, these experiments well performed in the same way as the room temperature tests, where high brines (1.0M) of NaCl and $CaCl_2$ and low brines (0.01) of NaCl and $CaCl_2$ were used. In both cases where the imbibition tests were continued after the production plateau had been reached, the BST cores were transferred carefully from high concentration to low concentration of brines. The produced amount of decanoic acid-dodecane was read off the burette and used to calculate the oil recovery. The model oil recovery and original oil model compounds in place have been computed using Equation 6.5 and Equation 6.6.The amount of decanoic acid-dodecane spontaneously imbibed by the BST core plugs were noted daily and is listed in Appendix C.4.

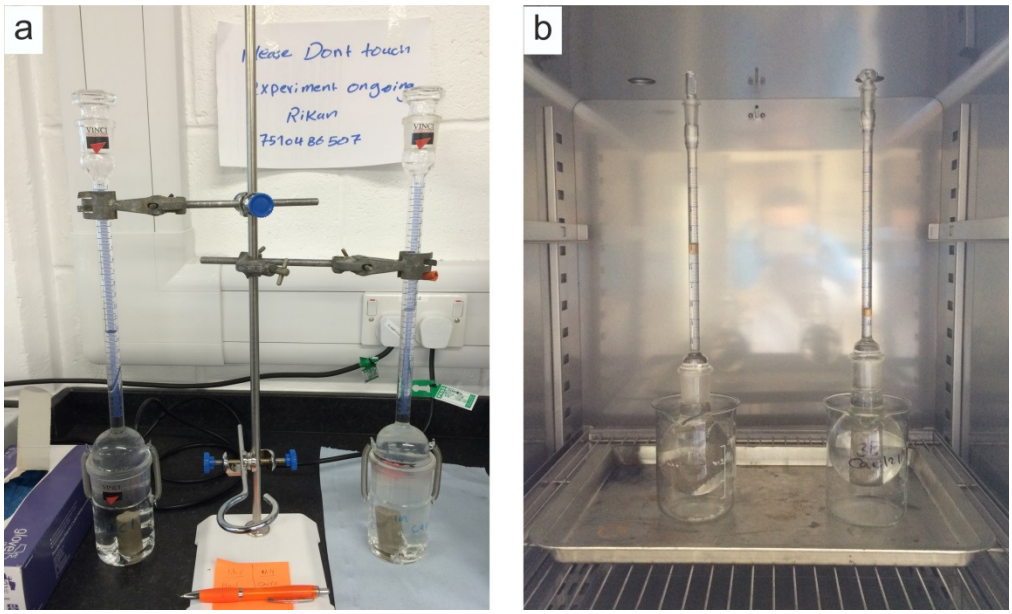

Figure 6.10: Imbibition flasks with BST core plugs under spontaneous imbibition showing: a) Imbibition flask showing BST and decanoic acid-dodecane produced by spontaneous imbibition with 1.0M of NaCl and $CaCl_2$ at room condition: b) Imbibition flask showing BST and decanoic acid-dodecane produced by spontaneous imbibition with1.0M of NaCl and $CaCl_2$ at 70 °C.

$$\text{Recovery}\ (\%) = \left(\text{Amount of oil}\ \frac{\text{produced}}{\text{OOIP}}\right) \times 100\% \qquad (6.5)$$

$$\text{OOIP} = (1 - S_{wi}) \times \text{PV} \qquad (6.6)$$

Where:

S_{wi} = Initial water saturation.
PV = Pore volume of the core (ml).

The results are presented as plots of oil recovery versus time in the following section. The recovery factor was calculated by using equation 6.7.

$$R = \frac{V_{prod}}{OOIP} \times 100\% \quad (6.7)$$

Where:

R = Oil recovery factor (%).
V_{prod} = Volume of oil produced (ml).
$OOIP$ = Original oil in place (ml).

6.2.3. Experimental Apparatus

In this chapter, a range of optical techniques, surface chemical techniques and core flooding equipment was used to analyse the wettability states of the BST in the presence of low and high concentrations of NaCl and $CaCl_2$ at scales ranging from micrometer to core scale.Full details of the instruments used are presented in Chapter 3.

6.2.3.1. Environmental Scanning Electron Microscopy

Environmental scanning electron microscope (ESEM) analysis was used for performing contact angle measurement. An FEI/Philips XL30 ESEM equipped with GSED and a Peltier stage capable of operating at +/-20 °C from ambient temperature (maximum range -5 °C to +60 °C). With the correct balance of temperature, pressure, and humidity, this is a system capable of condensing water onto a cooled solid surface, including samples of BST. A summary of the experimental sequences used is described in Chapter 5.

6.2.3.2. Drop-Shape Analyser

The wetting behaviors of BST were characterised using a commercial contact angle goniometer (Kruss DSA 100) (see Figure 5.6). The measurement is based on the sessile-drop method using aqueous drops placed on the solid substrate. The detail of the experimental process is described in Chapter 5. The contact angle of the drops was extracted from video snapshots using the tangent-fitting method in the data analysis

software provided with the instrument. Contact angles can be determined with a relative accuracy of ± 2°.

2.3.3. Organic Matter Quantity.

In this work, total organic carbon (TOC) of the untreated and treated BST thick slices (A3) in crude oil was measured by a Costech Elemental Analyser (ECS 4010) connected to a ThermoFinnigan Delta V Advantage isotope ratio mass spectrometer. For these measurements, thick BST slices each in the order of 20 mm diameter and approximately 20 mm thickness where aged in crude oil, after this half of the slices were kept and the other half were washed with low and high concentrations of NaCl and $CaCl_2$ brines. The slices were then dried and ground to a fine powder using an agate mortar and pestle. Approximately 10 mg of BST powder was then weighed out into tin capsules with no extra treatment and measured for TOC. Total carbon was obtained as part of the isotopic analysis using an internal standard (Glutamic Acid, 40.82 wt% C). Analytical error for the determination of wt% C was <0.3 wt%.

6.2.3.3. Zeta Potential Analyser

The surface charge and the surface potential of the solid/water (or oil/water) interfaces were determined by streaming potential measurements using an electrokinetic analyzer for solid surface analysis (SurPASS). A dilute electrolyte is circulated through the measuring cell containing the solid sample, thus creating a pressure difference. A relative movement of the charges in the electrochemical double layer occurs and gives rise to a streaming potential. This streaming potential, sometimes called the streaming current, is detected by electrodes placed on both sides of the sample (see Figure 5.10). Measured ζ potentials are converted to (diffuse layer) surface charges using Grahame's equation, more details on this can be found on Chapter 3 Section 3.9.4.

6.3. Results and Discussion

In the following subsections, the results of contact angle observations at the micro and macro scale, TOC measurements, ζ-potential measurements and spontaneous imbibition tests of BST are presented and discussed in the presence of low and high concentration of NaCl, and $CaCl_2$ solution. The main objective of this set of measurements is to investigate the wettability alteration by the change of water salinity and its relation to improved oil recovery during low-salinity water injection. Moreover, the effects of

temperature are discussed to investigate the efficiency of low-salinity water at different conditions. The pH of the brines used in measurements was not manipulated; pH is 6.5.

6.3.1. Contact Angle Measurements

The salinity effects on the wettability of a ternary system with BST in contact with brine and decanoic acid-dodecane and crude oil, respectively were tested. Brines of NaCl and $CaCl_2$ with a concentration of 0.001 to 1M were studied. The wettability was examined by both the pendant drop shape technique and the ESEM techniques. It should be noted, each measured data point in these two approaches is the average of at least three independent measurements. In addition, along with each data point, error bars are illustrated for better comparison between the various cases.

6.3.1.1. Drop-Shape/ Contact Angle Measurements

As it is stated earlier, pendant drop shape was used to image a droplet of water formed over a pre-treated and polished Berea sandstone surface. Prior to the measurements the samples were "flushed" with a brine of either $CaCl_2$ or NaCl of different concentration. The results of these macroscopic observations were divided into two sub-sections to examine the wettability behavior in aged-BST slices contacted with decanoic acid-dodecane and crude oil, respectively.

6.3.1.1.1. Macroscopic Observation of Aged Berea Slices in Decanoic Acid-Dodecane

To investigate the role of polar compounds on the wettability behavior of the BST surfaces, decanoic acid-dodecane was used as a model oil compound. Images of water droplets on the surface of the BST slices, "washed" with brines of different concentrations at room temperature and pressure, are shown in Figure 6.11. The figure shows a comparison between the contact angles of a water droplet with a high and low concentration of NaCl solution and $CaCl_2$ solution in the BST aged in decanoic acid-dodecane. The average of several readings obtained from each droplet was calculated and its shown in Table 6.2. All readings are listed in Appendix C.1. From the images, it can be clearly seen that there is a drastic decrease in the measured contact angle when the concentration of the NaCl brine (used to "wash" the surfaces) is decreased. Specifically, it dropped from a measured 101° using 1 M NaCl to 24° when using a 0.001M solution.

These results imply that the wettability of the BST was altered to more water-wet by exposure to NaCl solution at a concentration of 0.001M.

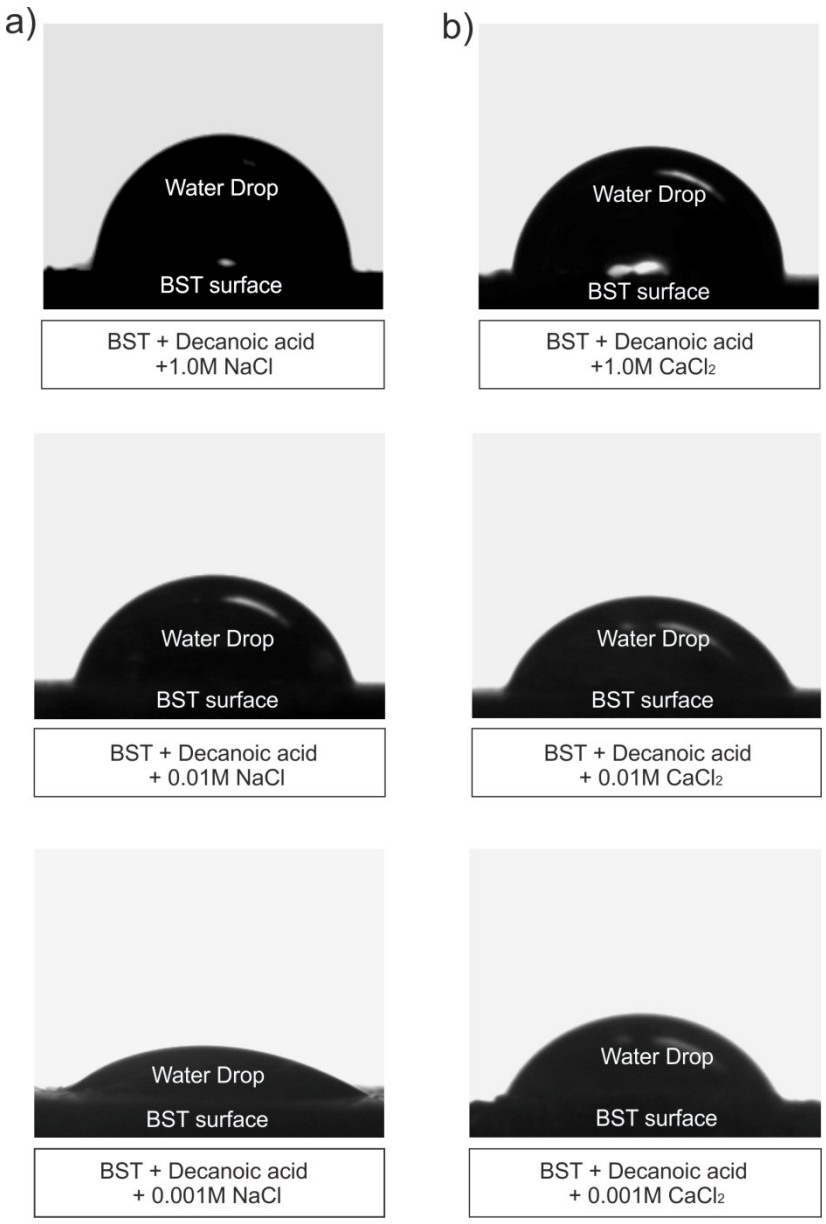

Figure 6.11: Contact angle optical images of water droplet on BST aged in decanoic acid-dodecane at room tempreature and pressure showing a) BST aged in decanoic acid-dodecane exposed to various NaCl concentrations; b) BST aged in decanoic acid-dodecane exposed to various $CaCl_2$ brine. These images were scaled up from the real size of 2.5±0.5 mm 2.5±0.5 mm.

Pictures of water droplets on the BST aged in decanoic acid-dodecane, after treatment with $CaCl_2$ solution at different concentrations, are shown in Figures 6.11b. The figure shows that the contact angle also decreases in value with a decrease in brine concentrations. As the concentration of $CaCl_2$ solution decreased from 1M to 0.001M, the average contact angle of the water droplet decreased from 93° to 66°.This implies that

wettability of the BST was altered to intermediate water-wetting by a low concentration of the $CaCl_2$ solution. This is the same trend observed for NaCl, but in this case, the total decrease in contact angle was of 27°, which is approximately 35% of the 77° decrease measured when using NaCl.

Table 6.2: Average contact angle of water droplets on BST aged in the decanoic acid-dodecane of NaCl solution and $CaCl_2$ solution along with their uncertainties at different concentrations.

Brines mol.kg-1	**NaCl**	**$CaCl_2$**
	Decanoic acid-dodecane	
	Theta (M) [deg]	**Theta (M) [deg]**
0.001	24.20	66.73
0.01	79.21	70.37
1	101.4	93.17

The average values of three different droplets at separate positions over each BST sample were plotted versus different brine salinities in Figure 6.12. This figure depicts the results of the six experiments to provide a complete picture of the effects of water salinity on contact angle. Figure.6.11 exposes significant features such as (1) there is a systematic effect of brine salinity on contact angle; (2) contact angle decreases as the brine concentration decreases; (3) the brine concentration has a characteristic point (at 0.001M NaCl solution) at which the water droplet was more spread on the aged BST surface, and (4) there is a constant decrease in the three solutions tried for both types of cations. In general, results in this set of experiments show a reduction in contact angle for all tested water droplet with the increase of water salinity over the range of 0.001M –0.01M.

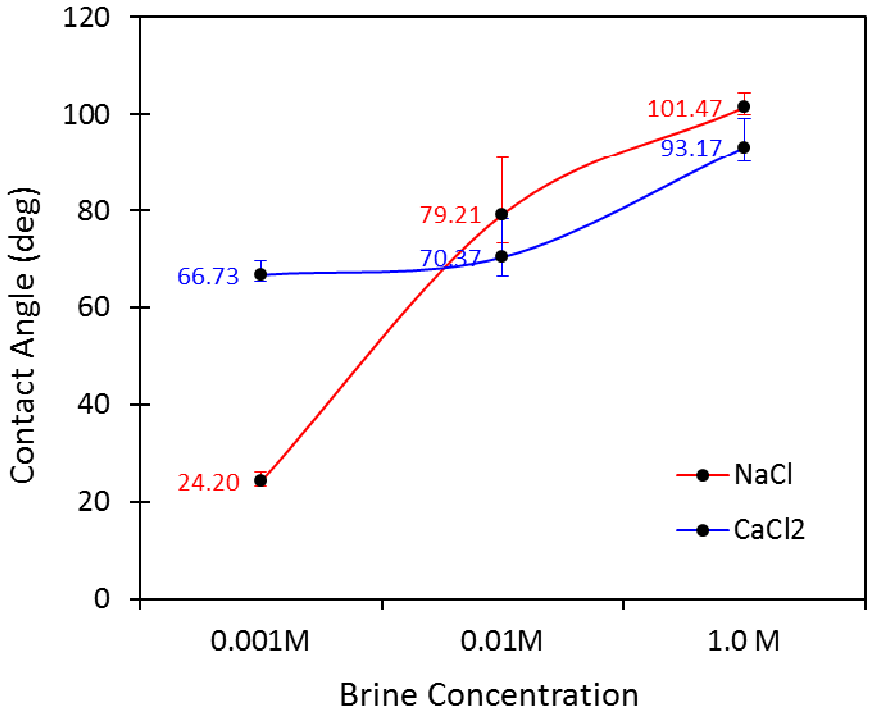

Figure 6.12: The average contact angle is plotted versus the ion concentration and shows the wetting states at the decanoic acid-dodecane BST surface at room tempreature and pressure. Error bars indicate standard deviations of several droplets.

A close examination in Figure 6.12 demonstrated that the contact angle of a water droplet is independent of NaCl concentration and drop is larger for Na^+, whereas the contact angle of a water droplet decreases as the concentration $CaCl_2$ salt in the solution decreases to 0.1M. However, a further decrease of $CaCl_2$ concentration to values lower than 0.01M causes a reverse trend. In other words, as the salinity decreases from 0.01M to 0.001M of $CaCl_2$ has almost no effect on the contact angle measured. It is also worth mentioning that, the system may be very sensitive to small differences in concentration at low concentrations. This shows that decanoic acid-dodecane is harder to desorb at $CaCl_2$ solution. Similar trends have also been observed in previous studies (Leirvik, 2010; Bera et al., 2016). These results are in agreement with the "expected" low-salinity effect as a decrease in the concentration/ion strength of the solution leads to a more water-wet surface. Also, it fits with the expectation that the presence of Ca^{2+} ions reduces the effectiveness of the low salinity solution in releasing oil from the reservoir (Rezaeidoust et al., 2010).

6.3.1.1.2. Macroscopic Observation of Aged Berea Slices in Crude Oil

Crude oil composition is, to some extent, dominated by polar organic compounds and thus it might be expected to behave similarly to decanoic acid-dodecane; to test this hypothesis, the same contact angle measurements described above were performed on crude oil-aged BST samples. Pictures of the water droplets on the surface of the BST slices, after being treated with NaCl and $CaCl_2$ brines at different concentrations, at room temperature and pressure, are shown in Figure 6.13.

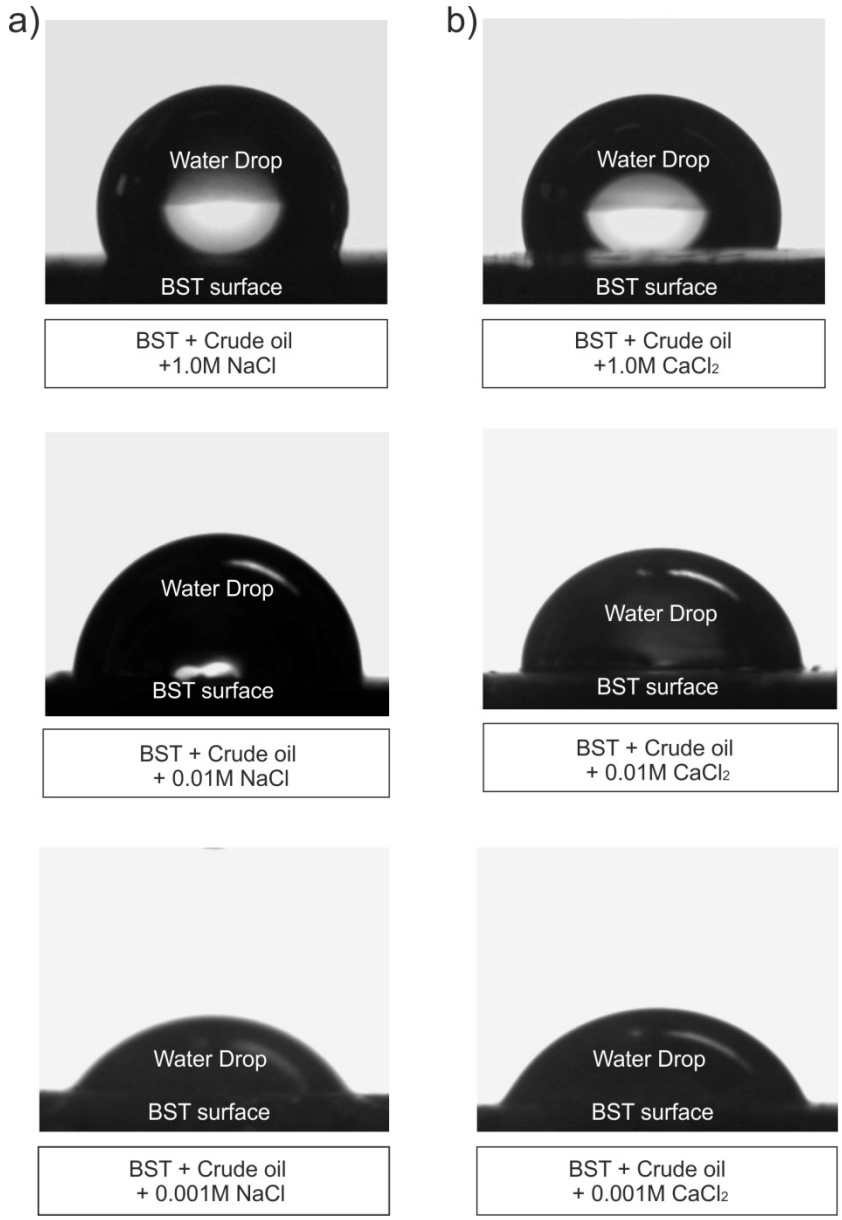

Figure 6.13: Contact angle images of water droplets on BST aged in crude oil at room tempreature and pressure. a) BST aged in crude oil during exposed to various NaCl concentrations. b) BST aged in crude oil exposed to various $CaCl_2$ concentrations. These images were scaled up from the real size of 2.5±0.5 mm 2.5±0.5 mm.

As was the case with the experiments performed with decanoic acid- dodecane, three different droplets were measured at separate positions over each BST sample, and then the average measurement was calculated and reported in Table 6.3. All measurements performed are listed in Appendix C.1.

Results show that the measured contact angle of the water droplet decreases from 131°, when the sample was treated with 1M NaCl to 41° when "flushed" with 0.001M NaCl, as shown in Figure 6.13a. This indicates that the wettability of the BST is heavily altered to be more water wet when decreasing the NaCl concentration, once again confirming the low salinity effect (Zekri et al., 2003; Shedid and Ghannam, 2004; Bera et al., 2012b).

Table 6.3: Average contact angle of water droplets on aged BST in crude oil of NaCl and $CaCl_2$ along with their uncertainties at different concentrations.

Brines mol.kg-1	**NaCl**	**$CaCl_2$**
	Crude oil	
	Theta (M) [deg]	**Theta (M) [deg]**
0.001	41.02	69.98
0.01	93.98	81.55
1	131.1	113.6

Images of water droplets on the BST aged in decanoic acid-dodecane, after treatment with $CaCl_2$ at different concentrations, are shown in Figures 6.13b, whereas the average contact angle values are shown in Table 6.3. Results show that the measured contact angle also decreases as the $CaCl_2$ concentration is decreased, going from 113° on those samples treated with 1M solutions to 70° on those treated with 0.001M solutions. This, again, implies that wettability of the BST was altered to a more water-wet state by a lower concentration of the $CaCl_2$ solution. The average values of contact angles of this group of experiments were plotted versus the different brine concentrations in Figure 6.14. This figure depicts the results of the six experiments to provide a complete picture of the effects of solution salinity on contact angle.

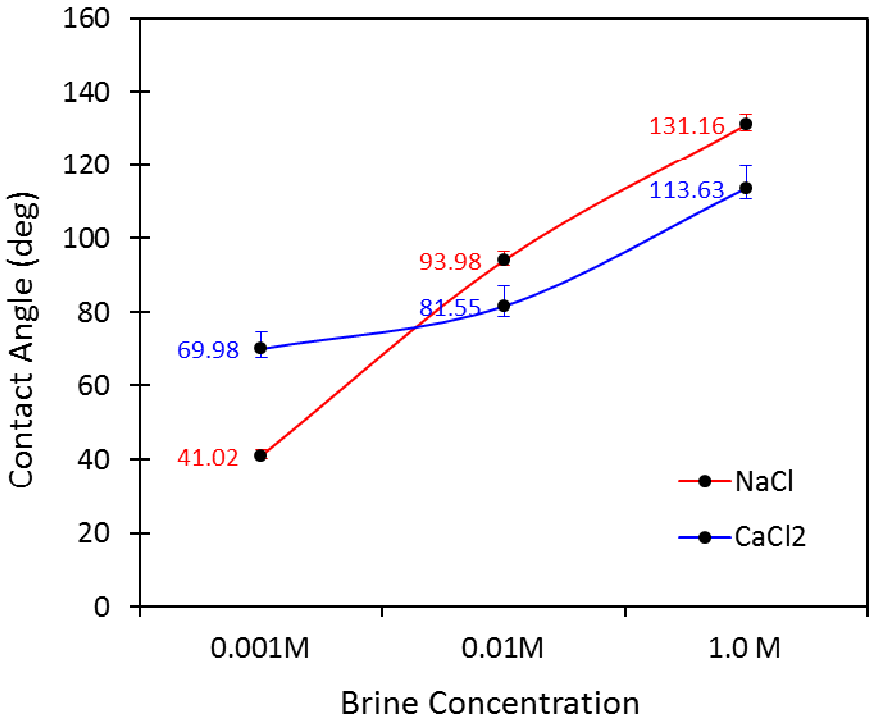

Figure 6.14: The average contact angle is plotted versus the ion concentration at crude oil shows the wetting states at BST-crude oil aged surfaces at room tempreature and pressure. Error bars indicate standard deviations of several droplets.

Figure.6.14 reveals significant features such as (1) there is a systematic effect of brine salinity on contact angle; (2) contact angle decreases as the brine concentration decreases from 1M to 0.001M; and (3) The total contact angle drop of NaCl-treated samples was 90°, which is more than twice of that measured for $CaCl_2$ treated samples (44°). The behavior of the measured contact angle on the BST surfaces when changing the brine matched the data reported by Buckley et al., (1996). They found that a water film is more stable at solutions of 0.1M NaCl, and this stability resulted in more water wet conditions.

As noted above, the $CaCl_2$ brine has a much smaller impact on reducing the contact angle, when compared to the NaCl solution, a behaviour that mimics that observed on the samples aged in decanoic acid-dodecane. This is a very important result as it not only corroborates the low salinity effect on a crude oil-aged sample, but also indicates that the use of decanoic acid-dodecane as a model oil compound on wettability-alteration experiments is valid. The results also indicate that the polar-acid groups are crucial in determining the wettability of the reservoir rock. These results suggest that the polar-acid groups, such as carboxylate, adsorb onto negatively charged mineral surfaces in BST

samples also through calcium bridges and reducing salinity is able to increase the electrostatic repulsive forces between mineral surfaces and carboxylate groups and then break calcium bridges to change the wettability behaviour of the BST surface to be more water-wet. These finding is supported by an experimental studies(Qi et al., 2013b; Yang et al., 2015). Finally, the observed trends are in agreement with findings in the literature of the wettability behaviors in sandstone rock. Alotaibi et al., (2010) investigated the effect of brine salinity on contact angle measurements by using two types of sandstone as rock surface, and three different brine solutions such as NaCl, $CaCl_2$, and $MgCl_2$. The researchers reported that the brine salinity had an effect on the rock wettability and that this impact is also related to the rock's mineralogy.

6.3.1.2. Environmental Scanning Electron Microscopy/ Contact Angle Measurements

In order to further investigate the role brine composition in the wettability of aged BST samples, experiments were performed using ESEM to obtain complementary information at the microscale.The ESEM was used to image the condensation process of water on polar compounds in both the oil model compound (decanoic acid in dodecane) and crude oil in detail on quartz surfaces.The average contact angle, which was also made of quartz crystal see Chapter 5, is representing a three droplets to provide a complete picture of the effects of brine salinity on wettability alteration in a different time interval. Due to instability in water droplets on quartz overgrowth in BST samples, the stabilized values of contact angles at the end of each experiment were selected to represent the wettability behaviour. The results of this microscopic observation were again divided into two sub-sections to examine the wettability behavior in BST slices aged with either decanoic acid-dodecane or crude oil, respectively.

6.3.1.2.1.Microscopic Observation of Berea Slices Aged in Decanoic Acid-Dodecane

Figure 6.15 shows ESEM photomicrographs of aged BST samples pretreated with NaCl (1M and 0.01M) before and after water condensation. Figure 6.15a shows an ESEM micrograph of a pretreated specimen (0.01M of NaCl) before the condensation process. The micrograph shows the presence of decanoic acid-dodecane over several quartz grains which clearly indicates that an oil-wet surface is retained, to some extent, after exposure to the 0.01 M NaCl brine. Condensation was started using the method described in Chapter 3,

and in this case, the formation of droplets was observed after 5.5 Torr have been achieved. ESEM micrographs taken after condensation (Figure 6.15b) show two different wetting behaviors coexisting in the imaged area.The first is represented by the formation of a water film across several mineral grains (right part of Figure 6.15b). A different wetting behaviour on the left part of the image is clear from the formation of well-defined water droplets over several quartz grains. These, high-contact angle water droplets indicating that certain grain surfaces remain primarily hydrophobic while the very low-angle droplets or films fo water relate to a more water-wet condition. The decanoic acid-dodecane coatings are on dertial quartz overgrowth crystal and apparently closely associated with clays, possible kaolinite as the clay morphology.

For the experiment performed with a high concentration (1.0M) solution, the condensation of water started to be observed after 6 Torr, as is shown in Figure 6.15.d. The pretreated sample is shown in Figure 6.15c. The ESEM micrograph in Figure 6.15d shows a series of well-defined water droplets that have nucleated over quartz surfaces. Some other areas of the image (left part) show the formation of a water film. The average measured contact angle for the water droplets is approximately 93^{o}, which represents an intermediate wetting condition in 1.0M of NaCl solution. The behavior in this sample is trapped water droplets with high contact angles surrounded by decanoic acid-dodecane.

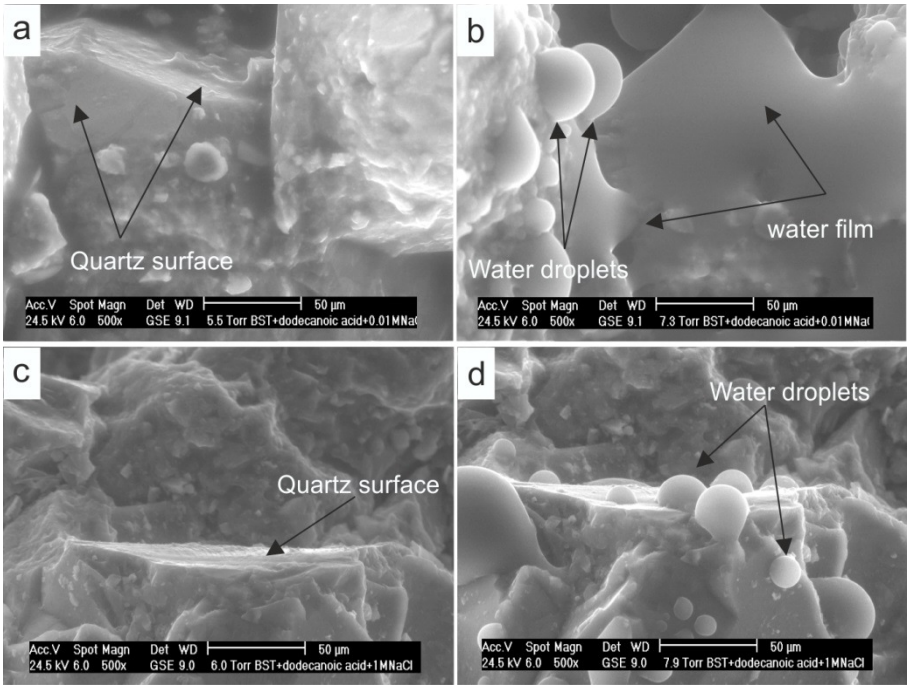

Figure 6.15: ESEM micrographs showing the wettability state on quartz surfaces in BST slices aged in decanoic acid-dodecane. a) BST sample preteated with 0.01M NaCl. Note a thin film of the decanoic acid-dodecane over a quartz overgrowth. b) The same surface shown in (a) with condensed water. Note that in some parts of the sample water developed into a, low contact angle, sheet-like cover on quartz grians,whereas in other quartz grains it formed well-defined droplets (see arrow) areas during the condensation at 5 °C and 7.3 Torr. c) Pretreated aged BST with 1.0M NaCl. d) The same surface shown in (c) is condensated at 5°C and 7.9 Torr. Note Condesend water appeared in the form of spherical droplets (high contact angle) on quartz overgrowth.

The same types of experiments were run in decanoic acid-dodecane aged samples treated with $CaCl_2$ solutions. ESEM photomicrographs of these experiments are shown in Figure 6.16 Figure 6.16a shows details of several relatively uncoated and clean quartz grains on a BST sample pretreated with 0.01 M $CaCl_2$. Once the vapour pressure inside the ESEM was increased, condensation was observed to start occurring at about 5.0 Torr. The ESEM micrograph in Figure 6.16b shows the formation of a few relatively large and isolated droplets of water with high contact angles, as well as the appearance of several, very small droplets over a very clean quartz surface. No droplets are visible over non-quartz surfaces. The average measured contact angle was approximately 93^o, which shows an intermediate wetting condition for the sample treated with 0.01M $CaCl_2$ solution. Water droplets with high-angle domes indicate that those surfaces remained primarily oil-wet. For the aged-BST sample treated with 1 M $CaCl_2$ solution (Figures 6.16c and6.16d), no significant changes of wetting conditions of the quartz surfaces were observed (see Figure 6.16) with respect to the initial oil-wet condition, as the average calculated contact angle

was about 134^{o}, which represents an oil-wet condition.The behavior in this sample, visually is trapped water droplets with high contact angles.

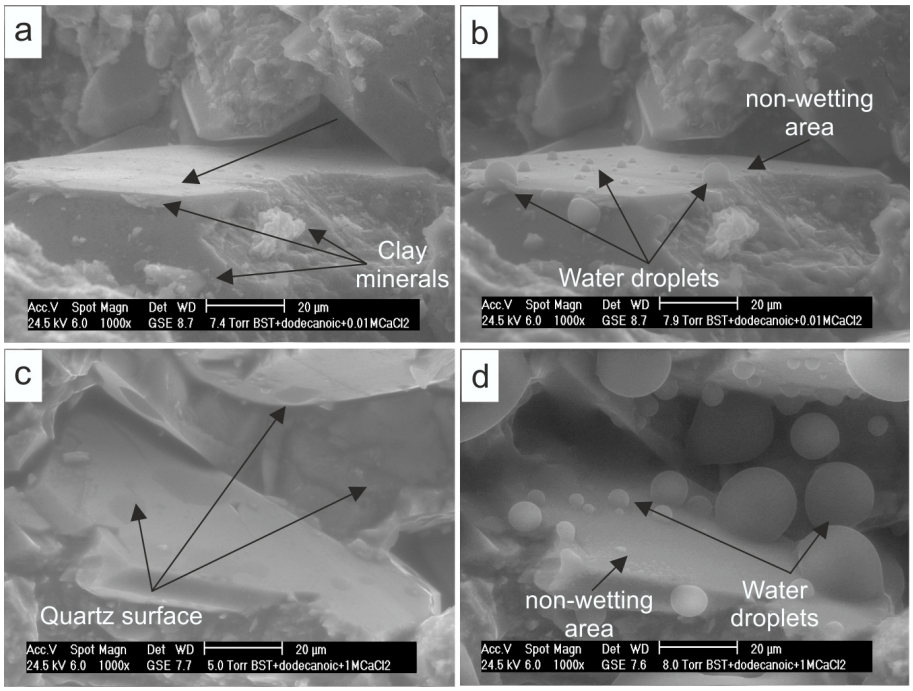

Figure 6.16: ESEM micrographs showing the wettability state on quartz surfaces in BST slices aged with decanoic acid-dodecane. a) Pretreated aged BST with 0.01M $CaCl_2$.Note the clay structure (arrow) on the quartz grain with well developed over growths. b) The same surface shown in (a) is condensated at 5 °C and 8 Torr. Note, condensed water appeared in the form of high dome shaped (water droplets) in contact with a quartz overgrowth. c) Pretreated aged BST with 1.0M $CaCl_2$. d) The same surface shown in (c) with condensed water at 5 °C and 7.9 Torr. Note Condesend water appeared in the form of spherical droplets (high contact angle) on quartz grians with well developed overgrowths.

To evaluate results, the average contact angles of one of each test in this subsection are reported in Table 6.4, and the summary result is listed in Appendix C.2.

Table 6.4: Average contact angle of water droplets over quartz surface in aged BST slices with the decanoic acid-dodecane of NaCl solution and $CaCl_2$ solution at different concentrations.

Brines mol.kg^{-1}	**NaCl**	**$CaCl_2$**
	Decanoic acid-dodecane	
	Theta (M) [deg]	**Theta (M) [deg]**
0.01	74°	93.05
1	115.57	134.50

The values of contact angles of this/group of experiments were plotted versus as a function of experimental time in Figure 6.17. This figure depicts the results of the three droplets to provide a complete picture of the effects of water salinity on contact angle.

Figure 6.17a (left) shows the evolution of contact angle as a function of time for the experiments performed on BST samples treated with NaCl. For both concentrations, droplets show a similar contact (~80°) radious halfway through the experiment, but this changes after 1494 seconds. After this time, the measured contact angle on the BST samples treated with 0.01M NaCl decreased to about 10°, water droplets form very low-angle domes or simply sheet over both quartz and clay surfaces indicating that a wettability alteration. It should be seen that the sheet of water is a result of changing contact angle as the grow in size (see Appendix C.2). In contrast, the measured contact angle on the BST sample treated with 1.0M of NaCl solution; the contact angle actually increased after the 1494 second mark. In this case, the water droplets formed high-angle contacts, indicating that the quartz surfaces remained primarily oil wet.

For the experiments performed with $CaCl_2$ solutions the evolution of the contact angle as a function of time (Figure 6.17b) shows a very different behaviour. In this case, water-advancing contact angles measured throughout the experiment were different from low and high concentrations.The contact angles measured in the samples treated with 0.01M of $CaCl_2$ solutions were observed to keep the same value ($\theta = 115°$) until the end of the experiment (1700 sec). Treatment with the 1.0M $CaCl_2$ solution resulted in increasing contact angles, from an initial value of ~80° to ~134°, throughout the duration of the experiment (1550 sec). It should be noted that raw data for each candidate droplet is presented in Appendix C.2

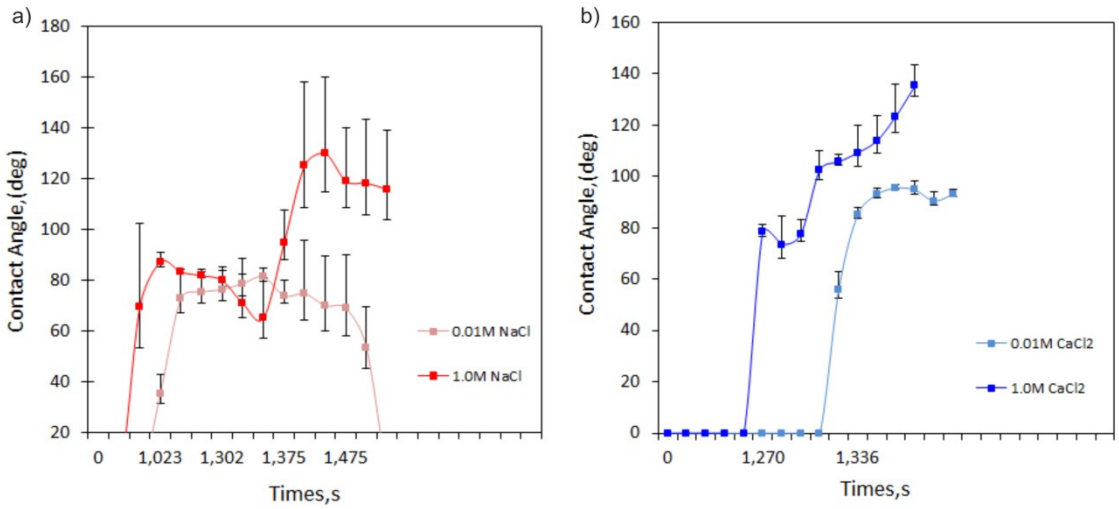

Figure 6.17: The average of dynamic contact angles plotted versus time for condensate on quartz surfaces in BST slices aged with decanaoic acid-dodecane, for each brine at 5°C. The left subfigure presents low(0.01M) and high(1.0M) concentration of NaCl solution. The right subfigure represents a low(0.01M) and high(1.0M) concentration of $CaCl_2$ solution. Error bars indicate standard deviations of at least three droplets. The width of calcualted error bar proves the effect of heterogeneity of wettability behavior on the quartz overgrowth crystal.

High-resolution ESEM provides direct evidence of decanoic acid (polar compound) residues coated on detrital quartz surface in association with clay minerals in BST.When the polar compounds are adsorbed onto the highly irregular quartz grain in BST under reservoir conditions, the original water-wet quartz grains may partly become oil-wet, allowing direct contact between decanoic acid-dodecane and quartz surfaces. Once a quartz grain or part of a grain becomes oil-wet, oil droplets may be trapped within healed microfractures or along quartz grain boundaries by diagenetic quartz overgrowth or through annealing of microfractures. An excellent discussion of the effects of roughness on wetting alteration by adsorption at mineral surfaces in sandstone rock is given by Hirasaki, (1991); Buckley, (1996); Bera et al. (2012); Yuan and Lee, (2013a). Clay minerals have been shown to have varying wettabilities (Jiang et al., 2011; Lebedeva and Fogden, 2011; Basmenj et al., 2016), which is the result of different oil adsorption properties.When in small separated crystals, kaolinite may show a water-wet condition, however, it may become more oil-wet when it is in the form of 5 µm wide booklets (Robin et al., 1998).The presence of clay minerals within the micro-cavities on the quartz surfaces, or nanoparticles like clay-shape over the quartz detrital surfaces in sandstone rock (Hassenkam et al., 2016; Kareem et al., 2016) may also be conducive to decanoic acid-dodecane adsorption on the quartz grains.

The results present, in the first instance, the wettability behaviors can be strongly correlated to the presence of clay minerals owing to their large surface area.The large surface area of clays makes them more susceptible to wettability alterations than any other components of the sandstone rock, and this may explain why such an effect is observed here.The observations from the ESEM images suggests a strong preference for the polar compound to be interacting with the clays (see Figure 6.1), inferring that clay-organic interactions exist in the aged BST samples. However, It can also be seen that there is a preference for the decanoic acid-dodecane to adsorb in the NaCl brine solution, and particularly a strong preference for the 0.01M concentration. These findings are in agreement with the experimental results issued by (Guan et al., 2003).They studied modifications in wettability behavior on mineral surfaces in sequences of the test at Peltier stage (ESEM) using polar compounds that are separated from the crude oil, and they reported the role of mineral surfaces in changing of the wetting characteristic on a micro-scale level.

6.3.1.2.2. Microscopic Observation of Aged Berea Slices in Crude Oil

ESEM photomicrograph of the effect of pretreatment with NaCl solutions on the wettability behavior on crude oil-aged BST slices are shown in Figure 6.18. Figure 6.18a shows an image of a BST sample pretreated with 0.01M NaCl at the start of the experiment. A large, flat, overgrowth of quartz is clearly visible in the centre of the image. Condensation started to be observed after 5.5 Torr. The ESEM micrograph in Figure 6.18b shows a series of low contact angle droplets forming over the overgrowth surface. These droplets have an average contact angle 51^{o}, which indicates a water-wet character in 0.01M of NaCl solution. It can also be seen that the finding is in not match with the experimental result and observation on BST surface aged by crude oil. The variation in results can be due to the effects of other component in BST samples such as feldspar and clay minerals.

For the experiments with samples treated with the 1M NaCl solution, water condensation started to be observed after 5.5 Torr, as is shown in Figure 6.18c. In this figure, several facets of a quartz overgrowth can be seen in good detail. The ESEM micrograph in Figure 6.18d shows the same BST surface after condensation, now a series of droplets can be seen to have formed over the surface. These have formed at specific positions, and do not cover the whole overgrowth surface. The calculated average contact angle is ~109^{o}, which represents the intermediate wetting state in 1.0M of NaCl

solution.The behavior in this sample is indicative of trapped water droplets with high contact angles on quartz overgrowth crystal.

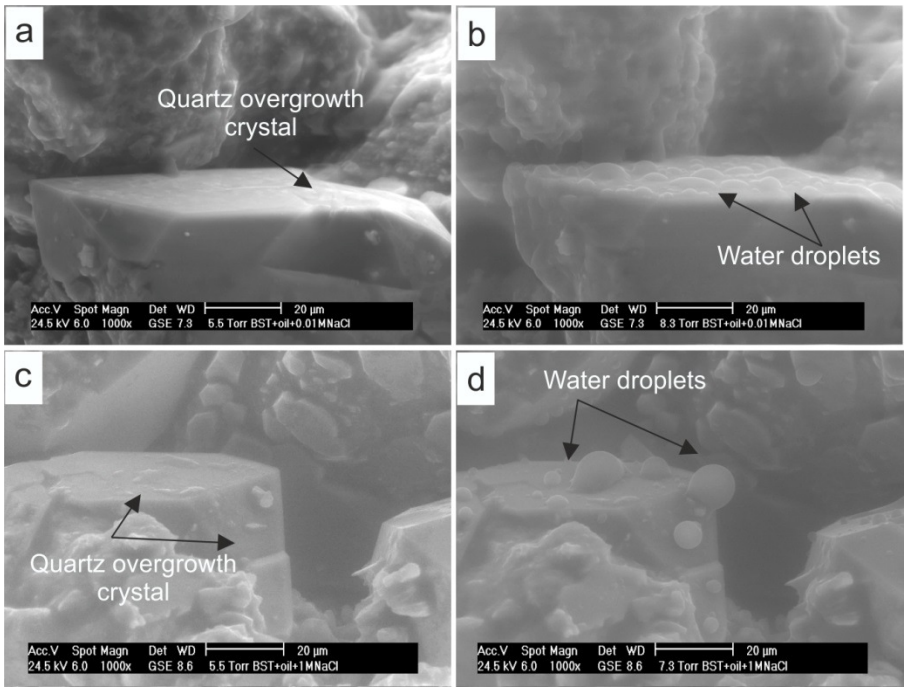

Figure 6.18: ESEM micrographs showing the wettability state on quartz surfaces in BST slices aged with crude oil. a) Pretreated aged BST with 0.01M NaCl. b) The same surface shown in (a) with condensed water at 5°C and 8.30 Torr. Note the low dome shaped droplets of water (low contact angle) on a quartz overgrowth (see arrow). c) Pretreated aged BST with 1.0M NaCl. d) The same surface shown in (c) with condensed water. Note Condensed water appeared in the form of droplets (high contact angle) on quartz overgrowth at 5 °C and 7.3 Torr.

The second batch of experiments was carried out using $CaCl_2$ solutions (0.01 and 1M). ESEM images of these are shown in Figure 6.19. It can be seen from ESEM images, the organic materials over the detrital quartz surfaces approve surfaces have been treated with crude oil (see Figure 6.19). This means that the contact angles of water droplets are not the artifact of the wettability behaviors of detrital quartz surfaces, however, indicating that the wettability state of an oil film and $CaCl_2$ solution over the surfaces.

Low concentration (0.01M) of $CaCl_2$ solution, the ESEM photomicrographs collected during in situ experiments, as can be seen in Figure 6.19a and Figure 6.19b. The condensed water started to be observed after 5.0 Torr, where the vapor pressure curves were in the same range of standard saturated vapor pressure curves. The ESEM micrograph in Figure 6.18b showed that the average calculated contact angle is $\theta = 90^o$ at 7.9 Torr, which shows intermediate wetting condition in 0.01M of $CaCl_2$ solution.The behavior in this test is

trapped water droplets with high contact angles surrounded by oil over the detrital quartz surface.

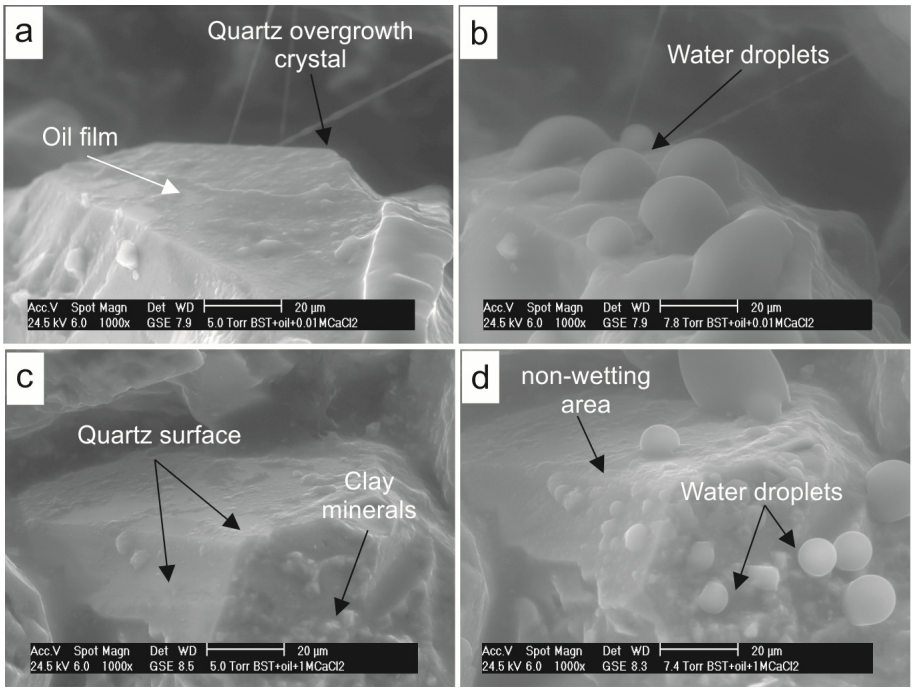

Figure 6.19: ESEM micrographs showing the wettability state on quartz surfaces in aged-BST slice with crude oil. a) Pretreated aged BST with 0.01M $CaCl_2$. Oil film (arrow) on quartz grian with well developed over growths. b) The same surface shown in (a) is condensated at 5 °C and 7.8 Torr. Note condensed water appered on the form of high dome shape (water droplets) in contact with a quartz overgrowth. c) Pretreated aged BST with 1.0M $CaCl_2$. d) The same surface shown in (c) is condensated at 5 °C and 7.4 Torr. Note Condesend water apperead on the form of spherical droplets on quartz grians with well developed overgrowths.

In high concentration of the $CaCl_2$ solution, the condensed water started to be observed after 5 Torr, as is shown in Figure 6.19c. The figure illustrates the BST slice aged in crude oil that was pretreated with 1M of $CaCl_2$ solution.The ESEM micrograph in Figure 6.19d shows that the average calculated contact angle is $\theta = 140^{o}$, which represents an oil-wet condition in 1.0M of $CaCl_2$ solution.The results obtained with the ESEM observed that the behavior in this experiment is showing trapped water droplets with high contact angles surrounded by oil. Quantitative analysis was undertaken in each of the NaCl and $CaCl_2$ concentrations, and the contact angle, therefore was measured.

The average contact angles of one of each test in this subsection are reported in Table 6.5 and listed in Appendix C.2.Results show the low and high concentration NaCl solution again provides a lower value of water droplets contact angle. Unlike the results in Figure

6.18, the results of $CaCl_2$ treatment under the same conditions shows that contact angle of water droplets has a high value, as can be seen in Figure 6.19.

Table 6.5: Average contact angle of water droplets over quartz surface in BST slices aged with crude oil and with deposited of NaCl and $CaCl_2$ at different concentrations.

Brines mol.kg-1	NaCl	$CaCl_2$
	Crude Oil	
	Theta (M) [deg]	Theta (M) [deg]
0.01	51.77	90
1	109.8	140.2

The variation of the wettability behaviors with time was measured for the low and high concentration NaCl and $CaCl_2$ brines, where the results for three droplets in each experiment are represented in Figure 6.20.

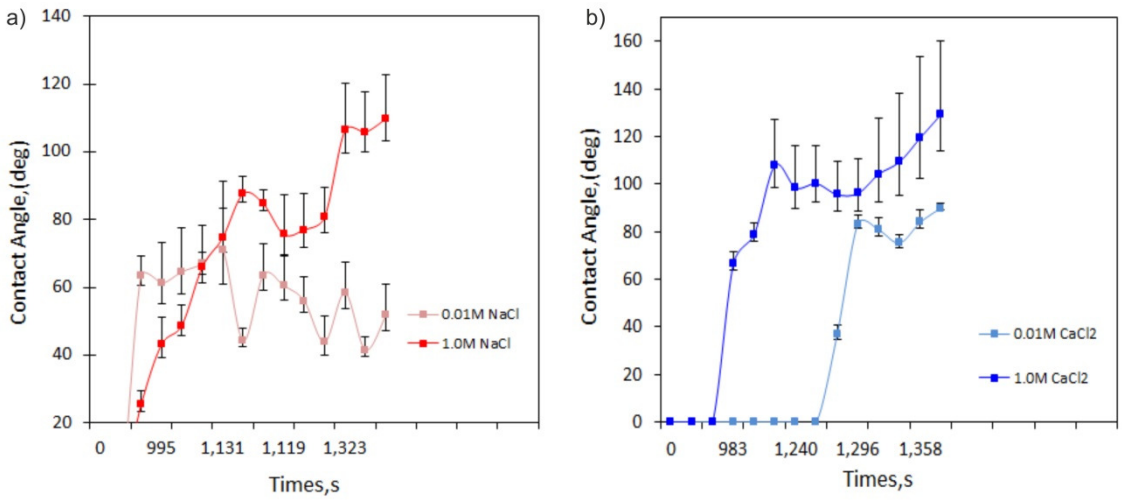

Figure 6.20: The average of dynamic contact angles plotted versus time for condensed water on quartz surfaces in BST slices aged with crude oil after contact with each brine at 5 °C. The left figure presents date for low (0.01M) and high (1.0M) concentration NaCl solutions. The right figure presents data for low (0.01M) and high (1.0M) concentration $CaCl_2$ solution.Error bars indicate standard deviations of at least three droplets. The width of calcualted error bar proves the effect of heterogeneity of wettability behavior on the quartz overgrowth crystal.

Figure 6.20a (left) shows the morphology of droplets changing as a function of time in 0.01M NaCl and 1M NaCl. In the low concentration NaCl solution, the morphology and contact angle of the droplets were constantly stable and kept the same shape and an angle between 50° and 70° at 1471s (see Appendix C.2).It is clear that the majority of quartz

surfaces in BST is coated with distinctly shaped non-organic aggregation, one is a cluster of small hexagonal kaolinite shaped crystals, and a separate cluster floating over the pore spacing. Previous studies (Lebedeva and Fogden, 2010, 2011) showed that the decreased salinity of sodium brines typically increased short-time adhesion and longer-time adsorption of oil on kaolinite, in agreement with Figure 6.20. A good match was also found in decanoic acid-dodecane experiments as can be seen in Figure 6.17.This also demonstrates the effects of 0.01M NaCl treatment on improving oil recovery in sandstone reservoirs.One possible explanation is that in the presence of divalent cations, Ca^{2+}, then cation bridges may be formed between like-charged negative condensate drops and quartz surfaces, which are also responsible for attracting the condensing water drops on the surface.

In contrast, in the case of high salinity monovalent Na^{+} brine cases, the experimental observations are different from those in low salinity brine cases.When 1M NaCl was exposed to the BST aged in crude oil under the same conditions the morphology and contact angle of the droplets were between 50° and 95° at 1471s, as shown in Figure 6.20a. The morphology and corresponding contact values of all candidate droplets, with time, for the low and high concentration of NaCl solution is presented in Appendix C.2. Micro-observation results indicate a high wettability dependence on both crude oil and brine types.However, for crude oil, and more concentrated brines, NaCl shows stronger oil wetting behavior than a low concentration of NaCl salt (See Table 6.5). Similar observations were reported in the work of Sayyouh et al. (1991), where wettability state on the sandstone surface was increased with increasing polar compounds. The presence of polar organic compounds and/or asphaltenes on water-wet quartz surfaces results in wettability alteration, which may allow direct contact between hydrocarbon and the water-wet quartz grains, leading to the formation of micro-size oil inclusions at the surface of quartz grains.

Figure 6.20b (right) shows the morphology of droplets changing as a function of time in 0.01M $CaCl_2$ and 1M $CaCl_2$. In low concentration $CaCl_2$ solution, the morphology and contact angle of the droplets were stable and at an angle between 87° and 92° at the 1450s, as shown in Figure 6.20b and Appendix C.2.It is worth highlighting, in particular, the distribution of the kaolinite and clay-like nanoparticles.Figure 6.19 clearly shows the quartz surface to be coated with clay minerals.

One may think that these clay are illite particles; however, studies have recently been shown to not necessarily be illite (Kareem et al., 2016, and Chapter 4). Studies on illite minerals alone indicate that illite is preferentially water-wet.However, kaolinite also shows a preference for water (Bantignies et al., 1997). Figure 6.1 also presents the high-resolution SEM of the quartz surfaces in BST.The figure shows two distinct shapes of non-organic aggregation. Previous studies (Lebedeva and Fogden, 2010, 2011) showed that decreased salinity calcium brines typically increased short-time adhesion of oil on kaolinite, in agreement with Figure 6.20. Nguele et al. (2015) reported perfectly water-wet behavior on Berea sandstone. He found that the contact angle of water droplets in BST surfaces increased, with decreased or increased salinity of $CaCl_2$. Again, oil-wet surfaces can be observed in Figure 6.20 (right). The figure shows the morphology of droplets changing as a function of time in 1M $CaCl_2$. Results show that the morphology and contact angle of the droplets are increased throughout the test between 70° to 140° at 1485 s as shown in Figure 6.20b.The morphology for all candidate droplets with time, and their correspond contact values can be found in Appendix C.2.

Finally, it should be noticed that differences in the values of contact angles measured with both techniques can be linked to differences in the environment surrounding the specimen. In addition, its important to consider that the contact angles represent liquid water/water-vapor/solid system inside the Peltier Stage. This implies that data obtained with the ESEM cannot be directly to reservoir environments. Such information on the relative wettability between reservoir components can be applied to actual reservoir conditions, where it can be utilized for example inducing whether the wettability characterstic of the reservoir rock are likely to be contributing towards production problems such as water blocking (the retention of water within pore spaces, interfering with oil flow).

6.3.2. Organic Geochemistry

6.3.2.1. Total Organic Carbon

Total organic carbon (TOC) was measured for BST slices aged with crude oil before and after being treated with low and high concentration NaCl solution and $CaCl_2$ solution (note, these were not the same sample, but two different samples aged in the same way).The summary of TOC content in all the BST slices aged with crude oil is presented in Appendix C.3.Results from the experiments are shown in Figure 6.21. It should be noted

that all the aged-BSTcore slices not treated with a brine solution had consistent oil content, suggesting there is a common factor contributing to the oil wetting behavior and that any large variation in TOC content after brine treatment can be attributed to this.It also shows the ability of an experiment or study of this type to be duplicated.

Figure 6.21a shows the TOC content of BST slices aged with crude oil, after being treated with 0.01M and 1M NaCl solutions.The amount of TOC content here is 5.4% and 5.5% by weight. From the figure, it can be seen that the 0.01M NaCl solution is significantly effective at displacing crude oil from BST slices aged with crude oil, compared to all the other studied brine compositions.Therefore, it can be seen that the drop in TOC as a percentage of the "initial" TOC for BST slices aged with crude oil after being treated with 0.01M NaCl solution is 2% (See Appendix C.3).This result aligns with the microscopic and macroscopic wettability observations(described above) that indicate that 0.01M NaCl solutions have the strongest capacity for changing wetting behavior.

After exposing the BST sample to 1M of NaCl solution (Figure 6.21a), no significant change to TOC content in BST sample was observed.Moreover, the drop in TOC as a percentage of the "initial" TOC for BST slices aged with crude oil after being treated with 1M NaCl solution is 0.7 % (See Appendix C.3). This confirms that the treated sample in 0.01M of NaCl solution can displace more oil than 1M of NaCl solution from the rock.

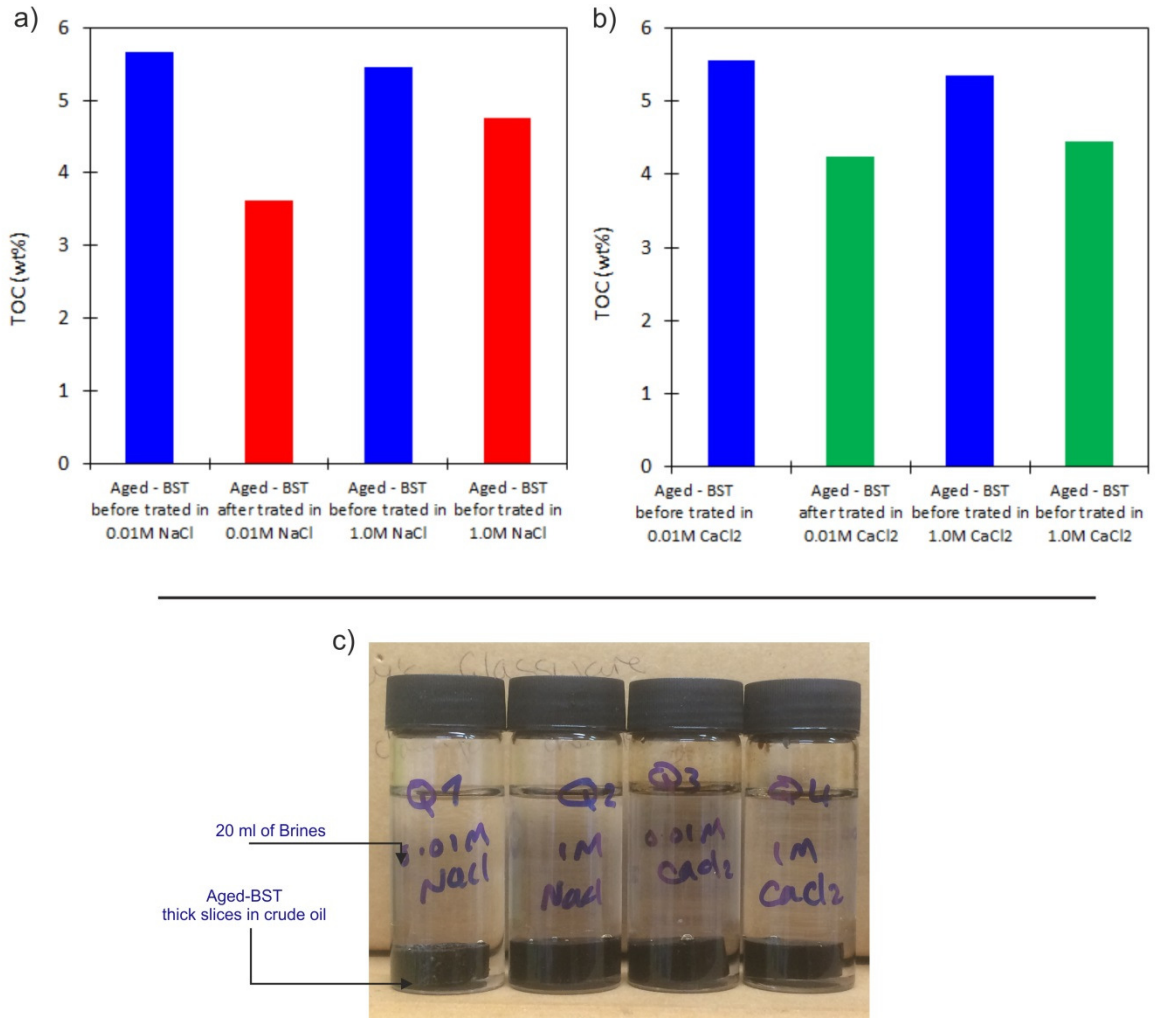

Figure 6.21:TOC in aged BST core slices. a) TOC content in BST aged with crude oil before and after flushing with 0.01M NaCl and 1.0M NaCl solution. b) TOC content in BST aged with crude oil before and after flushing with 0.01M $CaCl_2$ and 1.0M $CaCl_2$ solution.c) photograph showing aged-BST soaked in 20 ml of low and high concentration NaCl and $CaCl_2$ solutions.

The TOC of BST slices aged in crude oil was also measured on samples treated with low and high concentration $CaCl_2$ solutions, shown in Figure 6.21b. After 0.01M of $CaCl_2$ solution was exposed to the BST slices aged in crude oil, the TOC content of the BST as a percentage of the "initial" TOC decreased to (1.3%) (See Appendix C.3). Figures show that the treated aged-BST in 0.01M $CaCl_2$ solution has 4% TOC by weight. This confirms that oil has been displaced by brine in the pores of the BST. However, the presented results here show that pore system is still preferentially in an oil-wet condition. A similar result was found in Figure 6.21c. After exposing 1M $CaCl_2$ brine to the BST (Figure 6.21b), as can be seen, no significant change to TOC content (0.9%) was observed (See Appendix C.3). This indicates that that the treated sample in 0.01M of $CaCl_2$ solution can displace

more oil than 1M of $CaCl_2$ solution from the rock. It was noted that the 0.01M is the best solution for removing oil, and therefore at changing the wettability state of the rock.

It has previously been observed that the crude oil (containing asphaltenes and resins) induce varying wettabilities, depending on the type of clay minerals present in a rock (Clementz, 1977, 1982). All of the kinds of clay minerals present in BST samples (e.g., kaolinite, smectite, illite, and chlorite) are recognized as important in wettability changes. BST contains significant amounts of kaolinite.Studies on kaolinite mineral in shale rock indicated that kaolinite is preferentially oil-wet (Bantignies et al.,1997; Borysenko et al., 2009).However, illite showed a preference for water (Bantignies et al.,1997; Borysenko et al.,2009). Iron-rich chlorite is also claimed to be oil-wet(Worden and Morad, 2002). Petrographic analyses revealed that an iron-rich chlorite coating could give a stronger oil-wet character on quartz surfaces than the more common organic coating on other mineral surfaces.This suggests that in these samples, there are more hydrophobic surfaces than hydrophilic ones.

The amount of oil that can be displaced using different brines needs to be scaled to see how much volume of oil could be moved in full BST core plugs.It should be noted, the observed trend in oil displaced follows what you would “expect” from low-salinity EOR studies.Although using the core scale is relatively small, compared to the reservoir units, it provides a fast and reliable way to gain information for evaluating wettability states.

6.3.2. Oil Recovery by Imbibition Tests

Spontaneous imbibition is the third step in the integrated study to observe wettability alteration. The experiment was designed to aid and identify the wetting state of the BST core plugs aged with oil model compound (decanoic acid-dodecane) through measurements of oil recovery. As listed in Table 6.1, the initial water saturation for the four cores was 25%. The cores were treated and aged (the BST cores were aged with 1.0M decanoic acid-dodecane) as described under the experimental procedure, and the imbibition tests were run with different fluids. Spontaneous imbibition experiments were performed at room temperature and in an oven at reservoir temperature (70 °C) using low and high concentration of NaCl and $CaCl_2$ salts. Oil recovery by water imbibition displacement has concentrated on evaluating the relationship between time and oil production rate. The volumes of produced oil were recorded at intervals by using a graduated cylinder at the top of the Amott cells, and the oil recovery factor was calculated

as the percentage of original oil in place (% OOIP). In this work, the procedure of Cuiec (1984) using an Amott-wettability cell was followed.

For all cores, we have comparable parameters such as diameter, length, initial water saturation, porosity and air permeability. These parameters can be seen in Table 6.1. So, any difference in results is expected to be dependent mainly on other parameters such as the type of brine solution, the concentration of brine solution and temperature. All possible combinations of these three parameters were studied (see Figure 6.22). The results and the conclusion of the findings are presented in this chapter, while the oil model compound (decanoic acid/dodecane) used are described in Chapter 5. Since this type of experiment takes more than a year to complete, only four experiments were conducted, as can be seen in Figure 6.22.

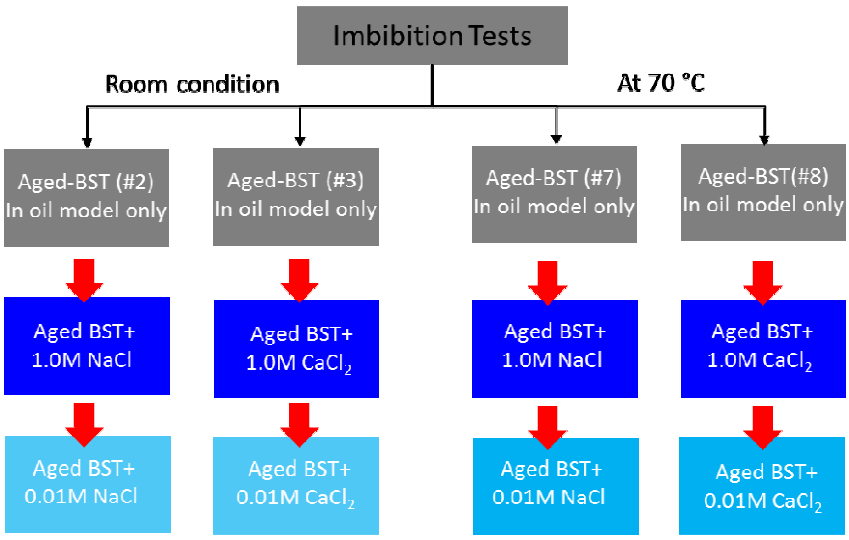

Figure 6.22: Spontineous imbibition sequences.

6.3.2.1. Decanoic acid-Dodecane Displacement at Room Condition

In the first series of imbibition tests, the experiment was designed to study the effect of ionic strength (concentration) and cation type (NaCl and $CaCl_2$). The cores were prepared/aged using decanoic acid-dodecane and then, where placed in contact to low and high concentration brines. As mentioned earlier, the imbibition tests were performed at room temperature (20 °C). The raw data of oil released recorded during the duration of the experiment is given in Appendix C.4. The decanoic acid-dodecane recovered as a function of the OOIP with time (day) was recorded. Therefore, the curves subsequently represent

decanoic acid-dodecane recovery (plotted on the y-axis). Depending on the efficiency of brine, the experiment was continued for 2-3 months until no more decanoic acid-dodecane was expelled from the BST core plug.

BST #2 (core plug): The core with $S_{wi} = 0.25$ was first aged with 1M decanoic acid-dodecane. The decanoic acid-dodecane recovery in a spontaneous imbibition process using 1.0M of NaCl solution reached a plateau of 15% of OOIP after 45 days, Figure 6.23. From the graph below it can been see that the recovery with 1M NaCl solution starts ten days after the start of the experiment, and then stops after 25 days at approximately 18% of the OOIP. The decanoic acid-dodecane imbibing out of the core sticks to the core surface in the form of films suggesting that this core is oil-wet, as shown in Figure 6.24.

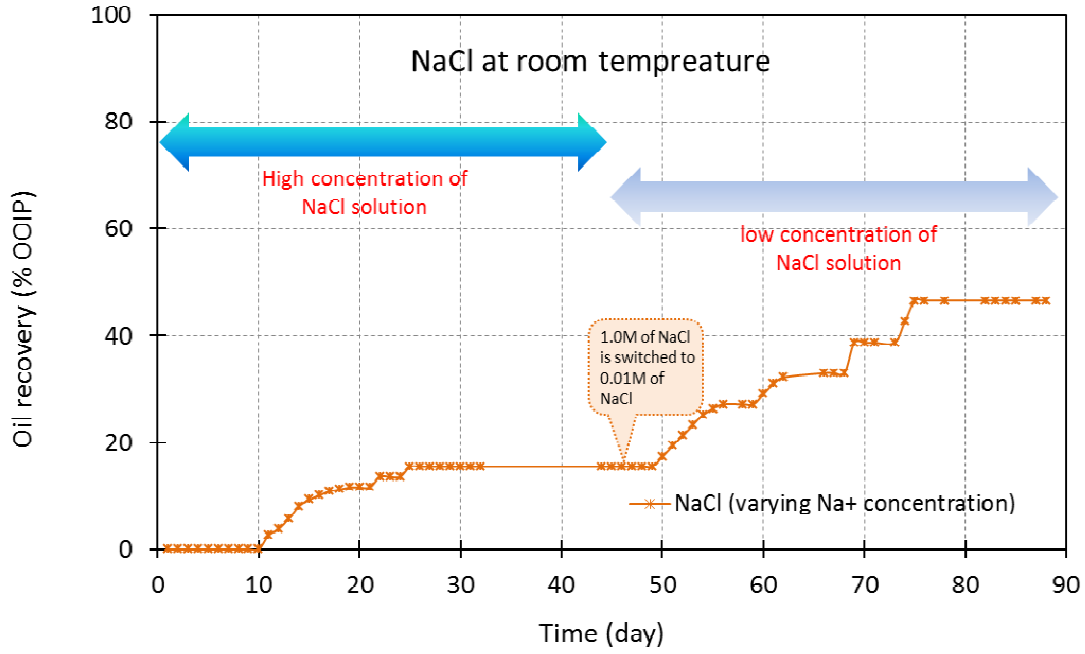

Figure 6.23: Spontaneous imbibition at room condition in BST#2 (core plug). The core had a $S_{wi} =$ 0.25 and saturated and was aged in decanoic acid-dodecane.

After this initial stage, the imbibing fluid was changed to 0.01M NaCl solution, which resulted in a sudden increase in decanoic acid-dodecane recovery and reached a first plateau of 30% of OOIP after ten days (55 days since the start of the experiment). A couple of days after the first plateau was reached, decanoic acid-dodecane recovery increased further to 46% of OOIP, finally reaching a limit after 80 days. These results verify previous work which previously verified that low concentration NaCl brine solutions are an excellent wettability modifier in sandstone rock (Suijkerbuijk et al., 2012; Shehata et al., 2015).

Table 6.6: Final recovery by spontaneous imbibitions at the presence of a low and high concentration of NaCl and $CaCl_2$ solution.

BST. No	Core plug properties				Type of Brines	Condition	Recovery (%OOIP)
	length (cm)	Diameter (cm)	k (mD)	Porosity (Φ)			
#2	5.02	1.9	200	21.83	1.0MNaCl 0.01MNaCl	At Room Temperature	15.0% 31.0%
#3	5.02	2.0	200	21.64	1.0M$CaCl_2$ 0.01M$CaCl_2$	At Room Temperature	19.5% 11.7%

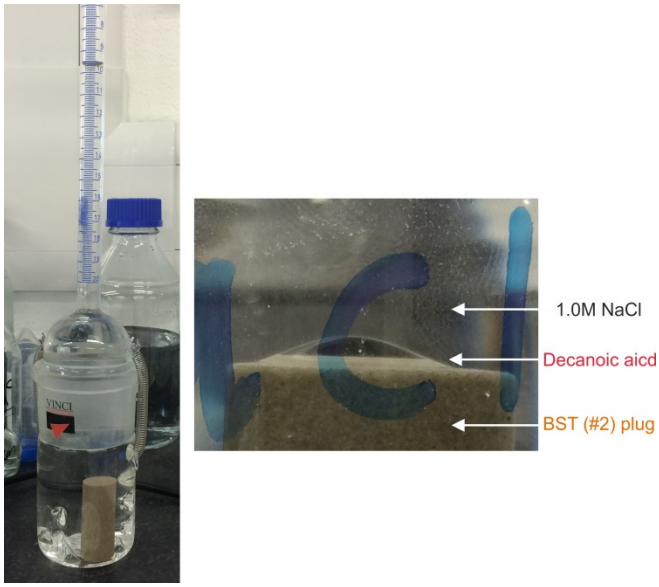

Figure 6.24: Imbibition cell with close up of the top surface of the BST core plug.

As expected, the core appeared less water-wet when 1M NaCl solution was used. Only ≈15% of OOIP was produced after spontaneous imbibition for 45 days (Table 6.6), compared to 0.01M of NaCl solution in the same core BST #2 (core plug), Figure 6.23.The higher recovery is firmly related to change in wettability caused by the concentration of Na^+. Results of this experiment show that the decanoic acid-dodecane/brine/BST interactions during exposure to 1 M NaCl solution has an effect, but 0.01M NaCl solution interacts more to modify the wettability of the mineral surfaces of the BST #2 (core plug). Therefore, the next test was performed using a decanoic acid-dodecane with 1M $CaCl_2$ and 0.01M $CaCl_2$.

BST #3 (core plug): This core, with S_{wi} = 0.25, was aged with 1M decanoic acid-dodecane and treated during the test with two $CaCl_2$ solutions. This brine composition has been used extensively by other researchers (Austad et al., 2010b; Sheng, 2010; RezaeiDoust et al., 2011; Fjelde et al., 2014).As expected, the core appeared less water-wet when the 1M $CaCl_2$ was used. Only ≈19% of OOIP was produced after spontaneous

imbibition with 1M $CaCl_2$ for 45 days, shown in Figure 6.25. The decanoic acid- dodecane imbibing out of the core plug sticks to the core surface in the form of thick-film suggesting that this core is oil-wet. The decanoic acid -dodecane was displaced spontaneously from the BST #3 (core plug) as the imbibing fluid was switched to 0.01M of $CaCl_2$. An additional recovery of ≈11% of OOIP was achieved within about 20 days, while the BST #2 (core plug) needed about 30 days in 0.01M of NaCl to produce an additional 30% of OOIP recovery. These results agree with previous studies, which have shown that multivalent metal ions in an injected brine, such as $Ca^{2+,}$ can act as bridges between the negatively charged functional groups of organic compounds and the clay minerals, leading to a smaller oil recovery (Anderson, 1986). Additionally, it was shown in the experimental study presented by Lager et al., (2006) that when multivalent cations existed in the brine of the formation, flooding with low salinity brine always led to higher oil recovery

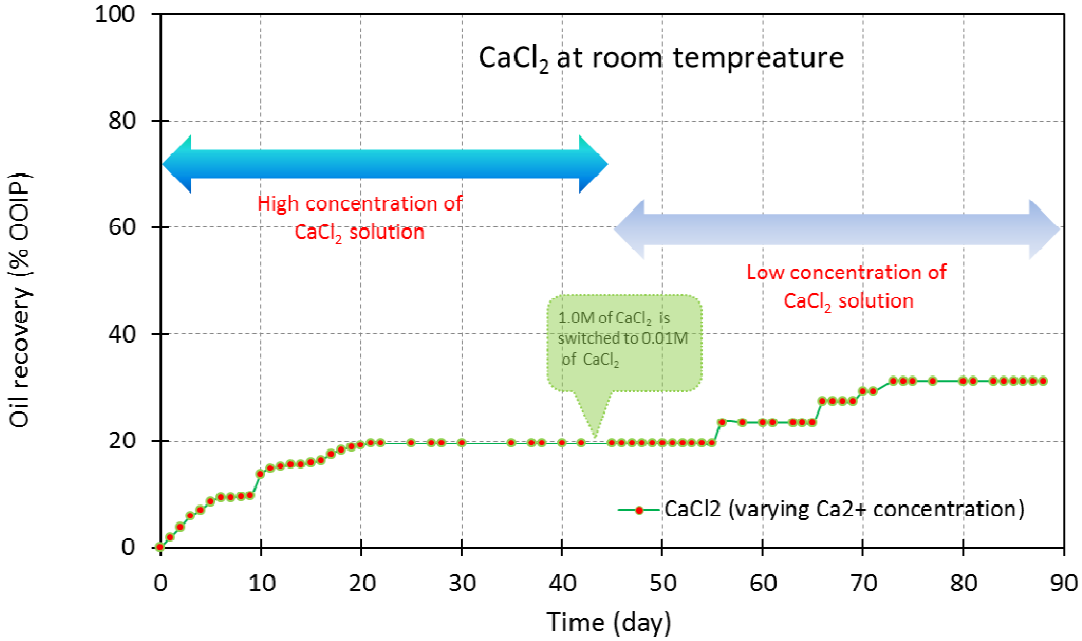

Figure 6.25: Spontaneous imbibition at room conditions in the BST#3 (core plug). The core had a S_{wi} = 0.25 and was saturated and aged with decanoic acid.

dependent on the ionic strength of Ca^{2+} in solution. The finding is consistent with wettability observations existing in Sections 6.3.1 in which 0.01M NaCl showed the better capability of changing wettability behavior from oil and intermediate-wet state to water-wet state at the end of the experiment.

6.3.2.2. Decanoic acid-Dodecane Displacement at 70 °C

In this part of the thesis, experiments were prepared to observe the potential of oil recovery by spontaneous imbibition at 70 °C, since one of the goals of this study was to

observe the wettability at different conditions, including temperature. Two BST core plugs, BST #7 and BST #8, with the same properties (regarding permeability and porosity) than cores #2 and #3 were used. Initial core properties are in Table 6.1, and the details on the oil model compounds and brines used in the experiments can be found in Chapter 5. The volume of the produced decanoic acid -dodecane was monitored and counted against time on a daily basis. Therefore, the curves subsequently represent decanoic acid-dodecane (oil model) recovery that is plotted on the y-axis. Depending on the efficiency of the brine, the experiment continued for 2-3 months until no more decanoic acid-dodecane was expelled from the BST core plug.

BST #7(core plug): The core was aged with1M decanoic acid-dodecane. The decanoic acid-dodecane recovery in a spontaneous imbibition process using 1M NaCl solution reached the plateau of ≈36 % of OOIP recovered after 25 days, as can be observed in Figure 6.26. From the figure, it can be noted that the performing experiment at 70 °C accelerate oil recovery in which decanoic acid-dodecane was produced from BST#7 in less than four days. In addition, since one of the goals of this study was to find the wetting behaviour, the decanoic acid- dodecane displaced by the imbibing NaCl appears to adhere to the core surface in the form of high contact angles ~ 100° (visual observation), suggesting that these cores are mixed-wet. Then the imbibing fluid was changed to 0.01M NaCl solution. This resulted in a sudden increase in decanoic acid-dodecane recovery and reached a plateau of ≈63% of OOIP recovered after 60 days (see Figure 6.26). The decanoic acid-dodecane recovery further rose to ≈70% of OOIP after 65 days, with no further recovery thereafter indicating that the decanoic acid-dodecane recovery plateau was reached.

It can be seen that the performing experiment at 70 °C accelerates decanoic acid-dodecane recovery by 10% in less than one day. This means the imbibition time decreased with an increased temperature. This faster oil production caused by imbibition at low concentration of NaCl salt in core BST#7 compare to the same core at high concentration of NaCl salt is explained by the fact that the low ionic strength of Na^+ changes wettability in core faster, as shown in the similar experiment at room condition (See section 6.3.2.1). This change in wettability shifts capillary pressure from negative to positive mobilising decanoic acid-dodecane with help also of gravity forces. Also, because brine solution is imbibing into the BST#7, its concentration is increasing along the core walls favouring a counter current movement as evidenced in Figure 6.26.

In the case of 0.01 M NaCl solution, the decanoic acid-dodecane recovery sharply increased and reached of a plateau of (37%) of OOIP after 45 days since introducing the aged core plug to 0.01 M NaCl. This result affirmed the importance of the existence of monovalent cations in the system and a drastic effect of temperature on the total recoverable oil. Lager et al. (2006) concluded that cation exchange between the mineral surface and the invading brine was the primary mechanism underlying the improved waterflood recovery seen by low salinity brine injection. A summary of the results of the experiments conducted in this study is shown in Table 6.7.

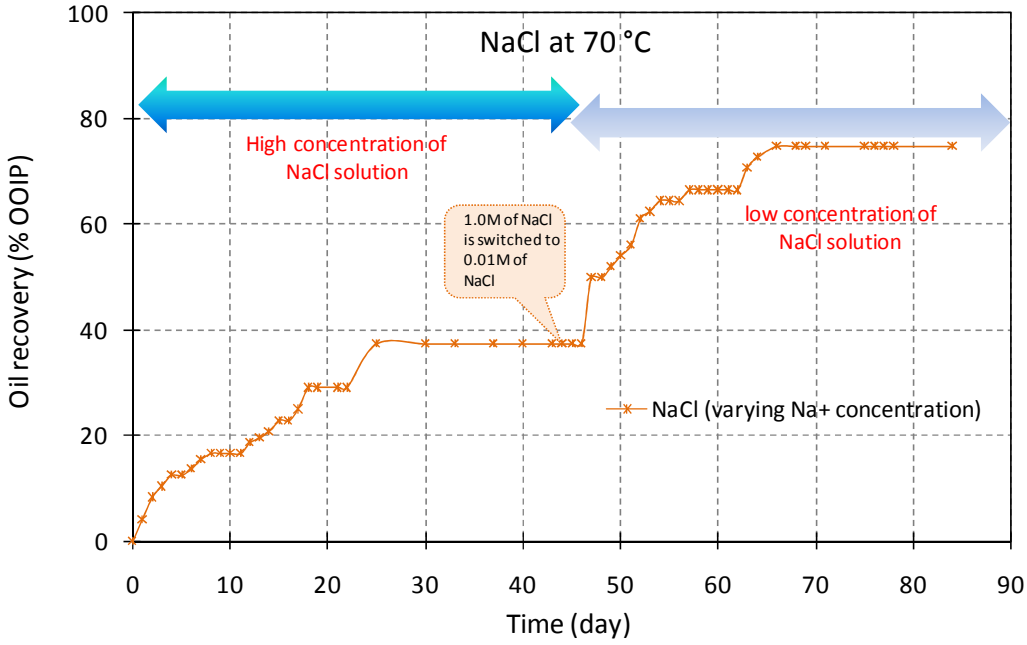

Figure 6.26: Spontaneous imbibition at 70 °C in to BST #7 (core plug). The core had a S_{wi} = 0.25 when saturated and aged with decanoic acid-dodecane.

Table 6.7: Final recovery by spontaneous imbibitions at the presence of low and high concentration of NaCl and $CaCl_2$ solution at 70 °C.

BST. No	Core plug properties				Type of Brines	Condition	Recovery (%OOIP)
	length (cm)	Diameter (cm)	k (mD)	Porosity (Φ)			
#7	5.0	1.9	200	20.73	1.0M NaCl 0.01M NaCl	At 70 °C (Inside an oven)	37.3% 37.3%
#8	5.0	1.9	200	22.31	1.0M $CaCl_2$ 0.01M$CaCl_2$	At 70 °C (Inside an oven)	26.7% 15.2%

In general, results indicate that the decanoic acid-dodecane recovery by spontaneous imbibition adjusted by temperature as well as an ionic number of monovalent Na^+ at 70 °C. Nevertheless, from the results obtained, the use of 0.01M NaCl can significantly improve

water imbibition and change wettability from oil and intermediate-wet to water-wet in the BST #7 (core plug). Hoffman and Kovscek (2010) indicated that the wettability of the reservoir rock was often the main parameter in thermal displacement efficiency. Tang and Morrow (1997) demonstrated that an increase in temperature frequently resulted in increased water-wetness and improved oil recovery, as observed here.

BST#8(core plug): Spontaneous imbibition of the BST #8 core using 1 M $CaCl_2$ brine solution as the imbibing fluid resulted in the decanoic acid-dodecane recovery of about 26% of OOIP after nearly 25days (Figure 6.27). The plateau in the recovery remains at 28% of OOIP after this, until 45 days, similar to what was obtained at the room temperature condition. A sudden increase in decanoic acid-dodecane recovery was detected when the imbibing fluid was changed to 0.01M of $CaCl_2$. The experiment was stopped when the recovery reached 35% of OOIP after 15 days without reaching the ultimate plateau in recovery. The cumulative decanoic acid-dodecane recovery reached 41% of OOIP after 25 days. It should be noted that, s noted with NaCl, the decanoic acid-dodecane migrating out of the core adheres to the core surface with droplets having low contact angles suggesting that these cores are mixed-wet. A summary of high-temperature results for these experiments is shown in Table 6.7 and Appendix C4. In general, these results indicate that the decanoic acid-dodecane recoveries by spontaneous imbibition under different wettabilities were more affected by temperature than the ionic content of a divalent cation such as Ca^{2+}. Furthermore, these results also align with the wettability observations presented in previous sections.

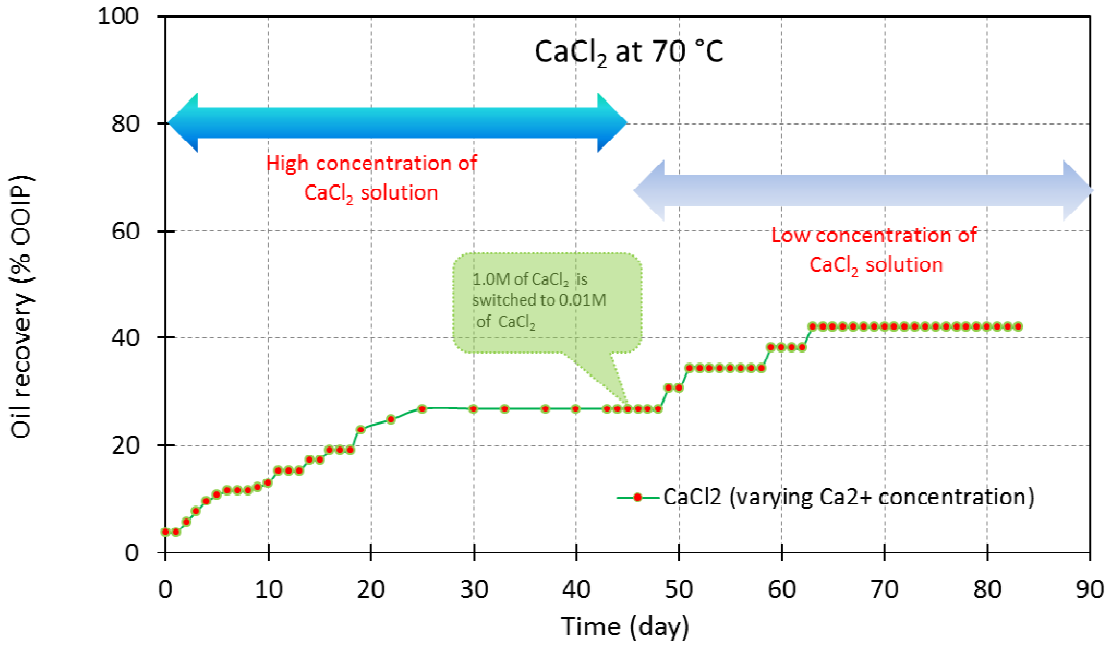

Figure 6.27: Spontaneous imbibition 70 °C in to BST #8 (core plug). The core had an initial water saturation, $S_{wi} = 0.25$ and saturated and aged with decanoic acid-dodecane.

In summary, the recovery by spontaneous imbibition of the BST plugs in the presence of low and high concentrations of NaCl and $CaCl_2$ in Table 6.6 and Table 6.7 shows that the BST #7 (core plug) has the higher recovering, closely followed by BST #2 (core plug), BST #8 (core plug), and BST #4 (core plug). Nasralla and Nasr-El-Din (2011a) stated that the relative absence of $CaCl_2$ in the injected brine allowed leaching of Ca^{+2} from the rock surface, and that resulted in changing the minerals surfaces, and hence higher oil recovery.The lack of change in wettability is the main reason why fluid imbibition is very low in some of the experiments compared to others.

It is clear that the decanoic acid-dodecane recovery as the OOIP shows the efficiency of the NaCl brine on improving decanoic acid-dodecane production compared to $CaCl_2$ solution.The fact that high and low concentrations of NaCl solution act quicker than the $CaCl_2$ solution in displacing oil compounds from BST core surfaces and promote higher imbibition and decanoic acid-dodecane recovery. The results are in good agreement with the literature. Nasralla and Nasr-El-Din (2011a) investigated the effects of injected brine on low salinity waterflood performance for sandstone rocks. NaCl and $CaCl_2$ brine solution were tested, with the NaCl brine giving the highest oil recovery. The results are in good agreement with the literature, though here the effect of temperature is tested.

6.3.2. Surface Charge on Sandstone, Berea Sandstone When Exposed to Potential Determining Ions

To have a better understanding of the role of surface charge in low salinity EOR, the zeta potential of the BST rock was measured. Zeta-potential measurements were conducted for BST grains (crushed) aged in decanoic acid-dodecane and crude oil, with NaCl and $CaCl_2$ brine at different salinities and compositions. The objectives of these measurements are to study the effect of brine on the electrokinetic charge of decanoic acid-dodecane /brine/BST interfaces and crude oil/brine/BST interfaces and relate these changes in electric charges to the oil displacement and contact angle results to explain how the wettability is altered by different brines.For each series of measurements, the concentration of divalent ion and monovalent ions present in a brine solution, i.e. Ca^{2+} or Na^{+}, was changed.

In this section, 0.001M, 0.01M, and1M brines were used, unlike the previous experiments when 0.01M and 1.0M were only used, see Table 5.2. In this test, as a starting point (to obtain a baseline for comparison purposes) a ζ potential measurement for untreated crushed BST and BST grains aged in decanoic acid-dodecane was carried out. In addition, the fluid composition in these measurements for streaming is KCl electrolytes at low ionic strength (0.1M). The experiment is repeated at four different flow rates and the stabilized voltage for each experiment plotted as a function of the stabilized pressure difference (more details can be found in methodology chapter). It should be noted, very few studies have investigated salt concentration relevant to the natural system (natural formation water is typically more saline than this).

The results achieved through ζ analysis give clear insight in this experiment.From Figure 6.28, it can be seen that the ζ potential at the untreated BST grains is -32.35 mV (negative). Previous studies have tested BST saturated with distilled water, or NaCl /KCl /KNO_3 electrolytes at low ionic strength (Shehata et al., 2015). The ζ potential of powdered BST samples have been reported (Kia, Hugh S. Fogler, et al., 1987; Moore et al., 2004). Thanh and Sprik (2015) reported that the ζ potential for the water flow through a water-saturated sample of BST is about -45 mV. This means our result is in agreement with literature. Furthermore, for BST grains aged in decanoic acid-dodecane, the ζ potential at the surface of aged-BST grains became positive (+4.6 mV). Although earlier researchers have observed that the crude oil give a negative ζ potential (Vinogradov and Jackson, 2015), it was observed that the surface charge of crud oil aged in BST grains became even

more positive (+7.97 mV)(see Appendix C4).It has been suggested that due to the electrical charge of asphaltenes, they might be potential candidates to control the magnitude and the sign of the ζ potential (Vega et al., 2009). In an experimental study of surface properties of asphaltenes, Parra-Barraza et al.(2003) have found that the volume of n-heptane is an important parameter that determines the electrical surface properties of asphaltenes. These data provide an indication that the aging procedure in the test was successful.

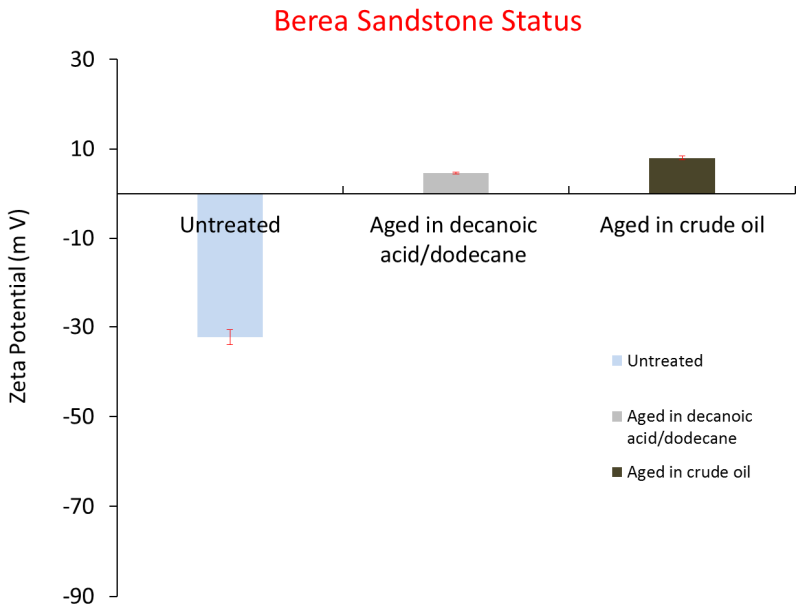

Figure 6.28: Results of ζ potential measurements for BST grains: untreated, and treated with decanoic acid-dodecane and with crude oil.Error bars indicate standard deviations of four independent measurments.

Zeta-potential (ζ) measurements for BST grains treated with different brines are depicted in Figure 6.29. Four runs were conducted for each sample and the average for each was taken. In all results, the standard error of the four different runs was often less than 4%. The parameters used for the ζ potential measurements and the data treatment are provided along with the raw data in Appendix C4.

Figure 6.29 shows the ζ potential of BST grains as a function of brine solution. The figure shows that as the salinity decreased, the ζ potential values become more negative. Zeta potential of BST grains in 0.001M of NaCl salt was -33.4 mV at room temperature and pH 7.8. Increasing the salinity to 0.1M of NaCl salt decreased the ζ potential values to -31.2mV at pH 7.5.1M of NaCl salt showed the lowest ζ potential values of -18.8 mV at pH 6.4. However, the highest negative charge was obtained by using 0.001M NaCl brine

solution.Zeta potentials of BST/brine interface at three different concentrations (2 kmg/l,10 kmg/land50 kmg/l) were determined in NaCl brine by (Nasralla and Nasr-El-Din, 2014b); BST in 2kmg/l of NaCl was the most negative clay for the whole pH range. Therefore, variation in the ζ potentials of BST grains with 0.001M $CaCl_2$ salt, 0.01M of $CaCl_2$ and 1M of $CaCl_2$ salt are shown in Figure 6.29. The values were -27.9mV at pH 7.2 and 26.4mV at pH 6.8 for 0.001M of $CaCl_2$ and 0.1M of $CaCl_2$ salt, respectively. Zeta-potential value for 1M $CaCl_2$ was -19.6mV at pH 6.4. BST grains in $CaCl_2$ concentrations give negative values for ζ potential at room temperature. As salinity decreases, the ζ potential becomes more negative.It should be noted, the values of ζ potential of BST grains with 0.001M of $CaCl_2$ and 0.1M of $CaCl_2$ are close to each other.In general, the ζ potential values for BST samples in both brines are showing a similar trend (see Figure 6.29).

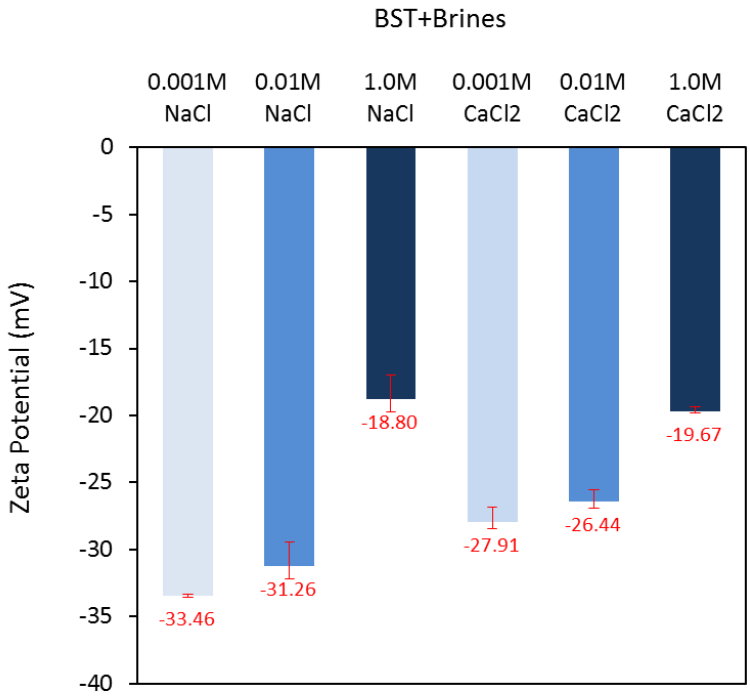

Figure 6.29: Impact of brine salinity on zeta potential at rock/brine interface for BST from pH 6 to 8. Error bars indicate standard deviations of 4 independent measurments.

As previously noted, both cation type and concentration have been shown to affect zeta potential significantly (Nasralla and Nasr-El-Din, 2014c). In general, NaCl brine solutions with BST showed strongly negative charges, unlike $CaCl_2$ solution. This results agree with observations performed by other researchers, for example, it has previously been observed that the sandstone rock and clay minerals have negative charges with brines (Kia, H. Scott Fogler, et al., 1987a; Hussain et al., 1996). Another study reported that the

surface charge becomes more negative for all types of clay minerals and two types of sandstone, Berea, and Scioto, when the water salinity was decreased (Alotaibi et al., 2011). An increase in the magnitude of surface charge at the brine/rock interface means that the repulsion forces between the like particles will be high. This is due to the negative charge in each of the interacting surfaces. As previously noted, greater repulsion forces between brine/rock interfaces let the water film surrounding the mineral in sandstone rock become thicker and more stable, which results in a water-wet condition(Nasralla and Nasr-El-Din, 2014a).The results suggest that the brine salinity has the highest effects on electrokinetic charges at the rock/brine interface in BST core samples (see Figure 6.29). The different ζ potential observed in NaCl brine solutions and $CaCl_2$ brine solutions, which showed the weakest water-wet behaviour when the brine concentration was 1.0M when compared to 0.01M, could be due to the effect the different ratio of monovalent to divalent cations. More investigation is necessary to identify the effects of brine and cations concentrations on the electrokinetic charge of both oil/brine and brine/rock interfaces. The ζ potential of BST in decanoic acid-dodecane and crude oil was measured for two different brine and three different concentrations; the results are presented in the following subsections.

6.3.2.1. Surface Charge of Decanoic Acid-Dodecane/Brine/Berea Sandstone

Zeta potential measurements were conducted for BST aged in decanoic acid-dodecane and treated with NaCl and $CaCl_2$ at different salinities.The results show the ζ potential as a function of Na^+ concentration for each of the three NaCl concentrations studied, and as a function of Ca^{2+} concentration for the three $CaCl_2$ brines examined. All ζ potential measurements taken are shown in Figure 6.30. Results show that the charges at the BST/brine and decanoic acid-dodecane/brine interfaces are negative with all ranges of the brine solution concentration.

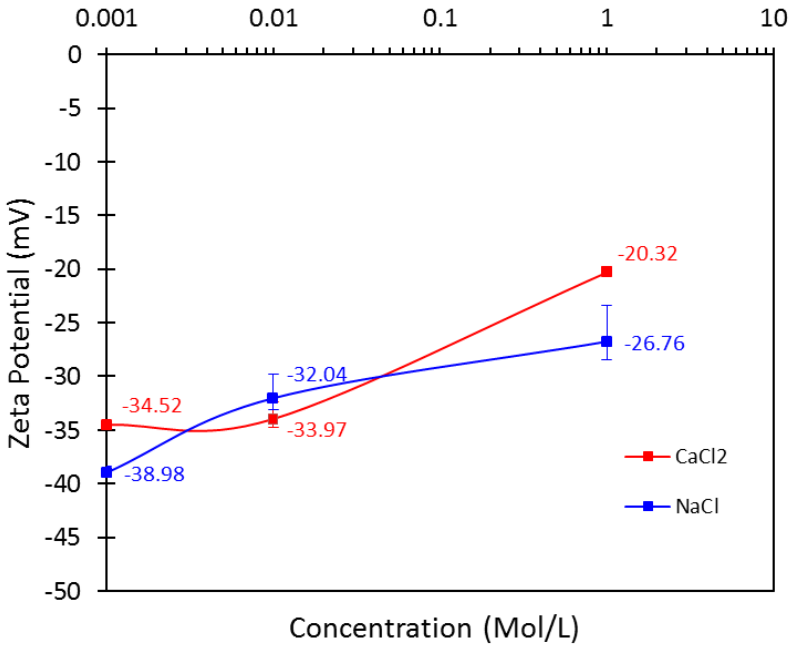

Figure 6.30: Effect of different brine (NaCl, and $CaCl_2$) and concentrations on ζ potential of BST grains aged in decanoic acid-dodecane. Error bars indicate standard deviations of 4 independent measurments.

It can be seen that ζ potential is -38.9 mV at 0.001M NaCl salt. The ζ potential becomes less negative as the salinity increases. The values were -32mV and -26.7 mV for 0.01M of NaCl and 1M of NaCl salt, respectively. As shown in Figure 6.30, the ζ increases slowly and shifts toward the less negative with the increasing concentration of NaCl solution, which is the same to the variation trend of the ζ potential in the BST grains treated with 0.001M and 0.1M of NaCl salt. However, there is a difference between ζ potential values for the BST grains exposed with 1M of NaCl and BST grains aged in decanoic acid-dodecane and treated with 1M of NaCl salt. This shows the impact of cation type and concentration on zeta potential at BST samples. The behaviour observed in these experiments agrees well with expectations from previous low-salinity investigations on BST surfaces (Nasralla et al., 2013a; Vinogradov and Jackson, 2015; Yang et al., 2015), i.e. that a high concentration NaCl solution will induce a more oil-wet state on the BST surface.With the increase of the NaCl concentration, the ion-exchange between the polar molecule and the ion on the BST surface is promoted and the most polar molecule is adsorbed onto the BST.These results suggest that Na^+ behave almost identically at room temperature, with little effect of overall concentration, and can have a significant impact on ζ potential.

The effect of Ca^{2+} concentration on the measured ζ potential was also investigated. Figure 6.30 shows the ζ potential as a function of Ca^{2+} concentration for each of the three $CaCl_2$ concentrations. In all cases, the measured ζ potential is negative; the least negative (or smallest in magnitude) ζ potential is observed for 1.0M of $CaCl_2$ solution, and the ζ potential becomes increasingly more negative as the $CaCl_2$ solution is diluted. It can be seen that ζ potential is -34.5 mV at 0.001M $CaCl_2$ salt. The negative values of were -33 mV and -20.3 mV for 0.01M of $CaCl_2$ and 1M of $CaCl_2$ salt, respectively. It should be noted, Ca^{2+} ions in 0.001M and 0.01M $CaCl_2$ solution changed the surface charge along a similar trend, as shown in Figure 6.30.However, the ζ potential of 1.0 M $CaCl_2$ solution rises along with the increase of concentration, which is the same to the variation trend of the ζ in the treated BST grains with all concentration of the $CaCl_2$ solution.This shows that the $CaCl_2$ concentration has generally less effect on the BST/brine and decanoic acid-dodecane/brine interfaces. As previously noted, compare to NaCl salt a $CaCl_2$ salt showed higher contact angle on BST slices aged in decanoic acid-dodecane, which shows the $CaCl_2$ does not have an influence on wettability behaviour.

Seen from the above experimental results, the brine salinity has a significant impact on electrokinetic charges at the rock/brine interface. Zeta-potential measurements for BST slice aged in decanoic acid-dodecane was positive (Figure 6.28), and as treated with brines, zeta-potential magnitude decreases until it reaches -38.9 mV and -34.5 mV with 0.001M of NaCl and $CaCl_2$, respectively. This can be explained as a result of decreasing the cation concentrations in the solution; decanoic acid carries negative charges and brine cations are positively charged. After treated BST slices aged in decanoic acid-dodecane with high and low brines concentration, high-salinity solution masks the high negative charges of decanoic acid-dodecane by a high concentration of positively charged cations (Nasralla et al., 2013b). Highly negatively charged can be related to a lower concentration of cations in brines, the negative charge of decanoic acid-dodecane is more dominant, and as a result, the oil/brine interface is strong and negatively charged.

6.3.2.2. Surface Charge of Crude Oil/Brine/Berea Sandstone

Following the model compound measurements, zeta potential measurements were conducted for crude oil aged BST at different brine salinities and compositions. The aim of these measurements was to study the effects of NaCl and $CaCl_2$ brine solution on the electrokinetic charge of BST/brine and oil/brine interfaces, and relate these changes to electric charges to compare with the wettability behaviors in a similar system to that which

contained the oil model compounds (decanoic acid and dodecane). All ζ potential measurements for crude oil with different concentrations of NaCl brine solution are shown in Figure 6.31. The results indicate that the charges at the oil/brine interface are negative with all ranges of brine salinity, which is the same to the variation trend of the ζ in the treated BST grains with all concentration of NaCl and $CaCl_2$ solutions (see Figure 6.29).

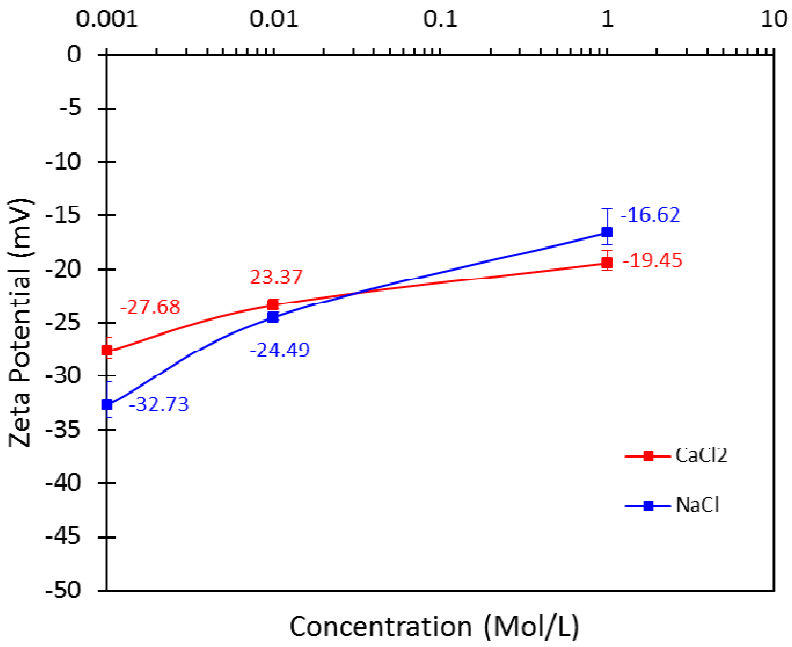

Figure 6.31: Effect of different brine (NaCl, and $CaCl_2$) and respective concentrations on ζ potential of BST grains aged in crude oil. Error bars indicate standard deviations of 4 independent measurments.

The oil/brine interface charge is significantly changed with lowering the NaCl concentration; the more reduction of ionic strength of Na^+, the more negatively charged the BST/brine and oil/brine interfaces. It can be seen from Figure 6.31 that the ζ potential is -32.7 mV at 0.001M NaCl brine concentration. Moreover, the ζ potential becomes less negative (-24.5 mV) with increasing ionic strength of Na^+ at 0.01M NaCl concentration. The ζ potential remains negative (-19.4 mV) regardless of increasing ionic number Na^+ at 1.0M of NaCl. Figure 6.31 illustrates that the ζ potential of BST grains aged in crude oil, treated with the NaCl concentrations was more negative at compared to the value obtained with native BST sample. This can be ascribed to deprotonation of surface hydroxyl groups that causes the minerals in BST grains aged in crude oil to be highly negatively charged after treatment with NaCl brine, resulting in a higher magnitude of the negative zeta potential.

Figure 6.31 shows ζ potential measurements for crude oil with different concentration of $CaCl_2$ brine solution. It can be seen that 0.001M $CaCl_2$ solution resulted in less negative charge at the oil/brine interface than 0.01M $CaCl_2$ solution, and the least negative charge was obtained by 1.0M $CaCl_2$ solution. The amount of change of charge is different from NaCl to $CaCl_2$ when compared to the same cation concentrations used. The electrokinetic charge at the oil/brine ($CaCl_2$) interface changed from -27.6 to -23.3 mV for 0.001M $CaCl_2$ solution and 0.01M $CaCl_2$ solution, respectively. Nevertheless, for 1.0M $CaCl_2$ brine solution, the charge was-19.4 mV.This evidences the effect of brine type and concentration on the electrokinetic charges.The changes of ζ potential in BST/brine and oil/brine interfaces were relatively similar with $CaCl_2$ brine compared NaCl, which shows that there is a relation between the surface charge of crude oil and type of brines.

Seen from the above experimental results, the brine salinity has a significant impact on electrokinetic charges at the rock/brine interface. Zeta-potential measurements for BST slice aged in crude oil was positive (Figure 6.28), and as treated with brines, zeta-potential magnitude decreases until it reaches -32.7 mV and -27.6 mV with 0.001M of NaCl and $CaCl_2$, respectively. The finding can be rationalised as due to the effect of high concentrations of NaCl solution increasingly shielding the high negative charge of oil by their high concentration of positively charged cations, since oil carries negative charges due to the organic acids in crude oil, and lower concentration of cation in low salinity, and as a result the oil/brine interface is strong and negatively charged. This explanation agrees with that similarly determined previously by Nasralla and Nasr-El-Din (2011a).They stated that the absence of $CaCl_2$ in the injected brine allowed leaching/ion exchange of Ca^{2+} from the sandstone rock surface that resulted in changing the rock surface charge, hence higher oil recovery was observed. Shehata et al. (2015) reported the role of ion exchange in produced oil by water flooding.They observed that the reservoir sandstone cores initially saturated with connate water containing divalent cations of Ca^{2+} showed higher oil recovery compared to those cores initially saturated with monovalent cations of Na^{+}.

In summary, water chemistry has a significant impact on the ζ potential for BST grain in brines as well as BST grains aged in decanoic acid-dodecane and BST grains aged in crude oil. Sodium chloride changed the charges at the BST grains aged in decanoic acid-dodecane and BST grains aged in crude oils to highly negative, which shows there is also a relation between surface charge and polar compounds each of oil model compounds and crude oil. It should be noted that the higher negative charge observed in BST grains aged

in decanoic acid-dodecane experiments than aged BST grains in crude oil.The results of this study are possible because less acidic components exist at the mineral surface in BST samples aged in crude oil (TAN = 1.2 mg KOH/g) compare to the BST samples aged in decanoic acid-dodecane (1M), and therefore repulsive electrostatic forces between the negatively charged oil components and the negatively charged mineral surface increase more to undermine or even break the ion bridges. The retention of polar oil components onto the reservoir rock mineral surface has been found to depend on both the composition of brine and/or the crude oil (Fjelde et al., 2013a).

In general, these studies observed that the brine salinity can play a fundamental role in shifting the electric charges at the interfaces of crude oil/BST and brine/BST to affect the interaction between the crude oil/brine and brine/BST interfaces, resulting in wettability. Reducing brine salinity is capable of increasing the repulsive forces between the negative rock surface and acidic components, resulting in wettability alteration toward a less oil-wet state (Yang et al., 2015).

6.4. Parameters Induced Wettability Modification of Berea Sandstone

Rock wettability is a function of the sign, and magnitude of electric charge at the oil/brine and brine/rock interfaces due to the repulsive or attractive forces generated between the oil/brine and brine/rock. In this section, from experimental results and discussions, this present work is used to validate and highlight dominant influences on the wettability alteration in the studied samples; more details and explanations are presented in the following subsection in this chapter.

6.4.1. Influence of Solution Multi-Cations and Ionic Strength on Low Salinity EOR

The contact angle technique was used to investigate the effect of solution cations and ionic strength of brines on the wettability of BST, and any wettability modification achieved through lowering the brine concentration. The BST slices, initially saturated with formation water and then aged either of decanoic acid-dodecane and crude oil, were subsequently treated with high and low salinity brines of NaCl and $CaCl_2$.

In this chapter, the average contact angles of water droplets at different length scales were reported. Figure 6.10 and Figure 6.12 shows a comparison between the water droplets observed with brines of the various salinities at the macroscale, in aged-BST samples in crude oil and decanoic acid-dodecane, respectively. The measured contact angles were

plotted as a function of the salt type and concentrations in Figure 6.12 and Figure 6.14. From the plotted data, it can be seen that in the aged-BST sample in decanoic acid-dodecane, the contact angle of a water droplet on the BST samples treated with a flood of low concentration NaCl brine solution were much lower than those of samples treated with a corresponding $CaCl_2$ brine solution. A similar trend of these results was observed in the microscopic wettability behaviour on the detrital quartz surfaces in BST (using ESEM) and reported in Tables 6.4 and 6.5, a result that is consistent with previous observations of the aged-BST surface surfaces in decanoic acid-dodecane and crude oil, respectively (Bera et al., 2012).

TOC content was used to investigate the influence of brine solution cations and ionic strength on the wettability modification through lowering the salinity of the brine. The results showed that a low ionic content of monovalent cations, Na^+, can remarkably change the wetting state of BST aged with crude oil more when compared with the same brine concentration of divalent cations, i.e. Ca^{2+} (see Figure 6.20).

Spontaneous imbibition was used to investigate the influence of brine solution cations and ionic strength on the wettability behavior of BST core plugs by lowering the salinity of the brine. The core plugs, initially saturated with FW then drained and aged with decanoic acid-dodecane, were subsequently imbibed with high-salinity brine followed by low-salinity brine (Table 5.1). From Figure 6.22, it can be seen that, during high salinity imbibition, the decanoic acid-dodecane recovery of core BST#2 aged by NaCl brine was a little lower than the BST#3 saturated with $CaCl_2$ brine. However, once the solutions were switched to low concentration, the decanoic acid-dodecane recovery was much higher for BST#2, imbibed by a lower concentration of NaCl brine in comparison to BST#3, in contact with lower concentration $CaCl_2$ brine. Therefore, cores BST#2 and BST#3 had a different decanoic acid-dodecane recovery at the end of the experiment, even though the salinities of the FW (used to pre-treat the cores prior to oil aging) were the same (Table 5.1). In a recent work by Yang et al. (2015), it was shown that the divalent cations Ca^{2+} of initial formation water can notably change the wettability toward more oil-wet, while the wetting state is independent of the concentration of Na^+. They observed that the higher the concentration of Ca^{2+} in injection solution, the more oil-wet the rock surfaces were. It was found that the retention of oil components was dominated by bonding of carboxylic groups to mineral surfaces through calcium bridges (Fjelde et al., 2013a).

In our experiments, decanoic acid is still dominated by the alkane chain and thus might be expected to behave similarly to a polar compound in crude oil. Then, the BST surface would be covered by the decanoic acid, and as a consequence, the BST surface changed to be more oil-wet due to the Ca^{2+} cations of formation water. Lowering the concentration of imbibing saline water can evidently improve the decanoic acid-dodecane recovery of BST#2 compared to BST#3. The results are possible because fewer cations exist between the acid group and mineral surface with the reduction of salinity, and then electrostatic repulsive forces between the negatively charged acidic group and the negatively charged mineral surface increase to undermine or even break the calcium bridges. Therefore, acidic components desorb from the rock surface, and the organic layers will be released to change the wettability to be less oil-wet. Then, EOR occurs. The reason why the EOR of BST#3 is gently higher than that of BST#2 in 1 M of $CaCl_2$, is because during imbibition BST#3, aged with a higher concentration of $CaCl_2$ can adsorb more acidic components by calcium bridges in comparison to BST#2, and then lowering salinity to 0.01M of $CaCl_2$ can release more pre-adsorbed acidic components for core BST#3 (Table 6.6).

These suggestions above are in accordance with the ζ potential of decanoic acid-dodecane/brine and brine/crushed BST interfaces. The effect of brine salinity and composition on ζ potential at BST grains aged in decanoic acid-dodecane//brine is shown in Figure 6.30. The 1 M of NaCl and $CaCl_2$ solutions resulted in weak positive charges (close to zero) at aged BST grains, while other 0.1M of NaCl and $CaCl_2$ solutions changed the charge from less negative to more negative. Lowering the concentration of NaCl or $CaCl_2$ solutions increased the magnitude of the negative charge at the BST grains/brine interface. These results demonstrate that the brine salinity can play a key role in altering the electric charges at the interfaces of decanoic acid-dodecane/brine and brine/mineral to affect the interaction between the decanoic acid-dodecane/brine and brine/mineral interfaces, resulting in wettability variation of the rock surface and, hence, the amount of produced oil by waterflooding.

6.4.2. Effect of the Mineralogy Surfaces on the Wettability States

In BST rocks, quartz is usually the dominant mineral (Ramirez et al., 1986; Churcher et al., 1991; Lai et al., 2015), but others minerals may be more significant in terms of activity. Although aged-BST has detrital potassium feldspar grains, it does also have clay minerals, which have different surface chemistry to that of quartz (Gray, 1966; Kareem et

al., 2016). Also, there may be pore coating minerals present in relatively small volumetric amounts that can have a controlling influence on the surface properties, though barely being discernible in either X-ray diffraction analysis of SEM.

The crude oil and decanoic acid-dodecane used previously were tested on the ideal quartz surface using the low and high brine solutions. The contact angles of water droplets were measured to observe and identify the roles of surface chemistry on wettability behaviours. In general, the wettability in multiple length scales shows the changes oil-wet state to more water-wet state with decreasing the concentration of NaCl to 0.1M compare with 0.01M of $CaCl_2$ in same non-flat quartz crystal in aged decanoic acid-dodecane at different experiment (see Figure 5.22 in Chapter 5). More precisely, pendant drop analysis shows the wettability of non-flat quartz crystal in aged decanoic acid-dodecane after treatment presence of 0.01M of NaCl solution was about 1.5 times greater than that in the BST slice aged in decanoic acid-dodecane with the same brine concentration (See Table 5.5 in Chapter 5 and Table 6.2 in Chapter 6). It has previously been shown that different wettability behaviour resulted for the same brine and crude oil for single mineral surfaces in isolation (Bantignies et al., 1997), which illustrates the potential effects of clay mineralogy, such as kaolinite and illite, to the efficiency of low concentration NaCl brine solutions in the BST slice.

More direct evidence for the effects of clay minerals on wettability behaviours was obtained using high-resolution SEM images to characterise the surfaces of detrital quartz overgrowths of pre-treated BST and post-treated BST core plugs, which interacted with decanoic acid-dodecane under various concentration at room temperature. It can be seen that some of the clay minerals have a different behaviour to the quartz mineral in the BST rock under specific conditions (see Figure 6.32).

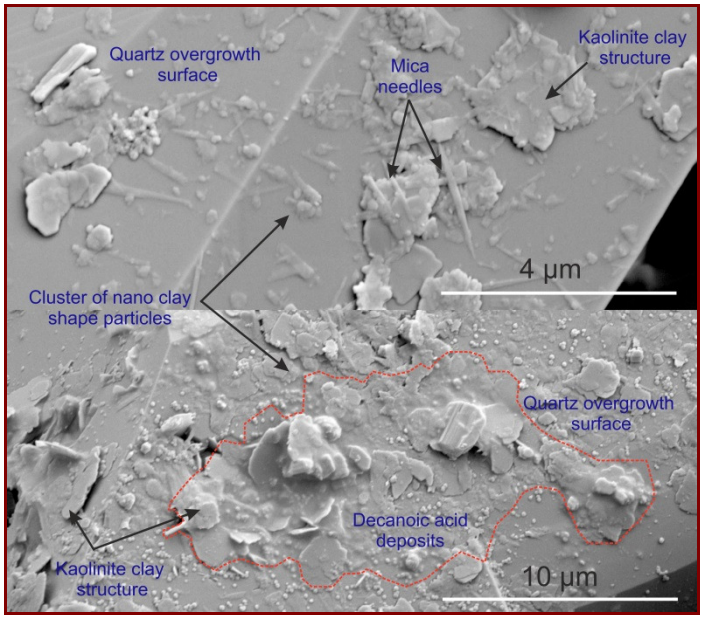

Figure 6.32: SEM high-magnification showing quartz overgrowth surfaces of the BST #2 core in: (top) higher magnification (scale bar 4 μm) close-ups of quartz overgrowth areas "before" imbibition test; (bottom) high magnification (scale bar 10 μm) showing decanoic acid-dodecane deposits (red line) on clay minerals structures after recovery by high and low concentrations imbibition brine (NaCl) at room temperature and pressure.

Figure 6.32 (top) presents the quartz overgrowth surface in untreated BST #2 core. The surfaces of quartz in selected BST core plugs was analysed without conductive coating to preserve the delicate nanoscale features. It was necessary to image the rock chip at 5.0 kV accelerating voltage to avoid surface charging. It can be seen that the clay-like nano minerals are present on all mineral surfaces, i.e. on pore surfaces from rocks that have never come into contact with oil or gas. After high and low concentration imbibition brine, the remnants of decanoic acid-dodecane on clay and clay-like nano minerals was observed on the quartz surface, Figure 6.32 (bottom). Morphologically, it can be observed that the remnant of decanoic acid-dodecane appears more on the clay minerals surfaces than quartz overgrowths surfaces.

It is also worth highlighting, in particular, the effects of the clay mineralogy such as kaolinite and illite to the efficiency of low concentration $CaCl_2$ brine solutions in BST rock. Figure 6.33 (top) presents the quartz overgrowth surface in untreated BST #3 core. Again, the detrital quartz surfaces were imaged at 5.0 kV to avoid surface charging and avoid destruction of the texture of detrital quartz surfaces which coating would result in.

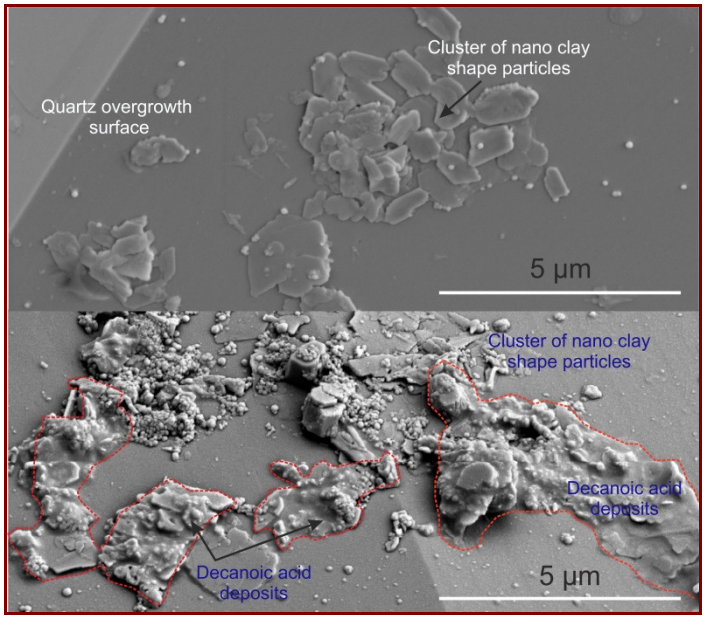

Figure 6.33: SEM high-magnification showing quartz overgrowth surfaces of BST #3 core in: (top) high magnification (scale bar 5 μm) close-ups of quartz overgrowth areas "before" imbibition test; (bottom) high magnification (scale bar 5 μm) showing decanoic acid-dodecane deposits (red line) on clay minerals structures after recovery by high and low concentrations imbibition brine ($CaCl_2$) at room temperature and pressure.

After exposure to high and low concentration imbibition brine, the remnants of decanoic acid-dodecane were commonly observed on clay minerals and clay-like nano minerals on the quartz surfaces, Figure 6.33 (bottom). It should be noted that the amount of remnant decanoic acid-dodecane in the BST#3 core was observed as a film over the clay minerals and the clay-like nano minerals on the quartz surfaces, rather than over the uncoated (clay-free) quartz overgrowth surfaces. It has recently been shown that the presence of Ca^{2+} in FW can largely enhance the adsorption of acidic polar compounds onto clay minerals (kaolinite and illite) by Yang et al., (2015). This concurs with previous publications (Hassenkam et al., 2011, 2016) that wettability can be largely correlated to the presence of clay minerals owing to their large surface area and oil-concentrating properties. The large surface area and permanent surface charge of clay minerals make them more susceptible to wettability alteration than any other components of the BST core samples. Surfaces that are analogues of minerals other than quartz are needed for further work on the interactions that dominate wetting alteration in sandstones rock, like BST, even though they are mainly composed of detrital quartz minerals.

6.4.3. Effect of Temperature

Spontaneous imbibition at 70 °C was conducted to confirm the effectiveness of temperature on wettability alteration and also, further studies evaluated the oil recovery potential of low salinity brine under ambient conditions. Since these experiments take more than a year to complete, only two experiments were conducted. Results presented in Figure 6.25 and Figure 6.26 showed that the decanoic acid-dodecane recovery profile at

high and low concentration brines of NaCl and $CaCl_2$ of the BST#7 core plug and the BST#8 core plug. It should be noted that from the previous results, a significant difference in the magnitude of the decanoic acid-dodecane recovery between the room temperature and high temperature (70°C) was observed Table 6.7.The decanoic acid-dodecane recovery in BST#7 core plug after 90 days was reached at ~80% at the presence of a high and low concentration of NaCl solution. However, in the BST#8 core plug after 90 days, the decanoic acid-dodecane recovery in the high and low concentration of $CaCl_2$ was reached ~ 41%. Results show that the EOR action of NaCl brines might be temperature dependent, especially in the BST#7 core plug, where 1.0M NaCl brine solution was changed with 0.01M NaCl brine solution Table 6.7. In contrast, the results from experiments performed with $CaCl_2$ do not show a clear trend with varying concentration in both conditions. This suggests the effects of NaCl floods may be enhanced under reservoir temperatures.

Results obtained with these cores suggest that even if kaolinite can play a major role in the recovery mechanisms, as proposed by Tang and Morrow (1999), and is more hydrophobic than other clays, additional oil recovery can be observed at high temperature. Overall, our experiments clearly show additional decanoic acid-dodecane recovery in the NaCl and $CaCl_2$ brines. The results can be explained by changing in viscosity and density of oil model compound, and this effect introduces an additional force on the oil drop across the BST core plug. It means the density of the phases differently along with viscosity, which in turn will significantly affect the contact angle of the oil phase. In previous work, Bera et al. (2012) have observed temperature effect on contact angle on the quartz surface. As the temperature of the liquid phase increases, the contact angle decreases due to the reduction of oil viscosity. In addition to this, when the pressure was kept constant, the surface charges of quartz mineral and kaolinite have been reported to always increase with increasing temperature in the range from 20 °C-80 °C (Rosenbrand and Kjøller., 2014).

Kaolinite minerals have a different charge on the two basal faces and the edges, due to the particular structure of the mineral crystal lattice (Grim, 1968; Gupta and Miller, 2010; Gupta et al., 2011). Gupta and Miller (2010) studied the surface charge on both, the aluminol and siloxane basal planes, of kaolinite, using atomic force microscopy, and found that the silica face is always negatively charged, whereas the luminol face charge was positively charged below pH ≈ 6, and negatively charge about that value. They found that the charge on both faces depends on pH, which clearly suggests that groups on the faces do

react with water whereby their charge presumably also depends on other parameters such as temperature.

It can be seen that steps can be observed on kaolinite faces of kaolinite particles in BST#7 before treatment Figure 6.34 (top); thereby faces might also have broken bonds (Brady et al., 1996; Żbik and Frost, 2009) which react with injection water to generate alkalinity. In previous work, Rosenbrand and Kjøller, (2014) have observed similar steps on kaolinite faces in a sample of Rotliegend sandstone, where the effectiveness of high temperature on the different faces of kaolinite particles were examined. There is a strong relationship between temperature, average charge density and the crystal shape and size of kaolinite (Rosenbrand and Kjøller, (2014). With a higher charge density on the edges than on the faces, the thicker crystal would have a more negative average charge density than thinner crystal Figure 6.34 (bottom). From the images, it can be seen that most of the kaolinite crystals in the BST open pores are commonly bigger than 10 µm, which would have more negative charge density during the imbibition test for BST#7. This means that the residual oil saturation is then not only dependent on temperature and brine salinity, but also dependant on the surface chemistry, as well as the morphology of minerals in studies, core samples.

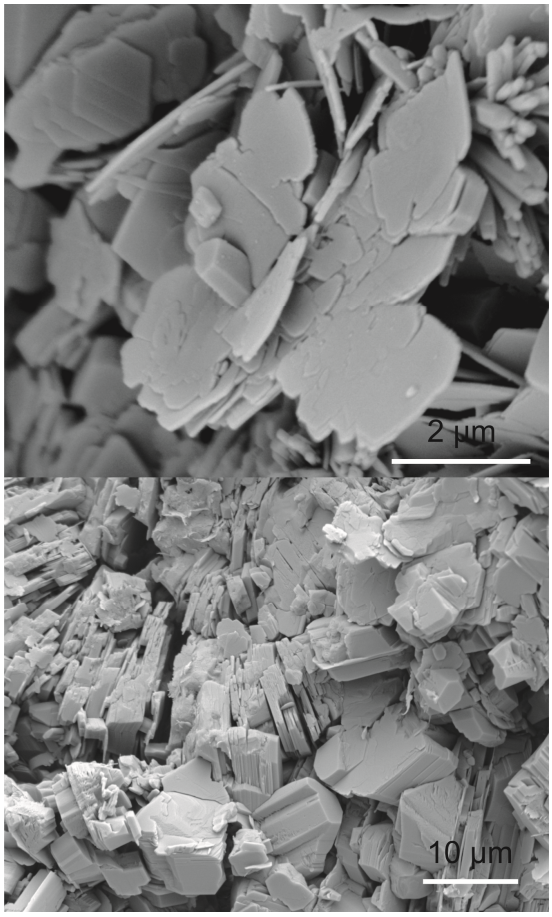

Figure 6.34: SEM at high-magnification showing the face of a kaolinite crystal in the BST#7 core plug; (top) Lines indicate that stacked layers do not have the same size, which results in steps on the particle face; (bottom) booklet of thick kaolinite crystal.

6.5.Conclusions

In this chapter, a series of experimental studies has sought to examine and to observe the potential changes in rock surface wettability state and also for the subsequent changes in the mineral surfaces in porous rock, which may occur as a result of the interaction of the polar compounds with the mineral surface during waterflooding enhanced oil recovery. This study also seeks to correlate the macroscopic wettability alteration with microscopic observations using ESEM. For this purpose, contact angle measurements using BST, crude oil, and decanoic acid/dodecane, two brines, and with different brine, concentrations were conducted to observe the effects of brine salinity on wettability alteration. In addition, the electrokinetic charges of oil/brine/BST interface and decanoic acid-dodecane/brine/BST interface were measured using ζ potential to explain how the wettability of BST rock could be altered by changing the brine salinity. The new contribution in the current work is that it provides a novel approach in combing experimental techniques: ESEM test, which allows

tracking the effect of brine salinity on the mineral surfaces in aged porous core samples. For the first time, this combination of techniques is applied in macro-scale to micro-scale experiments. Furthermore, the emphasis of rock interactions as a function of brine salinity and temperature was investigated during spontaneous imbibition. Integration of the results from these experiments provides a framework for understating oil/brine/rock interactions in terms of wettability behaviours. On the basis of these measurements, the following results have been found:

1 Wetting alteration of BST surfaces by interactions with decanoic acid and crude oil from the North Sea can be controlled by changing the low ionic strength solutions of monovalent Na^+ brine, compared with divalent Ca^{2+} brines. More water-wet conditions were observed by the pendant drop shape technique, whereas with a 0.001M of NaCl, wetting was less water-wet for the same brine concentration of BST aged in crude oil. This study proves that lowering the concentration of the NaCl brine solution results in wettability changing of the aged-BST surfaces. Low salinity NaCl solution resulted in more water-wet surfaces compare with corresponding $CaCl_2$ brine solution, as can be seen in previous work in this area. After the BST aged in crude oil was washed in two brine solutions, the exposed BST samples analysed by TOC reveals that the presence of low ionic strength solutions of monovalent Na^+ largely enhanced adsorption in comparison to Ca^{2+}. In addition, oil composition has a significant effect on the alteration of rock wettability.
2 Wetting changes observed in porous media (BST) using an ESEM technique show similar trends as measurements of wetting alteration on flat BST surfaces by the pendant drop shape technique, showing consistent effects between length-scales. The presences of clay minerals such as kaolinite associated with the hydrocarbon residues on quartz overgrowth surfaces have a significant effect on the wettability alteration process. This is the first time that the direct influence of brine solution on detrital quartz surfaces has been observed, and it can be seen that quantitative analysis of the wetting behaviors can give more insight toward an understanding of the oil/brine/rock interactions that is vital in future studies on EOR techniques. After BST aged in crude oil was washed in two brine solutions, the exposed BST samples analysed by TOC reveals that the presence of low ionic strength solutions of monovalent Na^+ largely enhanced desorption in comparison to Ca^{2+}.

3 The spontaneous imbibition decanoic acid-dodecane recovery ranged from 15 to 31% of OOIP for 1 M and 0.01M of NaCl solution at room temperature, respectively. On the other hand, decanoic acid-dodecane recovery ranged from 19 to 11% of OOIP at room temperature for 1M and 0.01M of $CaCl_2$ solution. As the experiments run at 70 °C in an oven, an ideational decanoic acid-dodecane recovery up to ~80 to ~41% of OOIP was observed by spontaneous ambition for the high and low concentration of NaCl and $CaCl_2$, respectively. Lowering the salinity of the imbibing brine can markedly improve oil recovery of cores saturated with NaCl brine compared to cores aged by $CaCl_2$ brine due to the role of the mineralogy in BST in EOR. Decreasing the salinity of either the NaCl solution or the $CaCl_2$ brine solution can change the brine/rock and crude oil/brine interfaces to be more negatively charged, leading to increased repulsive forces between the two interfaces. These results suggest that acidic components in decanoic acid-dodecane can adsorb onto the rock surface mainly through calcium bridges instead of sodium bridges or van der Waals forces to make the rock surface hydrophobic. Reducing the salinity of the imbibing brine is capable of increasing the repulsive forces between the negative rock surface and acidic components, resulting in wettability alteration toward less oil-wet, and then EOR occurs.

4 SEM photomicrographs of quartz overgrowth surfaces reveal that the quartz surfaces are commonly coated with clay particles and clay-like nanoparticles associated with the hydrocarbon residues that may have modified the wettability alteration.

6.6.References

Ahmed, T., 2010, Chapter 14 - Principles of Waterflooding, *in* Reservoir Engineering Handbook (Fourth Edition): Boston, Gulf Professional Publishing, p. 909–1095.

Alipour Tabrizy, V., R. Denoyel, and A. A. Hamouda, 2011, Characterization of wettability alteration of calcite, quartz and kaolinite: Surface energy analysis: Colloids and Surfaces A: Physicochemical and Engineering Aspects, v. 384, no. 1–3, p. 98–108, doi:10.1016/j.colsurfa.2011.03.021.

Alotaibi, M. B., R. Azmy, and H. A. Nasr-El-Din, 2010, A Comprehensive EOR Study Using Low Salinity Water in Sandstone Reservoirs: Society of Petroleum Engineers, doi:10.2118/129976-MS.

Alotaibi, M. B., R. A. Nasralla, and H. A. Nasr-El-Din, 2011, Wettability Studies Using Low-Salinity Water in Sandstone Reservoirs: SPE Reservoir Evaluation & Engineering, v. 14, no. 6, p. 713–725, doi:10.2118/149942-PA.

Al-Shafei, M. A., and T. M. Okasha, 2009, Wettability Studies at the Pore Level of Saudi Aramco Reservoirs: Society of Petroleum Engineers, doi:10.2118/126088-MS.

AlShaikh, M., and J. Mahadevan, 2014, Impact of Brine Composition on Carbonate Wettability: A Sensitivity Study: Society of Petroleum Engineers, doi:10.2118/172187-MS.

Anderson, W. G., 1986, Wettability Literature Survey- Part 1: Rock/Oil/Brine Interactions and the Effects of Core Handling on Wettability: Journal of Petroleum Technology, v. 38, no. 10, p. 1,125-1,144, doi:10.2118/13932-PA.

Austad, T., A. Rezaeidoust, and T. Puntervold, 2010a, Chemical Mechanism of Low Salinity Water Flooding in Sandstone Reservoirs: Society of Petroleum Engineers, doi:10.2118/129767-MS.

Austad, T., A. Rezaeidoust, and T. Puntervold, 2010b, Chemical Mechanism of Low Salinity Water Flooding in Sandstone Reservoirs: Society of Petroleum Engineers, doi:10.2118/129767-MS.

Bantignies, J.-L., C. C. dit Moulin, and H. Dexpert, 1997, Wettability contrasts in kaolinite and illite clays; characterization by infrared and X-ray absorption spectroscopies: Clays and Clay Minerals, v. 45, no. 2, p. 184–193.

Bantignies, J.-L., C. C. D. Moulin, and H. Dexpert, 1997, Wettability Contrasts in Kaolinite and Illite Clays : Characterization by Infrared and X-ray Absorption Spectroscopies: Le Journal de Physique IV, v. 7, no. C2, p. C2-867-C2-869, doi:10.1051/jp4:1997261.

Basmenj, A. K., A. Mirjavan, M. Ghafoori, and A. Cheshomi, 2016, Assessment of the adhesion potential of kaolinite and montmorillonite using a pull-out test device: Bulletin of Engineering Geology and the Environment, p. 1–13, doi:10.1007/s10064-016-0921-3.

Bera, B., M. H. G. Duits, M. A. Cohen Stuart, D. van den Ende, and F. Mugele, 2016, Surfactant induced autophobing: Soft Matter, v. 12, no. 20, p. 4562–4571, doi:10.1039/c6sm00128a.

Bera, A., A. Mandal, and T. Kumar, 2015, The Effect of Rock-crude Oil-fluid Interactions on Wettability Alteration of Oil-wet Sandstone in the Presence of Surfactants: Petroleum Science and Technology, v. 33, no. 5, p. 542–549, doi:10.1080/10916466.2014.998768.

Bera, A., K. S, K. Ojha, T. Kumar, and A. Mandal, 2012, Mechanistic Study of Wettability Alteration of Quartz Surface Induced by Nonionic Surfactants and Interaction between Crude Oil and Quartz in the Presence of Sodium Chloride Salt: Energy & Fuels, v. 26, no. 6, p. 3634–3643, doi:10.1021/ef300472k.

Bjørlykke, K., 2014, Relationships between depositional environments, burial history and rock properties. Some principal aspects of diagenetic process in sedimentary basins: Sedimentary Geology, v. 301, p. 1–14, doi:10.1016/j.sedgeo.2013.12.002.

Borysenko, A., B. Clennell, R. Sedev, I. Burgar, J. Ralston, M. Raven, D. Dewhurst, and K. Liu, 2009, Experimental investigations of the wettability of clays and shales: Journal of Geophysical Research: Solid Earth, v. 114, no. B7, doi:10.1029/2008JB005928.

Brady, P. V., R. T. Cygan, and K. L. Nagy, 1996, Molecular Controls on Kaolinite Surface Charge: Journal of Colloid and Interface Science, v. 183, no. 2, p. 356–364, doi:10.1006/jcis.1996.0557.

Brown, H. W., 1951, Capillary Pressure Investigations: Journal of Petroleum Technology, v. 3, no. 3, p. 67–74, doi:10.2118/951067-G.

Buckley, J. S., 1996, Mechanisms and consequences of wettability alteration by crude oils, Ph.D.: Heriot-Watt University.

Buckley, J. S., C. Bousseau, and Y. Liu, 1996, Wetting Alteration by Brine and Crude Oil: From Contact Angles to Cores: SPE Journal, v. 1, no. 3, p. 341–350, doi:10.2118/30765-PA.

Busscher, H. J., A. W. J. Van Pelt, H. P. De Jong, and J. Arends, 1983, Effect of spreading pressure on surface free energy determinations by means of contact angle measurements: Journal of Colloid and Interface Science, v. 95, no. 1, p. 23–27, doi:10.1016/0021-9797(83)90067-X.

Churcher, P. L., P. R. French, J. C. Shaw, and L. L. Schramm, 1991, Rock Properties of Berea Sandstone, Baker Dolomite, and Indiana Limestone: Society of Petroleum Engineers, doi:10.2118/21044-MS.

Clementz, D. M., 1982, Alteration of Rock Properties by Adsorption of Petroleum Heavy Ends: Implications for Enhanced Oil Recovery: Society of Petroleum Engineers, doi:10.2118/10683-MS.

Clementz, D. M., 1977, Clay Stabilization in Sandstones Through Adsorption of Petroleum Heavy Ends: Journal of Petroleum Technology, v. 29, no. 9, p. 1,061-1,066, doi:10.2118/6217-PA.

Cuiec, L., 1984, Rock/Crude-Oil Interactions and Wettability: An Attempt To Understand Their Interrelation: Society of Petroleum Engineers, doi:10.2118/13211-MS.

Dandekar, A. Y., 2013, Petroleum reservoir rock and fluid properties: Boca Raton, FL, CRC Press.

Fjelde, I., A. V. Omekeh, and Y. A. Sokama-Neuyam, 2014, Low Salinity Water Flooding: Effect Of Crude Oil Composition: Society of Petroleum Engineers, doi:10.2118/169090-MS.

Fjelde, I. F., A. P. Polanska, F. T. Taghiyev, and S. M. A. Asen, 2013a, Low Salinity Water Flooding: Retention of Polar Oil Components in Sandstone Reservoirs: doi:10.3997/2214-4609.20142611.

Flores, J. G., J. J. Elphick, F. Lopez, and P. Espinel, 2008, The Integrated Approach to Formation Water Management: From Reservoir Management to the Protection of the Environment: Society of Petroleum Engineers, doi:10.2118/116218-MS.

Fogden, A., 2011, Effect of Water Salinity and pH on the Wettability of a Model Substrate: Energy & Fuels, v. 25, no. 11, p. 5113–5125, doi:10.1021/ef200920s.

Gray, D. H., 1966, Formation Damage in Sandstones caused by Clay Dispersion and Migration: Clays and Clay Minerals, v. 14, no. 1, p. 355–366, doi:10.1346/CCMN.1966.0140131.

Grim, R. E., 1968, Clay mineralogy: McGraw-Hill, 616 p.

Guan, H., G. M. Graham, and A. Juhasz, 2003, Investigation of Wettability Alteration Following Scale Inhibitor Adsorption onto Carbonate and Clastic Reservoir Core Material - Static Tests and ESEM Studies: Society of Petroleum Engineers, doi:10.2118/80231-MS.

Gupta, V., M. A. Hampton, J. R. Stokes, A. V. Nguyen, and J. D. Miller, 2011, Particle interactions in kaolinite suspensions and corresponding aggregate structures: Journal of Colloid and Interface Science, v. 359, no. 1, p. 95–103, doi:10.1016/j.jcis.2011.03.043.

Gupta, V., and J. D. Miller, 2010, Surface force measurements at the basal planes of ordered kaolinite particles: Journal of Colloid and Interface Science, v. 344, no. 2, p. 362–371, doi:10.1016/j.jcis.2010.01.012.

Hancock, N. J., and A. M. Taylor, 1978, Clay mineral diagenesis and oil migration in the Middle Jurassic Brent Sand Formation: Journal of the Geological Society, v. 135, no. 1, p. 69–72, doi:10.1144/gsjgs.135.1.0069.

Hassenkam, T. et al., 2016a, Could Atomic-Force Microscopy Force Mapping Be a Fast Alternative to Core-Plug Tests for Optimizing Injection-Water Salinity for

Enhanced Oil Recovery in Sandstone? SPE Journal, v. 21, no. 3, p. 720–729, doi:10.2118/169136-PA.

Hassenkam, T. et al., 2016b, Could Atomic-Force Microscopy Force Mapping Be a Fast Alternative to Core-Plug Tests for Optimizing Injection-Water Salinity for Enhanced Oil Recovery in Sandstone? SPE Journal, v. 21, no. 3, p. 720–729, doi:10.2118/169136-PA.

Hassenkam, T., C. S. Pedersen, K. Dalby, T. Austad, and S. L. S. Stipp, 2011, Pore scale observation of low salinity effects on outcrop and oil reservoir sandstone: Colloids and Surfaces A: Physicochemical and Engineering Aspects, v. 390, no. 1–3, p. 179–188, doi:10.1016/j.colsurfa.2011.09.025.

Hirasaki, G. J., 1991, Wettability: Fundamentals and Surface Forces: SPE Formation Evaluation, v. 6, no. 2, p. 217–226, doi:10.2118/17367-PA.

Hoffman, B. T., and A. R. Kovscek, 2010, Efficiency and Oil Recovery Mechanisms of Steam Injection into Low Permeability, Hydraulically Fractured Reservoirs: Petroleum Science and Technology, doi:10.1081/LFT-120034187.

Hussain, S. A., Ş. Demirci, and G. Özbayoğlu, 1996, Zeta Potential Measurements on Three Clays from Turkey and Effects of Clays on Coal Flotation: Journal of Colloid and Interface Science, v. 184, no. 2, p. 535–541, doi:10.1006/jcis.1996.0649.

Jiang, T., G. J. Hirasaki, C. A. Miller, and S. Ng, 2011, Wettability Alteration of Clay in Solid-Stabilized Emulsions: Energy & Fuels, v. 25, no. 6, p. 2551–2558, doi:10.1021/ef2000079.

Kareem, R., P. Cubillas, J. Gluyas, L. Bowen, S. Hillier, and H. C. Greenwell, 2016, Multi-technique Approach to the Petrophysical Characterization of Berea Sandstone Core Plugs (Cleveland Quarries, USA): Journal of Petroleum Science and Engineering, doi:10.1016/j.petrol.2016.09.029.

Kia, S. F., H. S. Fogler, and M. G. Reed, 1987, Effect of pH on colloidally induced fines migration: Journal of Colloid and Interface Science, v. 118, no. 1, p. 158–168, doi:10.1016/0021-9797(87)90444-9.

Kia, S. F., H. S. Fogler, M. G. Reed, and R. N. Vaidya, 1987, Effect of Salt Composition on Clay Release in Berea Sandstones: SPE Production Engineering, v. 2, no. 4, p. 277–283, doi:10.2118/15318-PA.

Lager, A., K. J. Webb, and C. J. J. Black, 2007, Impact of Brine Chemistry on Oil Recovery.

Lager, A., K. . Webb, C. J. . Black, M. Singleton, and K. . Sorbie, 2006, Low salinity oil recovery an experimental investigation Paper, *in* Torndheim,Norway: Paper SCA 2006-36.

Lai, P., K. Moulton, and S. Krevor, 2015, Pore-scale heterogeneity in the mineral distribution and reactive surface area of porous rocks: Chemical Geology, v. 411, p. 260–273, doi:10.1016/j.chemgeo.2015.07.010.

Lebedeva, E. V., and A. Fogden, 2010, Adhesion of Oil to Kaolinite in Water: Environmental Science & Technology, v. 44, no. 24, p. 9470–9475, doi:10.1021/es102041b.

Lebedeva, E. V., and A. Fogden, 2011, Wettability alteration of kaolinite exposed to crude oil in salt solutions: Colloids and Surfaces A: Physicochemical and Engineering Aspects, v. 377, no. 1–3, p. 115–122, doi:10.1016/j.colsurfa.2010.12.051.

Leirvik, A., 2010, Evaluation of experimental methods to determine wettability: 29 p.

Marcussen, Ø., T. E. Maast, N. H. Mondol, J. Jahren, and K. Bjørlykke, 2010, Changes in physical properties of a reservoir sandstone as a function of burial depth – The Etive Formation, northern North Sea: Marine and Petroleum Geology, v. 27, no. 8, p. 1725–1735, doi:10.1016/j.marpetgeo.2009.11.007.

Moore, J., S. Glaser, F. Morrison, and G. M. Hoversten, 2004, The streaming potential of liquid carbon dioxide in Brea Sandstone: Geophysical Research Letters, v. 31, no. 17.

Mugele, F., I. Siretanu, N. Kumar, B. Bera, L. Wang, R. de Ruiter, A. Maestro, M. Duits, D. van den Ende, and I. Collins, 2016, Insights From Ion Adsorption and Contact-Angle Alteration at Mineral Surfaces for Low-Salinity Waterflooding: SPE Journal, v. 21, no. 4, p. 1,204-1,213, doi:10.2118/169143-PA.

Nasralla, R. A., M. A. Bataweel, and H. A. Nasr-El-Din, 2013, Investigation of Wettability Alteration and Oil-Recovery Improvement by Low-Salinity Water in Sandstone Rock: Journal of Canadian Petroleum Technology, v. 52, no. 2, p. 144–154, doi:10.2118/146322-PA.

Nasralla, R. A., and H. A. Nasr-El-Din, 2011a, Coreflood Study of Low Salinity Water Injection in Sandstone Reservoirs: Society of Petroleum Engineers, doi:10.2118/149077-MS.

Nasralla, R. A., and H. A. Nasr-El-Din, 2014a, Double-Layer Expansion: Is It a Primary Mechanism of Improved Oil Recovery by Low-Salinity Waterflooding? SPE Reservoir Evaluation & Engineering, v. 17, no. 1, p. 49–59, doi:10.2118/154334-PA.

Nguele, R., K. Sasaki, H. S. Al-Salim, Y. Sugai, and M. Nakano, 2015, Wettability Alteration in Berea Sandstone Cores by Contact Angle Measurements: Society of Petrophysicists and Well-Log Analysts.

Parra-Barraza, H., D. Hernández-Montiel, J. Lizardi, J. Hernández, R. Herrera Urbina, and M. A. Valdez, 2003, The zeta potential and surface properties of asphaltenes obtained with different crude oil/n-heptane proportions: Fuel, v. 82, no. 8, p. 869–874, doi:10.1016/S0016-2361(03)00002-4.

Polson, E. J., J. O. Buckman, D. G. Bowen, A. C. Todd, M. M. Gow, and S. J. Cuthbert, 2010, An Environmental-Scanning-Electron-Microscope Investigation Into the Effect of Biofilm on the Wettability of Quartz: SPE Journal, v. 15, no. 1, p. 223–227, doi:10.2118/114421-PA.

Potts, D. E., and D. L. Kuehne, 1988, Strategy for Alkaline/Polymer Flood Design With Berea and Reservoir-Rock Corefloods: SPE Reservoir Engineering, v. 3, no. 4, p. 1,143-1,152, doi:10.2118/14935-PA.

Prather, C. A., J. M. Bray, J. D. Seymour, and S. L. Codd, 2016, NMR study comparing capillary trapping in Berea sandstone of air, carbon dioxide, and supercritical carbon dioxide after imbibition of water: Water Resources Research, v. 52, no. 2, p. 713–724, doi:10.1002/2015WR017547.

Qi, Z., Y. Wang, H. He, D. Li, and X. Xu, 2013, Wettability Alteration of the Quartz Surface in the Presence of Metal Cations: Energy & Fuels, v. 27, no. 12, p. 7354–7359, doi:10.1021/ef401928c.

Ramirez, W. F., A. C. Oen, J. F. Strobel, J. L. Falconer, and H. E. Evans, 1986, Surface Composition of Berea Sandstone: SPE Formation Evaluation, v. 1, no. 1, p. 23–30, doi:10.2118/11972-PA.

Rezaeidoust, A., T. Puntervold, and T. Austad, 2010, A Discussion of the Low-Salinity EOR Potential for a North Sea Sandstone Field: Society of Petroleum Engineers, doi:10.2118/134459-MS.

RezaeiDoust, A., T. Puntervold, and T. Austad, 2011, Chemical Verification of the EOR Mechanism by Using Low Saline/Smart Water in Sandstone: Energy & Fuels, v. 25, no. 5, p. 2151–2162, doi:10.1021/ef200215y.

Robin, M., R. Combes, and L. Cuiec, 1998, Two SEM Techniques To Investigate Reservoir-Rock Wettability: Journal of Petroleum Technology, v. 50, no. 11, p. 77–79, doi:10.2118/1198-0077-JPT.

Rosenbrand, E., and C. Kjøller, 2014, Effect of temperature on sandstone permeability: Technical University of Denmark, Department of Civil Engineering, Mineral-fluid interaction.

Sayyouh, M. H., A. M. Hemeida, M. S. Al-Blehed, and S. M. Desouky, 1991, Role of polar compounds in crude oils on rock wettability: Journal of Petroleum Science and Engineering, v. 6, no. 3, p. 225–233, doi:10.1016/0920-4105(91)90015-F.

Shabib-Asl, A., M. A. A. Mohammed, M. Kermanioryani, and P. P. J. Valentim, 2014, Effects of Low Salinity Water Ion Composition on Wettability Alteration in Sandstone Reservoir Rock: A Laboratory Investigation: Journal of Natural Sciences Research, v. 4, no. 13, p. 34–41.

Shedid, S. A., and M. T. Ghannam, 2004, Factors affecting contact-angle measurement of reservoir rocks: Journal of Petroleum Science and Engineering, v. 44, no. 3–4, p. 193–203, doi:10.1016/j.petrol.2004.04.002.

Shehata, A. M., N. El-Din, and H. A, 2015, Spontaneous Imbibition Study: Effect of Connate Water Composition on Low-Salinity Waterflooding in Sandstone Reservoirs: Society of Petroleum Engineers, doi:10.2118/174063-MS.

Sheng, J., 2010, Modern Chemical Enhanced Oil Recovery: Theory and Practice: Amsterdam ; Boston, MA, Gulf Professional Publishing, 648 p.

Soraya, B., C. Malick, C. Philippe, H. J. Bertin, and G. Hamon, 2009, Oil Recovery by Low-Salinity Brine Injection: Laboratory Results on Outcrop and Reservoir Cores: Society of Petroleum Engineers, doi:10.2118/124277-MS.

Suijkerbuijk, B., J. Hofman, D. J. Ligthelm, J. Romanuka, N. Brussee, H. van der Linde, and F. Marcelis, 2012, Fundamental Investigations into Wettability and Low Salinity Flooding by Parameter Isolation: Society of Petroleum Engineers, doi:10.2118/154204-MS.

Tang, G.-Q., and N. R. Morrow, 1999a, Influence of brine composition and fines migration on crude oil/brine/rock interactions and oil recovery: Journal of Petroleum Science and Engineering, v. 24, no. 2–4, p. 99–111, doi:10.1016/S0920-4105(99)00034-0.

Tang, G. Q., and N. R. Morrow, 1997, Salinity, Temperature, Oil Composition, and Oil Recovery by Waterflooding: SPE Reservoir Engineering, v. 12, no. 4, p. 269–276, doi:10.2118/36680-PA.

Thanh, L. D., and R. Sprik, 2015, Zeta Potential Measurement Using Streaming Potential in Porous Media: VNU Journal of Science: Mathematics - Physics, v. 31, no. 4.

Vargha-Butler, E. I., M. Kashi, H. A. Hamza, and A. W. Neumann, 1986, Direct Contact Angle Measurements on Polished Sections of Coal: Coal Preparation, v. 3, no. 2, p. 53–75, doi:10.1080/07349348608905274.

Vega, S. S., R. H. Urbina, M. V. Covarrubias, and C. L. Galeana, 2009, The zeta potential of solid asphaltene in aqueous solutions and in 50:50 water + ethylene glycol (v/v) mixtures containing ionic surfactants: Journal of Petroleum Science and Engineering, v. 69, no. 3–4, p. 174–180, doi:10.1016/j.petrol.2009.08.014.

Vevle, J., 2011, NMR measurements of wettability alternation in Berea Sandstone.

Vinogradov, J., M. Z. Jaafar, and M. D. Jackson, 2010, Measurement of streaming potential coupling coefficient in sandstones saturated with natural and artificial brines at high salinity: Journal of Geophysical Research: Solid Earth, v. 115, no. B12, doi:10.1029/2010JB007593.

Vinogradov, J., and M. D. Jackson, 2015, Zeta potential in intact natural sandstones at elevated temperatures: Geophysical Research Letters, v. 42, no. 15, p. 2015GL064795, doi:10.1002/2015GL064795.

Wilson, M. J., L. Wilson, and I. Patey, 2014, The influence of individual clay minerals on formation damage of reservoir sandstones: a critical review with some new insights: Clay Minerals, v. 49, no. 2, p. 147–164, doi:10.1180/claymin.2014.049.2.02.

Worden, R., and S. Morad (eds.), 2002, Clay Mineral Cements in Sandstones: Malden, MA, Wiley-Blackwell, 520 p.

Yang, J., Z. Dong, M. Dong, Z. Yang, M. Lin, J. Zhang, and C. Chen, 2015, Wettability Alteration during Low Salinity Waterflooding and The Relevance of Divalent Ions in This Process: Energy & Fuels, doi:10.1021/acs.energyfuels.5b01847.

Yuan, Y., and T. R. Lee, 2013, Contact Angle and Wetting Properties: p. 3–34, doi:10.1007/978-3-642-34243-1_1.

Żbik, M. S., and R. L. Frost, 2009, Micro-structure differences in kaolinite suspensions: Journal of Colloid and Interface Science, v. 339, no. 1, p. 110–116, doi:10.1016/j.jcis.2009.07.038.

Zekri, A. Y., M. T. Ghannam, and R. A. Almehaideb, 2003, Carbonate Rocks Wettability Changes Induced by Microbial Solution: Society of Petroleum Engineers, doi:10.2118/80527-MS.

Zhang, P., M. T. Tweheyo, and T. Austad, 2007a, Wettability alteration and improved oil recovery by spontaneous imbibition of seawater into chalk: Impact of the potential determining ions Ca2+, Mg2+, and SO42−: Colloids and Surfaces A: Physicochemical and Engineering Aspects, v. 301, no. 1–3, p. 199–208, doi:10.1016/j.colsurfa.2006.12.058.

Chapter 7

Summary, Outlook for Future Research and Concluding Remarks

7.1. Introduction

The overall aims of the research presented in this thesis were to (*1*) perform a full "multi-scale" characterisation of Berea sandstone core plugs (Cleveland Quarries, USA); (*2*) investigate the role of brine composition and ionic strength on the wettability alteration oil-aged quartz substrates; (*3*) and oil-aged Berea sandstone as a model of sandstone reservoir. In this final chapter, the main conclusions of the work performed in this thesis are presented, along with their implications for understanding wetting alteration in core flood experiments. The potential application of this research for understanding EOR in reservoir rocks is discussed, along with potential limitations. The initial results from some nascent further investigations across different areas are discussed and suggestions made for future studies that could improve our understanding of the fundamental controls of low-salinity EOR. The chapter, and thesis, draws to a close with some concluding remarks reflecting on the main points learned from the studies presented here.

7.2. Summary

7.2.1. Petrophysical Characterisation of Berea Sandstone

This part of the thesis, mainly presented in Chapter 4, provides results of the most detailed, multi-length scale characterisation of the well-known Berea sandstone, up to date. BST has been used significantly in core flooding experiments over 25 years, as a proxy for

siliciclastic (sandstone) rocks. However, only incomplete characterisation data has been reported, especially with respect to the mineral distribution along pore walls. This knowledge is particularly crucial to understand any oil/brine/mineral interactions that may occur inside the pore space of the rock. For these reasons a multi length-scale, multi-technique characterisation effort was undertaken with an emphasis on quantifying the porosity as well as the identity of the minerals exposed to the open space, including nano-mineral phases. Four different BST samples, with 4 different permeability ranges (from < 50 mD, 50-100 mD. 100-200 mD, and 500-1000 mD) were studied.

Results from the characterisation study indicated that authigenic minerals, especially clay minerals, make up a small portion of the bulk rock volume (3.3% to 8%) but are over-represented at the pore surfaces and in pore spaces compared to the other major mineral constituents of the rock (quartz and feldspar). For the BST samples studied, kaolinite is the predominant pore lining mineral observed for three of the four permeability ranges studied. In the remaining sample (50-100 mD), illite is the predominant clay-mineral. Atomic force microscopy shows the presence of nano-sized particles with the shape and size of clay minerals on the surface of recrystallised quartz grains in a BST sample. Regardless of their origin and identity, the presence of these particles shows that the quartz grain surfaces in BST samples are more heterogeneous than previously assumed. Although we have shown that carbonate cement was somewhat localised throughout two of the BST specimens, silica-based cement is common in all of the BST cores studied and include both microcrystalline quartz and amorphous silica phases. Porosity shows a positive, albeit non-linear, correlation with permeability across the BST cores studied. Results show that permeability is mainly controlled by pore connectivity in the clay mineral matrix. In addition, there are likely to be significant pores in authigenic clays. Next to the pore connectivity, three-dimensional pore space showing both pore-to-pore and pore-to-pore-throat-to-pore relationships were also found to be important.

The results obtained in this characterization study illustrate the heterogeneity of even a “standard” rock across multiple scales. It also highlights the need to fully understand not only the overall mineralogical composition of the rock but more importantly what kind of phases are present in the pore spaces, including surface coating-nanoparticles, as these will play a crucial role in determining the wettability of the system and its response to different enhanced oil recovery methods. Therefore, it is recommended that this type of multi-scale characterisation be undertaken on both test outcrop core samples and reservoir core rocks

and, indeed, more studies of this type are emerging in the recent literature (Desbois et al., 2016).

7.2.2. Wettability Regime in Quartz-Based Substrates

The goal of this part of the thesis, presented in Chapter 5, was to elucidate the effect of ion identity and concentration on modifying the wettability of crude oil and model oil (decanoic acid/dodecane mixture) aged quartz surfaces of different roughness. This information is of primary importance for low salinity EOR in sandstone rocks, as a significant amount of pore space is still occupied by detrital quartz grains (with and without overgrowths), which will, therefore, be in contact with any oil present in the rock. A highlight of this study was the combination of traditional contact angle measurements at the millimetre scale with true microscopic imaging through the use of environmental scanning electron microscopy. The more significant conclusions of this part of the overall study are summarised below.

1. The effect of nano-roughness (<100 nm) on wettability was evaluated for the first time on a quartz surface. The effect of surface roughness on contact angles has been reported before, but always at roughness on the micron range. Our results show that surface roughness can have a major effect in changing the wetting characteristics of a decanoic acid-dodecane treated quartz crystal, as evidenced by ESEM contact angle measurements. In particular, it was observed that the increase of nanoroughness value from 3 nm to 50 nm makes the quartz crystal surface more oil-wet. For a flat quartz crystal aged in decanoic acid/dodecane, the contact angles were 77° and 120° after pretreatment with 0.01M and 1 M of NaCl salt, respectively. On the other hand, the contact angles values for 0.01M and 1M of $CaCl_2$ were 70° and 93° at a similarly aged surface. As the roughness of surface increases to 50 nm, an increase in the measured contact angles was observed. Contact angles at samples pre-washedwith 0.01M and 1M of NaCl salt were 90° and 115°, respectively. The value of contact angle in the presence of 0.01M and 1 M of $CaCl_2$ were 105° and 115°, respectively. From these results it can be concluded that, as the surface roughness increases, so too does the solid-liquid contact area, leading to a larger contact angle.
2. Additional clues regarding the variation of wettability with roughness were obtained through the observation of post-treatment quartz surfaces with atomic

force microscopy, which allowed to observe the remnants of decanoic acid/dodecane on the quartz surfaces after brine treatment. In addition, the direct measurement of adhesion over decanoic acid/dodecane remnants were used as a proxy for the total amount left on the surface. AFM observations showed remnant decanoic acid/dodecane after exposure to NaCl and $CaCl_2$ salts at two different concentrations (0.01M and 1M). In particular, $CaCl_2$ salt showed more decanoic acid/dodecane left on non-flat quartz surfaces, where it remained concentrated on grooves and other imperfections of the surface. 0.01M and 1M of $CaCl_2$ salt reduced the adhesion force between the decanoic acid and quartz surface to 4.0 nN and 8.0 nN, respectively. The lowest adhesion force, however, was observed in 0.01M of NaCl (2.5 nN). It can be seen from the results that the adhesion on quartz surface is sensitive to brine-type as well as their concentration. These results demonstrate that the mineral-fluid interactions depend on both morphological and chemical properties of quartz surfaces at the nanoscale and that these will play a crucial role in determining the "macroscopic" wettability of a quartz surface or even a quartz-rich rock.

3. Contact angle measurements using a non-flat quartz crystal, crude oil, decanoic acid-dodecane, and two brines, namely, NaCl and $CaCl_2$ at different concentrations were conducted at the macroscopic and microscopic scale to study the effect of brine salinity on wettability alteration. Macroscopically, the rate of wettability alteration of oil/brine/quartz system and decanoic acid-dodecane/brine/quartz system was different on both system. The results revealed that there are three dominant parameters which affect the contact angle, including (a) the presence of polar compounds in the crude oil and decanoic acid, (b) the type of salts, and (c) salt concentration. In addition, microscopic observation prove that decreasing brine salinity (to 0.01M of NaCl) results in a change in the wetting state of quartz surfaces from oil-wet (or mixed wet) to more water-wet. This effect is stronger on the crystal treated with 0.01M of NaCl salt than no that washed with 0.01M of $CaCl_2$ when both are considered under identical concentration. No significant change in wettability behaviour on crystals treated with 1.0M NaCl salt and 1.0M $CaCl_2$ brines implies that high salinity has less influence within the ranges studied. In general, due to differences (potentially asphaltene content) in crude oil, and the polar character of the decanoic acid, a dual effect can be observed for cation salt

concentrations. For the case of low concentration of NaCl, the polar character of the decanoic acid leads to a greater reduction in the contact angles compared with the asphaltene content in crude oil in all cases, although as the concentration of salt was increased, the effect of polar character on contact angle reduction is dominant. Also, no significant change in wettability for $CaCl_2$ salt was observed within the ranges studied in the ESEM studies.

4. The experimental observations suggest that the contact angle of the same system (decanoic acid-dodecane/brine/quartz) changes with temperature. The contact angle of a water droplet showed a reduction when the temperature increased, i.e. when the contact angles were measured at 5 °C in the ESEM compared with the same experiment at room temperature (25 °C). The contact angles values were 80° and about 80° to 100° for 0.01M and 1 M of NaCl salts, respectively. However, at room temperature (25 °C), the contact angles were 65° and 84° at 0.01M and 1M of NaCl (see Table 5.5 in Chapter 5), respectively. At the lower temperature, when 0.01M and 1M of $CaCl_2$ salts were used, the contact angles were 98° and 95 to 135°. However, at higher temperature conditions (25 °C), the contact angles were 73° and 86° in the presence of 0.01M and 1M of $CaCl_2$ salts respectively (see Table 5.5 in Chapter 5). It should be noticed that the error bars of the contact angle measurements at 5 degrees was commonly low, such even after taking uncertainties into account, the trends stand. These results agree with the works previoulsy published in the literature. Based on Bera et al. (2012), the interfacial interaction between decanoic acid-dodecane and the solution is also affected by temperature. As confirmed by Shedid and Ghannam, (2004) and Bera et al. (2012) the reduction in contact angle may also be attributed to the decrease in oil viscosity with the increase in temperature. The results obtained indicate that the decrease in contact angle of water droplets in the macroscopic investigation may also be attributed to the decrease in decanoic acid viscosity with the increase in temperature. In addition to this, a thermal gradient may act behind the some of the variation in contact angle results, which were obtained by *in-situ* experiment (ESEM), of water droplets on non-flat quartz aged in decanoic acid-dodecane. Overall, results from these experiments demonstrate that low-salinity water has a positive potential for enhancing oil recovery over a wide range of temperatures and that it is not limited to a certain temperature.

5. Zeta potential measurements were used to corroborate that a reduction in contact angle (and increased desorption of oil) as salinity decreased is likely to be due, at least in part, to the expansion of the electric double-layer. The ζ potential measurements for quartz powder aged in decanoic aciddodecane and quartz powder aged in crude oil with NaCl and $CaCl_2$ brines at different concentrations 0.001M, 0.01M and 1M were studied. Generally, results show that monovalent cations are more efficient in increasing the absolute values of ζ potential that divalent cations at the same concentration. Zeta potential became more negative while salinity of brines decreased. The resulting ζ potentials values for quartz powder aged in decanoic acid-dodecane are more negative than that of quartz powder aged in crude oil. Change of the electric charge at decanoic acid-dodecane/brine and quartz/brine interfaces or crude oil/brine and quartz/brine caused by low-salinity water is the primary reason for wettability alteration on quartz surfaces. When the electric charges became more negative at the crude oil/brine or decanoic acid-dodecane/brine and quartz/brine interfaces, the repulsion forces between quartz and decanoic acid-dodecane or/and crude oil increase and make the quartz surface more water-wet as a result of expansion of the electric double-layer and stabilizing of the water film surrounding the rock. Stability of the thin aqueous films is responsible for the adsorption and spreading of the condensed water onto the quartz crystal surface.This would cause a measurable change of wettability behaviour of the system.

7.2.3. Wettability Alteration in Berea Sandstone

The objective of this part of the thesis (see Chapter 6) was to examine the effects of cation type and concentration on the wettability behaviour of BST samples aged with either crude oil or a model oil (decanoic acid-dodecane mixture). Based on the experimental results, the following significant conclusions can be drawn:

1. Based on pendant drop shape measurements, contact angles indicate that the wetting alteration of a crude oil-treated BST and a decanoic acid/dodecane-treated BST is controlled by both, the oil composition and ionic strength of solutions. For both type of aging (crude oil and decanoic acid-dodecane), a decrease in the concentration of either NaCl or $CaCl_2$ solutions led to a change in the wettability to a more water-wet state. In both cases too, $CaCl_2$ showed a smaller overall effect in modifying the wettability state (a smaller reduction in contact angle was measured),

particularly when the concentration of the brine was reduced from 0.01 M to 0.001M. This in contrast to the NaCl brine which showed a continued reduction in contact angel for every reduction in concentration. The main effect of the type of oil on which the aging was performed was on the overall value of the contact angle measured, with those samples aged in crude-oil exhibiting a consistent 10 to 20 % higher value of contact angle. In other words, crude oil-aged samples consistently showed a more oil-wet state than those pretreated with decanoic acid. For the case of NaCl, the polar character of the decanoic acid leads to a greater reduction in the contact angles compared with the crude oil in all cases, although as the concentration of salt was increased, the effect of polar character on contact angle reduction is dominant. A similar result was observed in a decanoic acid/dodecane-treated quartz crystal when the aged surface pretreated with same salt concentration. Generally, due to the presence of asphaltenes in crude oil, and the polar character of the decanoic acid, a dual effect can be observed for cation salt concentrations.

2. The wettability behaviour BST was also studied using the ESEM technique. ESEM observations of the post treatment core chips have then allowed for the investigation the effects of brine solutions on detrital quartz surfaces. Crude oil, decanoic acid-dodecane,and two brines, NaCl and $CaCl_2$ at different concentrations (0.01M and 1M) were conducted to study the effect of brine salinity on wettability behaviour. For BST slices aged in decanoic acid-dodecane, the measured contact angles were 74° at 0.01M of NaCl solution and 115° 1M of NaCl solution. On the contrary, when the sample was treated with $CaCl_2$, the contact angles were 93° and 134° at 0.01M and 1M, respectively. For crude oil-aged samples treated, the contact angle decreased from 109° when the sample was treated with 1M NaCl to 51° when "flushed" with 0.01M NaCl. Results also show that the measured contact angle also decreases as the $CaCl_2$ concentration is decreased, going from 140° on those samples treated with 1M solutions to 90° on those treated with 0.01M solutions. ESEM measurements indicate a similar trend to that observed with the pendant drop method, i.e., a reduction in the concentration of both brines leads to more water wet conditions, with NaCl having the stronger effect. More importantly, the use of the ESEM allowed the observation of heterogeneous wetting behaviour

across adjacent quartz crystals, which may be the result of differences in the amount and type of clay minerals and nanoparticles exposed at each surface.

3. A TOC analysis investigation was conducted on oil-aged BST samples to assess the amount of oil left on the sample after treatment with different brines. Results show that the largest amount of oil was removed from samples after washing with 0.01M NaCl brines. On the contrary $CaCl_2$ consistently removed less oil at equal concentration when compared to NaCl.
4. The decanoic acid-dodecane recovery by spontaneous imbibition from - aged BST core plugs at room temperature indicated the effects of cation type and concentration on altering the wettability behaviour in BST. The imbibition results in NaCl solution show that the decanoic acid-dodecane recovery increased by 31% (OOIP) when the salinity of NaCl solution was decreased from 1.0M to 0.01M as determined by Ammot cell. The former concentration is only able to attain a 15 % recovery (OOIP). On the contrary, imbibition by $CaCl_2$ resulted in less total oil recovered, with 19.5% (OOIP) achieved by an initial treatment with a 1M solution, followed by an increase of only 11.7% after switching to 0.01M. Therefore, divalent cations (e.g. Ca^{2+}) in the brine hinder the low salinity effect with respect to the effects of monovalent cation-only brine(in the case of the Na^{+} and Ca^{2+} systems studied in this thesis).The observed results showed that cation type has an effect on decanoic acid-dodecane recovery, and it could be more dominant than the effect of cation concentration in the injected brine. At the core scale, therefore, enhancing oil recovery by low salinity brine is not only a function of the total dissolved salts in the injected brine but also the composition and ratios of the cations in the brine.
5. The experimental observations show that the wettability of the same system (decanoic acid/brine/BST) can be significantly affected by temperature. The decanoic acid recovery by spontaneous imbibition showed higher additional decanoic acid recovery when the temperature increased to 70°C, compared to that recovered at room temperature. Results show that the decanoic acid-dodecane recovery was improved by 28 % when immersed in 1.0M NaCl solution, and a further 37 % by 0.01M NaCl solution. Further investigation is needed to explain the effect of temperature on low salinity brine.
6. Mesurements of electrotokinetic charge using ζ potential was undertook to explain how the wettability of BST grains aged in decanoic acid-dodecane and BST grains

aged in crude oil were altered by changing the brine salinity at different concentrations (0.001M, 0.01M and 1M). In the case of the decanoic acid-dodecane-brine-BST system, the ζ potential was -38.9 mV at 0.001M NaCl brine concentration. Moreover, the ζ potential increased to -32 mV with increasing ionic strength of Na^+ at 0.01M NaCl concentration. The ζ potential remained negative -26.7 mV regardless of increasing ionic number Na^+ at 1.0M of NaCl. The effect of Ca^{2+} concentration on the measured ζ potential was also investigated. Results shown that ζ potential is -34.5 mV at 0.001M $CaCl_2$. The lareger values of -33 mV and -20.3 mV were measured for 0.01M of $CaCl_2$ and 1M of $CaCl_2$ salt, respectively. In the case of a crude oil-brine-BST system, the ζ potential was -32.7 mV at 0.001M NaCl brine concentration. It then increased to -24.5 mV with increasing ionic strength of Na^+ at 0.01M NaCl concentration. The ζ potential remained negative -19.4 mV regardless of increasing ionic number Na^+ at 1.0M of NaCl. For $CaCl_2$ brines ζ potential values changed from -27.6 to -23.3 mV for 0.001M $CaCl_2$ solution and 0.01M $CaCl_2$ solution, respectively. Nevertheless, for 1.0M $CaCl_2$ brine solution, the charge was -19.4 mV. In general, results show that monovalent cations are more efficient in increasing the absolute values of ζ potential that divalent cations at the same concentration. Zeta potential value became more negative while salinity of brines decreased. The resulting ζ potentials for BST grains aged in decanoic acid-dodecane is more negative than that of BST grains aged in crude oil in the range of 5 magnitudes. The results can be rationalised as due to the effect of high concentrations of NaCl salt increasingly shielding the high negative charge of crude oil by their high concentration of positively charged cations, since crude oil carries negative charges due to the organic acids in crude oil, and lower concentration of cation in low salinity, and as a result the crude oil/brine interface is strong and negatively charged. This explanation agrees with that similarly determined previously by Nasralla and Nasr-El-Din (2011a). Therefore, this would cause a measurable change of wettability behaviour of the system.

7.3. Conclusions/Implications of Results

Throughout this thesis the principal focus has been the application of a range of characterisation techniques to assess the mineral distribution at the pore surface as well as pore structure, the factors impact on mineral surface chemistry and ascertain how different cations affect the oil/water and oil/minerals surface from the experimental studies with broad implications to fully understanding what is happening in the sandstone reservoir during low salinity waterflooding EOR.

Berea core sandstones were subjected to a multi-scale analysis with an emphasis on determining the mineral composition and distribution at the pore surface as well as pore structure. From multiple length characterisations, the comprehensive understanding of mineral surface chemistry in reservoirs sandstone can play an essential role in determining oil/water and oil/minerals interactions and proposing further investigations. However, the surface characterisation can not only be achieved by using only microscopic methods as each technique can only cover a specific volume or area investigated with respect to resolution and dimension of observation.The methodology used in this study can be further applied to understanding the wider knowledge (new insight) into the sandstone rock characterisation, execution and analysis of core flood experiments in the lab, and oil and gas exploration in conventional and unconventional systems.

Although, clay minerals present in sandstone are more of interest to researchers than quartz in EOR technology, owing to their surface charge and exchangeable ions, the investigation in this thesis on ideal quartz surfaces showed that reduced salinity leads to a more water-wet state. This study has examined changes in surface wettability in a series of adhesion test on quartz surfaces; the results giving further insight into the role of nano-scale roughness on quartz surfaces in wettability alteration, also for the role of molecular level trenches on quartz surfaces to adsorb and accumulate the oil after reducing salinity, which may occur as a result of the different interaction of oil with the broken quartz crystal edges in the quartz surface.

To further improve our understanding of the role of quartz surfaces in porous media, a pretreated slice of Berea core sandstone were used in wettability experiments using ESEM. The effect of brine was consistent, reproducible and reversible. The results demonstrate that the quartz surface always contributes at least in part to the low salinity effect, decreasing oil wettability when salinity is low. In addition, it is much easier to observe general trends such as those described here-in, meaning that this experimental

study can give some valuable information to add to the understanding of low salinity EOR in sandstone rock.

7.4. Research Outlook

Although the studies presented here related to multi-length scale characterisation and wettability analysis on ideal quartz surfaces and sandstone surfaces, there still remain a number of fundamental questions to answer regarding the way that the technique works and to enable the optimisation of EOR deployment. On the basis of the work in this thesis, the topic that should be investigated further is what determines the fundamental controls on oil/water wettability of quartz surfaces. Through bringing together a range of *in situ* experimental (ESEM and AFM) and computational methods, the atomic level nature of these controls can be explored. This understanding will be of interest to ongoing EOR projects looking at a range of substrates.

Another important topic that should be investigated further is the role that clay minerals have in low-salinity waterflooding. For this purpose, several international groups with their industry partners have been exploring the nature of the clay/oil interactions. More recently, Durham University with the oil company BP has been conducting *in-situ* AFM experiments with large-scale molecular dynamics simulations to examine how different cations affect the oil/water and oil/clay structure(Underwood et al., 2015, 2016). This understanding will be of interest of oilfield applications and EOR projects.

At the University of Twente, they address fundamental aspects of the surface charge of clay mineral (e.g. kaolinite) in order to provide a rational scenario explaining many aspects of the success of low-salinity waterflooding (Mugele et al., 2014, 2016). Moreover, the functionalised tips with a carboxylic acid to model adhesion of polar components in crude oil to pore surfaces was used by a group of a researchers at the Nano-science Centre, University of Copenhagen (Hilner et al., 2015; Hassenkam et al., 2016). They will aim to find the role of nanoparticles attached to the sand grain surface as their result shown that the particles clearly respond to the low salinity effect.

Another topic to highlight is that pore-scale analysis during multi-phase flow behaviour in porous rocks will be required to design and predict oil recovery, from exploration to tertiary, while providing benchmarked predictions for input into field-scale models (Lai and Krevor, 2014; Krevor et al., 2015). Recently, the Department of Earth Science and Engineering at Imperial College London as part of the Digital Rocks Lab have

been tried to develop a robust methodology for identifying, quantifying, and characterising 3D pore space morphology and the distribution of mineralogy with the use of a combination of spectroscopic and X-ray tomography imaging techniques. Finally, develop a new and robust conceptual model to allow prediction of oil recovery during low salinity waterflooding EOR process is necessary, to bring together all the information garnered from multi-scale analysis in a constitutive framework.

7.5. References

Bera, B., M. H. G. Duits, M. A. Cohen Stuart, D. van den Ende, and F. Mugele, 2016, Surfactant induced autophobing: Soft Matter, v. 12, no. 20, p. 4562–4571, doi:10.1039/c6sm00128a.

Bera, A., K. S, K. Ojha, T. Kumar, and A. Mandal, 2012, Mechanistic Study of Wettability Alteration of Quartz Surface Induced by Nonionic Surfactants and Interaction between Crude Oil and Quartz in the Presence of Sodium Chloride Salt: Energy & Fuels, v. 26, no. 6, p. 3634–3643, doi:10.1021/ef300472k.

Desbois, G., J. L. Urai, S. Hemes, B. Schröppel, J.-O. Schwarz, M. Mac, and D. Weiel, 2016, Multi-scale analysis of porosity in diagenetically altered reservoir sandstone from the Permian Rotliegend (Germany): Journal of Petroleum Science and Engineering, v. 140, p. 128–148, doi:10.1016/j.petrol.2016.01.019.

Hassenkam, T. et al., 2016, Could Atomic-Force Microscopy Force Mapping Be a Fast Alternative to Core-Plug Tests for Optimizing Injection-Water Salinity for Enhanced Oil Recovery in Sandstone? SPE Journal, v. 21, no. 3, p. 720–729, doi:10.2118/169136-PA.

Hilner, E., M. P. Andersson, T. Hassenkam, J. Matthiesen, P. A. Salino, and S. L. S. Stipp, 2015, The effect of ionic strength on oil adhesion in sandstone – the search for the low salinity mechanism: Scientific Reports, v. 5, p. 9933, doi:10.1038/srep09933.

Krevor, S., M. J. Blunt, S. M. Benson, C. H. Pentland, C. Reynolds, A. Al-Menhali, and B. Niu, 2015, Capillary trapping for geologic carbon dioxide storage – From pore scale physics to field scale implications: International Journal of Greenhouse Gas Control, v. 40, p. 221–237, doi:10.1016/j.ijggc.2015.04.006.

Lai, P., and S. Krevor, 2014, Pore scale heterogeneity in the mineral distribution and surface area of Berea sandstone: Energy Procedia, v. 63, p. 3582–3588, doi:10.1016/j.egypro.2014.11.388.

Mugele, F., I. Sîretanu, N. Kumar, B. Bera, L. Wang, M. A. Maestro, M. H. G. Duits, H. T. M. van den Ende, and I. Collins, 2014, Charge Control And Wettability Alteration At Solid-liquid Interfaces, *in* Society of Petroleum Engineers journal, Tulsa, Oklahoma, USA: Society of Petroleum Engineers.

Mugele, F., I. Siretanu, N. Kumar, B. Bera, L. Wang, R. de Ruiter, A. Maestro, M. Duits, D. van den Ende, and I. Collins, 2016, Insights From Ion Adsorption and Contact-Angle Alteration at Mineral Surfaces for Low-Salinity Waterflooding: SPE Journal, v. 21, no. 4, p. 1,204-1,213, doi:10.2118/169143-PA.

Nasralla, R. A., and H. A. Nasr-El-Din, 2011a, Coreflood Study of Low Salinity Water Injection in Sandstone Reservoirs: Society of Petroleum Engineers, doi:10.2118/149077-MS.

Shedid, S. A., and M. T. Ghannam, 2004, Factors affecting contact-angle measurement of reservoir rocks: Journal of Petroleum Science and Engineering, v. 44, no. 3–4, p. 193–203, doi:10.1016/j.petrol.2004.04.002.

Underwood, T., V. Erastova, P. Cubillas, and H. C. Greenwell, 2015, Molecular Dynamic Simulations of Montmorillonite–Organic Interactions under Varying Salinity: An Insight into Enhanced Oil Recovery: The Journal of Physical Chemistry C, v. 119, no. 13, p. 7282–7294, doi:10.1021/acs.jpcc.5b00555.

Underwood, T., V. Erastova, and H. C. Greenwell, 2016, Wetting Effects and Molecular Adsorption at Hydrated Kaolinite Clay Mineral Surfaces: The Journal of Physical Chemistry C, v. 120, no. 21, p. 11433–11449, doi:10.1021/acs.jpcc.6b00187.

Appendix A

Multi-technique Approach to the Petrophysical Characterization of Berea Sandstone Core Plugs (Cleveland Quarries, USA)

Appendix A.1: Summary of point counting 52 thin sections

Table 1: Point counting category with QFL for the 52 studied thin sections from BST core samples.

Sample No	Sample ID		Quartz		K-feldspars %	Plagioclase %	Muscovite %	Quartz cement %	calcite %	Matrix %	Total	QFL%
			Monocrystalline %	Polycrystalline %								
	A1		65.6	17.8	5.1	1	1.2	1	0.1	8.1	99.9	84/7/9
1	B1		69.4	14.2	5	1.1	1.1	1.1	0	8	99.9	84/7/10
	A2		64.2	18.7	5.4	1	1	1	0.2	8.4	99.9	83/7/10
2	B2	BST.1	64.4	18.2	5.5	1.4	1.2	1.1	0.1	8	99.9	83/8/9
	A3		67.1	15.6	5.2	1.4	1.3	1	0	8.3	99.9	83/8/9
3	B3		64.8	18.2	5.2	1.3	1.2	1	0.1	8.1	99.9	83/8/10
	A4		64.3	17.9	5.2	1.2	1.1	1.2	1	8	99.9	82/8/10
4	B4		63.9	19.4	5	1.1	1	1.3	0	8.2	99.9	83/7/10
5	A5		63.1	21.4	4.3	1.5	1	1.3	0.2	7.1	99.9	84/7/9
	B5		62.4	22.9	4.2	1.3	1.3	1.2	0.1	6.5	99.9	85/7/9
6	A6		61.9	23.6	4.4	1.4	1.2	1.2	0	6.2	99.9	85/7/8
	B6		67.1	18	4.4	1.2	1.2	1.5	0	6.5	99.9	86/7/7
7	A7	BST.2	61.1	23.1	4.5	1.2	1.3	1.3	0.2	7.2	99.9	85/7/8
	B7		62.8	22.8	4.1	1.4	1.1	1.3	0.1	6.3	99.9	84/7/9
8	A8		61.8	22.9	4.2	1.5	1	1.2	0.1	7.2	99.9	86/7/8
	B8		62.8	21.4	4	1.6	1.3	1.4	0.2	7.2	99.9	85/7/9
9	A9		64	20.3	4.3	1.4	1.4	1.6	0.2	6.7	99.9	84/7/9
	B9		62.7	22.1	4.1	1.2	1.2	1.5	0.3	6.8	99.9	84/7/9
	A10		67.2	18.9	5.2	1.7	1.5	2.2	0.1	3.1	99.9	85/7/9
10	B10		67.2	18.9	5	1.7	1.3	2.4	0	3.4	99.9	86/8/6
	A11		60.4	25.4	5.6	1.6	1.4	2.3	0	3.2	99.9	86/8/6
11	B11	BST.3	60	26.4	5.3	1.5	1.3	2	0.1	3.3	99.9	86/9/6
	A12		64.1	22.6	5.3	1.6	1.4	1.9	0	3	99.9	87/8/5
12	B12		63.1	22.6	5.3	1.3	1.2	2.3	1	3.1	99.9	87/8/5
	A13		66.2	21	5	1.5	1.4	1.4	0.3	3.1	99.9	86/8/6
13	B13		63.9	22.2	5.1	1.7	1.3	2.2	0.1	3.4	99.9	87/8/5

Table 2: Point counting category with QFL for the 52 studied thin sections from BST core samples.

Sample No	Sample ID	Quartz		K-feldspars %	Plagioclase %	Muscovite %	Quartz cement %	calcite %	Matrix %	Total	QFL%
		Monocrystalline %	Polycrystalline %								
	A1		64.2	18.9	4.1	1.6	1.3	2.8	0	7	99.9	83/7/10
14	B1		63.1	19.9	4.6	1.5	1.1	2.8	0	6.9	99.9	83/7/10
	A2		64.4	20.1	4.3	1.4	1.2	1.2	0.1	7.2	99.9	85/7/8
15	B2		62.2	20.5	5.1	1.4	1.3	2.6	0	6.8	99.9	83/8/9
	A3		63.7	19.6	5.3	1.2	1.2	2.4	0	6.5	99.9	83/10/7
16	B3		63.2	19.2	5	1.4	1.3	2.6	0.1	7.1	99.9	83/8/9
	A4		64.3	18.5	4.8	1.2	1.4	2.5	0	7.2	99.9	83/8/9
17	B4		64.8	18	5.2	1.7	1.3	1.9	0	7	99.9	83/8/9
	A5	BST.3	63.1	19.7	5.2	1.2	1.3	2.3	0	7.1	99.9	83/7/10
18	B5		62.8	17.3	5.9	1.8	1.7	2.9	0.2	7.3	99.9	80/9/11
	A6		62.2	22.7	3.4	1.4	1.2	2.2	0	6.8	99.9	85/6/9
19	B6		62.1	20.9	5.1	1.6	1.3	2.1	0	6.8	99.9	83/8/9
	A7		63.9	18.6	5.2	1.5	1.2	2.3	0	7.2	99.9	83/8/9
20	B7		63.7	19.3	5.1	1	1.1	2.3	0.1	7.3	99.9	83/7/10
	A8		61.3	20.8	5.3	1.6	1.4	2.4	0	7.1	99.9	82/8/10
21	B8		65.1	17	5.4	1.7	1.5	2.3	0	6.9	99.9	82/9/9
	A9		62.7	18.9	5.7	1.2	1.6	2.6	0.1	7.1	99.9	82/9/9
22	B9		63.1	20.5	4.8	1.1	1	2.3	0.2	6.9	99.9	84/7/9
	A10		73.2	18.9	0.6	0	0.2	3.3	0	3.7	99.9	83/7/10
23	B10		75.6	15.3	0.9	0	0.2	3.4	1.1	3.4	99.9	92/1/7
	A11		78.7	13	0.6	0	0.5	2.9	0.4	3.8	99.9	91/1/8
24	B11	BST.4	78.2	14	0.5	0	0.4	3.4	0	3.4	99.9	92/1/7
	A12		70.2	16	0.8	0	0.3	5.4	0	3.2	95.9	92/1/7
25	B12		79.3	13.5	0.6	0	0.3	2.9	0.2	3.1	99.9	90/1/9
	A13		70.6	21.5	0.8	0	0.2	2.8	0.4	3.6	99.9	93/1/6
26	B13		72.9	19.2	0.9	0	0.1	3.2	0.2	3.4	99.9	92/1/7

Appendix A.2: Mineral weight percentage estimation from XRD, and process for estimating the area fraction from electron microscopy images.

Table 1: Weight percentage mineralogy of BST core specimens estimated from XRD.

Sample ID	Quartz	K-feldspar	Plagioclase	Muscovite	Calcite	Ankerite	Siderite	Anatase	Chlorite	Kaolinite	I/S-ML	
BST.1	81.4	5.1	1.4	1.2	0.1	1.6	0.7	0.2	0.8	3.6	3.8	99.9
BST.2	84.5	4.4	1.4	1.1	0.1	0.9	0.5	0.2	0.7	3.1	3.0	99.9
BST.3	82.7	5.3	1.7	1.4	0.0	0.8	0.8	0.1	0.7	3.5	2.9	99.9
BST.4	95.1	0.8	0.0	0.3	0.1	0.1	0.1	0.0	0.2	1.6	1.6	99.9

Table 2: Area of BST core specimens from BSE/EDX

Sample ID	Quartz	K-feldspar	Plagioclase	Calcite	Ankerite	Siderite	Anatase	Chlorite	Muscovite	Kaolinite	I/S-ML	
BST.1	61.1	1.3	1.3	0.0	9.5	2.9	2.8	0.9	4.4	13.9	2.1	99.9
BST.2	76.2	2.5	2.2	0.0	2.4	0.7	0.6	0.0	3.6	5.8	6.0	99.9
BST.3	75.0	2.4	1.6	0.0	5.6	0.7	0.2	6.6	0.0	5.2	2.7	99.9
BST.4	95.1	0.0	0.0	0.0	0.0	0.0	0.2	0.0	0.0	3.1	1.6	99.9

Appendix A.3: Parameters used for X-ray imaging and segmentation

BST samples were scanned by The XRadia/Zeiss XRM 410 which ensures maximum scan quality. Table 3.1 shows the field of view obtained.

Table 1: The XRM410 scan parameter for all three sample sizes, LFOV indicates a large field of view scan whilst SFOV indicates a small field of view scan.

Sample Size	Diameter (mm)	Height (mm)	Scan Type	Voxel Size (um)	Field of View (mm)	Scan Time (hr)
BST.1	20	50	LFOV	21	21x21	2.0
BST.1	10	10	SFOV	1.88	2.0 x 2.0	19
BST.1	10	10	SFOV	1.03	1.0x1.0	29
BST.2	20	50	LFOV	21	21x21	2.0
BST.2	10	10	SFOV	1.88	2.0 x 2.0	19
BST.2	10	10	SFOV	1.03	1.0x1.0	29
BST.3	20	50	LFOV	21	21x21	2.0
BST.3	10	10	SFOV	1.88	2.0 x 2.0	19
BST.3	10	10	SFOV	1.03	1.0x1.0	29
BST.4	20	50	LFOV	21	21x21	2.0
BST.4	10	10	SFOV	1.88	2.0 x 2.0	19
BST.4	10	10	SFOV	1.03	1.0x1.0	29

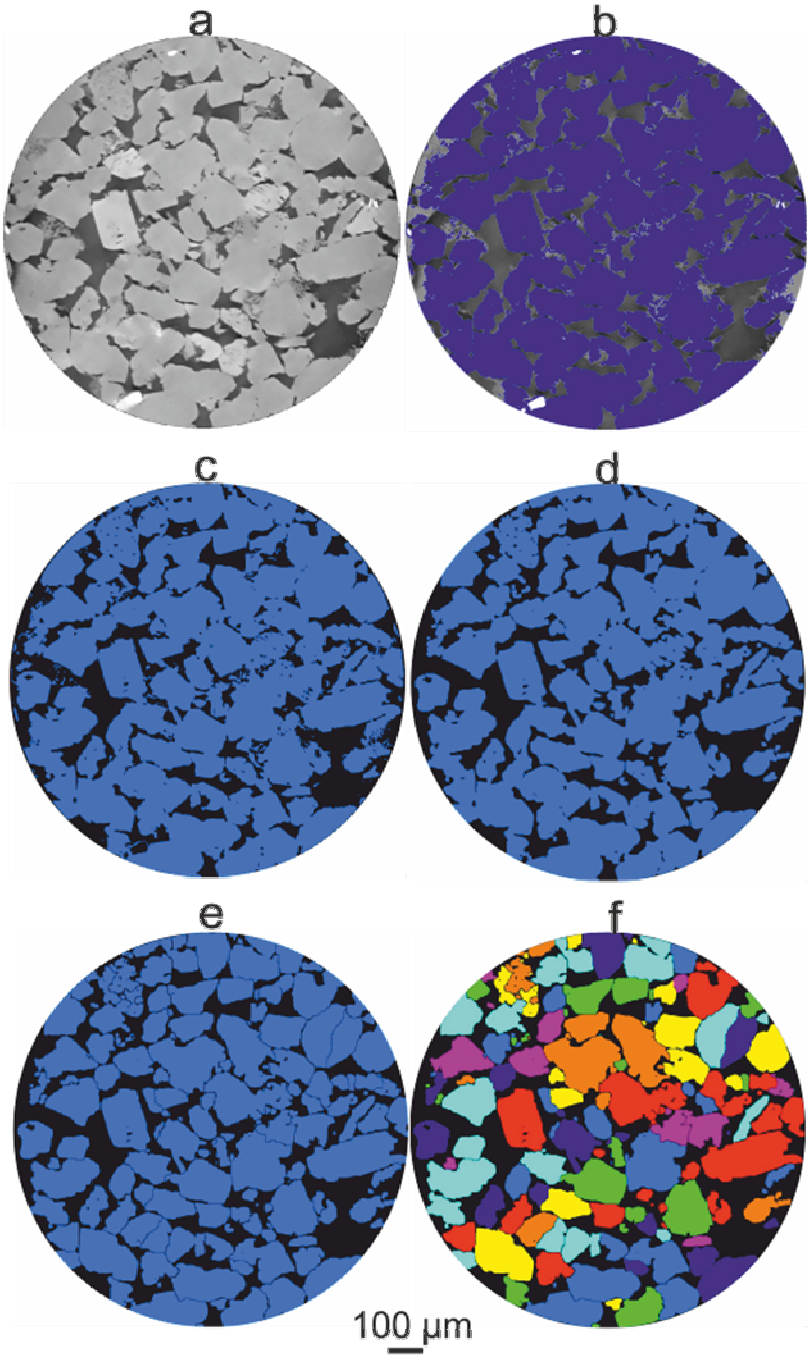

Figure 1: Example of detrital grain size analysis of a scanned BST core specimen by segmentation (with a resolution of 1.87 µm): a) micrograph image. b) The binary image of detrital grains after applying the thresholding module c) Binary image of BST after removing pores. d) Filtered detrital grains. e) Separated detrital grains. f) Separated detrital grains labelled.

Table 2: Equivalent diameters of detrital grains from selected BST core samples

BST.1		BST.2		BST.3		BST.4	
Diameter(μm)	Frequency	Diameter(μm)	Frequency	Diameter(μm)	Frequency	Diameter(μm)	Frequency
16.7	309.0	18.3	196.0	17.2	321.0	19.0	420.0
23.9	170.0	24.1	80.0	25.2	183.0	30.5	107.0
31.1	74.0	30.0	54.0	33.1	99.0	42.1	29.0
38.4	38.0	35.8	25.0	41.1	41.0	53.6	26.0
45.6	26.0	41.7	24.0	49.1	38.0	65.1	28.0
52.8	31.0	47.5	14.0	57.0	27.0	76.7	29.0
60.0	33.0	53.4	17.0	65.0	33.0	88.2	32.0
67.2	39.0	59.2	20.0	73.0	34.0	99.7	38.0
74.5	54.0	65.0	35.0	80.9	50.0	111.3	44.0
81.7	61.0	70.9	49.0	88.9	53.0	122.8	40.0
88.9	68.0	76.7	40.0	96.9	52.0	134.4	49.0
96.1	68.0	82.6	60.0	104.8	60.0	145.9	51.0
103.4	76.0	88.4	69.0	112.8	60.0	157.4	37.0
110.6	83.0	94.3	86.0	120.8	56.0	169.0	47.0
117.8	94.0	100.1	72.0	128.7	76.0	180.5	38.0
125.0	92.0	106.0	99.0	136.7	89.0	192.1	30.0
132.2	77.0	111.8	88.0	144.7	69.0	203.6	39.0
139.5	80.0	117.7	92.0	152.6	59.0	215.1	30.0
146.7	87.0	123.5	104.0	160.6	58.0	226.7	22.0
153.9	79.0	129.4	109.0	168.6	57.0	238.2	28.0
161.1	63.0	135.2	115.0	176.6	51.0	249.7	21.0
168.4	63.0	141.0	102.0	184.5	52.0	261.3	14.0
175.6	47.0	146.9	77.0	192.5	38.0	272.8	9.0
182.8	40.0	152.7	78.0	200.5	30.0	284.4	10.0
190.0	45.0	158.6	76.0	208.4	21.0	295.9	9.0
197.3	35.0	164.4	56.0	216.4	21.0	307.4	7.0
204.5	21.0	170.3	65.0	224.4	14.0	319.0	5.0
211.7	14.0	176.1	49.0	232.3	11.0	330.5	0.0
218.9	18.0	182.0	39.0	240.3	9.0	342.1	1.0
226.1	7.0	187.8	29.0	248.3	10.0	353.6	1.0
233.4	8.0	193.7	34.0	256.2	5.0	365.1	1.0
240.6	10.0	199.5	14.0	264.2	0.0	376.7	1.0
247.8	3.0	205.4	17.0	272.2	0.0	388.2	0.0
255.0	3.0	211.2	19.0	280.1	1.0	399.7	0.0
262.3	1.0	217.0	13.0	288.1	0.0	411.3	1.0
269.5	1.0	222.9	8.0	296.1	1.0		
276.7	0.0	228.7	5.0	304.0	0.0		
283.9	0.0	234.6	0.0	312.0	0.0		
291.1	0.0	240.4	3.0	320.0	0.0		
298.4	1.0	246.3	3.0	327.9	0.0		
305.6	0.0	252.1	4.0	335.9	0.0		
312.8	0.0	258.0	0.0	343.9	1.0		
320.0	0.0	263.8	3.0				
327.3	1.0	269.7	1.0				
		275.5	0.0				
		281.4	1.0				

Appendix A.4 AFM imaging

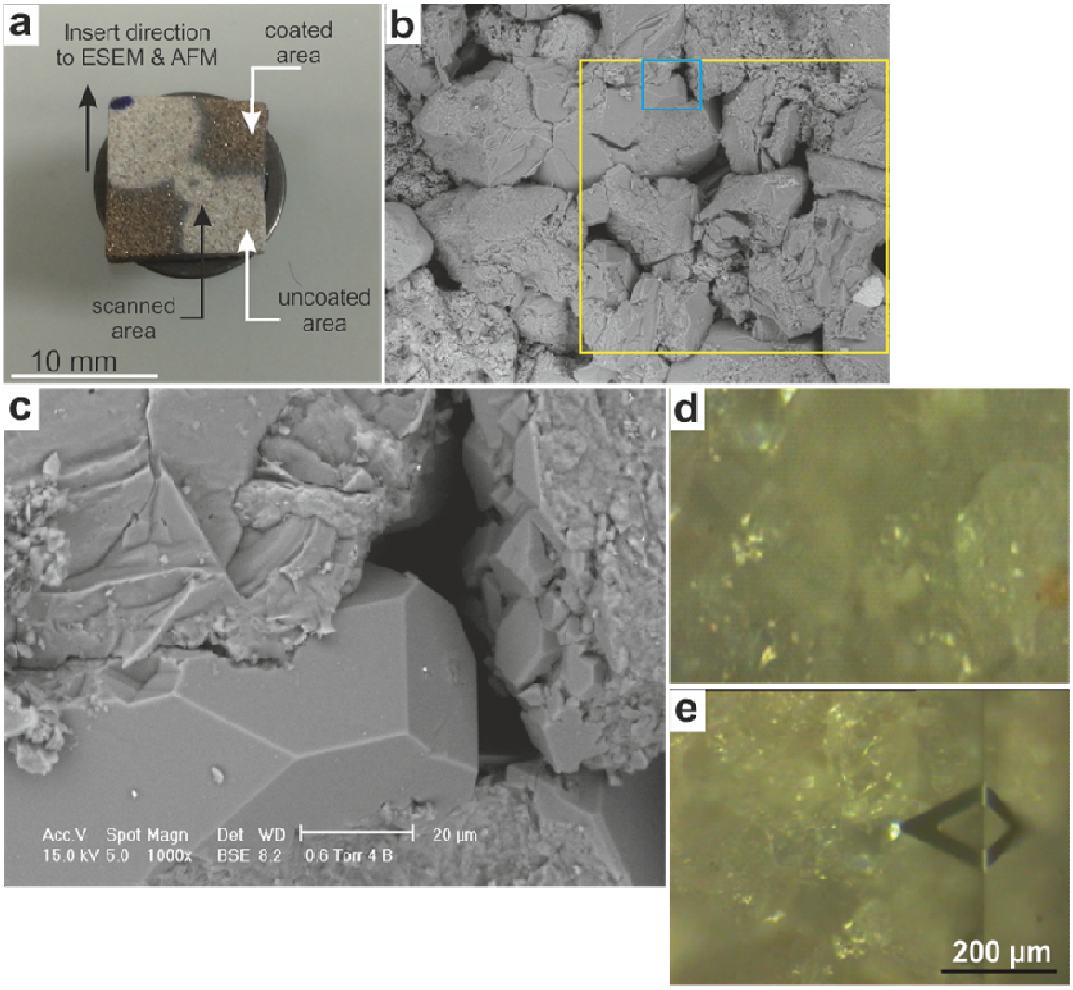

Figure 1: A process for imaging detrital quartz surface using SEM and AFM techniques. a) Uncoated BST chip. b) SEM image showing detrital grains in BST sample (Yellow Square) represents high light a location area, and blue square is a selected area for imaging. c) Enlargement of Blue Square from (b) showing a quartz overgrowth surface. d) Same area of image (b) under AFM optical microscopy. e) Approaching AFM tip toward a selected detrital quartz surface.

Journal of Petroleum Science and Engineering xx (xxxx) xxxx–xxxx

Contents lists available at ScienceDirect

Journal of Petroleum Science and Engineering

journal homepage: www.elsevier.com/locate/petrol

Multi-technique approach to the petrophysical characterization of Berea sandstone core plugs (Cleveland Quarries, USA)

Rikan Kareem[a], Pablo Cubillas[a], Jon Gluyas[a], Leon Bowen[b], Stephen Hillier[c,d], H. Christopher Greenwell[e,*]

[a] Department of Earth Sciences, Durham University, South Road, Durham DH1 3LE, United Kingdom
[b] Department of Physics, Durham University, South Road, Durham DH1 3LE, United Kingdom
[c] The James Hutton Institute, Craigiebuckler, Aberdeen AB15 8QH, United Kingdom
[d] Department of Soil and Environment, Swedish University of Agricultural Sciences, Box 7014, Uppsala SE-750 07, Sweden
[e] Department of Earth Sciences, Durham University, South Road, Durham, DH1 3LE, United Kingdom

ARTICLE INFO

Keywords:
Berea sandstone
Mineral characterization
Nonoparticles
Pore system
EOR

ABSTRACT

Berea sandstone has been used by the petroleum industry as a representative model siliciclastic rock for a number of years. However, only incomplete data has been reported in the literature regarding its petrographic, geochemical, and petrophysical properties. In particular knowledge of the mineral distribution along the pore walls is particularly scarce, despite the fact that mineral exposed in the pore space will be crucial in determining the rock-fluid interactions that occur during core-flooding experiments. In this paper, four Berea sandstone samples (with 4 different permeability ranges from < 50 mD, 50–100 mD. 100–200 mD, and 500–1000 mD) were subjected to a multi-technique characterization with an emphasis on determining the mineral composition, and distribution at the pore surface as well as pore structure and connectivity analysis. The mineral distribution was measured in two-dimensions by chemical mapping using energy dispersive X-ray spectroscopy–scanning electron microscopy (SEM–EDX). The bulk composition of the Berea sandstones was also measured by X-ray diffraction and micro-X-ray computed tomography. From this, it was found that authigenic minerals, especially clay minerals, make up a small portion of the bulk rock volume (3.3–8%) but are over-represented at the pore surfaces and in pore spaces compared to the other major mineral constituents of the rock (quartz and feldspar). The effective mineralogy, from the standpoint of rock-fluid interactions, is the mineralogy that predominates at pore surfaces. For the Berea sandstone samples studied, the effective mineralogy is represented, mainly, by kaolinite, illite, and chlorite. For 3 of the four permeability ranges studied, kaolinite is the predominant pore lining mineral observed. In the remaining sample (50–100 mD), illite is the predominant mineral. In addition to SEM, we used atomic force microscopy to show that the nano-sized particles with the shape and size of clay crystals are observed on the surface of recrystallised quartz grains in a Berea sample. Regardless of their origin and identity, the presence of these particles shows that the quartz grain surfaces in Berea sandstone are more heterogeneous than previously assumed. Carbonate cement was somewhat localized throughout two of the Berea sandstone specimens, however, quartz cement is common in all of the Berea cores studied and include both microcrystalline quartz and amorphous silica phases. The pore structure within the four different Berea samples was studied using a combination of X-ray computed tomography, mercury injection porosimetry and high resolution scanning electron microscopy. Results show that two Berea sandstone permeability ranges have a bimodal pore-throat-size distribution whereas the other two were dominated by a unimodal pore-throat size distribution. SEM imaging of the pore network showed that permeability is mainly controlled by pore connectivity in the clay mineral matrix. Next to the pore connectivity, three-dimensional pore space showing both pore-to-pore and pore-to-pore-throat-to-pore relationships are also important.

* Corresponding author.
E-mail address: chris.greenwell@durham.ac.uk (H.C. Greenwell).

http://dx.doi.org/10.1016/j.petrol.2016.09.029
Received 27 May 2016; Received in revised form 16 August 2016; Accepted 19 September 2016
Available online xxxx

Please cite this article as: Kareem, R.M., Journal of Petroleum Science and Engineering (2016), http://dx.doi.org/10.1016/j.petrol.2016.09.029

Appendix B

Wettability Regime in Quartz based Substrate

B.1. Contact Angle -ESEM

In this set of experiments clean, treated and untreated with brine, decanoic acid, and crude oil quartz crystals were examined using (Peltier stage) ESEM chamber. In our work, an average measured contact angles taken over at least three water droplets.

Table B1.1: The average of the dynamic contact angle of water droplets on treated non- flat quartz crystal with different concentration of each sodium chloride and calcium chloride.

No	NaCl		$CaCl_2$	
	0.01M	1.0M	0.01M	1.0M
1	56.85	92.80	54.26	69.66
2	45.32	101.23	62.86	73.68
3	54.34	106.04	78.17	76.67
4	75.90	95.93	62.50	68.46
5	63.01	84.18	67.16	67.06
6	47.56	71.90	75.58	109.95
7	65.35	83.82	64.24	87.50
8	47.58	82.23	74.26	82.50
9	24.63	80.89	74.89	87.87
10	62.95	76.19	67.60	63.52
11	75.75	75.67	73.46	102.54
12	43.21	76.49	77.05	93.03
13	29.18	75.18	74.15	55.46
14	38.73	83.05	81.86	57.36
15	45.95	79.30	86.90	54.58

Table B1.2: Summary of dynamic contact angle of water droplets on the flat-quartz crystal aged in decanoic acid/dodecane, were exposed to sodium chloride.

Type of sample	No	Times (sec)	Pressure (Torr)	Dynamic contact angle (θ)			
				Droplet 1	Droplet 2	Droplet 3	Average
Flat-Quartz + Decanoic acid-dodecane + 0.01M NaCl	1	1225	5.5	78.43	73.43	87.00	79.62
	2	1293	6.8	70.56	70.56	86.00	75.71
	3	1347	6.8	71.25	78.60	87.00	78.95
	4	1449	6.8	77.40	78.20	82.00	79.20
	5	1623	6.8	79.20	80.00	83.00	80.73
	6	1834	6.8	80.20	81.40	83.90	81.83
	7	1990	6.8	80.40	81.40	84.00	81.93
	8	2004	6.8	86.20	82.30	87.00	85.17
	9	2049	6.8	76.23	75.46	77.29	76.33
	10	2100	6.8	72.36	74.54	75.26	74.05
	11	2118	6.8	79.78	75.46	80.00	78.41
	12	2164	6.8	72.63	74.30	76.40	74.44
	13	2241	6.8	71.12	74.10	75.56	73.59
Flat-Quartz + Decanoic acid-dodecane+1.0M NaCl	1	1225	6.7	115.2	139.1	139.7	131.3
	2	1293	6.7	105.7	123.3	105.4	111.5
	3	1347	6.8	104.7	112.6	101.6	106.3
	4	1449	6.8	110.0	116.0	113.0	113.0
	5	1623	6.8	95.93	98.93	97.93	97.59
	6	1834	6.8	79.74	80.75	70.71	77.07
	7	1990	6.8	130.9	139.5	127.1	132.5
	8	2004	6.8	120.3	126.1	123.4	123.3
	9	2049	6.8	103.3	110.3	109.3	107.6
	10	2100	6.8	123.9	130.8	138.7	131.1
	11	2118	6.8	111.7	113.9	119.8	115.1
	12	2164	6.8	113.1	115.8	115.9	114.9
	13	2241	6.8	129.9	141.6	149.3	140.2

Table B1.3: Summary of dynamic contact angle of water droplets on the flat- quartz crystal aged in decanoic acid/dodecane, were exposed to calcium chloride.

Type of sample	No	Times (sec)	Pressure (Torr)	Dynamic contact angle (θ)			
				Droplet 1	Droplet 2	Droplet 3	Avearge
Flat-Quartz+Decanoic acid-dodecane+0.01M $CaCl_2$	1	0.00	5.5	120.2	123.3	123.2	122.2
	2	262	6.5	113.7	118.1	120.0	117.3
	3	391	6.8	51.10	47.15	50.19	49.48
	4	503	7.0	101.4	104.3	101.7	102.5
	5	611	7.1	103.8	106.6	105.3	105.2
	6	686	7.2	119.7	124.4	121.4	121.8
	7	793	7.3	93.12	101.1	97.18	97.16
	8	858	7.4	85.17	87.22	81.93	84.77
	9	926	7.4	49.14	43.20	45.26	45.87
	10	1030	7.4	65.85	71.10	70.33	69.09
	11	1099	7.4	66.45	65.00	64.45	65.30
	12	1140	7.4	37.00	38.21	32.30	35.84
	13	1165	7.4	45.21	50.32	50.26	48.60
Flat-Quartz+Decanoic acid-dodecane+1.0M $CaCl_2$	1	960	6.7	70.10	74.35	72.28	72.24
	2	1520	7.4	88.52	84.78	86.62	86.64
	3	1685	7.4	114.3	107.1	112.3	111.2
	4	1748	7.4	115.0	110.0	114.0	113.0
	5	1813	7.4	120.1	124.3	122.2	122.0
	6	1935	7.4	77.52	73.00	75.10	75.21
	7	1983	7.4	83.14	83.00	84.62	83.59
	8	2005	7.4	84.41	86.00	87.41	85.94
	9	2068	7.4	95.93	99.00	97.93	97.62
	10	2119	7.4	90.00	94.29	92.45	92.25
	11	2162	7.4	115.3	94.30	113.3	107.6
	12	2185	7.4	149.8	102.8	141.4	131.3
	13	2232	7.4	110.9	115.9	120.9	115.9

Table B1.4: Summary of dynamic contact angle of water droplets on the non- flat quartz crystal aged in decanoic acid/dodecane, were exposed to sodium chloride.

Type of sample	No	Times (sec)	Pressure (Torr)	Dynamic contact angle (θ)			
				Droplet 1	Droplet 2	Droplet 3	Average
Non-Quartz+Decanoic acid-dodecane+0.01M NaCl	1	0.00	5.60	0.00	0.00	0.00	0.00
	2	390	5.60	0.00	0.00	0.00	0.00
	3	444	5.80	101.9	0.00	0.00	33.99
	4	609	5.80	128.4	115.3	114.6	119.4
	5	1027	6.80	122.0	110.8	122.5	118.4
	6	1048	6.80	133.8	85.90	132.7	117.4
	7	1090	6.80	115.7	91.70	120.5	109.3
	8	1110	6.80	114.6	97.04	118.2	110.0
	9	1155	6.80	64.98	52.23	116.6	77.94
	10	1174	6.80	62.23	49.78	115.0	75.68
	11	1216	6.80	60.23	48.74	124.7	77.89
	12	1263	6.80	32.20	10.40	113.5	52.06
	13	1284	6.80	30.86	25.21	101.5	52.53
	14	1353	6.80	14.23	15.68	15.45	15.12
	15	1394	6.80	0.00	0.00	0.00	0.00
Non-Quartz+Decanoic acid-dodecane+1.0M NaCl	1	0.00	5.50	0.00	0.00	0.00	0.00
	2	7.00	5.50	0.00	0.00	0.00	0.00
	3	567	6.50	0.00	0.00	0.00	0.00
	4	688	6.60	84.54	69.37	0.00	51.30
	5	790	6.70	95.47	67.98	69.96	77.80
	6	843	6.80	101.5	76.39	79.19	85.71
	7	900	6.80	105.8	81.15	97.66	94.88
	8	919	6.80	120.8	104.4	100.4	108.5
	9	974	6.80	131.3	118.0	101.1	116.8
	10	1033	6.80	132.6	130.7	107.0	123.4
	11	1080	6.80	117.8	125.0	90.60	111.1
	12	1095	6.80	115.1	121.5	88.22	108.3
	13	1140	6.80	85.51	121.5	99.34	102.1
	14	1170	6.80	79.43	70.35	96.10	81.96
	15	1227	6.80	78.07	83.32	109.9	90.43
	16	1272	6.80	61.13	80.26	107.3	82.90
	17	1291	6.80	117.8	125.0	90.60	111.1
	18	1346	6.80	115.1	121.5	88.22	108.3
	19	1392	6.80	85.51	121.5	99.34	102.1
	20	1411	6.80	79.43	70.35	96.10	81.96
	21	1455	6.80	78.07	83.32	109.9	90.43
	22	1471	6.80	61.13	80.26	107.3	82.90

Table B1.5: Summary of dynamic contact angle of water droplets on the non- flat quartz crystal aged in decanoic acid/dodecane, were exposed to calcium chloride.

Type of sample	No	Times (sec)	Pressure (Torr)	Dynamic contact angle (θ)			
				Droplet 1	Droplet 2	Droplet 3	Avearge
Non-Quartz+Decanoic acid-dodecane+0.01M $CaCl_2$	1	265	5.50	0.00	0.00	0.00	0.00
	2	606	6.40	0.00	0.00	0.00	0.00
	3	1027	7.10	72.00	0.00	0.00	24.00
	4	1082	7.10	65.00	0.00	0.00	21.67
	5	1099	7.10	100.47	116.3	0.00	72.28
	6	1156	7.10	112.02	94.78	95.0	100.6
	7	1211	7.10	101.80	90.03	86.20	92.68
	8	1230	7.10	95.86	105.6	92.60	98.02
	9	1273	7.10	99.59	124.5	98.62	107.5
	10	1293	7.10	112.02	110.2	96.37	106.2
	11	1335	7.10	105.02	105.9	99.59	103.5
	12	1352	7.10	112.54	98.10	83.68	98.11
	13	1392	7.10	92.94	98.38	99.14	96.82
	14	1413	7.10	96.62	98.69	89.45	94.92
	15	1507	7.10	110.96	118.9	116.63	115.5
	16	1525	7.10	112.39	70.52	118.43	100.4
	17	1572	7.10	80.96	80.96	119.52	93.81
	18	1626	7.10	83.66	83.66	106.60	91.31
	19	1643	7.10	80.46	80.46	118.86	93.26
	20	1687	7.10	52.40	47.28	115.58	71.75
	21	1707	7.10	53.66	53.66	113.81	73.71
Non-Quartz+Decanoic acid-dodecane+0.01M $CaCl_2$	1.00	2358	1.50	0.00	0.00	0.00	0.00
	2.00	2652	4.50	83.62	81.78	83.62	83.01
	3.00	2707	5.00	85.92	82.07	80.40	82.80
	4.00	2819	5.20	87.29	84.06	82.07	84.47
	5.00	2814	5.40	89.86	90.00	82.33	87.40
	6.00	2870	5.60	90.80	91.97	91.91	91.56
	7.00	2888	5.80	93.37	97.93	82.37	91.22
	8.00	2942	6.00	91.59	115.6	95.54	100.9
	9.00	3015	6.20	92.94	113.2	92.04	99.41
	10.00	3066	6.40	95.21	120.0	88.46	101.2
	11.00	3121	6.60	96.48	120.3	91.15	102.5
	12.00	3176	6.80	94.91	91.02	91.02	92.32
	13.00	3229	7.00	95.55	95.82	95.82	95.73
	14.00	3289	7.00	132.8	123.4	123.4	126.6
	15.00	3315	7.00	112.6	117.7	122.8	117.7
	16.00	3370	7.00	122.1	128.6	128.6	126.5
	17.00	3374	7.00	119.5	128.1	128.1	125.3

B.2. Contact Angle -Drop Shape Analysis

The contact angle measurements were taken using Kruss DSA 100 drop shape analyser; the following contact angle results found in a set of experiment.

Table B 2.1: Summary of dynamic contact angle of water droplets on the non- flat quartz crystal aged in decanoic acid/dodecane, were exposed to sodium chloride.

Type of Tests	No.	Theta (M)[deg]	IFT [mN/m]	Type of Tests	Theta (M)[deg]	IFT [mN/m]	Type of Tests	Theta (M)[deg]	IFT [mN/m]
	1	56.1	15.59		76.6	16.45		89.1	12.23
	2	55.5	15.96		73.8	15.95		88.5	12.97
	3	55.1	16.61		72.4	15.74		87.3	12.55
	4	53.2	15.41		71.6	16.1		86.6	11.74
	5	52.8	16.76		68.2	17.87		86.1	13.75
	6	55.8	16.31		67.7	17.98		85.4	15.22
	7	54.9	15.93		66.9	18.33		85.6	14.99
	8	54.1	16.83		67.5	18.89		84.7	17.12
	9	56.4	16.42		62.1	16.46		84.5	11.78
	10	53.6	16.39		62.7	16.34		83.1	13.66
	11	54.6	15.97		63.6	15.68		83.8	13.99
	12	51.7	16.74		64.4	20.91		83.4	11.89
	13	52.4	16.35		66.1	19.14		83.6	10.99
	14	54	16.28		65.6	16.47		82.1	14.25
	15	53.9	16.63		65.5	21.29		81.5	15.87
Quartz	16	52.1	16.36	Quartz	63.7	18.47	Quartz	81	16.97
+Decanoic	17	50.3	16.25	+Decanoic	63.6	72.73	+Decanoic		
Acid-	18	53.7	15.15	Acid-	62.7	13.2	acid-		
dodecane	19	55	16.97	dodecane	62.4	16.11	dodecane		
+	20	52.7	15.87	+	62.4	13.83	+		
0.001M	21	54	16.12	0.01M	61.6	13.15	1.0M		
NaCl	22	52.7	16.14	NaCl	62.6	13.68	NaCl		
	23	55.8	17.04		63.4	16.27			
	24	54.6	17.3		62.4	14.76			
	25	52.5	17.15		62.1	15.25			
	26	52.6	15.74		62.1	13.24			
	27	53.7	15.73						
	28	52.2	17.55						
	29	53.7	16.23						
	30	53.9	15.35						
	31	53.8	15.7						
	32	53.3	16.92						
	33	53.9	15.02						
	34	52.7	15.51						
	35	53.5	15.36						
	36	53.9	14.92						
	37	53.8	15.28						

Table B 2.2: Summary of dynamic contact angle of water droplets on the non- flat quartz crystal aged in decanoic acid/dodecane, were exposed to calcium chloride.

Type of Test	No.	Theta (M)[deg]	IFT [mN/m]	Type of Test	Theta (M)[deg]	IFT [mN/m]	Type of Test	Theta (M)[deg]	IFT [mN/m]
	0	76	6.93		82	198.65		89.5	30.41
	1	74.4	8.28		79.2	109.41		86.9	30.95
	2	72.3	10.17		79.3	197.73		86.5	51.02
	3	72	10.25		78.6	66.16		86.5	51.2
	4	74.5	10.28		76.2	109.84		87.6	51.76
	5	71.1	11.4		75	63.5		87.6	94.37
	6	74.2	10.33		72.1	109.89		85.2	30.77
	7	72	10.35		72.5	199.55		85.9	51.3
Quartz	8	71.4	10.44	Quartz	72.8	66.56	Quartz	85.7	30.99
+Decanoic	9	72.2	9.34	+Decanoic	72.4	198.17	+Decanoic	85.4	30.68
Acid-	10	71.6	10.45	Acid-	72.6	112.33	acid-	85.9	19.84
dodecane+	11	71.5	10.47	dodecane+	72.6	106.21	dodecane+	85.6	31.04
0.001M	12	71.2	10.47	0.01M	72.9	67.81	1.0M	85.4	30.86
$CaCl_2$	13	71.6	10.11	$CaCl_2$	72.9	103.12	$CaCl_2$	85.1	31.08
	14	73.1	10.49		62.1	54.33		86.8	51.86
	15	71.6	10.06		72.4	113.73		86.9	30.99
	16	72.9	10.52		70.1	29.85		86.2	13.44
	17	70.9	10.59		70.7	186.24		85.3	13.41
	18	68.4	10.58		69.1	68.32		86.5	20.38
	19	68.3	10.58		71.1	68.34		85.4	15.55
	20	68.2	10.59		69.4	64.72		85.5	13.81
	21	72.7	10.6		70.6	38.03		84.5	13.83

Table B 2.3: Summary of dynamic contact angle of water droplets on the non- flat quartz crystal aged in crude oil, were exposed to sodium chloride.

Type of Test	No.	Theta (M)[deg]	IFT [mN/m]	Type of Test	Thet a(M)[deg]	IFT [mN/m]	Type of Test	Theta (M)[deg]	IFT [mN/m]
	1	52.80	9.66		89.50	13.0		107.3	4.30
	2	51.70	6.20		79.30	11.4		91.10	10.8
	3	52.70	6.35		90.60	13.2		91.60	7.03
	4	50.90	5.21		106.1	19.1		61.70	24.1
	5	50.20	5.61		85.80	19.7		59.40	9.13
	6	52.30	5.68		89.10	26.4		44.20	7.91
	7	52.50	6.09		110.9	30.5		80.00	11.2
	8	51.40	9.82		87.00	19.8		105.5	7.91
	9	45.00	8.51		86.40	20.7		108.7	8.40
	10	51.50	6.07		67.90	20.6		74.60	8.40
	11	52.40	5.74		109.1	21.0		73.60	14.8
	12	48.00	6.16		85.90	21.1		88.40	13.9
	13	50.60	6.06		90.00	21.2		92.80	11.8
	14	51.30	10.0		85.50	55.9		109.5	9.68
Quartz	15	51.80	5.39	Quartz	89.20	29.6	Quartz	74.60	11.5
+Crude	16	50.10	5.41	+Crude	90.80	31.3	+Crude	75.10	3.10
Oil	17	52.10	5.41	Oil	42.50	26.2	Oil	89.50	16.4
+0.001M	18	51.20	10.1	+0.01M	74.50	25.9	+1.0M	89.30	15.2
NaCl	20	54.30	5.46	NaCl	49.90	16.6	NaCl	90.70	8.08
	21	53.10	5.65		78.70	17.4		68.00	5.39
	22	54.50	6.26		79.30	15.5		90.80	5.37
	23	49.80	6.41		67.20	10.2		107.4	4.52
	24	60.00	7.63		81.60	17.0		104.3	4.03
	25	52.80	10.6		75.60	14.5		85.50	9.21
	26	51.20	7.67		45.50	18.2		93.90	12.7
	27	50.10	5.66		44.80	13.8		66.80	18.8
	28	50.30	7.65		46.10	10.2		87.60	12.7
	29	52.30	9.06		46.40	9.58		105.9	15.8
	30	53.70	15.4		43.40	9.55		83.10	93.1
	31	55.00	11.7		46.10	9.40		72.60	6.60
	32	48.40	5.70		44.50	9.55		78.00	51.2
	33	50.10	5.51		45.00	9.27		114.8	51.1
	34	44.40	10.7		44.40	9.32		87.50	30.6

Table B 2.4: Summary of dynamic contact angle of water droplets on the non- flat quartz crystal aged in crude oil, where exposed to calcium chloride.

Type of Test	No.	Theta (M)[deg]	IFT [mN/m]	Type of Test	Theta (M)[deg]	IFT [mN/m]	Type of Test	Theta (M)[deg]	IFT [mN/m]
Quartz +Crude oil+ 0.001M $CaCl_2$	1	70.70	11.37	Quartz +Crude Oil +0.01M $CaCl_2$	81.70	42.02	Quartz +Crude oil+ 1.0M $CaCl_2$	75.60	41.85
	3	77.90	13.42		77.60	46.18		74.90	61.19
	4	78.30	12.64		58.30	41.91		77.30	34.02
	5	76.90	7.32		84.00	41.99		74.50	54.69
	6	91.10	11.48		84.10	41.97		79.10	20.70
	8	83.30	11.34		78.40	42.00		96.90	34.13
	9	93.10	11.92		82.00	41.98		95.60	37.33
	10	81.40	11.17		80.60	41.75		90.40	61.97
	11	72.70	11.11		81.40	41.96		83.40	34.20
	12	72.70	11.59		101.40	41.78		85.40	61.93
	13	75.40	12.73		79.30	41.98		84.40	68.87
	14	68.70	11.90		84.90	50.68		76.90	34.10
	16	75.10	12.38		82.50	75.76		83.40	37.05
	17	77.70	13.25		82.60	43.80		90.90	7.40
	18	64.30	12.82		83.40	41.95		87.90	7.46
	19	99.20	12.95		73.60	44.50		79.60	10.79
	20	87.40	13.52		83.40	42.30		85.60	3.95
	21	60.00	11.91		86.00	41.96		90.20	7.51
	23	87.00	12.93		81.40	75.70		87.00	7.60
	24	78.90	10.04		82.10	75.52		76.60	5.62
	25	84.70	12.78		83.80	38.41		63.40	5.47
	26	78.70	10.32		82.90	75.68		97.50	7.65
	27	78.90	11.10		81.20	41.95		83.00	7.62
	28	76.80	11.24		80.60	75.77		98.60	4.03

B.3. Zeta potential

In this section of appendix, the summary of parameter for the zeta potential is given. The results for the zeta potential of all BST used in the potential testing are also given.

Table B3.1: Summary of results for zeta potential measurement for untreated quartz powder, treated in oil model compounds(decanoic acid in dodecane), and crude oil.

Sample	Ramp Nr	dU/dp [mV/mbar]	dU/dp R^2	dV/dp [ml/min/mbar]	dV/dp R^2	pH
Untreated Quartz	1	0.23	1.00	1.60	0.98	6.51
	2	0.24	1.00	-1.85	0.99	6.50
	3	0.23	1.00	1.89	0.98	6.52
	4	0.23	1.00	-1.96	0.99	6.53
Aged Quartz in Decanoic acid/dodecane	1	0.23	1.00	1.04	1.00	6.50
	2	0.28	1.00	-1.10	1.00	6.51
	3	0.22	1.00	1.07	0.99	6.45
	4	0.26	1.00	-1.07	0.99	6.50
Aged Quartz in crude oil	1	0.10	1.00	1.76	1.00	6.50
	2	0.12	1.00	-1.77	1.00	6.48
	3	0.10	1.00	1.81	1.00	6.50
	4	0.11	1.00	-1.75	1.00	6.58

We B07

Towards a Nanoscopic Understanding of Oil-sandstone Wettability - Implications for Enhanced Oil Recovery

R. Kareem* (Durham University), P. Cubillas (Durham University), H. Riggs (Durham University), C. Greenwell (Durham University) & J. Gluyas (Durham University)

SUMMARY

Due to the continuous rise in the demand for oil across the globe and diminishing availability of conventional sources, low salinity enhanced oil recovery (EOR) operations are increasingly deployed to extend crude production. Reservoir-rock wettability controls the low salinity effect, and it has been shown to be influenced by the presence of clay minerals, polar compounds in the crude oil and the activity of divalent ions. Nevertheless, a detailed understanding of the fundamental chemical and physical controls on the wetting behavior of reservoirs at the pore scale is still lacking. We have used quartz crystals as a model mineral surface to gain a better insight on sandstone oil/water wettability. The effect of the surface roughness and pre-treatment (using model oil compounds, dodecane and decanoic acid) on wettability has been studied. In addition, adhesion of decanoic acid to quartz surfaces was studied with atomic force microscopy (AFM). The wettability regime in quartz crystals was examined by using contact angle measurements with an environmental scanning electron microscopy (ESEM). Two different degrees of quartz crystal roughness were used. This allowed us to study the influence of nano-roughness on wettability while keeping the surface chemistry constant. Surface roughness of quartz and films was determined using atomic force microscopy (AFM) The quartz surfaces were studied without treatment and after being aged in , dodecane (non polar model oil phase) and decanoic acid mixtures (polar oil phase). The effect of brines on wettability alteration was studied by using range of brine concentration between 0.01 M to 1 M of NaCl, CaCl2, MgCl2, and KCl. AFM was used to study the oil-aged quartz crystals after brine treatment with the goal of observing any residual organic molecules. Results from these investigations show that dodecane-aged quartz crystals are more water whereas those pre-treated with decanoic acid are more oil wet. In addition, crystal with higher roughness are also more oil wet, this result can be explained by the presence of more remnants of decanoic acid than on the flat crystals (as seen by AFM).Overall, results from our investigations will contribute to increase our understanding and prediction of, the wetting behavior of the model mineral surfaces during low salinity water flooding IOR/EOR.

Appendix C

An Integrated Study of Wettability Alteration and Oil Recovery Improvement in Berea Sandstone as A-model of Sandstone Reservoir

C.1. Contact Angle -Drop Shape/Measurement

The contact angle measurements were taken using Kruss DSA 100 drop shape analyser; the following contact angle results found in a set of experiment.

Table C1.1: Summary of dynamic contact angle of water droplets on the BST surface aged in decanoic acid-dodecane, were exposed to sodium chloride solution.

Type of Test	No.	Theta (M)[deg]	IFT [mN/m]	Type of Test	Theta (M)[deg]	IFT [mN/m]	Type of Test	Theta (M)[deg]	IFT [mN/m]
	1	25.50	17.66		82.10	14.28		103.40	65.47
	2	24.90	17.49		89.80	13.70		103.60	113.25
	3	24.60	20.65		89.10	12.68		101.60	118.80
	4	24.20	23.51		78.60	11.13		105.50	119.32
	5	24.50	23.49		87.30	9.90		104.70	120.27
	6	24.30	21.13		87.70	9.45		102.70	44.35
	7	25.80	19.66		87.60	10.29		104.00	159.59
	8	27.60	17.58		87.30	10.27		101.00	27.83
	9	30.00	22.11		88.60	9.87		102.20	25.83
	10	28.60	23.17		87.70	63.11		102.10	32.56
	11	25.60	21.27		77.60	31.64		102.50	30.45
	12	25.90	20.68		85.10	39.30		101.90	34.08
	13	25.70	7.68		85.40	38.76		101.80	26.99
BST	14	25.70	45.13	BST+	84.50	48.29	BST	101.10	41.01
+Decanoic	15	25.20	32.80	Decanoic	84.20	43.79	+Decanoic	101.20	27.27
acid-	16	24.90	34.43	acid-	84.20	49.70	acid-	104.00	38.05
dodecane	17	23.50	35.33	dodecane	83.50	48.11	dodecane	105.00	51.20
+0.001M	18	23.50	35.26	+0.01M	80.10	49.87	+1.0M	103.00	50.35
NaCl	19	23.00	30.28	NaCl	82.90	82.90	NaCl	103.00	76.58
	20	23.70	26.73		82.60	40.14		103.40	50.62
	21	22.70	37.33		82.00	8.62		103.30	51.66
	22	22.20	65.65		84.50	10.42		102.90	32.24
	23	22.20	53.24		72.90	11.34		102.50	33.89
	24	22.00	37.66		73.70	11.63		101.90	31.33
	25	22.60	152.70		73.50	11.18		101.70	35.75
	26	22.60	32.24		71.20	10.90		101.40	25.37
	27	22.60	58.66		72.20	10.71		100.80	25.37
	28	22.60	58.15		71.70	11.22		95.40	25.37
	29	22.60	59.51		23.20	10.91		95.40	25.37
	30	22.80	75.92		71.30	11.60		95.10	69.95
	31	21.80	61.35		71.50	11.73		94.50	75.89
	32	21.10	87.63		71.00	11.57		94.30	80.34

Table C1.2: Summary of dynamic contact angle of water droplets on the BST surface aged in decanoic acid-dodecane, were exposed to sodium chloride solution.

Type of Test	No.	Theta (M)[deg]	IFT [mN/m]	Type of Test	Theta (M)[deg]	IFT [mN/m]	Type of Test	Theta (M)[deg]	IFT [mN/m]
BST +Decanoic acid-dodecane +0.001M $CaCl_2$	1	68.10	5.67	BST +Decanoic acid-dodecane +0.01M $CaCl_2$	59.80	61.41	BST +Decanoic acid-dodecane +1.0M $CaCl_2$	96.80	10.01
	2	71.70	6.98		74.50	61.45		67.50	8.25
	3	67.90	5.77		76.00	61.50		91.20	8.60
	4	70.90	8.35		90.40	61.82		97.90	10.13
	5	67.50	6.99		71.20	91.19		98.50	10.15
	6	64.20	8.27		71.20	129.36		97.40	10.17
	7	68.30	8.76		89.50	87.12		97.50	8.82
	8	66.60	5.59		72.30	62.07		99.20	8.78
	9	63.40	6.09		61.40	91.06		96.90	8.28
	10	64.30	9.95		75.80	61.90		95.30	9.40
	11	67.50	7.07		73.00	62.07		94.30	40.77
	12	66.90	9.97		87.00	11.88		91.30	74.38
	13	72.30	16.27		66.70	11.60		92.40	73.45
	14	67.00	15.99		66.00	12.48		93.30	73.73
	15	66.90	11.00		67.00	12.50		95.70	74.66
	16	67.10	16.31		62.80	11.94		91.90	41.26
	17	72.30	16.18		62.60	12.91		94.50	41.24
	18	66.60	16.25		64.70	11.13		99.10	41.74
	19	67.00	16.27		66.80	11.16		93.40	16.71
	20	67.00	10.03		70.30	10.96		89.40	16.71
	21	66.70	16.90		71.80	12.41		85.70	28.46
	22	66.50	39.20		60.80	11.97		91.40	25.45
	23	64.40	10.36		68.80	12.18		92.70	29.02
	24	64.40	72.43		63.40	12.19		92.50	38.86
	25	63.30	42.97		72.40	13.89		93.40	51.28
	26	61.00	15.52		68.30	12.96		92.10	94.28
	27	61.80	10.54		65.50	12.86		94.40	190.35

Table C1.3: Summary of dynamic contact angle of water droplets on the BST surface aged in crude oil, were exposed to sodium chloride solutoin.

Type of Test	No.	Theta (M)[deg]	IFT [mN/m]	Type of Test	Theta (M)[deg]	IFT [mN/m]	Type of Test	Theta (M)[deg]	IFT [mN/m]
	1	43.80	21.40		88.40	17.98		137.10	16.67
	2	43.40	27.75		88.10	18.69		137.00	25.90
	3	42.60	26.71		89.10	18.53		136.60	17.94
	4	42.40	26.96		93.30	18.66		135.80	17.96
	5	42.20	26.34		95.20	17.29		135.20	19.85
	6	42.80	28.70		96.20	18.11		135.00	18.80
	7	42.70	27.64		96.20	17.33		135.00	17.40
	8	42.40	28.53		96.40	17.33		134.50	18.89
	9	41.20	28.11		96.30	16.77		135.50	19.10
BST	10	41.80	36.86	BST	95.60	13.66	BST	134.50	15.89
+Crude	11	41.20	35.46	+Crude	95.50	12.18	+Crude	134.20	18.74
Oil	12	41.70	37.67	Oil	96.90	15.40	Oil	131.50	43.90
+0.001M	13	41.60	36.47	+0.01M	96.10	17.41	+1.0M	131.80	26.67
NaCl	14	40.90	37.01	NaCl	95.40	16.47	NaCl	131.00	21.84
	15	40.20	29.04		94.20	17.34		130.80	14.13
	16	39.90	34.51		94.80	17.94		132.30	22.20
	17	39.50	32.42		94.80	17.87		130.90	21.92
	18	39.10	47.25		94.10	16.74		130.10	21.97
	20	39.10	40.07		94.20	19.70		129.50	12.27
	21	39.10	32.17		93.70	20.61		129.50	22.05
	22	39.10	80.98		93.50	15.68		127.10	21.97
	23	38.50	50.22		93.60	46.10		127.30	20.96
	24	38.20	46.70		92.90	13.08		128.80	11.93

Table C1.4: Summary of dynamic contact angle of water droplets on the BST surface aged in crude oil, were exposed to calcium chloride solution.

Type of Test	No.	Theta (M)[deg]	IFT [mN/m]	Type of Test	Theta (M)[deg]	IFT [mN/m]	Type of Test	Theta (M)[deg]	IFT [mN/m]
	1	69.90	8.98		84.90	16.67		113.10	55.44
	2	65.60	9.27		80.40	25.90		113.00	12.18
	3	64.70	28.10		69.40	17.94		112.60	18.93
	4	64.30	36.32		75.60	17.96		112.80	11.84
	5	64.80	22.75		71.20	19.85		112.20	19.31
	6	68.20	15.36		77.10	18.80		112.00	35.49
	7	67.70	13.80		73.90	17.40		112.00	18.84
	8	67.40	14.10		79.70	18.89		141.50	21.76
	9	75.60	12.89		84.30	19.10		115.50	60.33
	10	76.20	13.77		90.10	15.89		114.50	43.00
	11	76.00	15.14		89.20	18.74		114.20	34.23
	12	76.10	16.01		85.90	43.90		113.50	43.31
	13	77.50	13.92		87.30	26.67		113.80	20.90
BST +Crude Oil +0.001M $CaCl_2$	14	75.40	13.55	BST +Crude Oil +0.01M $CaCl_2$	78.30	21.84	BST +Crude Oil +1.0M $CaCl_2$	113.00	62.00
	15	73.20	13.60		83.00	14.13		112.80	34.45
	16	72.50	8.94		82.30	22.20		112.30	62.66
	17	71.10	14.33		82.00	21.92		112.90	38.46
	18	70.80	13.34		79.80	21.97		112.10	34.56
	19	67.30	14.09		79.10	12.27		112.50	34.57
	20	64.80	12.29		81.10	22.05		112.50	34.53
	21	65.50	8.56		89.50	21.97		112.10	21.25
	22	64.90	11.91		86.40	20.96		112.30	35.04
	23				83.00	11.93		111.80	11.93
	24				83.30	8.37		111.20	8.37
	25				80.10	12.06		111.00	12.06
	26				76.90	9.11		112.40	9.11
	27				81.40	10.76		112.00	10.76
	28				88.10	10.79		112.00	10.79
	29							112.50	31.64
	30							112.70	12.41

C.2. Contact Angle –ESEM Measurement

In this set of experiments clean, treated and untreated with brine, decanoic acid-dodecane, and crude oil quartz crystals were examined using (Peltier stage) ESEM chamber. In our work, an average measured contact angles taken over several water droplets

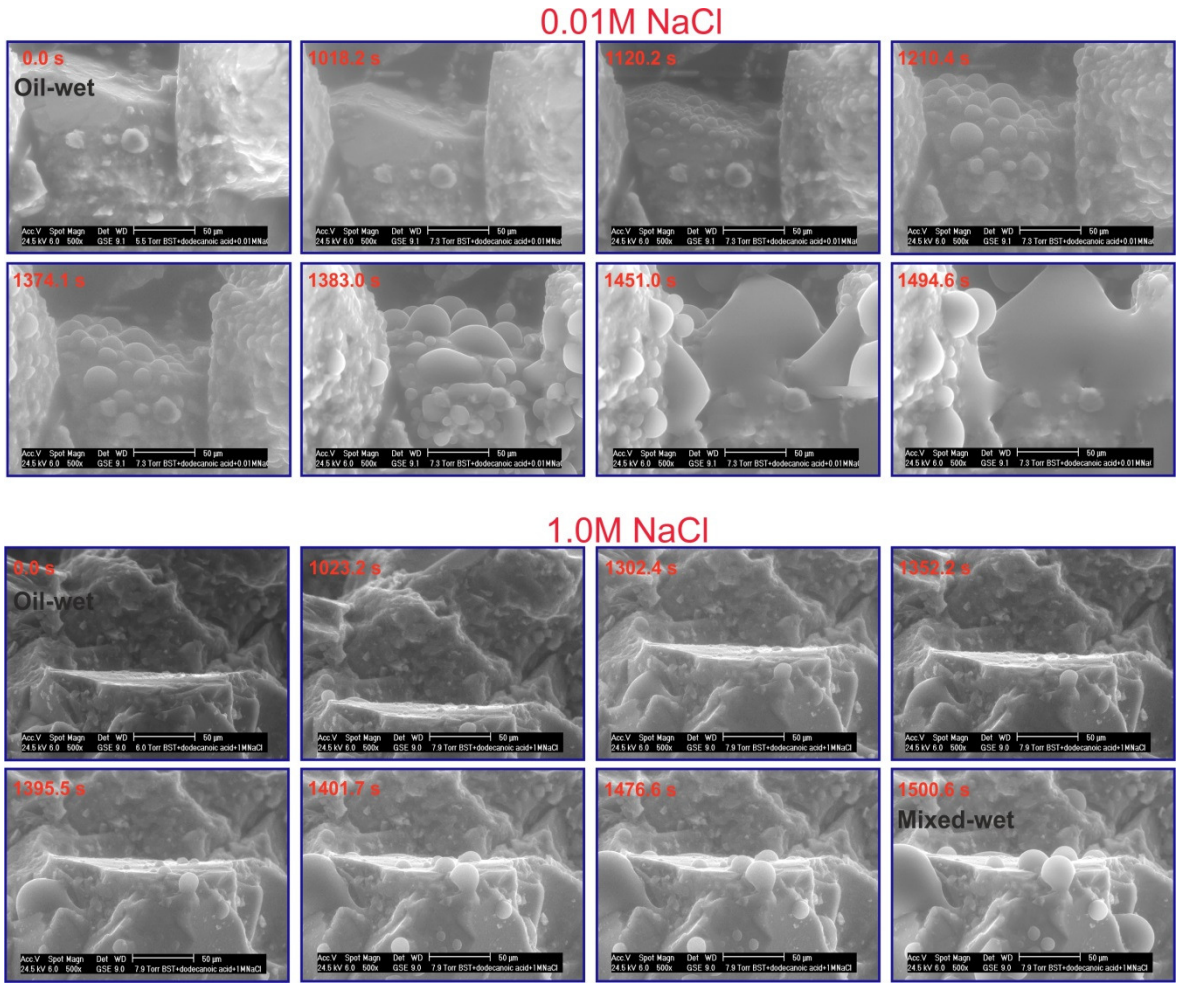

Figure C2.1 Photomicrographs show the variation of the contact angle with time in BST aged in decanoic acid-dodecane after injected with low and high brine concentration of sodium chloride solution inside the ESEM chamber at °C.

Table C2.1: Summary of dynamic contact angle of water droplets on the BST slcies aged in decanoic acid-dodecane, were exposed to sodium chloride solution.

Type of sample	No	Times (sec)	Pressure (Torr)	Dynamic contact angle (□)[deg]			
				Droplet 1	Droplet 2	Droplet 3	Average
BST+ Decanoic acid-dodecane +0.01M NaCl	1	0.0	5.50	0.00	0.00	0.00	0.00
	2	962.0	7.30	0.00	0.00	0.00	0.00
	3	1018.2	7.30	0.00	0.00	0.00	0.00
	4	1053.1	7.30	45.52	32.56	27.56	35.21
	5	1120.2	7.30	85.45	75.25	57.52	72.74
	6	1152.4	7.30	85.00	77.24	63.24	75.16
	7	1198.3	7.30	87.41	75.35	65.78	76.18
	8	1210.4	7.30	88.42	80.2.38	68.63	78.52
	9	1374.1	7.30	86.03	78.83	78.58	81.14
	10	1380.4	7.30	80.46	75.23	65.47	73.72
	11	1383.4	7.30	95.81	81.90	45.74	74.48
	12	1452.9	7.30	91.12	74.55	43.67	69.78
	13	1451.7	7.30	90.80	75.25	40.00	68.68
	14	1475.8	7.30	75.63	45.62	38.21	53.15
	15	1494.6	7.30	0.00	0.00	0.00	0.00
BST+ Decanoic acid-dodecane +1.0M NaCl	1	0.0	5.50	0.00	0.00	0.00	0.00
	2	754.3	6.00	0.00	0.00	0.00	0.00
	3	567.6	7.90	73.20	65.45	0.00	69.33
	4	1023.2	7.90	92.10	85.40	83.60	87.03
	5	1121.3	7.90	84.40	81.65	83.00	83.02
	6	1174.6	7.90	82.10	79.60	83.10	81.60
	7	1302.4	7.90	80.70	74.20	84.20	79.70
	8	1320.1	7.90	82.30	55.10	74.30	70.57
	9	1352.2	7.90	85.00	45.60	64.10	64.90
	10	1375.3	7.90	94.60	78.30	110.30	94.40
	11	1395.5	7.90	125.46	84.36	165.00	124.94
	12	1401.7	7.90	132.10	91.70	165.20	129.67
	13	1474.8	7.90	125.60	90.50	140.30	118.80
	14	1147.6	7.90	124.60	84.20	145.30	118.03
	15	1500.6	7.90	14.23	94.20	148.30	85.58

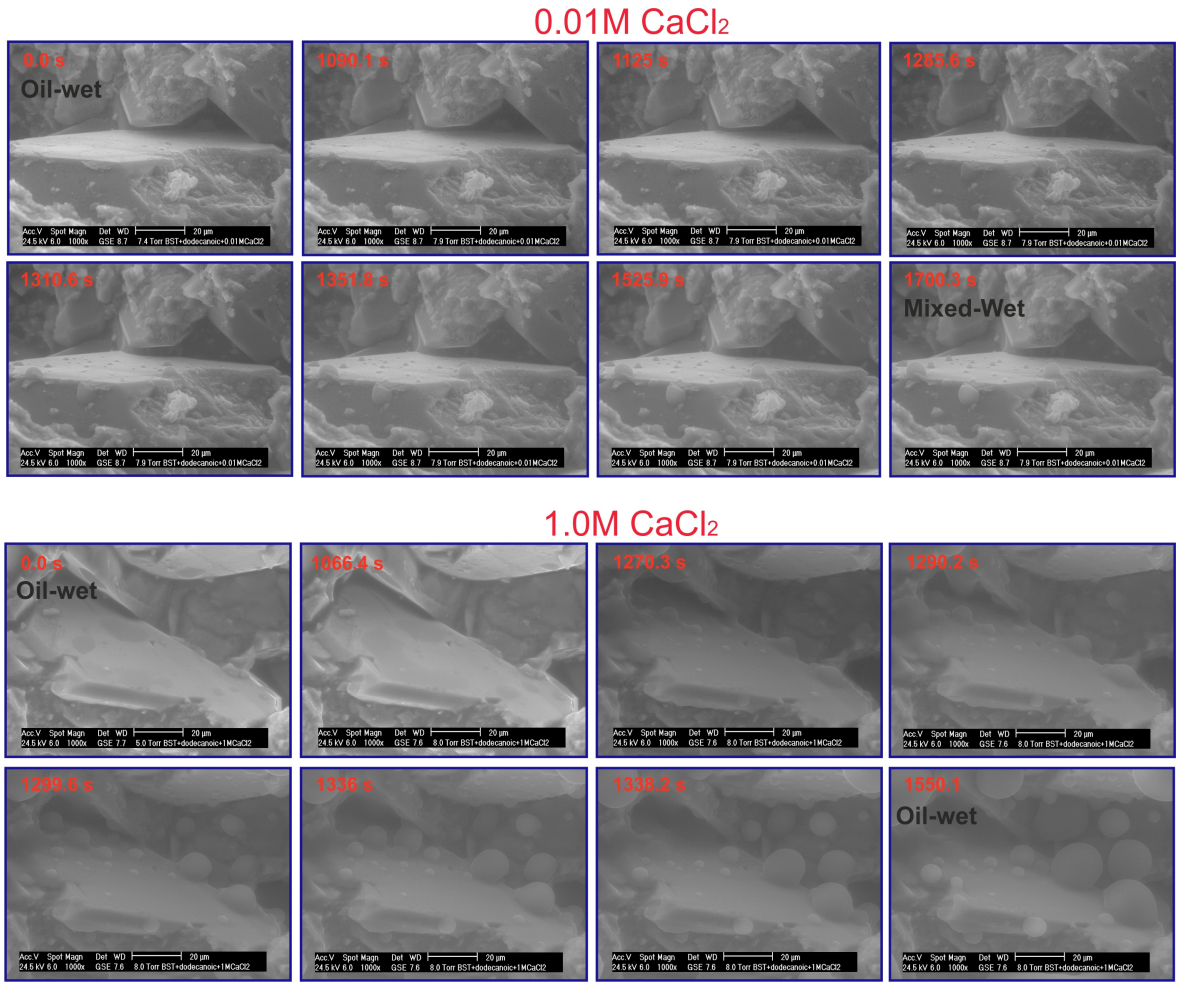

Figure C2.2 Photomicrographs show the variation of the contact angle with time in BST aged in decanoic acid-dodecane after injected with low and high brine concentration of calcium chloride solution inside the ESEM chamber at °C.

Table C2.2: Summary of dynamic contact angle of water droplets on the BST slcies aged in decanoic acid-dodecane, were exposed to calcium chloride solution.

Type of sample	No	Times (sec)	Pressure (Torr)	Dynamic contact angle (□)[deg]			
				Droplet 1	Droplet 2	Droplet 3	Average
BST+ Decanoic acid-dodecane+0.01M $CaCl_2$	1	0.0	5.00	0.00	0.00	0.00	0.00
	2	759.3	8.00	0.00	0.00	0.00	0.0
	3	985.6	8.00	0.00	0.00	0.00	0.0
	4	1090.1	8.00	0.00	0.00	0.00	0.0
	5	1100.1	8.00	0.00	0.00	0.00	0.0
	6	110.6	8.00	0.00	0.00	0.00	0.0
	7	1125.3	8.00	0.00	0.00	0.00	0.0
	8	1285.6	8.00	0.00	0.00	0.00	0.0
	9	1291.2	8.00	0.00	0.00	0.00	0.0
	10	1301.2	8.00	65.30	48.60	54.20	56.0
	11	1310.6	8.00	81.26	87.60	86.45	85.1
	12	1320.6	8.00	90.40	96.30	91.87	92.9
	13	1351.8	8.00	93.62	95.46	97.00	95.4
	14	1452.3	8.00	90.60	99.30	94.20	94.7
	15	1525.9	8.00	94.32	91.23	85.60	90.4
	16	1700.3	8.00	90.26	94.28	94.63	93.1
BST+ Decanoic acid-dodecane+1.0M $CaCl_2$	1	0.00	7.40	0.00	0.00	0.00	0.00
	2	650.30	7.90	0.00	0.00	0.00	0.00
	3	850.10	7.90	0.00	0.00	0.00	0.00
	4	1066.40	7.90	0.00	0.00	0.00	0.00
	5	1250.60	7.90	0.00	0.00	0.00	0.00
	6	1270.30	7.90	81.20	75.20	0.00	78.20
	7	1290.20	7.90	84.60	62.30	0.00	73.45
	8	1297.10	7.90	85.20	74.10	73.00	77.43
	9	1299.60	7.90	92.10	104.30	110.70	102.37
	10	1315.30	7.90	101.30	107.60	107.90	105.60
	11	1336.00	7.90	110.60	121.70	95.20	109.17
	12	1350.20	7.90	114.30	125.80	101.30	113.80
	13	1338.20	7.90	114.30	141.30	114.30	123.30
	14	1550.10	7.90	125.60	145.40	134.50	135.17

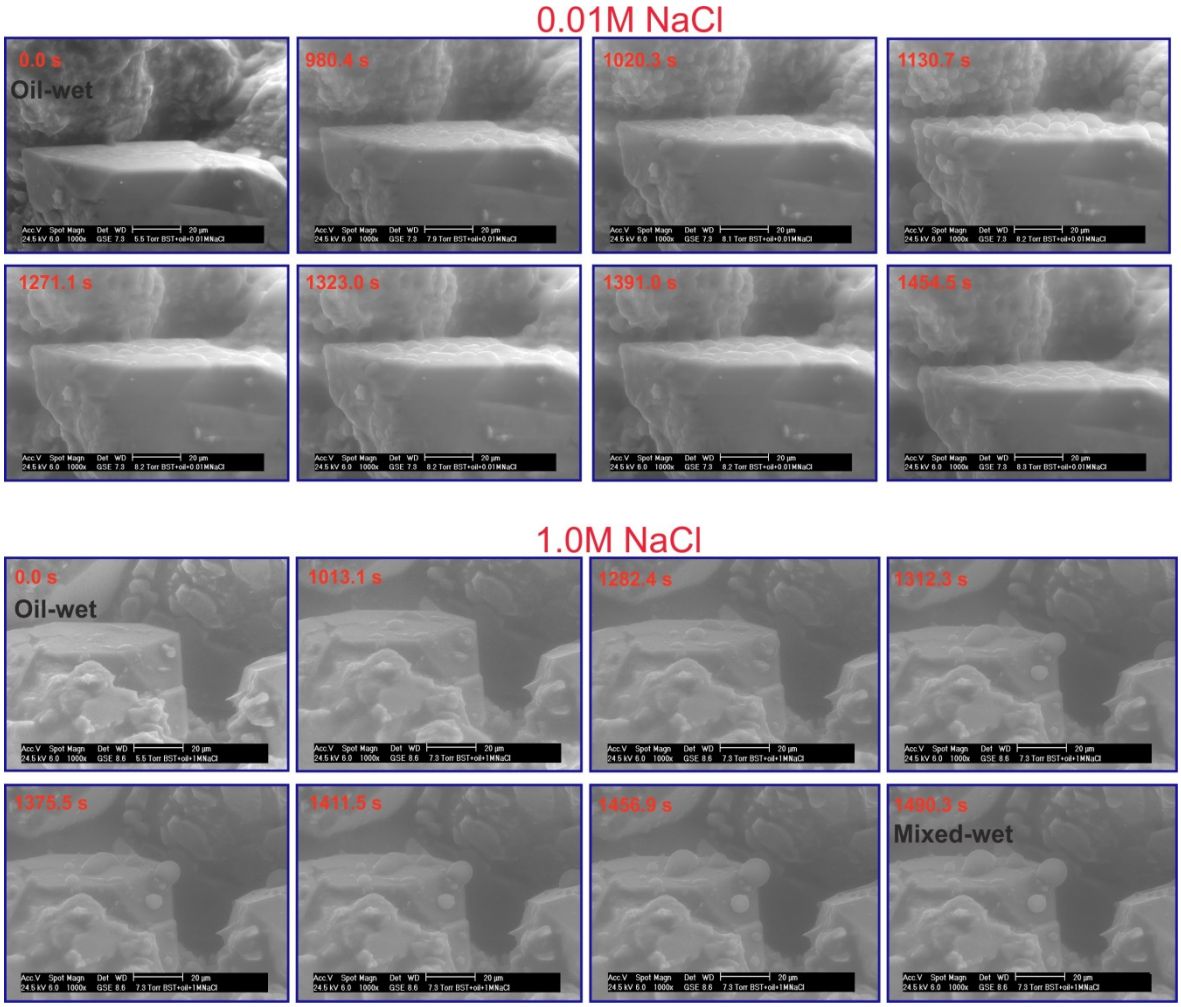

Figure C2.3 Photomicrographs show the variation of the contact angle with time in BST aged in crude oil after injected with low and high brine concentration of sodium chloride solution inside the ESEM chamber at °C.

Table C2.3: Summary of dynamic contact angle of water droplets on the BST slcies aged in crude oil, were exposed to sodium chloride solution.

Type of sample	No	Times (sec)	Pressure (Torr)	Dynamic contact angle (□)[deg]			
				Droplet 1	Droplet 2	Droplet 3	Average
BST+ Crude oil +0.01M NaCl	1	0	5.40	0.0	0.0	0.0	0.0
	2	745	6.00	0.0	0.0	0.0	0.0
	3	824	6.00	0.0	0.0	0.0	0.0
	4	983	6.00	0.0	0.0	0.0	0.0
	5	110	6.00	0.0	0.0	0.0	0.0
	6	1135	6.80	0.0	0.0	0.0	0.0
	7	1240	7.40	0.0	0.0	0.0	0.0
	8	1254	7.50	0.0	0.0	0.0	0.0
	9	1280	7.50	32.1	41.6	37.1	36.9
	10	1296	7.50	78.3	87.6	84.2	83.4
	11	1326	7.50	80.7	74.3	87.3	80.8
	12	1348	7.50	80.0	71.3	74.6	75.3
	13	1358	7.50	81.5	79.4	91.2	84.0
	14	1451	7.50	87.3	92.3	90.4	90.0
BST+ Crude oil +1.0M NaCl	1	0	5.5	0.0	0.0	0.0	0.0
	2	652	5.5	0.0	0.0	0.0	0.0
	3	1013	7.3	30.3	25.6	20.2	25.4
	4	1116	7.3	32.4	45.3	51.7	43.1
	5	1185	7.3	41.6	48.7	56.2	48.8
	6	1282	7.3	65.3	71.5	61.2	66.0
	7	1297	7.3	85.7	74.2	64.1	74.7
	8	1312	7.3	94.3	82.3	86.3	87.6
	9	1355	7.3	90.6	81.6	81.8	84.7
	10	1376	7.3	92.0	70.0	65.0	75.7
	11	1387	7.3	91.3	74.5	65.3	77.0
	12	1412	7.3	93.3	74.7	74.2	80.7
	13	1457	7.3	124.5	91.2	103.6	106.4
	14	1464	7.3	120.3	91.5	105.8	105.9
	15	1490	7.3	125.6	93.5	110.3	109.8

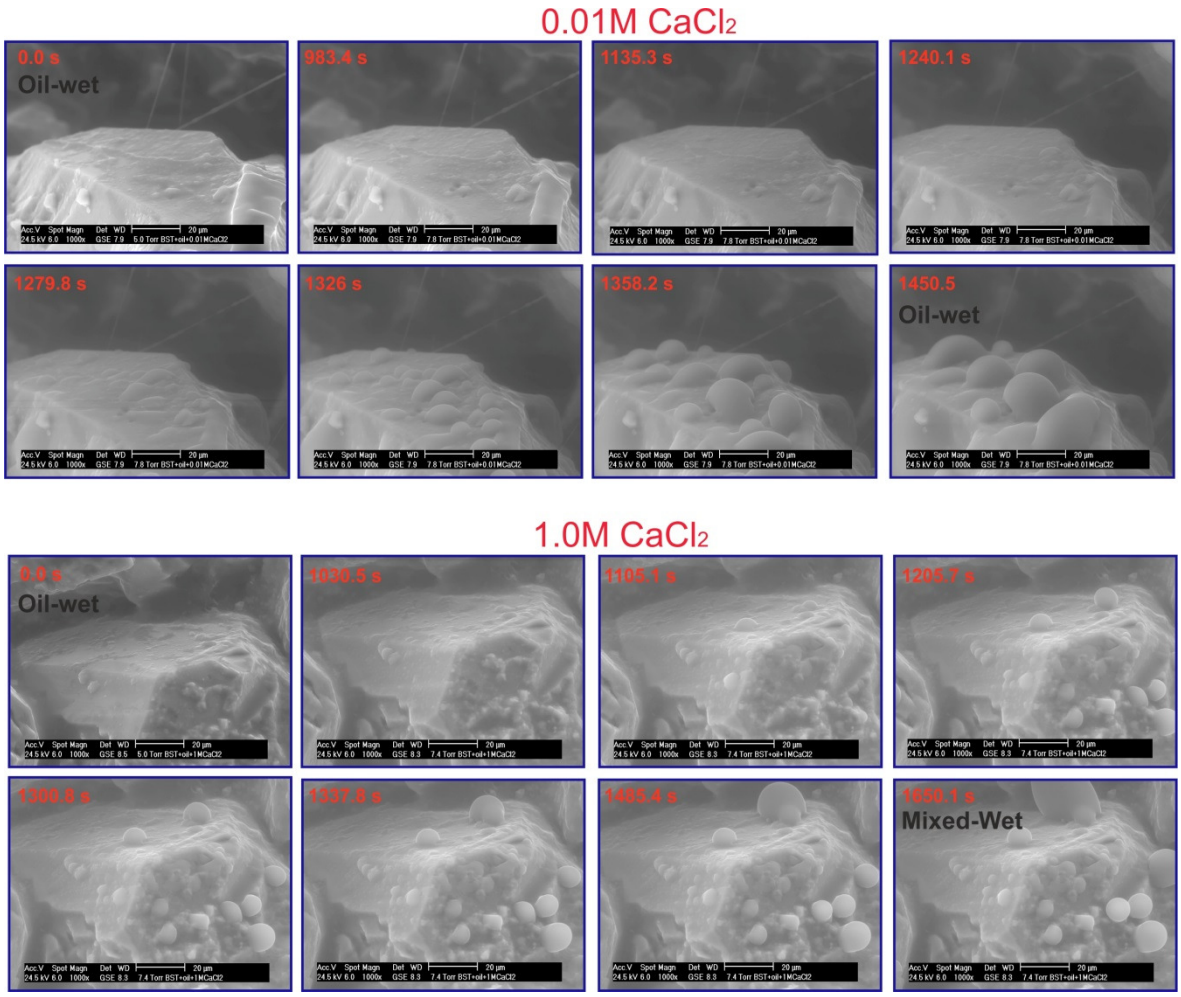

Figure C2.4 Photomicrographs show the variation of the contact angle with time in BST aged in crude oil after injected with low and high brine concentration of calcium chloride solution inside the ESEM chamber at °C.

Table C2.4: Summary of dynamic contact angle of water droplets on the BST slcies aged in crude oil, were exposed to calcium chloride solution.

Type of sample	No	Times (sec)	Pressure (Torr)	Dynamic contact angle (□)[deg]			
				Droplet 1	Droplet 2	Droplet 3	Average
BST+ Crude oil + 0.01M $CaCl_2$	1	0	5.40	0.0	0.0	0.0	0.0
	2	745	6.00	0.0	0.0	0.0	0.0
	3	824	6.00	0.0	0.0	0.0	0.0
	4	983	6.00	0.0	0.0	0.0	0.0
	5	110	6.00	0.0	0.0	0.0	0.0
	6	1135	6.80	0.0	0.0	0.0	0.0
	7	1240	7.40	0.0	0.0	0.0	0.0
	8	1254	7.50	0.0	0.0	0.0	0.0
	9	1280	7.50	32.1	41.6	37.1	36.9
	10	1296	7.50	78.3	87.6	84.2	83.4
	11	1326	7.50	80.7	74.3	87.3	80.8
	12	1348	7.50	80.0	71.3	74.6	75.3
	13	1358	7.50	81.5	79.4	91.2	84.0
	14	1451	7.50	87.3	92.3	90.4	90.0
BST+ Crude oil + 1.0M $CaCl_2$	1	0.0	5.4	0.0	0.0	0.0	0.0
	2	0.0	5.4	0.0	0.0	0.0	0.0
	3	1030.5	6.3	0.0	0.0	0.0	0.0
	4	1064.8	6.4	61.6	73.5	64.3	66.5
	5	1105.1	6.4	72.6	78.9	84.5	78.7
	6	1205.5	6.4	86.5	124.7	112.3	107.8
	7	1274.3	6.4	84.5	119.6	91.3	98.5
	8	1300.8	6.4	86.6	122.4	91.6	100.2
	9	1310.1	6.4	84.2	115.0	87.6	95.6
	10	124.6	6.4	87.3	116.4	84.6	96.1
	11	1337.8	6.4	81.6	94.6	136.4	104.2
	12	1387.6	6.4	81.0	98.4	148.7	109.4
	13	1485.4	6.4	82.6	110.5	165.3	119.5
	14	1529.8	6.4	95.6	121.8	170.6	129.3
	15	1650.1	6.4	110.3	135.2	175.3	140.3

C.3. Total Organic Carbon Test

In this set of experiments, the quantity of crude oil present within aged-BST is measured using total organic carbon (TOC).

Table C3.1: TOC of the sample selected for the study.

ID	Type of brines	TOC (wt%)	TOC (wt%)	d13 Corg	d13 Corg	TOC (wt%) average	TOC (wt%) Std dev	d13Corg average	d13Corg Std dev	TOC (wt%) BQ – AQ	d13Corg BQ – AQ
AQ1	-	5.563	5.765	-30.717	-30.695	5.664	0.143	-30.706	0.016		
BQ1	0.01M NaCl	3.550	3.707	-30.308	-30.279	3.63	0.11	-30.294	0.021	2.036	-0.413
AQ2	-	5.502	5.423	-30.132	-30.356	5.463	0.056	-30.244	0.158		
BQ2	1.0M NaCl	4.718	4.797	-30.376	-30.393	4.758	0.056	-30.385	0.012	0.705	0.140
AQ3	-	5.583	5.532	-30.042	-30.240	5.558	0.036	-30.141	0.140		
BQ3	0.01M $CaCl_2$	4.235	4.247	-29.905	-29.751	4.241	0.008	-29.828	0.109	1.317	-0.313
AQ4	-	5.338	5.386	-30.398	-30.549	5.362	0.034	-30.474	0.107		
BQ4	1.0M $CaCl_2$	4.452	4.440	-29.982	-29.798	4.446	0.008	-29.890	0.130	0.916	-0.583

AQ: Aged-BST with crude oil
BQ: Treated aged-BST in brines

C.4. Spontaneous Imbibition Test

In the present appendix the rates recorded during the experiment of the Amott cells at the the spontaneous imbibition test is given.The results for the oil reocvery factor on all the cores used in the imbibition testing are also given.

Table C4.1: Summary of the imbibition data of the BST #2 in high and low sodium chloride at room tepreature and pressure.

# 2 (BST)+1.0M NaCl at room condition				# 2 (BST)+ 0.01M NaCl at room condition			
No	Date	Production (ml)	R	No	Date	Production (ml)	R
1	14/06/2016	0.00	0.00	1	27/07/2016	0.40	15.50
2	15/06/2016	0.00	0.00	2	28/07/2016	0.40	15.50
3	16/06/2016	0.00	0.00	3	29/07/2016	0.40	15.50
4	17/06/2016	0.00	0.00	4	30/07/2016	0.40	15.50
5	18/06/2016	0.00	0.00	5	31/07/2016	0.40	15.50
6	19/06/2016	0.00	0.00	6	01/08/2016	0.40	15.50
7	20/06/2016	0.00	0.00	7	02/08/2016	0.45	17.44
8	21/06/2016	0.00	0.00	8	03/08/2016	0.50	19.38
9	22/06/2016	0.00	0.00	9	04/08/2016	0.55	21.32
10	23/06/2016	0.00	0.00	10	05/08/2016	0.60	23.26
11	24/06/2016	0.07	2.71	11	06/08/2016	0.65	25.19
12	25/06/2016	0.10	3.88	12	07/08/2016	0.68	26.36
13	27/06/2016	0.15	5.81	13	08/08/2016	0.70	27.13
14	28/06/2016	0.21	8.14	14	09/08/2016	0.70	27.13
15	29/06/2016	0.24	9.30	15	10/08/2016	0.70	27.13
16	30/06/2016	0.26	10.08	16	11/08/2016	0.75	29.07
17	01/07/2016	0.28	10.85	17	12/08/2016	0.80	31.01
18	02/07/2016	0.29	11.24	18	13/08/2016	0.83	32.17
19	03/07/2016	0.30	11.63	19	17/08/2016	0.85	32.95
20	06/07/2016	0.30	11.63	20	18/08/2016	0.85	32.95
21	10/07/2016	0.30	11.63	21	19/08/2016	0.85	32.95
22	11/07/2016	0.35	13.57	22	20/08/2016	1.00	38.76
23	12/07/2016	0.35	13.57	23	21/08/2016	1.00	38.76
24	13/07/2016	0.35	13.57	24	22/08/2016	1.00	38.76
25	15/07/2016	0.40	15.50	25	24/08/2016	1.00	38.76
26	16/07/2016	0.40	15.50	26	25/08/2016	1.10	42.64
27	17/07/2016	0.40	15.50	27	26/08/2016	1.20	46.51
28	18/07/2016	0.40	15.50	28	27/08/2016	1.20	46.51
29	19/07/2016	0.40	15.50	29	29/08/2016	1.20	46.51
30	21/07/2016	0.40	15.50	30	03/09/2016	1.20	46.51
31	25/07/2016	0.40	15.50	31	04/09/2016	1.20	46.51
32	27/07/2016	0.40	15.50	32	05/09/2016	1.20	46.51
33	27/07/2016	0.40	15.50	33	06/09/2016	1.20	46.51
34	27/07/2016	0.40	15.50	34	08/09/2016	1.20	46.51
35	27/07/2016	0.40	15.50	35	09/09/2016	1.20	46.51

Table C4.2: Summary of the imbibition data of the BST #3 in high and low calcium chloride at room tepreature and pressure.

# 3 (BST)+1.0M CaCl2 at room condition				# 3 (BST)+ 0.01M CaCl2 at room condition			
No	Date	Production (ml)	R	No	Date	Production (ml)	R
1	14/06/2016	0	0.00	1	26/07/2016	0.5	19.52
2	15/06/2016	0.05	1.95	2	27/07/2016	0.5	19.52
3	16/06/2016	0.1	3.90	3	28/07/2016	0.5	19.52
4	17/06/2016	0.15	5.86	4	29/07/2016	0.5	19.52
5	18/06/2016	0.18	7.03	5	30/07/2016	0.5	19.52
6	19/06/2016	0.22	8.59	6	31/07/2016	0.5	19.52
7	20/06/2016	0.24	9.37	7	01/08/2016	0.5	19.52
8	21/06/2016	0.24	9.37	8	02/08/2016	0.5	19.52
9	22/06/2016	0.245	9.57	9	03/08/2016	0.5	19.52
10	23/06/2016	0.25	9.76	10	04/08/2016	0.5	19.52
11	24/06/2016	0.35	13.67	11	05/08/2016	0.5	19.52
12	25/06/2016	0.38	14.84	12	06/08/2016	0.6	23.43
13	26/06/2016	0.39	15.23	13	08/08/2016	0.6	23.43
14	27/06/2016	0.4	15.62	14	10/08/2016	0.6	23.43
15	28/06/2016	0.4	15.62	15	11/08/2016	0.6	23.43
16	29/06/2016	0.41	16.01	16	13/08/2016	0.6	23.43
17	30/06/2016	0.42	16.40	17	14/08/2016	0.6	23.43
18	01/07/2016	0.45	17.57	18	15/08/2016	0.6	23.43
19	02/07/2016	0.47	18.35	19	16/08/2016	0.7	27.33
20	03/07/2016	0.48	18.74	20	18/08/2016	0.7	27.33
21	04/07/2016	0.49	19.13	21	19/08/2016	0.7	27.33
22	05/07/2016	0.5	19.52	22	20/08/2016	0.7	27.33
23	06/07/2016	0.5	19.52	23	21/08/2016	0.75	31.24
24	09/07/2016	0.5	19.52	24	22/08/2016	0.75	31.24
25	11/07/2016	0.5	19.52	25	24/08/2016	0.8	31.24
26	12/07/2016	0.5	19.52	26	25/08/2016	0.8	31.24
27	14/07/2016	0.5	19.52	27	26/08/2016	0.8	31.24
28	19/07/2016	0.5	19.52	28	28/08/2016	0.8	31.24
29	21/07/2016	0.5	19.52	29	01/09/2016	0.8	31.24
30	22/07/2016	0.5	19.52	30	02/09/2016	0.8	31.24
31	24/07/2016	0.5	19.52	31	04/09/2016	0.8	31.24
32	26/07/2016	0.5	19.52	32	05/09/2016	0.8	33.19
33	26/07/2016	0.5	19.52	33	06/09/2016	0.8	33.19
34	27/07/2016	0.5	19.52	34	07/09/2016	0.8	33.19
35	28/07/2016	0.5	19.52	35	08/09/2016	0.8	33.19
36	29/07/2016	0.5	19.52	36	09/09/2016	0.8	33.19
37	30/07/2016	0.5	19.52	37	10/09/2016	0.8	33.19
38	31/07/2016	0.5	19.52	38	11/09/2016	0.8	33.19

Table C4.3: Summary of the imbibition data of the BST #7 in high and low sodium chloride at 70 °C inside an oven.

# 7 (BST)+1.0M NaCl at 70 °C				# 7 (BST)+ 0.01M NaCl at 70 °C			
No	Date	Production (ml)	R	No	Date	Production (ml)	R
1	18/07/2016	0.00	0.00	1	03/09/2016	0.90	37.34
2	19/07/2016	0.10	4.15	2	04/09/2016	1.20	49.79
3	20/07/2016	0.20	8.30	3	05/09/2016	1.20	49.79
4	21/07/2016	0.25	10.37	4	06/09/2016	1.25	51.87
5	22/07/2016	0.30	12.45	5	07/09/2016	1.30	53.94
6	23/07/2016	0.30	12.45	6	08/09/2016	1.35	56.02
7	24/07/2016	0.33	13.69	7	09/09/2016	1.47	61.00
8	25/07/2016	0.37	15.35	8	10/09/2016	1.50	62.24
9	26/07/2016	0.40	16.60	9	11/09/2016	1.55	64.32
10	27/07/2016	0.40	16.60	10	12/09/2016	1.55	64.32
11	28/07/2016	0.40	16.60	11	13/09/2016	1.55	64.32
12	29/07/2016	0.40	16.60	12	14/09/2016	1.60	66.39
13	30/07/2016	0.45	18.67	13	15/09/2016	1.60	66.39
14	31/07/2016	0.47	19.50	14	16/09/2016	1.60	66.39
15	01/08/2016	0.50	20.75	15	17/09/2016	1.60	66.39
16	02/08/2016	0.55	22.82	16	18/09/2016	1.60	66.39
17	03/08/2016	0.55	22.82	17	19/09/2016	1.60	66.39
18	04/08/2016	0.60	24.90	18	20/09/2016	1.70	70.54
19	05/08/2016	0.70	29.05	19	21/09/2016	1.75	72.61
20	06/08/2016	0.70	29.05	20	23/09/2016	1.80	74.69
21	08/08/2016	0.70	29.05	21	25/09/2016	1.80	74.69
22	09/08/2016	0.70	29.05	22	26/09/2016	1.80	74.69
23	12/08/2016	0.90	37.34	23	28/09/2016	1.80	74.69
24	17/08/2016	0.90	37.34	24	02/10/2016	1.80	74.69
25	20/08/2016	0.90	37.34	25	03/10/2016	1.80	74.69
26	24/08/2016	0.90	37.34	26	04/10/2016	1.80	74.69
27	28/08/2016	0.90	37.34	27	05/10/2016	1.80	74.69
28	01/08/2016	0.90	37.34	28	11/10/2016	1.80	74.69
29	02/09/2016	0.90	37.34	29	11/10/2016	1.80	74.69
30	03/09/2016	0.90	37.34	30	11/10/2016	1.80	74.69
31	04/09/2016	0.90	37.34	31	11/10/2016	1.80	74.69
32	04/09/2016	0.90	37.34	32	11/10/2016	1.80	74.69
33	04/09/2016	0.90	37.34	33	11/10/2016	1.80	74.69
34	04/09/2016	0.90	37.34	34	11/10/2016	1.80	74.69
35	04/09/2016	0.90	37.34	35	11/10/2016	1.80	74.69

Table C4.4: Summary of the imbibition data of the BST #8 in high and low calcium chloride at 70 °C inside an oven.

# 8 (BST)+1.0M CaCl2 at 70 °C				# 8 (BST)+ 0.01M CaCl2 at 70°C			
No	Date	Production (ml)	R	No	Date	Production (ml)	R
1	18/07/2016	0.00	3.82	1	04/09/2016	0.70	26.8
2	19/07/2016	0.10	3.82	2	05/09/2016	0.70	26.8
3	20/07/2016	0.10	5.74	3	06/09/2016	0.80	30.6
4	21/07/2016	0.15	7.65	4	07/09/2016	0.80	30.6
5	22/07/2016	0.20	9.56	5	08/09/2016	0.90	34.4
6	23/07/2016	0.25	10.71	6	09/09/2016	0.90	34.4
7	24/07/2016	0.28	11.47	7	10/09/2016	0.90	34.4
8	25/07/2016	0.30	11.47	8	11/09/2016	0.90	34.4
9	26/07/2016	0.30	11.47	9	12/09/2016	0.90	34.4
10	27/07/2016	0.30	12.24	10	13/09/2016	0.90	34.4
11	28/07/2016	0.32	13.00	11	14/09/2016	0.90	34.4
12	29/07/2016	0.34	15.30	12	15/09/2016	0.90	34.4
13	30/07/2016	0.40	15.30	13	16/09/2016	1.00	38.2
14	31/07/2016	0.40	15.30	14	17/09/2016	1.00	38.2
15	01/08/2016	0.40	17.21	15	18/09/2016	1.00	38.2
16	02/08/2016	0.45	17.21	16	19/09/2016	1.00	38.2
17	03/08/2016	0.45	19.12	17	20/09/2016	1.10	42.1
18	04/08/2016	0.50	19.12	18	21/09/2016	1.10	42.1
19	05/08/2016	0.50	19.12	19	22/09/2016	1.10	42.1
20	08/08/2016	0.50	22.95	20	23/09/2016	1.10	42.1
21	11/08/2016	0.60	24.86	21	24/09/2016	1.10	42.1
22	16/08/2016	0.65	26.77	22	25/09/2016	1.10	42.1
23	19/08/2016	0.70	26.77	23	26/09/2016	1.10	42.1
24	23/08/2016	0.70	26.77	24	27/09/2016	1.10	42.1
25	26/08/2016	0.70	26.77	25	28/09/2016	1.10	42.1
26	30/08/2016	0.70	26.77	26	29/09/2016	1.10	42.1
27	31/08/2016	0.70	26.77	27	30/09/2016	1.10	42.1
28	01/09/2016	0.70	26.77	28	01/10/2016	1.10	42.1
29	02/09/2016	0.70	26.77	29	02/10/2016	1.10	42.1
30	03/09/2016	0.70	26.77	30	03/10/2016	1.10	42.1
31	04/09/2016	0.70	26.77	31	04/10/2016	1.10	42.1
32	04/09/2016	0.70	26.77	32	05/10/2016	1.10	42.1
33	04/09/2016	0.70	26.77	33	06/10/2016	1.10	42.1
34	04/09/2016	0.70	26.77	34	07/10/2016	1.10	42.1
35	04/09/2016	0.70	26.77	35	08/10/2016	1.10	42.1

C.5. Zeta Potential Test

In this section of appendix, the summary of parameter for the zeta potential is given. The results for the zeta potential of all BST used in the potential testing are also given.

Table C5.1: Summary of results for zeta potential measurement for untreated BST grains, treated in oil model compounds(decanoic acid-dodecane), and crude oil.

Sample	Ramp Nr	dU/dp [mV/mbar]	dU/dp R^2	dV/dp [ml/min/mbar]	dV/dp R^2	pH	Conductivity [mS/m]	Gap Height [μm]	ζ [mV]
Untreated BST	1	0.23	1.00	1.60	0.98	6.51	15.94	0	-32.7
	2	0.24	1.00	-1.85	0.99	6.53	15.94	0	-34.1
	3	0.23	1.00	1.89	0.98	6.50	15.93	0	-30.7
	4	0.23	1.00	-1.96	0.99	6.45	15.97	0	-31.8
Aged BST in decanoic acid/dodecane	1	0.23	1.00	1.04	1.00	6.50	17.76	0	4.28
	2	0.28	1.00	-1.10	1.00	6.53	17.81	0	5.08
	3	0.22	1.00	1.07	0.99	6.50	17.81	0	4.36
	4	0.26	1.00	-1.07	0.99	6.63	17.77	0	4.66
Aged BST in crude oil	1	0.10	1.00	1.76	1.00	6.50	25.63	0	7.67
	2	0.12	1.00	-1.77	1.00	6.57	25.66	0	8.22
	3	0.10	1.00	1.81	1.00	6.59	25.65	0	7.67
	4	0.11	1.00	-1.75	1.00	6.50	25.66	0	8.31

Table C5.2: Summary of results for zeta potential measurement for treated BST in different concentrations for each sodium chloride and calcium chloride.

Sample	Ramp Nr	dU/dp [mV/mbar]	dU/dp R²	dV/dp [ml/min/mbar]	dV/dp R²	pH	Conductivity [mS/m]	Gap Height [μm]	ζ [mV]
BST+0.001M NaCl	1	-0.17	1.00	3.21	0.99	7.88	15.31	0.00	-33.55
	2	-0.15	0.99	-4.24	0.96	7.78	15.31	0.00	-29.02
	3	-0.17	1.00	3.10	0.98	7.80	15.31	0.00	-32.57
	4	-0.15	0.94	-2.55	0.91	7.74	15.31	0.00	-29.90
BST+0.01M NaCl	1	-0.16	1.00	2.35	0.98	7.50	16.20	0.00	-33.55
	2	-0.16	1.00	-3.11	0.98	7.54	16.21	0.00	-33.23
	3	-0.16	1.00	2.26	0.98	7.60	16.21	0.00	-33.47
	4	-0.16	1.00	-3.24	0.98	7.43	16.22	0.00	-33.61
BST+1.0M NaCl	1	-0.16	1.00	1.72	0.99	6.50	9.86	0.00	-19.91
	2	-0.14	1.00	-1.75	0.97	6.43	9.83	0.00	-16.90
	3	-0.17	1.00	2.18	1.00	6.60	9.83	0.00	-21.16
	4	-0.14	1.00	-1.83	0.97	6.50	9.82	0.00	-17.24
BST+0.001M $CaCl_2$	1	-0.15	1.00	3.08	0.98	7.20	10.21	0.00	-19.47
	2	-0.15	1.00	-3.48	0.98	7.25	10.22	0.00	-19.37
	3	-0.16	1.00	3.68	0.99	7.30	10.22	0.00	-20.14
	4	-0.15	1.00	-3.74	0.98	7.25	10.23	0.00	-19.69
BST+0.01M $CaCl_2$	1	-0.17	1.00	1.81	0.98	6.80	13.75	0.00	-28.63
	2	-0.16	1.00	-1.57	0.98	6.84	13.78	0.00	-26.64
	3	-0.17	1.00	2.04	0.98	6.82	13.79	0.00	-29.26
	4	-0.16	1.00	-1.64	0.98	6.78	13.81	0.00	-27.12
BST+1.0M $CaCl_2$	1	-0.11	1.00	2.01	0.99	6.50	19.33	0.00	-26.30
	2	-0.10	1.00	-1.87	0.98	6.40	19.34	0.00	-25.15
	3	-0.12	1.00	2.41	1.00	6.45	19.34	0.00	-27.62
	4	-0.11	1.00	-2.54	0.99	6.40	19.36	0.00	-26.71

Table C5.3: Summary of results for zeta potential measurement of BST aged in decanic acid-dodecane at the presence of different concentration for each sodium chloride and calcium chloride.

Sample	Ramp Nr	dU/dp [mV/mbar]	dU/dp R^2	dV/dp [ml/min/mbar]	dV/dp R^2	pH	Conductivity [mS/m]	Gap Height [μm]	ζ [mV]
BST+0.001M NaCl	1	-0.20	0.98	5.24	0.97	8.04	15.6	0.00	-39.9
	2	-0.19	0.98	-4.51	0.97	8.03	15.6	0.00	-39.0
	3	-0.19	1.00	4.64	0.98	8.03	15.6	0.00	-38.2
	4	-0.19	0.99	-4.47	0.97	8.03	15.7	0.00	-38.7
BST+0.01M NaCl	1	-0.13	1.00	4.03	0.99	7.86	18.9	0.00	-29.8
	2	-0.15	1.00	-3.97	0.98	7.86	18.9	0.00	-34.4
	3	-0.13	1.00	4.25	0.98	7.86	18.9	0.00	-29.8
	4	-0.15	1.00	-3.40	0.97	7.86	19.0	0.00	-34.2
BST+1.0M NaCl	1	-0.10	1.00	4.97	0.99	7.86	20.8	0.00	-25.7
	2	-0.13	1.00	-6.24	0.99	7.86	20.9	0.00	-22.8
	3	-0.11	1.00	5.22	0.99	7.86	20.9	0.00	-26.6
	4	-0.13	1.00	-6.04	0.99	7.86	20.9	0.00	-31.9
BST+0.001M $CaCl_2$	1	-0.16	1.00	3.04	1.00	8.04	16.3	0.00	-34.2
	2	-0.17	1.00	-3.13	1.00	8.04	16.3	0.00	-34.9
	3	-0.16	1.00	3.03	1.00	8.04	16.3	0.00	-34.4
	4	-0.16	1.00	-3.00	1.00	8.04	16.4	0.00	-34.6
BST+0.01M $CaCl_2$	1	-0.16	1.00	1.84	0.99	7.86	16.5	0.00	-32.4
	2	-0.18	1.00	-1.80	0.99	7.86	16.5	0.00	-36.4
	3	-0.16	1.00	2.06	0.99	7.86	16.5	0.00	-32.8
	4	-0.17	0.99	-1.64	0.98	7.86	16.5	0.00	-34.4
BST+1.0M $CaCl_2$	1	-0.09	1.00	1.30	0.98	7.86	19.2	0.00	-20.6
	2	-0.08	0.99	-1.09	0.97	7.86	19.2	0.00	-19.6
	3	-0.09	1.00	1.40	0.98	7.86	19.2	0.00	-20.2
	4	-0.09	1.00	-1.22	0.97	7.86	19.2	0.00	-21.0

Table C5.4: Summary of results for zeta potential measurement of BST aged in crude oil at the presence of different concentration for each sodium chloride and calcium chloride.

Sample	Ramp Nr	dU/dp [mV/mbar]	dU/dp R^2	dV/dp [ml/min/mbar]	dV/dp R^2	pH	Conductivity [mS/m]	Gap Height [μm]	ζ [mV]
BST+0.001M NaCl	1	-0.22	1.00	0.80	0.98	8.02	17.6	0.00	-32.2
	2	-0.24	1.00	-1.02	0.99	8.02	17.6	0.00	-32.0
	3	-0.22	1.00	1.01	0.97	8.02	17.6	0.00	-35.2
	4	-0.24	1.00	-1.07	0.99	8.02	17.6	0.00	-31.1
BST+0.01M NaCl	1	-0.24	1.00	0.95	0.98	8.02	18.0	0.00	-24.2
	2	-0.24	1.00	-0.82	0.99	8.02	18.1	0.00	-24.2
	3	-0.24	1.00	1.03	0.98	8.02	18.1	0.00	-24.3
	4	-0.24	1.00	-0.80	0.98	8.02	18.1	0.00	-25.0
BST+1.0M NaCl	1	-0.18	1.00	3.98	0.98	8.02	16.4	0.00	-15.7
	2	-0.16	0.99	-3.26	0.99	8.02	16.5	0.00	-16.7
	3	-0.18	1.00	3.70	0.99	8.02	16.5	0.00	-18.4
	4	-0.16	1.00	-3.47	1.00	8.02	16.5	0.00	-15.7
BST+0.001M $CaCl_2$	1	-0.29	1.00	1.26	0.99	8.02	16.4	0.00	-27.5
	2	-0.30	1.00	-1.18	1.00	8.02	16.4	0.00	-27.3
	3	-0.29	1.00	1.34	0.99	8.02	16.4	0.00	-26.1
	4	-0.28	1.00	-1.08	0.98	8.02	16.4	0.00	-27.6
BST+0.01M $CaCl_2$	1	-0.26	0.99	0.79	0.98	8.02	10.3	0.00	-23.5
	2	-0.26	1.00	-1.18	0.97	8.02	10.3	0.00	-23.3
	3	-0.27	1.00	1.09	0.99	8.02	10.3	0.00	-23.2
	4	-0.27	1.00	-1.06	0.98	8.02	10.3	0.00	-23.2
BST+1.0M $CaCl_2$	1	-0.09	1.00	0.08	1.00	8.04	18.7	0.00	-20.4
	2	-0.09	0.97	-0.12	1.00	8.04	18.7	0.00	-20.8
	3	-0.08	1.00	0.07	1.00	8.04	18.7	0.00	-17.9
	4	-0.08	0.97	-0.11	0.97	8.04	18.7	0.00	-18.6

Tu SBT2 10

Insights of Berea Sandstone Wettability Alteration as A-model of Sandstone Reservoir through Contact Angle Measurement

R. Kareem* (Durham University), P. Cubillas (Durham University), H. J. Riggs (Durham University), J. Gluyas (Durham University), D.R. Gröcke (Durham University) & H.C. Greenwell (Durham University)

SUMMARY

Enhanced oil recovery (EOR) methods target the residual ca. 50 % of crude oil, found coating the pore surfaces of sandstone reservoirs. Low salinity water flooding EOR involves the injection of waters with low salt concentrations into the reservoir. These methods, through a contested mechanism, alter the wettability of the reservoir rock and promote oil displacement. In this work, we have used environmental scanning electron microscopy (ESEM) to measure and assess the change in wettability on oil-treated detrital quartz grains from Berea sandstone and model single-crystal high-quality quartz. Crude oil, as well as a "model-oil" (decanoic acid) where used. Wettability alteration was brought by flushing the pre-treated crystals with low concentration brines (0.01M) of different composition (NaCl, CaCl2, MgCl2, and KCl). Results show that, in the case of quartz surfaces from Berea sandstone, NaCl has the greater effect in changing the wettability state from oil wet to water wet. Results are noticeably aligned with total organic carbon (TOC) data. In contrast, the model-quartz crystals do not show great changes in wettability. The variation in results is probably due to the influence of nano-mineral coatings in the sandstone's quartz crystals, as observed by high-resolution SEM. These results also highlight the importance of using natural mineral surfaces in the EOR study.